Conference Program

January 25-27, 2013

Bangkok, Thailand

2013 BBENS

2013 Bangkok International Conference on Biological Engineering & Natural Science

2013 ICEAI

2013 International Congress on Engineering and Information

Contents

Instructions for Oral /Poster Presentations

Welcome and thank you for your contribution. To ensure each session going smoothly and all attendees enjoy your presentation and opportunities interacting with presenters, please take care of the followings.

Oral Presentation

Equipment Provided by the Conference Organizer:

1. Laptop Computer (MS Windows Operating System with MS PowerPoint & Adobe Acrobat Reader)
2. Built-in LCD Projector with Screen
3. Cable Microphone
4. Whiteboard, Flip Chart

Materials Provided by the Presenters:

5. File(s) in Microsoft PowerPoint or PDF format

Duration of Each Presentation:

6. Regular Oral Session: approximately 15 minutes for each oral presentation, including 3 minutes for Q&A.
7. Please check the conference program online for the precise date and time of your presentation session.
8. Presenters are suggested to enter the specific session room 5 minutes earlier before the session begins.

Poster Presentation

Materials Provided by the Conference Organizer:

9. X Racks & Base Fabric Canvases (60cm×160cm, see the figure below)
10. Adhesive Tapes or Clamps

Materials Prepared by the Presenters:

11. Home-made Poster(s)

Requirement for the Posters:

12. Material: Abstract/Full paper printed on a poster/A4 paper(s) which can be posted on the Canvases
13. Size: smaller than 60cm×160cm
14. Content: The research findings in the poster presenter's abstract/ full paper

Conference Schedule

Friday, January 25, 2013
Committee Meeting (Committee Only)

Saturday, January 26, 2013

Time	Information
08:15-16:30	Registration (2F)
08:45-10:15	Oral Session Beta I, Biomedical Engineering
10:15-10:30	**Tea Break / Poster Session- Engineering A**
10:30-12:00	Oral Session Beta I, Environmental Science
12:00-13:00	**Lunch Time**
13:00-14:30	Oral Session Beta I, Natural Sciences I
14:30-14:45	**Tea Break / Poster Session- Biomedical Engineering & Civil Engineering**
14:45-16:15	Oral Session Beta I, Natural Sciences II

Sunday, January 27, 2013

Time	Information
08:15-16:30	Registration (2F)
08:45-10:15	Oral Session Beta I, Engineering I
10:15-10:30	**Tea Break / Poster Session- Engineering B**
10:30-12:00	Oral Session Beta I, Engineering II Oral Session Gamma, Engineering III
12:00-13:00	**Lunch Time**
13:00-14:30	Oral Session Beta I, Information
14:30-14:45	**Tea Break / Poster Session - Chemical Engineering & Natural Sciences**

Monday, January 28, 2013
Bangkok City Tour

Conference Organization

Conference Committee

C H OH, National University of Singapore

Lim Koon Ong Pk, Universiti Sains Malaysia

Parin Chaivisuthangkura , Srinkharinwirot University

Zulkifli Hj. Shamsuddin, Universiti Putra Malaysia

Avinash C. Sharma, GGS Indraprastha University

E. Shaji, University of Kerala

A. M. Chandra, University of Calcutta

Chien-Cheng Chang, National Taiwan University

Programme Committee

Aidy b. Ali, University of Putra Malaysia

K.Ananthanarayanan, Indian Institute of Technology

Ram Prakash Bharti, Indian Institute of Technology Roorkee

Henskens, Frans, University of Newcastle

P K Garg, Indian Institute of Technology Roorkee

M L Kansal, Indian Institute of Technology Roorkee

Kaushik Kumar, Birla Institute of Technology Mesra

Dattaram. B, Indian Institute of Technology

Xiaomei Li, Southeast University

S.P. Mehrotra, Indian Institute of Technology Kanpur

D. P. Mishra, Indian Institute of Technology

Bhaskarwar A.N., Indian Institute of Technology Delhi

Ojha, C.S.P., IIT of Roorkee

Dhaval Patel, National University of Singapore

International Committee

Stephen Redmond, the University of New South Wales

J. Gao, The University of Hong Kong

P.K.Barhai, Birla Institute of Technology

Singh, Gauri Shankar, Indian Institute of Technology Roorkee

Mohd. Nasir Mohd. Desa, Universiti Putra Malaysia

Aliakbar Roodbari, Shahroud University of Medical Sciences

Olivia J Fernando, Annamalai University

K. Padmakumar, Kerala University Campus

John Hearne, Royal Melbourne Institute of Technology

Hamed M. El-Shora, Mansoura University

Huabei Jiang, the University of Florida

Special Thanks

Session Chairs

Sierin Lim, Nanyang Technological University

B C Meikap, University of KwaZulu-Natal

Norman Y. S. Woo, The Chinese University of Hong Kong

Eakphan Thangthong, Chulalongkorn University

Felix T. S. Chan, the Hong Kong Polytechnic University

Jyri Rajamäki, Laurea University of Applied Sciences

Program - Oral Sessions

Biomedical Engineering

Pullman Bangkok King Power, 2F Meeting Room BETA I

2013/1/26 Saturday 08:45-10:00

Session Chair: Sierin Lim

BENS71

Automatic Detection of the Signature of Expertise in the Ocular Scanpath through Machine Learning

Claudio Desperati | *Università Vita-Salute San Raffaele*
Giuseppe Boccignone | *University of Milan*
Mario Ferraro | *University of Turin*
Sofia Crespi | *Università Vita-Salute San Raffaele*
Carlo Robino | *Università Vita-Salute San Raffaele*

BENS143

Protein-protein Interaction in a Nanocapsule

Sierin Lim | *Nanyang Technological University*
Kang Yu | *Nanyang Technological University*
Ning Mao | *Nanyang Technological University*

BENS199

Fabrication and Characterization of Phosphate Glass/Hydroxyapatite Scaffold for Palate Repair

Pornpatima Yenbut | *Chiang Mai University*
Wassanai Wattanutchariya | *Chiang Mai University*

BENS200

Fabrication and Characterization of Composite Porous Scaffold by Chitosan-Gelatin/Hydroxyapatite for Bone Filler Application

Whattanapong Changkowchai | *Chiang Mai University*
Wassanai Wattanutchariya | *Chiang Mai University*

BENS71

Automatic detection of the signature of expertise in the ocular scanpath through machine learning

Giuseppe Boccignone[a], Mario Ferraro[b], Carlo Robino[c], Sofia Crespi[d], Claudio de'Sperati[d,*]

[a]**Dipartimento di Informatica – Università degli Studi di Milano**, via Comelico 39, 20135 Milano, Italy
E-mail address: Giuseppe.Boccignone@unimi.it

[b]**Dipartimento di Fisica – Università degli Studi di Torino**, via Giuria 1, 10100 Torino, Italy
E-mail address: ferraro@ph.unito.it

[c]**Laboratory of Action, Perception, Cognition – Università Vita-Salute San Raffaele,** 2Easy s.r.l., Via Mascagni 14, 20122 Milano, Italy
E-mail address: carlo.robino@2easyweb.it

[d]**Laboratory of Action, Perception, Cognition – Università Vita-Salute San Raffaele**, via Olgettina 58, 20132 Milano, Italy
E-mail address: crespi.sofiaallegra@gmail.com

[d]**Laboratory of Action, Perception, Cognition – Università Vita-Salute San Raffaele**, via Olgettina 58, 20132 Milano, Italy
E-mail address: desperati.claudio@unisr.it

ABSTRACT

The automatic recognition of individual traits and competences through behavioral analyses is an intensely pursued goal. Here we applied machine learning to classify expertise from the oculomotor behavior (scanpath) of 21 novice and 21 expert billiard players while they were freely watching a filmed billiard match with no specific task, and ad-hoc, occluded billiard shots with a trajectory prediction task. By using saccade amplitude and direction as features, a Relevance Vector Machine classified correctly which group – novice or expert – the observers belonged to, with an accuracy of 83% and 77% respectively for the match and the shots. Interestingly, for simple shots (2 cushions) the classification accuracy decreased to 69%, while for difficult shots (5 cushions), where expertise could indeed make the difference, it reached 86%. These results provide direct proof that the signature of expertise is hidden in the ocular scanpath, at least in the particular domain of billiard sports, and that it can be accurately detected at the individual level with proper test stimuli – even very natural ones – and suitable data mining.

Keyword: Psychophysiology, Eye movements, Expertise, Billiards, Relevance Vector Machine

1. INTRODUCTION

The automatic detection of expertise from indirect psychophysiological indexes is

a goal that is as valuable as challenging. Eye movements seem to be very promising in this respect, as they may contain enough information to tell apart experts from non-experts (the "expert's eye"). Indeed, the gaze shifts of novices and experts differ in several domains of knowledge and competence [1,2,3,4,5,6,7,8,9,10]. We have recently provided evidence that exploratory eye movements can distinguish between novice and expert billiard players when they are watching billiards under controlled conditions [11]. Whereas novices tended to adopt a strategy based on mental trajectory extrapolation, experts monitored with the gaze certain diagnostic points along the ball trajectory. The question arises as to whether the differences between experts and novices could be detected in the individual patterns of eye movements, or whether they are visible only in the group data, as in previous work. The present study addressed this question by applying machine learning techniques to eye movement data, with the goal of classifying any single observer as being a billiard expert or novice. The Support Vector Machine (SVM) is a widely used technique to classify noisy signals (see [12], including, quite recently, eye movement data [13]. To overcome the known limitations of SVM [14], here we have exploited a Relevance Vector Machine (RVM, [14], which has recently attracted much interest in the research community but has never been used with eye movement data.

2. MATERIALS AND METHODS

The analyses presented in this study have been applied to the raw data taken from [15]; the reader is referred to that study for further details.

2.1 Participants

Forty-two healthy participants volunteered in the experiment. Half of them were elite billiard players, recruited on the basis of their national rank.

2.2 Stimuli and recording procedures

The stimuli were movies of a real billiard match or individual simplified shots, which were watched on a computer screen. The stimuli were prepared in advance by videorecording them from the top of the billiard table. Basically, observers were presented 48 controlled shot ultimately directed towards the central skittle, with no spin. The most important difference among them was that they could be short (2 cushions) or long (5 cushions). The shots could be directed towards the right or the left, or the towards the upper or the lower side of the table, in a balanced design. There were 2 repetitions for each shot. The final part of the trajectory was occluded, and the observers' task was to tell whether or not the ball would strike the skittle (there were actually 3 versions for each shot, in one version the central skittle is pulled down, in the other two versions the ball passes just by the skittle on the right or the left).

The other typology of visual stimulus consisted of a piece of a real billiard match, again videorecorded from the top. In the match, two professional players (the opponents) alternated in making a shot in which a cue ball (own's ball) should be directed towards the target ball (the opponent's ball) in such a way that the latter – but not the former – would pull down as many skittles as possible (there were 5 skittles in the central region of the table) and/or the third ball (the small red ball). On the computer screen, the size of the billiard table was 13 x 27 cm. The movie lasted 5 minutes and contained 11 shots, alternating at a natural pace between the two

opponents. The shots were obviously different for complexity, orientation, number of cushions, ball velocity, spin. The duration of each shot, defined as the time during which at least one ball was in motion, varied between 8 and 13 seconds.

The billiard match was always presented first, followed by a pseudo-random sequence of the individual shots. The duration of the experiment was about 20 minutes. When the stimulus was the match, observers had been instructed to pay attention to the events in order to answer to some general question afterwards. With the individual shots, the task was instead to predict whether or not the ball would strike the skittle, through a keypress. In this prediction task, experts performed better than novices with both the long and the short shots, and in terms of both accuracy and response times [15].

Observers watched the stimuli seating about 57 cm in front of the computer screen, with the head resting on a forehead support. Eye movements were acquired through infrared video-oculography (Eyegaze System, LC Technologies; sampling frequency: 60 Hz; nominal accuracy: 0.45 deg). Monocular recordings were performed unobtrusively via a remote camera mounted below the computer screen. Fixations were identified by means of a simple dispersion criterion: We defined gaze samples as belonging to a fixation if they were located within an area of 25 pixels (corresponding to 0.67 deg) for a minimum duration of 6 video frames (corresponding to 100 ms).

2.3 Data analysis

The problem of distinguishing billiard experts from novice observers, by assessing their oculomotor behavior, can be formulated as a classification procedure in a supervised learning setting. More precisely, if X denotes the space of input variables representing features derived from observer eye movements and the space of output variables i.e. the expert/novice label, the training dataset produced along eye-tracking recording can be defined as the set $Z = \{(\mathbf{x}_n, \ell_n) \in X \times \mathbf{I} \mid \mathrm{n} = 1, \ldots, \mathbf{N}\}$. The learning step implies the use of Z together with any other prior knowledge for finding a function $f: X \longrightarrow \mathbf{I}$ out of a class $\mathcal{F}$ of functions that encodes the estimated dependency. The result function f is assumed to produce an efficient prediction of the expert/novice assignment given a new feature vector $\mathbf{x}$. A flexible and popular set of candidates for $f(\mathbf{x})$ is that of the form $f(x; w) = \sum_{i=1}^{M} w_i \, \phi_i(x) = w^{\dagger} \phi(x)$ where the output is a linearly-weighted sum of M, generally nonlinear and fixed, basis functions. Analysis of functions of such type is facilitated since the adjustable parameters (or 'weights') w appear linearly in the equation, and the objective is to estimate 'good' values for those parameters (learning stage). Note that, although the model is linear in the parameters, it may still be highly flexible as the size of the basis set, M, may be very large.

Together with good generalization performance, which can be achieved by many methods proposed in the statistical machine learning literature [12] a key feature of any classification approach is to find a sparse representation of predictors, in which they contain relatively few non-zero w_i parameters. Sparsity is an attractive concept; it offers elegant complexity control, feature extraction, the potential for elucidation of meaningful input variables along with the practical benefits of computational speed and compactness. In this perspective, the SVM is a sparse linearly-parameterized

model for regression and classification that has attracted considerable interest [12], which considers a restriction of the $f(x;w)$ model, namely:

$$f(x;w) = \sum_{i=1}^{N} w_i K(x, x_i) + w_0 \quad , \qquad (1)$$

where $K(x, x_i)$ is a kernel function, defining one basis for each example $\mathbf{x}_n$ in the training set. Sparsity is achieved by considering the subset of kernel functions, those associated with training samples x_n that lie on the margin separating classes (the support vectors). A number of significant and practical disadvantages of the support vector learning methodology have been identified [14]. To overcome such limitations the RVM has been proposed. RVMs are based on a Bayesian treatment of the linear model (1), with an appropriate prior that results in a sparse representation.

Following the standard probabilistic formulation, the targets ℓ_n can be considered as samples from the model with additive noise $\ell_n = f(\mathbf{x}_n; \mathbf{w}) + \varepsilon_n$, where in turn ε_n are independent samples from a noise process generated by amean-zero Gaussian with variance σ^2; hence, $p(\ell_n |\mathbf{x}) = \mathcal{N}(\ell_n |f(\mathbf{x}_n), \sigma^2)$, where the notation specifies a Gaussian distribution over the target labels with mean $f(x_n)$. Unlike the SVM, the RVM explicitly encodes the criterion of model sparsity as a prior over the model weights w. The Bayesian formulation of the regression problem in the RVM allows for a prior structure that explicitly encodes the desirability of sparse representations. This is done by complementing the standard likelihood function with an "automatic relevance determination" (ARD) prior over the weights, $p(w | \alpha) = \prod_{n=1}^{N} \mathcal{N}(w_n |0, \alpha_n^{-1})$, with α a vector of $N+1$ hyperparameters that has the effect of "switching off" basis functions for which there is no evidence in the data (see [14] for details).

For a two-class problem such as the one we are dealing with, , sparse Bayesian classification can be obtained generalizing the linear model by applying the logistic sigmoid link function $\sigma(f)$

to function *f* and by adopting the Bernoulli distribution for the data likelihood, . In the learning stage, the parameters α, w of the model are computed through an iteration procedure (the EM algorithm) until convergence is achieved.

The feature set *X* has been defined in order to capture the oculomotor behavior of the observers. To this end, for each observer, given the sequence of fixation and saccades $\{r_t, s_t\}_{t=1}^{T}$, we represent his scanpath in terms of saccade amplitudes and directions $\{l_t, \theta_t\}_{t=1}^{T}$, where l_t is determined as the Euclidean distance between the positions at the beginning of the saccade and at the landing position, and

, being the saccade horizontal and vertical displacements. The magnitude of saccades and their direction are suitable descriptors for characterizing oculomotor behavior tendencies [16] and have been successfully employed for stochastic modeling eye movements on videos [17].

Since we assume that the scanpath is the result of an underlying stochastic process [17], we summarize the random sample $\{l_t, \theta_t\}_{t=1}^{T}$ through their empirical distribution function (histogram), which we denote as the random vectors

and , respectively, where the vector dimension *J* represents the number of bins of the histogram.

When considering short and long shots both histograms where computed by aggregating the 2 repetitions for each shot. For all types of shot (short, long and match) *J =6*.

Finally, the feature vector $\boldsymbol{x}$ capturing the oculomotor behavior of a single observer is obtained by concatenating the two vectors, $\boldsymbol{x} = [\boldsymbol{h}_l \quad \boldsymbol{h}_\theta]^\dagger$, thus giving rise to a $2 \times J$ dimensional feature vector. For *N=42* observers we have a set $\{\boldsymbol{x}_n\}_{n=1}^{42}$ of such random vectors, where $\boldsymbol{x}_n$ stands for the feature vector related to the *n*-th observer. By associating the corresponding label we eventually obtain the complete data set $Z = \{(\boldsymbol{x}_n, \ell_n) \in X \times \mathbf{I} \mid \mathrm{n} = 1, \ldots, \mathbf{N}\}$.

Learning and classification on *Z* were accomplished by adopting the classic Leave-one-out procedure [18]. To keep data analysis conditions straight, the kernel function *K* was shaped in the form of a linear kernel [12,14,18].

3. RESULTS

Expert and novice observers exhibited *prima facie* rather similar fixation patterns (**Figure 1**), although some differences were occasionally apparent, at least as a qualitative impression when looking at the cumulative scanpath over time, condensed in single snapshots. We know from our previous study [15]that the distribution of basic oculomotor parameters such as fixation duration and gaze shifts amplitude did not differ significantly between experts and novices with individual billiard shots as stimuli. Nonetheless, some subtle but consistent differences in the spatio-temporal allocation of gaze have been observed, to the extent that the different "looking style" of experts and novices allowed to parse the video stream of the billiard match into individual shots [11].

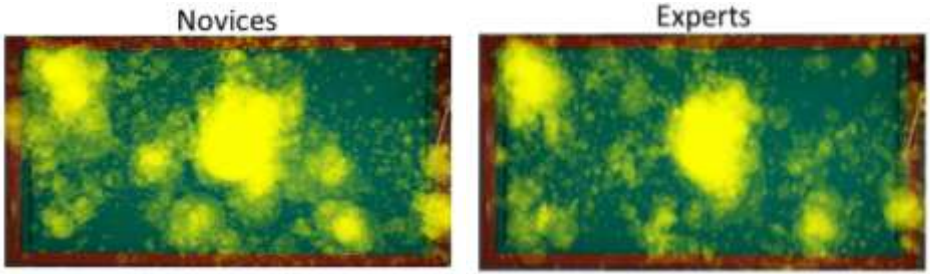

Figure 1. Fixation maps across the 5 minutes of billiard match viewing. Each yellow spot represents an individual fixation, whose diameter is proportional to the fixation duration. All fixations from all subjects are superimposed.

We present here the results of the analysis with a machine learning approach. As input features, we used the concatenation of saccade amplitude and direction. With a linear kernel (length=6), the capability of the classifier to distinguish between experts and novices was remarkably high. The Relevance Vector Machine classified correctly which group – novice or expert – the observers belonged to with an accuracy of 83% and 77%, respectively for the match and the shots. Interestingly, for the short shots the classification accuracy decreased to 69%, while for the long shots, where expertise could indeed make the difference, it reached 86%.

Table 1. Performance of the binary classifier, for the three typologies of shots (M, Match; SS, Short Shots; LS, Long Shots).Pc, percent correct; d', d prime; C, response criterion; A' estimate of the area under the ROC curve.

	M	**SS**	**LS**
Pc	83%	69%	86%
d'	1.944	1.015	2.133
C	0.094	0.204	0.000
A'	0.900	0.778	0.916

In Table 1 is reported the performance of the classifier for the three stimulus categories expressed in terms of percent correct, together with additional quantities derived within the framework of signal detection theory [19]. We computed the well-known distance index d', as well the index A', which is an estimate of the area under the ROC curve and which is equivalent to the proportion of correct responses. We did not provide the so-called Equal Error Rate (the point on the ROC curve where misses and false alarms coincide), because, given the symmetry of the estimated ROC, the same information is conveyed by 1-A'. Further, although in principle the classifier is expected to be bias-free, we also computed the response criterion C, which revealed a slight tendency to misclassify more often the expert observers, taking them for novices (misses, or false negatives), rather than mistaking a novice for an expert (false alarms, or false positives). The raw accuracy data and the signal detection indexes were in perfect agreement, and showed a very high discriminability of experts and novices despite apparently similar fixation patterns (Figure 1). In terms of differential classification, 21 observers (50%, 12 novices and 9 experts) were classified correctly in all three stimulus categories (Shot shots, Long shots, and Match), while 16 observers (38%) were classified correctly in two stimulus categories, and 5 observers (12%) in one stimulus category. None was always misclassified. Overall, 90% of novices and 86% of experts were classified correctly in at least two stimulus

categories.

4. DISCUSSION

In this study we have successfully applied a machine learning approach (RVM) to eye movements data in order to classify individual observers as billiard experts or novices. To explore various testing conditions, we have administered to 42 subjects, either novice or top billiard players, different visual stimuli and tasks, all representing filmed, real billiard events: A portion of a match, containing shots of variable complexities, and several *ad-hoc* individual shots, with either 2 cushions or 5 cushions. The match stimulus was associated to a free-viewing observation condition, while for the individual shots, which were occluded in the second part of the trajectory, the trajectory prediction task placed implicitly a significant constraint on the deployment of visuospatial attention. That is, we had 2 constrained stimulus conditions (the shots) and one relatively unconstrained stimulus condition (the match). The overall classification accuracy, expressed as percent correct and averaged across stimulus types and observer expertise, scored a respectable 79%.

Remarkably, the classification accuracy was higher with the long shots (86%) and lower with the short shots (69%), with a somewhat intermediate level when the stimulus was the match (83%). This finding is in keeping with the idea that the individual scanpath provides indication of the degree of expertise that is actually exerted. In fact, the long shots had a more complex geometry than the short shots, and in fact the behavior of experts and novices differed more than for the short shots, both in predicting the trajectory and in terms of fixation maps [15]. In other words, it is especially with the long shots that expertise makes the difference. The billiard match, in turn, contained professional shots of variable length and difficulty, as well as pauses between shots; moreover, the shots in the match were much less predictable and with more variables (e.g., many more options as to the geometry and the goal) than the controlled individual shots. Thus, at least at the qualitative level, the classifier performance correlated with the actual expertise level required to understand the stimulus. This underscores the importance of selecting a proper stimulus in order to extract expertise from the scanpath through a classifier. Although it did not represent the highest performance, it is striking that the classifier yielded a so high accuracy with the match as stimulus (83%). Considering the uncontrolled variability of a real match, we think this is a remarkable result.

Despite much work should still be done to optimize the present approach, perhaps by testing additional features or feature combinations, or by using other classifiers, we think these preliminary data provide clear evidence of the success of applying the RVM to eye movement data in detecting expertise. At variance with previous studies [1,2,3,4,5,6,7,8,9,10,20], including our own one [15], here we have been able to classify experts and novices individually, which is a necessary step in order to pursue the goal of automatic expertise detection based on psychophysiological indexes.

5. ACKNOWLEDGMENTS

This work received partial financial support from the Italian Ministry of Instruction, University and Research (grant PRIN 2008RBFNLH_002 to C.d.S.) and Stanib program.

6. REFERENCES

1. Pihko E, Virtanen A, Saarinen VM, Pannasch S, Hirvenkari L, et al. (2011) Experiencing art: the influence of expertise and painting abstraction level. Front Hum Neurosci 5: 94.
2. Nodine CF, Locher PJ, Krupinsky EA (1993) The Role of Formal Art Training on Perception and Aesthetic Judgment of Art Compositions. Leonardo 26: 219-227
3. Zangemeister WH, Sherman K, Stark L (1995) Evidence for a global scanpath strategy in viewing abstract compared with realistic images. Neuropsychologia 33: 1009-1025.
4. Vogt S, Magnussen S (2007) Expertise in pictorial perception: eye-movement patterns and visual memory in artists and laymen. Perception 36: 91-100.
5. Humphrey K, Underwood G (2009) Domain knowledge moderates the influence of visual saliency in scene recognition. Br J Psychol 100: 377-398.
6. Nodine CF, Kundel HL, Lauver SC, Toto LC (1996) Nature of expertise in searching mammograms for breast masses. Acad Radiol 3: 1000-1006.
7. Donovan T, Manning DJ (2007) The radiology task: Bayesian theory and perception. Br J Radiol 80: 389-391.
8. Underwood G (1998) Eye guidance in reading and scene perception. Amsterdam ; New York: Elsevier. xi, 466 p. p.
9. Chase WG, Simon H (1973) Perception in chess. Cognitive Psychology 4: 55-81.
10. Reingold EM, Charness N, Pomplun M, Stampe DM (2001) Visual span in expert chess players: evidence from eye movements. Psychol Sci 12: 48-55.
11. Robino C, Crespi S, Silva O, de'Sperati C (2012) Parsing visual stimuli into temporal units through eye movements. Proceedings of the Symposium on Eye Tracking Research and Applications. Santa Barbara, California: ACM. pp. 181-184.
12. Vapnik V (1998) Statistical Learning Theory: John Wiley.
13. Lagun D, Manzanares C, Zola SM, Buffalo EA, Agichtein E (2011) Detecting cognitive impairment by eye movement analysis using automatic classification algorithms. J Neurosci Methods 201: 196-203.
14. Tipping ME (2001) Sparse Bayesian Learning and the Relevance Vector Machine Journal of Machine Learning Research 1: 211-244.
15. Crespi S, Robino C, Silva O, de'Sperati C (2012) Spotting expertise in the eyes: billiards knowledge as revealed by gaze shifts in a dynamic visual prediction task. Journal of Vision 12, p. 1-19.
16. Tatler BW, Vincent BT (2008) Systematic tendencies in scene viewing. Journal of Eye Movement Research 2: 1-18.
17. Boccignone G, Ferraro M (2012) Gaze shift behavior on video as composite information foraging. Signal Processing-Image Communication.
18. Hastie T, Tibshirani R, Friedman J (2001) The Elements of Statistical Learning. Data Mining, Inference and Prediction: Springer.
19. Macmillan NA, Creelman CD (2005) Detection Theory: A User's Guide (2nd ed.): Lawrence Erlbaum Associates.
20. Gregori-Grgic R, Balderi M, de'Sperati C (2011) Delayed perceptual awareness in rapid perceptual decisions. PLoS One 6(2): 1-10.

BENS143

Modification of Protein-protein Interaction in a Nanocapsule

Kang Yu, Ning Mao, and Sierin Lim*
Bioengineering Division, School of Chemical and Biomedical Engineering
NanyaSng Technological University, 70 Nanyang Dr., Singapore 637457
E-mail address: SLim@ntu.edu.sg

ABSTRACT
The vault nanocapsules are promising carriers in protein-based drug delivery. However, limited studies have been reported on effectively controlling the drug release during delivery. It is hypothesized that the rate of content release is related to the interaction between the major vault protein (MVP) and the interaction domain (INT) of vault poly(ADP-ribose)-polymerase. The MVP domains that specifically interact with INT have been identified and is referred to as iMVP. In this report, a few key amino acids of iMVP on the interaction interface were replaced with histidines to impart pH-sensitive response. In contrast to the wild type soluble iMVP, the mutants are produced as insoluble proteins.
Keywords: vault, nanocapsule, protein-protein interaction, histidine modification

1. INTRODUCTION

Protein nanocapsules, such as Ferritin and E2 protein, have been shown to be promising as carriers for contrast agents and small molecule drugs [1-3]. The nature derived template provides precise spatial control resulting in highly uniform structures while the proteinaceous nature allows for facile modification. Vault, a ribonucleoprotein nanoparticle, is ubiquitous in most living eukaryotic system, with dimensions of 72.5 × 41.0nm[4].It has been shown to be non-toxic, non-immunogenic, and stable in wide pH and temperature ranges[5]. The large lumen of vault is made of the major vault proteins (MVP) that self-assemble to form a barrel-like nanocapsule. A shuttle peptide named the interaction domain (INT) located at the C-terminus of the vault poly(ADP-ribose)-polymerase (GenBank accession No. AF158255; aa 1563-1724), is known to attach to the inner side ofthe vault shell through a unique protein-protein interaction. Fusion of therapeutic agents to the INT N-terminus facilitates the encapsulation of the therapeutic agents within the vault[5].Introduction of some functional peptides on the vaults have successfully transport vaults to target cells [6].

Vault has a dynamic structure that involves half-vault exchanges[7]. During the open state, content might be freed from or held within the lumen depending on the association/dissociation between MVP and INT. However, controlling the releaseof therapeutic agents from the vaults interior remains a challenge. Since the tumor microenvironment is mildly acidic (pH 6-7) due to the hypoxic environment and residues from anaerobic metabolism, the ability to control the molecular release at specific pH is favorable. Histidinehas been demonstrated to induce repulsive interactions between protein subunits upon pH change from 7.4 to 5.0 [8, 9].The histidineimidazole side-chain has a pKa value of 6.1. At pH 7.4, ~10% of the side chains are positively charged while at lower pH the proportion increases.Upon pH

change, multiple histidines that are strategically located within the Debye radius at the interface will induce enough repulsive forces to trigger disassembly or separation between protein subunits.

In this study, we isolated the MVP domains that specifically interact with INT which is referred to as iMVP. Histidines were subsequently introduced to replace key amino acids on the iMVP located at the interaction interface. The production of the recombinant iMVP and hisditine-substituted iMVP were examined.

2. MATERIALS & METHODS

Histidine-substituted Protein Designs–The interacting amino acids were identified by visualizing the structures using PyMOL. The structure of the INT was predicted using I-TASSER server (http://zhanglab.ccmb.med.umich.edu/I-TASSER/) and the interaction with MVP was simulated using online protein docking software (http://vakser.bioinformatics.ku.edu/resources/gramm/grammx). The crystal structure of MVP (PDB No. 2QZV) shows that the interaction surface of iMVP (aa113-276) is mostly negatively charged. To modify the interactions between iMVP and INT, several amino acids were replaced to pH-responsive histidines on iMVP (Table 1). The LDL and VDA on iMVP were selected based on their proper distances to INT residues. The amino acids EE were modified to Ala-Ala as control.

Site-Directed Mutagenesis– Primers with the desired mutation sites were designed (Table 1) and the genes were amplified using PCR. The sequence was confirmed by sequencing and the mutant fragments of iMVP were subclonedintopET-28afor tagging with 6xHisat the N terminus to ease purification. All histidine-tagged proteins from the are denoted by His-, i.e. His-iMVP and His-INT.

Table 1. The mutant constructed at the iMVP interface to investigate the effect of histidine substitution.

Constructions	Oligonucleotides
LDL/3H (L213H/D214H/L215H)	5’-GTC TTT GAA GAG GTC cat catcat GTG GAT GCT GTG ATC-3’ (forward) 5’-GAT CAC AGC ATG CAC atgatgatg GAG CTC TTC AAA GAC-3’ (reverse)
VDA/3H (V216H/D217H/A218H)	5’-GAG GTC CTG GAT CTG cat catcat GTG ATC CTT ACA GAA-3’ (forward) 5’-TTC TGT AAG GAT CAC atgatgatg CAG ATC CAG GAC CTC-3’ (reverse)
EE/AA (E210A/E211A)	5’-CTC CCA GCT GTC TTT gcggcg GTG CTG GAT CTG GTG-3’ (forward) 5’-CAC CAG ATC CAG CAC cgccgcAAA GAC AGC TGG GAG-3’ (reverse)

Protein production and purification–His-INT andHis-iMVPvariants were produced in *E. coli*BL21(DE3) grown in LB broth with 50 mg/L Kanamycin according to the recommended protocol (Stratagene). The production was induced by IPTG at optimum concentration for specific construct. The proteins were purified with affinity chromatography (HisTrap HP column, GE Healthcare).

3. RESULTS AND DISCUSSION

Replacement of native amino acids on the iMVP that are located at the interaction interface with INT is hypothesized to impart pH response providing additional cargo release control to the vault. To identify the amino acid residues on the iMVP that interact closely to the INT, a docking simulation was performed using the online software. The results of the docking simulation were used to evaluate the amino acid residues on the iMVP that are within the Debye radius to the INT residues. Solvent accessibility of the interface is important in the protonation of the histidine residues and was examined as shown by the molecular surface (Fig.1).

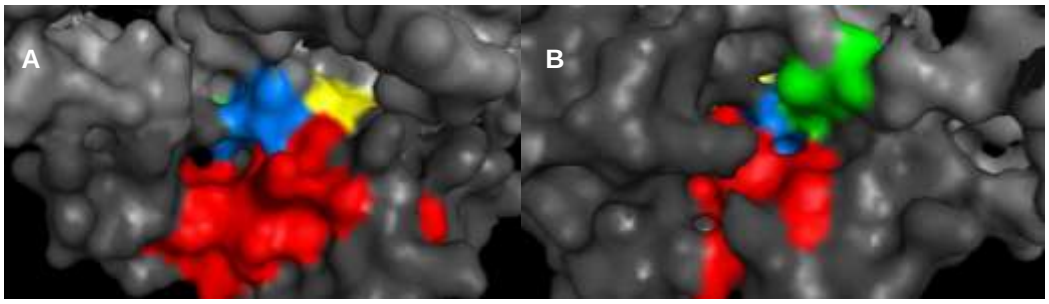

Figure 1. Front (A) and back (B) view of surface structure showing selected iMVP residues for mutation: E210/E211(yellow); L213/D214/L215 (blue);V216/D217/A218 (green); INT residues (red). Figures were generated using in PyMOL [10].

Figure 2 highlights the identified residues on iMVP that are proposed to be interacting with INT within the Debye radius and are solvent accessible.

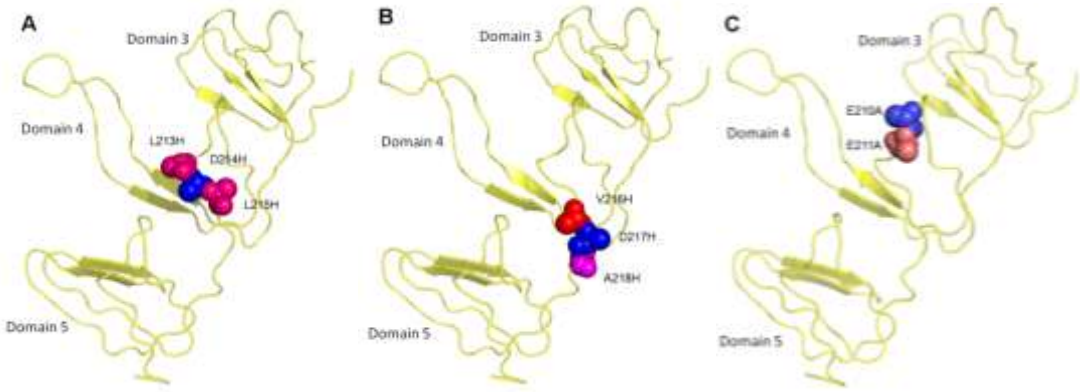

Figure 2. Mutation sites on iMVP domains3, 4 and 5. (A) LDL/3H (L213H/D214H/L215H), (B)VDA/3H(V216H/D217H/A218H),(C) EE/AA(E210A/E211A).

The recombinant protein productions in this study were optimized. His-INT was produced by adding 1 mM IPTG for 3 hours at 37ºC. The gene expression of His-iMVP and its mutants were induced by addition of 0.1 mM IPTG for 16 hours at 20ºC. Upon harvest, the cells were lysed and the protein production was analyzed using SDS polyacrylamide gel electrophoresis (Fig. 3). Both His-iMVP mutants, LDL/3H and VDA/3H, were produced as insoluble proteins (Fig. 3, lanes 4 and 6) while His-iMVP EE/AA were not produced in either soluble or insoluble fractions (Fig. 3, lanes 1 and 2). The unmodified His-iMVP and His-INT were expressed as soluble proteins and were subsequently purified (Fig. 3, lanes 7 and 8). The summary

of protein production is presented in Table 2.

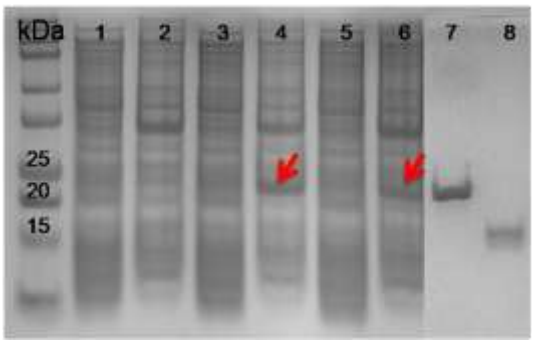

Figure 3. SDS-PAGE gel of proteins production. Lane 1: His-iMVP EE/AA soluble fraction; 2: His-iMVP EE/AA insoluble fraction; 3: His-iMVPLDL/3H soluble fraction; 4:His-iMVPLDL/3Hinsoluble fraction; 5:His-iMVPVDA/3H soluble fraction; 6:His-iMVPVDA/3Hinsoluble fraction; 7: purified His-iMVP, 8: purified His-INT. Red arrows indicate the expected proteins.

Table 2.Summaryof protein productions.

Protein variants	Mutated interface	Expressed in *E. coli*	Soluble for purification
His-iMVP	No	Yes	Yes
His-iMVPLDL/3H	Yes	Yes	No
His-iMVPVDA/3H	Yes	Yes	No
His-iMVP EE/AA	Yes	-	-
His-INT	No	Yes	Yes

The insoluble production of the histidine-substituted His-iMVP mutants is speculated to be due to the change in electrostatic interactions within the protein. To analyze the interactions, the surface potentials of His-iMVP mutants were computed and displayed using PyMOL (Fig. 4). The side-chain charges of the key area of interaction site on iMVP were compared between wild type and mutant on Table 3. As shown in Figure 4 and Table 3, the vicinity of the mutant residues LDL and VDA is negatively charged at pH 5-7.4. Upon introduction of the positively charged histidines, the electrostatic interaction might be disrupted leading to protein misfolding. As a result, His-iMVP LDL/3H and VDA/3H are much less soluble than wild type His-iMVP. Since the gene expression involves many factors, such as control at transcription and translation levels, the non-production of His-iMVP EE/AA is relatively complex to explain. In addition, the alanine replacements might cause interference on the EE interactions which were identified to have both negative and positive charged neighbors in vacuum electrostatics analysis (Fig. 4C).

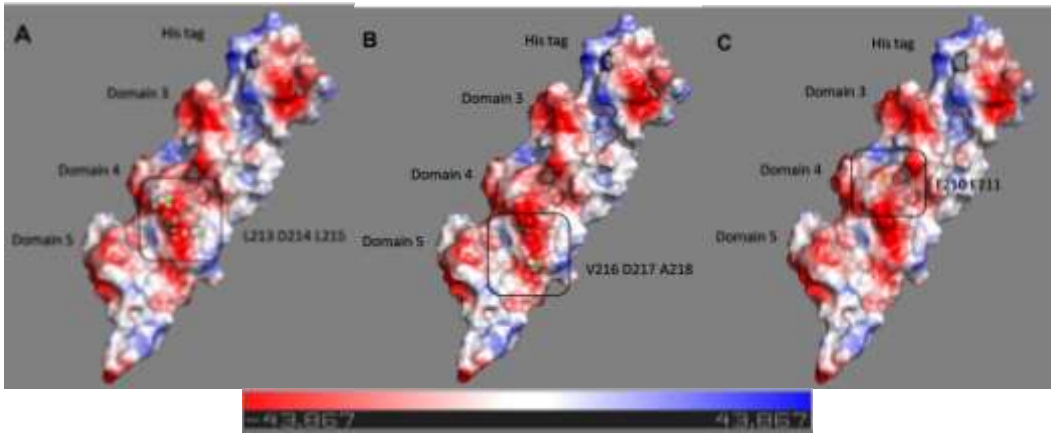

Figure 4.Vacuum electrostatics of His-iMVP drawn by PyMOL. (A) LDL/3H (L213H/D214H/L215H), (B)VDA/3H(V216H/D217H/A218H).

Table 3.Side-chain charges of the key interaction sites on iMVP.

Residue #	iMVP	LDL/3H	VDA/3H	EE/AA
209	F	F	F	F
210	E (-)	E (-)	E (-)	**A**
211	E (-)	E (-)	E (-)	**A**
212	V	V	V	V
213	L	**H (+)**	L	L
214	D (-)	**H (+)**	D (-)	D (-)
215	L	**H (+)**	L	L
216	V	V	**H (+)**	V
217	D (-)	D (-)	**H (+)**	D (-)
218	A	A	**H (+)**	A

For all designed iMVP mutants, attempts to lower the expression temperature to 20°C and alter inducer concentrations to 0.1 mM did not produce soluble proteins. Subsequent investigations required soluble proteins and could not be performed with these variants.

4. CONCLUSIONS

His-iMVP and His-INT were successfully produced as soluble proteins in *E. coli*. However, attempts to replace amino acids on the iMVP interacting interface with histidines resulted in insoluble proteins. To further investigate the interactions between iMVP and INT, it is important to produce soluble proteins. Modifications on the INT may be possible alternatives to the iMVP modifications.

5. ACKNOWLEDGMENTS

The wild-type plasmids for MVP and INT were generous gifts from Prof. Leonard Rome at University of California, Los Angeles. The work was partially supported by the Singapore Ministry of Education Academic Research Funds Tier 1 (RG33/07).

6. REFERENCES

[1] Ren, D., F. Kratz, and S.W. Wang. Protein nanocapsules containing doxorubicin as a pH-responsive delivery system. *Small*, 2011. 7(8): p. 1051-1060.
[2] Sana, B., C.L. Poh, and S. Lim. A manganese-ferritin nanocomposite as an ultrasensitive T 2 contrast agent. *Chemical Communications*, 2012. 48(6): p. 862-864.
[3] Sana, B., E. Johnson, K. Sheah, C.L. Poh, and S. Lim. Iron-based ferritin nanocore as a contrast agent. *Biointerphases*, 2010. 5(3): p. 48-52.
[4] Goldsmith, L.E., M. Pupols, V.A. Kickhoefer, L.H. Rome, and H.G. Monbouquette. Utilization of a Protein "Shuttle" to Load Vault Nanocapsules with Gold Probes and Proteins. *ACS Nano*, 2009. 3(10): p. 3175-3183.
[5] Buehler, D.C., D.B. Toso, V.A. Kickhoefer, Z.H. Zhou, and L.H. Rome. Vaults engineered for hydrophobic drug delivery. *Small*, 2011. 7(10): p. 1432-1439.
[6] Kickhoefer, V.A., M. Han, S. Raval-Fernandes, M.J. Poderycki, R.J. Moniz, D. Vaccari, M. Silvestry, P.L. Stewart, K.A. Kelly, and L.H. Rome. Targeting Vault Nanoparticles to Specific Cell Surface Receptors. *Acs Nano*, 2009. 3(1): p. 27-36.
[7] Yang, J., V.A. Kickhoefer, B.C. Ng, A. Gopal, L.A. Bentolila, S. John, S.H. Tolbert, and L.H. Rome. Vaults are Dynamically Unconstrained Cytoplasmic Nanoparticles Capable of Half Vault Exchange. *ACS Nano*, 2010. 4(12): p. 7229-7240.
[8] Peng, T. and S. Lim. Trimer-based design of pH-responsive protein cage results in soluble disassembled structures. *Biomacromolecules*, 2011. 12(9): p. 3131-3138.
[9] Dalmau, M., S. Lim, and S.W. Wang. Design of a pH-dependent molecular switch in a caged protein platform. *Nano Letters*, 2009. 9(1): p. 160-166.
[10] Schrödinger, L., The PyMOL Molecular Graphics System, Version 1.3r1. 2010.

BENS199

Fabrication and Characterization of Phosphate Glass/Hydroxyapatite Scaffold for Palate Repair

Pornpatima Yenbut[a], Wassanai Wattanutchariya [b,*]
[a]Biomedical Engineering Center, Faculty of Engineering, Chiang Mai University,
239 Huaykeaw Road, T.Suthep, A. Muang, Chiang Mai, Thailand
Email address: jajah109@gmail.com

[b]Biomedical Engineering Center, Faculty of Engineering, Chiang Mai University,
239 Huaykeaw Road, T.Suthep, A. Muang, Chiang Mai, Thailand
Email address: wassanai@eng.cmu.ac.th

ABSTRACT
Bone grafting is the standard treatment for cleft palate patients. However, a downside to this method is that it requires multiple surgeries to fill the gap in the mouth. Bone tissue engineering can be employed as a solution to this problem to fabricate artificial bone based on synthetic biomaterials. The objectives of this study focus on preparing phosphate glass and hydroxyapatite (HA) as well as developing appropriate forming conditions for scaffold based on the polymeric replication method. Various glass compositions and sintering temperature were examined in this study in order to investigate scaffold structure, strength, biodegradability and pH. Amount of CaO and the sintering temperatures were varied in order to explore their impacts on scaffold properties. Results from XRD clearly show that phosphate glass and HA can be successfully synthesized by using natural materials. In addition, it was found that polymeric foam replication can be successfully used for scaffold fabrication. The scaffold microstructure revealed the appropriate pore size for bone tissue engineering, which is in the 240 – 360 μm range. According to the results, it was found that biodegradability can be regulated by amount of CaO used. For example, specimens with the highest level of biodegradability were obtained from 30 mol% of CaO composition. On the other hand, scaffold containing 40 mol% of CaO and sintering at 750 °C were revealed to have the highest compressive strength, 6.54 MPa. Nonetheless, specimens fabricated from these conditions resulted in base condition for pH testing, which could be toxic to living cells.

Keywords: Phosphate glass, Hydroxyapatite, Biomaterials, Bone tissue engineering

1. INTRODUCTION

Cleft palate is an opening at the roof of the mouth caused by a birth defect. This abnormality can affect facial appearance, resulting in eating and speaking problems as well as ear infections. Srinagarind Hospital in Thailand treated 1,950 cleft lip and palate patients from 1984 – 2007, according to recent studies. Patient numbers have been increasing in the past few years [1].

Current treatment for cleft palate includes the use of prosthetic devices and surgery. A surgical technique known as palatoplasty has been used for palate

reconstruction. Bone grafting is used in this technique to fill in the bone gap and create bone matrix to support growth in the cleft area. The tibia, mandible, ilium, and ribs are donor sites for harvesting bone grafts. While bone grafting has been used successfully, it has several short comings; patients must have multiple operations to achieve successful bone grafting, operations can be painful, wounds can become infected, and donor sites can fracture, among other problems [2].

Bone tissue engineering has been introduced as a new treatment technique for cleft palate repair in order to address the aforementioned issues. This procedure regenerates damaged bone by implanting scaffold to provide mechanical support for gap areas [3]. In addition, scaffolds for bone tissue engineering should be osteoconductive, biocompatible, and biodegradable. Therefore, several materials have been introduced as biomaterials for bone tissue engineering, including tricalcium phosphate, HA, bioactive glass, and biopolymers [4]. These biomaterials can be synthesized from both chemical substances and natural products. For example, HA can be synthesized from coral [5], bovine bones [6], and seashells [7] and the sol-gel method can be used to synthesize silica-based bioactive glass from chemical substances [8]. Nonetheless, such materials have limitations in regard to their mechanical, biodegradability, and other properties [9]. Phosphate glass was therefore chosen as a biomaterial for scaffold fabrication in this research since it offers controllable biodegradation and good biocompatibility. However, phosphate glass has weak mechanical properties. Therefore, HA was added to enhance the scaffold's mechanical properties because it has good mechanical properties and is chiefly composed of calcium and phosphate, important minerals in human bone. In addition, natural materials like mollusk shell and bovine bone were used to synthesize phosphate glass and HA respectively, because of their biocompatibility.

Several techniques have been employed to produce scaffold, including freeze-drying [10], slip casting [11], solid freeform fabrication [12], and polymeric foam replication [13]. In reviewing the above techniques, polymeric foam replication was selected due to the advantage it offers in producing scaffold with controllable pore size and porosity, an important condition in cleft palate treatment.

2. MATERIALS AND METHODS

2.1 Preparation of materials

2.1.1 Hydroxyapatite

Bovine bone was boiled at 150 °C for three days. It was then immersed in hydrogen peroxide for two days in order to dispose of organic substances. Bovine bone was subsequently calcined at 850°C for three hours, before being ground into powder.

2.1.2 Calcium oxide

Mollusk shell was soaked in hydrogen peroxide for two days. It was then calcined at 900°C for three hours, before being ground into powder.

2.1.3 Phosphate glass

Three varieties of phosphate glass were synthesized by mixing $NH_4H_2PO_4$, NaH_2PO_4, and CaO. The amount of $NH_4H_2PO_4$ was kept constant at 45 mol%. However, the ratio of Ca/Na was varied: 30/25, 35/20, and 40/15. The mixtures were

subsequently melted at 1000°C for 30 minutes before being ground into powder. Glass codes and their compositions are shown in Table 1.

Table 1 Phosphate glass compositions and code

Glass code	P_2O_5 (mol%)	CaO (mol%)	Na_2O (mol%)
$P_{45}Ca_{30}Na_{25}$	45	30	25
$P_{45}Ca_{35}Na_{20}$	45	35	20
$P_{45}Ca_{40}Na_{15}$	45	40	15

2.2 Fabrication of phosphate glass/hydroxyapatite scaffold

Each group of phosphate glass was mixed with HA before being added to 40 wt% concentration of polyvinyl alcohol (PVA) solution. Polyurethane foam (pore size 200 – 400 µm) was cut to the size of 10 x 10 x 15 mm for use as scaffold templates. After the foam was immersed in phosphate glass/HA slurry, the scaffold templates were dried at room temperature for a minimum of 12 hours. In order to attain the scaffolds, they were then heated at 400°C for two hours, burning out the polyurethane foam. Finally, the scaffolds were sintered for three hours at 600°C, 675°C and, 750°C, respectively. Table 2 shows scaffold type and composition.

Table 2 Type of scaffold and its compositions

Type of scaffold	Composition of scaffold	
Type 1	HA	$P_{45}Ca_{30}Na_{25}$
Type 2	HA	$P_{45}Ca_{35}Na_{20}$
Type 3	HA	$P_{45}Ca_{40}Na_{15}$

2.3 Characterizations

2.3.1 X-ray diffraction analysis (XRD)

XRD analysis was used to investigate phases of synthetic material powders. The data were collected from a Bruker D8 Advance, using Cu K_α radiation. Voltage and current were set at 40 kV and 40 mA. The data were analyzed from 10° - 100° 2θ with a 0.04°/s scanning rate.

2.3.2 Scanning electron microscope analysis (SEM)

Pore morphology was examined through SEM analysis. The scaffolds were sputter coated with gold before being examined with a JBM-5910LV.

2.3.3 Degradation behavior

In order to test degradation ability, the scaffolds were immersed in Phosphate buffered saline (PBS) at 37°C for seven days. Initial scaffold weight was noted as M_0. After seven days scaffolds were washed with deionized water. Dry scaffolds were weighed as M_t. The following formula was used to calculate degradation percentage:

(1)

2.3.4 Mechanical properties

A compression test was used to evaluate the scaffolds' mechanical behavior. Specimens are approximately 10x10x15 mm in size. A Universal Testing Machine (Instron 5566) was used to perform the tests with crosshead speed 1 $mm.min^{-1}$.

3. RESULT AND DISCUSSION

3.1 Chemical characterization by XRD

The XRD spectra of bovine bone HA were compared with JCPDS-ICDD Card no. 9 – 432[14]. Figure 1 shows that all significant peaks of the bovine bone powder matched JCPDS – ICDD. Results clearly indicate that HA could be synthesized by using this methodology. The CaO – base powder pattern derived from mollusk shell is shown in Figure 2. The main CaO – base powder peaks were found at 2θ = 29.47°, 47.87° and 49.05°, which are characteristic peaks of calcium carbonate and at 2θ = 32.14°, 37.22°, 53.57°, 64.24° and 67.49°, characteristic peaks of calcium oxide [15]. The results confirm that CaO – base powder can be derived from mollusk shell at 900 °C. Figure 3 shows the XRD spectra of prepared phosphate glass. It is evident that no peaks exist in the pattern, indicating that prepared phosphate glass is rather amorphous material.

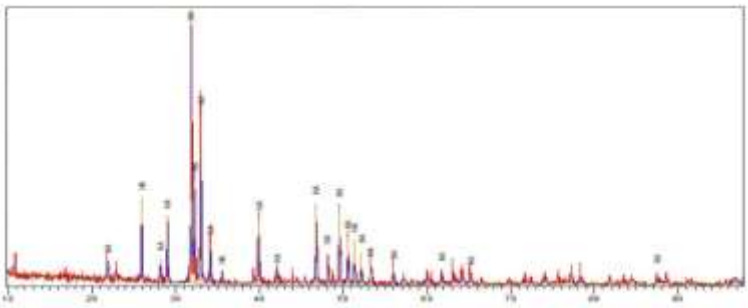

Figure1. XRD pattern of HA extracted from bovine bone

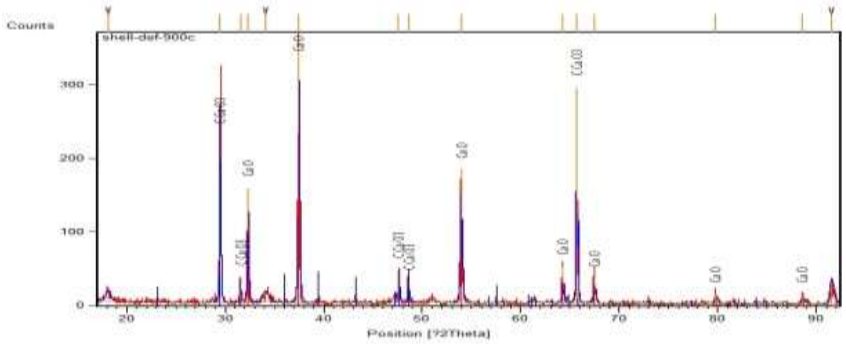

Figure2. XRD pattern of CaO derived from mollusk shell

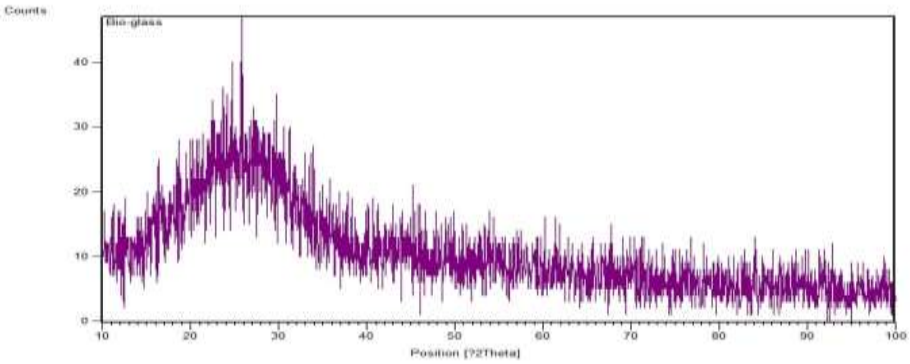

Figure3. XRD pattern of phosphate glass

3.2 Pore structure characterization by SEM

Since, the experiments determined that sintering at 600 °C was not sufficient to fabricate scaffolds, the scaffolds sintered at 675 °C and 750 °C were considered and studied. Figure 4 shows SEM images of phosphate glass/HA scaffolds using polymeric foam replication at 675 °C and 750 °C. The phosphate glass/HA scaffold structure is porous, sharing similarities with human trabecular bone [7]. Phosphate glass/HA scaffold pore size was found to be in the 240 - 360 µm range. These results surpass the minimum pore size requirement, which is considered to support tissue in-grow that 100 µm. In addition, the SEM images show that sintering temperature affected scaffold structure: at 675 °C (Figure 4a) more porous structure was observed than at 750 °C (Figure 4b). Given that the melting point of phosphate glass is approximately 850 – 900 °C, phosphate glass particles melted when scaffold was sintered at near melting point temperature. Therefore, scaffold sintered at 750 °C contained less porous structure than scaffold sintered at 675 °C. Consequently, sintering temperature may have an effect on mechanical properties.

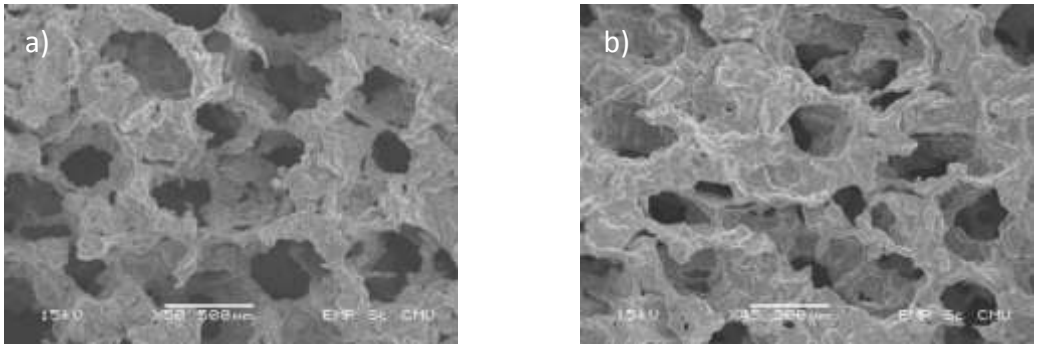

Figure 4. SEM images of phosphate glass/HA scaffolds
a) sintered at 675°C b) sintered at 750 °C

3.3 Scaffold degradation

Scaffolds were immersed for seven days in PBS, demonstrating weight loss in phosphate glass/HA scaffold and PBS pH percentage, as seen in Table 3. The table also indicates that increasing the amount of CaO in phosphate glass causes a decrease in scaffold degradation. Similar results have been reported by Ahmed et al. [16] and Franks et al. [17]. They conclude that when concentration of Ca^{2+} ions in solution increases, degradation decreases. Because increasing Ca^{2+} ions in solution causes ionic strength increases, it can be stated that ionic strength has an effect on degradation. Increasing scaffold – sintering temperature has the same effect. However, degradation percentages among Type 2 and Type 3 scaffolds were found to be similar. pH was shown as base in Type 2 and Type 3. However, in Type 1, pH was shown as neutral. Since pH conditions for cell culture are in the 6.9 – 7.4 range, [18] Type 1 scaffold shows good pH conditions for cell culture.

Table 3 Degradation test and pH of scaffold after immersing in PBS for seven days

Type of scaffold	Scaffold sintering temperature (°C)	Degradation (%)	pH
Type 1	675	17.8	7.0
Type 2		4.3	8.8
Type 3		4.0	9.0
Type 1	750	15.3	7.3

Type 2		0.6	9.0
Type 3		0.2	9.2

3.4 Mechanical properties

As discussed earlier, sintering temperature affected porous structure, which caused variation in compressive strength: the more porous the scaffold, the less compressive strength it has. As shown in Table 4, when sintering temperature increased, compressive strength increased. For Type 1, at 675 °C compressive strength is 0.18 MPa. However, at 750 °C compressive strength is 1.84 MPa. Type 2 and Type 3 compressive strength also increased when temperature was increased: from 2.22 MPa and 2.35 MPa to 3.70 MPa and 6.54 MPa, respectively. Type 2 and Type 3 scaffolds thereby show good compressive strength for bone tissue engineering since the trabecular bone compressive strength range has been reported as 2 – 12 MPa [9]. Compared with previous research [7, 19], compressive strength of scaffold obtained from phosphate glass/HA is higher than scaffold derived from only HA.

Table 4 Compressive strength of scaffold at different sintering temperatures

Type of scaffold	Scaffold sintering temperature (°C)	Compressive strength (MPa)
Type 1	675	0.18
Type 2		2.22
Type 3		2.35
Type 1	750	1.84
Type 2		3.70
Type 3		6.54

4. CONCLUSION

HA and phosphate glass were successfully synthesized by using local material as a precursor and it was possible to fabricate phosphate glass/HA scaffold by using polymeric foam replication. Appropriate pore size for bone tissue engineering was obtained in the 240 – 360 µm range. Degradation rate could be regulated by varying CaO amount. Although Type 2 and Type 3 scaffolds produced good compressive strength, they didn't provide appropriate pH condition for cell culture. Proper pH condition for cell culture was only found in Type 1. In conclusion, phosphate glass code$P_{45}Ca_{30}Na_{25}$ is the best candidate found in this study to fabricate scaffold for cleft palate repair since it can provide neutral pH and can degrade. 750 °C would be an appropriate temperature for producing scaffold because at this temperature good compressive strength can be fabricated. Nevertheless, the ratio between phosphate glass and HA should be studied in order to improve the biological and mechanical properties of scaffold.

5. REFERENCES

[1] Orathai L, Suteera P, Vasana C, Supitcha U, Bowornsilp C. Statistics of Patients with Cleft Lip and Cleft Palate in Srinagarind Hospital 1984-2007, *Srinagarind Medical Journal*, 2009. 24(3): 240-246.

[2] Jennifer LM, Dominick PC. Tissue Engineering Solutions for Cleft Palates, *Journal of Oral and Maxillofacial Surgery*, 2007. 65: 2503-2511.

[3] Wang X, Nyman JS, Dong X, Leng H, Reyes M. Fundamental Biomechanics in Bone Tissue Engineering, Morgan & Claypool, 2010, pp.1-15.
[4] Lichte P, Pape HC, Pufe T, Kobbe P, Fischer H. Scaffolds for bone healing: Concepts, materials and evidence. *Injury: International Journal of the Care of the Injured*, 2011, 42: 569-573.
[5] Sivakumar M, Sampath KTS, Shantha KL, Panduranga R. Development of hydroxyapatite derived from Indian coral. *Biomaterials*, 1996, 17: 1709 -1714.
[6] Barakat NAM, Myung SK, Omran AM, Faheem AS, Kim HY. Extraction of pure natural hydroxyapatite from the bovine bones bio waste by three different methods. *journal of materials processing technology*, 2009, 209: 3408 - 3415.
[7] Yun Y, Qingqing Y, Ximing P, Zhenqing H, Qiqing Z. Biphasic calcium phosphate macroporous scaffolds derived from oyster shells for bone tissue engineering. *Chemical Engineering Journal*, 2011, 173: 837-845.
[8] Saboori A, Rabiee M, Moztarzadeh F, Sheikhi M, Tahriri M, Karimi M. Synthesis, characterization and in vitro bioactivity of sol-gel derived SiO_2-CaO-P_2O_5-MgO bioglass**.** *Materials Science and Engineering C*, 2009, 29: 335- 340.
[9] Mohamed. NR, Delbert ED, Bal BS, Qiang F, Steven BJ, Lynda FB, Antoni PT. Review: Bioactive glass in tissue engineering. *Acta Biomaterialia*., 2011, 7: 2355-2373.
[10] Masoud M, Mohammad R, Mahmoud A, Saied M. Biomimetic formation of apatite on the surface of porous gelatin/bioactive glass nanocomposite scaffolds. *Applied Surface Science*, 2010, 257: 1740-1749.
[11] Qiang F, Mohamed. NR, Bal BS, Wenhai H, Delbert ED. Preparation and bioactive characteristics of a porous 13-93 glass, and fabrication into the articulating surface of a proximal tibia.*Wiley Inter Science* , 2007: 222-229.
[12] Hutmacher DW, Sittinger M, Risbud MV. Review: Scaffold-based tissue engineering: rationale for computer-aided design and solid free-form fabrication systems. *TRENDS in Biotechnology*, 2004, 22: 354 -362.
[13] Schwartzwalder K, Somers AV. Method of Making a Porous Shape of Sintered Refractory Ceramic Articles, *United Stated Patent*, No. 3090094, 1963.
[14] JCPDS-ICDD Card No.9-432. International Center for Diffraction Data. Newtown Square, PA, 2000**.**
[15] Jutika B, Ashim JT, Dhanapati D. Solid oxide derived from waste shells of Turbonilla striatula as a renewable catalyst for biodiesel production, *Fuel Processing Technology*, 2011, 92: 2061-2067.
[16] Ahmed I, Lewis M, Olsen I, Knowles JC. Phosphate glasses for tissue engineering: Part 1. Processing and characterization of a ternary-based P_2O_5-CaO-Na_2O glass system. *Biomaterials*, 2004, 25: 491-499.
[17] Franks K, Abrahams I, Knowles JC. Development of soluble glasses for biomedical use Part I: In vitro solubility measurement. *Journal of Materials Science: Materials in Medicine*, 2000, 11: 609 -614.
[18] Freshney RI. Defined Media and Supplements. In *Culture of Animal Cells a Manual of Basic Technique 5th edition*, 2005, pp.115-128.
[19] Jo IH, Shin KH, Soon YM, Koh YH Lee JH, Kim HE. Highly porous hydroxyapatite scaffolds with elongated pores using stretched polymeric sponges as novel template. *Materials Letters*, 2009, 63: 1702 -1704.

Fabrication and Characterization of Composite Porous Scaffold by Chitosan-Gelatin/Hydroxyapatite for Bone Filler Application

Whattanapong Changkowchai[a,*], Wassanai Wattanutchariya[b]
[a]Biomedical Engineering Center, Faculty of Engineering, Chiang Mai University,
239 Huaykeaw Road, T.Suthep, A. Muang, Chiang Mai, Thailand
Email address: aum31350@hotmail.com

[b]Biomedical Engineering Center, Faculty of Engineering, Chiang Mai University,
239 Huaykeaw Road, T.Suthep, A. Muang, Chiang Mai, Thailand
Email address: wassanai@eng.cmu.ac.th

ABSTRACT
Chitosan-gelatin and hydroxyapatite was widely used as a material in bone tissue engineering application which can be extracted from squid pen. The structure of chitosan is similar to glycosaminoglycans which is the major component of the extracellular matrix of bone and cartilage. Gelatin can be obtained by thermal denaturation and chemical degradation of collagen, which has known to be good for cell viability. Hydroxyapatite has a chemical composition similar to the mineral tissue in human body, which can be activated new bone formation. In this research, Mollusk shell was used as a precursor of hydroxyapatite synthesis and freeze drying method was employed for fabricating the porous structure. An investigation on a development of porous bone scaffold was carried out in order to identify a proper mixing ratio between chitosan, gelatin and hydroxyapatite which yields appropriate biodegradability, porosity and swelling property for bone filler application. The results of the study showed that the degradability decreased by increased chitosan-gelatin and hydroxyapatite concentration. The porosity was increased by decreased chitosan-gelatin and hydroxyapatite concentration. The swelling property was increased by increased chitosan-gelatin and decreased hydroxyapatite concentration. SEM technique showed opening pore structure of porous scaffolds. Consequently, this developing bone porous scaffold as a bone filler seems to be a promising activated new bone formation that can be implemented in medical applications.

Keywords Chitosan, Gelatin, Hydroxyapatite, Porous scaffold, Bone filler

1. INTRODUCTION

Bones are rigid organs that support and protect various organs of the body. Bone defect and bone lost from diseases, trauma or tumor resections require special treatment for these bones to be repaired [1]. The bone repairment is subjected to intensive investigation in human health care. In general, bone graft has been recognized as a standard method for the reconstructive orthopedic surgery [2]. There are 3 types of bone or tissue substitution used in bone graft application including allograft, autograft and xenograft. Allograft is a bone or soft tissue that is transplanted from one individual to another in the same species. Allograft has many advantages such as osteoinductive and strong mechanical properties. However, the disadvantage of allograft is that diseases from donor such as HIV, hepatitis or cancer can be

transmitted to the receiver. Autograft or autologous bone is a bone tissue from one site to another in the same individual. The main feature of this graft is excellent biocompatibility, which does not stimulate host inflammatory response. Although autograft has a desirable property, the treatment procedure may cause long lasting pain and uncomfortable to the patient. Furthermore, there is a risk of wound infection at site of surgery [3] Xenograft is cells or sections of tissue that removed from one species and grafted on or into a different species. Materials widely used as xenograft are bovine bone [4] and mollusk shell [5]. However, the bioactivity properties of xenograft are weaker than allograft and autograft.

To improve the property of Xenograft, a new treatment technique for bone or tissue repair called bone tissue engineering has been introduced. Bone tissue engineering is a procedure to regenerate damaged bone by implanting cells, proteins, and scaffold to provide mechanical support for gap areas [6]. This technique helps develops. Thus, many researches focus on the development of artificial bone substitutes by bone tissue engineering technique for repairing bone defect [7]. Bone substitute morphology has many forms such as compact and porous structure. Compact structure is good mechanical strength for used as bone replacement. Porous structure is suitable for cell attachment and blood supply for used as bone filler.

Bone tissue engineering creates the biological material that provides the option to implantation and prosthesis. It can be used for bone repairing in many fields including maxillofacial, orthopedic, craniofacial, and plastic surgery, which are mostly concern about biocompatibility, non-toxicity, bioactivity, high osteoconductivity, and degradation rate. The approach of bone tissue engineering deals with three main bases: osteoconductive biomaterial scaffolds, osteogenic cells and osteoinductive molecules [8]. Materials widely used in bone tissue engineering are including hydroxyapatite (HA), chitosan and gelatin. HA has a chemical composition similar to the mineral tissue in human body. Furthermore, HA could be synthesized from many natural resources with calcium based structure such as bovine bone, mollusk shell and coral. Chitosan is a polysaccharide which can be synthesized from crustacean shell and squid pen. Structure of chitosan is similar to glycosaminoglycans which is the major component of the extracellular matrix of bone and cartilage [9, 10]. Gelatin can be obtained by thermal denaturation and chemical degradation of collagen [11], which has known to be good for cell viability [12].

Several methodologies have been used for fabricating porous scaffold in bone tissue engineering such as sintering, salt leaching and freeze drying process. Sintering process has been employed to form a porous structure by using high temperature to bond substance together as well as burn out organic phase of material [13]. Salt leaching is another technique that demonstrated feasibility of highly porous scaffold forming; however, it also revealed some basic limits of this technique as the prolonged contact of particles with water, requirement for salt removal [14]. Hence, freeze dying method was chosen to fabricate the porous scaffold because it can form highly opening pore structure, stability and easy handling [15].

This study focuses on the preparation of bone graft using natural based materials such as HA, chitosan, and gelatin. The combination of these three biomaterials could synergy the physical property and bioactivity of the bone graft in order to apply as bone filler. The implementation of this study bone defect or bone lost repairment in

orthopedic surgery, maxillofacial as well as craniofacial applications.

2. EXPERIMENTAL

2.1 Materials

Chitosan based on squid pens extraction was purchased from Taming Enterprises Co., Ltd, Thailand. Gelatin, ammonium di-hydrogen phosphate ($NH_4H_2PO_4$), Sodium Hydroxide (NaOH) and phosphoric acid (H_3PO_4) were purchased from Sigma Aldrich Co., Ltd.

2.2 Preparation of HA

Mollusk shell was used as a raw material to synthesis HA by wet chemical precipitation method. Mollusk shells was calcined at 850°C for 5 hours and then grind in ball mill for 12 hours to obtain $CaCO_3$ powder. In order to achieve HA with appropriate ratio of Ca/P at 1/0.5, $CaCO_3$ was dissolved in ammonium di-hydrogen phosphate ($NH_4H_2PO_4$) solution and adjust pH 9-10 by phosphoric acid (H_3PO_4) then stirred the solution for 2 hours then precipitate the solution at room temperature for 12 hours. Next, filtered the solution and washed the powder for 3 times, dried it at 110°C in hot air oven for 12 hours then calcined at 800°C for 12 hours to obtain HA powder

2.3 Preparation of chitosan-gelatin solution

Chitosan solution was prepared by mixing of 97.88% deacetylation chitosan with 1% acetic acid solution. Then, gelatin was added into chitosan solution with the ratio of chitosan: gelatin at 1:1 and agitate the solution at 37°C for 12 hours to form a chitosan-gelatin solution.

2.4 Preparation of porous bone scaffold

In order to investigate the effect of materials on the property of developing porous bone scaffold, HA was added to chitosan-gelatin solution and stirred for 24 hours for thoroughly dispersion. The resultant solution was transferred to 24 well culture plates and pre-frozen at -20°C for 12 hours following by freeze drying in lyophillizer at -40°C for 48 hours to obtain porous scaffolds. Then scaffolds was neutralized by 2% sodium hydroxide (NaOH) and washed with deionized water before repeating the freeze drying process one more time. The mixture design was used as An experimental design based on mixture design technique was implemented to investigate the effect of chitosan-gelatin/hydroxyapatite compositions to the product properties.

2.5 Characterization

Characterization of porous bone scaffold was employ to show the characteristic of the result structures such asbiodegradability, morphology, porosity and swelling property.

- X-ray diffraction analysis (XRD) analysis was used to investigate the synthetic material powders' phase of hydroxyapatite. The data was collected from a Bruker D8 Advance, using Cu Kα radiation. Voltage and current was set at 40 kV and 40 mA.
- Biodegradability of the scaffolds was characterized by in vitro study. The scaffolds were immersed in PBS medium containing lysozyme (10,000 U/ml) at 37°C for 7 days. Initial weight of the scaffold noted as W_0 and after 7 days the scaffold were washed in deionized water to remove ions adsorb on surface and

then freeze dry. The dry weight of the scaffold was noted as W_t. The degradation of the scaffold calculates by the following formula (1).

(1)

- The porosity of the porous chitosan-gelatin/HA scaffolds with different concentration can be determined by Archimedes' principle. Ethanol was selected as the displacement liquid as it permeates through the scaffolds without swelling or shrinking the matrix. The scaffolds (dry weight, W_d) were immersed in the ethanol for 5 min and the weights of scaffolds in ethanol noted as W_l. The scaffolds were taken out and the liquid on the surface will be removed by filter paper. The weight of the wet scaffold was noted as W_w. The porosity of the chitosan-gelatin/HA scaffold could be obtained by formula (2).

(2)

$$\text{Porosity (\%)} = \frac{Ww\text{-}Wd}{Ww\text{-}W1} \times$$

- Swelling property was determined by the percentage of water absorption. Dry weight of scaffold is noted as W0. Then, porous scaffolds were immersed in PBS buffer solution at PH 7.4 and temperature 37°C for 24 hours. After that, surface adsorbed water was removed by filler paper. Wet weight of scaffolds after taken out from PBS buffer solution was noted as W_w. The ratio of swelling can be determined by using the formula (3)

(3)

$$\text{Swelling ratio} = \frac{Ww\text{-}}{Wl}$$

- Pore structure morphology was examined by scanning electron microscope analysis (SEM). The scaffolds was sputter coated with gold before being examined with a JBM-410LV

3. RESULT AND DISCUSSION

HA powder that synthesized from mollusk shell was characterized by using X-Ray Diffraction. Diffractogram showed the XRD pattern of synthesized HA at 700°C, the peak resembled naturally occurring bone apatite with respect to degree of crystalline and structural morphology as show in the Figure 1. Figure 2 shows the porous bone scaffolds composite fabricated from freeze dried method.

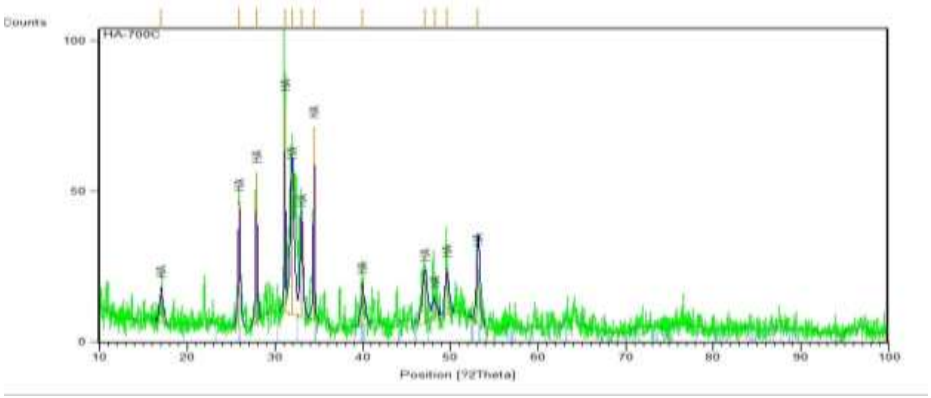

Figure 1. XRD pattern of hydroxyapatite synthesized from mollusk shell

Figure 2. Porous scaffold composite with highly porous and opening pore structure

The ratio of chitosan-gelatin/hydroxyapatite was varying by mixture design generated by MINITAB software version 15. Biodegradability, porosity and swelling properties of the porous scaffold were showed in Table 1. To investigate the degradability of the structure, the porous scaffold was soaking in PBS solution with lysozyme after 7 days. The degradation rate shows that when increased the concentration of chitosan-gelatin, the porosity of scaffold was decreased and when increase the concentration of HA, the rate of the scaffold was decreased. Porosity of the scaffold shows that when increased the concentration of chitosan-gelatin, the porosity of scaffold was decreased and when increased the concentration of HA, the porosity was decreased. The swelling property also shows reverse proportion to the concentration of HA in the mixture. [15, 16].

Table1. Properties of porous scaffold with various ratios by mixture design using MINITAB version 15

Chitosan-Gelatin concentration (%w/w)	**HA (%w/w)**	**1%Acetic acid Solution (%w/w)**	**Biodegradability (%)**	**Porosity (%)**	**Swelling property (%)**
1.37	1.50	97.13	44.23	91.46	93.24
3.13	2.50	94.37	20.87	89.37	94.32
2.30	2.00	95.70	23.94	92.59	93.10
0.50	1.00	98.50	56.32	94.65	90.76

Chitosan-Gelatin concentration (%w/w)	HA (%w/w)	1%Acetic acid Solution (%w/w)	Biodegradability (%)	Porosity (%)	Swelling property (%)
4.00	3.00	93.00	18.12	88.56	94.15
1.37	1.50	97.13	43.52	91.42	92.45
0.50	3.00	96.50	31.22	90.15	80.45
4.00	1.00	95.00	35.50	92.84	96.88
4.00	3.00	93.00	17.65	88.76	94.23
3.13	1.50	95.37	38.45	91.95	95.66
1.37	2.50	96.13	28.78	89.88	89.66
0.50	3.00	96.500	30.84	90.15	81.89
1.37	2.50	96.13	28.64	89.84	88.35
3.13	2.50	94.37	21.06	89.59	94.48
0.50	1.00	98.50	55.96	94.55	89.74
3.13	1.50	95.37	38.45	91.74	95.45
2.30	2.00	95.70	24.82	91.86	92.95
4.00	1.00	95.00	35.45	92.32	95.45

The pore structure morphology of porous bone scaffold was opening pore structure with micropore and macropore as show in figure 3. Opening pore structure is good for blood supply and cell attachment [12]. The pore size of chitosan-gelatin/HA composite scaffold varied from 50-350 μm as measured by SEM. With increase concentration of chitosan-gelatin, the pore size decreased, which is in accordance with previously reported literature [16] and ASTM F2450-10.

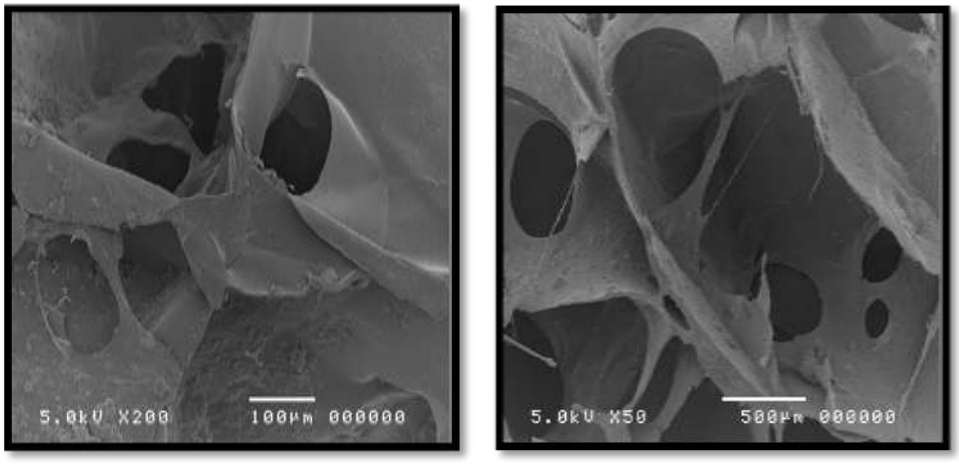

Figure3 Micropore and Macropore structure of porous bone scaffold

4. CONCLUSION

An investigation on developing porous bone scaffold was carried out in order to identify a proper mixing ratio between chitosan, gelatin and HA, which could yield appropriate biodegradability, porosity and swelling property for bone filler application. In this study, 5 levels of mixing ratio between chitosan-gelatin and HA were used and

varied by the mixture design technique. According to the test results, the degradability decreased by increased chitosan-gelatin and HA concentration. In the meantime, the porosity was increased by decreased chitosan-gelatin and HA concentration, while the swelling property was increased by increased chitosan-gelatin and decreased HA concentration. Furthermore, SEM technique showed opening pore structure of porous scaffolds which proper for blood supply and cell attachment. Consequently, this developing bone porous scaffold as a bone filler seems to be a promising activated new bone formation that can be implemented in medical applications.

5. REFERENCES

[1] Gauthier O, Müller R, von Stechow D, Lamy B, Weiss P, Bouler J-M, Aguado E and Daculsi G. *In vivo bone regeneration with injectable calcium phosphate biomaterial: A three-dimensional micro-computed tomographic, biomechanical and SEM study*. Biomaterials, 2005. 26(27): 5444-5453.

[2] Mehta M, Schmidt-Bleek K, Duda GN, Mooney DJ. *Biomaterial delivery of morphogens to mimic the natural healing cascade in bone.* Advanced Drug Delivery Reviews 2012; 64(12):1257-76.

[3] Venkatesan J, Qian Z-J, Ryu B, Ashok Kumar N, Kim S-K. *Preparation and characterization of carbon nanotube-grafted-chitosan - Natural hydroxyapatite composite for bone tissue engineering*. Carbohydrate Polymers 2011; 83(2):569-77.

[4] Barakat NAM, Khil MS, Omran AM, Sheikh FA, Kim HY. *Extraction of pure natural hydroxyapatite from the bovine bones bio waste by three different methods*. Journal of Materials Processing Technology 2009; 209(7):3408-15.

[5] Vecchio KS, Zhang X, Massie JB, Wang M, Kim CW. *Conversion of bulk seashells to biocompatible hydroxyapatite for bone implants.* Acta Biomaterialia 2007; 3(6):910-8.

[6] wang X, Nyman JS, Dong X, Leng H, Reyes M. *Fundamental Biomechanics in Bone Tissue Engineering*. Morgan & Claypool 2010:1-15.

[7] Cai X, Tong H, Shen X, Chen W, Yan J, Hu J. *Preparation and characterization of homogeneous chitosan-polylactic acid/hydroxyapatite nanocomposite for bone tissue engineering and evaluation of its mechanical properties*. Acta Biomaterialia 2009; 5(7):2693-703.

[8] Vachiraroj N, Ratanavaraporn J, Damrongsakkul S, Pichyangkura R, Banaprasert T, Kanokpanont S. *A comparison of Thai silk fibroin-based and chitosan-based materials on in vitro biocompatibility for bone substitutes.* International Journal of Biological Macromolecules 2009; 45(5):470-7.

[9] Thein-Han WW, Misra RDK. *Biomimetic chitosan-nanohydroxyapatite composite scaffolds for bone tissue engineering*. Acta Biomaterialia 2009; 5(4):1182-97.

[10] Li Z, Ramay HR, Hauch KD, Xiao D, Zhang M. *Chitosan-alginate hybrid scaffolds for bone tissue engineering.* Biomaterials 2005; 26(18):3919-28.

[11] Panzavolta S, Fini M, Nicoletti A, Bracci B, Rubini K, Giardino R, et al. *Porous composite scaffolds based on gelatin and partially hydrolyzed α-tricalcium phosphate.* Acta Biomaterialia 2009; 5(2):636-43.

[12] Kim H-W, Kim H-E, Salih V. *Stimulation of osteoblast responses to biomimetic nanocomposites of gelatin-hydroxyapatite for tissue engineering scaffolds*. Biomaterials 2005; 26(25):5221-30.

[13] Baino F, Verné E, Vitale-Brovarone C. *3-D high-strength glass ceramic scaffolds*

containing fluoroapatite for load-bearing bone portions replacement. Materials Science and Engineering: 2009; 29(6):2055-62.

[14] Cannillo V, Chiellini F, Fabbri P, Sola A. *Production of Bioglass® 45S5 - Polycaprolactone composite scaffolds via salt-leaching*. Composite Structures 2010; 92(8):1823-32.

[15] Zhao F, Grayson WL, Ma T, Bunnell B, Lu WW. *Effects of hydroxyapatite in 3-D chitosan-gelatin polymer network on human mesenchymal stem cell construct development*. Biomaterials 2006; 27(9):1859-67.

[16] Peter M, Ganesh N, Selvamurugan N, Nair SV, Furuike T, Tamura H, Jayakumar R. *Preparation and characterization of chitosan-gelatin/nanohydroxyapatite composite scaffolds for tissue engineering applications*. Carbohydrate Polymers2010. p. 687-94.

Environmental Science

Pullman Bangkok King Power, 2F Meeting Room BETA I

2013/1/26 Saturday 10:30-12:00

Session Chair: B C Meikap

BENS78

Wetland, Wastewater and Wealth: A Unique Case of East Kolkata Wetlands

Anindya Basu | *University of Calcutta*

BENS124

Investigating the Potential Impact of Coal Seam Gas Mining on Aquifers and the Surface Environment

John Bradd | *University of Wollongong*

Tim Cohen | *University of Wollongong*

Sam Marx | *University of Wollongong*

Solomon Buckman | *University of Wollongong*

Emma Kiekebosch-Fitt | *University of Wollongong*

BENS152

Abatement of Gaseous and Dust Air Pollutants by A Gas-Liquid Contacting Towers

B C Meikap | *University of Kwazulu-Natal*

BENS205

High Dominance of Hydrogenotrophic Methanogens in Three Different Full-Scale Anaerobic Sewage Sludge Digesters

Changsoo Lee | *Ulsan National Institute of Science and Technology*

Jaai Kim | *Ulsan National Institute of Science and Technology*

BENS165

The Usage of Water Steam Data Provided From GNSS in Meteorology

Seyit Ali Yilmaz | *Selçuk Üniversitesi*

BENS78

Wetland, Wastewater and Wealth: A Unique Case of East Kolkata Wetlands

Anindya Basu
Department of Geography,Women's Christian College, Kolkata, India

1. CONCEPT

Wetlands are one of the most important ecosystems, which have multiple utilities. These are lands, transitional between terrestrial and aquatic systems where the water level is at or near the surface. According to *Ramsar Convention* (1971), wetlands are, " areas of marsh, fen, peat land or water, whether natural or artificial, permanent or temporary, with water that is static or flowing, fresh brackish, or salt, including areas of marine water the depth of which at low tide does not exceed six metres". Wetlands are not only considered important for waterfowls, but are also for a whole range of wise-use practices. That includes fisheries, tourism, bio-diversity conservation, waste recycling etc. The list of sites under Ramsar convention increased significantly. So has been the number of participating countries. East Calcutta Wetlands (ECW), on August, 2002 was been designated as Ramsar site. For the Asian Bureau (1991) wetlands covers "estuaries and deltas, salt marshes, mangroves and mud flats, coastal lagoons, fresh water lakes and marshes oasis, salt marshes, seasonal flood plain wetlands, swamp forests, rivers and streams, man managed systems such as rice fields, fish ponds and reservoirs."

The East Kolkata Wetland, the study area, is the vast low lying area on the east towards which the city is inclined and plays the role of a sink. This 12,500 hectare area which is located at 88°20'E to 88°35'E and 20°25'E to 20°35'E.

Fig: 1 Cropped image from Google Earth, 2012 and Fig: 2 Base Line Document Action Plan, Creative Research Group, December 1997

2. BACKDROP

The East Kolkata Wetlands fall within the South Bengal ecotone. The eastward

shift in the course of the main flow of the river Ganga brought metamorphic changes in the process of delta building. This affected the flow of a number of distributaries. Mouths of some of the streams opened directly into the Bay of Bengal and were influenced by tidal action. One such channel was Bidyadhari. Extensive saltwater marshes existed between River Hugli and River Bidyadhari. The tidal flow from the Bay of Bengal used to increase salinity in water. Change in pattern of delta building and human interference contributed to the reduction of the spill area. With the cessation of tidal influx it got converted into a vast derelict swamp.

The natural elevation of city Calcutta is six to seven metres along the levee of the river Hooghly and bit lesser at the existing wetland sites. Given these geo-climatic factors, the sewerage planning authority could not realize the natural gradient of the city in early days. In 1803 the city drainage was directed artificially to the river Hooghly. It took fifty more years to come to grip with the problem. Beleghata canal was excavated in 1810 and circular canal was dug in 1829. The then Governor General of India, Lord Wellesley appointed a committee to examine the problems and submit recommendations. The committee approved a combined scheme for the disposal of (a) storm water, (b) sewage and (c) dry weather flow.

Mr. William Clarke, Chief Sanitary Engineer, prepared a new detailed drainage scheme which was finally completed in 1884. Piscicultre and fish market was initiated successfully from 1870's. But several interferences including human intervention led to increased siltation, Finally in 1928, Bidyadhari was declared dead. In 1943, the out fall system was changed from south-east to the Kulti Gung. With the diversion of city sewage and storm water into the salt lakes and the deterioration of river Bidyadhari there was a gradual change in aquatic environment from saline to non-saline.

Kolkata lies on the edge of the delta area, where the surface gradients are very low. The micro topography varies widely because of the changing patterns of the natural drainage network. Delta landscapes are characterized by relatively flood-safe high levees along the banks of the major rivers. Further away from the river, spill basins and swamps dominate. Kolkata's original growth pattern followed the flood-safe levees along the banks of the Hooghly. The expansion particularly went north, away from the delta. The massive influx of refugees after partition in 1947 led to further urbanization in the east and south-east. The original drainage and canal system of the city became ineffective because of the newly urbanized areas. This situation has improved somewhat owing to infrastructure investment in the 1980s and 1990s. Systematic research on East Kolkata Wetlands began only in the 1980s on behalf of the state government.

Fig 3: Base Line Document Action Plan, Creative Research Group, December 1997

Table:1 Mouzas under East Calcutta Wetlands and Waste Recycling Region

Police Station	**Total Area (in hectare)**	**Percentage**
Bhangar	4548.58	36.00
Bidhannagar (S)	2100.00	17.00
Sonarpur	4416.83	35.50
Tiljala	1426.73	11.50
Total	12492.14	100.00

3. CONCEPT OF VALUATION

Environmental degradation associated with development and population growth is visible all over. Both economists and natural scientists have appreciated this environmental consciousness that has emerged in the context of development debate. While economists tend to emphasize on short term goals, environmentalists emphasize on the long term ones. There is also a dispute about how to value environment. It can be argued that the accounting approach will give an under estimation due to minimum coverage and economic approach may give an over estimation due to subjective valuation. The price of environmental amenities may be a difficult proposition but that needs to be addressed. Economic valuation of environmental resources and consequently their impact assessment can make decisions on resource utilization and allocation more meaningful. Going beyond anthropocentrism, the valuation problems become issues of deep philosophy.

Wetland ecosystem provides goods and services to the society and therefore is valuable to us. Measuring such values becomes important when sections of these wetlands are found to be lost in favour of some developmental activities without any comparative assessment of the value of the land vis-à-vis that of wetlands, which existed there. The method of Contingent Valuation, obtains the consumers' willingness to pay to conserve the wetlands. While, the Economic Valuation method can also act as an effective tool for decision-making.

The wastewater enters the wetlands through a network of canals and feed the fishponds. On the way, the sunlight acts as a purifying agent on the sewage, which

triggers biochemical reactions. Each hectare of a shallow water body can remove about 237 kg of BOD per day. This helps in the reduction of coliform bacteria prone to be pathogenic which even conventional mechanical sewage treatment plants may not be able to fully eliminate. The wetlands that act as bio-treatment plant and treat the sewage without involving any cost. The wetland also helps in removing heavy metals, like lead, chromium, etc. by ion exchange. On the basis of 11 sampling sites it had been found that as distance increases from pumping stations concentration of organic nitrogen, dissolved phosphorous, lead and chromium is lowered.

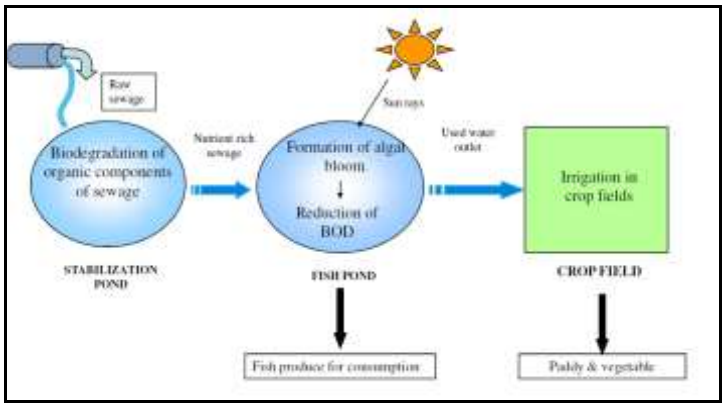

Fig 4: IWMED, 2001

According to a survey conducted by Indian Statistical Institute, Kolkata, EKW saved the state government from an expenditure of at least Rs. 400 crores for construction of sewage treatment plant. Besides, sewage fed fishing is an important economic activity in this region. The total potential loss of fish production was estimated to be 7076 quintals per annum, which was equivalent to a loss of Rs 14.15 million (2001). The effluent from the fishponds serve as water source for the fields located further south-east and is beneficial for them.

The challenging task of evaluating EKW, a transformed ecosystem where human beings are as integral to as the aquatic flora, fauna was also taken up by Department of Business Management, University of Calcutta. The three major economic benefits derived from are:

i) Cost of treating the sewage
ii) Cost of waste water as fish feed
iii) Cost of irrigation water.

Table 2: Beneficial Role of Wetlands

Functional Parameters	**Components**
i) Hydrology	•Flood control •Ground water recharge •Dissipation of erosive forces
ii) Water Quality	•Waste water treatment
iii) Habitat	•Rich in biodiversity
iv) Socio-economic	•Consumptive use value (eg. Food chain support) •Non-consumptive use value

	(eg. Recreation)

The list of other indirect values is also not negligible involving flood control, livelihood support, extensive food chain, carbon sequestration, micro-climate stabilization.

4. ROLE OF PISCICULTURE: THE MOST UNIQUE FEATURE

Wastewater flows through fish ponds covering about 4,000 ha, within the East Kolkata Wetlands, facilitating a wide range of physical, biological and chemical processes which help improve the quality of the water. Consequently this wetland system is popularly known as the kidney of the city and has been described as one of the rare examples of resource recovery activity region. The wetland also supports the livelihoods of local residents through the sewage-fed fisheries and other socio-economic activities like garbage farming, paddy farming etc. K.M.C.'s share of responsibility is to ensure that the waste-water reaches the outfall channels through the pumping stations. Thereafter, it's the duty of the fisheries to draw the required amount of water.

Table:3 Pumping Stations

Name of Basin	**Area of Basin (sq.km)**	**Terminal Pumping Station**
Town System	19.13	Palmer's Bridge Pumping Station
Suburban System	25.69	Ballygunge Drainage Pumping Station
Maniktala System	8.91	Dhapa Lock Pumping Station
Tangra-Topsia System	5.17	Topsia Pumping Station
Tollygunge-Pancannagram System	36.00	Chowbaga Pumping Station
Bagjola System	6.07	Bagjola Pumping Station

There are more than 154 big fisheries or bheries, as they are known locally. The most important function performed by these wetlands is to recover nutrients from a major proportion of the 1,300 million litres of wastewater discharged from the city daily. The total area of sewage-fed fisheries is around 3,900 ha, privately owned bheris account for 93% of this area, farms managed by co-operatives cover 6% and ponds managed by the State Government account for less than 1%. Large areas of the fisheries are taken on lease and operated by commercial producers, however, several fisheries became cooperatives, either registered or non-registered, because of the inability of the owners to sustain their fishing activities owing to land reforms and past problems with the labour unions. The fisheries range in size from over 50 ha down to around 5 ha. Various sewage canals supply water to these fisheries, and the water enters the fisheries either via gravity, by siphoning or pumping. Production is mainly sold through wholesale markets at Bantala, Bamanghata, Choubaga and Chingrighata nearby. From these four major sources fish are distributed to retail markets scattered throughout the core of the city, but there is also increasing evidence that fish are increasingly being transported out and marketed in provincial towns. Recent field surveys showed that 8,500 people are directly engaged in sewage-fed fisheries, of which about 90% are from local villages falling within the EKW, the

others mainly coming from adjoining areas.

The fish species in wetlands largely depend on plankton in their younger stage. With the age and growth in size, these tend to feed on larger prey and organic matter from the sewage water. Previously the fish fauna in the East Calcutta Wetland system was composed of both brackish water and fresh water forms. But after the large-scale intervention by the owners through sewage fed cultivation of only few number of fresh water fish species are recorded from these wetlands. The wetland owners commonly culture the survey results showed that 37 fish species are recorded of which 14 species and 23 species are recorded as wild fish species. The most common ones are Rui, Katla, Mrigel, Bata, Telapia, Carp etc.

The major phases of fish raising involve: pond preparation, primary fertilization, fish stocking, secondary fertilization, fish harvesting.

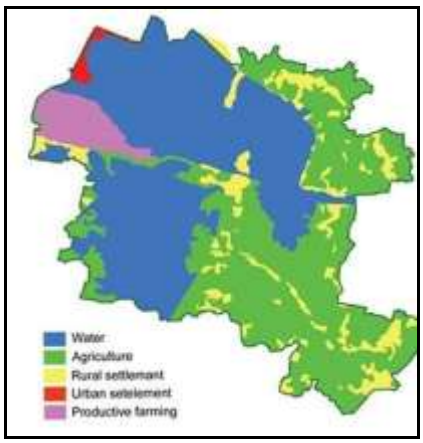

Fig 5: Department of Environment, Government of West Bengal, 2000

Table 4: Types of Land use

Land use	Area
Water bodies	5,852 ha (about 3,899 ha used for fish farming)
Agricultural land	4,960 ha
Garbage farming	603 ha
Rural settlement	1,235 ha
Urban settlement	91.5 ha
Total area	12,500 ha

5. ISSUES FACED

Unregulated Urban Development

Encroachment of urban settlements has only increased over Kolkata's history, and is one of the largest factors threatening the health of the wetlands. While environmentalists advocate the preservation of the wetlands, speculators are exerting increasing pressure for the right to develop areas for residential and industrial purposes. The wetland is bordered by the city of Kolkata to the west, Salt Lake township to the northwest, and the new township of Rajarhat to the north-east. The Eastern Metropolitan Bypass also runs along the western side of the wetlands making

the area easily accessible. In combination these factors are making it increasingly difficult to protect the EKW from developers and real estate agents. The various regulations for the conservation area are often flouted. Sonarpur, which has the maximum of 20 mouzas out of 32 mouzas that come under conservation, has witnessed greatest land conversions.

Table 5: Conversion of Some Bheris

Name of Bheries	Present Location
Bidyadhari Spill Cooperative Fisheries	Vidyasagar,Laboni B.S. Market
Knakrimari Bheri	Atomic Research Centre
Boro Bheri	Baisakhi, Digantika
Daser Bheri	Mayukh Bhavan
Nortala Khas Bheri	Salt
Kansar Bheri	Baisakhi Housing
Bager Bheri	Jhilmil
Kajar Bheri	Industrial Estate
Hansar Bheri	Industrial Estate

Uncontrolled Industrial Pollution

Of immediate concern for human health is the build up of some industrial pollutants, such as chromium in the wastewater. This toxic metal has been discharged by the numerous tannery operations previously located in the EKW. Though many of the tanneries have been relocated some still remain. Small scale industries are difficult to monitor and particularly prone to discharging toxic effluents, lead smelters are of particular concern for their heavy metal contamination. These toxins are taken into the fish populations, making the fish unsafe for human consumption at higher levels

Gradual Siltation

It has reduced the quantity of sewage flowing to the fisheries and made many of the fish ponds much shallower; consequently production has reportedly declined. Maintenance of required water-depth is needed for growth of quality spawn, fry, fingerlings.

Dwindling Wastewater Availability

Not only does siltation affect production by decreasing the volume of water in fishponds, it also prevents the effective distribution of wastewater. Uncertain wastewater supplies for aquaculture managers and seasonal water shortages are significant challenges. The Calcutta Drainage Outfall (CDO) division of Irrigation and Waterways department is in charge of sewage supply while KMC is responsible for pumping of water. There have been instances of failure to properly maintain sluice gates and run the pumping system regulating the storm weather flow and the dry weather flow channels of the Kolkata drainage system in line with the requirements of farmers in the area. As a consequence, sewage-fed agriculture is on the verge of collapse. A number of lift irrigation facilities installed on drainage channels which could have alleviated some of these problems are now mostly defunct.

Inconclusive Land Tenure

As mentioned earlier, there are various forms of ownership of sewage-fed fishponds in Calcutta. There is a small cluster of co-operative sewage-fed fishponds in the region.

Owner-managed fishponds are the oldest practice of wastewater-fed pond management in the wetlands. This form of management is, however, dwindling fast on account of then uncertainties that prevail in this area. Farmers tend to refrain from making significant investments in their lands and operations because of uncertainty about property rights and land holding, given intense development pressure.

Loss of Bio-diversity

Informal and illegal changes of land use threaten the ecological balance of the area, as do unplanned encroachments on the fringes of the region. In the marshy land east of Kolkata, 248 species of birds and 22 species of mammals were observed in the 1960s. More recent surveys have found the number of bird species reduced by almost 85 percent.

Various Governing Bodies

In the case of the EKW, the major agencies that should facilitate conservation and development include the Department of Land and Land Records, the Department of Irrigation & Waterways, the Ministry of Fisheries, Ministry of Agriculture, and the Department of the Environment along with West Bengal Pollution Control Board [WBPCB] and Institute of Wetland Management and Ecological Design [IWMED]. Participation of the Kolkata Municipal Corporation, Panchayats, District Administration of 24-Parganas (North) and 24-Parganas (South), various NGOs and CBOs (community-based organisations) is also required. East Kolkata Management Authority was formed in 2005 to look after the whole region. Management Plan for East Kolkata Wetlands was chalked out in 2008. It should be emphasised in this context that ground level coordination, control and management are often impeded because of the existence of a plethora of often contradictory legislation originating from different authorities.

Legislation affecting EKW

- The Environment (Protection) Act, 1986
- The West Bengal Inland Fisheries Act (amended in1993)
- The West Bengal Town and Country (Planning & Development) Act, 1979
- Water (Prevention and Control of Pollution) Act, 1974 (Amended 1988)
- The National Conservation Strategy and Policy Statement on Environment and Development of 1992
- The East Kolkata Wetlands (Conservation and Management) Act, 2006

Probable Solutions

- About 3 mt wide and 30-40 cm deep silt-traps are constructed at the edges of the ponds to trap some of the silt load and should be periodically.
- Water hyacinths by breaking up the surface waves those reduce the erosion of the pond banks and the method is much cheaper than the expensive alternatives like stone or concrete to strengthen the banks and also provide shade to fishes during the scorching summers.
- Fisheries do not provide year round employment as fish production drops during the winter months. So, to supplement the irregularity in income and to attract the young generation who are losing interest in pisciculture, part of the wetland can be launched as a site for eco-tourism. promoting picnic spots at Sukantanagar bheri, Natar bheri and involving local community in such projects.

Sustainability is another variable that has to be kept in mind. Close observation has revealed a complex array of problems and issues facing the wetlands community, economy and ecology. With the march of urbanisation the rural context is increasingly in transition, creating a complex socioeconomic parameter. Only by understanding this complexity and by ensuring the participation of all stakeholders related to the EKW, and in particular the traditional farming communities can any policy development or planning activity achieves success. Development and conservation cannot leave behind the populace for whom it is intended.

6. REFERENCES

Books:

Bunting, S., Kundu, N. and Mukherjee, M. Situation Analysis of Production Systems and Natural Resources in Peri-Urban Kolkata. Stirling, UK: University of Stirling, 2002

Ghosh, Dhrubajyoti, Ecology and Traditional Wetland Practice: Lessons From Wastewater Utilisation In The East Calcutta Wetlands, Worldview, 2005

Kundu, N. Planning the Metropolis, A Public Policy Perspective, Minerva Associates, Calcutta, India 1994

Martin, S. Reuse of Urban Waste Water and Human Excreta, EAWAG/ SANDEC, Switzerland, 2001

Papers in Journals:

Gupta, R. and Gangopadhyay, S. G., 'Peri-Urban Agriculture and Aquaculture', Economic and Political Weekly, Vol. 41, No. 18, 2006, pp. 1757-1760

Kundu, N. Planning for Aquatic Production in East Kolkata Wetlands, *Urban Agriculture Magazine*, RUAF, No. 14, 2005, pp.24-26

Raychaudhuri, S., Mishra, M., Nandy, P. and Thakur, A.R. 'Waste Management: A Case Study of Ongoing Traditional Practices at East Calcutta Wetland', American Journal of Agricultural and Biological Sciences 3 (1), 2008, pp.315-320

Reports:

'Assignment Report on Water Supply and Sewage Disposal: Greater Calcutta', World Health Organisation, 1960

Management of Urban and Peri-Urban Wetlands: A Rapid Appraisal Programme for Fragile Areas, IWMED, Kolkata, 1988

Workshop Proceedings:

Bunting, S., Kundu, N., Punch, S. and Little, D. East Kolkata Wetlands and Livelihoods Workshop Proceedings. Stirling, UK: University of Stirling, 2001

Edwards, Peter (2005) 'Waste Water Fed Aquaculture: State-of the-Art', Aquaculture and Aquatic Resources Management Programme, School of Environment Resources and Development, Asian Institute of Technology, 2005

BENS124

A Methodology for the Rapid Assessment of the Potential Impact and Hazard of Coal Seam Gas Mining on Aquifers and the Environment

John M. Bradd[a,*], Emma Kiekebosch-Fitt[b], Tim J. Cohen[c], Sam K. Marx[d], Solomon Buckman[e]

[a]**University of Wollongong**, Wollongong NSW 2522
E-mail address: jbradd@uow.edu.au

[b]**University of Wollongong**, Wollongong NSW 2522
E-mail address: emkf419@uowmail.edu.au

[c]**University of Wollongong**, Wollongong NSW 2522
E-mail address: tcohen@uow.edu.au

[d]**University of Wollongong**, Wollongong NSW 2522
E-mail address: smarx@uow.edu.au

[e]**University of Wollongong**, Wollongong NSW 2522
E-mail address: Solomon@uow.edu.au

ABSTRACT

The potential environmental impacts and hazards of coal seam gas mining in Australia are highly contentious and poorly understood. Concerns have been raised by communities, and the Australian government has incorporated management tools and strategies to address these concerns. The primary environmental issue associated with coal seam gas mining would be on the aquifers above the target coal seam. If the upper aquifers are affected in terms of quantity and quality, then there are cumulative impacts to the surface environment such as groundwater dependent ecosystems and surface waters. This paper will examine the Australian situation with regard to coal seam gas mining and present a methodology for rapid assessment of the potential impacts and hazards of coal seam gas extraction on aquifers and surface environments. A GIS analysis method for developing broad scale potential impact and hazard criterion for aquifers above the target coal zone are discussed. Current investigations and future research and development opportunities are explored.

1. INTRODUCTION

Coal Seam Gas (CSG) extraction is a thriving industry as an alternative source of non-renewable energy, particularly in eastern Australia where there are large coal reserves. There are indeed significant challenges for this industry as governments and community aim to keep the industry accountable for any potential impacts extracting this energy resource may have on the sub-surface (aquifers) and surface (land-vegetation-water) environments. To address the issues related to potential environmental impacts of CSG, the Australian Government are using a regulatory framework involving legislative and policy instruments that assist in managing the fine balance between economic, environmental and social issues.

Recently, the New South Wales (NSW) government launched the NSW Aquifer Interference Policy and Strategic Land Use Policy. The NSW Aquifer Interference Policy defines the protection of NSW aquifers, balancing the water use requirements of towns, farmers, industry and the environment. It details how potential impacts to aquifers should be assessed, and how this information is provided to the relevant planning process. As part of the Strategic Land Use Policy, all new major projects for mining or petroleum which have the potential to affect agricultural resources or industries must submit an Agriculture Impact Statement. Whilst these government regulatory instruments provide the framework for companies to be responsible for any potential impacts their CSG mining activities may have on the environment, each assessment should be underpinned by good scientific investigation on a case by case basis.

The objectives of this study were to provide a preliminary assessment of the potential impacts and hazards of CSG mining activities at a regional scale, and devise a rapid assessment methodology to determine basic criteria for estimating the potential impacts and hazards of CSG activities on the environment using the Sydney Basin as a case study.

2 SITE DESCRIPTION

The study area has been defined as three New South Wales Catchment Management Authority (CMA) areas; the Hawkesbury-Nepean, Sydney Metropolitan and the Southern Rivers (Figure 1), based on federal government funding initiatives. The Hawkesbury-Nepean and Sydney Metropolitan catchments completely lie within the Sydney Basin. Only the northern area of the Southern Rivers Catchments form part of the Sydney Basin. The Sydney Basin is a large sedimentary basin on the east coast of Australia covering almost 50,000 km^2. The Southern Coalfields and Western Coalfields lie within this basin. The Southern Coalfields affect all three CMA regions and the Western Coalfields affect the western section of Hawkesbury-Nepean region. The southern section of the Southern Rivers Catchment area is not affected by coal mining or CSG activity due to the lack of coal present.

The Sydney Basin is dominated by six major stratigraphic units that gradually thin from the centre of the basin to the margins. Overlying the intensely folded Palaeozoic basement lie the marine sediments and coal measures of the Talaterang and Shoalhaven Groups, which progressively thin from 1,000 m at the coast (near Nowra) to approximately 45 m thick at Tallong (50 km further west). The Talaterang Group is made up of the Clyde Coal Measures and the shallow marine Wasp Head Formation. Overlying the Talaterang Group is the 300 to 900 m thick Shoalhaven Group. Bowman, [1] and Eyles et al., [2] state that the Shoalhaven Group consists of lithic sandstones interbedded with shale and mudstone, which were deposited in a marine or marine-influenced environment.

At the top of the Shoalhaven Group, alternating layers of sandstones and siltstones are capped by volcanic rocks, and are interbedded with the upper Budgong Sandstone and the base of the Illawarra Coal Measures as detailed by Carr and Jones [3]. Above the Shoalhaven Group is the economically significant Illawarra Coal Measures. This 240m thick deltaic sequence consists of lithic sandstone units interbedded with thinner units of coal, sediments and shale. The maximum thickness of the coal

measures is 520m in the northern section of the coalfield according to Hutton [4].

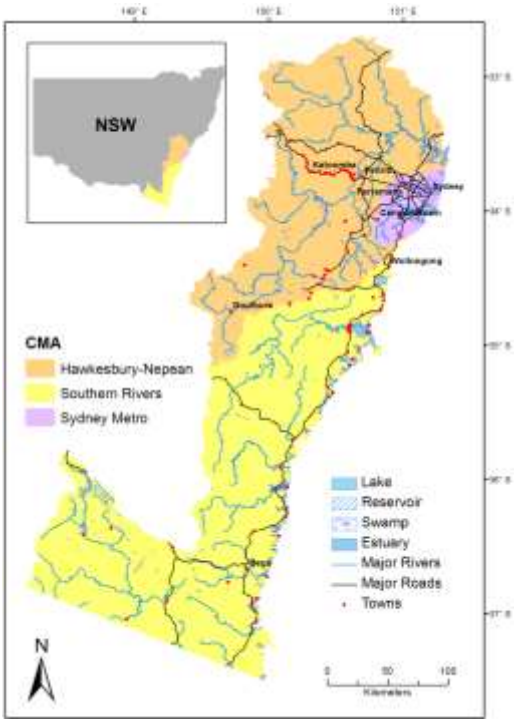

Figure 1. Investigation area highlighting the three catchment management areas.

The erosional surface at the top of the Bulli coal is overlain by the Triassic sequence, namely the Narrabeen Group and Hawkesbury Sandstone. The Narrabeen Group comprises lithic to quartz lithic sandstones, shales and claystones and has a thickness ranging from 300 to 500 m. This group also contains the Bald Hill Claystone unit, a largely continuous aquitard/aquiclude, capping the Narrabeen Group. The Bald Hill Claystone unit has been identified as an important impermeable unit in restricting the migration of water and gas into adjoining aquifer systems as discussed by Haworth [5].

3 COAL SEAM GAS EXTRACTION AND ANTICIPATED ENVIRONMENTAL IMPACTS

Evaluation of the aquifer and surface environment characteristics of the study area is possible by understanding the extraction process. In order to extract the gas from the coal seam, the pressure in the seam is reduced by pumping the groundwater from the coal seam. This dewatering process causes the vertical hydraulic gradient between lithologies to be potentially affected, depending on the degree of hydraulic connectivity (leakage coefficient) between lithological units. Hydrogeological characterisation of a CSG site, in particular the properties of permeability and porosity, are of fundamental importance in understanding and assessing potential impacts of CSG.

To release the gas, water must be extracted by drilling a well into the target coal seam, reducing the pressure and allowing the gas to flow. One of the major concerns raised in regards to drilling is the possibility of cross-aquifer contamination.

The clearing of surface vegetation to enable infrastructure development, such as access roads, can lead to a modification of surface water hydrology and a reduction in

habitat. The clearing of vegetation is likely to increase the extent of erosion and therefore has the potential to enhance stream sedimentation rates, resulting in degradation of water quality.

Hydraulic fracturing, or 'fracking', is the process by which a coal seam (or any other hydrocarbon-bearing deposit) can be 'stimulated' by forcing fluids at high pressure into the reservoir unit to create an artificial network of fractures and increase the permeability of a seam. The fluid is normally composed of water, a 'proppant' (typically sand) to hold the fractures open, and a chemical solution that will vary depending on the geology of the site (Rutovicz *et al.*, [6[). The consequences of fractures extending beyond the target coal seam include the possibility of fracking fluids entering overlying strata, possible cross contamination of aquifers, excess water production, and inefficient depressurisation of the coal seam according to Colmenares and Zoback [7].

4 A METHODOLOGY FOR RAPID ASSESSMENT OF POTENTIAL IMPACTS AND HAZARDS

4.1 Definitions and rationale

For the purposes of this study, 'impact' is defined as the likely level of effect on the environment if CSG is to occur based on pre-determined criteria. In this case, the predetermined criteria are based on the location of coal geology and geological fault density. 'Hazard' is defined as any source of potential damage, harm or adverse effect on the environment by existing or potential CSG activity (based on existing coal titles and current CSG activity). Based on this definition, hazard can only occur if there is a likely source (i.e. coal titles).

A defined objective criterion for assessing potential impact and hazard was used. Impact was divided into three basic categories of 'low', 'medium' and 'high'. Hazard was divided into three categories: 'existing', 'existing and potential expansion', and 'potential'. Existing refers to where current CSG activity is occurring, potential expansion refers to where there is a coal title but no current activity is occurring, and potential refers to areas where coal reserves exist but no titles are held.

Fractures form part of the potential impact criteria since fractures act to increase the permeability and connectivity of the strata overlying the target coal seam. Consequently, increased fracture density in an area has the potential to increase the impact of CSG. According to CSIRO [8], coal seam gas is typically extracted from coal seams at depths of 300 to 1000 m. Generally at shallower depths CSG would be expected to have naturally vented from the coal seam to the surface through permeable overlaying bedrock fractures and faults. It is therefore reasonable to assign a low CSG potential impact when the depth to the coal seam is 0 - 200 m, as it has previously been released to the environment.

4.2 Data

Geospatial datasets for the study area were obtained from government agencies including primary and derived Geographical Information Systems (GIS) layers. NSW Statewide Geology data based on the 1:250 000 geological map sheets, was the primary dataset for determining the spatial distribution of geological units, particularly coal. Coal depth was determined from the Department of Primary

Industries geological contour maps expressing depth to each geological unit. In addition, fault and fracture GIS data was used in the analysis of potential impacts also.

Aquifer data was collated from both borehole data and derived GIS layers including Groundwater Management Areas (GWMAs). The boredata was collated from the NSW Office of Water's "Pinneena" dataset. GWMAs were also based on the geology primary dataset. Since geology is the key data for the assessment, a description of the geology and hydrogeology is presented below.

4.3 GIS Analysis Methodology

The impact assessment was performed using GIS analysis based on the criteria described previously for the decision rules. For the potential impact assessment, the Triassic sediment thickness was used as a proxy for the depth to the top of the Permian coal measures and reclassified into the three depth categories: 0 - 200, 200 - 500 and >500 m. Fault density was determined using the ArcMap tool 'Line Density', which calculates the density of linear features in the neighbourhood of each unit area. Here, a large radius parameter was chosen to produce a more generalised fault density map. The fault density was then classified into areas of high, medium and low density. This was a method based on natural groupings of data values and was determined statistically by finding adjacent feature pairs, between which there was a relatively large difference in data values. The decision matrix for CSG potential impact is presented in Table 1.

Table 1: Decision matrix for CSG impact using thickness of the Triassic formation and fault density

	Triassic Sediment Thickness (m)			
Fault Density	***0-200***	***200-500***	***>500***	***No Triassic strata found in area***
High	Low	High	High	Low
Medium	Low	High	Medium	Low
Low	Low	Medium	Medium	Low

A GIS hazard layer was created based on the classification matrix shown in Table 2 by overlaying the coal titles with the spatial extent of the Permian coal measures. This simple analysis resulted in a layer defining areas which contained current coal titles (existing hazard), Permian coal measures (potential hazard), both (existing and potential expansion) or none (no hazard).

Table 2: CSG and coal mining extraction hazard identification matrix based on the presence of Permian lithology and the existence of current coal titles (currently mined or not mined)

	Permian Coal Measures	
Coal Title	***Present***	***Not Present***
Present + current mining	Existing	No hazard

Present + not mined currently	Potential Expansion	No hazard
Not present	Potential	No hazard

The hazard assessment of CSG mining on aquifer and surface environments was based on location of current coal mining titles and the location of the Permian coal measures. An existing hazard was defined as an area that contained a current coal mining title. An area was classified as a "potential expansion" hazard when it fell within the boundary of the Permian coal measures but did not contain a current coal mining title. GWMAs classified as "existing" and "Potential" hazard refer to GWMAs that fall into areas containing both existing and potential hazards. These can be considered areas where expansion of a current lease is possible. It was considered that there is no hazard for aquifers and surface environmental features where Permian coal measures and thus no coal titles existed.

5 RESULTS AND DISCUSSION

The likely impacts on groundwater, surface water and ecosystems vary according to the hydrogeological characteristics, the proximity to CSG mining, the amount of groundwater extraction and the extent of the aquifer connection. Figure 2 shows the potential impact associated with CSG mining on groundwater based on the scale of groundwater management areas. At this scale of data analysis, the level of impact on groundwater management areas is spatially broad since analysis is based on lithological information associated with coal depth and geological fault/fracture density. A high CSG impact will be associated with coal lithology below 500 m depth and high fracture density. This will mean that the total spatial extent of a groundwater management area will be shown as a high impact area even if only part of the area has those particular lithology and fracture density characteristics. In regard to hazard to coal seam gas extraction, the analysis was based on current coal titles and presented in Figure 3. If a coal title was found to lie within a groundwater management area, the whole groundwater management area would be indicated as having a high hazard. This limitation is based on the scale issue of regional datasets.

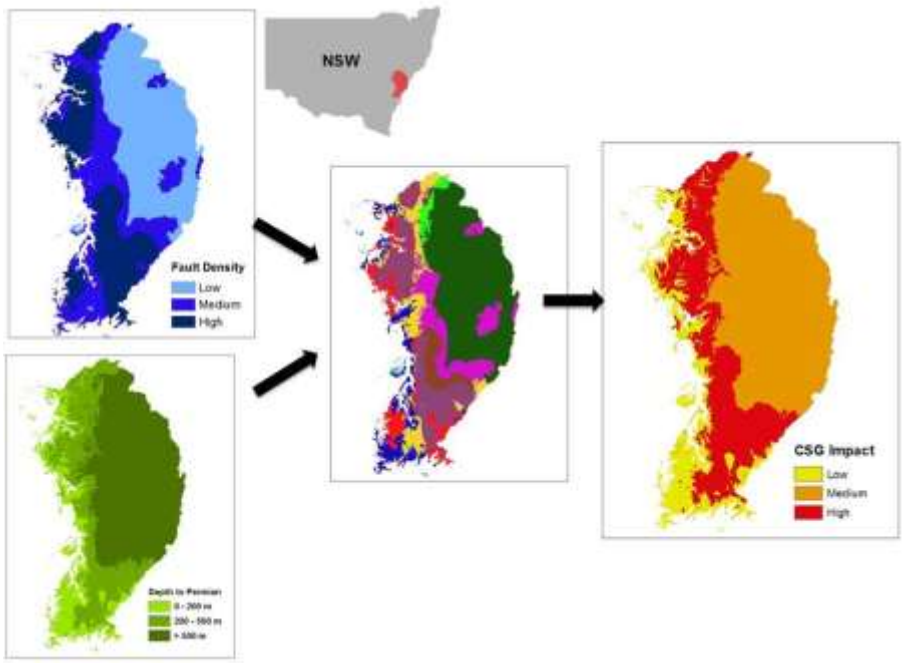

Figure 2: An illustration of the GIS analysis process and the resulting GIS potential impact layers for Coal Seam Gas within the Sydney Basin. The full study area has not been included since that any area beyond the coal measures boundary was assumed to be low impact.

Based on the specified GIS analysis described previously, the aquifers that have high hazard from both current operations, and from the potential to expand, are the shallow Hawkesbury-Nepean alluvial aquifer associated with the main river systems of the Hawkesbury-Nepean catchment, and the deeper Hawkesbury Sandstone aquifer that lies above the Southern Coalfields. Both aquifer systems provide reliable yields for stock and domestic use as well as in some cases irrigation for agriculture. In the northern area of the Southern Rivers CMA, most of the Hawkesbury-Nepean CMA and Sydney Metropolitan CMA, aquifers have a high existing and potential hazard from CSG extraction.

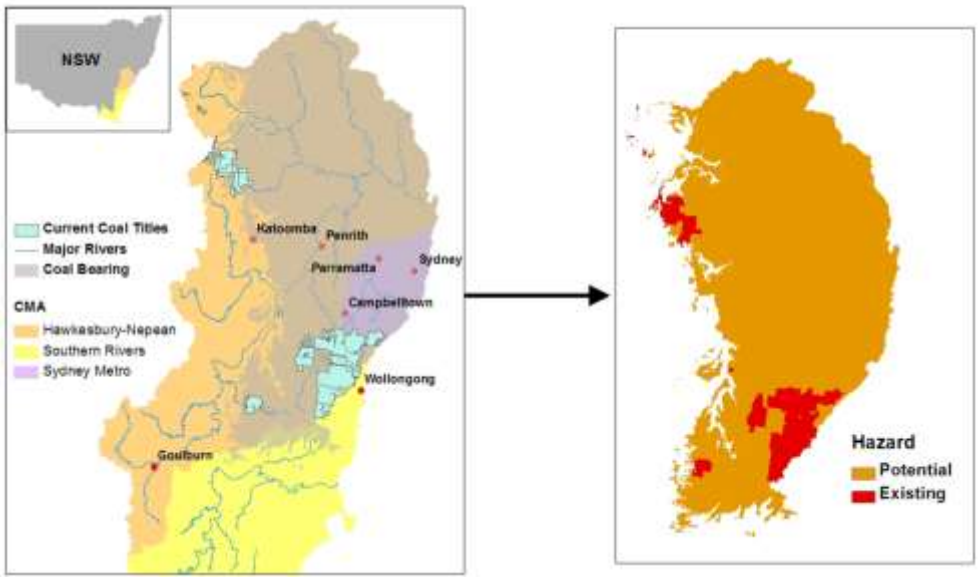

Figure 3: The resulting GIS hazard layer developed from locations of current coal

titles and the extent of Permian coal measures. Aquifers and environmental features that do not fall within the limits of potential or existing hazards are classified as 'No Hazard.'

6. CONCLUSION

The results of this initial rapid assessment of potential impacts and hazards of CSG activity on aquifers and the surface environment, and the associated GIS analysis, will provide government a useful tool for implementing environmental management strategies. It is recommended that areas within the study area identified as having a high potential impact should require a more detailed level of environmental impact assessment than an area with medium or low potential impact. These high areas occur where coal seams are at least 200m below ground level and where significant fracture density occurs. Existing hazard areas for CSG relate to where CSG titles (or coal mining titles) currently occur.

It is suggested that future research and development should focus on collecting data on aquifer/aquitard characterisation through pumping test analysis in order to determine leakage coefficients. This would enable a better understanding of the hydraulic connectivity between aquifers just above the CSG target coal seam and subsequent connection to surface water systems. This would give more confidence in model input parameters which ultimately guide the decision making process for whether a CSG mining activity should go ahead or not.

7. ACKNOWLEDGMENTS

A number of people contributed to various phases of the investigation and are gratefully acknowledged; Heidi Brown, Emma Burkhart, Ashlee Clarke, Nicole Cook, Stephen Cullen, James Daley, Alexi Gavin, Ren Hu, Matt Lemcke, Andrew Lowe, Thomas McMahon, Luke McNeilage, Kaitlyn O'Mara, Garth Nagle, Sam Robson, Carolyn Silveri, Joe Stammers, and Mick Stevens. The work was funded as a consultancy through the Southern Rivers, Hawkesbury-Nepean and Sydney Metropolitan Catchment Management Authorities under the Federal Government Bioregional Assessment Program administered by the Department of Sustainability, Environment, Water, Population and Communities (SEWPaC).

8. REFERENCES

[1] Bowman, N. Southern Coalfield, Upper Shoalhaven Group, and Illawarra Coal Measures. In *Herbert, C & Helby, R. (Eds) A Guide to the Sydney Basin*, Department of Mineral Resources, Geological Survery of New South Wales, 1973.

[2] Eyles, C., Eyles, N & Gostin, V. Facies and allostratigraphy of high-latitude, glacially influenced marine strata of the Early Permian southern Sydney Basin, Australia. *Sedimentology,* 1998 Vol. 45 pp121-162.

[3] Carr, P. & Jones, B. The influence of paleoenvironment and lava flux on the emplacement of submarine, near shore Late Permian basalt lavas, Sydney Basin (Australia). *Jn of Volcanology and Geothermal Research.* 2001, Vol 38, no. 2, pp313-328.

[4] Hutton, A. Geological setting of Australasian coal deposits. In *Kininmonth, R. & Baafi, E (eds.) Australasian Coal Mining Practice.* Carlton, Victoria: The Australasian Institute of Mining and Metallurgy. 2009.
[5] Haworth, R. The shape of Sydney by its urban geology. *Quaternary International,* 2003, Vol 103, pp41-55.
[6] Rutovicz, J., Harris, S., Kuruppu, N. & Dunstan, C. Drilling down. Coal Seam Gas: A background paper. *Institute for Sustainable Futures, University of Technology.* 2011.
[7] Colmenares, L.B. & Zoback, M.D. Hydraulic fracturing and wellbore completion of coalbed methane wells in the Powder River Basin, Wyoming: implications for water and gas production. *AAPG Bull,* 2007, No. 1, pp51-67.
[8] CSIRO. What is coal seam gas? Viewed 22 October 2012, http://www.csiro.au/news/coal-seam-gas>.

BENS152

Abatement of Gaseous and Dust Air Pollutants by A Gas-Liquid Contacting Towers

B. C. Meikap
University of Kwazulu-Natal, Department of Chemical Engineering, UKZN,
Durban, South Africa
E-mail address: meikap@ukzn.ac.za

Air pollution is considered to be most dangerous among the pollutants as it has no boundaries and becomes uncontrollable once emitted. There are varieties of matter emitted into the atmosphere by natural and anthropogenic sources. Typical pollutants include particulate matter such as ash, smoke, dust, fumes, mist and spray; inorganic gases such as sulfur dioxide, hydrogen sulfide, nitric oxide, ammonia, carbon monoxide and hydrogen fluoride; olefinic and aromatic hydrocarbons; and radioactive compounds. They originate from burning of fossil fuels and other industrial activities like, mineral processing, transportation and transformation. Thus, the air pollution is a man-made pollution that had its origin at the time of invention of fire itself.

The evolution of air pollution from its sources to its areas of impact is governed by transport and transformation. Acids, smog and dust explosions are the common consequences of air pollution. These fine particles can be emitted by many sources like tailpipes of vehicles, smoke stacks and chimneys of both residential and industrial parks [C. Seigneur 2005]. The particles smaller than 2.5microns are denoted as PM2.5, these are associated with a range of respiratory and cardiovascular disease. Several epidemiological studies have indicated a strong association between elevated concentrations of inhalable particles (PM10) and increased mortality and morbidity It also influences many atmospheric processes including cloud formation, visibility, solar radiation and precipitation, and plays a major role in acidification of clouds, rain and fog . The National Ambient Air Quality Standards for particulate matter, based on human health impacts are as follows: for PM2.5, the three year average of 98th percentile of 24 hour average concentrations at each population-oriented monitor must not exceed 65 µg / m-3, and the three year average arithmetic mean concentration from single or multiple community-oriented monitors must not exceed 15 µg / m-3. For PM10, the fourth highest 24-h concentration over 3 years must not exceed 150 µg / m-3, and the three year average annual mean concentration must not exceed 50 µg / m-3.

Due to stringent emission standards (150mg/Nm3) laid by State and Central Pollution Control Boards in regard with the EPA standards, almost all these units have installed electrostatic precipitators having almost 99% efficiency in removing the fine dust particles. In spite of installing the particulate control equipments, certain technical limitations like in coal based DRI rotary kilns; dense fume is directly emitted through kiln cap during startup period of the kiln for a period of 8 to 10hrs.

Wet scrubbers are used to remove either gaseous or particulate contaminants from effluent gas streams. A very high percentage removal of SO2 can be achieved from air–SO2 mixture in the modified multi-stage bubble column without using any additives or pre-treatment .

Wet scrubbers remove particles from gas streams by capturing the particles in liquid droplets or in sheets of scrubbing liquid (usually water) and then separating the

droplets from the gas stream. Several process variables affect particle capture; they include particle size, the size of liquid droplets, and the relative velocity of the particle and the liquid droplets, with particle size being the most important parameter. In general, larger particles are easier to collect than smaller ones. The key to effective particle capture in a wet scrubber is creating a mist of tiny droplets that act as collection targets: usually, the smaller the droplet and the more densely the droplets are packed, the better the ability to capture smaller-sized particles

In the present study a gas-liquid contacting wet scrubber have been used to simultaneously remove the dust and gaseous pollutants from industrial flue gases. It has been found that in spray scrubbers many parameters like the size range, velocity and concentration of the particles at which they are emitted at the source, the operating parameters like the droplet size, velocity, droplets population density, residence time and temperature of the scrubbing liquid influences the particle scrubbing efficiency. The experiments conducted on the scrubbing of particulate matter (fly-ash) in spray a spray scrubber using water droplets as scrubbing liquid. Results indicate that a removal efficiency of around 93% was achieved which can bring down the pollution load to a considerable level.

BENS205

High dominance of hydrogenotrophic methanogens in three different full-scale anaerobic sewage sludge digesters

Jaai Kim[a], Changsoo Lee[b,*]
[a]School of Urban and Environmental Engineering, Ulsan National Institute of Science and Technology (UNIST), Ulsan 689-798, Republic of Korea
E-mail address: jaai@unist.ac.kr

[b]School of Urban and Environmental Engineering, Ulsan National Institute of Science and Technology (UNIST), Ulsan 689-798, Republic of Korea
E-mail address: cslee@unist.ac.kr

EXTENDED ABSTRACT

Due to the ability to stabilize pollution load and produce methane simultaneously, anaerobic digestion (AD) is today gaining increasing attention with the increasing demand for protecting the environment and developing alternative energy sources. AD is a series of biological reactions mediated by extremely diverse microbes which can be broadly grouped into hydrolyzing/acidifying bacteria (acidogens) and methane-producing archaea (methanogens). Performance of an AD process basically depends on the concerted activity of microbes involved and, therefore, a good understanding of the underlying ecology is required for stable and efficient AD. However, our understanding of AD at the microbial community level is still limited, potentially leading to process upset or failure in field-scale anaerobic digesters.

Recent development and application of culture-independent molecular techniques provided useful tools to explore microbial communities in complex mixed-culture environments. Such approaches have more recently been extended to studies of waste/wastewater environments including AD, leading to a better insight into AD microbial ecology. However, although our knowledge of AD microbial ecology has been extensively improved in some points, the majority of previous studies have been limited to non- or partly quantitative approaches that often lead to difficulties in comparing community structures of different ecosystems. Although many studies on AD microbial community have recently been made using quantitative and/or qualitative approaches to better understand the process fundamentals, to our knowledge, little has been reported on the investigation of both quantitative and qualitative microbial community structures in full-scale sewage sludge digesters. Given that the treatment of sewage sludge is the major practical application of AD today, this knowledge gap deserves more research attention.

This study therefore investigated the quantitative and qualitative microbial community structures in three full-scale anaerobic digesters (D1–D3) treating domestic or industrial sewage sludge of different origins: D1 and D3 treating domestic sewage sludges from treatment plants A and B, respectively, and D2 co-digesting waste oil and grease (WOG) collected from local restaurants and industrial sewage sludge from plant A. Different molecular techniques, denaturing gradient gel electrophoresis (DGGE) for qualitative analysis and real-time polymerase chain reaction (PCR) for quantitative analysis, were simultaneously applied to examine AD microbial communities. Eight out of eleven bacterial DGGE sequences

were not affiliated with known species (<97% sequence similarity). A sequence among them was not even assigned to any known phylum, indicating that this population might represent a novel bacterial lineage. The other seven were classifiable at the phylum level but showed poor sequence similarities of < 94% to any known species. One of them, detected only in D2, was affiliated with the order *Clostridales* which is a metabolically highly versatile group involving several species capable of producing lipase and degrading long-chain fatty acids under anaerobic conditions. This indicates that the microbe corresponding to this band sequence may be involved in the degradation of WOG in D2. On the other hand, all eleven archaeal sequences were assigned to known methanogen species (≥97% sequence similarity) belonging to only two orders: seven to hydrogenotrophic *Methanomicrobiales* and four to aceticlastic *Methanosarcinales*. All *Methanosarcinales*-related sequences were assigned to the geneus *Methanosaeta* feeding only on acetate, indicating that *Methanosaeta* strains are responsible for acetate-utilizing methanogenesis in all digesters. Among the *Methanomicrobiales*-related microbes, on the other hand, *Methanospirillum* and *Methanolinea* strains were suggested to be the major drivers of hydrogen-utilizing methanogenesis in D1 and D2 and in D3, respectively.

The clustering analysis of DGGE profiles showed that the archaeal community structures in D1 and 2 were closely related (Dice similarity index (S_D), 87.5%), with D3 being remotely related to the others (S_D, < 51.2%). The high similarity between D1 and D2, may be attributable to the use of D1 sludge for starting up of D2. The distant relationship of D3 to D1 and D2 reflects the alternative occurrences of *Methanospirillum*- and *Methanolinea*-related bands. The bacterial community structures in three digesters were distantly related to one another with fairly even distances (S_D, 62.5-64.3%), indicating no significant influence of the initial inoculation of D2 with D1 sludge. This may be due to the much more diverse and dynamic nature of bacteria than archaea in AD environments.

Real-time PCR assay revealed that, based on the 16S rRNA gene abundance, *Methanomicrobiales* overwhelmingly dominates the methanogen community (>94% of the total methanogen population) in all digesters. This is in agreement with the archaeal DGGE results showing the dominant occurrence of *Methanospirillum*- and *Methanolinea*-related bands in all digesters. Hydrogenotrophic methanogens, particularly *Methanomicrobiales* populations, are therefore likely the main drivers of methanogenesis in the digesters studied regardless of the different feeds. Intriguingly, our observation is contrary to the conventional understanding that aceticlastic methanogens generally dominate methanogen community in stable anaerobic digestion environments, suggesting the need for further studies on the behaviors of and interactions between different trophic groups of methanogens under different substrate conditions.

Keyword: Anaerobic digestion; hydrogenotrophic methanogens; microbial community structure; sewage sludge; waste oil and grease (WOG)

Acknowledgements

This work was supported by the 2012 Research Fund of Ulsan National Institute of Science and Technology (UNIST) through a Future Challenge Project.

BENS165

The Usage Of Water Steam Data Provided From GNSS in Meteorology

Seyit Ali Yilmaz
Selçuk Üniversitesi, Türkiye
E-mail adrress: seyit@selcuk.edu.tr

ABSTRACT
The data obtained from Constant GBS (SGBS) networks which are established generally for the aim of geodesic, geodynamic and navigation studies also contribute to the meteorological studies.
In this study, hourly temperature and pressure values measured by present meteorological sensors in SGPS stations as well as water vapor values (PWV) that can be converted into rain by taking the advantage of GPS observations will be calculated for Middle Anatolian Region. The values of GPS_IPWV obtained as a result of calculation will be confirmed with the radiosonde data and will also be compared with MM5 weather forecast model results used in State Meteorological Service (DMI). This study, which covers Middle Anatolian Region, will be carried out by using the data belonging to two radiosonde stations of DMI that are present in Ankara and Isparta.
In this study, the consistence between PWV values calculated from GPS values and PWV values obtained from MM5 model and radiosonde will be examined. It is evaluated with this preliminary study that the GPS meteorology studies which has been just present in Turkey will be more economical and meaningful from the point of both geodesy-geophysicist and meteorologists to use present station data of DMI instead of establishing a meteorology sensor in every SGPS station in order to use for GPS calculations.

Natural Sciences I

Pullman Bangkok King Power, 2F Meeting Room BETA I

2013/1/26 Saturday 13:00-14:30

Session Chair: Norman Y. S. Woo

BENS74

Production of Ampiphilic Surfactant Molecule from Saccharomyces Cerevisiae Mtcc 181 and Its Protagonist in Nanovesicle Synthesis

Akila Srv | *St. Josephs College of Engineering*

BENS79

Expression of Cystic Fibrosis Transmembrane Regulator in Osmoregulatory Tissues of Sea Bream

Norman Y. S. Woo | *The Chinese University of Hong Kong*

Teresa W. S. Yuen | *The Chinese University of Hong Kong*

BENS88

Alternative Energy Resource and Power Generation in Selected Block of Hugli, West Bengal

Lopamudra Basu | *Sivanath Sastri College*

BENS89

Environmental Conditions Vulnerable to Fluoride Contamination of Drinking Water in Parts of Birbhum District and Impact on Human Health

Bhaswati Ray | *Sivanath Sastri College*

BENS96

The Scenario-based Water Release of Caldera Lake in Mt Baekdusan Volcano Eruption

Khil Ha Lee｜*Daegu University*
Sung Wook Kim｜*GI Co Ltd.*
Sang Hyun Kim｜*Pusan National University*
Sung Hyo Yun｜*Pusan National University*

BENS81

Cloning of Lipase Gene from a Thermophilic Bacterium

Rashidah Abdul Rahim｜*Universiti Sains Malaysia*
Liong Jia Hui｜*Universiti Sains Malaysia*
Darah Ibrahim｜*Universiti Sains Malaysia*

BENS74

Production Of Ampiphilic Surfactant Molecule From Saccharomyces Cerevisiae Mtcc 181 And Its Protagonist In Nanovesicle Synthesis

Akila Srv
St. Josephs College of Engineering
Email: akitzu93@gmail.com

ABSTRACT
Microbial expel appears to nurture in the field of medicinal sciences. Surface active compounds from microbes though imply in several areas, its biodegradability and amphillic property outspread greatly in improving drug delivery. Current work transmit on applicability of biosurfactant in nanovesicle synthesis, saccharomyces cerevisiae was proficient in producing biosurfactant using groundnut oil as a carbon source. Chemical structure was predicted to be lactonic sophorolipid using FTIR, HPTLC and GCMS analysis. Property of biosurfactant was determined using oil displacement test and Emulsification index. Nanovesicle was synthesised using cholesterol and biosurfactant in equal proportion by hand shaking method. SEM analysis was used to determine shape and size of the nanovesicle. Surface charge and size of the vesicle was evaluated by Zeta potential measurement. Biosurfactant displays emulsification property and its amphillic structure proficient in vesicle shape, size and stability. We effectively studied the vesicle forming ability of biosurfactant and this is the first report on the prospect of extracellular secretion of biosurfactant from Saccharomyces cerevisiae. Glycolipid of this yeast appears to support nanovesicle formation and this formulation can be exploited for better drug entrapment and release kinetics in the field of Pharmaceutical sciences.

Keywords: Bio surfactant, Saccharomyces cerevisiae, Emulsifier, Sophorolipid, Nano vesicle Drug entrapment

1. AIM

Aim of this work is to produce surfactant from Saccharomyces cerevisiae and its application in nanovesicle synthesis.

(I). Production and purification of Biosurfactant

(II). Physicochemical characterization of Biosurfactant

- Oil displacement test
- Emulsification index

(III). Identification of molecules by Thin layer Chromatography

- Thin layer chromatography for protein
- Thin layer chromatography for lipid
- Thin layer chromatography for carbohydrate

(IV). Quantification of Biosurfactant

- Estimation of protein by Lowry's method:
- Estimation of Carbohydrates by Phenol Sulphuric acid method
- Estimation of Lipid by Vanillin Sulphuric acid:

(V). Structural characterization of Biosurfactant

- High performance thin layer chromatography
- Fourier transform infrared spectroscopy
- Gas chromatography Mass spectroscopy

(VI). Application of Biosurfactant from *Saccharomyces cerevisiae* in Nanovesicle synthesis

- Synthesis of Nanovesicle by hand shaking method
- Morphological identification by optical microscopy
- Size and shape Analysis by Scanning Electron Microscopy
- Size and charge analysis by Zeta potential

2. MATERIALS AND METHODS

MATERIALS:

Microorganism and Media

Saccharomyces cerevisiae MTCC181 was used in this study. It was obtained from Microbial Type Culture Collections (MTCC), Chandigarh, India. The organism was maintained on YPD agar slant at 4^0C and it was sub cultured periodically.

Chemicals

Chemicals used in the analysis were of laboratory grade. It was purchased from Lobachemie Pvt. Ltd, Mumbai, India and Merck chemicals, India.

METHODOLOGY

Cultivation of microorganism

25ml of yeast extract peptone dextrose broth was prepared, sterilized, inoculated with fresh culture of *Saccharomyces cerevisiae* MTCC181and was incubated at 300Cfor 24 hrs. This is the seed culture for the production of surfactant.

Production of biosurfactant (Cooper, D.G *et al.*, 1983)

Mineral salt medium was prepared, Sterilized, inoculated with 5% seed culture of *Saccharomyces cerevisiae* MTCC181 and it was kept for shaking at 150 rpm for 4 days. The biomass was separated by centrifugation at 8,000 rpm for 15 minutes; the supernatant was collect for screening of surfactant.

Screening of surfactant by oil displacement test (Suppasil Maneerat *et al*., 2007)

The selected strains were compared by measuring of the diameter of the clear zones occurred when a drop of a biosurfactant-containing solution was placed on an oil-water surface.50 ml of distilled water was added to a large petri dish (15 cm diameter) followed by the addition of 20 µl of crude oil to the surface of water and 10 µl of supernatant of culture broth was added. The diameter of clear zones of triplicate assays from the same sample was determined.

Emulsification index (e24) (David Cameron *et al.*, 1988)

The emulsifying capacity was evaluated by an emulsification index (E24). The E24 was determined by adding 2 ml of mustard oil and 2 ml of the sample in test tube. It was vortex at high speed for 2 min and allowed to stand for 24hours.The E24 index was given as percentage of the height of emulsified layer (cm) divided by the total height of the liquid column (cm).

The percentage of emulsification index was calculated by using the following equation.

$$E24 = \frac{\text{Height of emulsion formed x 100}}{\text{Total height of solution}}$$

Purification of Biosurfactant by Solvent Extraction (Salwa Mohd Salleh *et al.*, 2011)

The culture was centrifuged at 12000 rpm, and the cells were removed. The supernatant was extracted with a mixture of the extraction solvents with the following ratio methanol/chloroform/1-butanol, 1:2:1 by Vol). The mixture was kept in magnetic stirrer for 6hrs at 200 rpm. After 6hrs 2 layer of precipitation were obtained. The upper layer was discarded. Lower layer was collected, and the pH was converted in to acidic (pH 2) using 6N hydrochloric acid. And it was further purified using ice cold acetone in the ratio of 1:4, and kept refrigerated at 4^0C for 12 hrs. Precipitate was separated by centrifugation at12000 rpm for 15min, further the precipitate was dried in hot air oven for overnight.

Identification of molecules by Thin Layer Chromatography

Principle

TLC is based on the principle of separation. The separation depends on the relative affinity of compounds towards stationary and mobile phase. The compounds under the influence of mobile phase (driven by capillary action) travel over the surface of stationary phase, during this movement the compounds with higher affinity to stationary phase travel slowly while the others travel faster. The separation of components in the mixture is achieved by TLC method.

Once separation occurs components are visualized as spots at respective level of travel on the plate. Their nature or characters were identified by means of suitable detection techniques.

a. Identification of amino acid by TLC method was followed according to Saeger, S *et al.,* 2005

b. Separation of lipids by TLC method was followed according to Christie, W.W**.** *et al*, 2010.

c. As far as carbohydrate separation is concerned, the procedure given by G. Walker *et al*., 1964 was followed.

Quantification of Biosurfactant

A. Estimation of protein by Lowry's Method (Lowry *et al.,* 1951)

Principle

The phenolic group of tyrosine and tryptophan residues (amino acid) in a protein will produce a blue purple color complex, with maximum absorption in the region of 660 nm wavelength, with Folin- Ciocalteau reagent which consists of sodium tungstate molybdate and phosphate. Thus, the intensity of color depends on the amount of these aromatic amino acids present and will thus vary for different proteins.

Procedure

0.1, 0.2, 0.3, 0.4 and 0.5ml of the working standard was pipetted out into a series of test tube. 0.02ml, 0.04ml, 0.06ml of the sample was pipetted out in two other test tubes. Make up the volume to 1ml in all the test tubes. A tube with one ml of water serves as the blank. Add 3ml of alkaline copper reagent to each tube including the blank. Mix well and allow standing for 10min, and then add 0.5ml of Folin's Ciocalteau reagent, mix well and incubate at room temperature in the dark for 30min. Absorbance was

measured at 660nm in spectrophotometer. Plot the absorbance against protein concentration to get a standard calibration curve.

B. Estimation of Lipid by Phospho - Sulfo Vanillin reagent (Jacques Izard *et al.*, 2003)

Principle

Lipids react with sulfuric acid to form carbonium ions which subsequently react with the vanillin phosphate ester to yield a purple complex that is measured photo metrically.

Procedure

0.02ml, 0.04ml, 0.06ml of the sample was mixed with 3ml of vanillin reagent. Make up the volume to 1ml in all the test tubes. A tube with one ml of water serves as the blank. And it was well vortex, Heated at 95°c for 10 mins. Then it was later cooled. Absorbance was observed at 536nm after incubated at 40°c for 15mins in spectrophotometer.

C. Estimation of Carbohydrate estimation by Dinitro Salicylic acid method (DNS) method (Miller, 1972)

Principle

This method tests for the presence of free carbonyl group (c=o), the so called reducing sugar. This involves the oxidation of the aldehyde functional group present in the sample, for example; in glucose and the ketone functional group in fructose. Simultaneously 3, 5 dinitrosalicylicacid (DNS) is reduced to 3amino, 5 nitro salicylic acid under alkaline conditions.

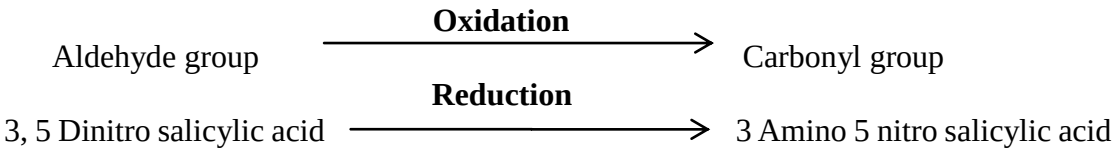

The above reaction scheme shows that one mole of sugar will react with one mole of 3, 5 dinitrosalicylicacid. Different reducing sugars generally yield different colour intensities; thus it is necessary to calibrate for each sugar. In addition to the oxidation of the carbonyl groups in the sugar, other side reactions such as the decomposition of sugar also compete for the availability of 3, 5 dinitrosalicylicacid.

Procedure

3ml of DNS reagent was added in 0.02ml, 0.04ml, 0.06ml of the sample in a test tube. Make up the volume to 1ml in all the test tubes. A tube with one ml of water serves as the blank. Heat the mixture at 90º C for 5-15 minutes to develop the red-brown color, and 1 ml of a 40% potassium sodium tartrate (Rochelle salt) solution was added. After cooling to room temperature in a cold water bath, record the absorbance with a spectrophotometer at 575 nm.

High performance thin layer chromatography

HPTLC were performed on CAMAG Linomat 5 “Linomat 5_ 150423” using HPTLC silica gel 60F254 plate as stationary phase with plate size of 8x 10 cm, chloroform and methanol (2:1) used as solvent system.

Fourier Transform Infrared Spectroscopy (FTIR) (Nelly Christova *et al*., 2003)

Principle

Infrared spectroscopy has been a workhorse technique for materials analysis in the laboratory for over seventy years. An infrared spectrum represents a fingerprint of a sample with absorption peaks which correspond to the frequencies of vibrations between the bonds of the atoms making up the material. Because each different material is a unique combination of atoms, no two compounds produce the exact same infrared spectrum. Therefore, infrared spectroscopy can result in a positive identification (qualitative analysis) of every different kind of material. In addition, the size of the peaks in the spectrum is a direct indication of the amount of material present. With modern software algorithms, infrared is an excellent tool for quantitative analysis.

Procedure

One milligram of purified biosurfactant was ground with 100mg of Potassium bromide and pressed with 7500 kg for 30 sec to obtain translucent pellet. The infrared spectra were recorded on Bruker Optics FT-IR system within the range of 500 to 4000 cm-1 wave number.

Gas chromatography and Mass spectroscopy

Principle

Gas-Liquid chromatography - involves a sample being vapourised and injected onto the head of the chromatographic column. The sample is transported through the column by the flow of inert, gaseous mobile phase. The column itself contains a liquid stationary phase which is adsorbed onto the surface of an inert solid.

Procedure

Surfactant sample meant to acid hydrolysis, further it is dissolved in 80% ethanol and then injected(1µl) in to GC-MS-QP 2010 [Shimadzu] equipped with the capillary inlet and the mass selective detector, set scan from 40 – 1000 m/z at a scan rate of 1.2 scans per second. The capillary column used was a VF-5ms of length 30m, diameter 0.25mm and full thickness 0.25um. Column oven temperature was 70^{o}C with the injector temperature of 240^{o}C.The oven temperature was programmed from 70^{o}C to 300^{o}C for 3min.The ion source temperature was set to be 200^{o}C and the interface temperature was 240^{o}C. The carrier gas helium at a flow rate of 1.5ml/min with spilt ratio set as 10.

Preparation of Nanovesicles in Hand shaking method (Mohamed S. El-ridy *et al.*, 2012)

10mg of Biosurfactant sample and 10 mg of cholesterol i.e. 1:1 ratio in round bottom flask. Dissolve the mixture well in ether. Evaporate the solvent at room temperature. Adapt the flask to the temperature of 50 to 60◦C and Shake well for about 15 minutes. Store the formulation in refrigerator for further process.

Characterization of Nanovesicle by optical microscopy

A drop of Nanovesicle solution was placed over a clean glass slide, and it was observed under microscope.

Scanning Electron Microscopy analysis of Nanovesicle

SEM is capable of magnifying images up to 200.000 times achieving high resolution pictures of the surface and determining the size distribution of Nanovesicle.

The dehydrated Biosurfactant were dispersed in ethanol before analysis. The morphology of the synthesized biosurfactant was characterized by SEM (Hitachi

S4800, Japan) using an accelerating voltage of 0.1–30 kV.

Measurement of zeta potential

Nanovesicle sample was set at a power level of +200 V by an ultrasonic generator (Sonics-Vibracell ultrasonic processor). Size and surface charge of vesicle were measured at room temperature (250c) with a Malvern zeta analyzer.

3. RESULTS

Oil Displacement test:

Calculation:

Diameter of the oil layer was measured as 5.9cm

Oil Displacement Area (ODA) = 22/7 (Radius) ^{2} Cm2

Radius = Diameter /2

= 5.9cm/2

= 2.95

ODA = 22/7 $(2.95)^2$

= 22/7 * 8.70

= 27.342 cm^2

10µl of Biosurfactant sample has displacement area of 27.342 cm^2

Emulsification index:

Calculation:

$$E24 = \frac{\text{Height of emulsion formed}}{\text{Total height of solution}} \times 100$$

= 1.9/3.3 *100

= 57.5%

4. QUANTIFICATION OF BIOSURFACTANT

A. Estimation of protein by Lowry's method

TABLE –Estimation of protein by Lowry's method

PARTICULARS	**B**	**S1**	**S2**	**S3**	**S4**	**S5**	**T1**	**T2**	**T3**
Volume of standard (BSA) (ml)	-	0.1	0.2	0.3	0.4	0.5	0.02	0.04	0.06
Concentration of standard (µg)	-	100	200	300	400	500	-	-	-
Volume of distilled water (ml)	1	0.9	0.8	0.7	0.6	0.5	0.98	0.96	0.94
Alkaline copper reagent (ml)	3	3	3	3	3	3	3	3	3

Folin's Ciocalteau reagent (ml)	0.5	0.5	0.5	0.5	0.5	0.5	0.5	0.5	0.5
Optical density at 260nm	0.00	0.07	0.14	0.22	0.27	0.32	0.02	0.03	0.05

S1 to S5– Standard, B – Blank, T1 to T3 - Biosurfactants sample.

Calculation:

Concentration of unknown = $\frac{Absorbance\ of\ unknown}{Absorbance\ of\ standard}$ **x** Concentration of standard

= 0.03/0.204*300

= 44µg/ml

1ml of surfactant contains 44 micrograms of proteins

B. Estimation of Lipid by Vanillin Sulphuric acid

TABLE - Estimation of Lipid by Vanillin Sulphuric acid

PARTICULARS	**B**	**S1**	**S2**	**S3**	**S4**	**S5**	**T1**	**T2**	**T3**
Volume of standard Oleic Acid(ml)	-	0.1	0.2	0.3	0.4	0.5	0.02	0.04	0.06
Concentration of standard(µg)	-	100	200	300	400	500	-	-	-
Volume of distilled water(ml)	1	0.9	0.8	0.7	0.6	0.5	0.98	0.96	0.94
Vanillin reagent(ml)	3	3	3	3	3	3	3	3	3
Optical density at 260nm	0.00	0.390	0.507	0.835	1.128	1.331	0.386	0.743	0.987

S1 to S5– Standard, B – Blank, T1 to T3 - Biosurfactants sample.

Calculation:

Concentration of unknown = $\frac{Absorbance\ of\ unknown}{Absorbance\ of\ standard}$ **x** Concentration of standard

= 0.705/ 0.8382*300

= 252.32µg/ml.

1ml of surfactant contains 252.32 microgram of lipid compounds.

C. Estimation of Carbohydrates by Dinitro salicylic acid method

TABLE - 6. 7. C.4. Estimation of Carbohydrates by Dinitro salicylic acid method

PARTICULARS	**B**	**S1**	**S2**	**S3**	**S4**	**S5**	**T1**	**T2**	**T3**
Volume of standard (glucose) (ml)	-	0.1	0.2	0.3	0.4	0.5	0.02	0.04	0.06

Concentration of standard (µg)	-	100	200	300	400	500	-	-	-
Volume of distilled water (ml)	1	0.9	0.8	0.7	0.6	0.5	0.98	0.96	0.94
DNS reagent (ml)	3	3	3	3	3	3	3	3	3
40% Rochelle salt (ml)	1	1	1	1	1	1	1	1	1
Optical density at 260nm	0.00	0.86	1.20	1.46	1.64	1.88	0.38	0.52	0.89

S1 to S5– Standard, B – Blank, T1 to T3 - Biosurfactants sample.

Calculation:

Concentration of unknown = $\frac{Absorbance\ of\ unknown}{Absorbance\ of\ standard}$ **x** Concentration of standard

= 0.596/1.408*300

= 126.98µg/ml

1ml of surfactant contains 126.98 microgram of carbohydrates.

High performance thin layer chromatography

6.6. A. Standard1: Rhamnose sugar

GRAPH – 6.8.A.1 HPTLC for Rhamnose Sugar

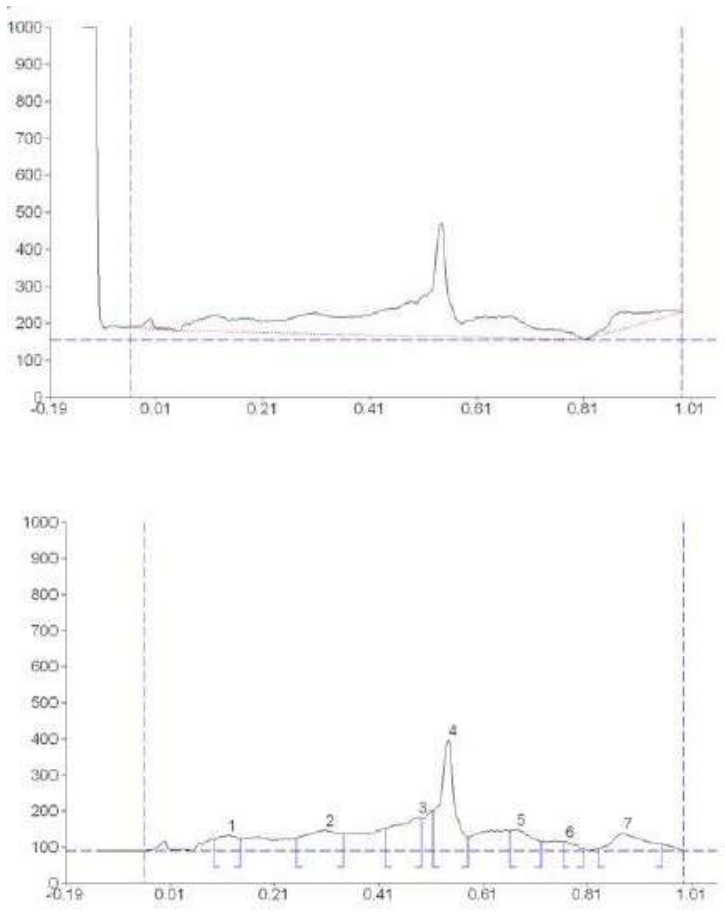

TABLE. HPTLC for Rhamnose Sugar

Peak	Start Rf	Start Height	Max Rf	Max Height	Max %	End Rf	End Height	Area	Area %	Assigned substance
1	0.10	32.0	0.12	43.8	6.87	0.15	32.9	1630.6	7.09	unknown *
2	0.26	34.9	0.31	57.7	9.06	0.35	46.7	3622.9	15.74	unknown *
3	0.43	61.3	0.49	93.2	14.63	0.50	90.0	4311.2	18.74	unknown *
4	0.52	111.7	0.55	307.1	48.23	0.58	38.4	7750.1	33.68	unknown *
5	0.67	56.0	0.68	59.6	9.36	0.73	27.0	2231.4	9.70	unknown *
6	0.77	25.5	0.77	27.1	4.26	0.81	6.2	586.5	2.55	unknown *
7	0.83	7.2	0.89	48.3	7.59	0.96	18.8	2878.7	12.51	unknown *

Standard 2: Sodium deoxycholate (surfactant)
GRAPH –HPTLC for Sodium deoxycholate

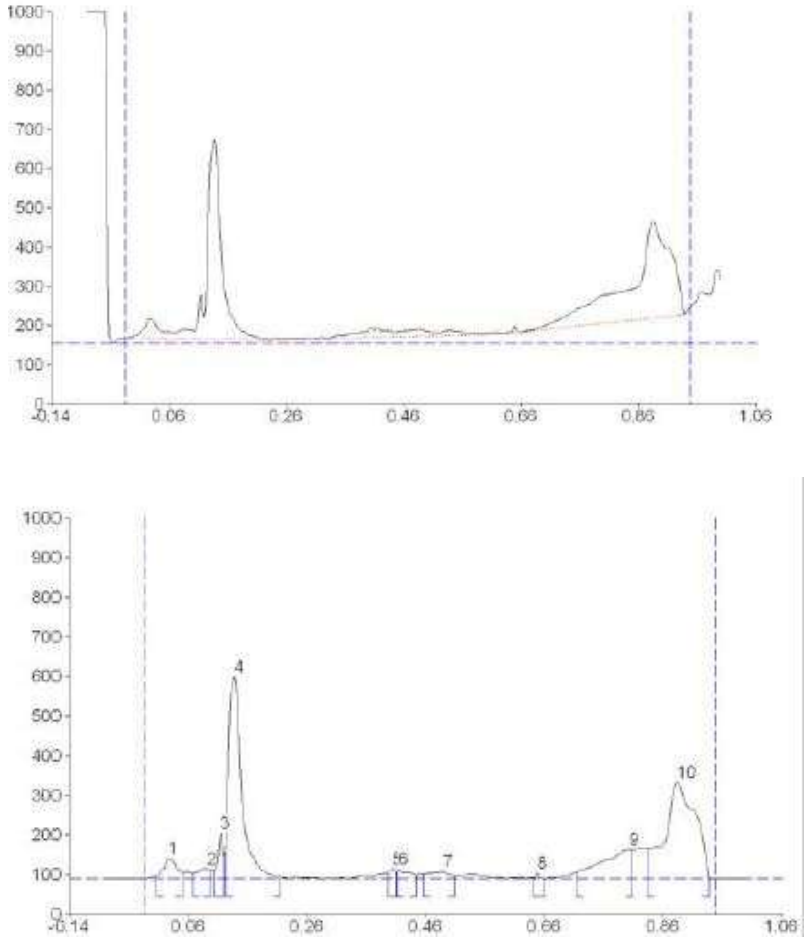

TABLE –HPTLC for Sodium deoxycholate

Peak	Start Rf	Start Height	Max Rf	Max Height	Max %	End Rf	End Height	Area	Area %	Assigned substance
1	0.00	7.9	0.02	51.9	4.70	0.05	16.1	1123.4	3.63	unknown *
2	0.06	14.0	0.09	25.5	2.31	0.09	22.2	521.6	1.69	unknown *
3	0.10	21.1	0.11	115.4	10.45	0.12	57.7	969.9	3.14	unknown *
4	0.12	68.6	0.13	509.4	46.15	0.21	4.8	11184.4	36.16	unknown *
5	0.39	13.2	0.40	25.5	2.31	0.41	17.3	250.0	0.81	unknown *
6	0.41	19.0	0.41	24.5	2.22	0.44	10.1	480.3	1.55	unknown *
7	0.45	12.2	0.49	18.2	1.65	0.51	7.4	645.7	2.09	unknown *
8	0.64	1.0	0.65	15.3	1.38	0.66	0.2	74.4	0.24	unknown *
9	0.71	16.4	0.80	73.6	6.66	0.81	73.1	3610.1	11.67	unknown *
10	0.83	75.3	0.88	244.5	22.15	0.94	3.2	12068.1	39.02	unknown *

Standard 3: fatty acid mixture
GRAPH –HPTLC for fatty acid mixture

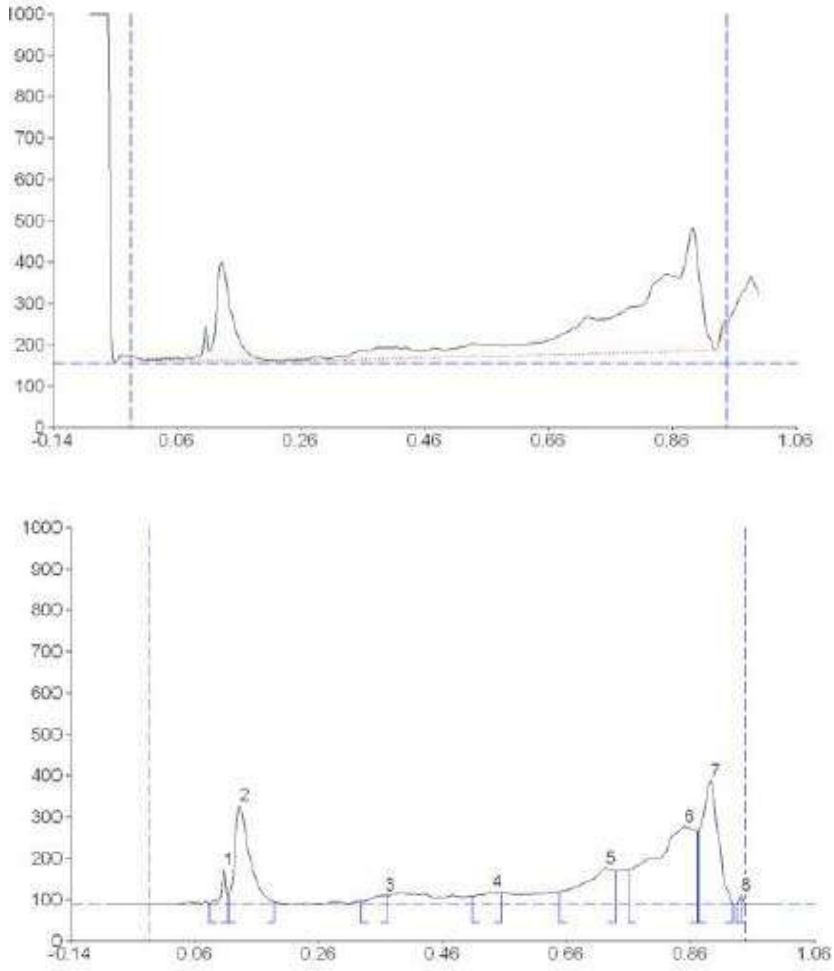

TABLE –HPTLC for fatty acid mixture

Peak	Start Rf	Start Height	Max Rf	Max Height	Max %	End Rf	End Height	Area	Area %	Assigned substance
1	0.08	3.7	0.10	83.0	8.59	0.11	22.2	641.9	1.96	unknown *
2	0.11	23.9	0.13	238.1	24.63	0.19	5.4	5610.3	17.09	unknown *
3	0.33	6.8	0.36	22.2	2.30	0.37	21.6	589.2	1.79	unknown *
4	0.51	19.3	0.54	30.5	3.16	0.55	27.2	1031.3	3.14	unknown *
5	0.65	28.4	0.72	87.2	9.03	0.74	80.6	4438.2	13.52	unknown *
6	0.76	83.7	0.85	187.2	19.37	0.87	175.5	12904.1	39.31	unknown *
7	0.87	176.6	0.89	297.0	30.73	0.93	1.2	7505.9	22.86	unknown *
8	0.93	1.7	0.94	21.3	2.20	0.94	19.1	108.9	0.33	unknown *

Sample: Biosurfactant
GRAPH - HPTLC for Biosurfactant

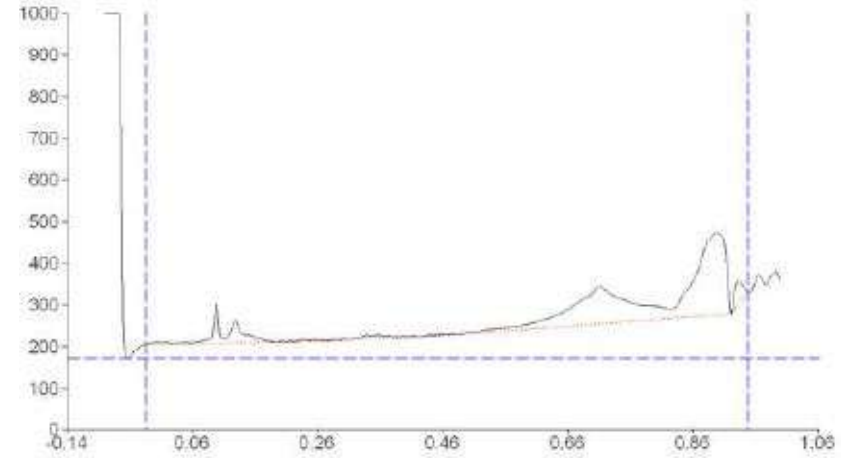

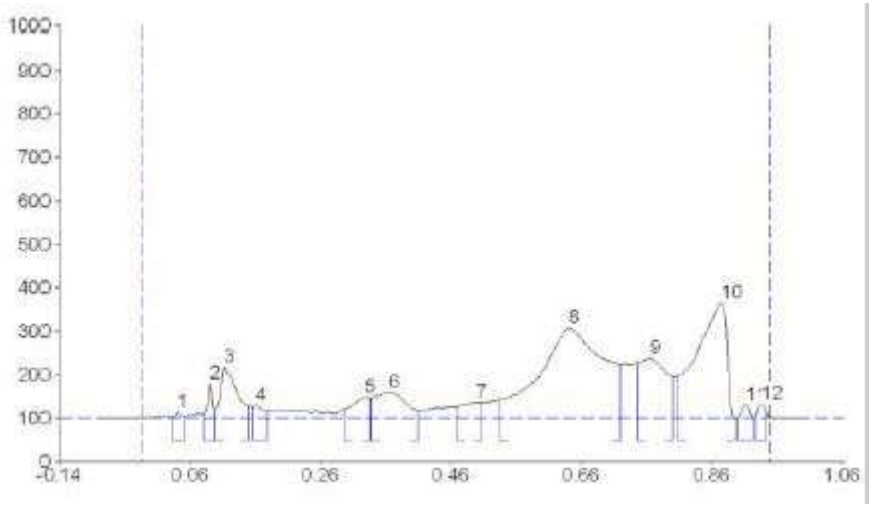

TABLE –HPTLC for Biosurfactant

Peak	Start Rf	Start Height	Max Rf	Max Height	Max %	End Rf	End Height	Area	Area %	Assigned substance
1	0.03	2.6	0.04	14.6	1.37	0.05	3.5	113.0	0.24	unknown *
2	0.08	9.4	0.09	80.8	7.59	0.09	15.7	525.0	1.12	unknown *
3	0.09	17.9	0.11	117.4	11.03	0.14	30.7	2765.1	5.91	unknown *
4	0.15	26.3	0.16	30.9	2.91	0.17	19.4	470.0	1.01	unknown *
5	0.29	21.0	0.33	48.4	4.55	0.33	48.1	1262.3	2.70	unknown *
6	0.33	47.9	0.36	59.9	5.63	0.41	19.2	2778.7	5.94	unknown *
7	0.47	27.3	0.50	37.7	3.55	0.50	36.6	1104.4	2.36	unknown *
8	0.53	42.4	0.64	207.9	19.53	0.72	122.7	19647.6	42.02	unknown *
9	0.74	126.3	0.76	138.3	13.00	0.80	96.0	5618.4	12.02	unknown *
10	0.81	97.0	0.87	264.1	24.82	0.89	0.6	11776.4	25.19	unknown *
11	0.90	0.8	0.91	30.5	2.87	0.92	0.7	348.4	0.75	unknown *
12	0.93	2.0	0.93	33.6	3.16	0.94	18.1	348.5	0.75	unknown *

Gas chromatography-Mass Spectroscopy

GRAPH – Gas chromatography-Mass Spectroscopy

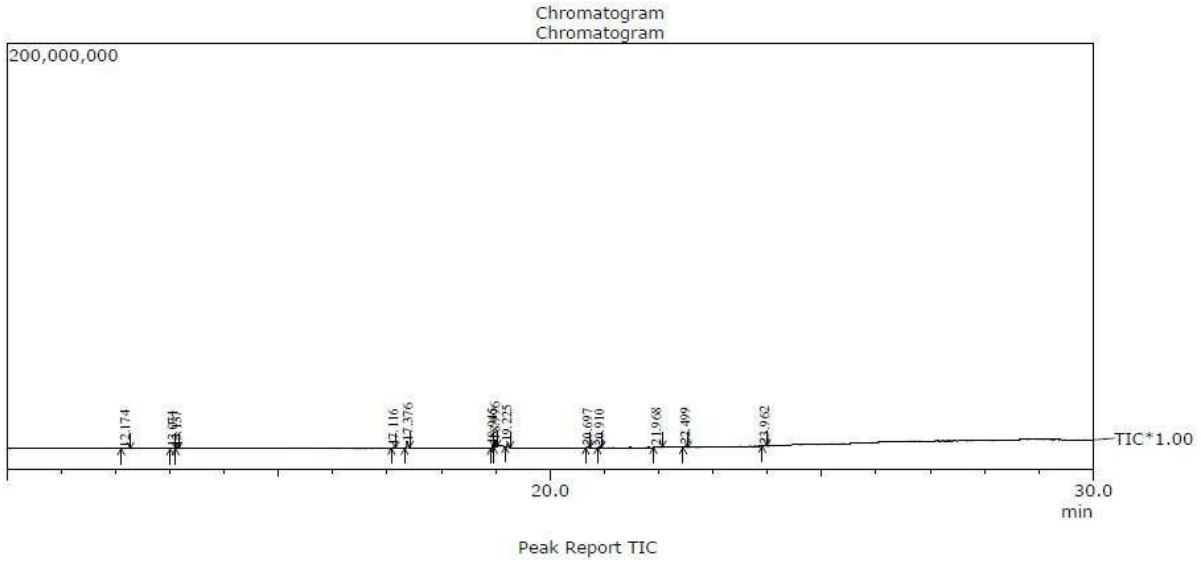

TABLE –Gas chromatography-Mass Spectroscopy

PEAK#	R.TIME	AREA	AREA%	NAME
1	12.174	753643	3.06	PHENOL, 2,4-BIS(1,1-DIMETHYLETHYL)-
2	13.071	370999	1.51	1-Hexadecanol
3	13.137	433406	1.76	DODECANOIC ACID, ETHYL ESTER
4	17.116	892233	3.62	Dibutyl phthalate
5	17.376	6169722	25.06	HEXADECANOIC ACID, ETHYL ESTER
6	18.945	1095659	4.45	ETHYL (9Z,12Z)-9,12-OCTADECADIENOATE
7	18.996	4873416	19.80	Ethyl Oleate
8	19.225	3665015	14.89	OCTADECANOIC ACID, ETHYL ESTER
9	20.697	1387390	5.64	9-Octadecenoic acid, 12-hydroxy-
10	20.910	767272	3.12	Octadecyl trifluoroacetate
11	21.968	1764373	7.17	CYCLODODECASILOXANE, TETRACOSAMETHYL-
12	22.499	1545133	6.28	Nonadecanoic acid, ethyl ester
13	23.962	898883	3.65	Ethyl tetracosanoate
		24617144	100.00	

Fourier Transform Infrared Spectroscopy

GRAPH –Fourier Transform Infrared Spectroscopy

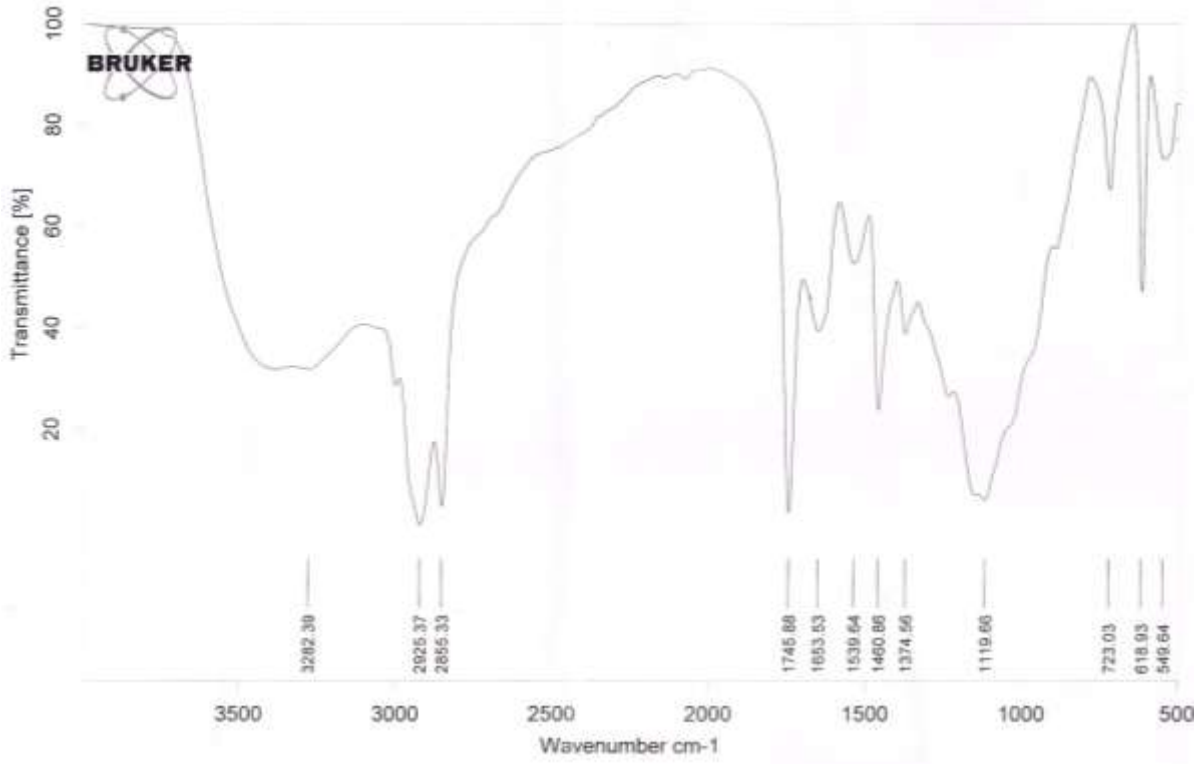

Zeta potential analysis for nanovesicle

TABLE –standard value of the zeta potential

Zeta potential (mv)	**Stability of the particle**
0 to +/- 5	Rapid coagulation or floculation
10 to +/- 30	Incipient stability
30 to +/- 40	Moderate stability(Thatipamula *et al*, 2011)
40 to +/- 60	Good stability
More than +/-61	Excellent stability

Zeta potential analysis for biosurfactant formulated nanovesicle was measured to be -8.73(mV) and electrical conductivity was 36.8 (Ms/cm).The DLS analysis of size of the nanovesicle were measured using zeta analyser were found to be 152d.nm.and the corresponding values are tabulated.

Results

			Diam. (nm)	% Volume	Width (nm)
Z-Average (d.nm):	152.0	**Peak 1:**	223.1	23.5	98.52
PdI:	0.457	**Peak 2:**	39.94	71.1	13.81
Intercept:	0.858	**Peak 3:**	5477	5.5	629.8
Result quality :	Good				

5. DISCUSSION

Identification of exosecretion of surfactant molecules from Saccharomyces cerevisiae MTCC 181 were analysed and it was characterised, further implemented in nanovesicle synthesis.

Culture condition:

Saccharomyces cerevisiae is a species of yeast having more beneficial role in fermentation industry. As per the instruction of Microbial type culture condition (MTCC), YEPD medium were used for the cultivation, the most commonly used rich medium for growing Saccharomyces cerevisiae when special conditions are not required. It provides an excess of amino acids, nucleotide precursors, vitamins, and essential metabolites needed for optimal cell growth. Yeast cells divide every ~90 min when grown in YPD during the exponential phase of the growth cycle (P. N. MC Donald, 2001)

Surfactant production:

Surfactant is a significant molecule for microorganism for its various physiological activities (Ron & Rosenberg, 2001). Mineral salt medium is commonly used for production of biosurfactant; carbon, nitrogen and electrolytes are the major sources of nutrients. 2% ground nut oil was used as the carbon source for the production of surfactant (Sarubbo, L.A. *et al*., 2007). Mineral salt medium containing crude oil as a carbon source can be used for surfactant production (Rahman *et al.,* 2002). Hydrophobic carbon source will enhance the synthesis of surfactant molecule and also it is an indirect screening method as the growth on hydrophobic carbon source confirms the presence of surfactant **(**Ramakrishna Sen., 2008).

Screening of surfactant:

Screening of surfactant is commonly based on its interaction with hydrophobic molecules because of amphiphilic nature. Oil spreading test is simple and reliable method for screening of surfactant molecule (Ramakrishna Sen., 2008). 10µl culture supernatant was added on oil surface, a clear halo zone of diameter was measured as 5.9cm and the oil displacement area was found to be 27.34 cm^2. Increase in the area of the circle signifies the surfactant activity. Emulsification test is first method used for screening for surfactant it will just confirm the presence of surfactant. In our study Groundnut oil used as hydrophobic compound and emulsification index was found to be 57.5 % which is the carbon source used for surfactant production. Preethy chandran et al., 2011 stated that all biosurfactant isolated from yeast species exposed emulsification activity over a pH range from 2 to 10 hence it is very useful in both acidic and alkaline condition and showed emulsification activity of 60% in the temperature range of 10 – 100^0C which is very applicable at extreme temperature.

Purification and Quantification of surfactant:

Initial purification is based on the separation of hydrophilic compounds using solvents like chloroform, methanol and n-propanol which separate the surfactant into separate layer and further ice cold acetone and 6N Hydrochloric acid will reduces the dielectric charges of the molecules which precipitate the surfactant molecules. Purified surfactant contains 44 microgram of protein, 130 microgram of carbohydrates and 252 micrograms of lipid molecules. Vegetable oil used as a carbon source may increase the

sugar and lipid content of surfactant in the class of glycolipid, composition of surfactant varies depends on the carbon sources (Ramakrishna Sen., 2010).

Characterisation of surfactant:

Thin layer chromatography

Non – specific spray method were used for the analysis lipid molecules by spraying with Vanillin Sulphuric acid reagents, brown spots confirms the presence of lipid molecules (Christie, W.W., Han, X. 2010) and carbohydrates were screened under Uv light , blue spot determines the presence of sugar compound. Glycolipids of *saccharomyces cerevisiae* were studied and a fatty acid derivative of sugar moiety was identified by Renuka Malhotra *et al*., 2005. TLC of protein spots (purple) were identified using Ninhydrin spray solution according to Sager *et al*., 2005.

High performance thin layer chromatography (HPTLC)

Surfactant sample exposed different patterns in HPTLC with R.f values 0.03 - 0.05, 0.08 – 0.09, 0.09 – 0.14, 0.15 – 0.17, 0.29 – 0.33, 0.33 – 0.41, 0.47 – 0.50, 0.53 – 0.72, 0.74 – 0.80, 0.81 – 0.89, 0.90 – 0.92 and 0.93 – 0.94. The peak 0.09 – 0.14 and 0.15 – 0.17 is relates to glycolipid class of acidic sophorolipid. The peak 0.29 – 0.33, 0.33 – 0.41, 0.47 – 0.50 and 0.53 – 0.72 is relates to glycolipid class of lactone sophorolipid and fatty acid derivatives. The peaks 0.74 – 0.80, 0.81 – 0.89, 0.90 – 0.92 and 0.93 – 0.94 is relates to sophorolipid surfactant (Sachin shah, 2002). The purified fraction of surfactant from Saccharomyces cerevisiae comes under glycolipid class of biosurfactant and its peaks typically bear a resemblance with sophorolipid. Similar study were observed from lactonic and acidic class of sophorolipid exhibited five to six patterns of R.f 0.59, 0.48, 0.37, 0.22, 0.07 in thin layer chromatography by Albert Lumanlan Ussher., 2002 and Copper et al., 1983 identified glycolipid fractions of surfactant using thin layer chromatography showed R.f value of 0.31, 0.21, and 0.07 from yeast organism.

Fourier Transform Infrared Spectroscopy (FTIR)

Surface active compounds from *Saccharomyces cerevisiae* were absorped between 500 – 3500 wavenumber cm^{-1} and the transmittance are 3282.39 cm^{-1}, 2925.37 cm^{-1}, 2855.33 cm^{-1}, 1745.88 cm^{-1}, 1653.53 cm^{-1}, 1539.64 cm^{-1}, 1460.86 cm^{-1}, 1374.56 cm^{-1}, 1119.66 cm^{-1}, 723.03 cm^{-1}, 618.93 cm^{-1} and 549.64 cm^{-1}. All transmittance peak data's were measured using standard IR values. The peak 3282.39 cm^{-1} relates to broad spectrum of O-H stretch of phenolic or alcoholic group (Aniruddha B. Pandit *et al*., 2012) and also it may corresponds to N-H medium stretch which can be secondary amide structure (Gazhal, E.A *et al* ., 2010); further this peak has a strong C-H stretch of Alkynes group. The peak 2925.37 cm^{-1} and 2855.33 cm^{-1} corresponds to asymmetrical (CH_2) and symmetrical (CH_2) stretching of methylene group (Aniruddha B. Pandit *et al*., 2012) and also matches with aliphatic chain of C-H stretch which is usually less useful in determining structure. Carbonyl stretching (C=O) of Ketone, Ester and Carboxylic group were measured in the peak of 1745.88 cm^{-1} and the peak 1653.53 cm^{-1} correspond to C=O stretching of Amide group, these carbonyl stretch is one of the strongest absorption which is very useful in structure determination and this absorption may contribute from lactones, ester or acidic forms of sophorolipid (Aniruddha B. Pandit *et al*., 2012). Aromatic C=C bending correspond to the peak 1539.64 cm^{-1} which has strong asymmetrical stretch of nitro (NO2) compound and also N-H bend of amines and amide groups. The band peak at 1460.86 cm^{-1} corresponds to C-O-H plane bending of carboxylic acid (COOH) and also C-H=O of aliphatic aldehyde (Aniruddha B.

Pandit *et al*., 2012 & Gazhal, E.A *et al*., 2010). This peak may further relate to scissoring and bending of C-H alkanes group. The transmittance peak of 1374.56 cm^{-1} was matches with C-H plane bend and vibration at CH_3 bends. It also corresponds to strong symmetrical stretch of –NO2 compound. The band peak 1119.66 cm^{-1} relates with C-O, C-O-C stretch of alkyl aryl esters (Gazhal, E.A *et al*., 2010) and also medium stretches in C-N amine group. The 723.03 cm^{-1} peak corresponds to aromatic C-H bending, phenyl ring substitution. C-Cl stretches of acid chloride and alkyl halide relates to the peak 723.03 cm^{-1} and 618.93 cm^{-1}. The peak 549.64 cm^{-1} corresponds to R –Cl stretch of alkyl halides. From FTIR pattern, it manifest lactonic forms of surfactant are common among yeast species.

Gas chromatography and Mass spectroscopy

Hydrolysed surfactant sample showed 13 GC/MS peak, peak 3, 5, 8, 12 and 13 relates to similar base peak at 88 (m/z) comes under fatty acid esters class of decanoic acids and their structure were identified and partitioned using MS library (NIST08s, WILEY8 & FAME). Individual fatty acid can be used produce novel sophorolipid, the incorporation of fatty acid from Palmitic acid was directly observed. A similar study was accomplished with hydrocarbons from tetradecane to docosane (14 – 20 carbon) molecule (Albert Lumanlan Ussher., 2002). The peak 1- Hexadecanol and dodecanones of peak 6, 3, 11 and 13 have also been successfully incorporated into sophorolipid. Alcohol such as 1- dodecanol, 2- dodecanol, 1- hexadecanol, 1-tetradecanol, 2,13- tetradecandiol, 2,15- hexadecandiol and ketones such as 2-dodecanones , 3- dodecanones have all can be successfully incorporated into sophorolipids (Brakemeier et al., 1995; Brakemeier et al., 1998). 9th peak of retention time 20.910 and mass peak 161(m/z) is found to be 12- hydroxy octadecanoic acid is pretend to be hydroxy fatty acid esters of sophoroside for a reason that it can bind glycosidically to several residues of sugar molecule to form glycosidic acid(Spencer et al., 1967). The peak 7 was ethyl oleate an exosecretion of fatty acid molecules by yeast organism. From the data surfactant of Saccharomyces cerevisiae has fictitious to have sophoroside of hydroxy fatty acid derivatives.

Application in Nanovesicle synthesis

Surface active compound of sophorolipid has the tendency of forming nanovesicle; addition of cholesterol decrease the size of nanovesicle .A similar study of rhamnolipid surfactant in the concentration of 2.6 mM used for vesicle synthesis and using transmission electron microscopy the size of nanovesicle has been reduced when addition of cholesterol was implemented; this vesicle has 80% of drug entrapment efficiency was reported by Ratana Rujiravanit, (2011). Morphology of the vesicles was analysed using optical microscope at 45x showed spherical vesicle. Scanning electron microscopy showed uniformity in size and shape of the vesicle, 150nm of vesicle size were observed in Zeta analyser and negative charge of the vesicle shows incipient stability. The general dividing line between stable and unstable suspensions is generally taken at either +30mV or -30mV Particles with zeta potentials more positive than +30mV or more negative than -30mV are normally considered stable. Vesicle stability plays vital role in drug loading capacity but anionic charge of the surfactant vesicle may delay better delivery of drug molecules. (Noordman, W.H, *et al*., 2000).

6. SUMMARRY AND CONCLUSION

Biosurfactant production was identified in Saccharomyces cerevisiae MTCC 181 using ground nut oil as a carbon source and its properties were identified by oil displacement test and emulsification activity. Thin layer chromatographic technique exposed positive spots for protein, carbohydrates and lipids of the surfactant. Quantification of surfactant was measured by calorimetric method showed increase concentration of lipids but proteins are in very low concentration than carbohydrate molecules. Sophorolipid peaks were recognized from HPTLC peaks and the Lactonic form of sophorolipid was identified from Fourier transform infrared spectroscopy. Hydroxy fatty acid derivative of sophorolipid was identified in GC/MS analysis and this surfactant was used in nanovesicle synthesis. Glycolipid class of sophorolipid was identified in Saccharomyces cerevisiae and it surface active property extended its role in nanotechnology.

7. BIBLIOGRAPHY

Abu-Ruwaida, A. S., Banat, I. M., Haditirto, S., Salem, A., Kadri, M. 1991b "Isolation of biosurfactant-producing bacteria product characterization and evaluation", Acta Biotechnologica 11: 315-324

As¸c¸i, Y., Nurbas, M., Ac¸ikel, Y. S. 2007. "Sorption of Cd (II) onto kaolin as a soil component and desorption of Cd (II) from kaolin using rhamnolipid biosurfactant," Journal of Hazardous Materials, vol. 139, no. 1, 50–56.

Asmer, H .J., L., Slegmund, W., Fritz ., Wrey V. 1988. "Microbial production, structure elucidation and bioconversion of sophorose lipid" JAOCS, 65: 1460-1466.

Alvaro Silva Lima., Ranulfo Monte Alegre. *2009. "Evaluation of emulsifier Stability of biosurfactant Produced by Saccharomyces lipolytica CCT-0913". Brazilian archives of biology and technology an international journal. Vol: 52(2): 285-290.*

Albert Lumanlan Ussher. 2002. Analysis of sophorolipids by Candida bombicola. Master of Engineering thesis. Department of Biological Sciences, University of Alberta, 1-117.

Bayoumi, R.A., Haroun, B.M.,Ghazal, E.A. and Maher, Y.A. 2010. Structural Analysis and Characteristics of Biosurfactants Produced by Some Crude Oil Utilizing Bacterial Strains. Australian Journal of Basic and Applied Sciences, 4(8): 3484-3498,

Cabib, E., Roberts, R.1982. "Synthesis of the yeast cell wall and its regulation". Annu Rev Biochem 51, 763–93.

Cameon, D. R., Cooper, D.G., Neufeld, R.J. 1988. "The mannoprotein of saccharomyces cerevisiae is an effective bioemulsifier". Applied Environ.Microbiol, 54(6):1420-1425.

Chen C, Baker S, Darton R. 2007. The application of a high throughput analysis method for the screening of potential biosurfactants from natural sources. J Microbiol Methods; 70:503-510.

Christie, W.W., Han, X. 2010. "Lipid Analysis - Isolation, Separation, Identification and Lipidomic Analysis", Oily Press, Bridgwater, U.K, 4th edition, 446.

Christie, W.W. 1990. "Has thin-layer chromatography had its day? Lipid Thin-layer chromatography of lipids", W.W. Christie lipid library.aocs.org 6 Technology, 2, 22-23.

Christie, W.W., Dobson, G. 1999. "Thin-layer chromatography-revisited, Lipid Technology", 11, 64-66.

Michael C. Cirigliano and George M Carman. 1985, Purification and

Characterization of Liposan, a Bioemulsifier from Candida lipolytica, Applied and Environmental Microbiology, 846-850.

Cooper, D. G., Paddock, D. A. 1983, "Production of a Biosurfactant from *Torulopsis bombicola*", Applied and Environmental Microbiology, Jan. 1984, 173-176 Vol. 47, Received 20 June 1983/Accepted 25 October 1983.

Dastgheib, S.M.M., Amoozegar, M.A., Elahi, E., Asad S., Banat, I.M. 2008. "Bioemulsifier production by a halothermophilic Bacillus strain with potential applications in microbially enhanced oil recovery". Biotechnology.

David G. Cooper and D. A. Paddock. 1984. Production of a Biosurfactant from Torulopsis bombicola. Applied and environmental microbiology, Jan. 1984, 173-176.

David, R., Cameron David G., Cooper., Ron J. Neufeld. 1988. "The Mannoprotein of Saccharomyces cerevisiae is an Effective Bioemulsifier". Applied and Environmental Microbiology, June 1988, 1420-1425 Vol. 54, No. 6, Received 13 November 1987/Accepted 17 March 1988.

Deleu, M. and Paquot, M. 2004. From Renewable Vegetables Resources to Microorganisms: New Trends in Surfactants C.R.Chimie.7:641-646.

Desai, J., Banat, I.M. 1997 **"**Microbial Production of Surfactant and Their Commercial

Potential". American Society for Microbiology, *61*(1), 47-64.

Desai, J. D., Banat, I. M. 1997. "Microbial production of surfactants and their commercial potential". Microbiology and Molecular Biology Reviews 61: 47-64.

Deziel, E., Lepine, F., Milot, S., Villemur, R. 2000. "Mass spectrometry monitoring of rhamnolipids from a growing culture of *Pseudomonas aeruginosa* Strain 57RP". Biochimica et Biophysica Acta 1485: 145-152.

Franzetti, A., Caredda, P., Ruggeri, C., La Colla, P., Tamburini, E., Papacchini, M., Bestetti, G. 2009. "Potential applications of surface active compounds by Gordonia sp. strain BS29 in soil remediation technologies", Chemosphere, doi:10.1016/j.chemosphere.2008.12.052

Gautam, K.K., Tyagi, V.K. 2006. "A Review of Microbial Surfactant", Journal of Oleo Science, *55*(4), 155-166.

Guerra-Santos, L., Kappeli, O., Fiechter, A. 1986. "Dependence of Pseudomonas aeruginosa continuous culture biosurfactant production on nutritional and environmental factors", Applied Microbiology and Biotechnology 24: 443-448.

Healy, M.G., Devine, C.M., murphy, R. 1996."Microbial production of biosurfactants". Resour, conserve, Recy., 18(1):41-57.

Hu Y, Ju L-K (2001) Purification of lactonic sophorolipids by crystallisation. J Biotechnol 87: 263–272.

Jacques Izard., Ronald, J., Limberger. 2003, "Rapid Screening Method for Quantitation of Bacterial Cell Lipids from whole cells", Department of Biomedical Sciences, USA, Received 30 January 2003; received in revised form 22 April 2003; accepted 9 June 2003.

Karanth, N. G. K., Deo, P. G., Veenanadig, N. K. 1999. "Microbial biosurfactant and their importance". Current Science 77: 116-126

Karanth, N. G. K., Deo, P. G., Veenanadig, N. K. 2005. "Microbial production of biosurfactants and their importance". Pesticide Residue Abatement Lab, Food Protectants and Infestation Control Department, Central Food Technological Research Institute, Mysore.

Kim, H.S., Yoon, B.D., Choung, D.H., Oh, H. M., Katsuragi, T., Tani, Y. 1999 "Characterization of a biosurfactant, mannosylerythritol lipid produced from

Candida sp". SY16. Appl. Microbiol. Biot; 52, 713-21.

Kim, S. H., Lim, E. J., Lee, S. O., Lee, J. D., Lee, T. H. 2000. "Purification and characterization of biosurfactants from *Nocardia* sp. L-417". Biotechnology and Applied Biochemistry 31: 249-253.

Kwon, S. Y., Kim, M. W. 2001. Langmuir 17 8016.

Laith Al-Araji1., Raja Noor Zaliha Raja Abd., Rahman., Mahiran Basri., Abu Baker Salleh. *2007*. "Microbial Surfactant", *Asia Pacific Journal of Molecular Biology and Biotechnology, 2007, Vol. 15 (3): 99-105, Received 3 May 2007 / Accepted 15 August.*

Lang S, Wullbrandt D. 1999. Rhamnolipids-biosynthesis, microbial production and application potential. Appl. Microbiol. Biotechnol, 51:22–23

Lowry, O.H., Rosebrough, N.J., Farr, A.L., and Randall, R.J. 1951, "The original method of Protein Estimation", J.Biol.Chem, 193: 265.

Maneerat, S. 2005. "Biosurfactants from marine microorganisms", Songklanakarin J. Sci. Technol., 27(6) : 1263-1272

Maneerat, S., Phetrong, K. 2007, "Isolation of biosurfactant-producing marine bacteria and characteristics of selected biosurfactant", Songklanakarin J. Sci. Technol., 29(3) : 781-791

Meesters PAEP., Huijberts GNM., Eggink G. 1996. "High‐cell‐density cultivation of the lipid accumulating yeast *cryptococcus curvatus* using glycerol as a carbon source". Appl Microbiol Biotechnol; 45:575‐79.

Miller, G.L. (1972). Anal. Chem., 31, p. 426.

Mohamed S. El-ridy., Alia A. Badawi., Marwa M. Safar., Amira M., Mohsen. 2012. "Niosomes as a novel pharmaceutical formulation encapsulating the hepato protective drug silymarin". International Journal of Pharmacy and Pharmaceutical Sciences ISSN- 0975-1491 Vol 4, Issue 1, Received: 2 Sep 2011, Revised and Accepted: 26 Oct 2011.

Mukherjee, S., Das, P., Sen, R. 2006 **"**A Review of Towards Commercial Production of Microbial Surfactants", Trends in Biotechnology, 24(11), 509-515.

Mulligan, C. N., Yong, R. N., Gibbs, B. F., James, S., Bennett, H. P. J. 1999. "Metal removal from contaminated soil and sediments by the biosurfactant surfactin," EnvironmentalScience and Technology, vol. 33, no. 21, pp. 3812–3820.

Nabi, S. A., Khan, M. A. 2003. "Selective TLC Separation of Lysine and Threonine in Pharmaceutical Preparations". Department of Chemistry, Aligarh Muslim University, India, Journal of the A. S. S. B. T. American Society of Sugar Beet Technologists No. 13.

Nelly Christovaa., Borjana Tulevaa., Zdravko Lalchevb., Albena Jordanovac., and Bojidar Jordanovd. 2003. "Rhamnolipid Biosurfactants Produced by *Renibacterium salmoninarum 27BN* During Growth on *n*-Hexadecane",received April 10/May 28.

Neu, T. 1996. "Significance of bacterial surface-active compounds in interaction of bacteria with interfaces". Microbiol. Rev. 60: 151-166.

Noordman, W.H., M.L. Brusseau and D.B. Janssen. 2000.Adsorption of a multicomponent rhamnolipid surfactant to soil. Environ Sci Technol,. 34(5):83-838.

Gholamreza Dehghan Noude , Fariba Sharififar, Mehdi Khatib, Effat Behrava and Masoud Ahmadi Afzadi. 2010. Study of aqueous extract of three medicinal plants on cell membrane–permeabilizing and their surface properties, African Journal of Biotechnology.9 (1), 110-116.

Orathai Pornsunthorntawee, Sumaeth Chavadej, and Ratana Rujiravanit. 2011. Characterization and encapsulation efficiency of rhamnolipid vesicles with cholesterol addition. Journal of Bioscience and Bioengineering, 112 (1), 102–106.

Paweena Dikit., Suppasil Maneerat., Hatairat Musikasang., Aran H-kittikun. 2010. "Emulsifier properties of the mannoprotein extract from yeast isolated from sugar palm wine, Department of Industrial Biotechnology", Faculty of Agro-Industry, Prince of Songkla University, Hat Yai, Songkhla 90112, Thailand.

P.N Mc Donald, 2001.Methods in Molecular Biology, Vol. 177, Two-Hybrid Systems: Methods and Protocols, copy rights by Humana Press Inc., Totowa, Japan.

Priscilla., Amaral., Maria Alice., Coehlo., Isabel., Marracho., Joao., Coutinho. 2008. "Biosurfactant from yeast: Characteristics, Production and Application".

Preethy Chandran., Trichosporon asahii. 2010. "Biosurfactant Production and Diesel Oil Degradation by Yeast Species *Trichosporon Asahii* Isolated from petroleum Hydrocarbon contaminated soil", International Journal of Engineering Science and Technology, Vol. 2(12), 6942-6953.

Rahman, K. S. M., Rahman, T. J., Lakshmanaperumalsamy, P., Marchant, R., Banat, M., 2002c. "Emulsification potential of bacterial isolates with a range of hydrocarbon substrates". Acta Biotechnol., 23(4):335-345.

Rahman, K.S.M., Street,G., lord, R., Kane, G., Rahman,T.J., Marchant, R ., Banat, I.M. 2006. "Bioremediation of Petroleum sludge using bacterial Consorium with Biosurfactant in: Environment Bioremediation Technology", Singh, S.N., Tripathi R.D (Eds).Springer Publication, PP: 391-408.

Ramakrishna Sen. 2008. Biosurfactant, Landes Bioscience and Springer science + Business Media. Copy rights at Landes Biosciences

Ramakrishna Sen. 2010. Biosurfactant, Landes Bioscience and Springer science + Business Media. Copy rights at Landes Biosciences

Renuka Malhotra ., Balwant Singh. 2005. "Glycolioids of Saccharomyces cerevisiae cell", Journal of Biological Sciences 5(3): 253-256.

Ron E, Rosenberg E. 2001. Natural roles of biosurfactants. Environ Microbiology, 3(4):229-236.

Ron, E., Rosenberg, E. 2002. "Biosurfactants and oil bioremediation", Current Opinion in Biotechnol. 13: 249-252

Sachin Shah. 2002. Dry column chromatography technique used for the purification of different forms of sophrolipids produced by *Candida bombicola*. PhD thesis, University of Pune, Chapter (3), 1-31.

Saeger, S. L., Slabaugh, M. R. 2005. Safety-scale Laboratory Experiments for General, Organic, and Biochemistry for Today, Amino Acids and Proteins, CHEM 209 Lab, Spring, 4th Ed., 387.

Salwa Mohd Salleh., Nur Asshifa Md Noh., Ahmad Ramli Mohd Yahya. 2011. "Comparative study: Different recovery techniques of rhamnolipid produced by *Pseudomonas aeruginosa* USMAR-2" International conference on Biotechnology and Environment Management, IPCBEE vol.18, Singapore.

Sarubbo, L.A., Farias, C.B.B., and Campos-Takki, G.M. (2007) Co-utilization of canola oil and glucose on the production of a biosurfactant by *Candida lipolytica*. *Curr. Microbiol*. **54**, 68-73.

Sheppard, J. D., Cooper, D. G. 1990. "The effect of a biosurfactant on oxygen transfer in a cyclone column reactor", Journal of Chemical Technology and Biotechnology 48: 325-336.

Frank H. Stodola, Maria H. Deinema, and J. F. T. Spencer. 1967. Extracellular

Lipids of Yeasts. Bacteriological Reviews, 194-213.

Suppasil Maneerat, Kulnaree Phetrong, 2007. "Isolation of biosurfactant-producing marine bacteria and characteristics of selected biosurfactant", Songklanakarin J. Sci. Technol, 29(3): 781-791.

Torabizadeh, H., Shojaosadati, S.A. Tehrani, H.A. 1996. "Preparation and Characterisation of Bioemulsifier from *Saccharomyces cerevisiae* and its Application in Food Products", Lebensm.-Wiss. u.-Technol., 29, 734–737, (Received August 2, 1995; accepted January 12, 1996)y

Van Dyke., Couture, M. I., Brauer, P. M., Lee, H., Trevors, J. T. 1993. "*Pseudomonas aeruginosa* UG2 rhamnolipid biosurfactants: Structural characterisation and their use in removing hydrophobic compounds from soil". Can. J. microbial, 39(11):1071-1078.

Vishal J. Parekha, Vandana B. Patravaleb, Aniruddha B. Pandit (2012) Mango kernel fat: A novel lipid source for the fermentative production of sophorolipid biosurfactant using *Starmerella Bombicola NRRL*-Y 17069. Annals of Biological Research, 3 (4):1798-1803

G.'Walker, J. R., Ricci, B. A., Goodwin, J. C. 1964. "Thin-layer chromatography of sugar beet carbohydrates", received for publication, august 20.

BENS79

Expression of cystic fibrosis transmembrane conductance regulator in osmoregulatory tissues of sea bream

Norman Y. S. Woo, Teresa W. S. Yuen
School of Life Sciences, The Chinese University of Hong Kong, Shatin, N.T., Hong Kong SAR, China
Email: normanwoo@cuhk.edu.hk
Email: biosumsum@yahoo.com.hk

ABSTRACT
A partial CFTR gene sequence was obtained from the gills of silver sea bream (GenBank Accession no. EF017215), from which specific oligonucleotides were obtained for detection of CFTR mRNA expression. A thorough tissue distribution analysis of CFTR in silver sea bream was performed and it was found that CFTR was expressed at high levels in the primary osmoregulatory organs, i.e. gill, intestine, and pituitary, and to a lesser extent, in opercular epithelium, spleen, urinary bladder, liver and heart, suggesting that CFTR may be involved in the osmoregulatory processes in fish.

Keywords: CFTR, osmoregulation, euryhalinity

1. INTRODUCTION

The ability of euryhaline fishes to maintain ionic homeostatis in varying salinities depends on an intricate interplay of their osmoregulatory organs, of which the gills, kidneys and intestines are the most crucial. In these ion-transporting epithelia and especially the gills, specialized mitochondrion-rich cells (MRCs), also known as chloride cells (CCs), are the site of salt secretion. CCs express various types of ion pumps, transporters and channels to facilitate transepithelial chloride (Cl^-) transport [4]: they are namely basolateral Na^+, K^+-ATPase, apical cystic fibrosis transmembrane conductance regulator (CFTR), basolateral $Na^+/K^+/2Cl^-$ co-transporter (NKCC) and basolateral potassium (K^+) channel. Considerable research has been done on the key ionomotive enzyme Na^+, K^+-ATPase [14] and its involvement in teleostean osmoregulation, however, there is a relative scarcity of work on other ion transporters, such as the chloride transport channel CFTR.

Mammalian CFTR is a plasma membrane cAMP-regulated Cl^- channel that belongs to the family of ATP-binding cassette (ABC) proteins and is gated in response to binding and hydrolysis of ATP [4]. Following the identification of the human CFTR gene and its association with the pathology of cystic fibrosis [17], various fish CFTR homologs have been cloned, such as CFTRs from dogfish *Squalus acanthias* [13], killifish *Fundulus heteroclitus* [18] Atlantic salmon [1], fugu *Takifugu rubripes* [2] and striped bass *Morone saxatilis* [9].

Considerable evidence suggests that piscine CFTR is a Cl-transporter and is actively involved in osmoregulation. CFTR is highly expressed the major osmoregulatory organs such as gill, opercular epithelium and intestine of seawater

(SW)-adapted killifish [18]. CFTR mRNA expression and the localization of CFTR channels on CCs were salinity-dependent in killifish, particularly, the mRNA expression in gills showed a nine-fold increase 24 hours after exposure of freshwater (FW)-adapted killifish to SW [18]. Immunocytochemical study revealed that CFTR was present in the apical membrane of CCs for ion secretion in SW [19]. CFTR was also detected in the opercular epithelium of FW-adapted killifish, but they were diffusely localized near the basolateral membrane of CCs, when killifish were subjected to SW exposure, CFTR became re-distributed progressively from the cytosol and finally inserted onto the apical membrane of CCs [11]. Most of the enterocytes of marine killifish showed CFTR immunofluorescence on the basal portion and were involved in salt absorption in the intestine, but there was about 20% of enterocytes which exhibited apical distribution of CFTR and the author suggested that this subgroup of chloride channels may be involved in salt secretion [12].

The present study aims at confirming CFTR mRNA expression in the main osmoregulatory epithelia of sea bream. A partial CFTR gene sequence was obtained from the gills of silver sea bream, from which specific oligonucleotides were obtained for detection of CFTR mRNA expression in tissue distribution experiments. Tissue distribution profile was constructed to aid further understanding of this chloride channel in relation to osmoregulation.

2. MATERIALS AND METHODS

Experimental fish

Silver sea bream (*Sparus sarba*) were acclimated to seawater aquaria for 1 month and fed a pellet diet [21] daily ad libitum. Feeding was terminated 24 h before sacrifice and fish were killed by spinal transection. Various tissues were collected and stored in 500 μl of Tri-Reagent (Molecular Research Center, Cincinnati, OH) until analysis.

Total RNA extraction, reverse transcription and cloning

CFTR gene in silver sea bream was cloned using semi-quantitative reverse transcriptase polymerase chain reaction (RT-PCR). Total RNA was extracted according to manufacturer's instruction (Molecular Research Center, Cincinnati, OH), quantified by spectrophotometry at 260 nm and purity was assessed by gel electrophoresis using 2% agarose gel. Total RNA was used for synthesizing first strand cDNA by reverse transcription using oligo dT primer and MuLV Reverse Transcriptase (Gibco-BRL, Gaithersburg, MD; 200 U/μl). The resultant cDNA template was used for the polymerase chain reaction (PCR). Multiple alignments of several published teleost CFTR genes (killifish, AF000271, [18]; fugu, AJ271361, [2]; Atlantic salmon, AF155237 and AF161070, [1]; puffer fish, AE017192, [2]) were constructed using ClustalW to identify highly conserved gene regions, from which gene-specific primers were designed using the Primer3 program. The following primer sets were used to amplify a specific region of silver sea bream CFTR gene:

R-domain:
Forward 5'-CCTTTTACCCACCTGGACCT-3'
Reverse 5'-CCTCCTCTACCTGATCGTCCT-3'
(product size = 583 bp)

R-domain to membrane spanning region:
Forward 5'-GGGGTTCGTGAACTTTCTGA-3'
Reverse 5'-ATGATTCGGCCTGTCTTCAT-3'
(product size = 780 bp)

Specific sequences of CFTR gene fragments were amplified from gill of silver sea bream using *Taq* DNA polymerase. Thermal cycling of PCR reactions was performed as follows: 30s denaturation at 94^{o}C, followed by 30s annealing at 60^{o}C, followed by a 1-min extension step at 72^{o}C for 30 cycles. PCR products were separated according to size by gel electrophoresis in 2% agarose gels with ethidium bromide staining and cloned using a Topo TA cloning kit (Invitrogen). Multiple clones of each fragments were sequenced bidirectionally, and the partial CFTR gene sequences obtained were deposited in GenBank database with the Accession no. EF017215.

Tissue distribution profile of CFTR

CFTR mRNA expression level was assessed in brain, pituitary, gill, opercular epithelium, anterior intestine, stomach, posterior intestine, spleen, urinary bladder, liver, kidney, heart, gonad and muscle. Preparation of first strand cDNA from these tissues was the same as those previously described. Primers specific to silver sea bream CFTR were designed using the Primer3 program from the partial sequence of silver sea bream CFTR obtained. The primers had the following sequences:

Forward 5'-GTCACCAGCAAGTTTGAGCA-3'
Reverse 5'-CGGGTACCACAGAGAATTTCC-3'
(product size = 478 bp)

PCR amplification was performed with cycle parameters of 30s denaturation at 94oC, followed by 30s annealing at 60oC, followed by a 30s extension step at 72oC for 33 cycles. Before initiating experiments, the linear range of the PCR for the primer set was determined. These cycling parameters (33 cycles, 60oC annealing) were chosen to ensure that the set of primers resulted in reactions that were within the exponential amplification phase of the PCR for all templates. PCR products were separated according to size by gel electrophoresis in 2% w/v agarose gel and stained with ethidium bromide. The PCR products were visualized by ultraviolet illumination and quantified by densitometry using QuantityOne software (Bio-Rad).

3. RESULTS

Cloning of CFTR gene

Partial sequence of silver sea bream CFTR gene flanking part of the R domain and the membrane spanning regions was obtained (Fig. 1). Multiple sequence alignment revealed that the partial sequence of silver sea bream CFTR was 80% similar to killifish CFTR and 84% similar to fugu CFTR at the nucleotide level.

Tissue distribution profile of CFTR

Using the set of primers designed from the partial sequence of silver sea bream CFTR, amplification yielded a fragment of about 500 bp with strong signals in gill, anterior intestine, posterior intestine and pituitary, and weak signals in opercular epithelium, spleen, urinary bladder, liver and heart tissues. No CFTR expression could be detected in brain, stomach, kidney, blood, muscle and gonad (Fig. 2).

```
   0       GTAACAGAGA AAGAGATCTT TGAAAAATGT GTCTGTAAAC TTATGGCCTC CAAGACTCGT ATTGTGGTCA CCAGCAAGTT TGAGCATCTC AAACGAGCAG
 100       ACAAAATCCT GCTGCTGCAC AACGGAGACT GCTATTTCTA CGGCACCTTC TCAGAGCTGC AGGCCCAGCG TCCTGACTTC AGCTCCCTCC TCCTCGGCCT
 200       GGAAGCCTAT GACAACATCA ATGCAGAGAG ACGCAGCTCC ATCCTCACGG AAACTCTCCG CAGGGTCTCT GTCGATGAAA CAGCTGGCTT CCGAGGCCCA
 300       GAGCCAATTC GACAGTCGTT CCGCCAGCAA CCCCCTCCAA TGATCATCTC TGGATCCCAA GGACATCCTG GAAGTGATGG CTACCCAGAA AAACGCAAAC
 400       AGTCTCTAAT CCTTAACCCC CTGGCAGCTG CACGCAAGTT CTCCTTCATT GGGAACTCCC AACAGACTGC AAATCCTCCC CAGTCCAGTT CAATAGAAGA
 500       TGGGGTTCGT GAACTTTCTG AGAGGAAATT CTCTGTGGTA CCCGAGGATG ATCAAGTAGA GGAGGTGCTT CCCAGGGGTA ATGTATACCA TCATGGGCTG
 600       CAGCACTTCA ACGGGCAGCG GCGTCAGTCT GTCCTGGCGT TCATCACCAA CTCTCAGGGC CAGGAGCGCA GAGAGCAGAT TCAGTCCTCC TTCAGAAAAA
 700       AACTGTCCAT CACACCGCAG TGTGACCTGG CGCCCGAGCT GGACATTTAT GCCCGCCGTC TGTCCAAGGA CAGCGTCTAT GACATTAGTG AGGAGGTGGA
 800       TGAGGAAGAC ATGGAGCAAT GCTTTGCAGA TCAGCGTGAG AACATCTTTG AAACTACCTC ATGGAGCACC TACCTGCGCT ACATCACCAC CAACAAGAGC
 900       TTAGTCTATG TCCTAATTTT CATCGTCTTT GTCTTCATCA TTGAGGTTGC TGGTTCAGTC ATCGGCATTT TCCTCATAAC TGACACGATT TGGAGGGATG
1000       GCGCCAACCC TTCATCACCC AACTACATTG ATGAGCAGCA CGTCAATGCC TCATCAACCC CAGTCCACCT GGCAGTCATC GTCACACCAA CCAGCGCTTA
1100       CTACATTATC TACATCTATG TGGCCACATC AGAGAGCGTG CTGGCCCTGG GATTCTTCAG GGGTCTCCCA TTAGTGCACA CATTACTCAC TGTGTCTAAA
1200       AGATTGCATG AACAGATGCT AAGCGCTGTA ATACGAGCCC CCATGGCTGT ACTCAACACT ATGAAGACAG GCCGAATC
   0     VTEKEIFEKC VCKLMASKTR IVVTSKFEHL KRADKILLLH NGDCYFYGTF SELQAQRPDF SSLLLGLEAY DNINAERRSS ILTETLRRVS VDETAGFRGP
 100     EPIRQSFRQQ PPPMIISGSQ GHPGSDGYPE KRKQSLILNP LAAARKFSFI GNSQQTANPP QSSSIEDGVR ELSERKFSVV PEDDQVEEVL PRGNVYHHGL
 200     QHFNGQRRQS VLAFITNSQG QERREQIQSS FRKKLSITPQ CDLAPELDIY ARRLSKDSVY DISEEVDEED MEQCFADQRE NIFETTSWST YLRYITTNKS
 300     LVYVLIFIVF VFIIEVAGSV IGIFLITDTI WRDGANPSSP NYIDEQHVNA SSTPVHLAVI VTPTSAYYII YIYVATSESV LALGFFRGLP LVHTLLTVSK
 400     RLHEQMLSAV IRAPMAVLNT MKTGRI
```

Figure 1. Nucleotide and deduced amino acid sequence of *Sparus sarba* branchial CFTR cDNA clone responsible for part of the R-domain and membrane spanning regions. Nucleotides and amino acids are numbered on the left-hand side. These sequences have been deposited with GenBank (Accession no.: EF017215).

Figure 2. Agarose gel with PCR products from different tissues of *Sparus sarba* under ultraviolet illumination. Order of tissues is 1: brain, 2: gill, 3: opercular epithelium, 4: anterior intestine, 5: stomach, 6: posterior intestine, 7: spleen, 8: urinary bladder, 9: liver, 10: kidney, 11: heart, 12: blood, 13: gonad, 14: negative control, 15: ladder, 16: pituitary and 17: muscle.

4. DISCUSSION

The presence of a characteristic CFTR R domain demonstrates that the presently obtained silver sea bream gene fragments are true CFTR homologs, which are distinct from other members of the ABC superfamily of transporters [18]. Alignment of other cloned teleost CFTR homolog shows that the R-domain is the region with the least homology among all species. In mammalian CFTR, this domain was also termed the regulatory domain which consisted of 241 amino acids, where some of the amino acids contained charged side chains [16]. In addition, there were strong consensus sequences for phosphorylation by protein kinase A (PKA) and protein kinase C (PKC). This clustering, especially the PKA phosphorylation sites, suggested the role of R-domain on regulating CFTR activity would probably act through phosphorylation [16].

A thorough tissue distribution analysis of CFTR in silver sea bream was performed and it was found that CFTR was present at high levels in the primary osmoregulatory organs, i.e. gill, intestine, and pituitary, and to a lesser extent, in opercular epithelium, spleen, urinary bladder, liver and heart.

CFTR is primarily responsible for transport of chloride ions (Cl^-) [18]. In the currently accepted model for ion transport in SW-adapted teleosts, SW chloride cells are named for their ability to secrete Cl^- actively from the basolateral side to the apical side of the cell [10]. In an immunolocalization study, CFTR appeared to be restricted to the apical membrane in the apical crypts of chloride cells from SW-adapted mudskippers [19]. Our result indicated a high expression of CFTR in the gill of silver sea bream, which is consistent with the finding that this tissue contains an abundance of these specialized chloride cells. It must be emphasized that the present experiments cannot provide direct evidence for localization of CFTR in the chloride cells, but can only demonstrate the abundant expression in gill tissue, although the importance of the chloride cells in the osmoregulatory physiology of the sea bream has been amply demonstrated [5] and [6].

The opercular epithelium of SW-adapted killifish was rich in chloride cells, and CFTR mRNA expression levels in gill and opercular epithelium were similar [18]. These opercular chloride cells in killifish also showed CFTR immunofluorescence which is restricted to the

apical membrane [11]. Our results showed a lesser amount of CFTR expression in the opercular epithelium of silver sea bream relative to its branchial expression. There are two possibilities that could possibly account for such result, either the opercular epithelium of SW-adapted silver sea bream is not rich in chloride cells, or there is a differential role of opercular epithelium between the two species of fish with respect to chloride secretion by CFTR.

Marine teleosts drink SW, and absorb salts and fluid across the esophageal and intestinal epithelia that have high osmotic permeability. Almost all ingested water and monovalent ions are absorbed in parallel by the intestine of SW teleosts [8]. Killifish CFTR was expressed in the posterior intestine at levels comparable with gill tissues, as detected by Northern blot analysis [18]. Marshall et al. [12] investigated the electrophysiology of anterior and posterior sections of intestine of SW killifish and found both tissues responded in a similar manner and revealed CFTR localization on the basolateral side of the intestine of SW killifish. Our findings in the anterior and posterior intestine of silver sea bream are consistent with the previous study in killifish, and suggest an absorptive role of CFTR in the intestine of silver sea bream. Absorptive cells endowed with similar transport mechanisms as gill chloride cells have been localized in the intestines of many fish species [8] including the sea bream, in which the main ion transporter Na^+, K^+-ATPase has been localized [20].

In contrast to killifish, there is no detectable CFTR expression in brain of silver sea bream. CFTR mRNA and protein were found to be present within the rat and human brains, in areas regulating sexual differentiation and function [15]. In addition, it is surprising that the pituitary of silver sea bream was found to have a high expression of CFTR. Pituitary is the production site of prolactin which is a well-known freshwater adapting hormone in fish including the sea bream [7], and also that of growth hormone, which is involved with osmoregulation in SW in some fish species [3]. Therefore, modulation of CFTR mRNA level may have an effect of prolactin or growth hormone secretion from the pituitary, which in turn affects the osmoregulatory mechanisms of fish.

5. ACKNOWLEDGMENT

This work is partially supported by a Research Grants Council (Hong Kong) General Research Grant (CUHK 477111).

6. REFERENCES

[1] Chen J M, Culter C, Jacques C, Boeuf G, Denamur E, Lecointre G, Mercier B, Cramb G, Ferec C. A combined analysis of the cystic fibrosis transmembrane conductance regulator: implications for structure and disease models. *Molecular Biology and Evolution* 2001, 18: 1771-1788.

[2] Davidson H, Taylor M S, Doherty A, Boyd A C, Porteous D J. Genomic sequence analysis of *Fugu rubripes* CFTR and flanking genes in a 60 kb region conserving synteny with 800 kb of human chromosome 7. *Genome Research* 2000, 10: 1194-1203.

[3] Deane E E, Woo N Y S. Modulation of fish growth hormone levels by salinity, temperature, pollutants and aquaculture related stress: a review. *Reviews in Fish Biology and Fisheries* 2009, 19: 97-120.

[4] Hirose S, Kaneko T, Naito N, Takei Y. Molecular biology of major components of chloride cells. *Comparative Biochemistry and Physiology* 2003, 136B: 593-620.
[5] Kelly S P, Chow I N K, Woo N Y S. Alterations in Na^+-K^+-ATPase activity and gill cell morphometrics of juvenile black sea bream (*Mylio macrocephalus*) in response to salinity and ration size. *Aquaculture* 172: 351-367, 1999.
[6] S. P. Kelly, and N. Y. S. Woo, The response of sea bream following abrupt hyposmotic exposure. *Journal of Fish Biology* 1999, 55: 732-750.
[7] Kwong A K Y, Woo N Y S. Prolactin-releasing peptide, a possible modulator of prolactin in the euryhaline silver sea bream (*Sparus sarba*): a molecular study. *General and Comparative Endocrinology* 2008, 158: 154-160.
[8] Loretz C A. Electrophysiology of ion transport in teleost intestinal cells. In: *Cellular and Molecular Approaches to Fish Ionic Regulation*. Eds. Wood, C. M. and Shuttleworth, T. J. Academic Press, Inc.: San Diego. 1995, pp. 25-56.
[9] Madsen S S, Jensen L N, Tipsmark C K, Kiilerich P, Borski R J. Differential regulation of cystic fibrosis transmembrane conductance regulator and Na^+, K^+-ATPase in gills of striped bass, *Morone saxatilis*: effect of salinity and hormones. *Journal of Endocrinology* 2007, 192: 249-260.
[10] Marshall W S, Bryson S E. Transport mechanism of seawater chloride cells: an inclusive model of a multifunctional cell. *Comparative Biochemistry and Physiology* 1998, 119A: 97-106.
[11] Marshall W S, Lynch E M, Cozzi R R F. Redistribution of immunofluorescence of CFTR anion channel and NKCC co-transporter in chloride cells during adaptation of the killifish *Fundulus heteroclitus* to sea water. *Journal of Experimental Biology* 2002a, 205: 1265-1273.
[12] Marshall W S, Howard J A, Cozzi R R F, Lynch E M. NaCl and fluid secretion by the intestine of the teleost *Fundulus heteroclitus*: involvement of CFTR. *Journal of Experimental Biology* 2002b, 205: 745-758.
[13] Marshall J, Martin K A, Picciotto M, Hockfield S, Nairn A C, Kaczmarek L K. Identification and localization of a dogfish homolog of human cystic fibrosis transmembrane conductance regulator. *Journal of Biological Chemistry* 1991, 266: 22749–22754.
[14] McCormick S D. Methods for nonlethal gill biopsy and measurement of Na^+, K^+-ATPase activity. *Canadian Journal of Fisheries and Aquatic Sciences* 1993, 50: 656-658.
[15] Mulberg A E, Weyler R T, Altschuler S M, Hyde T M. Cystic fibrosis transmembrane conductance regulator expression in human hypothalamus. *Neuroreport* 1998, 9: 141-144.
[16] Riordan J R. CFTR Function. In: *Cystic Fibrosis–Current Topics*. Eds. Dodge, J. A., Brock, D. J. H. and Widdicombe, J. H.. John Wiley & Sons Ltd.: New York. 1993, pp. 157-173.
[17] Riordan J R, Rommens J M, Kerem B S, Alon N, Rozmahei R, Grzelczak Z, Zielenski J, Lok S, Plavsic N, Chou J L, Drumm M L, Iannuzzi M C, Collins F S, Tsui L C. Identification of the cystic fibrosis gene: cloning and characterization of complementary DNA. *Science* 1989, 245: 1066-1073.
[18] Singer T D, Tucker S J, Marshall W S, Higgins C. A divergent CFTR homologue: highly regulated salt transport in the euryhaline teleost *F. heteroclitus*. *American Journal of Physiology* 1998, 274: C715-C723.
[19] Wilson J M, Randall D J, Donowitz M, Vogl A W, Ip A K Y. Immunolocalization of ion-transport proteins to branchial epithelium mitochondria-rich cells in the mudskipper (*Periophthalmodon schlosseri*). *Journal of Experimental Biology* 2000, 203: 2297-2310.
[20] Wong M K S. Characterization of the renin-angiotensin system in silver sea bream (*Sparus*

sarba): Perspectives in salinity adaptation. PhD thesis, The Chinese University of Hong Kong, 2005.
[21] Woo N Y S, Kelly S P. Effects of salinity and nutritional status on growth and metabolism of *Sparus sarba* in a closed seawater system. *Aquaculture* 1995, 135: 229-238.

BENS88

Alternative Energy Resource and Power Generation in Selected Block of Hugli, West Bengal

Lopamudra Basu
Lecturer Department of Geography, Sivanath Sastri College, 23/49 Gariahat Road,
Kolkata700029, West Bengal
E-mail address: basulopa24@gmail.com

1. INTRODUCTION

The entire world produces carbon dioxide which is released into the atmosphere every day. The amount is expected to increase with years' time. This increased content of carbon dioxide is the main cause of global warming. The best way to restrict the global warming is to replace and retrofit current technologies with alternatives that have better performance but emits less carbon dioxide. Reducing energy use is also seen as a key solution to the problem of reducing greenhouse gas emissions. This can be possible with what is better known as alternative resource. Alternative resources are renewable and therefore have no undesired consequences. With the rise of population the energy requirements are also likely to increase. Energy efficiency and renewable energy are said to be the *twin pillars* of sustainable energy policy.

Our topic in question is that how energy can be efficiently managed so that in one hand it will emphasise the economy and on the other hand it will be eco-friendly. For this there are 2 ways open to us, either reduce the consumption of power or substitute the same with renewable energy sources. The reduction of power consumption can be achieved either by controlling the consumption level, avoiding wastage or following energy efficient systematic programmes. However, power generation output will have a little impact, but the positive side will be individual's lesser payment of electric bills at the end of the month.

The systematic energy efficiency programmes and its successful implementation nowadays is a widespread thought. All over the world, including the developing & underdeveloped countries, the research & development system is giving priority to achieve energy efficiency system by upgrading technologies. About 16% of the global energy consumption comes from renewable. The share of renewable in the generation of electricity is about 3%.

2. APPROACH

For almost three decades, the U.S. Department of energy has been exploring advanced technologies that help to reduce energy waste and create the efficiency needed for prolonged economic growth. There are wonderful opportunities in India to apply these technologies. The key focus of this paper is to examine the use of alternative source of energy for an eco friendly environment. An analysis of various scenarios of energy demand and supply has been carried to provide a representation of the different technologies and sectoral energy demands. The magnitude of total energy requirements was estimated along with the economic, environmental implications of India's alternative energy pathways. This paper also tries to explore the

possibilities of use of alternative resources in generation of power with rice husk. For the same Hugli district of West Bengal has been selected which has an abundance of availability of rice husk.

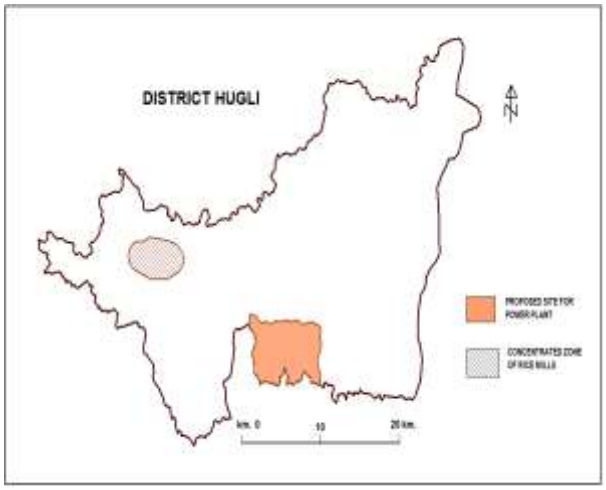

Fig I

3. METHODOLOGY

The location of rice mills were collected from Government of West Bengal and the Rice mill associations of Hugli district. Primary survey was conducted to assess the productivity of rice along with the consumption and the husk generated. The information regarding the price of rice husk and transportation cost was also collected. The estimation of capacity of power plant from rice husk has been based on secondary data.

4. POWER SCENARIO IN INDIA AND WEST BENGAL

With India's energy demand expected to double by 2030, there is a pressing need to develop innovative ways to conserve energy. The industrial sector consumes about half of the total energy available in India. The industry and transport sector have highest potential for saving energy. From FIG II it can be seen that the domestic sector has the highest potential for energy saving in West Bengal.

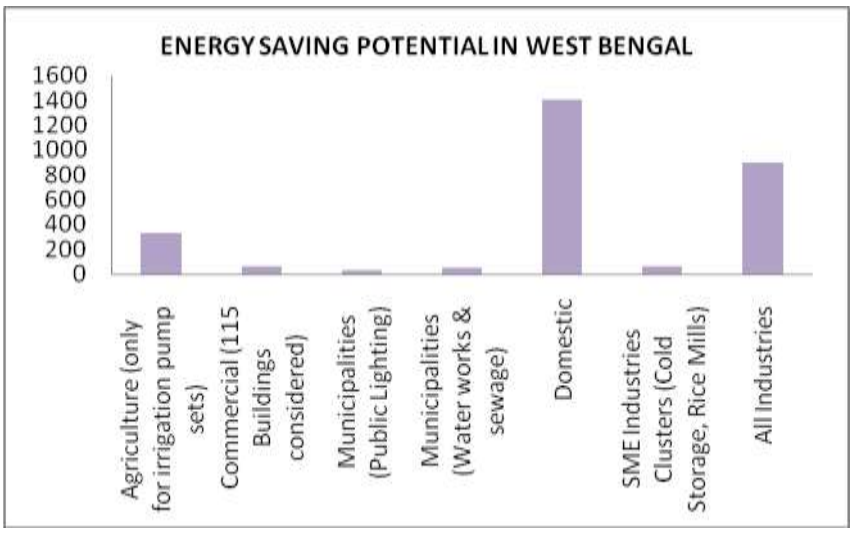

Fig II

However the potential for energy saving in the industrial sector is likely to come down because of maximum consumption of power. The increasing numbers of industries results in immense pressure on consumption. The ratio between the growth of industries and energy saving unit comes down. The introduction of latest technologies in the transport sector might lead to the increasing energy saving.

In India the total commercial energy consumption is estimated to increase from 285 million tonnes of oil equivalent in 2001 to 2123 in 2031. It has been studied that if the economy grows at the rate of 6.7% the commercial energy requirement would be 1579 million tonnes of oil equivalent by 2031. However, the energy requirement other than the commercial sector is expected to be very high. It could be as high as 3351 million tonnes of oil equivalent. This might become possible because of using advanced coal and gas based power generating technologies. Studies revealed that the energy consumption can be reduced to 15% - 25% in 2031. Alternate sources can be exploited to curb the country's energy requirement. It is seen that the commercial energy consumption shows a steady rise by 2030. In West Bengal total installed generating capacity is about 7601 MW in 2008. The state sector accounts for about 5508 MW. However, in 2010-11 the generation of electricity from hydro, nuclear, renewable and thermal has been estimated to be 712 BkWh. With the increasing demand for energy the generation of energy is expected to rise by 3000 BkWh.

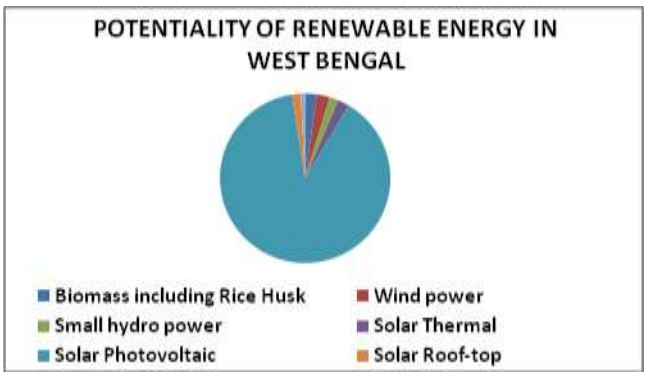

Fig III

The strong positive correlation between energy use and human development is well recognised and a substantial increase in per capita energy consumption is anticipated while attaining an acceptable level of well-being amongst the citizens.

5. STATUS OF ELECTRICITY SUPPLY AND CONSUMPTION IN WEST BENGAL

Renewable energy can be particularly suitable for developing countries. In rural and remote areas, transmission and distribution of energy generated from fossil fuels can be difficult and expensive. Producing renewable energy locally can offer a viable alternative. With the increasing population the requirement and the cost of energy is expected to rise rapidly.

The primary fuel used in the residential sector in the state is predominantly biomass and fossil fuels. In rural West Bengal, Firewood/Biomass is reported as the predominant fuel for cooking in 74% of the households, with dung cake (4%), LPG (4%) and the remaining using other fuel sources including coke/coal.

In West Bengal, 96% of the current electricity generation, is from coal-based generating stations, while the remaining is mostly from hydro-power sources. The state sector has an installed electricity generation capacity of 10,398 MW (2010). The State level Perspective Power Planning Committee (2006) has projected the aggregate demand for electricity to be between 66,368 and 71,351MU by 2021, based on scenario generated from economic trends, assuming a rise of 4% for the domestic segment, 6% for commercial and 3.5% for industry. The peak demand is projected to be between 8,937 and 10,871 MW in 2021 increasing to about 14,730 MW by 2031. Electricity generation in the state is mostly coal-based (96%) at the Thermal Power Stations.

6. ENERGY CONSUMPTION IN RURAL SECTORS OF WEST BENGAL

India has a population of 1.2 billion, 70% of which is concentrated in the rural sector. Therefore, the rural energy needs should be taken care of as the rural poor do not have the purchasing power to articulate their needs. Moreover, many of the villages are still without electricity. In West Bengal only 49 percent of the rural households have access to electricity. It is assumed that rural penetration could improve up to 75% by 2015. This indicates about 3-4 million unconnected households, who could be use biomass or kerosene for lighting and cooking.

Biomass power & cogeneration programme is implemented with the main objective of promoting technologies for optimum use of state's biomass resources for grid power generation. Biomass materials used for power generation include bagasse, rice husk, straw, cotton stalk, coconut shells, soya husk, jute wastes, groundnut shells, saw dust etc.

The current availability of biomass in India is estimated at about 500 million metric tons per year. Studies sponsored by the Ministry have estimated surplus biomass availability at about 120 – 150 million metric tons per annum covering agricultural and forestry residues

corresponding to a potential of about 18,000 MW. The state of West Bengal on the other hand has the potentiality of about 3000MW. The eastern states of West Bengal, Orissa and Bihar (covering 15 talukas) account for about 18-25% of surplus biomass as a percentage of total biomass.

7. ELECTICITY GENERATION WITH THE HELP OF RICE HUSK

Using biomass to produce electricity is 80 percent more efficient than transforming the biomass into biofuel. In addition, the electricity option would be twice as effective at reducing greenhouse-gas emissions. Biomass is plant matter used to generate electricity with steam turbines & gasifiers or produce heat, usually by direct combustion. The term Biofuel and Biogas refer to fuels derived from Biomass, from agricultural and domestic waste and by anaerobic digestion of sewage. Biomass is sustainable and generally carbon neutral because the carbon released in the combustion process is offset by the carbon trapped in the organic matter by photosynthesis during its growth.

In the state of West Bengal the situation urges the need for an introduction of alternative fuel for generation of power. A 5MW power plant for electricity generation can be planned to set up in the Hugli district of West Bengal. Jangipara block of Hugli district has been chosen for setting up of the power plant. The project envisages generation of power to support the energy deficit in the entire district. According to the earlier definition of village electrification a village is classified as electrified if electricity is being used within its revenue area. But the new definition suggests that the basic infrastructure such as distribution transformer and or distribution lines is made available in the inhabited locality within the revenue boundary of the village including at least one hamlet/Dalit Basti as applicable. Secondly any of the public places like Schools, Panchayat Office, Health Centres, Dispensaries, Community centers etc. avail power supply on demand. Thirdly the number of household electrified should be minimum 10%.

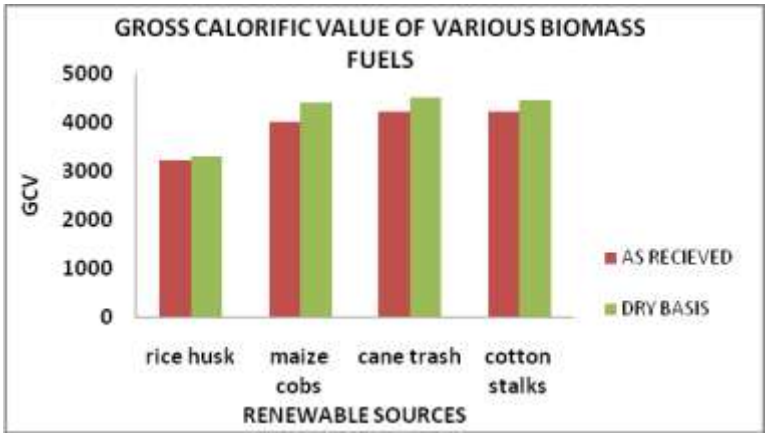

Fig IV

For setting up the power plant rice husk has been used as fuel. This serves as the best fuel for AFBC (Atmospheric classic Fluidised Bed Combustion System) boilers. West Bengal has a potential to generate 600 mw of biomass energy as enough husk available from the 1,300 rice mills and at least one lakh husking mills in the state. The calorific value of the rice husk is about 3300 to 3500 kcal/ kg husk with low ash content. More over the ash composition has 75-87%

silica which can be easily disposed off. The silica produced often serves as good fertilizer for the agricultural sector. The rice husk ash has other alternative uses. The husk ash has been used by many steel plants in generating good quality steel. It prevents the rapid cooling of the steel ensuring uniform solidification. Besides, it also acts as an excellent insulator with low thermal conductivity. The diagram shows that cane trash, maize cobs, cotton stalks have low residues but are highly toxic and cannot be easily disposed.

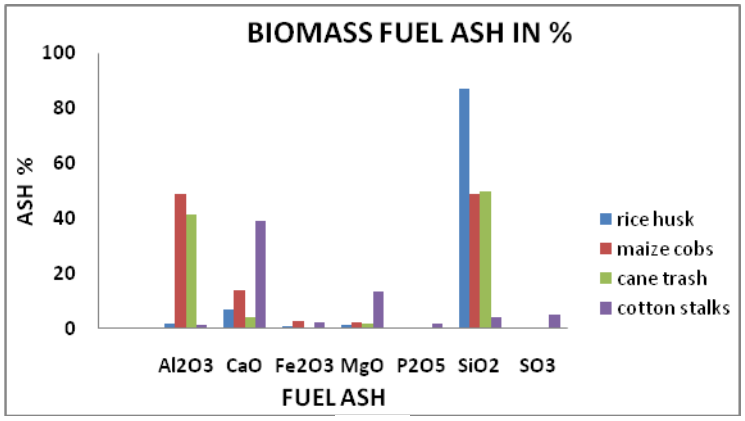

Fig V

West Bengal accounts for 17% of total rice production. Rice husk is nothing but a bi-product of rice. Amongst 2 types of rice parboiled and atap, output of husk from atap is appreciably high having high calorific value. The variations in efficiency largely depend on the characteristics of the resources.

There are 103 modern rice mills in Hugli district, out of which 88 are located in Arambagh subdivision. These mills are situated within 15 km radius of the subdivision. Net annual surplus availability of rice husk from rice mills in Hugli district has been estimated to be 66955 tonne of which 85.65% (57247 tonne) is generated in Arambagh subdivision. The power plant can operate year round with surplus rice husk. It has been estimated that 1.3kg of rice husk is required to generate 1 unit (1 kWh) of electricity. The annual electricity generation for the entire district has been estimated to be 51503846 kWh/year. Average proximate analysis of husk is also essential in case of setting up of the power plant. Rice husk has 19.8% fixed carbon and 17.5% ash. This remains the standard value. Any increase in the amount of fixed carbon and ash will have a negative impact. The more the ash carbon content in the husk, the calorific value comes down. This deteriorates the efficiency of the boiler and therefore requirement of the husk will increase. The annual consumption of rice husk for 5 MW power plant has been estimated to be 55801 ton. The husk is available in abundance in the summer months rather than in the winter season. Along with the availability of the husk, the price has also been taken into account. Price ranges between Re. 0.70- Re. 1.00/ kg in summer, rises in winter. Adding the transportation cost the price has been estimated to about Rs. 1.20/ Kg.

The power plant project would be beneficial not only for the meeting the energy crisis in Hugli but also the agricultural sector where additional energy is required. It aims toward employment generation in the rural sector too. According to WBSERC (West Bengal State Electricity Regulatory Comission) directives the thermal power producing company using fossil

fuel are liable to purchase 3% green power of their total generation capacity. The biomass based power plant can be beneficial for the same.

8. CONCLUDING OBSERVATION

Biomass, a broad term for all organic matter, is currently regarded as renewable energy source which will contribute to the world's energy supply in the future.

Throughout the country massive programmes on renewable energy utilization have been launched. However, larger application on a sustainable basis is essential. From the above discussion it can be concluded that the demand for energy will show a steady rise in all sectors with the growth and development of energy. It will not be possible to reduce or check the consumption level; rather an alternative arrangement of resource has become essential. Government of India, from 1980-2005 have taken up major policies to increase the energy efficiency in the industrial sectors. It has also set an ambitious target of "power for all" by 2009. A major challenge, however, is to make renewable sources competitive with fossil fuels and nuclear plants.

Use of cleaner fuel; support to small, medium and large scale industries; shift towards tapping waste heat for process heat; use of bio diesel fuel etc. are some of the recommended measures that can be taken for a cleaner and greener environment.

9. REFERENCES

1. XI plan proposals for new and renewable energy, Ministry of New and Renewable Energy, Government of India, December, 2006.
2. Anil Kumar Jain, Design Parameters for a Rice Husk Throatless Gasifier Reactor, Agricultural Engineering International: the CIGR Ejournal, Manuscript EE 05 012. Vol VIII. May, 2006.
3. S. Dasappa, P J Paul, H S Mukunda, N. K. S. Rajan, G Sridhar G., H V Sridhar, Biomass gasification technology- a route to meet energy needs, Current Science, Vol. 87, No. 7, 10 October 2004
4. F A Agblevor, S. Besler, R J Evans, Inorganic compounds in biomass feedstock: Their role in char formation and effects on the quality of fat pyrolysis oils. In proceedings of biomass pyrolysis oil properties and combustion meeting edited by Milne, T. A.,M Estes Park, National Renewable Energy Laboratory, Golden, CO, NREL-CP-430-7215, , 77-89, September 26-28, 1994
5. Gangesh Upadhyay, R D Sharma, J B S Girdhar, B M L Garg, Sudhir Mohan, Biomass power potential in India- an overview, Biomass based decentralized power generation, Proceedings of the national seminar, 7-43. 2005
6. P S Pathak, T A Khan, P Sharma, Biomass production its utilization and surplus for energy generation in India. In: Biomass management and energy purposes- Issues and strategies, Editors B S Pathak , N S L, Srivastava. Technical publication No. SPRERI/2005/2, Sardar Patel Renewable Energy Research Institute, Vallabh Vidyanagar (Gujarat), 10-35, 2005
7. Ministry of New and Renewable Energy (MNRE), Annual report, 2008- 2009

BENS89

Environmental Conditions Vulnerable to Fluoride Contamination of Drinking Water in Parts of Birbhum District and Impact on Human Health

Bhaswati Ray
Department of Geography Sivanath Sastri College, 23/49 Gariahat Road Kolkata 700029, India
E-mail address: bhaswati173@gmail.com

ABSTRACT

Fluoride incidence in ground water has turned out to be a serious environmental hazard in Bibhum district in recent times. Certain environmental conditions aid the weathering and leaching processes that dissolve fluoride from the fluoride bearing rocks and increase the vulnerability of ground water to fluoride contamination. An exponential increase in the number of hand pumps during the last three decades and the tapping of fluoride rich aquifers has exposed the population to excess fluoride most commonly through drinking water. While small concentrations of fluoride are known to stimulate teeth and bone formation, a concentration of more than 1.5ppm results in the accumulation fluoride in the hard and soft tissues of the human body causing serious health hazards. In this study an attempt has been made to explore the environmental conditions of Birbhum district to assess its vulnerability to fluoride incidence in ground water. Villages were selected from the vulnerable parts of the district that use ground water for drinking and irrigation. The population of these villages was then examined to determine the impacts of fluoride on human health at different fluoride concentration levels. Based on the symptoms, the population may be categorized as those suffering from dental, skeletal and non-skeletal fluorosis. The study would help create awareness about the environmental conditions that increase the risk of fluoride contamination of ground water and fluorosis.

Keywords: fluoride, vulnerability, contamination, environmental hazard, fluorosis

1. INTRODUCTION

Incidence of fluoride in ground water is a natural phenomenon, influenced by local and regional geological settings and hydro geological conditions. The chief source of fluoride in ground water is the fluoride bearing minerals in rocks and sediments. Certain rocks like basalt, granite, gneiss, shale, clay, limestone, sandstone and phosphorite has been identified as major sources of fluoride poisoning in ground water (Agarwal et. al. 1997 [1]).

2. POPULATION EXPOSED TO FLUORIDE CONTAMINATED DRINKING WATER IN INDIA

The fluoride belt in India stretches from Punjab in the north to Tamilnadu in the south and from Gujarat in the west to Assam in the east (Fluorosis Research and Rural Development Foundation, 1999 [3]). According to Rajiv Gandhi National Drinking Water Mission 1991the

bedrock of the Indian peninsula consists of a number of fluoride bearing minerals like fluorite, topaz, apatite and rock phosphate, phosphatic nodules and phosphorite. Health problems caused by the intake of excess fluoride, most commonly through drinking water, has become more acute in India during the last three decades with excessive dependence on ground water for purposes of drinking. Various government programmes like The Accelerated Rural Water Supply Programme launched in 1971-72 and The National Drinking Water Mission of 1986, renamed as the Rajiv Gandhi National Drinking Water Mission in 1991 and the drive to bypass effluent at the surface encouraged the tapping of groundwater. These decades saw an exponential increase in the number of privately owned pump sets and wells (Narain, 2003 [5]). Testing and monitoring of water quality did not receive the desired attention because of the inadequacy of infrastructure. Under such circumstances high fluoride aquifers are being unknowingly tapped.

3. PERMISSIBLE FLUORIDE AMOUNT IN DRINKING WATER

Fluoride is an essential ion for all living beings and helps in the formation of dental enamels and in the proper development of bones. When consumed in inadequate quantities of less than 0.5ppm it causes health problems like dental carries, lack of formation of dental enamel and deficiency of mineralization of bones especially among children. However, at high concentrations of more than 1.5ppm it causes various kinds of physiological disorders. Fluoride helps in the normal mineralization of bones and in the formation of dental enamel, but can cause dental fluorosis and adversely affect the central nervous system, bones, and joints at high concentrations (Agarwal et al., 1997 [1]). 'Fluorosis' describes the state of toxicity of the trace element fluorine (referred to as fluoride in ionic state) within an organism. The permissible upper limit of fluoride in drinking water has been fixed at 1.5ppm by the World Health Organisation. Bureau of Indian Standards has reduced the level to 1.0ppm with an emphasis on 'lesser the better'.

4. HEALTH PROBLEMS ASSOCIATED WITH EXCESS FLUORIDE IN DRINKING WATER

Ingestion of excess fluoride results in its accumulation in the hard and soft tissues of the human body and creates various kinds of discomforts. Based on the symptoms, the population affected by fluoride contaminated drinking water can be categorised as those suffering from dental, skeletal and non-skeletal fluorosis.

Dental fluorosis is a hypomineralisation of tooth enamel characterised by discoloured, blackened, mottled or chalky-white teeth. Dental fluorosis reflects an increasing porosity of the surface and sub-surface enamel, causing the enamel to appear opaque and discoloured. White and yellow discolouration of teeth turns brown and presents itself in horizontal streaks. The fluorosis affected teeth often loose enamel under normal masticatory stress. Cavities initiated in dentin then spread much faster and involve the pulp. The teeth would be pitted and perforated and may even be chipped off. Loss of teeth at an early age is common in endemic areas.

Chronic intake of excess fluoride can also lead to severe and permanent bone and joint deformations of skeletal fluorosis. The main complaints of patients suffering from skeletal fluorosis are severe pain and stiffness in the neck, backbone and joints as well as in the pelvic

girdle. Pain is associated with rigidity and restricted movement of cervical and lumber spine, knee and pelvic joints as well as the shoulder joints. The increasing immobilization of joints due to contractures lead to flexion deformities of hip, knee and other joints resulting in severe disability. Perforations in the backbone gets constricted due to the deposition of calcium fluoroapatite leading to excess pressure on nerves and blood vessels that culminate in paralysis. Crippling deformity is associated with abnormally increased convexity of the thoracic spine and lateral curvature of vertebral column, curved legs, knocked knees and paralysis of lower part of the body. Abortions, still births and deformed children are common in endemic areas because of calcification of the foetal blood vessels.

Among the symptoms of non-skeletal fluorosis, gastro-intestinal complaints are often the early warning signs of fluoride toxicity in endemic areas (Gandhi National Drinking Water Mission, 1994 [6]). The complaints include nausea, acute abdominal pain, intermittent diarrhoea and gas formation, tenderness in stomach, bloated feeling and loss of appetite. Nervousness, depression, polyurea and excessive thirst, painful rashes, male infertility are also regarded as common symptoms of fluoride toxicity.

It is indicated in relevant literature that the symptoms of fluoride toxicity vary with variations in the amount of fluoride in drinking water. According to a report published by World Health Organisation in 1970, fluoride concentration level in drinking water up to 1ppm helps in the reduction of dental carries. At more than 1.5ppm it results in mottled teeth and pitting on the surface while at more than 6ppm fluoride contamination causes both dental and skeletal fluorosis. Yet higher levels of more than 10.0ppm fluoride in drinking water are responsible for crippling skeletal fluorosis. At 50.0ppm, fluoride results in hormonal changes while acute doses of 2.5-5gm may even result in death.

5. THE STUDY AREA

Fluorosis is not a localised problem in India. 20 states have been identified as endemic for fuorosis. An estimated 66.62 million people are at risk out of which 6 million are children below the age of 14 years. West Bengal was identified as endemic for fluorosis in 1996-97. According to the State Water Investigation Department, Birbhum is the worst affected district in West Bengal in terms of clinical manifestations of fluorosis. Fluoride concentration in groundwater is between 10ppm to 16ppm (Central Ground Water Board, 1999 [2]). Hence Birbhum district has been chosen as the study area. It is located in the south western part of West Bengal, between 23°32’30’’N and 24°35’10’’N latitudes and between 87°5’25’’E to 88°01’40’’E longitudes. Covering a significant part of the western shield area, Birbhum district faces a number of physical environmental constraints including the presence of fluoride bearing rocks.

6. OBJECTIVES OF THE STUDY

- To explore the environmental conditions of Birbhum district that are vulnerable to fluoride contamination of drinking water
- To identify the impact of excess fluoride in drinking water on human health among the population of the selected areas of district.

7. RESEARCH METHODOLOGY APPLIED

Literature survey was undertaken to identify the environmental conditions responsible for fluoride contamination of groundwater, the chief source of drinking water in the district. An assessment of the environmental conditions of Birbhum district helped identify the areas within the district that are vulnerable to fluoride contamination.

Pilot survey was conducted in the vulnerable parts of the district for symptoms of fluorosis among the rural population. The residents were also questioned to judge their perception about the quality of drinking water in their villages and their awareness about fluorosis.

Drinking water samples were then collected from the tube wells of the villages located in the vulnerable parts of Birbhum district in which the population showed symptoms of fluorosis. These samples were then tested for estimating the concentration of fluoride.

Primary survey was conducted in two villages with varying amounts of fluoride in drinking water to explore the health impacts of excess fluoride in drinking water at various fluoride concentration levels.

The scope of the study is restricted to the signs of fluoride toxicity on the teeth and bones of a person because these signs are visible and easy to identify. For identifying the effects of excess fluoride on the gastro-intestinal and nervous systems and on the hormones are not easy and one has to depend on detailed medical reports or on the perception of the affected population. Such study is of immense important but needs to be dealt with separately. Hence it has been kept outside the purview of this work.

8. ENVIRONMENTAL CONDITIONS VULNERABLE FOR FLUORIDE INCIDENCE IN GROUND WATER

The concentration of fluoride in groundwater depends on the concentration of fluoride bearing minerals in rock types and mainly on their decomposition and dissolution activities through rock water interactions.

As rain water percolates through the soil, it comes in contact with the rocks and minerals present in the aquifer materials. The rainwater gets enriched in CO_2 from soil, air and biochemical reactions of bacteria and organic matter during its downward movement. The dissolution of CO_2 tends to enhance the hydrogen ion concentration in groundwater.

$$CO_2 + H_2O \rightarrow H_2CO_3$$
$$H_2CO_3 \rightarrow H + HCO_3$$

Alkaline water with a high pH of 7.6 to 8.6 and a high bicarbonate concentration is more conducive for fluoride dissolution in groundwater from soils, weathered rocks and fluorite. It results in the precipitation of calcium carbonate and release of fluorine.

$$CaF_2 + 2HCO_3 \rightarrow CaCO_3 + 2F + H_2O + CO_2$$

It is probable that high fluoride in groundwater is formed as a result of evapotranspiration under arid and semi-arid conditions. The dry climate with high evaporation increase the ion concentration in water and precipitation of soil carbonates occur. Fluoride and pH has positive correlation, indicating that higher alkalinity of water promotes leaching of fluoride and thus affects concentration of fluoride in groundwater (and Ahmed, 2001 [7]).

9. ENVIRONMENTAL CONDITIONS OF BIRBHUM DISTRICT

Climatic environment

The prevailing temperature and rainfall condition in Birbhum district indicates a sub-tropical climate. Oppressive hot dry summers, high humidity and rainfall during the monsoon season are some of the characteristics of the climate of Birbhum. The average temperature is 12.7°C in winter and 39.4°C in summer season. The annual rainfall is 1400mm in the western part of the district and reduces to 1100mm in the eastern part. Mid-June to September is the season of the south-west monsoon and accounts for 78.28 % of the total annual rainfall. Conditions in the pre-monsoon season are semi-arid to arid that increases the fluoride concentration as indicated in relevant literature.

10. GEOLOGICAL SETTING AND HYDRO-GEOLOGICAL CONDITION

Fluoride bearing rocks like basalt, granite, gneiss, shale, clay, limestone and sandstone occur in the western and south-western parts of Birbhum district. Rajmahal Traps, Laterites and Quaternary sediments have fluoride level up to 19.5 ppm in Birbhum district (Central Ground Water Board, 1999 [2]). Laterites occur in Muraroi-I, Nalhati-I, parts of Rampurhat-I and Rampurhat-II, basalts form the bed-rock in Nalhati-I and Rampurhat-I, granite and gneiss in Muhammad Bazar, Rajnagar, in parts of Dubrajpur, parts of Suri-I and Suri-II and in parts of Khoyrasol. Quaternary sediments predominate in parts of Suri I and Suri II, in parts of Dubrajpur and in parts of Khoyrasol.

Ground water occurs under both water table conditions as well as under confined conditions in deeper aquifers (at a depth of 60m to 100m). In the Basaltic region in western parts of the district, secondary porosity develops due to cooling cracks, joints, fissures, open flow junctions and fractures. Near ground porosity is accentuated by weathered rock or laterite cap over hard basalt. Usually contains phreatic water. In the fractures and fissures, ground water occurs in a semi-confined state. The very proximity to the rocks makes the water in these cracks and joints rich in fluoride. The vesicular/ fractured Trap horizons serve as good potential for ground water resources at a depth of 60m to 100m due to their

inter-connected channel ways. In the Archaean crystalline granites and gneisses, ground water occurs under water table and semi-confined conditions in the weathered and fractured zones.

Further, the water samples collected and secondary sources reveal that the ground water of the district is alkaline with the pH ranging mostly from 7.4 to 8.8 that aid the dissolution of fluoride from geological formations. The district also suffers from acute scarcity of water during the drier months of the year. Hence the people of Birbhum depend heavily on ground water for

the purposes of irrigation and drinking. It is evident from the fact that in Birbhum district there is an 8m fall in the level of ground water from post-monsoon to pre-monsoon season (Moulick, 1996 [4]). Hence the C.D. Blocks occupying the western and south-western parts of Birbhum district has been identified as vulnerable for fluoride contamination (Fig.1).

Fig. 1: Parts of Birbhum district vulnerable to fluoride contamination

11. HEALTH IMPACTS OF EXCESS FLUORIDE IN DRINKING WATER IN CASE STUDY VILLAGES

Tapaspur mauza of C.D. Block Dubrajpur has been selected from the areas underlain by the Quaternary sediments. Atla mauza in C.D. Block Rampurhat-I is from the laterite covered areas.

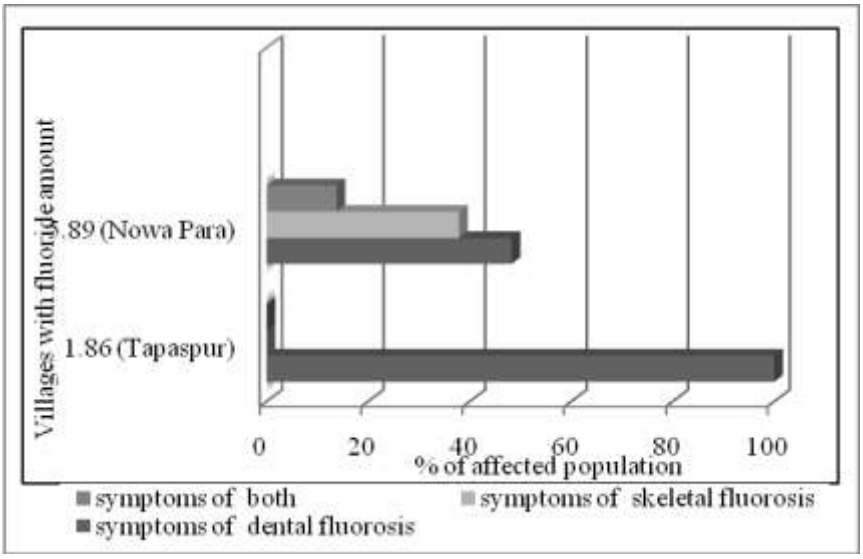

Fig. 2 Symptoms of fluorosis at different fluoride amounts in drinking water

In Tapaspur mauza, only one tube well located near Adarsha Sangha has fluoride above the permissible limit. The fluoride amount is 1.86ppm. 43 households located near the tube well were found to be consuming the contaminated water even when a couple of tube wells located at a short distance has fluoride within the permissible limit. Most of the villagers were reluctant to fetch water from the tube well not located nearest to the house. Besides population of rural India are conscious of their community and prefer to remain within the confines of the locality where the community resides for their needs. A total population of 241 persons residing in these 43 households was hence surveyed.

At this low level of fluoride concentration in drinking water, only 31 persons showed symptoms of fluorosis. The affected population comprises of 12.86 per cent of the total population exposed to fluoride contaminated drinking water (Fig. 3). All of them, however, showed symptoms of dental fluorosis (Fig. 2). Such a condition suggests that at less than 2ppm fluoride in drinking water, the bones remain unaffected by excess fluoride. It is only the teeth that are affected.

For 6 persons the symptoms were slight aberrations in translucency ranging from a few white flecks to occasional white spots. For 16 persons the symptoms were small opaque areas scattered in not more than 25 per cent of teeth surface particularly in the tip of cusps, bicusps and second molars. For these 22 persons comprising of 9.13 per cent of the total surveyed population, symptoms of fluorosis are just beginning to show on the teeth of an individual and hence may be diagnosed as very mild dental fluorosis as indicated by Dean in 1954. As the disease progresses, the white opaque areas become more extensive covering nearly 50 percent of teeth surface. Brown stains are occasionally apparent on superior incisors. Such symptoms were seen in 7 persons indicating that they suffer from mild forms of dental fluorosis. Thus, at this low fluoride amount 2.90 per cent of the total population exposed to the fluoride rich drinking water suffer from mild dental fluorosis.

Only in case of 2 persons, all enamel surfaces were affected with brown stains and signs of

attrition (Fig. 3). Signs of moderate dental fluorosis were thus seen among only 0.83 per cent of the surveyed population. It may be noted that the identification mild and moderate forms of dental fluorosis is based on the work of Dean in 1954.

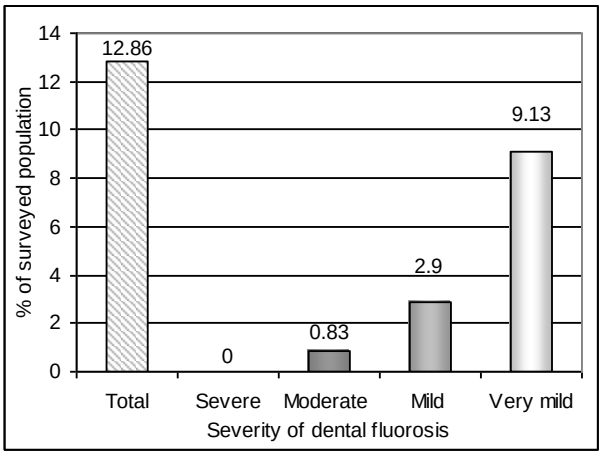

Fig. 3 Symptoms of dental fluorosis in Tapaspur

It is thus evident that at more than 1.5ppm of fluoride in drinking water the population gets affected by fluorosis. But the symptoms show that it is only the teeth that are affected by various forms of dental fluorosis ranging from slight aberrations in translucency to brown stains and a pitted surface.

In Atla mauza the village under study is Nowa Para where all tube wells have fluoride above the permissible limit. This is a small village with 32 households consuming the fluoride contaminated

drinking water. The average fluoride concentration level is 5.89ppm. One tube well with fluoride above 14ppm has already been sealed. The total population under study is 159 persons belonging to these 32 households. 58 persons comprising of 36.48 per cent of the total population

exposed to high fluoride drinking water are affected by the disease (Fig. 4). 28 persons or 48.28 per cent of the total affected population showed symptoms of dental fluorosis while another 22 persons accounting for 37.93 per cent of the total affected population were found to be affected by skeletal fluorosis. In case of the remaining 8 persons or 13.79 per cent of the affected population both the teeth and bones were found to be affected by excess fluoride in drinking water (Fig. 1).

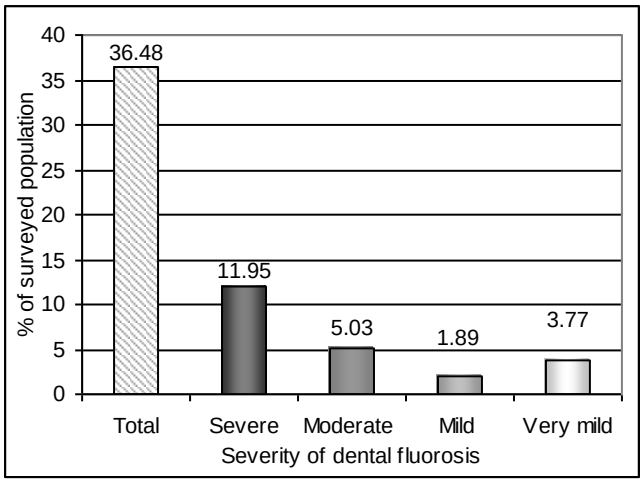

Fig. 4 Symptoms of dental fluorosis in Nowa Para

6 persons comprising of 3.77 per cent of the total surveyed population showed symptoms of very mild dental fluorosis. For 2 persons the symptoms of dental fluorosis were slight aberrations in translucency ranging from a few white flecks to occasional white spots. Another 4 persons showed small opaque areas scattered in not more than 25 per cent of teeth surface covering the tip of cusps, bicusps and second molars. The white opaque areas became more extensive covering nearly 50 percent of teeth surface for 3 persons with thin white lines and occasional brown stains visible on the superior incisors. Mild dental fluorosis has hence affected 1.89 per cent of the surveyed population. Only in case of 8 persons all enamel surfaces were affected with brown stains and signs of attrition. Thus at more than 5ppm fluoride in drinking water 5.03 per cent of the surveyed population suffer from moderate dental fluorosis. The percentage of population suffering from moderate fluorosis increases compared to the population surveyed in Tapaspur. The condition of the teeth worsened in case of 19 persons with all enamel surfaces badly affected. Browns stains were more marked, pitting of teeth surface became apparent and the teeth had a corroded appearance. Dental fluorosis thus turned severe for 11.95 per cent of the surveyed population (Fig. 4).

Apart from the effect on the teeth of an individual, excess fluoride is also known to affect the bones of an individual. It starts with occasional stiffness in spine, mild pain in joints, neck and in the lower back. These symptoms affect the bones at the initial stages and hence are associated with very mild forms of skeletal fluorosis in relevant literatures. 11 persons comprising of 6.92 per cent of the total surveyed population were noticed with such signs of fluoride toxicity. Fluorosis being a bone softening disease, deformities in bones particularly curvature of legs and knocked knee were also visible among 4 persons or 2.52 per cent of the surveyed population. In the next stage chronic joint pain associated with rigidity and restricted movement of the cervical and lumber spine, knees and pelvic joints are common. The affected population are unable to touch their feet, are unable to sit on the floor as well as get up without a support. Such symptoms were apparent among 13 persons. Skeletal fluorosis thus turned moderately severe for 8.18 per cent of the surveyed population. Severe crippling effects on the skeleton include curvature of the thoracic spine, lateral curvature of the vertebral column and paralysis on the lower part of the body. The number of persons affected by the severe or crippling form of fluorosis is 2, accounting for 1.26 per cent of the total population surveyed in this village (Fig. 5).

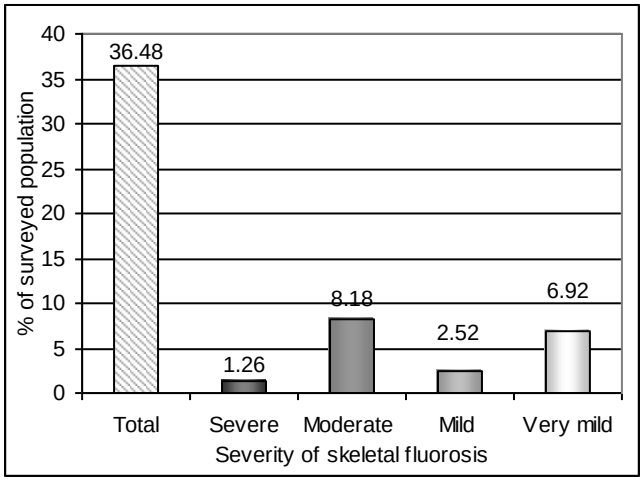

Fig. 5 Symptoms of skeletal fluorosis in Nowa Para

Out of the persons affected by both dental and skeletal fluorosis, fluoride was seen to have affected both the teeth and the skeleton of 8 persons. It was noticed that 4 persons showed symptoms of moderate forms of both dental and skeletal fluorosis while another 3 had severe dental fluorosis with moderate skeletal fluorosis. Skeletal fluorosis is mild for another person affected by severe dental fluorosis. Dental fluorosis appears to turn severe faster than skeletal fluorosis.

It is thus evident that at more than 5ppm fluoride in drinking water the population gets affected by fluorosis. But the symptoms show that it is not only the teeth that are affected by various forms of fluorosis, effects of fluoride toxicity are also evident on the skeleton of the affected population.

12. Major findings from the study

From the above study it is evident that the environmental conditions of the western parts of Birbhum district makes it vulnerable to fluoride contamination of drinking water. These environmental conditions include the presence of fluoride bearing rocks, semi-arid environment particularly in the summer and the pre-monsoon season, the alkaline nature of ground water and dependence on ground water for purposes of drinking.

The percentage of population affected by fluorosis depends on the fluoride amount in drinking water. At 1.86ppm fluoride in drinking water only 12.86 per cent of the population consuming fluoride contaminated drinking water show symptoms of fluorosis. As the fluoride amount increases to more than 5ppm, the percentage of population suffering from fluorosis increases. It is 36.48% of the population exposed to fluoride contaminated drinking water.

The other important observation is that the health impacts of fluoride toxicity vary as the fluoride amount in drinking water varies. At low fluoride amount effect is more pronounced on the teeth of an individual. In fact at less than 2ppm fluoride in drinking water only the teeth show signs of fluoride toxicity. As the fluoride amount increases to more than 5ppm impacts of excess

fluoride is evident on both the teeth and the bones of an individual.

The symptoms of dental and skeletal fluorosis also vary with the variations in the amount of fluoride in drinking water. Occasional opaque areas are identified on the teeth of an individual covering 25 per cent to 50 per cent of teeth surface at a fluoride amount of less than 2.0ppm in drinking water. All enamel surfaces show brown stains and a pitted appearance at a fluoride amount of more than 5ppm.

Deformities in bones particularly curvature of legs and knocked knee, chronic joint pain associated with rigidity and restricted movement of the cervical and lumber spine, knees and pelvic joints are also common. These people are unable to touch their feet and are unable to sit on the floor as well as get up without a support. These symptoms of skeletal fluorosis are, however, apparent only at a fluoride amount above 5ppm.

Along with the assessment of health impacts at various concentrations of fluoride in drinking water, the study is also likely to increase the awareness level about fluorosis as intended. Awareness about the symptoms will also increase. It is particularly important because the early warning signs of fluoride toxicity are often ignored and mistaken for more common and less harmful diseases.

13. REFERENCES

[1] Agarwal, V. Vaish, A.K. and Vaish, P. Groundwater Quality-Focus on Fluoride and Fluorosis in Rajasthan. *Current Science, Vol. 73, No. 9,* 1997 pp 743- 746

[2] Central Groundwater Board *High Fluoride Groundwater in India, Occurrences, Genesis and Remedies.* Ministry of Water Resources, Government of India, Faridabad, 1999.

[3] Fluorosis Research and Rural Development Foundation *State of Art Report on the Extent of Fluoride in Drinking Water and the Resulting Endemicity in India.* Fluorosis Research and Rural Development Foundation, New Delhi, 1999.

[4] Moulick, B. Groundwater Scenario in West Bengal. Paper Presented in the *Seminar on Aquifer Characteristics and Groundwater Management in Eastern India.* Department of Geological Sciences, Jadavpur University, Kolkata, 1996 pp 18-26

[5] Narain, S. Pumping out Poison – Too Much Arsenic and Fluoride in India's Groundwater Causes Millions to Suffer. *Down To Earth,* Vol. 1, No. 22, 2003 pp 36 – 41

[6] Rajiv Gandhi National Drinking Water Mission *Prevention & Control of Fluorosis in India-Health Aspects,* Volume 1, Ministry of Rural Development, Government of India, New Delhi,1994.

[7] Saxena, V. K. and Ahmed, S.: Dissolution of Fluoride in Groundwater, A Rock-Water Interaction Study. *Environmental Geology,* Vol. 40, Issue 9, 2001 pp 1084- 1087

BENS96

The Scenario-based Water Release of Caldera Lake in Mt Baekdusan Volcano eruption

Khil-Ha Lee[a,*], Sung-Wook Kim[b], Sang-Hyun Kim[c], Sung-Hyo Yun[d]
[a]**Civil Engineering, Deagu University**, Jillyang, Gyeongsan, Gyeongbuk 712-714 S, Korea
E-mail address: Klee@daegu.ac.kr

[b]**GI Co Ltd.**, Yeonsan, Yeonje, Busan 611-839, Korea
E-mail address: suwokim@chol.com

[c]**Department of Environmental Engineering, Pusan National University**, Busandaehak-ro 63beon-gil, Geumjeong-gu, Busan 609-735, Korea
E-mail address: kimsangh@pusan.ac.kr

[d]**Department of Earth Science Education, Pusan National University,** Busandaehak-ro 63beon-gil, Geumjeong-gu, Busan 609-735, Korea
E-mail address: yunsh@pusan.ac.kr

ABSTRACT

The Mt Baekdusan volcano that is located between the border of China and North Korea is known as a potential active volcano. The volcano disgorged up to 30 cubic kilometers of magma, or 10 times as much as the farmed Krakatoa eruption in 1883 in a violent, explosive eruption around 1000 AD. Smaller eruptions have occurred at roughly 100-year intervals since then, with the last one in 1903. The volcano is showing signs of waking from a century-long slumber recently. The volcanic ash may spread up to the northeastern of Japan and there is a need for the development of various forecasting techniques to prevent and minimize economic and social damage. Floods from lake-filled calderas may be particularly large and may cause significant hydrologic hazards for this reason. This study focuses on the amount of break-out flood from failures of the caldera lake in the Mt Baekdusan and constructing a hygrograph that is expected during eruption considering the geological conditions. The release of water is treated hydraulically as a dam break and a physically-based dam break model was used to compute the amount of water. The ordinary differential equation was numerically solved using the finite difference method and Newton-Raphson iteration method was used to solve nonlinear equation. As a preliminary test, three scenarios were conducted. The main results show that it will take about 6 hours to blank the 2 km^3 of water from the instantaneous lake collapse and the maximum discharge will be approximately $5.0x10^6$ $m^3/\sec$. This simulation approach stresses the potential flood hazard represented by the huge volume of water in the caldera lake, the unique geography, and the limited control capability and will contribute to build a geohazard map for the decision-makers and practitioners.

Keywords: Volcanic flood, Volcano, Caldera lake, Dam break, hazard

Acknowledgments

This research was supported by a grant [2012-NEMA12-100-01010000-2012] from the Volcanic Disaster Preparedness Research Center sponsored by National Emergency Management Agency of Korea.

BENS81

Cloning of Lipase Gene from a Thermophilic Bacterium

Rashidah Abdul Rahim*, Liong Jia Hui and Darah Ibrahim
School of Biological Sciences, Universiti Sains Malaysia, 11800, Penang, Malaysia
Email: rashidahrahim@gmail.com

ABSTRACT

Thermostable enzymes have received increasing attention because of their relevance for both basic and applied research. In biotechnology, novel opportunities might be offered by their catalytic activity at high temperature and, in some cases, unusual specificity. In this study, the lipase gene was cloned from a thermophilic bacterium *Bacillus licheniformis* IBRL-CHS2, originated from Cangar Hotspring, Malang, Indonesia. Lipase is glycerol ester hydrolase that catalyses the hydrolysis of triglycerides to free fatty acids and glycerol. *Bacillus licheniformis* IBRL-CHS2 cultured in optimum medium pH 8 at 50^{o}C to optimize the growth. The genomic DNA of *Bacillus licheniformis* IBRL-CHS2 was extracted using modified CTAB method. Lipase gene from the extracted gDNA was amplified by Polymerase Chain Reaction (PCR) using the designed forward and reverse primers (BLF and BLR, respectively). The PCR product was purified using QiAquick Gel Extraction Kit. The amplified lipase gene was then inserted into plasmid DNA (pGEM ®-T Easy vector) that acted as a vector for lipase gene at multiple cloning sites (MCS) of α-peptide coding region of β-galactosidase of *lac*Z. The competent *Escherichia coli* JM109 cell prepared was used as a host for plasmids to house recombinant plasmids and allowed them to multiply through DNA replication and multiplication of *Escherichia coli* cells. Plasmids were transformed into the competent *Escherichia coli* cells and blue-white screening was conducted to screen the recombinant plasmids. Recombinant plasmids were extracted and digested for DNA sequencing.

Natural Sciences II

Pullman Bangkok King Power, 2F Meeting Room BETA I

2013/1/26 Saturday 14:45-16:15

Session Chair: Chong Kim Wong

BENS93
Phytoplankton Characteristics in the Coastal Waters of Hong Kong Determined by HPLC Analysis of Pigments
Chong Kim Wong | *The Chinese University of Hong Kong*
Chi Hung Tang | *The Chinese University of Hong Kong*
Alle An Ying Lie | *University of Southern California*
Ying Kit Yung | *Hong Kong Government Environmental Protection*

BENS137
Air Quality at Traffic Intersection Points in Kolkata City: An Efficient Intervention Policy

Sukla Bhaduri | *University of Calcutta*

BENS138
Etrospect and Prospect of Biodiversity Conservation in the Fragile Ecosystems of Sundarban Region in Ganga Delta
Ranjan Basu | *University of Calcutta*

BENS163
Analysis on the Secretome Encoded in the Chromosome and Plasmid Genome of Ralstonia Solanacearum GMI1000
Xiaogang Zhou | *Yunnan Academy of Agriculture Science*
Maolin Sun | *Yunnan Academy of Agriculture Science*

BENS191
Association Study of Enrichment and Optimization for Bacteria Source and Fermentative Hydrogen Production from Biomass
Tao Li | *Zhengzhou University*

BENS93

Phytoplankton Characteristics in the Coastal Waters of Hong Kong Determined by HPLC Analysis of Pigments

Chong Kim Wong[a,*], Chi Hung Tang[b], Alle An Ying Lie[c], Ying Kit Yung[d]
[a]Simon F.S. Li Marine Science Laboratory, School of Life Sciences, The Chinese University of Hong Kong, New Territories, Hong Kong SAR
E-mail address: chongkimwong@cuhk.edu.hk

[b]Simon F.S. Li Marine Science Laboratory, School of Life Sciences The Chinese University of Hong Kong, New Territories, Hong Kong
E-mail address: charles_mail@hotmail.com

[c]Department of Biological Sciences, University of Southern California, 3616 Trousdale Parkway, Los Angeles, California 90089, USA
E-mail address: alie@usc.edu

[d]Mater Policy and Planning Group, Hong Kong Government Environmental Protection Department, Hong Kong SAR
E-mail address: ykyung@epd.gov.hk

ABSTRACT
The coastal waters of Hong Kong have been considered to consist of three zones: A western estuarine zone heavily influenced by the discharge of the Zhujiang (Pearl River), an eastern oceanic zone that is exposed to water currents from the South China Sea, and a central transitional zone in between. Zonal differences in hydrography have led to different utilization and management of the marine waters. As biological communities are often affected by environmental factors, we used HPLC analysis of phytoplankton pigments to investigate whether zonal differences exist in the phytoplankton communities of Hong Kong's marine environment. Results showed that while there is obvious zonal differences in salinity and nutrient concentrations, especially during the summer, the phytoplankton communities found around Hong Kong showed an overall > 40% similarity during both summer and winter.

Keywords: Marine Biology, Coastal ecology, Phytoplankton pigments

1. INTRODUCTION

The coastal environment of Hong Kong is diverse. Situated between the borders of temperate and tropical climatic zones, the sub-tropical waters of Hong Kong is influenced by water currents from the South China Sea and the Taiwan Strait [1]. In addition, the Zhujiang (Pearl River), with a watershed of 228,000 km2, discharges > 300 km3 of riverine water annually into the western part of Hong Kong [1-2]. The intensity of the influence exerted by the various oceanic currents and the Zhujiang changes seasonally, creating a marine environment that is highly heterogeneous both spatially and temporally. Morton [1] proposed that the coastal waters of Hong Kong can be

considered to consist of three hydrographic zones: an estuarine zone on the west, an oceanic zone on the east, and a transitional zone in between (Figure 1). The western estuarine zone is highly influenced by the discharge of the Zhujiang, and is characterized by reduced salinity and high nutrient concentrations, especially when the river flow is increased during the rainy season in summer. The eastern oceanic zone, on the other hand, resembles a more typical marine environment, with relatively higher salinity and lower nutrient concentrations.

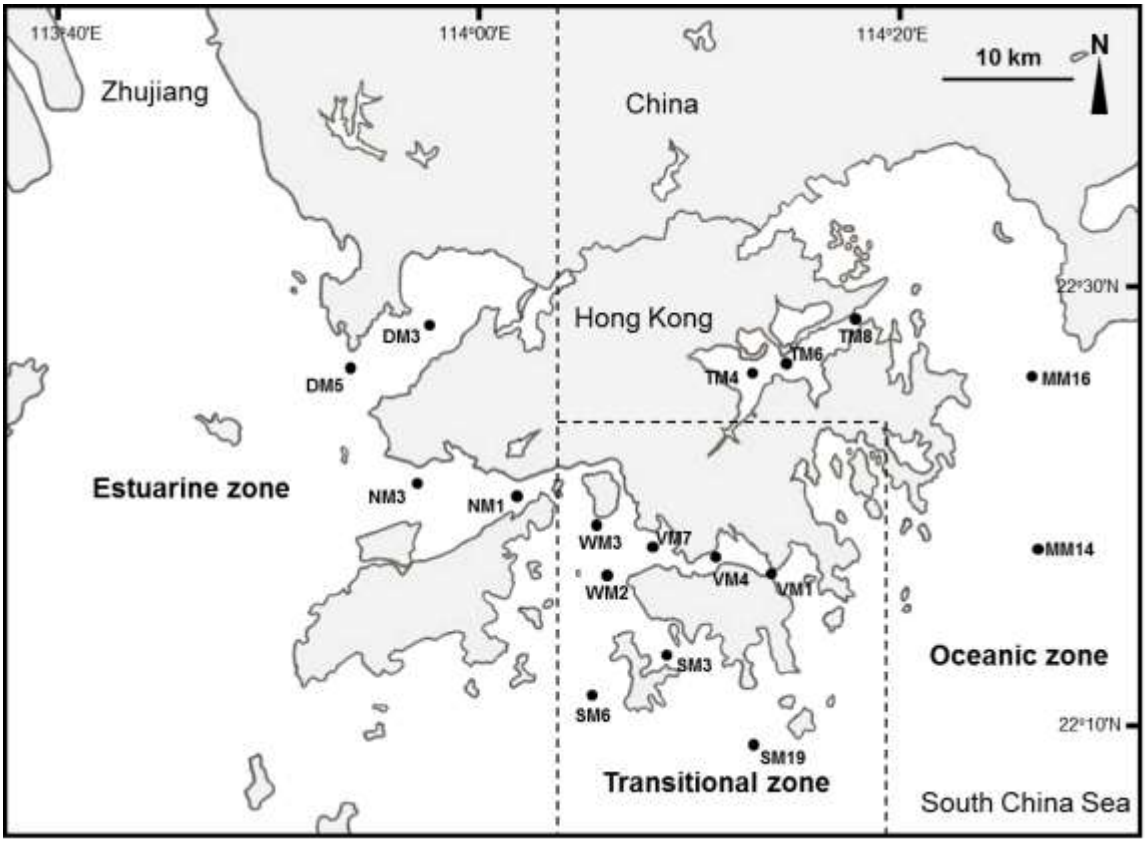

Figure 1. Map of Hong Kong showing the three zones, and 17 sampling stations.

Such division can basically be noted by the utilization and management of Hong Kong's coastal waters. Most of the designated fish and shellfish culture zones lie within and near the eastern oceanic zone [3], where the conditions are more suitable for marine fish culturing. Designated areas of secondary-contact recreation, such as rowing, fishing, and canoeing, are mainly located on the eastern side of Hong Kong [3]. The Hong Kong Environmental Protection Department (HKEPD) divided Hong Kong's marine waters into ten Water Control Zones (WCZ) and established Water Quality Objectives (WQO) as water quality criteria for each WCZ. The location and delineation of the WCZ reflect, to a certain extent, the aforementioned zonation of Hong Kong's marine waters.

As biological communities are influenced by environmental conditions, the aim of our study is to use phytoplankton pigments to investigate whether the phytoplankton communities in Hong Kong's coastal waters can also be divided according to the physico-chemical zonations. Studies on phytoplankton in Hong Kong have largely been based on microscopy identification and quantification of diatoms and dinoflagellates (e.g. [4-5]). However, in addition to being

time-consuming, microscopic analysis requires a high level of taxonomic expertise, and is limited to larger sized phytoplankton with recognizable external features. The detection of various phytoplankton pigments by high-performance liquid chromatography (HPLC) has gained popularity in recent years as it provides an efficient and unambiguous method of characterizing phytoplankton communities (e.g. [6-7]). As some pigments are unique or restricted to certain groups of phytoplankton, taxonomic composition of the phytoplankton community can be estimated according to the presence of these "marker pigments" [8] (Table 1).

Table 1. Marker pigments detected in this study, their abbreviation, and representative algal groups.

Marker pigment	**Abbreviation**	**Phytoplankton group**
Peridinin	Peri	Dinoflagellates
Fucoxanthin	Fuco	Diatoms
19-hex-fucoxanthin	19-hex	Prymnesiophytes
Alloxanthin	Allo	Cryptophytes
Lutein	Lut	Green algae
Zeaxanthin	Zea	Cyanobacteria
Chlorophyll *b*	Chl-*b*	Green algae
Divinyl chlorophyll *a*	D Chl-*a*	*Prochlorococcus*
Chlorophyll *a*	Chl-*a*	All phytoplankton

2. MATERIALS AND METHODS

Surface water samples were collected from 17 stations around Hong Kong's coastal waters (Figure 1) in July 2009 (Summer) and January 2010 (Winter) during HKEPD's cruises for Hong Kong marine water monitoring. Seawater was first filtered through a 200 μm mesh to remove large metazoans. Subsamples of 1000 mL were then filtered onto a GF/F (Whatman) filter for HPLC analysis using methods described in [9]. Physico-chemical parameters, including temperature, salinity, total nitrogen (TN), total phosphorus (TP), and SiO2 concentrations were measured, analyzed, and provided by the HKEPD.

3. RESULTS

Table 2 shows the mean physico-chemical parameters for each zone in summer and winter. Temperature did not differ among the three zones. Salinity was lower, and nutrient concentrations were higher in the estuarine zone than in the other zones, especially in the summer. HPLC analyses detected the presence of 9 marker pigments (Table 1), with Chl-a, Fuco and Allo common in all zones in both summer and winter. 19-hex and Chl b were also present in most samples in both season, while Zea was only found during the summer in the estuarine and oceanic zones (Figure 2). Lut was only found in the estuarine zone during the summer. In addition to the 9 marker pigments, the accessory pigments chlorophyll c3, chlorophyll c2, 19-but-fucoxanthin, neoxanthin, violaxanthin, diadinoxanthin, myxoxanthin, diatoxanthin, and α-/β-carotene appeared in some samples. Using all 18 detected pigments, a clustering analysis was performed for each season using the multivariate statistical software PRIMER v.6. The results did not show a division of the phytoplankton communities according to hydrographical

zonation (Figure 3).

Table 2. Mean temperature, salinity, total nitrogen (TN), total phosphorus (TP), and SiO_2 concentrations of each zone in summer 2009, and winter 2010. "BD" indicates below the detection limit of 0.02 mg L^{-1} for TP, and 0.05 mg L^{-1} for SiO_2.

Season	Region	Temperature (^oC)	Salinity	TN (mg L^{-1})	TP (mg L^{-1})	SiO_2 (mg L^{-1})
Summer	Estuarine	29.05 (28.31 – 29.85)	15.49 (14.13 – 17.57)	1.23 (1.06 – 1.57)	0.05 (0.02 – 0.09)	3.98 (3.10 – 4.80)
	Transi-tional	27.46 (25.87 – 29.01)	28.19 (26.38 – 31.53	0.41 (0.26 – 0.51)	0.03 (BD – 0.03)	0.57 (BD – 1.70)
	Oceanic	29.46 (27.00 – 30.75)	29.64 (28.32 – 30.74)	0.17 (0.13 – 0.24)	BD	0.33 (0.08 – 0.51)
Winter	Estuarine	18.76 (17.37 – 20.86)	31.17 (28.91 – 32.10)	0.86 (0.41 – 1.79)	0.08 (0.04 – 0.20)	0.81 (0.52 – 1.20)
	Transi-tional	19.19 (17.99 – 21.07)	32.42 (31.92 – 33.20)	0.40 (0.17 – 0.58)	0.04 (BD – 0.06)	0.75 (0.61 – 0.90)
	Oceanic	19.14 (16.86 – 20.86)	32.16 (31.77 – 32.30)	0.19 (0.13 – 0.23)	0.04 (BD – 0.04)	0.39 (0.11 – 0.89)

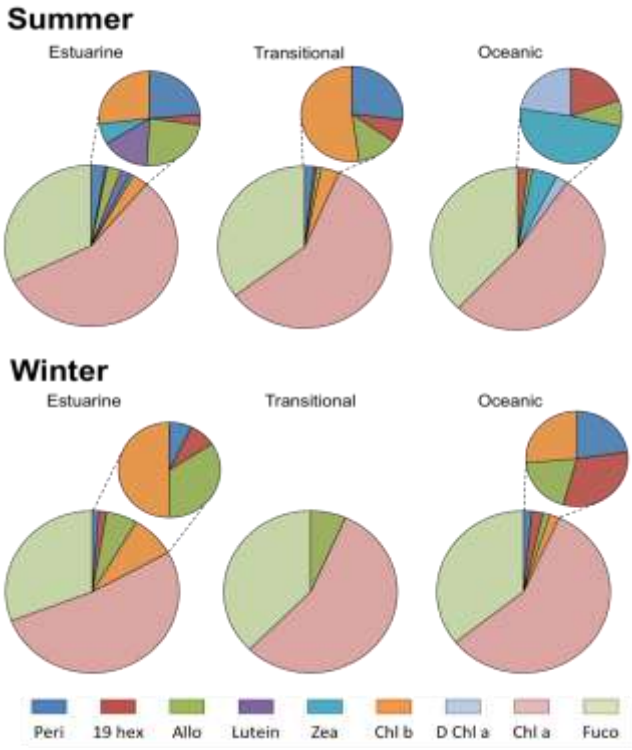

Figure 2. Mean composition of marker pigments detected by HPLC. Refer to Table 1 for the full name of marker pigments and its representative algal group.

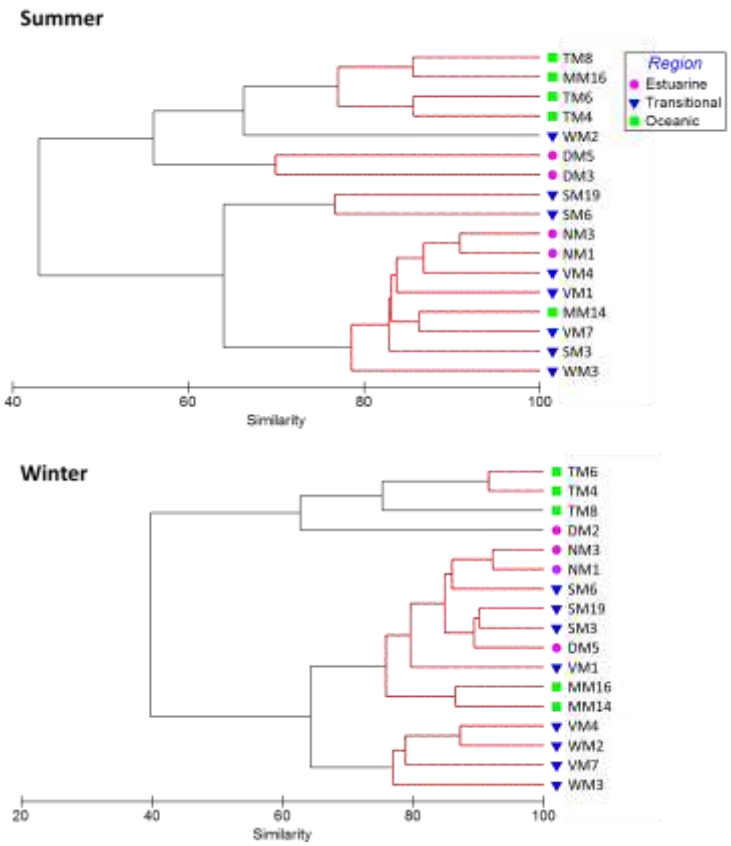

Figure 3. Clustering analysis using the 18 phytoplankton pigments detected by HPLC. Red lines indicate insignificant differences between the pigment signatures (SIMPROF, $p > 0.05$).

4. DISCUSSION

Zonation of Hong Kong's coastal waters was especially obvious during the rainy season in summer, as a layer of nutrient-rich estuarine water covered the western part of Hong Kong. In contrast to Morton's [1] suggestion that the central transitional zone can also be affected by the Zhujiang, high salinity suggests that the marine water in the central part of Hong Kong was not heavily influenced by the river.

Fuco was the most abundant accessory pigment in all samples (Figure 2). While Fuco can be found in diatoms as well as groups such as prymnesiophytes and chrysophytes, its prevalence, combined with microscopic analyses [9], suggests that diatoms are a major component of the phytoplankton communities. While dinoflagellates are regarded as important causative organisms of red tides in Hong Kong's coastal seas [4], Peri, an unambiguous marker for dinoflagellates, was rare or absent in most samples. This may be due to the fact that not all dinoflagellates possess Peri [6]. Restriction of Zea, a marker pigment for cyanobacteria, to the summer matches the general description of the group's preference for warmer waters [10]. Lut, a marker pigment for green algae, was unique to the estuarine zone, while D Chl-a, a marker pigment for the cyanobacteria Prochlorococcus, was unique to the oceanic zone. Prochlorococcus is known to prefer oligotrophic waters [11].

Results of the clustering analysis based on the pigment signatures did not show any distinct clustering of the phytoplankton communities according to hydrographical zones. The phytoplankton communities showed > 40% similarity in both seasons. Therefore, while the coastal waters of Hong Kong can be divided into different zones according to physic-chemical parameters, analysis of phytoplankton pigments revealed no distinct zonal separation of the phytoplankton community in both summer and winter.

5. REFERENCES

[1] Morton B. An introduction to Hong Kong's marine environment with special reference to the north-eastern New Territories. In *Proceedings of the First International Marine Biological Workshop: The Marine Flora and Fauna of Hong Kong and Southern China*. Hong Kong, 1980, pp. 25 – 53.

[2] Zhang S, Lu X X, Higgitt D L, Chen C A, Han J, Sun H. Recent changes of water discharge and sediment load in the Zhujiang (Pearl River) Basin, China. *Global and Planetary Change*, 2008, 60: 365-380.

[3] Hong Kong Environmental Protection Department, 2010. *Marine water quality in Hong Kong for 2009*. Environmental Protection Department, The Government of Hong Kong Special Administrative Region- Hong Kong.

[4] Lam C W Y, Ho K C. Phytoplankton characteristics of Tolo Harbour. *Asian Marine Biology*, 1989, 6:5-18.

[5] Yung Y K, Wong C K, Yau K, Qian P Y. Long-term changes in water quality and phytoplankton characteristics in Port Shelter, Hong Kong, from 1988-1998. *Marine Pollution bulletin*, 2001, 42:981-992.

[6] Jeffrey S W, Vesk M. Introduction to marine phytoplankton and their pigment signatures. *Phytoplankton pigments in oceanography: guidelines to modern methods* (Jeffrey S W, Mantoura R F C, Wright S W eds.). UNESCO Publishing-Paris, 1997, pp 37-84.

[7] Sherrard N J, Nimmo M, Llewellyn C A. Combining HPLC pigment markers and ecological similarity indices to assess phytoplankton community structure: an environmental tool for eutrophication? *Science of the Total Environment*, 2006, 361:97-110.

[8] Roy S, Chanut J-P, Gosselin M, Sime-Ngando T. Characterization of phytoplankton communities in the lower St. Lawrence Estuary using HPLC-detected pigments and cell microscopy. *Marine Ecology Progress Series*, 1996, 142:55-73.

[9] Lie A A Y, Wong C K. Selectivity and grazing impact of microzooplankton on phytoplankton in two subtropical semi-enclosed bays with different chlorophyll concentrations. *Journal of Experimental Marine Biology and Ecology*, 2010, 390: 149-159.

[10] El-Shehawy R, Gorokhova E, Fernández-Piñas F, del Campo F F. Global warming and hepatotoxin production by cyanobacteria: What can we learn from experiments? *Water Research*, 2012, 46:1420-1429.

[11] Partensky F, Hess W R, Vaulot D. Prochlorococcus, a marine photosynthetic prokaryote of global significance. *Microbiology and Molecular Biology Reviews*, 1999, 63:106-127.

BENS137

Air Quality at Traffic Intersection Points in Kolkata City: An Efficient Intervention Policy

Sukla Bhaduri
Department of Geography, **University of Calcutta**, 35, Ballygunge Circular Road, Kolkata-700019, India
E-mail address: suklabhaduri@gmail.com

ABSTRACT

Kolkata is one of the densely populated cities of India with about 24,252 persons per sq. km which is one of the highest in the country.The old industries are situated in the heart of the city which are mostly polluting industries, together with rapidly growing automobile population, proportionately low road coverage are some of the constraints which affect the city's air quality to a large extent. Over the last decade, the government has taken steps and has given high priority to improve the city's air quality and its urban agglomeration.The Pollution Control Board monitors ambient air quality in Kolkata, and other areas of the state through vast air quality monitoring network of 59 stations, of which 25 monitoring stations are in Kolkata city. The air pollution from industrial sources is mostly under control as Pollution Control Board has made it mandatory for cleaner fuel use.

The automobile exhaust is now recognized as a major source of air pollution in a city. It is estimated that 48 percent of the air pollution load of the city of Calcutta is contributed by automobiles as the transport scenario has changed drastically with economic reform in India. The travel demand has increased; number of registered vehicles is on rise and corresponds to some 52 percent growth since the last decade with less than 7 percent of effective road space leading to high automobile density, disproportionately low percentage of road network, congestion, accidents and effect on air quality. The traffic movement on the other hand is also affected by poor standard of road maintenance, old vehicles, traffic mix and large number of pedestrians. Therefore it is decided that major emphasis of air quality will be on automobile. Tangible steps were taken for controlling auto emission in the city and its surroundings. Pollution and its regulation start dominating the agenda of public policy in India since the adoption of new economic policy in July, 1991. According to Air Pollution Index (API) of US-EPA all the major traffic intersection points reflects high level of pollutants with few exceptions. Therefore an attempt has been made in this paper to assess the air quality of the city and the intervention policies taken thereof.

Keywords: Automobile exhaust, Economic reform, Travel demand, Air Pollution Index, Traffic intersection points

1. INTRODUCTION

Kolkata city with a population of 4.48 million is the 7th largest city of India in 2011 located at West Bengal state of India. However the metropolitan Kolkata hold a population around 14.1 million in 2011 making it the third most populous metropolitan area in India. Located on the

east bank of the Hooghly river, it is the principal commercial, cultural, and educational centre of East India, while the Port of Kolkata is India's oldest operating port as well as its sole major riverine port. As of 2008, its economic output as measured by gross domestic product ranked third among South Asian cities, behind Mumbai and Delhi. As a growing metropolitan city in a developing country, Kolkata confronts substantial urban pollution, traffic congestion, poverty, overpopulation, and other logistic and socioeconomic problems.

Kolkata, which is under the jurisdiction of the Kolkata Municipal Corporation (KMC), has an area of 187.33 km2 with a density of population density was 24,252 /km2 (62,810 /sq mi). This represents a decline of 1.88% during the decade 2001–11. The east–west dimension of the city is comparatively narrow, stretching from the Hooghly River in the west to roughly the Eastern Metropolitan Bypass in the east—a span of 9–10 km (5.6–6.2 mi). The north–south distance is greater, and its axis is used to section the city into North, Central, and South Kolkata.

The major sources of air pollution in Kolkata city are the industries and automobiles. The other sources include construction activities, re-suspension of road dust, burning of coal in slum areas, biomass burning etc.[1]

Although 34 percent [1] of total registered vehicles of the state are registered within Kolkata, a large number of vehicles registered in the districts within Kolkata Metropolitan Area (KMA) also ply on the streets of the core city areas. Most of these vehicles are petrol driven. Besides a large number of diesel driven taxis, buses, minibuses, trucks and other commercial vehicles also ply on the city streets.

2. REGULAR AIR QUALITY MONITORING AT KOLKATA

National Environmental Engineering Research Institute (NEERI) started monitoring of air quality in early 1970's. Subsequently, in 1984 the Central Pollution Control Board and in 1992 the State Pollution Control Board (SPCB) started monitoring. At present SPCB is monitoring air quality at 19 stations throughout the year. The stations are- Dunlop bridge, Tollygunge, Ultadanga, Picnic Garden, Minto Park, Shaymbazar, Beliaghata, Mominpore, Baishnabghata, Topsia, Salt Lake, Rajarhat, Moulali, Behala Chowrasta, Hyde Road, Gariahat, Paribesh Bhawan and Raj Bhawan etc. The parameters monitored are SPM, RPM, SO2 and NO2. The analysis of this data indicates that the pollutant of prime concern is Respirable Particulate Matter (RPM) which is roughly equivalent to PM10.[5]

Table I: Traffic Profile of Kolkata City at a glance

Latitude	22°23'47'' N
Longitude	88°23'34''E
Area	187.33 Sq. km
Population of Kolkata	4,486,679 (2011)
Population Density	24,252 person/sq km
Long Arterial System	1416.4 Km
New Flyovers	6
Total vehicles	12,02,983
Vehicle Density (per km)	823

Total slow moving vehicles	26,156
Road Intersections with signals	180
Traffic Crossings with count down timers	150
Traffic Crossings under CCTV Coverage	13
Air pollution cases	2,465
Air horn cases	774
Percentage of pollution from transport sector	48

Source: Public Vehicles Department

Kolkata city has registered a high vehicular population since 1991, due to economic liberalization as well as de-licensing of auto industry. From 1996 to 2007 the number of vehicles has a growth of about 1.89 times.[2] The slow moving vehicles has a declining trend from 2004 to 2007, (28,557 to 26,156, a decrease of about 2,401 numbers).

Table II: Vehicular Profile of Kolkata City

Growth of Motor Cars	Maximum observed in 2002-03 about 6.5%. The trend continued as more banks are willing to pay more car loans with facilities of EMI
Growth of Autos	This para- transit mode is on rise though has downfall in 2008 due to scraping of two stroke autos by the Government. However the four stroke autos are meeting the urban demand and has a big rise of 26.8% in 2009-10
Growth of Buses and Mini Buses	Increasing trend has been observed over the last three years with the introduction of JNNURM buses. The maximum increasing rate in 2009-10 is 18.27% whereas mini buses has a steady growth rate of 8%
Growth of Two-wheelers	A major mode providing door to door accessibility and enjoying increasing popularity among the youth for speed. The increasing trend is observed since 2001.

Source: Tabulated by author

3. TRAFFIC INTERSECTION POINTS

A fume study has been conducted on selected traffic intersection points in Kolkata by generating primary data during 2009 under a UGC sponsored project of interdisciplinary nature by the University of Calcutta. The following are some of the observation made on the basis of such study assisted by an NGO named as Envirocheck. West Bengal Pollution Control board has already started monitoring the emission of fumes in their latest agenda. It is to be noted that the road-space in Kolkata is much lower than the prescribed national norm and moreover the pressure of the vehicles both of public and private category is increasing day by day. For this the average speed of the moving vehicles is getting slower, the stoppage time at the traffic intersection points are increasing which lead to greater air pollution. Moreover, many vehicles are not well maintained by the owners and not well monitored by the concerned authorities so the emission of fumes is quite high. White fumes are generally emitted due to fuel-air mixture or excess oil burning. While, black fumes occur mainly due to coolant burn-off in the oil due to

leakage. It is mostly common in older vehicles. During the study, the vehicles have been classified into four categories- two wheelers (motorcycles, scooters), three wheelers (auto rickshaws), four wheelers (cars), six wheelers (buses, trucks). For data collection from the survey stations, three time slots have been selected; i)from 9.00-10.15 am to cover the high traffic of the office-going period , ii)from 14.00-15.15 pm to cover the scenario of the afternoon period, iii)from 17.00-18.15 pm to cover the evening rush.

B.B.D. Bag Crossing- Out of around 2,150 fume-emitting vehicles surveyed highest number of six wheelers have been noted, followed by four wheelers and two wheelers. The number of three wheelers is very negligible because in this area the route permit for auto rickshaws is not issued. Emission of white fumes score over that of the black fumes in all categories of vehicles. Cases of black fume emission are comparatively high for six wheelers. The pressure of the vehicles is highest during 10.00-10.15 am then it dips a bit minor fluctuations and again peaks up in the evening slot.

Ultadanga crossing-In this station the number of four wheelers is the highest about 1600 out of 4,800 total number of fume-emitting vehicles observed; which is about one-third. While, two and three wheelers mostly emit white fumes, four and six wheelers contribute to the white fumes too though at a lesser rate. From the diurnal vehicular flow pattern it can be seen that the number of all sorts of vehicles plying is highest during the evening 17.20 pm onwards. In general, the vehicular pressure over here is very high because Ultadanga serves as a link between the city proper and Salt lake region and through the nearby railway station suburban connection is also established.

Esplanade Masjid More Crossing- In this station about 2,300 plying fume-emitting vehicles has been recorded out of which four wheelers form the majority. The number of three wheelers is very negligible because in this area the route permit for auto rickshaws is not issued. Emission of white fume is much higher than that of the black fumes in all kind of vehicles. The vehicular flow is highest during the morning slot spanning from 9.20-10.15 am, when the office going traffic is at its peak.

Ballygunge Phanri Crossing- The total number of fume-emitting vehicles recorded at this point is around 2,500. Two, three, four and six wheelers come in ascending order if their number is taken into account. Here also the cases of black fume emission are much lower than that of white fumes. The vehicular flow is high in the morning, followed by a dip in the afternoon, while in the early part of the evening the flow increases with a sharp fall in the later half though a rising trend can be noticed after that phase. Since, the station is located in an area which is neither fully commercial nor residential but is of a rather complex entity the vehicular flow pattern is different from other stations.

Topsia Crossing- The number of fume-emitting four wheelers is really high, about 1,100 in this station, two, six and three wheelers follow the suit, which is about 1,500 taken all these categories together. The proportion of white fume emitting vehicles is much higher. The diurnal flow of the vehicles does not show much variation, though it dips a bit during the afternoon.

Mahatma Gandhi Road and Rabindra Sarani Crossing- About 1,000 fume-emitting four

wheelers have been detected. Six, three and two wheelers about 600 in number also contribute to the air pollution. The number of vehicles emitting black fumes is negligible. The vehicular flow pattern is very unusual compared to other stations. The flow peaks during the afternoon slot specially from 15.00-15.15 pm.

Shyambazar Five Point Crossing- This station is an important point of north Kolkata so the pressure of vehicles is quite high. About 3,200 fume-emitting vehicles have been detected out of which six and four wheelers form the chunk. Incidence of black fume is quite low. From the diurnal vehicular flow it is seen that the rush of the vehicles is maximum during the morning session, from 9.00-9.55 am.

Behala Tram Depot- Behala is a sprawling residential area of the city. 2,350 fume-emitting vehicles are noted. The share of three, four and six wheelers is almost equal while the two wheelers are comparatively lesser in number. Emission of white fume is much higher than that of the black one. The vehicular flow here is bit different from that of those commercial stations. The diurnal flow is stable throughout with a slight increase during the afternoon, no such office time pressure can be noticed here.

Moulali Crossing- It is one of the most busiest and congested point of the city. The commercial center's nearness to the Sealdah station is one of the factors behind the congestion. The total score of fume-emitting vehicles is about 2,800. Four wheelers contribute to the air pollution most, followed by two and six wheelers. Black fume emission is comparatively much lower. Due to some constraints the survey of vehicular flow has been conducted for a lesser span. The vehicular pressure is much higher during the morning slot.

Tollygunge Metro Crossing- Tollygunge serves as the connecting point between the city proper and the expanding areas in the south-eastern section of the metropolis. Only in this station it is seen that among all categories of fume-emitting vehicles, three wheelers lead in the pack. The share of white fume emitted surpasses the black fume formidably. The diurnal vehicular flow shows a descending trend as the day passes by.

4. CHANGES PERCEIVED IN THE PHYSICAL ENVIRONMENTS DUE TO AIR POLLUTION

While carrying out the study at the different traffic intersection points it was found that smog was the most common effect. While, at few stations change in the colour of the foliage was also detected, apart from several other minor effects.[3]

5. HEALTH HAZARDS FACED

Due to the respiratory particulate matters breathing problem is the most common ailment faced by the respondents. The residents have also complained about irritation in eye and dust allergy in some cases.

Kolkata has the highest vehicular density per km among all Mega- cities of India and normal speed in Kolkata at present is 19 km per hour [2]. But there are problems which are worthy to

note.

- Lack of integration of transportation and land use.
- Critical parking conditions, especially in the down town or CBD.
- High air pollution and noise level in high traffic density corridor.
- Unsustainable and low capacity road based public transport system.
- High increase of personalized vehicles and unregulated growth of Intermediate Passenger Transport.
- Shortage of long term transport plan and programmes which are capital intensive, low return and low gestation period
- Deregulation, privatization and de-investment of public transport undertakings.
- High energy consumption

6. THE MAIN DRAWBACKS

Inadequate and poor quality of public transport has led to increasing use of personalized vehicles.[4] Roads in the cities have inadequate facilities for pedestrians, cyclists and cycle rickshaws; pavements are fast disappearing and even where they exist, they have been transformed to parking places for private vehicles. Vehicle ownership in these cities has increased with rising household incomes, aspirations for better quality of life, enabling a market environment for vehicle purchase, increasing trip lengths and inadequate public transport system. The heavy concentration of private motor vehicles in metropolitan cities has been one of the key reasons for congestion, increased travel times, pollution and accidents. The improved approach for easy traffic flow, cleaner air, better fuel technology the following are some of the options that can be taken---

- ✓ Reduction in private vehicles on road
- ✓ Increase in public transport and non motorized rider ship
- ✓ Cleaner vehicle fleet

These in turn would have a significant impact on the energy consumption levels and CO2 emissions produced. Again analysis of daily RPM data at different monitoring stations based on USEPA air quality index indicated that 80 percent of the days of the year RPM levels at the monitoring stations located at residential areas remained at safe level while at major traffic intersection points reaches at alarming situation which may cause serious health impact on exposed population.

7. KEY PLANS

It is important that the cities in India recognize energy use and CO2 emissions from their transport sector as well as other transport emissions and Kolkata is no exception.As a key issue of concern, it is demanding immediate and proactive action. Urban transport plans and projects need to be viewed from these perspectives.

1. A better transport planning with modal shift to public transport
2. Extensive public transport facilities and non-motorized modes in urban areas in order to discourage personalized vehicles.
3. Clean fuel, retiring old polluting vehicles, promoting use of electric vehicles and use of mass transport system

4. Integrated land-use planning, public transport at its maximum and NMT in cities should be given thrust.

Like all other metropolitan cities, Kolkata also needs a better traffic management programmes to reduce the air pollution syndrome. Kolkata city can reduce the air pollution by either increasing the road capacity or by reducing the traffic (demand). The following are some of the options for better management of air quality in Kolkata city.

1. New construction of roads and flyovers together with expansion of road width, 2. Reducing the traffic demand, 3. Congestion pricing, 4. Road space rationing, 5. Increasing road infrastructure, 6. Proper traffic management 7. One way road system to improve the vehicular speed, 8. Use of public mode of transport, 9. Vertical parkways must be designed to increase road space, 10. Separation of lanes for user groups, 11. A manual or uniform traffic control device standards, 12. Limitation on car license issue, 13. Restricting slow moving vehicles on major transit routes, 14. Removal of hawkers from the footways, 15. Banning all meetings and processions on weekdays

8. ACKNOWLEDGEMENT

I acknowledge University Grants Commission for funding this UGC sponsored major UPE Project entitled "Spatial Concentration of Pollution and Morbidity Impact in the City of Kolkata: Efficient Intervention Strategies" to which I act as principal Investigator.

9. REFERENCES

1. West Bengal Pollution Control Board. The Clean Air Document-Final Report of the Project (WBPCB-ICEF) *Pollution Prevention and Waste Minimisation of Small Scale Industrial Units in Kolkata Metropolitan Area.* March 2007, Kolkata, pp 7-12.
2. Kolkata Traffic Police. Annual Report, We care for you. 2008, Kolkata.
3. Envirocheck. Ambient Air Quality Monitoring and Traffic Survey under a *Project Spatial concentration of Pollution and Morbidity Impact in the City of Kolkata: Efficient Intervention Strategies* under University of Calcutta , P.I. Sukla Bhaduri, 2009.
4. Bhaduri Sukla. Growth of Personalized Vehicles in Mega-cities of India and its Impact in *Indian Journal of Regional Science*, ed. C.R.Pathak, Vol.XXXX, No.1, June, 2008.Kolkata pp 21-33.
5. West Bengal Pollution Control Board. ADB Report, Air Quality Management, Vol.V, 2005, New Delhi, pp 1-20.

BENS138

Etrospect and Prospect of Biodiversity Conservation in the Fragile Ecosystems of Sundarban Region in Ganga Delta

Ranjan Basu
Department of Geography, **University of Calcutta,** 35, Ballygunge Circular Road, Kolkata-700019, India
E-mail address: basu_ranjan2045@yahoo.com

ABSTRACT

Sundarban region of Ganga delta is composed of a combination of multiple ecosystems. World's largest mangrove ecosystem is intertwined here with estuarine ecosystem which maintains a reciprocal relationship with marine ecosystem of the Bay of Bengal. Fresh water ecosystem and agricultural landscape are lying adjacent to the northern boundary of the forest. Such multiplicity of ecosystems in the frontier of terrestrial and marine environment has led to fragility of ecosystems often aggravated by human interference. Forest-society interface in the perspective of over-exploitation of forest and aquatic resources by the villagers and straying of tigers beyond the limit of forest opens new vistas of research questions.

Since the decrease of fresh water flow through the tidal part of River Ganga after construction of Farakka barrage, salinity of soil and water has been enhanced. Aftermath of the tropical cyclone 'Aila' few years back was far more devastating through destruction of earthen embankments and consequent brackish water inundation of the interfluves. Enhanced salinity of soil and water along with high level of pollution in Ganga water has induced changes in the species combination. Some mangrove and few faunal species have either become endangered or extinct. Deforestation, plundering of timber and non-timber forest resources and poaching of animals are also responsible for loss of biodiversity in this littoral forest. Fishing with fine nylon nets has reduced estuarine and shallow marine biodiversity. Mono-culture of prawn has squeezed biodiversity base of inland water-bodies. Introduction of high yielding varieties of paddy replacing indigenous species of paddy has deteriorated the situation. With such a perspective, this paper aims at formulation of strategies for revival of wild, aquatic and crop diversity through sustained utilization of the natural resource base and restoration of eco-friendly relations between the poverty stricken village society and the rest of the biotic world.

Keywords: Salinity, Forest-society interface, Over-exploitation, Monoculture, High yielding varieties

1. INTRODUCTION

Sundarban region of India is located in the eastern state of West Bengal occupying the lowest part of the Ganga delta which has been segmented by various distributaries. Such a littoral tract, experiencing tidal waves everyday from the Bay of Bengal, has given birth to wild mangrove ecosystem with highly diversified floral and faunal species. Estuaries, forming a separate ecosystem are maintaining a linkage between the terrestrial and marine ecosystem. The entire area is witnessing fresh water discharge through the river Ganga, locally known as Hugli and its

distributaries in one part of the day and counter flow of brackish water in the other part. Agricultural landscape associated with fresh water pond ecosystem can be found beyond the wild environ. Association of so many ecosystems in the proximity of sea have made all of them fragile while coming under the onslaught of natural hazards like cyclone and earthquake or under over exploitation by the human society because the delicate balance is consequently lost. Obviously three dimensions of biodiversity-- species, gene and ecosystem all are adversely affected.

2. AREA UNDER STUDY

Sundarban region is composed of 102 islands of which 48 are still under the cover of forest and rest of the 54 have already been deforested with subsequent conversion to arable land studded with human settlements, orchards and tanks. Northern limit of this region is known as Dampier and Hodges line. The river Hugli and the international boundary between India and Bangladesh form the western and eastern limits of the region respectively. In terms of administrative identity this region is a combination of 19 Community Development Blocks out of which 13 are under the jurisdiction of South 24 Parganas district while six other C.D blocks are under the district of North 24 Parganas. The western stretch of forest and swamp lies between 21°30′40″ and 22°37′30″ north latitudes and 88°4′30″ and 91°14′ east longitude. The total geographical area of Indian Sundarban is about 9,630 sq. km. The Sundarban region is extended to Bangladesh also which is not coming under the purview of this study.

In 4th century B.C the region was known as Gangahridi. It was depicted even in Ptolemy's map. But the correct description of its northern limit was given by Hunter [1]. From the report of O′Malley [2] it is evident that in the year 1781 the then Magistrate of Jessore District Mr. Henckel initiated the process of deforestation for agriculture and human settlement. In fact selling of forest area was started in 1770 under the initiative of the then District Collector of 24 Parganas. He divided the entire forest area into different lots to rich fortune seekers who were instrumental to mass scale deforestation thus inflicting immense injury to floral and faunal diversity [3]. Greater the volume of migrants, higher was the pace of forest recession. Such aggressive destruction of the forest ecosystem has led to squeezing the forest area to 86,442.74 hectares. In fact the forest policy under colonial period was not conducive to conservation [4].

What happened about hundred years after initiation of state sponsored deforestation that can be revealed from the following data on land use :

Table 1: Categories of Land Use in Sundarban Region (1883)

Serial	Categories	Area in Sq.km
1	Arable land	1,087
2	Forest	3,967
3	Rivers and Canals	1,884
4	Others	603
	Total Area	**7,541**

Source: Maitra et.al, 2000

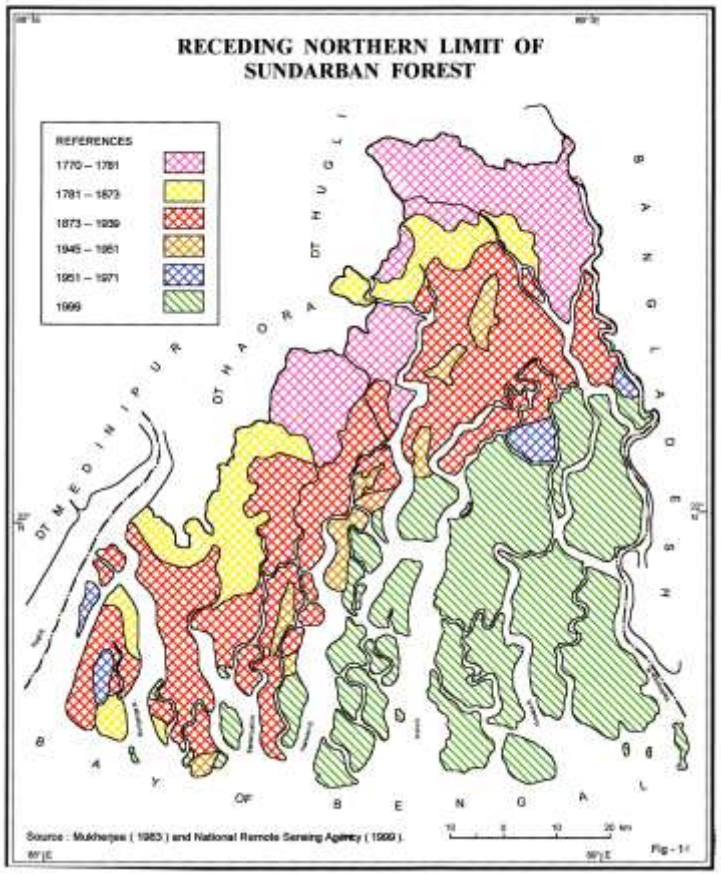

Fig.1

The process of land reclamation gained momentum during the world wars and continued even after partition of India. Use of the reclaimed land was diversified during the plan period in the name of regional development which can be clarified from the following table:

Table 2: Transformed Pattern of Land Use in Sundarban Region (1997 – 98)

Serial	Categories	Area in hectare
1	Net Area Sown	304,834.00
2	Pasture and Orchard	3,527.00
3	Cultivable Waste Land	6,828.00
4	Homestead	3,937.70
5	Forest	86,442.74
	Total Area	**405,569.44**

Source: Government of West Bengal

3. GROWTH OF HUMAN POPULATION

Population size in the Sundarban region of India has increased very fast. Even in 1921 when undivided Bengal recorded negative growth of population, even then this region witnessed positive growth. During the World War Two, this region experienced migration from the affected urban areas. After independence from the colonial rule along with a package deal of

partition of India, the same region experienced huge influx of refugees from erstwhile East Pakistan (now Bangladesh). The second spell of influx was recorded in 1971 when Bangladesh was liberated from Pakistan. Apart from cross-border migration, the Sundarban Region has allowed inter-district migration from the neighbouring East Medinipur and North 24 Parganas. Natural growth rate is also high in the poverty stricken rural society here which follows labour intensive mode of production. All these have resulted in very high density of population leading to worsening of man: land ratio. Decennial growth rate (2001–2011) of this region is 18.05 percent and density is 819 persons / sq.km. Highest density was recorded in Jaynagar I and lowest in Sagar island [5]. At a certain point of time it crosses even the carrying capacity of the saline/alkaline soil. Such a surplus population with overwhelming presence of a section living below the poverty line (BPL) has no other alternative but to exploit natural resources readily available in this region either in the forest or in the estuaries. Most of the land is mono-cropped and therefore rest of the six months in the span of a year, they have to work hard for mere sustenance of a big family.

4. FRAGILE FOREST ECOSYSTEM AND DECREASING BIODIVERSITY

Eight states and one union territory of India are endowed with mangrove forest. Out of the total area under such forest Sundarban of West Bengal has a share of 43.63 percent. This forest protects the human society from the natural hazard of cyclone and tsunamis because it absorbs high velocity wind, tidal surge and sea waves. In the eastern coast of India wherever mangrove forest has been uprooted in the name of development, there the local people paid the penalty in the form of Super Cyclone in September, 1999 and tsunamis in December, 2004. This ‘green buffer’ acts a shield against any natural hazard having its origin in the sea.

Sundarban is one of the 269 ‘Biosphere Reserves’ spread over 74 countries of the world. ‘Tiger Reserve’ was created here in 1973, ‘Crocodile Project’ in 1976 along with three other Reserve Forests in Sajnekhali, Lothian and Holiday Islands. This forest was recognized as ‘National Park’ in 1984 and as ‘World Heritage Site’ in 1987. In the year 1989 it was declared as ‘Biosphere Reserve’. Sundarban contains 64 species of mangrove variety. This littoral forest is the abode of 40 species of mammals, 45 species of reptiles, 150 species of birds, 200 species of fish, 40 species of crabs, 25 species of prawn and 6 species of frogs. Two horn Rhino and water loving wild buffalo have become extinct in the nineteenth century. Gradually hog deer and barking deer, Indian Muntjse and soft shell turtle also suffered extinction. Gangetic dolphin is rare now. So many mangrove species have become endangered as revealed from the recent surveys (Table – 3).

Table 3: List of Endangered Flora in Sundarban

Serial	Common Name	Scientific Name
1	Kankra	*Bruguier gymnorhiza*
2	Golpata	*Nipa fruticams*
3	Sundari	*Heritiera fomes*
4	Goran	*Ceriops sp.*
5	Keora	*Sonneratia sp.*
6	Ohundhal	*Xylocarpus granalum*
7	Passur	*Xylocarpus mekongensis*

Source: Arboretum – Swaminathan Project Forest (Bakkhali)

Impact of this endangered state of many mangrove species has led to the disturbance in the mangrove ecosystem which is highly sensitive and responds to any change promptly, being a dynamic ecosystem. The list of endangered fauna in Sundarban is lying with the fifth schedule and after necessary amendments since 1972, the following table has been prepared:

Table 4: List of Endangered Fauna in Sundarban

Serial	Common Name	Scientific Name
1	Estuarine Crocodile	*Crocodylus porosus*
2	Gharial	*Gavialis gangeticus*
3	Olive back Logger Head Turtle	*Lepidochelys olivacea*
4	Common Batagur	*Batagur baska*
5	Gangetic soft-shelled Turtle	*Trionyx gangeticus*
6	Water Monitor	*Varanus salvator*
7	Yellow Monitor	*Daranus flaviscense*
8	Indian Monitor	*Varanus bengalensis*
9	Python	*Python molusus*
10	Olive Ridley Turtle	*Lepidochelys olivacea*

Source: Naskar, 1999

Various anthropogenic factors are responsible for such a state of affairs [6]. These endangered species are falling prey to the greed of saw mill owners and poachers on one hand and hunger associated with need for essential commodities (e.g. fuel) of the poor people on the other. It should be realized that forest-society interface is very sensitive.

In fact diversified relationship among flora and fauna governed the issue of biodiversity in Sundarban forest. Brackish tidal waves, saline-alkaline soil and the mangrove species maintain a *symbiotic* relationship. Herbivores divide the forest horizontally and vertically depending on their food habit and nesting habit. Deer occupy the lowest stratum, monkeys stay in the middle and avi-fauna dominate the top most branches of the trees. Since they are not competitors to others they usually maintain a relationship of *peaceful coexistence.* In niche- overlap, competition for food and shelter is the order while deer and tiger have an eternal *prey-predator* relationship. In case any one of such intricate relationship is disturbed the food chain is susceptible to collapse. Initially they become vulnerable followed by the endangered stage and ultimately leading to extinction which is suggestive of loss of biodiversity [7]. Reduction in fresh water discharge through the last stretch of river Ganga, known as Bhagirathi-Hugli has allowed tidal waves to become stronger which has been reflected in higher salinity of the forest soil. Endangered state of the Sundari trees and dominance of Byne seems to be bio-indicator of increasing salinity of soil and water in the mangrove forest [8].

5. DECREASING BIODIVERSITY IN AQUATIC ECOSYSTEMS

There are two groups of people in Sundarban region who are dependent on marine or estuarine or pond ecosystem. Many of them are engaged in organized fishing throughout the year while others have taken it as a supplementary profession whenever necessary. Fishing trawlers

operate in the Bay of Bengal through the estuaries using fine nylon nets in which non target small fishes are also trapped. Their attempt for maximization of catch inflicts immense injury to the aquatic food web ultimately culminating in loss of biodiversity. Oil spill from the vessels and other waste materials thrown on the water have their own capacity to pollute. Because of the existence of numerous urban- industrial units in the long profile of the river Ganga, municipal and industrial waste materials released in the river ultimately aggravate the water pollution scenario through escalation of BOD which is detrimental to riverine or estuarine biodiversity [9].

Thousands of unorganized persons inclusive of house wives and school dropouts get engaged in fishing with rudimentary devices. Apart from small fishes, they collect crabs and prawn seeds. Such large scale catch of the needy as well as greedy careless people has an adverse impact on estuarine biodiversity.

In last two decades rich fishermen has concentrated on monoculture of prawn and lobster in the inland fishing pools locally known as bheri. This has altered the traditional fish combination of the pond ecosystem too.

Government of India initiated Ganga Action Plan way back in 1985. Even after completion of first two phases little justice has been done to abatement of water pollution because the authority along with the concerned state governments are more interested in beautification of the strand.

6. CONCLUSION

Sundarban with its combination of so many ecosystems is providing unique opportunity of utilizing multi-layer resource base on one hand and rendering service to the mankind as green buffer to natural hazards. Inflicting injury to the biotic resources of such a littoral tract either through deforestation or through over-exploitation of selected species is ultimately taking its toll on terrestrial or aquatic biodiversity. Pakhirala, once selected as sight for Bird Sanctuary in Sundarban has failed to attract the migratory birds. Introduction of high yielding varieties (HYV) of paddy in-lieu of indigenous varieties has depleted diversity of crops in agricultural landscape. Most of the people in the rural society of Sundarban are poor but they are blessed with rich endowment of biotic resources. Conservation of biodiversity will assure steady supply of food, fuel and building materials to these Below Poverty Line (BPL) people in the hunger belt of Sundarban. Apart from legal and administrative measures, mass awareness campaign and environmental movement can perform the role of safety valve to biodiversity conservation.

7. REFERENCES

1. Hunter, W.W. (1875): A Statistical Account of Bengal, Vol. I, Districts of the 24 Parganas and Sundarbans; Trubner and Co., London, pp 43-63.

2. O′Malley, L.S.S. (1914): Bengal District Gazetteers, 24 Parganas, The Bengal Secretariat Book Depot, Kolkata, pp 32-75.

3. Kanjilal, T. (2000): Nature, Man and Development in Sundarban; ed. Ghosh, T; West Bengal- The District of South Twenty Parganas; Department of Information and Culture, Government of West Bengal, Kolkata; pp 429-432.

4. Mukherjee, K.N. (2002): Sundarban: Histogenesis, Hazards and Nemeses, ed. Basu, S.R.; Changing Environmental Scenario of the Indian Subcontinent; acb Publications; pp 263-282.

5. www.censusindia.gov.in accessed on 24.11.2012.

6. Naskar, K.R. and Mandal, R.N. (1999): Ecology and Biodiversity of Indian Mangroves; Daya Publishing House, Vol. 2, Kolkata, pp 20-30.

7. Ghosh, A.K. ed. (1998): Report on the status of West Bengal, Department of Environment, Government of West Bengal, Kolkata; pp 72-82.

8. Ghosh, A.K. ed. (2008): Status of Environment in West Bengal- A Citizen's Report; Society for Environment and Development, Kolkata; pp 109-126.

9. Basu, R. (2004): Biodiversity under Threat- An Overview with Special Reference to West Bengal; ed. Singh, S, Sharma, H.S, De, S.K.; Geomorphology and Environment; acb Publication, Kolkata; pp 450-462.

Association Study of Enrichment and Optimization for Bacteria Source and Fermentative Hydrogen Production from Biomass

Tao Li[a,*], Yan-hong, Li[b], Bao-zeng Ren[c]
[a]**School of Chemical Engineering and Energy, Zhengzhou University**, 100, Science Avenue, Zhengzhou, Henan, 450001, China
E-mail address: litao_0912@126.com

[b]**School of Chemical Engineering and Energy, Zhengzhou University**, 100, Science Avenue, Zhengzhou, Henan, 450001, China
E-mail address: yanhongl2000@zzu.edu.cn

[c]**School of Chemical Engineering and Energy, Zhengzhou University**, 100, Science Avenue, Zhengzhou, Henan, 450001, China
E-mail address: Renbz@zzu,edu.cn

ABSTRACT
The enrichment for strains plays a crucial role in the technology of bio-hydrogen production from Biomass. In this paper, the effect of methods of enrichment strains to the bio-hydrogen production results was studied. The strains was pretreated with forcing aeration + heat shock in NaOH solution. And the pretreatment process was optimized with orthogonal design. The results showed that strains pretreated with heat shock 10 min + forcing aeration 20 min in NaOH solution (0.25 %) had obtained better bio-hydrogen production at pH 6.0 in batch experiments. The maximum cumulative hydrogen yield obtained from the two substrate are 345. 26 mL/g-sucrose and 114.85 mL/g-cornstalk respectively; the maximum hydrogen production rate are 8.65 mL/ mL/(L·g-cornstalk·h) and 14.27 mL/(L·g-sucrose·h) respectively; the highest concentration of biohydrogen are 55 % and 61 % respectively.

Keywords: biohydrogen production, cornstalk, sucrose, enrichment of strains, optimization

1. INTRODUCTION

One of the greatest challenges that mankind has to face in the 21st century is to find “green” energy sources for the replacement of fossil fuels and ensuring sustainable development[1]. As an ideal energy carrier, hydrogen generates high energy content per unit (118.2 kJ/g) with none of greenhouse gases produced from its combustion process. Among several methods of hydrogen production, bio-hydrogen production has received considerable attention because of its higher conversion rate of H_2 in the absence of light source as well as the various kinds of the substrates used [2]. The existing research on biohydrogen production by dark fermentation has shown that the production rates need to be optimized and improved. The key influencing factors of the biohydrogen production technology mainly include the enrichment strains, pretreatment of substrate [3-6], process control parameters [7-10], structural performance of fermentation reactor [11-13], etc. Among all the influence factors above, the enrichment of strains is a very important one which is related to the activity, stability and life of hydrogen producing bacteria. So a lot of

researchers have taken research on various aspects of enrichment of different strains to improve the efficiency of biohydrogen production [14-16]. Some of pretreatment conditions such as heat shock, medium solution, pH stress, and forcing aeration have been widely used to enhance the enrichment of strains and accordingly increase the efficiency of biohydrogen production. Although the current research has made some achievements，it was still out of distance from industrialized production. Based on this, the main objectives of this study were to improve the effects of the enrichment of strains for biohydrogen production. Pass by the optimization of the pretreatment process with orthogonal design, the suitable process conditions would be obtained.

2. MATERIALS AND METHODS

2.1 experimental raw material

Bacteria source is cow dung compost which was collected from the cow breeding base in the western suburb of Zhengzhou; The substrates is cornstalks which was collected from the farmland in the western suburb of Zhengzhou. Sucrose was purchased from Hualian supermarket. And all the reagents (mass fraction purity $\geq$ 0.99) used are analytically pure which were purchased from Tianjin Kermel Chemical Reagent Development Center. The composition (/L) of nutrient solution is NH_4HCO_3 2.0 g, KH_2 $PO_4$1.0 g, $MgSO_4 \cdot 7H_2O$ 100 mg, Na_2MoO_4 $\cdot 2H_2O$ 10mg, NaCl 10 mg, $CaCl_2 \cdot 2H_2O$ 10 mg, $MnSO_4 \cdot 7H_2O$ 15 mg, $FeCl_2$ 2.78 mg, which was slightly modified from Lay [17].

2.2 Experimental procedure

2.2.1 The enrichment of strains of biohydrogen production

In order to inhibit the activity of methanogenic bacteria and Hydrogenophilales bacteria and strengthen the activity of hydrogen production microorganism, the cow dung compost was pretreated by pretreatment conditions such as heat shock, medium solution, forcing aeration, or pretreated by combination methods with two or three pretreatment conditions.

2.2.2 The pretreatment of the substrate

Before the corn-stalk used as substrate were degraded by microorganisms, it were ground separately by a vegetation disintegrator (FZ-102, 250 kw, Beijing Yong Guang Ming Medical Appliance Factory, China) to pass 40-mesh screen. The grinding sample was employed as substrate of biohydrogen production in the experiments, then the mixture of the ground corn-stalks was pretreated by a synthetic method [18].

2.2.3 The experiments

The batch experiments were carried out with 250 mL serum vials as batch reactors filled with 200 mL comprising the mixture of the composts, the pretreated corn-stalks, and nutrient solution. These vials were gassed with nitrogen gas to remove oxygen and the headspace of the reactors to keep the anaerobic environment. The bottles were incubated at 37±1 ℃ and operated in an orbital shaker with a rotation speed of 120 rpm to provide better contact among substrates. The volume of biogas was determined using glass syringes of 5–50 mL.

2.3 Analytical methods

The pH values inside the reaction system were determined by a microcomputer pH-vision 6071. The hydrogen gas percentage (H_2 %) was determined by comparing the sample biogas

with a standard of pure hydrogen using a gas chromatograph (GC, Agilent 4890D) equipped with a thermal conductivity detector (TCD) and 6-foot stainless-steel column packed with Porapak Q (80/100 mesh). The operational temperatures of the injection port, the oven and the detector were 100 ℃, 80 ℃ and 150 ℃, respectively. Nitrogen was used as the carrier gas at a flow rate of 20 mL·min^{-1}. The concentrations of the volatile fatty acids (VFAs) and the alcohols were analyzed using another GC of the same model with a flame ionization detector (FID) and an 8-ft stainless-steel column packed with 10 % PEG-20M and 2 % H3PO4 (80/100 mesh). The temperature of the injection port, the detector and the oven were 220, 240 ℃ and a programmed column temperature of 130–175 ℃, respectively. Nitrogen was used as the carrier gas at a flow rate of 20 mL·min^{-1}. The flow rate of hydrogen and air was 30 mL·min^{-1}. Hydrogen gas yield was calculated from the headspace measurement of gas composition and the total volume of biogas produced at each time interval using the mass balance equation:

$$V = V_0 y_i + \sum V_i y_i \quad (1)$$

where V is the cumulative H_2 gas volumes at the current; V_0 is the volume of headspace of vials; V_i is the biogas volume discharged from the vials at the time interval (i); y_i is the fraction of H_2 gas discharged from the vials at the time interval (i).

3. RESULTS AND DISCUSSION

3.1 Optimization enrichment of strains by orthogonal design method

Based on prophase research, we have obtained the basic process conditions of enrichment of strains. The conditions obtained were at the initial pH 7.0, concentration of NaOH 0.25% (mass fraction), heat shock time 16 min, and forcing aeration time 30 min. Under in these conditions, the cumulative H_2 yield were 305. 8 mL/g-sucrose and 106 mL/g-cornstalk. In order to optimize the process conditions and improve the efficiency of biohydrogen production, the orthogonal design method was used. During the optimization experiments, the fermentation reaction was carried out with 250 mL serum vials. The fermentation condition of temperature was fixed at 37 ℃, concentration of substrate was sucrose fixed at 10 g/L. According to Table 1, (level and factor of orthogonal design), 9 groups of experiments were carried out in the batch reactors and the experimental results of the orthogonal design are shown in Tables 2-6.

Table 1 Level and factor of orthogonal design

Level	Factor			
	NaOH concentration (% mass fraction)	Heat shock time （min）	Forcing aeration time（min）	Initial pH
1	0.1	10	20	6
2	0.25	15	30	7
3	0.5	20	40	8

Table 2 A L_9 (3^4) orthogonal array and experimental results

No.	A	B	C	D	The indexes	
					cumulative H_2 yield（mL/g）	Average H_2 evolution rate(mL/(g•h))
1	1	1	1	1	318.9	9.14

2	1	2	2	2	233.2	6.68
3	1	3	3	3	184.1	8.69
4	2	1	2	3	178.9	9.77
5	2	2	3	1	276.4	13.06
6	2	3	1	2	290.9	13.75
7	3	1	3	2	190.7	10.42
8	3	2	1	3	266.8	6.06
9	3	3	2	1	294.3	6.51

Table 3 Results of intuitive analysis of cumulative H_2 yield

Mean value	A	B	C	D
1	245.4	229.5	292.2	296.5
2	248.7	258.8	235.5	238.3
3	250.6	256.4	217.1	209.9
Range	5.2	29.3	75.1	86.6

Table 4 Results of variance analysis of average H_2 evolution rate

Factor	Square of deviance	Freedom	F ratio	Critical value	Significance
A	41.636	2	0.007	4.460	
B	1589.496	2	0.282	4.460	*
C	9202.249	2	1.634	4.460	**
D	11697.342	2	2.077	4.460	**
Error	22530.72	8		α=0.05	

*, ** and Blank represent more significant different, significant different and no significant different, respectively.

Table 5 Results of intuitive analysis of average H_2 evolution rate

Mean value	A	B	C	D
1	8.1	9.8	9.7	9.6
2	12.2	8.6	7.7	10.3
3	7.7	9.7	10.7	8.2
Range	4.53	1.18	3.1	2.1

Table 6 Results of variance analysis of average H_2 evolution rate

Factor	Square of deviance	Freedom	F ratio	Critical value	Significance
A	36.965	2	2.426	4.460	**
B	2.530	2	0.164	4.460	
C	14.564	2	0.956	4.460	**
D	6.912	2	0.454	4.460	*
Error	60.94	8		α=0.05	

*, ** and Blank represent more significant different, significant different and no significant different, respectively.

It indicated that the cumulative hydrogen yield obtained from the Taguchi L9 orthogonal array experiments ranged from 178.9 to 318.9 mL/g-sucrose (Table 2). Based on the maximum hydrogen yield the optimum formulation was A1B1C1D1.(Run 1). And the optimal enrichment

of strains conditions were at the the initial pH 6.0, concentration of NaOH 0.1 %, heat shock time 10 min, and forcing aeration time 20 min. Under such condition, the maximum cumulative hydrogen yield was 318.9 mL/g-sucrose. However, the optimum formulation from response curve of orthogonal design, was A3B2C1D1, not A1B1C1D1. From table 3, it can be found that the order. And it indicated that the average H_2 evolution rate from the Taguchi L9 orthogonal array experiments ranged from 6.06 to 13.75 mL/(g-sucrose•h) (Table 5). Based on the maximum average H_2 evolution rate the optimum formulation was A2B3C1D2.(Run 6). Under such condition, the maximum average H_2 evolution rate was13.75 mL/(g-sucrose•h). However, the optimum formulation from response curve of orthogonal design, was A2B1C3D2, not A2B3C1D2.

To obtain each factor, the variance analysis were performed as shown in table 4 and 6. Based on the analysis of the experimental results we determined that forcing aeration time had the largest influence on the biohydrogen production process from the enrichment-determined factor levels, and fermentation initial pH was more influential than heat shock time and NaOH concentration. They also show that the NaOH concentration was the most neglected important factor for enrichment of strains for biohydrogen production.

The analysis of the important enrichment factors shows that forcing aeration time, fermentation initial pH, heat shock time and the NaOH concentration, the four factors we considered affected the enrichment of strains for biohydrogen production in an interaction-dependent way with the first being the most important factor. Therefore, operating at a proper enrichment conditions are preferable to biohydrogen production by cow dung compost. In summary, the optimization result was A2B1C1D1 as follows: the initial pH 6.0, concentration of NaOH 0.25 %, heat shock time 10 min, and forcing aeration time 20 min.

3.2 The verification experiments and Kinetic modeling

Based on the optimization result, the verification experiments were carried out in 250 mL serum vials. The substrate used was cornstalk and sucrose. The results of the biohydrogen were listed in table 7.

Table7 Results of verification experiments.

substrate	concentration of substrate (g/l)	cumulative H_2 yield (mL/g)	maximum H_2 evolution rate mL/(L·g·h)	highest hydrogen concentration %
cornstalk	15	114.85	8.65	55
sucrose	10	345.26	14.27	61

From table 7, it can be found that the optimal formulation resulted in a maximum cumulative hydrogen yield of 345. 26 mL/g-sucrose and 114.85 mL/g-cornstalk, which was higher than that of the orthogonal design method formulation of A1B1C1D1 (318.9 mL/g-sucrose). Moreover, a maximum H_2 evolution rate of 8.65 mL/ mL/(L·g-cornstalk·h) and 14.27 mL/(L·g-sucrose·h) which was higher than that of the orthogonal design method formulation of A2B3C1D2(13.75(L·g-sucrose·h)). Meanwhile, a maximum H_2 concentrations obtained are 55 % (cornstalk) and 61%(sucrose).

4. CONCLUSIONS

In this work, the enrichment of strains of biohydrogen production by use different substrates cornstalk and sucrose was investigated. The effects of condition of enrichment strains was optimizated by orthogonal design method. The key four enrichment factors forcing aeration time, fermentation initial pH, heat shock time and the NaOH concentration which we considered in an interaction-dependent way with the first being the most important factor of biohydrogen production. The optimization result was as follows: the initial pH 6.0, concentration of NaOH 0.25 %, heat shock time 10 min, and forcing aeration time 20 min. Based on this, a maximum cumulative hydrogen yield of 345. 26 mL/g-sucrose and 114.85 mL/g-cornstalk, H_2 evolution rate of 8.65 mL/ mL/(L·g-cornstalk·h) and 14.27 mL/(L·g-sucrose·h), and H_2 concentrations 55 % (cornstalk) and 61%(sucrose) are obtained.

5. ACKNOWLEDGMENTS

This research was supported by the National Natural Science Foundation of China (Grant No. 21171147，20871106)

6. REFERENCES

[1] P. Bakonyi, N. Nemestóthy, É. Lövitusz, et al. “Application of PlacketteBurman experimental design to optimize biohydrogen fermentation by E. coli (XL1-BLUE)”, International journal of hydrogen energy, 2011, 36(21), 13949-13954.

[2] Kapdan IK, Kargi F. “Biohydrogen production from waste materials”, Enzyme and Microbial Technology, 2006, 38(5): 69-82.

[3] Fan Yaoting，Zhang Gaosheng，Guo Xinyong，et al. Biohydrogen production from beer lees biomass by cow dung compost[J]. Biomass&Bioenergy，2006，30：493-496.

[4] Hidayet Argun，Fikret Kargi，Ilgi K. Kapdan. Effects of the substrate and cell concentration on bio-hydrogen production from ground wheat by combined dark and photo-fermentation[J]. International Journal of Hydrogen Energy，2009，34: 6181-6188.

[5] R.S. Prakasham，T. Sathish，P. Brahmaiah. Biohydrogen production process optimization using anaerobic mixed consortia: A prelude study for use of agro-industrial material hydrolysate as substrate[J]. Bioresource Technology，2010，101（14）：5708-5711

[6] Arunsri Fangkum, Alissara Reungsang. Biohydrogen production from mixed xylose/arabinose at thermophilic temperature by anaerobic mixed cultures in elephant dung[J]. International Journal of Hydrogen Energy，2009，34（23）: 6181-6188.

[7] Germán Buitrón，Carolina Carvajal. Biohydrogen production from Tequila vinasses in an anaerobic sequencing batch reactor: Effect of initial substrate concentration, temperature and hydraulic retention time[J]. Bioresource Technology，2010，101：9071–9077.

[8] R.S. Prakasham，P. Brahmaiah，T. Sathish，et al. Fermentative biohydrogen production by mixed anaerobic consortia: Impact of glucose to xylose ratio[J]. International Journal of Hydrogen Energy，2009，34（23）: 9354-9361.

[9] Thomas A. Kotsopoulos, Ioannis A. Fotidis, Nikolaos Tsolakis, Gerassimos G. Martzopoulos. Biohydrogen production from pig slurry in a CSTR reactor system with mixed cultures under hyper-thermophilic temperature (70 ℃)[J]. Biomass and Bioenergy，2009，33（9）：

1168-1174.
[10] A. Tenca，A. Schievano，F. Perazzolo，et al. Biohydrogen from thermophilic co-fermentation of swine manure with fruit and vegetable waste: Maximizing stable production without pH control[J]. Bioresource Technology，2011，102（18）：8582-8588.
[11] E. Castello´，C. Garcı´a y Santos，T. Iglesias，et al. Etchebehere. Feasibility of biohydrogen production from cheese whey using a UASB reactor: Links between microbial community and reactor performance[J]. International Journal of Hydrogen Energy，2009，34（14）：5674-5682.
[12] Eduardo Lucena Cavalcante de Amorim，Aruana Rocha Barros，Ma´rcia Helena Rissato Zamariolli Damianovic，et al. Anaerobic fluidized bed reactor with expanded clay as support for hydrogen production through dark fermentation of glucose[J]. International Journal of Hydrogen Energy，2009，34(2)：783-790.
[13] Hidayet Argun，Fikret Kargi. Bio-hydrogen production from ground wheat starch by continuous combined fermentation using annular-hybrid bioreactor[J]. International Journal of Hydrogen Energy，2010，35（12）：6170-6178.
[14] Yokoi T.，Tokushige J.，Hirose S.，et al.Hydrogen production by immobilized cells of aciduric enterobacter aerogenes strain HO-39[J]. Journal of Fermentation and Bioengineering，1997，83(5)：481-484.
[15] Yuan-Yuan Wang，Ping Ai，Cheng-Xiao Hu，et al. Effects of various pretreatment methods of anaerobic mixedmicroflora on biohydrogen production and the fermentation pathway of glucose[J]. International Journal of Hydrogen Energy，2011，36（1）：390-396.
[16] Myoung-Joo Lee, Ji-Hyeon Song, Sun-Jin Hwang. “Effects of acid pre-treatment on bio-hydrogen production and microbial communities during dark fermentation”, Bioresource Technology, 2009, 100(3): 1491-1493
[17] Fan YT, Li CL, Lay JJ, Hou HH, Zhang GSh. Optimization of initial substrate and pH levels for germination of sporing hydrogenproducing anaerobes in cow dung compost. Bioresource Technology, 2004, 91(2): 189–93
[18] ZENG Zhao-gang, SUN Xue-xi，LI Tao, et al. Study on the impact of corn straw pretreatment on anaerobic fermentation for hydrogen. 2010, 28(2): 59-61

BENS163

Analysis on the secretome encoded in the chromosome and plasmid genome of *Ralstonia solanacearum* GMI1000

ZHOU Xiaogan[a], SUN Maolin[b,*]

[a]Biotechnology and Genetic Germplasm Institute, Yunnan Academy of Agricultural Sciences, Kunming 650223, China；
Key Laboratory of Agricultural Biotechnology of Yunnan Province, Kunming 650223, China
E-mail address: zxg88@163.com

[b]Biotechnology and Genetic Germplasm Institute, Yunnan Academy of Agricultural Sciences, Kunming 650223, China；
Key Laboratory of Agricultural Biotechnology of Yunnan Province, Kunming 650223, China
E-mail address: maolin.sun@163.com

ABSTRACT

Total 5,129 amino acid sequences have been analysed from the chromosome and plasmid of the potato pathogens *Ralstonia solanacearum* GMI1000 genome. 263 ORFs of the secreted protein have signal peptides which included 178ORFs of chromosome (5.2% of proteins encoded in whole genome sequences) and 85ORFs of plasmid (5.1% of proteins encoded). 150 ORFs are type I and 28 ORFs are type II, 13 ORFs (11 ORFs type I and 2 ORFs type II) have the RR-motif structure, 116 ORFs have predicable function and the 62 ORFs were unknown in all signal peptides of secreted proteins encoded by chromosome genome. 73 ORFs are type I and 12 ORFs are type II , 3 ORFs have the RR-motif structure (only type I), 59 ORFs have predicable function and the 26 ORFs were unknown in the plasmid. The plasmid and chromosome could have very high Pro-source relationship in the evolutionary, as the secreted protein encoded of both are very close in the amino acids composition, and signal peptidases cleavage position. The functins of those secreted protein were described. The important functions was result in the interaction with various factors between the species and environment in a long-term evolution. But the type IV secreted protein of pilin signal peptides and the type III secreted protein encoded by the *hrp* gene , which the functions of both two typs can be described, had been not found in the secreted protein of signal peptides.

Keywords: Potato, *Ralstonia solanacearum* GMI1000, signal peptide secreted protein

1. INTRODUCTION

Potato bacterial wilt (BW) caused by *Ralstonia solanacearum* is a important bacterial disease in the potato production regions of the tropic -subtropic zone mainly. The pathogen has extensive host range including major solanaceae crops such as potato, tomato and tobacco[1]. The researches of *R..solanacearum* had been focused on bio-chemistry and genetics. It is become the model system to analyse the pathogenic process of plant bacteria[2]. Also, it is suitable material to research the adaptive functional regulation, as it can survive in the host-lack soil environment[3].

In 2002, Salanoubut et al finished the whole genome sequence analysis of model strain GMI 1000 of *Ralstonia solanacearum* [4]. It is 5.8 Mb with two replicons----a chromosome DNA of 3.7 Mb and a plasmid DNA of 2.1 Mb. The whole genome codes 5,129 putative proteins. Chromosome codes all the protein essential for its living, while plasmid codes control relative enzymes for primary metabolism, including animo acid and synthase of cofactor. If the plasmid missed, it should results in nutrition auxotrophic mutant for the strain. The analysis of the plasmid DNA suggests that the coded protein influents significantly on different environment adaptance as well as pathogenicity of the pathogen, and the plasmid carries whole hrp gene of strain, this gene cluster is necessary for BW. also the plasmid carries some gene to codes and turned into flagellum, and to controls polysaccharide synthesis outside the cell [4,5].

Basd on the protein synthesized in the cytoplasm be transported through a certain direction to a certain position in or outside the cells , the cell could maintain the normal living activity [6]. Blobel ect (1975) put forward that there was a part of specific order in the polypeptide chain .It guides the protein synthesis on the cisternal endoplasmic reticulum and gets into endoplasmic reticulum. The signal peptides had been cut by signal peptidase thus create ,and become relative mature protein,before the protein synthesis finished, this is signal hypothesis. This theory called signal peptides.has been proved by a lot of experimental evidence, and provided the method to decide the gene-coding amino acid sequence can excrete signal peptidase or secretory protein by the bio-information technology[7]. Signal peptides are generally made up by ten to sixty amino acid residues, and divided into three parts by a H-region which contains six to fifteen amino acid residues with hydrophilic N-terminal and C-terminal regions the two sides[8]. N-terminal are alkaline amino acid residues with positive charge, while C-terminal are parts rich in D-Ala. H-region plays an important part in the peptide transmembrane and accurate allocation. According to the difference of the signal peptides composition and cleavage site signal peptides recognition motif domain, there are four types of signal peptides[9]: signal peptidase I[10], signal peptidase II[11,12], Comc signal peptides[13] and bactericin-pheromone peptides[14]. This report was made by the seven types software,SignalP 3.0、TMHMM 2.0,THUMBUP、big-PI、TargetP 1.01、Lipop 1.0、TatP 1.0. to anlysied the presentation the secretory protein of *Ralstonia solanacearum* GMI1000.

2. MATERIALS AND METHODS

The studying materials are total 5,129 reported protein amino acid sequences from http://gib.genes.nig.ac.jp/single/index.php?spid=Rsol_GMI1000, among 3,448 protein amino acid are encoded by Chromosome Genome , and 1,681 protein amino acid are encoded by Plasmid Genome of *Ralstonia solanacearum* **GMI1000** . Seven protein predicting softwares were use for analysis of the secreted proteinsencoded. **SignalP3.0** (http://www.cbs.dtu.dk/services/SignalP/):Firstly, the whole GMI1000 Genome was preliminary screened by using the 3 parameters from Dscore and Smean in SignalP-NN and Cmax in SignalP-HMM. The potential secretory proteins with the signal peptides were confirmed by Cmax＞0.49，and Smean＞0.5 in the amino acid sequences , meanwhile, the Cmax cutting site was used as the cutting site of the signal sequences. based on the default of this software. **TMHMM2.0** (http://www.cbs.dtu.dk/services/TMHMM/) and **THUMBUP** (http://sparks-informatics.iupui.edu/Softwares-Services_files/thumbup.htm) The two softwares are used to predict whether the protein contain the transmembrane domain structure, if this

protein may play a role as a membrane receptor, also maybe is a anchored proteins located on the membrane, by this way, we identified that the proteins with transmembrane domain lack the secretory signal peptides. **big-PI predictor** (http://mendel.imp.ac.at/gpi/gpi_server) : It is Used to identify the GPI-anchor point of protein, the proteins without GPI-anchor point can be identified as potential secretory proteins. **TargetP1.01** (http://www.cbs.dtu.dk/services/TargetP/): To Predict the numbers and location of the target peptides in the subcellular organelle, then to confirm that the signal sequences are or are not the cell-penetrating signal peptides. **LipoP1.0**(http://www.cbs.dtu.dk/services/LipoP/) : To predict the cutting site of secretory protein signal peptidase from *R..solanacearum* GMI 1000 (the pathogen is an negative bacteria), acording to the typs of negative bacteria. **TatP 1.0**(http://www.cbs.dtu.dk/services/TatP/): To Predict the cutting site of the secretory protein signal sequence RR-motif from the pathogen.

3. RESULTS AND ANALYSIS

The Numbers and Length of secretory protein signal peptide encoded by genome:

After measured and calculated the GM1000 Genome, total 5,129 amino acid sequences are fit for the aforementioned algorithm routines of the seven softwares simultaneously, among these, 263 are the proteins encoded by the Genome carried solubility secretory signal peptide (5.2% of the whole amino acid sequences). 178 secretory proteins encoded by the chromosome genome (5.2% of proteins encoded by the chromosome genome). 85 secretory proteins encoded by the plasmi genome (5.1% of proteins encoded by the plasmid genome). To contrast the percentage of the secretory proteins is same almostly from both chromosome and plasmid genome, it indicate that both could have the relativity. The length of the signal peptide is between 13~37 amino acids,average of 24 amino acids residues from 178 secretory proteins encoded by chromosome genome.The length of the signal peptide is between 13 and 44 amino acids, average of 24 amino acids residues from 85 secretory proteins are encoded by plasmid genome. 19 signal peptides carry 20 amino acids and then 17 secretory signal peptides contian 22 amino acids in the chromosome secretory proteins . 11 signal peptides carry 24 amino acids, and other 10s have 22 amino acids in the plasmid secretory proteins (Fig.1). The shortest ORF of secretory protein encoded by chromosome genome is 67 amino acids, the longest is 1,070 amino acids, average of 293 amino acids. The shortest ORF of secretory protein encoded by plasmid genome is 58 amino acids, the longest is 1,330 amino acids, average of 332 amino acids. The length of most secretory protein ORFs have 101~200 amino acids, it is 53 ORFs from the chromosome and 23 ORFs from the plasmid , other ORFs have length 301~400 amino acids, 40 ORFs from the chromosome and 19 ORFs from the plasmid(Fig.2).

The composition of amino acids of secretory protein signal peptide encoded by genome:

The amino acid types of secretory protein signal peptide encoded respectively by chromosome and huge plasmid have been analysed systematically. There are 51.67% nonpolar amino acids, 24.22% polar amino acids, 9.07% basic amino acids carring gram-positive charge, 15.04% acidic amino acids carring gram-negative charge in secretory protein signal peptides from chromosome .there are 48.5% nonpolar amino acids, 26.34% polar amino acids, 8.45% basic amino acids carring positive charge,16.71% acidic amino acids carring negative charge in the secretory protein signal peptides from plasmid.The alanine (A) and leucine (L) are more abundent , glutamic acid (E) is the most less in the compostion of the both amino acid secretion

signal peptide. The frequencies of distribution of the 20 kinds of amino acid are very close in the signal peptide between chromosome and plasmid, The threonine (T) and asparagine (N) is almost the same, the difference of threonine (T) is 0.1%, the difference of asparagine (N) is only 0.02%, the difference of alanine (A) is the most notable 2.11%(Fig.3). The reserch showed that most amino terminal signal sequence could be identified and cut by the signal peptidase Spase enzyme , than the cutting the mature proteins are transported to different parts of the cell, while the signal peptide is decomposed by the signal peptide enzyme. After analysed the cleavage site of secreted protein signal peptide from the chromosomes and giant plasmid of GMI1000 genome ,the result showed that the left -3 position of cleavage site composted by a number of alanine amino acids (A), chromosomes have 67.98%, giant plasmids have 67.06%;-2 bit composted by 14.61% histidine (H) and 13.48% alanine (A) in the chromosome, and alanine (A) and histidine (H) have the largest numbers with the proportion of 12% in the giant plasmid; -1bit have the largest numbers alanine (A), the chromosome 88.2% and the giant plasmid 81.18%. The right +1 position of signal sequence cleavage sites have the largest numbers Glutamine (Q), 33.15% in the chromosomes and 25.24% in the plasmids. +2 bit composted by the16.29% alanine (A) in the chromosome ,and the 18.82% threonine (T) in the giant plasmid ; +3 bit composted by the 14.61% alanine (A) in the chromosome ,and 16.47% proline (P) in the giant plasmid. The composition of amino acids of secretory protein signal peptide was same almorstly(Tab. 1,2,3).

The analysis on the types and structures of the secreted protein of signal peptide :

150proteins were signal peptide type I in the 178 secreted protein of chromosome , 73 proteins were signal peptide type I in the 85 secreted protein of plasmid . They were indentified by the compositon of three kinds of protein components, including an ATP-enzyme complexes via the ABC-type transport system wich can regulate the transmembrane transport the proteins without the participation of themedia. The type I N-terminal signal peptide carrys 2 to 3 positive charged amino acids (K or R) mainly , or 5 to 11 positive charged amino acids. 113 proteins have the typical structure of AXA, accounting for 75.3% in the those 150 type I. The AXA structure is composed by the H-domain carring an average of 19 to 20 hydrophobic amino acids, and C-domain that is -3 to -1 position of the amino acids , A is alanine, X refers to any other amino acid [15]. The type II protein secretion signal peptide, alsoknown as lipoprotein signal peptide, the typical structure of C-domain is: L-(A / S) – (A / G), the cleavage site after amino acid cysteine +1 (C), thus forming a conservative L-(A / S) – (A / G)-C's Lipobox typical structure, the structure of the lipoprotein to be cut can still anchored in the plasma membrane. 28 proteins were the type II ,19 signal peptides have the Lipobox typical structure (67.86% in type II) in the 178 secreted protein of chromosome. 12 proteins were the type II , 4 signal peptides have the Lipobox typical structure (33.33% in type II) in the 85 secreted proteins of plasmid. RR-motif-based signal peptide is contained in the signalpeptide RRX-# - # structure, R refers to the arginine, X refers to any other amino acid, # refers tohydrophobic amino acids, the structure of signal peptide secreted regulatory proteins into the Tat pathway [16] , mainly through a combination of the cofactor redox protein folding on translocation. 13 signal peptides of the secretion protein of chromosome carry RR-motif structure, among 11 are belong to type I , and 2 are type II. 3 signal peptides of plasmid carry RR-motif structure only . For this, the part of coding proteins of chromosome genome could be transported by the Tat pathway .The type Ⅳ (Comc) and type Ⅲ (bacteriocin - pheromone) of the secreted protein signal peptide are described to transfer the effecter protein molecules to the host cells . The both types of signal

peptide would been found in the secreted protein of GMI1000, but used those softwares can not to predict the two types of signal peptide [17].

The functional analysis of secreted proteins in the GMI1000 genome-wide:

To check the relationship of homology to the known amino acid sequence and secreted protein in *R.. solanacearum* GMI1000. 116 ORFs have predicable function and the 62 ORFs were unknown in all signal peptides of secreted proteins encoded by chromosome genome. 59 ORFs have predicable function and the 26 ORFs were unknown in the plasmid. The functions of those known proteins are focused to join in variouse enzymes and relative proteins mainly which are necessary in the cell metabolism, such as decarboxylase, hydrolase, oxidoreductase, esterase, cytochrome c, lectin class, and the cell regulation of transport, the structural of cell surface . The functions of secreted proteins are described from the chromosome and plasmid (Tab.3, 4). It is obvious that these functions plays an important role to maintan an normal activities in the organisums.

4. DISCUSSION

Though limited softwares can not predict out the type Comc (type IV) of signal peptides and the type Bactericin-pheromone (type III) signal peptides , by compared the functional ,2 type IV secretory proteins of signal peptides were infered in the chromosome , coding RSc2675 and RSc1213, 3 type III secretory proteins of signal peptides were infered in the plasmid DNA secretory protein signal peptides, Coded by *hrp* gene , coding RSp0947, RSp1460 and RSp0099. The function of type III secretory protein is conservative in plant and animal pathogenic bacteria, And causes the disease by transmitting the functional protein into the host cells[18 · 19]. After anlysed the signal peptides secretory protein subcellular organelles by the Target P, 3 proteins were unknown secretory pathways , 30 proteins were located at the chondriosome, called type M secretory pathway, 145 proteins were secreted to the periplasmic space, called type M in the chromosome DNA secretory protein. 8 proteins were unknown secretory pathways, proteins were located at the chondriosome, 69 proteins were secreted to the periplasmic space in the plasmid DNA secretory protein. The type S proteins have the most large proportion , and approach a major secretory pathway , proved the hypothesis of "GNB secretory protein secretes directly to periplasmic space and extracellular medium" [20].

The most researches of the secretory protein signal peptide of pathogenic bacteria were interest in the secretory protein of signal peptide of chromosome genome. To compare GMI1000 contains the chromosome and giant plasmid genome.The proportion of the amino acid sequences of both genomes separately was same almorstly (5.2% in chromosome DNA and 5.1% plasmid DNA), the proportion of (G+C) purities was compared in the process of both genomes sequencing, chromosome is 67.04% and plasmid is 66.86%. The compositions of the signal peptidase cleavage position -1~+3 amino acid were quite affiliation. Based on those results, the chromosome and plasmid could have the relationship of evolution closely . The plasmid may originate from the chromosome, and than it formed the self-renewing DNA ,became an indepdent substance gradually in the long evolution process.

The announcement of *Ralstonia solanacerum* GMI1000 whole genome sequence (WGS) means the research on this pathogenic microbes comes to a functional genome era. Moe than

ten*Ralstonia solanacearum* extracellular proteins have been separated and tested, the most of thome are secreted directly to extracellular medium by type II and III secretory system, and at least two types of extracellular proteins are relative to BW pathogenicity. Although a lot of functions of the secretory protein has been proved from the chromosome and plasmid genome, such as the importance of the chromosome on vital movements,cellular metabolism, purine and pyrimidine biosynthesis, DNA cloning and repairing and cell division, the giant plasmid secreted protein plays a key part on the controlling of basal metabolism, amino acids biosynthesis, and host plant infection. How many potential secretory proteins are real secretory proteins, what condition the proteins are secreted to extracellular, and what functions do they have in host-environment interaction, all problemes will be focused in the next step.

5. FIGURES AND TABLES

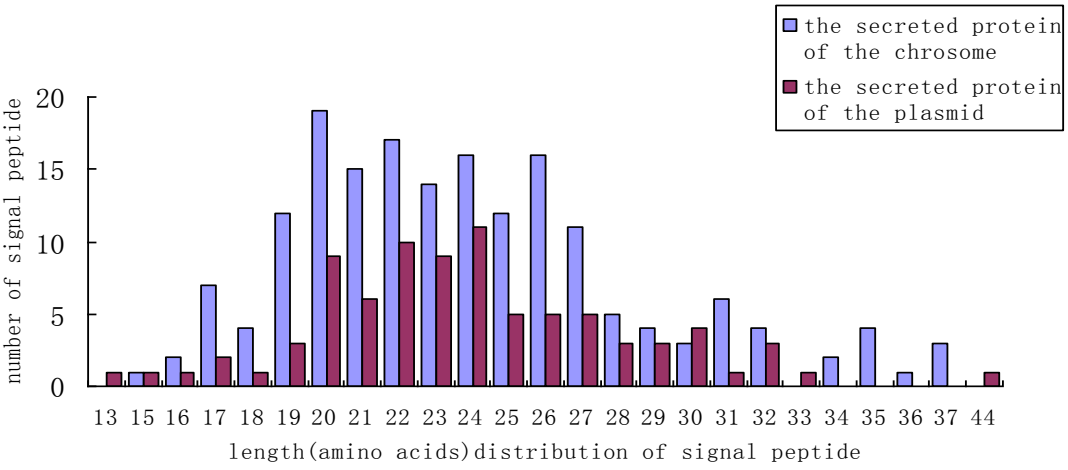

Fig.1 Secreted protein distribution and number of signal peptide in GMI1000 whole genome

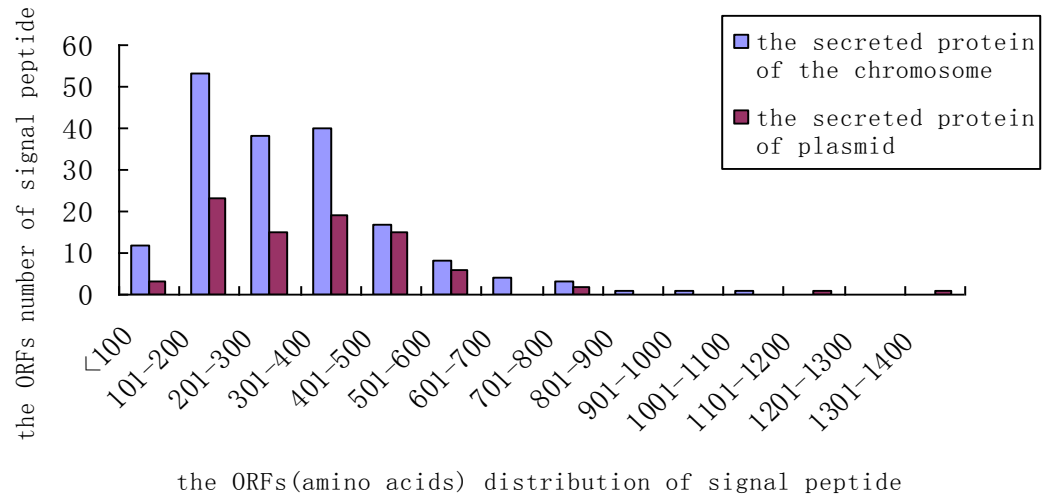

Fig.2 Secreted protein ORFs(amino acids) distribution and number of GMI1000 whole genome

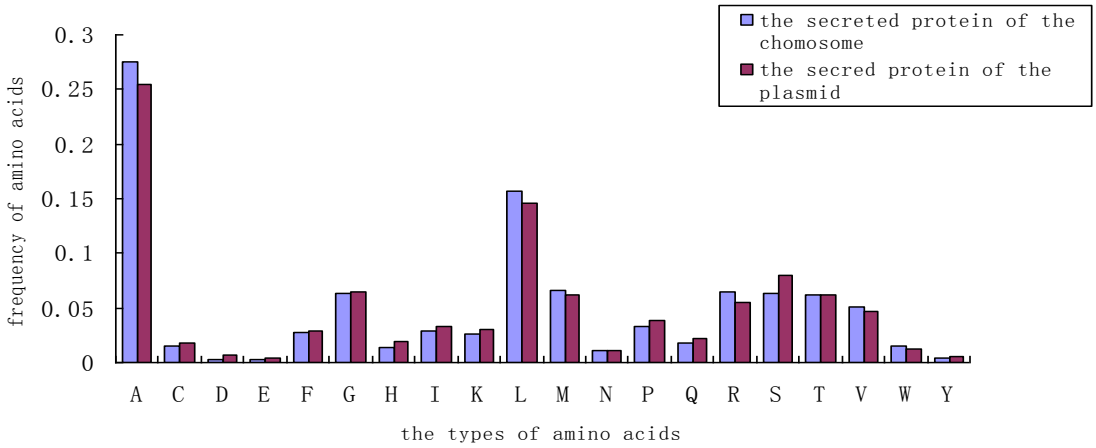

Fig.3 Secreted protein amino acids frequency of signal peptide in GMI1000 whole genome

Table 1 Secreted protein amino acids distribution of signal peptide cleavage position in GMI1000 chromosome genome

-3	Number	-2	Number	-1	Number	1	Number	2	Number	3	Number
A	121	A	24	A	157	A	34	A	29	A	26
C	1	C	2	G	16	C	29	D	22	C	2
F	1	D	1	Q	1	D	9	E	10	D	9
I	2	E	1	R	2	E	10	G	19	E	4
L	23	F	13	S	2	F	1	H	2	F	2
M	3	G	11	total	178	G	9	I	3	G	17
S	10	H	26			H	1	K	1	H	1
T	4	I	2			I	1	L	4	I	4
V	13	L	21			K	3	M	1	K	8
total	178	M	3			L	3	N	7	L	9
		N	3			N	2	P	19	M	2
		P	3			Q	59	Q	5	N	6
		Q	17			R	4	S	23	P	24
		R	14			S	4	T	23	Q	5
		S	14			T	4	V	10	R	5
		T	3			V	4	total	178	S	18
		V	6			Y	1			T	23
		W	9			total	178			V	9
		Y	5							Y	4
		total	178							total	178

Table 2 Secreted protein amino acids distribution of signal peptide cleavage position in GMI1000 plasmid genome

-3	Number	-2	Number	-1	Number	1	Number	2	Number	3	Number
A	57	A	12	A	69	A	18	A	14	A	6
E	1	C	3	G	13	C	12	C	2	C	1
G	3	D	1	S	2	D	4	D	4	D	3
I	1	E	1	V	1	E	5	E	6	E	2
L	6	F	6	total	85	G	3	G	8	F	4
M	4	G	3			H	2	L	2	G	4
S	4	H	12			L	1	N	2	H	3
T	3	K	1			M	1	P	8	I	2
V	6	L	7			N	2	Q	4	K	2
total	85	M	3			Q	24	S	15	L	10
		N	1			R	5	T	16	P	14
		Q	10			S	3	V	4	Q	4
		R	2			T	2	total	85	R	1
		S	11			V	1			S	11
		T	3			W	1			T	5
		V	2			Y	1			V	9
		W	4			total	85			W	1
		Y	3							Y	3
		total	85							total	85

Table 3 Description of secreted protein in Ralstonia solanacearum GMI1000 chromosome

gene code	ORF length(AA)	Initiation amino acid	termination amino acid	description
cell metabolism				
RSc0337	496	Met	Ile	polyphenol oxidase with tyrosine hydroxylase activity oxidoreductase protein
RSc0049	418	Met	Gly	probable 3-carboxymuconate cyclase protein
RSc2547	795	Met	Gln	Probable acyl-homoserine lactone acylase transmembrane protein
RSc1833	297	Met	Phe	probable cog4313, involved in meta-pathway of phenol degradation protein
RSc1717	216	Met	Gly	probable esterase protein
RSc2921	623	Met	Asp	Probable gamma-glutamyltranspeptidase precursor protein
RSc3086	103	Met	Ala	probable high-potential iron-sulfur precursor (hipip) protein
RSc2290	95	Met	Arg	probable iron oxidase precursor oxidoreductase protein
RSc2987	219	Met	Arg	probable oxidoreductase cytochrome c-type protein
RSc3310	353	Met	Lys	probable phosphate-binding periplasmic precursor (pbp) abc transporter protein
RSc2653	543	Met	Arg	probable protease protein
RSc3262	431	Met	Gly	probable sulfide dehydrogenase flavocytochrome c oxidoreductase protein
RSc0813	379	Met	Arg	probable sulfite:cytochrome c oxidoreductase (subunit a) oxidoreductase protein

RSc0097	483	Met	Leu	putative alkaline phosphatase lipoprotein transmembrane
RSc0098	467	Met	Leu	putative alkaline phosphatase protein
RSc2214	339	Met	Asp	putative beta-lactamase-like, zn-dependent hydrolase protein
RSc0206	342	Met	Arg	putative cog1073, hydrolase of the alpha/beta superfamily protein
RSc3256	270	Met	Arg	putative cytochrome c-related protein
RSc2328	259	Met	Arg	putative hydrolases or acyltransferases (alpha/beta hydrolase superfamily) protein
RSc1241	309	Met	His	putative rhizopine-binding precursor protein
RSc0629	104	Met	Ser	putative oxidoreductase cytochrome c552 precursor protein
RSc0772	429	Met	Gln	putative oxidoreductase dehydrogenase (cytochrome c subunit) protein
RSc0999	115	Met	Lys	putative periplasmic cytochrome type-c oxidoreductase protein
RSc1000	133	Met	Lys	putative periplasmic cytochrome type-c oxidoreductase protein
RSc2452	189	Met	Asp	putative phospholipase d/transphosphatidylase protein
RSc0319	700	Met	Ala	probablenon-hemolyticphospholipasec (phosphatidylcholine cholinephosphohydrolase) protein
RSc0153	314	Met	Gln	putative zn-dependent protease with chaperone function protein
cell processes and transported				
RSc2864	385	Met	Arg	probable abc-type branched-chain amino acid transport systems, periplasmic component abc transporter protein
RSc0011	398	Met	Gln	probable acriflavin resistance lipoprotein a precursor
RSc3182	583	Met	Phe	probable activation/secretion protein
RSc3329	382	Met	Asn	probable amino-acid-binding periplasmic (pbp) abc transporter protein
RSc1264	438	Met	Glu	probable glycerol-3-phosphate-binding periplasmic lipoprotein
RSc2340	215	Met	Gln	probable outer-membrane lipoprotein carrier precursor
RSc1886	525	Met	Lys	probable periplasmic dipeptide transport protein precursor
RSc1017	319	Met	Thr	probable ribose abc transporter, periplasmic ribose-binding abc transporter protein
RSc1791	343	Met	Arg	probable solute-binding periplasmic (pbp) abc transporter protein
RSc2368	182	Met	Asn	probable superoxide dismutase cu-zn precursor protein
RSc2261	308	Met	Gln	putative amino-acid-binding periplasmic (pbp) abc transporter protein
RSc1609	375	Met	Thr	putatived-alanyl-d-alanine-endopeptidase (penicillin-bindingprotein)
RSc3051	580	Met	Arg	putative bacterial extracellular solute-binding family 1; abc transporter protein
cell envelope structure				
RSc2380	209	Met	Gly	probable bacterial outer membrane transmembrane protein
RSc3065	261	Met	Phe	probable cog3713, mipa like outer membrane v transmembrane protein
RSc2760	353	Met	Phe	probable ipr001702 outer membrane (porin) protein
RSc1084	364	Met	Phe	probable outer membrane p2; transmembrane protein
RSc0595	729	Met	Phe	probable outer membrane receptor protein
RSc0736	172	Met	Tyr	probable peptidoglycan-associated lipoprotein precursor
RSc1516	451	Met	Ser	putative membrane-bound lytic murein transglycosylase-like lipoprotein
RSc2815	245	Met	Ser	putative transglycosylase protein
RSc2675	1070	Met	His	putative type 4 fimbrial biogenesis pily1-related protein
RSc1213	263	Met	Asp	putative type 4 fimbrial biogenesis protein

Table 4 Description of secreted protein in Ralstonia solanacearum GMI1000 megaplasmid

gene code	ORF length(AA)	Initiation amino acid	termination amino acid	description
cell metabolism				
RSp0947	258	Met	Leu	probable gluconate 5-dehydrogenase oxidoreductase protein
RSp0899	284	Met	Glu	probable hydratase/decarboxylase; protein
RSp0212	520	Met	Ala	probable lignostilbene-alpha,beta-dioxygenase related enzyme protein
RSp1201	187	Met	Phe	probable lipid a deacylase protein
RSp1370	423	Met	Pro	probable periplasmic copper-binding nosd protein
RSp1366	340	Met	Thr	probable thiamine biosynthesis apbe transmembrane protein
RSp1653	125	Met	Thr	putative cytochrome c oxidase subunit II oxidoreductase protein
RSp1453	363	Met	Gln	putative cytochrome c protein
RSp1652	309	Met	Thr	putative metallophosphoesterase/phosphohydrolase protein
RSp0168	200	Met	Ile	putative protein prenyltransferase
RSp0824	353	Met	Val	putativegluconolactonase (d-glucono-delta-lactone lactonohydrolase) protein
cell processes and transported				
RSp1447	386	Met	Arg	probable abc-type branched-chain amino acid transport systems, periplasmic component abc transporter protein
RSp0550	590	Met	Tyr	probable activation/secretion protein
RSp1445	556	Met	Phe	probable activation/secretion protein
RSp1535	583	Met	Phe	probable activation/secretion protein
RSp0013	386	Met	Lys	probable amino acid-binding periplasmic (pbp) abc transporter protein
RSp1575	283	Met	Ile	probable amino-acid-binding periplasmic (pbp) abc transporter protein
RSp0817	491	Met	Ala	probable outer membrane drug efflux lipoprotein
RSp0481	255	Met	Gln	probable substrate-binding periplasmic (pbp) abc transporter protein
RSp1140	298	Met	Asn	probable substrate-binding periplasmic (pbp) abc transporter protein
RSp0290	488	Met	Arg	probable type I secretion system, outer membrane chanel lipoprotein
RSp1468	311	Met	Phe	putative cog4313, involved in meta-pathway of phenol degradation protein
RSp0100	703	Met	Phe	putative ferrisiderophore receptor protein
RSp1283	414	Met	Trp	putative lamb type porin transmembrane protein
RSp0106	257	Met	Pro	putative molybdate-binding periplasmic protein
RSp1599	483	Met	Arg	putative outer membrane drug efflux lipoprotein
cell envelope structure				
RSp0916	296	Met	Asp	probable vacj-related lipoprotein
RSp1240	427	Met	Lys	putative membrane-bound lytic murein transglycosylase b protein
RSp1456	490	Met	Pro	putative outer membrane lipoprotein
virulence				
RSp0847	1330	Met	Gly	probable awr type III effector family protein
RSp1460	274	Met	Asp	putative type III effector protein
RSp0099	1127	Met	Leu	type III effector protein awr1

6. ACKNOWLEDGMENTS AND LEGAL RESPONSIBILITY

Thanks to the helpful warmthly of Dr. Greg. Forbes Who is plant pathologist from International Potato Center in editing the manuscript. This work is supported by the national Sci-foundation,China(No.31060021) and Provincal Sci-foundation, Yunnan.(2008ZC100M).

7. REFERENCES

[1] Hayward A C · Biology and epidemiology of bacterial wih caused by *Pseudorllotla sololloc earlzm* · *Annu Rev Phytopathol*.1991，29：65～87.

[2] Staskawicz, B. J.,Mudgett, M. B., Dangl, J. L. & Galan, J. E. Common and contrasting themes of plant and animal diseases. *Science*, 2001, 292：2285～2289.

[3] Granada, G. A. & Sequeira, L. Survival of Pseudomonas solanacearum in soil, rhizosphere and plant roots. Can. J. *Microbiol*. 1983,29：433～440.

[4] Salanoubat M · S Genin · F Artiguenave，*et a1* · Genome sequence of the plant pathogen *Ralstonia solanacearum* · Nature，2002，415：497～502.

[5] Genin S，C Boucher · *Ralstonia solanacearum*：secrets of a major pathogen umeiled by analysis of its genome · *Mol Plant Pathol* ，2002 · 3：l1l～ll8 ·

[6] Harold Tjalsma, Albert Bolhuis,Jan D, *et a1* · Signal Peptide-Dependent Protein Transport in *Bacillus subtilis*:a Genome-Based Survey of the Secretome. *Microbiology and Molecular Biology Reviews*, 2000, 515～547.

[7]Zhang cheng-gang,He fu-chu. Bioinfornation methods and practice. Beijing: Science press ,2002,67～69.

[8]Martoglio B，Dobberstein B.Signal sequence：more than just greasy peptides.*Trends Cell Biol,* 1998,10：410～415.

[9] Harold T.Albe rt B.Jan D H.*et al.*Signal peptide-dependent protein tran spo rt in Bacillus subtilis：a genome—based survey of the secretome.*Microbiology and Molecular Biology Reviews*.2000，9：515～547 ·

[10]Tjalsma H.Bolhuis A，van Roosmalen M L，*et a1* · Functional analysis of the secretory precursor processing machinery of Bacillus subtilis： identification of a eubacterial homolog of archaeal and eukaryotic signal peptidases. *Genes*,1998.12：2318～ 2331 ·

[11] Tjalsma H，Kontinen V P ◦ Pra gai z，et a1 · The role oflipoprotein processing by signal peptidase Ⅱin the Gram-positive eubacterium Bacillus subtilis：signal peptidases Ⅱis required for the efficient secretion of a-amylase · a non
-lipopretein. *Journa of Biology Chemistry*.1999.274：1698～ 1707 ·

[12] Tjalsma H，ZanenG，Venema G，*et a1* · Th epotential active site of the lipoprotein-specific (type Ⅱ) signal peptidase of Bacillus subtilis · *Journa of Biology Chemistry*，1999，275：25102～25108.

[13] Chan g Y S，Dubnau D · ComC is required for the processing and translocation of ComGC，a pilin-like competence protein of Bacillussubtilis · *MolecularMicrobiology* ，1995，15：543～551.

[14] Paik S H，Chakicherla A，Hansen J N · Identification and characterization of the structural and transporter genes for，and the chemical and biological properties of， sublancin 168，anovel lantibiotic produced by Bacillus subtilis 168 · *Journa of Biology Chemistry*，1998, 273：23134～23142.

[15] Harold Tjalsma,Albert Bolhuis,Jan D.H.Jongbloed. Signal peptide-dependent protein t ransport in *Bacillus subtilus*: a Genome-based survey of the secretom. *Microbiology and*

Molecular Biology Reveiws，2000:515～547.
[16] Kam ten H ，Andreas G，Maurice S， *et a1*． PrediSi：Pred iction of signal peptides and their cleavage positions Nucleic Acids Research，2004，32 (Web Server issue)：W375～W379．
[17] Pugsley AP .The complete general secretory pathway in gram-negative bacteria. *Microbiol Rev, 1*993,57:50～108.
[18] Staskawicz, B. J.,Mudgett, M. B., Dangl, J. L. & Galan, J. E. Common and contrasting themes of plant and animal diseases. *Science*，2001，92：2285～2289.
[19] Cornelis, G. R. & Van Gijsegem, F. Assembly and function of type III secretory systems. *Annu. Rev.Microbiol*,2000，54, 735～774.
[20] Pugsley A P The complete general secretory pathway in gram · nagative bacteria · *Microbiol Biotechnol*，1993，57，50～ 108.
[21] Schell M A · Control of virulence and pathogenicity genes of *Ralstonia solanacearum* by an elaborate sensory network · *AnnuRev Phytopathol*，2000，38：263～292 · Berks BC, Sargent F, Palmer T The Tat protein export pathway. *Mol Microbiol* ,2000, 35:260～274.

Engineering I

Pullman Bangkok King Power, 2F Meeting Room BETA I

2013/1/27 Sunday 08:45-10:00

Session Chair: Eakphan Thangthong

E189
Some Novel Techniques of Analog Multiplication using Operational Amplifiers
Chinnathambi Selvam | *IIT Madras*

E190
Degradation of Methylene Blue in Cathode of Microbial Fuel Cell with Gold Nanoparticles Catalyst '
Hiep Thi Han | *Yeungnam University*

E194
Overview on the Factors Affecting Pavement Interlayers Bond Strength
Fung Lung Chang | *Universiti Teknologi Malaysia*
Haryati Yaacob | *Universiti Teknologi Malaysia*
Mohd. Rosli Hainin | *Universiti Teknologi Malaysia*
Ahmad Safuan A. Rashid | *Universiti Teknologi Malaysia*

E198
A Study on Development of Fatigue Tester Simulating Operating Condition for the Dropper of Overhead Catenary System
Yongseok Kim | *Sungkyunkwan University*
Haochuang Li | *Sungkyunkwan University*
Jea Mean Koo | *Sungkyunkwan University*
Chang Sung Seok | *Sungkyunkwan University*
Heungchai Chung | *Korea Railroad Research Institute*

E207
The Application of Model-based and Integrated Process Improvement Methodology for Metal Sheet Coating Factory
Eakphan Thangthong | *Chulalongkorn University*
Jeerapat Ngaoprasertwong | *Chulalongkorn University*

E189

Some Novel Techniques of Analog Multiplication using Operational Amplifiers

K.C.Selvam
Department of Electrical Engineering, Indian Institute of Technology, Madras Chennai - 600 036, India
kcselvam@ee.iitm.ac.in

Abstract
The following novel techniques for analog multiplication using operational amplifiers are proposed in this paper. (1) Sigma Delta Multiplier (2) Sigma Integrated Multiplier. (3) Sigma Sampled Multiplier and (4) Sigma Single Slope Multiplier. In all the above 4 techniques, the constant of multiplication is dependent upon two reference voltages. Employing precision sources for the reference voltages, one can achieve an acceptable level of accuracy. Verification of the feasibility of the circuit configurations are established by way of test results on a proto type.
Keyword：Integrator; Switch; Comparator; Monostable Multivibrator; Peak detectors.

1. Introduction

There are several methods for analog multiplication. They are: logarithmic function generation, quarter-squarer multiplication, multiplication employing FETs, triangle averaging multiplication, magneto resistance multiplication [1], transconductance multiplication [2], and double dual slope multiplication [3]. If the width of a pulse train is made proportional to one voltage and the amplitude of the pulses to a second voltage, then the average value of pulse waveform is proportional to the product of two voltages, is called Time Division Multiplier [4],[5]. The TSY multiplier [4] requires a highly linear, symmetrical and stable frequency triangular wave generator. This multiplier is simplified by T. S. Rathore [6] without using triangular wave generator and using difference integrator, difference comparator, amplitude modulator and averaging circuit. Another way of simplification was done by Greg. D .Johnson [7] where he used dual slope integrator, comparator, switches and low pass filter. Now I propose novel types of analog multiplication using a sigma generator as basic building block for all the types. Both sigma generator and the proposed methods are implemented using opamps.

2. Sigma Generator

The sigma generator plays an important role in the proposed novel techniques of analog multiplier. Its circuit diagram using op amps is shown in Fig. 1 and the associated waveforms are shown in Fig. 2. As shown in Fig. 2, the sigma generator produces (1) a sawtooth wave VS of peak value of VR2 and period of T, where VR2 is a constant reference voltage. (2) a short pulse wave form VC of period T and (3) rectangular pulse waveform VP of period T whose ON time δT is proportional to one input Voltage +V1.

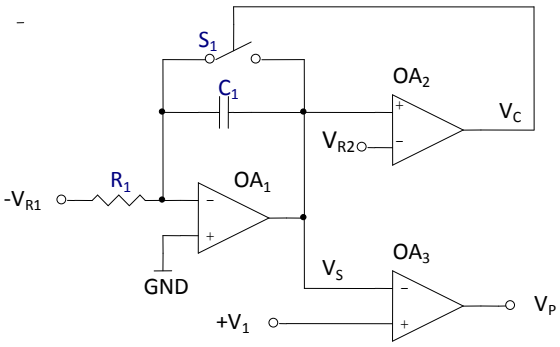

Fig. 1 Circuit diagram of Sigma Generator

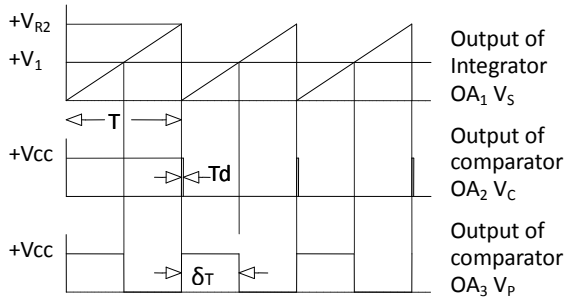

Fig. 2 Output waveforms of Sigma Generator

The sawtooth wave is generated by charging a capacitor at a specified rate and then rapidly discharging it with a switch [8]. In Fig. 1, the opamp OA_1 as an integrator forces the feedback capacitor C_1 to charge at a rate set by the input current whose value is V_{R1}/R_1. During the capacitor charge, the comparator OA_2 output is LOW state and the switch S_1 is OFF state. The output of integrator V_S is then

$$V_S = \frac{1}{R_1 C_1}\int_0^t V_{R1}\,dt = \frac{V_{R1}}{R_1 C_1}t \qquad (1)$$

When the output of integrator OA_1 exceeds the another reference voltage V_{R2}, the comparator OA_2 output goes HIGH and the switch S_1 shorts the capacitor C_1, hence V_S comes down to 0V. After a very short delay time Td, the comparator output returns to LOW and the switch S_1 opens allowing C_1 to resume charging. The cycle therefore repeats itself at a period (T+Td). The waveforms at cardinal points in the circuit are shown in Fig. 2, From Eqn (1) and the fact that at time t = T, Vs = V_{R2}, we get

$$T = \frac{V_{R2}}{V_{R1}} R_1 C_1 \qquad (2)$$

It should be noted here that the integration was done over the period T. The actual period is (T+Td), As Td <<T, Td can be neglected with negligible errors in the end result. The input voltage $+V_1$ is compared with the sawtooth wave V_S thus generated by the comparator OA_3. A rectangular pulse train V_P is produced at the output of comparator OA_3. Its ON time or width δ_T on will be

$$\delta_T = \frac{V_1}{V_{R2}} T \qquad (3)$$

Now we will see how this sigma generator is used to develop four types of analog multiplier.

3. Sigma Delta Type Multiplier

This is also called as Time Division Multiplier or Pulse width – Pulse hight multiplier. Its circuit diagram is shown in Fig. 3 and associated waveforms in Fig. 4.

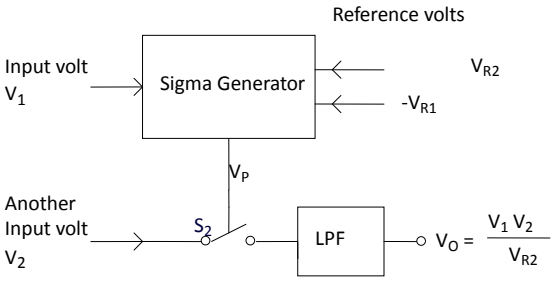

Fig. 3 Circuit diagram of Sigma Delta type Multiplier

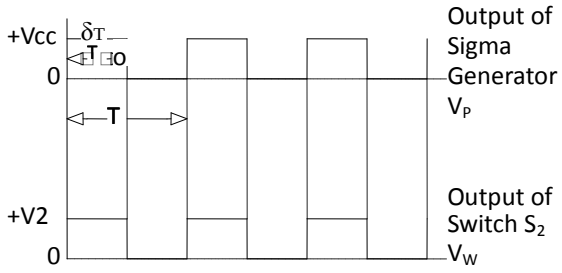

Fig. 4 Associated waveforms of Fig.3

The switch S_2 in Fig. 3 connects another input voltage V_2 to the Low Pass Filter (LPF) only during the ON time δ_T of pulse train V_P. As shown in Fig. 4, another pulse train V_W is generated at the output of switch S_2. The LPF output V_O is the average value of pulse train V_W,

$$V_O = \frac{1}{T}\int V_2 \, dt = \frac{V_2}{T}\delta_T$$

$$V_O = \frac{V_1 V_2}{V_{R2}} \qquad (4)$$

4. Sigma Integrated Type Multiplier

A pulse train whose ON time proportional to one voltage is generated. Another input is integrated during the ON time of the pulse. The peak value of the integrated output is proportional to the product of two voltages. The circuit diagram of sigma integrated type multiplier is shown in Fig. 5 and its associated waveforms in Fig. 6. The switch S_3 shorts the capacitor C_2 during OFF time of the pulse train V_P. During the ON time δ_T, the integrator OA_4 integrates the input voltage $-V_2$. The output of the integrator OA_4 will be

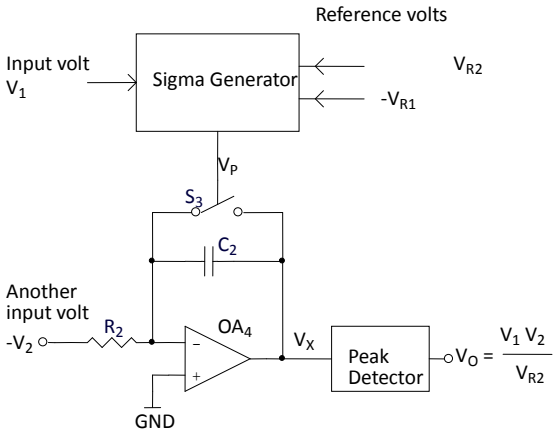

Fig . 5 Circuit Diagram of Sigma Integrated type Multiplier

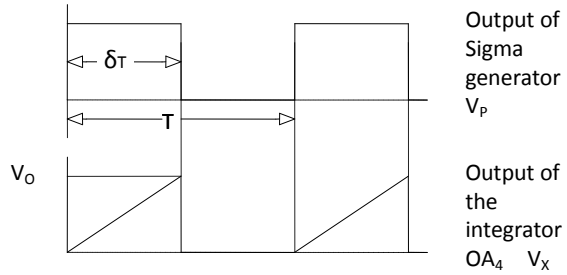

Fig. 6 Associated waveforms of Fig.5

$$V_X = \frac{1}{R_2 C_2}\int V_2 \, dt = \frac{V_2}{R_2 C} \delta_T \qquad (5)$$

$$= \frac{V_2 V_1}{R_2 C_2 V_{R2}} T$$

$$V_X = \frac{V_1 V_2 R_1 C}{V_{R1} R_2 C_2}$$

If $R_1 = R_2$ and $C_1 = C_2$

$$V_X = \frac{V_1 V_2}{V_{R1}} \qquad (6)$$

The peak detector at the output of integrator OA_4 gives the peak value. Hence $V_O = V_X$.

5. Sigma Sampled Type Multiplier

A sawtooth wave of period T whose peak value is proportional to one input voltage is sampled by a sampling pulse whose position over the period T is proportional to another input voltage. The sampled output is proportional to the product of two input voltages. The sigma sampled type multiplier is shown in Fig. 7 and its associated waveforms in Fig. 8. The output pulse train V_P from sigma generator is given to a monostable multivibrator whose output V_M is a short pulse during falling edge of the pulse train V_P. The second input $-V_2$ is given to the integrator OA_5. Its output will be

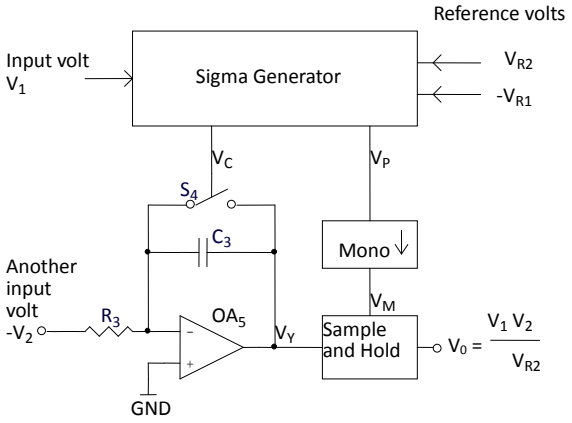

Fig. 7 Circuit diagram of Sigma Sampled type Multiplier

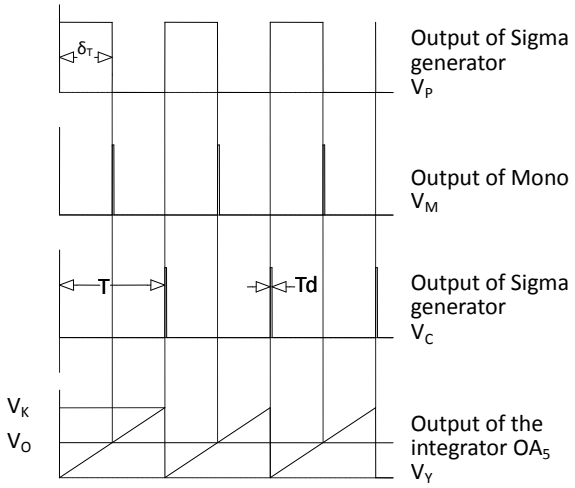

Fig. 8 Associated Waveforms of Fig. 7

$$V_Y = \frac{1}{R_3 C_3}\int_0^t V_2 dt = \frac{V_2}{R_3 C_3} t \qquad (7)$$

Another sawtooth wave V_Y is generated at the output of OA_5 with same time period T and a peak value of V_K. From the waveforms shown in Fig. 8 and from equation (7) and the fact at time t = T, $V_Y = V_K$.

$$V_K = \frac{V_2 V_{R\ 2} R_1 C}{V_{R1} R_3 C_3}$$

If $R_1=R_3$, $C_1=C_3$ then

$$V_K = \frac{V_{R2}}{V_{R1}} V_2 \qquad (8)$$

This sawtooth V_Y is sampled with the sampling pulse V_M as shown in Fig. 7. From the waveforms shown in Fig. 8

$$V_O = \frac{V_K}{T}\,\delta_T \qquad (9)$$

$$V_O = \frac{V_1 V_2}{V_{R1}} \qquad (10)$$

6. Sigma Single Slope Multiplier

A short pulse train whose period T proportional to one input voltage is generated. Another input voltage is integrated during the period T. The peak value of the integrated output is proportional

to the product of two input voltages.The circuit diagram of single slope multiplier is shown in Fig. 9 and its associated waveforms in Fig. 10. The short pulse from sigma generator V_C controls switch S_5. It shorts the integrating capacitor C_4 during short duration Td. The another input voltage $-V_2$ is integrated by the integrator OA_6 during the period T. The output of integrator OA_6 will be

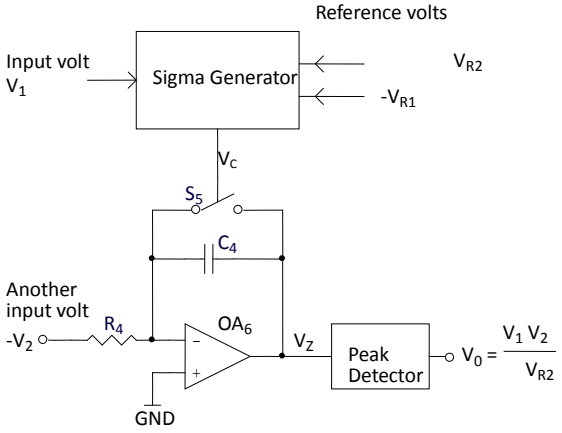

Fig. 9 Circuit diagram of Sigma Single Slope Multiplier

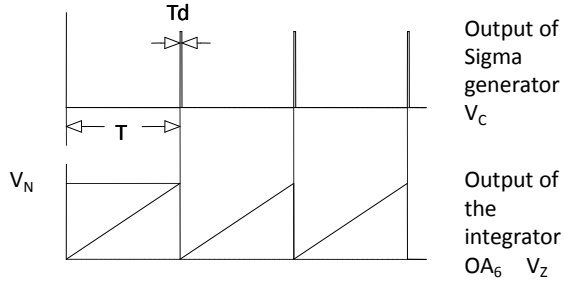

Fig. 10 Associated Waveforms of Fig. 9

$$V_Z = \frac{1}{R_4 C_4}\int_0^t V_2 \, dt = \frac{V_2}{R_4 C_4} \qquad (11)$$

From the waveforms shown in Fig. 10 and the fact that at
t = T, $V_Z = V_N$

$$V_N = \frac{V_2}{R_4 C_4} T$$

$$= \frac{V_2 V_{R2}}{R_4 C_4 V_{R1}} R_1 C_1$$

Let us assume $V_{R2} = V_1$ in the sigma generator and $R_1=R_4$ and $C_1 = C_4$, we get

$$V_N = \frac{V_1 V_2}{V_{R1}}$$

The sawtooth wave V_Z generated at the output of OA_6 is given to a peak detector to get the peak value V_N.

$$V_O = V_N.$$

$$V_O = \frac{V_1 V_2}{V_{R1}} \qquad (12)$$

7. Experimental Results and Conclusion

The proposed circuits were tested in our laboratory. OP 07 IC was used for all opamps. CD 4053 IC is used for all switches. CD 4528 IC was used for monostable multivibrator. Conventional circuits for peak detector and sample & Hold circuits using opamps were used. The test results are shown in Tables 1-4.

Input V_1=1.2V

V_2 (mV)	Experimental V_O (mV)	Calculated V_O (mV)	Error %
1028	0242	0246	-1.6
2028	0480	0486	-1.2
3033	0720	0727	-0.9
4033	0960	0967	-0.7
5066	1208	1215	-0.5

Table 1 Test results for sigma delta type multiplier

Input V_1=3.59V

$-V_2$ (mV)	Experimental V_O (mV)	Calculated V_O (mV)	Error %
504	304	301	0.996
700	420	418	0.478

2000	1183	1196	-1.086
3000	1770	1795	-0.947
5000	2980	2991	-0.367

Table 2 Test results for sigma integrated type multiplier

The offset in all opamps will cause an error in the result and hence it should be nulled. In all the multipliers the input voltage V_1 must be positive polarity only. However

Input V_1=2.9V

$-V_2$ (mV)	Experimental V_O (mV)	Calculated V_O (mV)	Error %
1000	0600	0588	0.3
2000	1190	1160	0.8
3000	1780	1740	1.1
4000	2360	2320	1.1
5000	2930	2900	0.8

Table 3 Test results for sigma sampled type multiplier

Input V_1=2.5V

$-V_2$ (mV)	Experimental V_O (mV)	Calculated V_O (mV)	Error %
1000	0510	0500	0.33
2000	1008	1000	0.26
3000	1506	1500	0.20
4000	2000	2000	0.00
5000	2510	2500	0.33

Table 4 Test results for sigma single slope multiplier

Another input voltage V_2 may be either positive or negative voltage. Hence the proposed all multipliers are of two quadrant type. ± Vcc is the power supply voltage to circuit and maximum voltage of both the inputs and reference voltages should be ±Vcc only.

8. Acknowledgement

The author is highly indebted to Prof. Dr. Enakshi Bhattacharya, Prof. Dr. V.Jagadeesh Kumar and Dr. Bharath Bhikkaji, Department of Electrical Engineering, Indian Institute of Technology, Madras, for their constant encouragement throughout the work. He also thanks (1) Mrs. Latha Selvam for circuit drawing and (2) Mr. I. M. Mithun for manuscript formatting.

9. References

[1] S. Kataoka, " Multiplying action of the magnetoresistance effect on semiconductors and its application to power measurements" Proc IEEE (London),Vol.III, pp 1937-1947, 1964.
[2] B. Gilbert, " A precise four quadrant multiplier with sub nanosecond response" IEEE J Solid State Circuits, pp 365-373, December 1968.
[3] J.K Stockton, " Proposed quarter-squares double dual slope digital wattmeter" Electronic Letters, Vol.16, pp 819-820, October 1980.
[4] M.Tomata, T.Sugiyama & K. Yamaguchi, " An electronic multiplier for accurate power measurements" IEEE Transactions on Measurement and Instrumentation, Vol.IM-17, no.4, December 1968.
[5] C.Selvam, " A simple and low cost pulse time multiplier" IETE Students Journal, pp 207-211, July-December 1993.
[6] T.S Rathore and B.B Bhattacharyya, "A new type of analog multiplier" IEEE Transactions on Industrial Electronics, Vol.IE-31, No.3, August 1984.
[7] Greg J.Johnson, " Analysis of the Modified Tomata-Sugiyamma-Yamaguchi Multiplier" IEEE Transactions on Instrumentation and Measurement,Vol.IM-33, No.1, March 1984.
[8] Sergio Franco, "Design with operational amplifiers and analog Circuits" Third Edition, Tata McGraw-Hill publishing company pp:476-478.

E190

Degradation of Methylene Blue in Cathode of Microbial Fuel Cell with Gold Nanoparticles Catalyst

Han Thi Hiep
20956089@ynu.ac.kr
m16nhim@yahoo.com

The corresponding author: Moo Hwan Cho

Abstract

Methylene blue (MB) is one of phenol-thiazine dyes which are used as probes to determine the catalytic activity of AuNPs [1, 2]. In this work, for the first time we present the degradation of MB in cathode of microbial fuel cell (MFC) with gold nanoparticles (AuNPs) catalyst. The mechanism of MB degradation has been studied under anaerobic (N2 bubbling) and microaerobic (no N2 bubbling) conditions. To investigate the catalytic activity of AuNPs on MB degradation, two MFC systems with AuNPs and without AuNPs (control MFC) were operated simultaneously. The MFCs consisted of two identical chambers (anode and cathode) separated by Nafion membrane. Each chamber had the effective volume of 250 mL. In anode chamber, an electrochemical active biofilm (EAB) was developed on plain carbon paper in artificial wastewater (sodium acetate and trace mineral salts). In cathode chamber was filled with pH 3 phosphate buffer solution and MB at the concentration of 0.05mM (16mg/L). AuNPs was synthesized in our lab using stainless steel method. 50 mL of AuNPs aqueous solution was sonicated for 5 min before adding to cathode chamber. The degradation of MB was evaluated from the decrease in absorbance of MB using a UV spectrophotometer (Optizen 2120 UV). Voltage was recorded every 2 min by using a digital multi-meter(Agilent).

The results show that under anaerobic condition, MB was not mineralized, just formed leuco-methylene blue (LMB). And this LMB was immediately oxidized to MB when it was exposed to air. As shown in Fig.1, MB peak was disappeared while an absorption peak at 256 nm appeared, which is confirmed the formation of LMB. It means that all the MB was reduced to LMB after 5 h. In MFC, electrons and protons are transferred from anode to cathode, where MB serves as an electron acceptor to produce semi-reduced MB, MB*. This MB* disproportionates to form MB and the doubly reduced form of MB, i.e. LMB or it reacts with e- and H+ to yield LMB in reaction [3]. It is clearly shown in Fig.1b that after certain time, the transformation from MB to LMB significantly faster in the presence of AuNPs. Here AuNPs behave as electron relay, which were facilitated for the reduction from MB to LMB. The results supported the previous study [3].

Same experiment was performed under microaerobic condition (no N2 bubbling). The results show that both of MB and LMB peaks were reduced with time (Fig. 2a, b). There was blue-shifted peak which indicated the formation of demethylated dyes [4]. As clearly shown in Fig. 3, the reaction rate with the presence of AuNPs catalyst was two times faster than that without the presence of AuNPs catalyst. As previously reported [3], electrons accumulate in the AuNPs to yield Au(e-), where oxygen receives electron to be superoxide radical, O2.-. O2.- is highly active oxidizing species to degrade MB. This mechanism explained the reason why MB degradation was enhanced with AuNPs catalyst.

In conclusion, we found that the complete degradation of MB in cathode of MFC occurs only under microaerobic condition and AuNPs. In this case, AuNPs improve the MB degradation reaction rate to be twice of control.

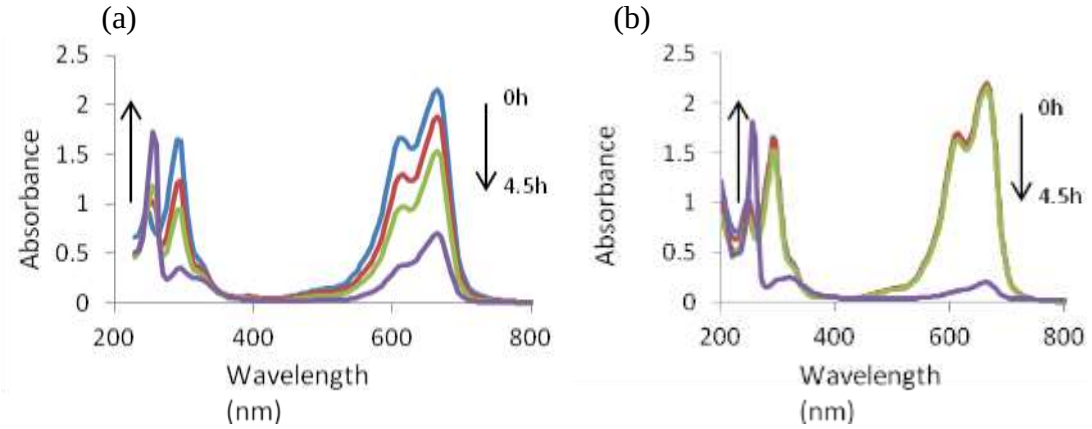

Fig. 1 Absorption spectral change of MB aqueous solution in cathode of MFC without AuNPs (a) and with AuNPs (b) under anaerobic condition.

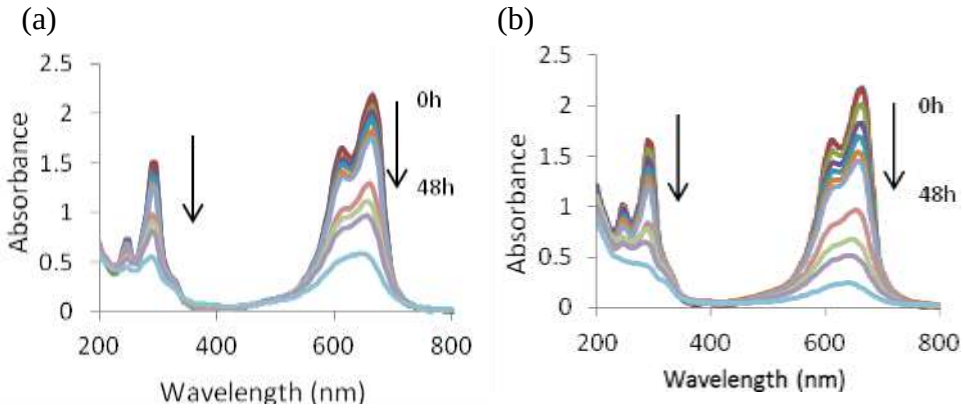

Fig. 2 Absorption spectral changes of MB aqueous solution in cathode of MFC without AuNPs (a) and with AuNPs (b) under microaerobic condition.

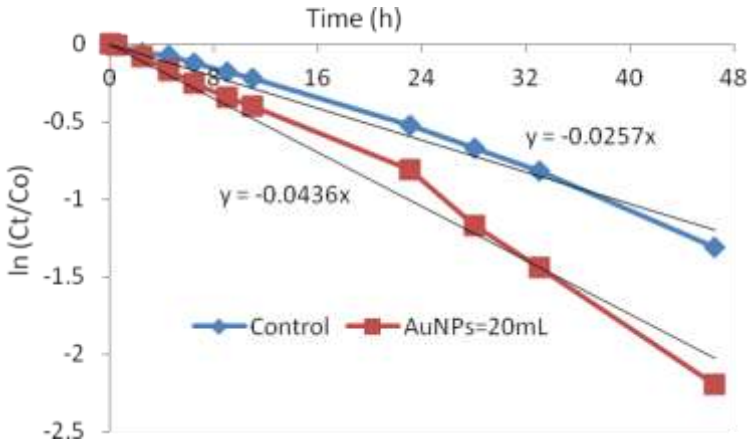

Fig. 3. Degradation rate of MB in cathode of MFC with AuNPs catalyst and without AuNPs (control) under microaerobic condition.

Keyword: Methylene blue, Gold nanoparticles, Microbial fuel cell, Demethylation, Catalyst.

Acknowledgments
This research was support by 2012 Yeungnam University Grant.

References

[1] U. P. Azad, V. Ganesan, M. Pal, Catalytic reduction of organic dyes at gold nanoparticles impregnated silica materials: influence of functional groups and surfactants, *Journal of Nanopartilce Research, 2011, Vol. 13*, pp. 3951-3959.
[2] N.Gupta, H. P. Singh, R. K. Sharma, Single-pot synthesis: plant mediated gold nanoparticles catalyzed reduction of methylene blue in presence of stannous chloride, *Colloids and Surfaces A: Physicochemical and Engineering Aspects 2010, Vol. 367,* pp. 102–107.
[3] C. Yogi, K. Kojima, T. Takai, N. Wada, Photocatalytic degradation of methylene blue by Au-deposited TiO2 film under UV irradiation, *Journal of Material Science, 2009, Vol. 44*, pp. 821-827.
[4] T. Zhang, T. Oyama, A. Aoshima, H. Hidaka, J. Zhao, N. Serpone, Photooxidative N_demethylation of methylene blue in aqueous TiO2 dispersions under UV irradiation, *Journal of Photochemistry and Photobiology A: Chemistry, 2001, Vol. 140,* pp. 163-172.

E194

Overview on the Factors Affecting Pavement Interlayers Bond Strength

Chang Fung Lung
Department of Geotechnics and Transportation, Faculty of Civil Engineering, Universiti Teknologi Malaysia, 81310 Skudai, Johor, Malaysia.
flchang2@live.utm.my

Haryati Yaacob
Department of Geotechnics and Transportation, Faculty of Civil Engineering, Universiti Teknologi Malaysia, 81310 Skudai, Johor, Malaysia.
haryatiyaacob@utm.my

Mohd. Rosli Hainin
Department of Geotechnics and Transportation, Faculty of Civil Engineering, Universiti Teknologi Malaysia, 81310 Skudai, Johor, Malaysia.
roslihainin@utm.my

Ahmad Safuan A. Rashid
Department of Geotechnics and Transportation, Faculty of Civil Engineering, Universiti Teknologi Malaysia, 81310 Skudai, Johor, Malaysia.
ahmadsafuan@utm.my

The corresponding author: Chang Fung Lung

Abstract
Performance of bond developed between the asphaltic concrete pavement layers is an important aspect in flexible pavement construction. Good bonding between the flexible pavements layering mechanism will ensure the pavement to behave like a monolithic structure in distributing traffic loadings to the base material. A common practice to provide adhesion between pavement layers is to apply a layer of tack coat during construction. Pavement distress related to poor bonding is no longer a new issue worldwide. Delamination and slippage failures are the two most common distresses related to insufficient level of adhesion. Generally, bond developed in a pavement is related to several factors. This paper aims to provide an overview on some pre-determined factors as specified in respective specification. These factors in particular interest include tack coat types, tack coat application rates, surface types and temperature. Each of the factors can significantly affect the interface bond strength in a pavement. While the pavement thickness might be a potential factor that affects the interface bond strength, the research carried out to investigate further on the relationship of the thickness and interlayer bonding is very limited. In order to optimize the bond developed between the pavements interlayers, each factor needs to be carefully monitored, both in design stage and construction stage.

Keyword: Interlayer bond strength, tack coat, adhesion, delamination

1. Introduction

Several real cases on pavement distress reported due to insufficient bond strength had end up in an extensive research on pavement interface bond strength over the past 20 years [1-2]. These distresses include delamination and slippage as shown in Figure 1. Uzan et al. [3] are among the first researcher to get involved in as early as 1978 which then later attracts the interest of different researcher worldwide. Subsequently, a variety of testing devices [4] with different features have been developed, alongside with the testing procedures as well as conceptual understanding and data analysing and interpretation. At the same time, possible factors in affecting the pavement bond strength were also identified, with detail research conducted to optimize the bond strength between pavement interlayers. In order to increase the pavement bond strength, tack coat is often applied to ensure the structural integrity of the pavement. Typically, pavement bond strength depends greatly on the pre-determined factors like types of tack coats, the application rates and the designed mix as outlined in the guideline from respective agencies. Nevertheless, the bond strength between pavement layers also closely related to temperature, which is often included as pre-determined testing parameters for the modern pavement interface bond strength testing device. This paper aims to provide an overview on these pre-determined factors on affecting the bond strength between pavement layers from the previous researches.

Figure 1: Distresses associated to insufficient bonding encountered on a pavement.

2. Factors Affecting Pavement Bond Strength

2.1 Tack Coat Types

Existing literature reveals that there are different types of tack coat materials being used to provide adhesion between layers of asphaltic concrete pavement. These materials include asphalt emulsion, penetration grade asphalt and cutback asphalt. Out of the three, asphalt emulsion is favoured as it is capable to be applied at lower temperature and more environmental friendly. This corresponds well to series of survey conducted on the types of tack coat applied in construction [5-6]. There are two categories of asphalt emulsion – cationic emulsion and anionic emulsion. Both are accepted to be served as tack coat depending on the types of aggregates used to produce the premix.

Selection of particular types of tack coat to be applied in construction often subjected to the local practices and specifications. A series of comprehensive studies to evaluate the effect of tack coat types and the pavement bond strength marked an inconsistency in the results. Mohammad et al. [7] in 2005 investigate the influence of two types of performance grade asphalt, PG 64-22 and PG 76-22M, and 6 emulsions, CRS-2P, CRS-2L, SS-1, CSS-1, SS-1h, and SS-1L in providing the bonding strength between pavement layers using laboratory fabricated specimens with different application rates. The simple shear test was conducted at two temperatures using

Superpave Shear Tester. The test results indicate that applying certain types of tack coat tends to improve the bonding between the specimens, but emulsion CRS-2P and CRS-2L manage to provide significantly higher interface bond strength. West et al. [8] did similar testing using two asphalt emulsion CRS-2, CSS-1 and a performance grade asphalt PG64-22 on several field projects. Interface testing is later conducted using the NCAT bond strength device, which resulted in PG64-22 manage to provide higher bond strength compare to the asphalt emulsion tack coat. Discrepancy in the testing result by both researchers might be associated with the viscosity of the tack material, where CRS-2P is much more viscous compare to PG64-22 as mentioned by al-Qadi et al. [9]. Besides viscosity, dilution of emulsion is also attributing to the bonding capabilities of pavement layers [10]. Further information pertaining to emulsion dilution has been published elsewhere [11]. Despite this, there is no information on the dilution of emulsion provided in both researches. Only residue of CRS-2P (65%) and CRS-2L (69%) is known, while an assumption of 60% residue is made for both emulsion applied on site by West et al. [8]. This will certainly be another possible explanation that the interface bond strength tested using CRS-2P and CRS-2L is much greater than CRS-2 and CSS-1. After all, different types of tack coat materials will end up providing different degree of adhesion, depending on the test setup. Different types of best tack coat may be identified from different experimental work, but these tack coats will hardly remain the best when in used with other testing configuration.

2.2 Tack Coat Application Rates

Tack coat application rate varies accordingly to the specifications set by respective authorities. In fact, it is always in the interest of the researchers to get to know the exact rate of tack coat to be applied in the construction based on different construction site conditions, which is extremely difficult to predict in nature. Neither too much nor too little tack coat applied can have catastrophic effect to the adhesion between pavement interlayers. Excessive tack coat caused slippage while insufficient tack coat might end up with poor adhesion. In fact, many researchers agreed that there exist an optimum application rate of tack coat, but the optimum rate can be a function of tack coat type, application rate, surface condition and also temperature [3, 8, 12]. A major concern when dealing with tack coat application rate is the confusion in the application rate itself, whether the rate as specified includes the water added or the residual asphalt contents. Both rates are presentable, but in order to avoid ambiguity, a clear notification should be provided.

A series of publication from different agencies revealed different range of tack coat rate to be applied. In United States, survey on tack coat application practice is conducted by Cross et al. [5] and Paul et al. [6]. A residual application rate of 0.15 to 0.70l/m^2 is reported by Cross et al. [5] while Paul et al. [6] claimed that the application rate of tack coat varies from as low as 0.06l/m^2 up to a maximum of 0.26l/m^2. The difference may be explained by several reasons. First, the respondents in both surveys have minor difference. Next, the application rates by Paul et al. are the outcome from distributed questionnaire to the engineers while application rates by Cross et al. refer to the specification from respective respondents. It is also interesting to note that tack coat application rate is not one of the survey questions by Cross et al. [5]. Finally, the time for the conducted survey has an interval of 7 years, which in return that there might be possible updates relating to tack coat practice within that period of time. In Malaysia, it is specified that the application rate of tack coat ranges in between 0.25l/m^2 to 0.55l/m^2 for dense and gap graded mixture, while open graded mixture like porous asphalt requires 0.50l/m^2 to 1.0l/m^2 [13].

However, all the above mentioned application rate does not take into consideration the condition of the pavement to be paved. Hansen [14] suggested two residual asphalt application rates based on the pavement conditions. The ranges of application as specified are 0.09l/m^2 to 0.23l/m^2 for a new pavement surface while for milled surface, the range varied from 0.23l/m^2 to 0.36l/m^2. Lavin [15] in his publication claimed that tack coats are usually applied at a rate of 0.2l/m^2 to 1.0l/m^2 of pavement surface area. At the same time, he recommended that for milled pavement, tack coat application rate of as high as 1.0l/m^2 can be adopted to cater the grooves left over by the milling machine. As for newly constructed overlay, he suggested that tack coat is not needed to provide the bonding between the asphaltic concrete layers. Even if it is insisted to apply tack coat, the application rate should be relatively light, which is usually less than 0.30l/m^2. While most publications discussed the importance of applying tack coat in construction, construction without tack coat (zero application rates) but end up with sufficient bond is also reported [16]. Although the guideline on the application rate of tack coat is readily available, in most cases, still tack coat are applied empirically based on the practical experience of contractors and consultants [17].

2.3 Surface Types

Surface types in this context refer to the designed mix or the surface texture used in the construction of asphalt overlay. These include dense graded, open graded, gap graded and concrete pavement adopted in construction. Previous construction favoured dense graded mix as wearing course, but the introduction of open graded mix like porous asphalt, gap graded mix like stone mastic asphalt and concrete pavement have gain popularities in the modern road construction. The later types of mix can provide extra features which are not possessed in dense graded mix. Surface types contribute to interface bonding through the mixture characteristics, which indicates that the shear resistance is governed by the frictional force between types of mix used to construct the wearing course and binder course.

Chen and Huang [18] conducted an experimental work on the effect of different types of mix on the interlayer bonding. An illustration of combination of mix types like Dense Graded Asphaltic Concrete (DGAC), Porous Asphalt Concrete (PAC) and Stone Mastic Asphalt (SMA) to produce dual layer sample is as shown in Figure 2. They formed a mix combination of DGAC-DGAC, PAC-DGAC and PAC-SMA.

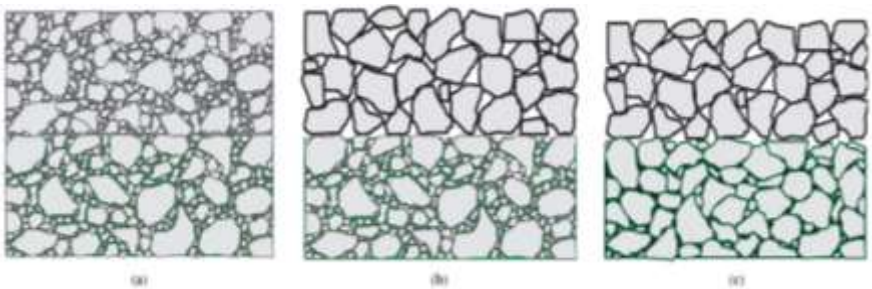

Figure 2: Combination of different mix types, (a) DGAC-DGAC, (b) PAC-DGAC and (c) PAC-SMA. [18]

Test results showed the highest interface shear strength in DGAC-DGAC combination, followed by PAC-DGAC and PAC-SMA. The concept of contact surface area best explained the phenomenon. Combination of DGAC-DGAC experienced full interface in contact fully utilised

the applied tack coat for maximum bonding. Reduction in surface area in contact in PAC-DGAC and PAC-SMA hence resulted in lower bonding. But, the combination of PAC-DGAC and PAC-SMA will have advantage of greater friction when normal stress is provided by Ancona Shear Testing Research and Analysis (ASTRA) device [19] used in this experimental work. This eventually produced an interlocking mechanism between the porosity nature of PAC and SMA, resulting in comparable shear strength as DGAC-DGAC combination with lesser surface area in contact. This is the consequences of residual shear stress after the shearing resistance provided by tack coat has been fully overcome. Similar observation was reported by other researchers using different shear testing device, with or without normal stress being applied [8, 20-21].

2.4 Temperature

Temperature in this context refers to the testing temperature for which the specimens are tested for the shearing strength. It is normally provided by the testing devices equipped with temperature control. The temperature simulates the real pavement performance when exposed to the climatic condition. When tack coat is subjected to higher temperature, the stiffness will be significantly reduced, thus results in variation of shearing resistance under hot weather, yet subjected to the traffic loadings. The effect of temperature on the bonding performance of pavement normally comes together in the presence of normal stress, which in real cases, stresses from vehicles travelling on the road. Many studies [8, 18, 22-24] have been carried out pertaining to the temperature and the interface shear strength. Most of the testing is carried out in a temperature ranged from 20°C to the maximum of 60°C. Limited research was carried out for testing temperature of 0°C and lower. This might be that tack coat is more critical at higher temperature, where failures are most likely to occur. A wide range of testing temperature should be adopted since the exact temperature conditions at which a shear failure may occur in a pavement is always unknown.

As far as temperature factor is concerned, a common trend as agreed shows that shear strength is inversely proportional to temperature. As asphalt is highly temperature dependent, it will gradually lose it cohesive properties when there is an increase in the surrounding temperature. The asphalt becomes less viscous, less stiff, and fails to perform the binding properties. An illustration of the asphalt molecules maybe depicts by Figure 3. At lower temperature, the asphalt molecules are less reactive. Coalescent of these molecules is the key of the cohesive nature of the asphalt. However at higher temperature, the asphalt after storing sufficient energy will then overcome the Van der Waals attraction between the molecules. The uni-directional movements of these molecules is the main reason for the asphalt to loss the binding properties. This as well explained the statement for which higher testing temperature results in lower shearing strength.

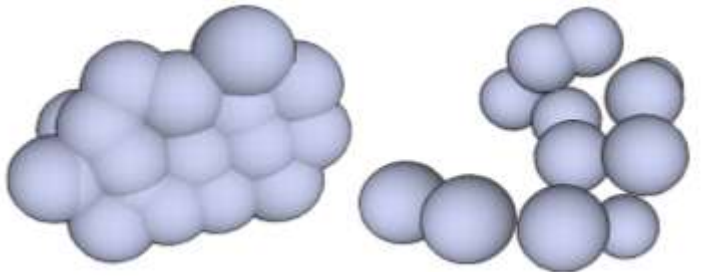

Molecules at lower temperature **Molecules at higher temperature**

Figure 3: Illustration of asphalt molecules at lower temperature and higher temperature.

When there is traffic loadings exerted, especially from heavy trucks and buses, the pavement condition at this stage will be critical. Sudden braking, acceleration and deceleration as well as turning at sharp corners will induce big impact of shear stresses which can seriously affect the pavement performance. As tack coat has gradually lost the cohesive properties with increasing temperature, the shearing resistance between layers will only be governed by the friction from the aggregate interlocking between the layering mechanisms.

3. Conclusion

This paper outlined some of the common factors affecting the bond strength between pavement interlayers. All of the factors are equally important and should be well taken care of in order to ensure the proper bonding in a pavement. From the literature, numerous interface shear tester have been developed through extensive research. Direct shear test however have been widely adopted to perform interface shear strength test though tensile test and torsion test can be occasionally encountered in certain device. While most research focused on the above mentioned factors, limited research however focused on the effect of thickness of the wearing course in pavement interface bond strength. Theoretically, sufficient lift thickness is certainly beneficial to resist shear stresses exert by the traffic. Within a thicker lift of pavement, the shear stress will be distributed in a wider perspective, minimizing the effect of direct shearing on the pavement interface, which is most likely to take place in a thinner pavement lift. As lift thickness might be associated with compaction difficulties and inadequacy, further research and experimental approach need to be carried out to investigate the effect of the pavement lift thickness and the interface bond strength.

4. Acknowledgement

The authors would like to extend their gratitude to Malaysia Ministry of Higher Education (MOHE) and the Universiti Teknologi Malaysia Research grants (GUP Tier 2 Vote 06J52) for the financial support in this research project.

References

[1] Chen, D.H., Slippage failure of a New Hot-Mix Asphalt Overlay. *Journal of Performance of Constructed Facilities, 24(3), 2010,* p. 258-264.

[2] Pavement Interactive, De-Bonding of HMA Pavements/Case Studies. 2008; Available from: http://www.pavementinteractive.org/article/de-bonding-of-hma-pavementscase-studies/.

[3] Uzan, J., M. Livneh, and Y. Eshed., Investigation of Adhesion Properties Between Asphalt Concrete Layers, *Proceedings of the Association of Asphalt Paving Technologists, 47, 1978,* p. 495-521

[4] Raab, C., M.N. Partl, and A.E.H.O.A.E. Halim, Evaluation of Interlayer Shear Bond Devices For Asphalt Pavements. *The Baltic Journal of Road and Bridge Engineering, 4(4), 2009,* p. 186-195.

[5] Cross, S.A. and P.P. Shrestha, Guidelines for Using Prime and Tack Coats, 2005.

[6] Paul, H, and J. Scherocman, Friction Testing of Tack Coat Surfaces. *Transportation Research Record: Journal of the Transportation Research Board, 1616, 1998,* p. 6-12.

[7] Mohammad, L.N., Z. Wu, and M.A. Raqib, Investigation of the Behavior of Asphalt Tack Interface Layer, 2005.

[8] West, R.C., J. Zhang, and J. Moore, Evaluation of bond strength between pavement layers, 2005, NCAT.

[9] Al-Qadi, et al., Tack coat optimization for HMA overlays: Laboratory testing, 2008.

[10] Tandon, V. and I. Deysarkar, Field Evaluation of Tack Coat Quality Measurement Equipments, *International Journal of Pavements, 4(1-2), 2005,* p. 25-37

[11] Caltrans, Tack Coat Guidelines, 2009, State of California, Department of Transportation, Division of Construction.

[12] Mohammad, L.N., et al., Measurement of Interlayer Bond Strength Through Direct Shear Test, in *3rd International Conference Bituminous Mixtures and Pavements, 2002*

[13] JKR, Section 4: Flexible Pavement, in Standard Specification for Road Works2008, Jabatan Kerja Raya.

[14] Hansen, K., Avoid Slippage By Using Good Tack Coat Practices, *Idaho Technology Assistance Newsletter, 2008.*

[15] Lavin, P.G., Asphalt Pavements, 2003: *Spon Press, Taylor and Francis Group,* p. 223

[16] Cooley, L.A., No tack Inlay on Milled Surface, Project Report, 1999.

[17] Raab, C. and M. Partl, Laboratory Study on Interlayer Bonding Using Cationic Tack Coats, *7th International RILEM Symposium on Advanced Testing and Characterisation of Bituminous Materials, 2009,* p. 3-12.

[18] Chen, J.S. and C.C. Huang, Effect of Surface Characteristics on Bonding Properties of Bituminous Tack Coat. *Transportation Research Record: Journal of the Transportation Research Board, 2180, 2010,* p. 142-149

[19] Santagata, E., F. Canestrari, and F.A. Santagata, Laboratory Shear Testing of Tack Coat Emulsion, *Proceedings of 1st World Congress on Emulsion, 1993.*

[20] Sholar, G.A., et al., Preliminary Investigation of a Test Method to Evaluate Bond Strength of Bituminous Tack Coats. *Journal of the Association of Asphalt Paving Technologists,73, 2003,* p. 23-52

[21] Kruntcheva, M., A. Collop, and N. Thom, Properties of Asphalt Concrete Layer Interfaces. *Journal of Materials in Civil Engineering, 18(3), 2006,* p. 467-471.

[22] Canestrari, F. and E. Santagata, Temperature effects on the shear behaviour of tack coat emulsions used in flexible pavements. *International Journal of Pavement Engineering, 6(1), 2005,* p. 39-46.

[23] Kim, H., et al., Numerical and Experimental Analysis for the Interlayer Behavior of Double-Layered Asphalt Pavement Specimens. *Journal of Materials in Civil Engineering, 23(1), 2011,* p. 12-20.

[24] Raab, C. and M.N. Partl, Temperature dependency of interlayer shear testing, *Transport Research Arena Europe, 2010*.

E198

A Study on Development of Fatigue Tester Simulating Operating Condition for the Dropper of Overhead Catenary System

Yongseok Kim
Graduate School of Mechanical Engineering, Sungkyunkwan University, Suwon, Kyenggi-do, 440-746, Korea
dmsnake@skku.edu

Li Haochuang
Graduate School of Mechanical Engineering, Sungkyunkwan University, Suwon, Kyenggi-do, 440-746, Korea
lihaochuang@126.com

Jea-Mean Koo
Department of Mechanical Engineering, Sungkyunkwan University, Suwon, Kyenggi-do, 440-746, Korea
kjm9000@hanmail.net

Chang-Sung Seok
Department of Mechanical Engineering, Sungkyunkwan University, Suwon, Kyenggi-do, 440-746, Korea
seok@skku.edu

Heungchai Chung
Korea Railroad Research Institute, Uiwang, Kyenggi-do, 437-757, Korea
hchung@krri.re.kr

Kiwon Lee
Korea Railroad Research Institute, Uiwang, Kyenggi-do, 437-757, Korea
kenlee@krri.re.kr

Sam-Young Kwon
Korea Railroad Research Institute, Uiwang, Kyenggi-do, 437-757, Korea
sykwon@krri.re.kr

The corresponding author: Chang-Sung Seok

Abstract
The Dropper enables the overhead contact wire to supply the electricity stably by supporting the overhead contact wire and maintaining it in a horizontal position. The Dropper consists of wire rope and clampers connecting the wire rope with messenger wire and contact wire. During the operation, the droppers are exposed to repeated mechanical bending and tensile stresses caused by the passage of pantographs of trains running in high speed. From the previous researches investigating the failures of droppers in real operation, various failure cases have been reported

including clampers and wire ropes. Therefore, it is highly necessary to develop test device and method of dropper which can simulate real operate condition (repeated bending and tensile).

Thus, in this study, real operating conditions of droppers were analyzed by investigating previous researches and the test device of dropper was developed. Also, fatigue characteristics of droppers were evaluated using the developed test device. Fatigue tests on the droppers (applied to the trains operating up to 150km/h) were conducted at high stress condition for accelerated test.

Keyword: dropper, fatigue test, wire rope, test device of dropper

1. Introduction

The technology for high speed railway has been competitively developed recently, and the maximum speed of train has been continuously updated by leading countries. Infra system for high speed railway, as well as high speed train itself, is an important issue to develop an high speed railway system.[1] Especially, the durability of dropper which supports an overhead contact wire has become an important issue since disruptions to services caused by failure on dropper has been recently reported. [2]

Fig. 1 shows the simple catenary system and dropper. Dropper is normally exposed to static tensile stress caused by the weight of contact wire. However, when a train passes, it is exposed to dynamic stress since the dropper become slack due to the uplift of contact wire and become tight again due to the weight of the contact wire. This dynamic loading condition is difficult to be obtained by mathematical approach and subject to other factors such as the condition of contact wire, the speed of the train, and the interval between droppers. Therefore, a lot of researches on the loading hysteresis of dropper have been conducted to investigate the failure mechanism of the dropper.

In this study, the loading conditions and fracture cases were discussed by investigating the previous reports synthetically. Also, a fatigue test method on dropper was introduced and fatigue tester was developed based on British Standard, BS EN 50119:2009[3]. Lastly, fatigue tests on the droppers(applied to the trains operating up to 150km/h) were conducted at high stress condition for accelerated test.

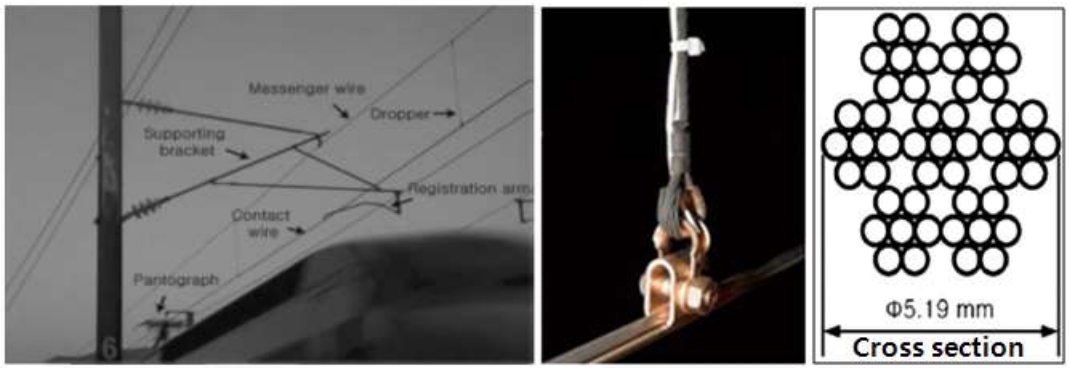

Fig. 1 Contact line with droppers at the supports[1]

2. Analysis on Loading Condition of Dropper During Operation

The researches on loading condition of dropper during operation have been reported. Previous researches are summarized in this section to understand the relation between the speed of the train and the stress in the dropper.

Lee, et al.[4] measured the stain of dropper that occurred during operation by attaching strain gage on the clamp and transformed it into load. According to the report, maximum dynamic load was 108N when the train speed was 91km/h. Also, Lee, et al.[2,5] measured the loading condition of dropper with the same method by a driving test at 300km/h. It is reported that the load varies up to 63N according to the location of the droppers. The maximum dynamic load was 240N which is more than double compared to the previous case (91km/h). Therefore, the speed of train is an important factor deciding the life of droppers. Lee, et al.[6] evaluated the loading hysteresis of the dropper at two different train speed(150km/h, 180km/h) using a loading prediction system for droppers.

Considering the reports mentioned, it can be known that the maximum load and vibration increases as the train speed increases.

3. Fatigue Tester for Dropper

3. 1 Development of Fatigue Tester for Dropper

All the papers[2,4,5,6] mentioned above report that the droppers are exposed to extremely complex fatigue loading condition. Therefore, simulating the exact loading hysteresis is not rational method to evaluate the life of the droppers. Also, BS EN 50119: 2009 suggests using an alternate load and compression cycle.

Therefore, in this study, the fatigue tester using an alternate load and compression cycle was developed. The fatigue tester is designed to simulate the condition of droppers(slack and tight). In addition, fatigue tests on the droppers with various loads were performed to obtain P-N curve.

The Details of the fatigue tester are as follows.

(1) Figs. 2 shows the mechanism of the tester. A geared motor, cranks, rod and levers are used to life up the droppers. The cranks transformed a rotary motion of the motor into reciprocating motion of the levers(<90o). To minimize the power consumption, the levers are located at symmetric position. The levers lift up the weight using the droppers up to 60mm.
(2) The droppers are exposed to fatigue load lifting up the weight repetitively. Each weight is attached on linear motion guide to minimize the horizontal vibration.
(3) The contact condition is simulated by using the clamps used in real operation. The clamps are connected to the real contact wire.
(4) Applied load on dropper is measured using the load cell installed at the top of each dropper.
(5) Uniform springs are installed between the droppers and the weights to minimize impact load on the droppers. Dynamic load caused by vibration and impact load is less than 10% of total load applied to the droppers. The test load can be changed from 98 to 989N using combinable three weights (98, 196, 392N).
(6) A proximity sensor is installed in front of the motor to count the test cycle.
(7) It is designed to test maximum 6 droppers at the same time.
(8) Fig. 3 shows the load hysteresis of the developed tester. It is observed that the tester has elaborate reproducibility. Also, temporary load drop is observed at the peak point due to the vibration occurring when the dropper is becoming tight, which also happens in real operation.

3. 2 Fatigue Test on Dropper

The fatigue tests on the droppers (used for 150km/h-train) were performed. To reduce the test time, accelerated test was performed with high loads. Fig. 4 shows the test result. Applied load-life relation of the dropper was obtained as equation (1). Maximum allowed load at required life can be calculated from equation (1).

$$P = 282 \cdot N^{-0.261} \quad (1)$$

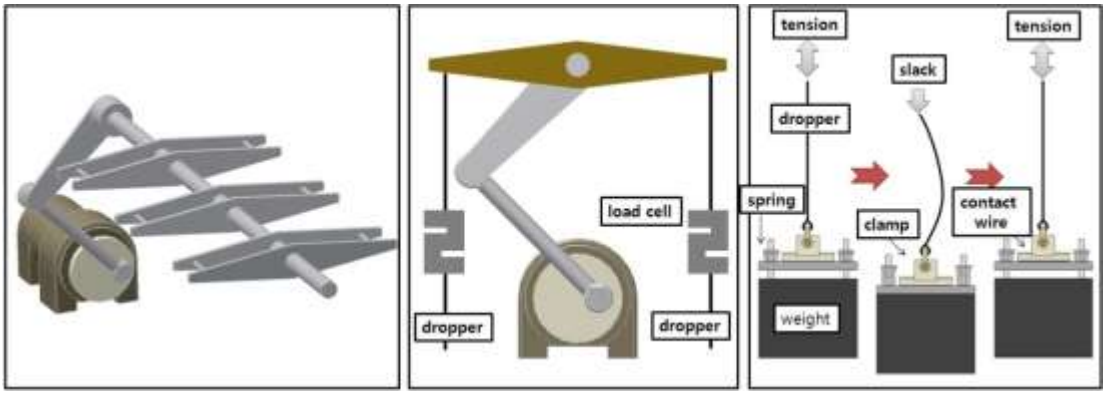

Fig. 2 Mechanism of the dropper fatigue tester

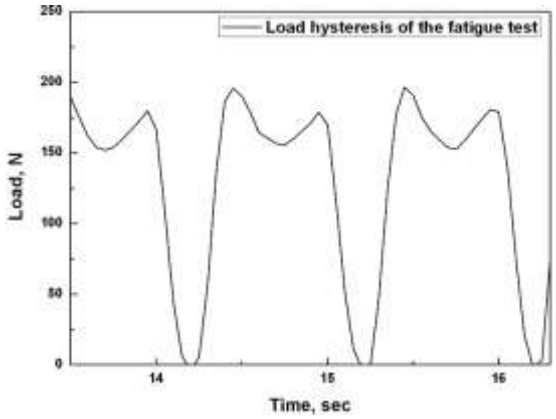

Fig. 3 Load hysteresis of the fatigue test

4. Conclusion

1. Previous researches on load conditions of droppers are summarized. The maximum load and vibration increases as the train speed increases. Therefore, the speed of train is an important factor deciding the life of droppers.
2. The fatigue tester using an alternate load and compression cycle was developed, which simulates the condition of droppers (slack and tight). The tester elaborates the same motion reproducibility, according to the load applied to dropper (Fig. 3). Also, temporary load drop is observed at the peak point due to the vibration occurring when the dropper is becoming tight, which also happens in real operation.
3. The fatigue tests on the droppers (used for 150km/h-train) were performed. To reduce the test time, accelerated test was performed with high loads. Applied load-life relation of the dropper was obtained.

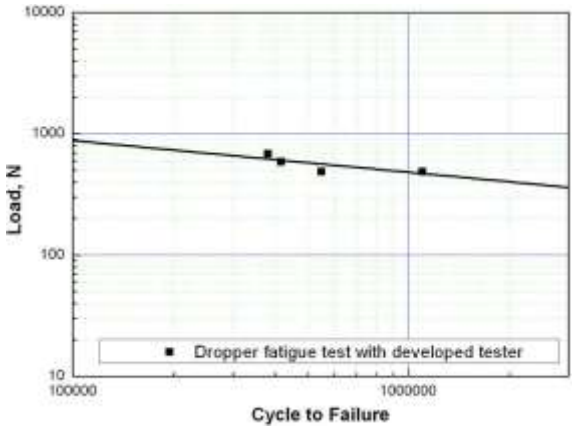

Fig. 4 The result of fatigue test with developed tester

5. Acknowledgment

This work is financially supported by Ministry of Land, Transport and Maritime Affairs(MLTM) through a research project "Development of Infra Technology for 400km/h High Speed Rail".

6. References

[1] Ki-Young Um, Development of Test-bed and infra technologies for 400 km/h high speed rail way, Railway Journal, the Korean Society for Railway, Vol. 15(4), pp. 55-60, 2012

[2] Gi-chun Lee, Tae-hoon Lee, Jong-woo Lee, Mechanical Loads of Dropper for High Speed Electric Railway, Railway Journal, the Korean Society for Railway, Vol. 14(3), pp. 222-227, 2011

[3] BS EN 50119:2009, pp. 76-77

[4] Kiwon Lee, Younghyeon Cho, Sanghoon Chang, Hyungchul Kim, Prediction of the force on the dropper according to the pre-sag, Proceedings of 2009 Autumn Conference of the Korean Society for Railway, the Korean Society for Railway, 972-977, 2009

[5] Tae-Hoon Lee, Yong-Joo Jeon, See-Bin Lee, Kyoung-Il Choi, Sang-Gil Han, Young-Sik Park, Ki-Bum Park, A Study on the Fracture Cause of Dropper Wire in Catenary System for Korea High Speed Railway, Proceedings of 2009 Summer Conference of the Korean Institute of Electrical Engineers, 14-17

[6] Kiwon Lee, Yonghyeon Cho, Young Park, Byungil Min, Samyoung Kwon, Chang-Sung Seok, Safety Assurance of Dropper Clamp in Overhead Catenary System(I), Proceedings of 2007 Spring Conference of the Korean Society for Railway, the Korean Society for Railway, 10-13, 2007

E207

The Application of Model-based and Integrated Process Improvement Methodology for Metal Sheet Coating Factory

Eakphan Thangthong
The Department of Industrial Engineering, Faculty of Engineering
Chulalongkorn University, Bangkok, Thailand
Eakphan@gmail.com

Jeerapat Ngaoprasertwong
The Department of Industrial Engineering, Faculty of Engineering
Chulalongkorn University, Bangkok, Thailand
Jeerapat.n@chula.ac.th

Abstract
The Model-based and Integrated Process Improvement Methodology (MIPI) is a business process improvement methodology which also concentrates on the improvement of process and aligns with organization vision and mission. This study focuses on the application aspect of MIPI to improvement of coating process. A case study is conducted in Metal Sheet Coating Process that identifies business needs and the problems by using Pareto chart. The main problems were the error setting coater machine and coater machine breakdown. These two problems were found out the root problems by why-why analysis. After that, the two problems were solved by using industrial engineering tools and techniques. This study will be useful and helpful to both practitioners and researchers.
Keyword: Business Process Improvement, MIPI Methodology, Coating Process

1. Introduction

The metal packaging business grows up continuously because the food industry has significantly expanded in every country. Moreover, recently the trend of using metal package has increased continually in food products. Furthermore, the metal coating industry is the upstream of metal packaging industry, so metal sheet coating companies have been forced to improve their businesses for increasing competitive ability. Many organizations chose Business Process Improvement (BPI) in improving processes. This is because Business Process Improvement is a revolutionary approach and the structural Business Process Improvement helps organizations to analyze and improve the operational process by focusing on wastes reduction and increasing efficiency and effectiveness. Model-based and Integrated Process Improvement (MIPI) is one of Business Process Improve Methodologies that created by Sola Adesola and Tim Baines in 2005. Their research is the doctorate research that describes a structural and procedural guidance for improving business processes.

The objective of this paper is to reduce production time loss in metal sheet coating process in metal sheet coating factory by using MIPI methodology.

2. Theoretical Background

Model-based and Integrated Process Improvement Methodology (MIPI) is a systematic approach

from the result of research by Sola Adesola and Tim Baines on Cranfield University in 2005. This methodology describes procedural step by step guide to assist organizations in business improvement project. The MIPI methodology consists of seven steps as guidance for process improvement [1]. Additionally, each step of MIPI methodology contains a hierarchical structure including aim, actions, people involved, outcome, checklists, hints and tips, and relevant techniques. Therefore, the result of using this approach is that organizations will understand their current process and also will provide a good plan to improve their business operation in the future.

In process improvement applications of Model-based and Integrated Process Improvement methodology (MIPI), this research focuses on identification and implementation of targeted solutions. In this paper the seven steps of MIPI methodology is applied as follow table 1

Table 1: MIPI Descriptions

Step	Description
1. Understand business needs	Identify the problem according to strategy and mission of organization
2. Understand the process	Identify the business process architecture and Define current process
3. Model analyze process	Identify and verify the root causes of problem
4. Redesign process	Find the solutions that will eliminate the root causes of problem
5. Implement new process	Plan the implementation for testing new solutions
6. Assess new process and methodology	Check the result of implementation and Revise the new approach
7. Review new process	Develop monitoring process and a plan to meet targets

3. Application of MIPI methodology on metal sheet coating process

3.1 Understand business needs

Currently, many process improvement programs are not useful because these programs do not align with organizational goals. Hence, it is very important that each organization should understand their business needs before they select process improvement programs to improve their businesses. Therefore, the authors studied the business needs of metal sheet coating factory firstly. The authors found that there are 3 operations including Inspection, Coating and logistic operation in the metal sheet coating factory. Furthermore, the vision of organization is that the factory will be the leader of metal coating and growing up continually by emphasizing the quality of products and service and also develop employees for business competition in the present and future. The missions of company are to improve production and machines to be the highest efficiency and also develop employees and the quality of products continually for increasing competitive ability in the world market. However, the metal sheet coating factory had the high backlog, so this organization wanted to improve its productivity. Therefore, the time loss of each operation was analyzed. It was found that according to fig. 1, the coating operation was the highest time loss. Consequently, the company selected the coating operation to improve

the productivity and efficiency by production time loss reduction for achieving its vision and missions.

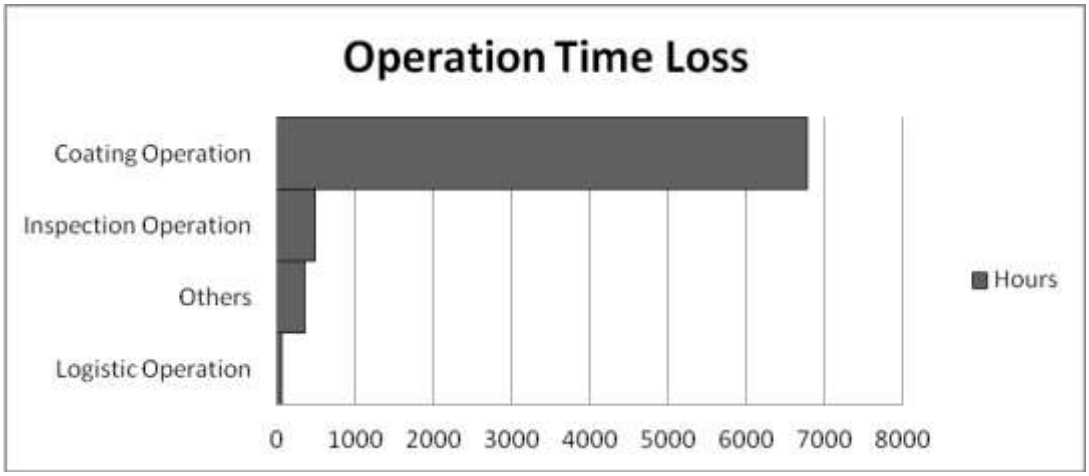

Fig. 1: The operation time loss in metal sheet coating factory

3.2 Understand the process

The second step helps the organizations to understand their current business process. Also this step is very useful to analyze and define the problems of business process. In Understand the process step, authors used the flow process chart to study the current coating process. It was observed that the coating process consists of five activities including preparing process (Feeder and Infeed system), coating process, over process, Inspection and storage.

3.3 Model analyze process

It is necessary to analyze the current internal downtime that is the production time loss in the coating process and also to identify the main problem of coating process. This paper used Pareto Chart to identify this problem. From fig. 2, the main problem of production time loss was the coater machine.

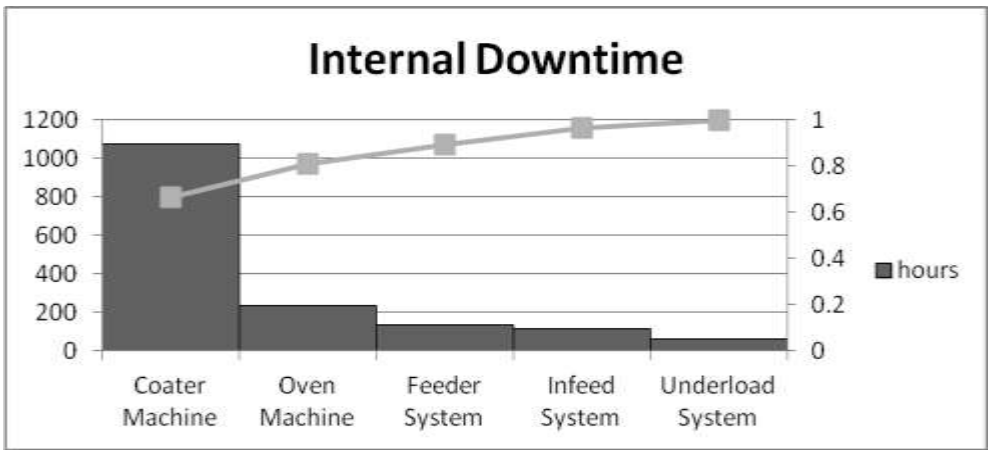

Fig. 2: Pareto Chart of problems in coating process

Furthermore, the coater machine problem was analyzed by brainstorm. The result is that the main

causes of coater machine problem were the error setting machine after Changing over new job and coater machine breakdown which caused failure gadget including rubber roll and Scraper Blade. After that, the two causes were studied to find out the root causes by why-why analysis because this method is a question asking technique to find and identify the true root cause of problem [2].

Why-1	Coater machine breakdown
Why-2	Failure gadgets
Why-3	Lack of checking
Why-4	No process control plan and Standard Work

Table 2: The root cause of machine breakdown

Why-1	Error setting coater machine
Why-2	Doing wrong setting method
Why-3	Employee set up coater machine by their own experience
Why-4	No Standard Work Instruction

Table 3: The root cause of error setting coater machine

According to table 2 and 3, the root causes of machine breakdown and error setting coater machine were no process control plan and standard work instruction. After that, this paper would find solutions to solve the two main problems in the next step.

3.4 Redesign process

In the redesign process step, the two main problems must be improved. The work in this step was divided into two parts which consist of coater machine breakdown and error setting machine problems.

Coater machine breakdown

Work Instruction is a suitable guidance for training any level of employees because the instructional material introduces the important concepts and steps of working that the employees

should think about as their working [3]. Additionally, Process Control Plan is an effective tool that helps organizations to decrease the variability of equipment such as the failure of equipment and make the corrective changes [4]. From the result of third stage, the root causes of coater machine breakdown were no Work Instruction and Process Control Plan. Therefore, the authors would use the theory of Preventive maintenance, that is corrective actions to maintain equipment and machines before they fails [5], to create Work Instruction and Process Control Plan for solving coater machine problem.

Error setting coater machine

The process of setting coater machine consisted of 13 activities and the setting time was 15 minutes. However, the employees could not set the coater machine at once. They used 2 or 3 round to set the coater machine. This resulted in the production time loss. Therefore, the authors used the theory of ECRS including Eliminate (E), Combine (C), Rearrange (R) and Simplify (S) to improve the setting process of coater machine because this approach is an effective technique for improvement into all process[6].

3.5 Implement new process

The step of Implement new process is an implement plan for testing new solutions. There are seven coater machines in the Metal Packaging Factory. The authors chose one machine to test new solutions for solving problems both coater machine breakdown and error setting machine.

3.6 Assess new process and methodology

In the assess new process and methodology step, the results of testing new solutions must be checked. The checking results were divided into two parts which consist of the implement results of coater machine breakdown and error setting machine.

The implement result of Coater machine breakdown

Work Instruction and Process Control Plan are appropriated tools for improvement process. The average production time loss of coater machine breakdown problem in machine one were 17 hours in 9 months ago. From fig. 3, the production time loss of coater machine breakdown problem has been decreased by 30% after applying these approaches.

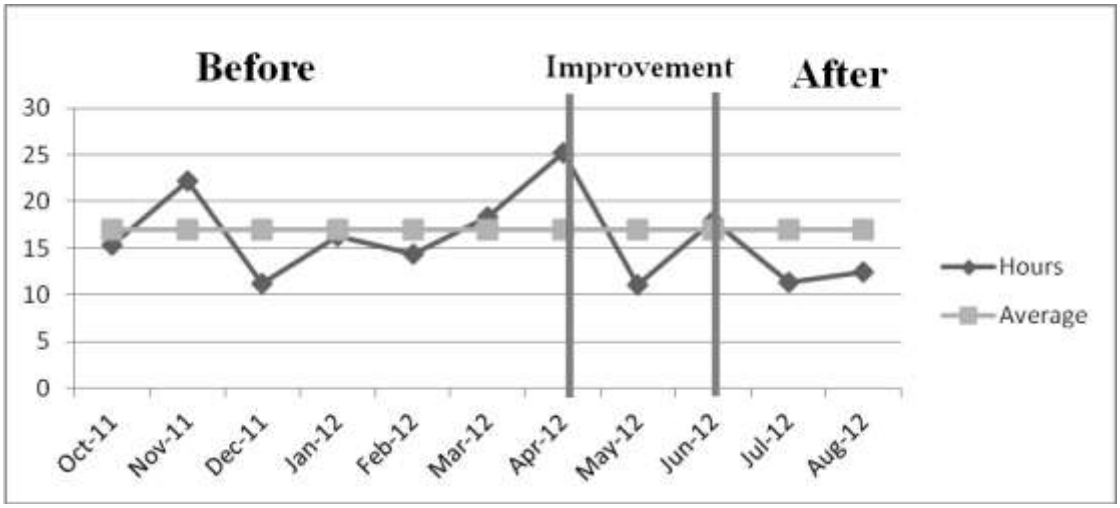

Fig. 3: The production time loss of coater machine breakdown problem in machine one

The implement result of Error setting coater machine

After applying ECRS technique, the activities of setting coater machine were rearranged and simplified. Consequently, the new activities of setting coater machine are 14 activities. Although the number of activities in setting coater machine has been increased, the employees can set the coater machine in once time setting and also they use time no more than 25 minutes for setting coater machine.

3.7Review new process

The step of review new process is to make a plan to meet targets and develop monitoring process. The work in this stage used Process Improvement Matrix (PIM) to develop the action plan. This is because this approach helps organization to create the roadmap of process improvement plans and current process status and also the Process Improvement Matrix approach identifies supporting processes and training that may be necessary to achieve the business process improvement [7]. Each action plan is clearly explained by three color coding. The first color is red (R) to the activity that need immediately attention. The second color is yellow (Y) to the activity which is operating and the third color is green (G) to the activity that is a recent success. The Process Improvement Matrix for coater machine problem as follows:

Process Improvement Matrix for Coater Machine problem **Action Plan**	**Factory Manager**	**Production Manager**	**Head Coater**	**Coater Engineer**	**Head Worker**
Coater machine breakdown* and *Error setting machine breakdown					
Analyze Problem		G	G	G	G
Improvement process			G	G	G
Test implement plan				G	G
Review a new plan	Y	Y	Y	Y	Y
Train employees			Y	Y	Y

Table 4: Process Improvement Matrix for Coater Machine problem

4. Result and Discussion

After the implementation of Model-based and Integrated Process Improvement Methodology (MIPI) in the metal sheet coating factory, the coating process has achieved obvious improvement. The results of improvement as follows:

- The production time loss of coater machine breakdown problem is below 15 hours per month.
- The employees can set coater machine at once and also the overall time of setting coater machine is no more 25 minutes.
- The results of coating process improvement help the coater company to improve the productivity of metal packaging production.

- The staffs feel very happy with the results of improvement and they will use the MIPI methodology to improve other business processes in the future.

The results of coating process improvement are significant evidence that the implementation of MIPI methodology creates the process improvement programs which are very efficient and effective to reduce the production time loss of coating process. The results of improvement were that the production time loss of coating process has been decreased and the effective setting coater machine of employees has been increased. Finally, the results of implementation confirm that the step-by-step of MIPI methodology can help organizations to improve their business processes efficiently and effectively.

5. Conclusion

The result of this research study is the presentation of the implementation of Model-based and Integrated Process Improvement Methodology (MIPI) to improve the coating process in the metal sheet coating factory. This approach emphasizes on the selection of problem for improvement. After applying MIPI methodology, it found that the metal sheet coating factory could achieve the target quickly because the MIPI methodology helps the factory to select correctly the problem which is the main barrier for achieving vision and missions, also aligns with the factory needs.

It is different with the original improvement process methodologies such as Lean, Six sigma and Engineering Management. These approaches do not consider the major problem that affects directly the business operation of organizations. Consequently, in certain situations, some process improvement programs are not useful with organizations after applying the original improvement process methodologies. Finally, the implementation of MIPI methodology is beneficial investment for operation improvement because this approach helps the organizations to create the process improvement programs which are very efficient and align with organizational vision and mission for business process improvement.

6. References

[1] S. Adesola, T. Baines, "Developing and evaluating a methodology for business process improvement," *Emerald Business Process Management*, vol. 11, No. 1, pp. 37-46, 2005

[2] U. Murugaiah, S. J. Benjamin, M. S. Marathamuthu and S. Muthaiyah, "Scrap loss reduction using the 5-whys analysis," *Emerald International Journal of Quality and Reliability Management* Vol. 27 No. 5, pp. 527-540, 2010

[3] H. Munby, M. Zanibbi, C. Poth, N. L. Hutchinson, P. Chin and A. Thornton, "Enhancing workplace learning for adolescents: the use of metacognitive instruction," *Emerald* Education and Training, Vol. 49 No. 1, pp. 8-24, 2007

[4] C. Hagemeyer, J. K. Gershenson and D. M. Johnson, "Classification and application of problem solving quality tools A manufacturing case," *EmeraldThe TQM Magazine* Vol. 18 No. 5, pp. 455-483, 2006

[5] S. I. Mostafa, "Implementation of proactive maintenance in the Egyptian Glass Company," *Emerald Journal of Quality in Maintenance Engineering*, Vol. 10 Iss: 2 pp. 107 - 122, 2004.

[6] J. Bai, H. Yao and L. Sun, "Standard Operation Research of Axle Box Key Production Line Process," IEEE International Conference on Information, Innovation Management and Industrial Engineering, 2011, Vol. 5, pp. 436-439.

[7] L. Janis, P. Kellye and A. Robert, *Process Improvement Matrix: A Tool For Measuring Progress Toward Better Quality*, Austin TZ, Vol. 10, No. 0, 1995

Engineering II

Pullman Bangkok King Power, 2F Meeting Room BETA I

2013/1/27 Sunday 10:30-12:00

Session Chair: Felix T. S. Chan

E210
A study on Bonding Strength and Fatigue Life of Caulking Part of Washing Machine
Suk Woo Hong | *Sungkyunkwan University*
Sang Soo Ahn | *Sungkyunkwan University*
Jeong Hoon Kang | *Samsung Electronics*
In Cheol Jang | *Samsung Electronics*
Jae Mean Koo | *Sungkyunkwan University*
Chang Sung Seok | *Sungkyunkwan University*

E227
Mathematical Modeling and Vibration Experiment for Multiple Electrostatic Precipitator Modules
Jin Ho Kim | *Yeung Nam University*
Ji Hyun Choi | *Yeung Nam University*
Bum Lee | *Yeung Nam University*
Su Jeong Lee | *Yeung Nam University*

E229
Optimization of Leaf Spring with High Fatigue Life Applied To Horizontal Linear Vibrating Actuator
Jin Ho Kim | *Yeung Nam University*
Ki Bum Lee | *Yeung Nam University*
Jae Hee Kim | *Yeung Nam University*
Ji Hyun Choi | *Yeung Nam University*
Su Jeong Lee | *Yeung Nam University*

E234
Fabricate Shoetrees Using Four-Axis NC Machines
Alan C Lin | *National Taiwan University of Science and Technology*
Tzu Kuan Lin | *National Taiwan University of Science and Technology*

E236
Estimation of Mechanical Properties of Thermal Barrier Coating measured by Nano-Indentation
In Hwan Shin | *Sung Kyun Kwan University*
Chang Sung Seok | *Sung Kyun Kwan University*
Jae Mean Koo | *Sung Kyun Kwan University*
SungHo Yang | *KPS Gas Turbine Technology Service Center*

E241
A Two-stage Priority based Genetic Algorithm for Closed-loop Supply Chain Network
Felix T. S. Chan | *The Hong Kong Polytechnic University*
Y.T. Chen | *Hong Kong Polytechnic University, Hong Kong*
S.H. Chung | *Hong Kong Polytechnic University, Hong Kong*

E210

A study on Bonding Strength and Fatigue Life of Caulking Part of Washing Machine

Suk-Woo Hong
Graduate School of Mechanical Engineering, Sungkyunkwan University,
300 Chunchun-dong, jangan-gu, Suwon-si, Kyunggi-do, 440-746, Korea
hong3418@naver.com

Sang-Soo Ahn
Graduate School of Mechanical Engineering, Sungkyunkwan University,
300 Chunchun-dong, jangan-gu, Suwon-si, Kyunggi-do, 440-746, Korea
sangsoo01@hanmail.net

Jeong-Hoon Kang
Advanced R&D Team, Digital Appliances, Samsung Electronics Co. Ltd.,
Maetan 3-dong, Yeongtong-gu, Suwon-si, Kyunggi-do, Korea
jhoon.kang@samsung.com

In-Cheol Jang
Advanced R&D Team, Digital Appliances, Samsung Electronics Co. Ltd.,
Maetan 3-dong, Yeongtong-gu, Suwon-si, Kyunggi-do, Korea
sueisa.jang@samsung.com

Jae-Mean Koo
School of Mechanical Engineering, Sungkyunkwan University,
300 Chunchun-dong, jangan-gu, Suwon-si, Kyunggi-do, 440-746, Korea
kjm9000@hanmail.net

Chang-Sung Seok
School of Mechanical Engineering, Sungkyunkwan University,
300 Chunchun-dong, jangan-gu, Suwon-si, Kyunggi-do, 440-746, Korea
seok@skku.edu

The corresponding author: Chang-Sung Seok

Abstract
Caulking joining is one of the joining methods that have an advantage to easily manufacture and assemble, and to decrease the cost of product. Though the design on caulking process is very important in order to obtain the satisfactory strength, the research on caulking joining is insufficient. Therefore, in this paper, the tensile and fatigue test for an evaluation of caulking part shapes of washing machine drum were conducted. Also, the caulking process was simulated by finite element analysis and the residual stress of caulking part shapes was evaluated.
Keyword: Caulking, Mechanical Bonding, Press Joining

1. Introduction

Recently, in the washing machine industry, the velocity of spin-dry was faster in order to decrease electricity usage, and the drum of washing machine is directly influenced by high spinning speed over the 1000rpm. Such a drum is made by caulking press joining or welding joining. The welding joining has high strength, but, the corrosion can easily occur to it and it has a high cost as compared with caulking joining. Because of such reasons, caulking press joining is using in washing machine industry, but caulking press joining has low strength as compared with welding joining. Recently, there are several studies on methodical and numerical analysis but those are insufficient, yet.[1~5]

Therefore, in this study, the bonding strength of the caulking part was evaluated by tensile test and fatigue test. Also, the caulking process was simulated by finite element analysis and the residual stress of caulking part shapes was evaluated.

2. Specimen and test method

In this study, as shown in Fig. 1 (a), 40mm × 150mm specimen was collected from caulking of the 4 kinds of drum, and the hydraulic test machine of Instron Co. Ltd(Model 8802) and the hydraulic grip were used for tensile test and fatigue test. The tensile and fatigue test were performed in the direction of allow in Fig. 1 (b). Considering the drum velocity at bursting, the tensile test speed was set in 50mm/min. And the fatigue test was set in sine wave, 10Hz and stress ratio R=0.1.

3. Tensile Strength and Fatigue Life of Caulking

The shapes of A~D drum are shown in Fig. 2, and tensile test result is shown in Table 1. The average of tensile strength has greatly changed depending on shape of caulking. The drum A and C almost coincide in deviation of about 2MPa, and drum B and D in deviation of about 15MPa, respectively. Also, the tensile strength of the drum A and C was larger about 50MPa than that of Drum B and D. After the tensile test was finished, the fatigue test was performed, and the results are shown in Fig. 3. As the results, the tensile strength of the drum A and C were evaluated higher than that of the drum B and D, but the result of the fatigue life is an opposite tendency. In conclusion, the tensile strength and fatigue life are not proportion. Also, the tensile strength and the fatigue life are heavily influenced by shape of caulking. Therefore, the shape of caulking is a highly important variable. In addition, the crack initiated at the folding part of the caulking like Fig. 4. Consequently, in this study, the finite element analysis was performed depending on shape of the caulking, and the residual stress was drawn from the folding part of the caulking.

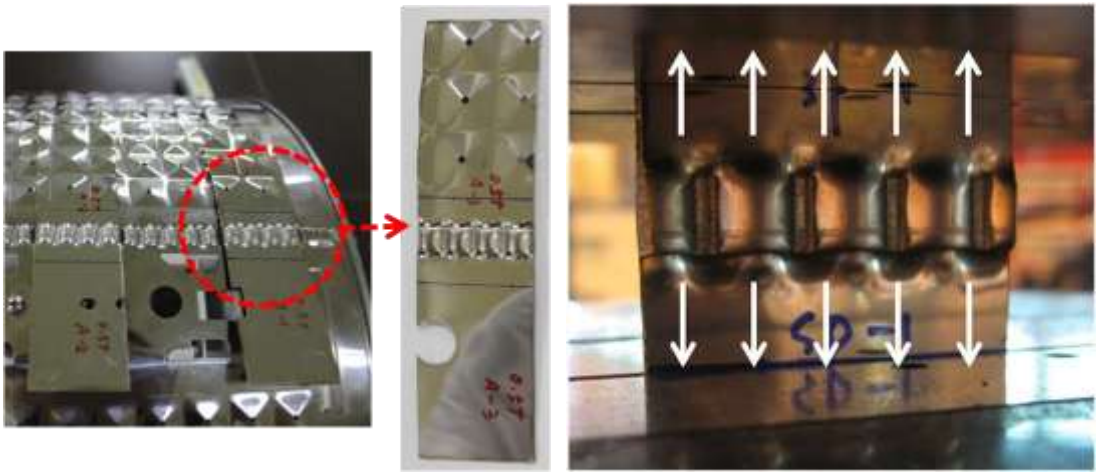

(a) (b)

Fig. 1 (a) The specimen collected from caulking part of drum, (b) Picture of load direction

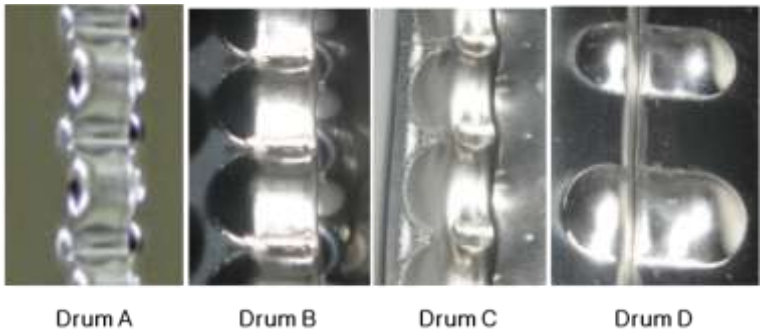

Fig. 2 Shape of caulking

4. Residual Stress by Finite Element Analysis

In this study, the Autodyn was used for simulation of the caulking process. The analysis was performed after the dense mesh was applied to the folding and inflexion part, because the crack occurs at the folding part of the caulking.

Table 1 Results of tensile test according to shape of caulking

Drum A		Drum B	
0.5t		0.5t	
No.	Tensile Strength(MPa)	No.	Tensile Strength(MPa)
Ave.	222.1	Ave.	171.3
Drum C		Drum D	
0.6t		0.7t	
No.	Tensile Strength(MPa)	No.	Tensile Strength(MPa)
Ave.	226.0	Ave.	156.7

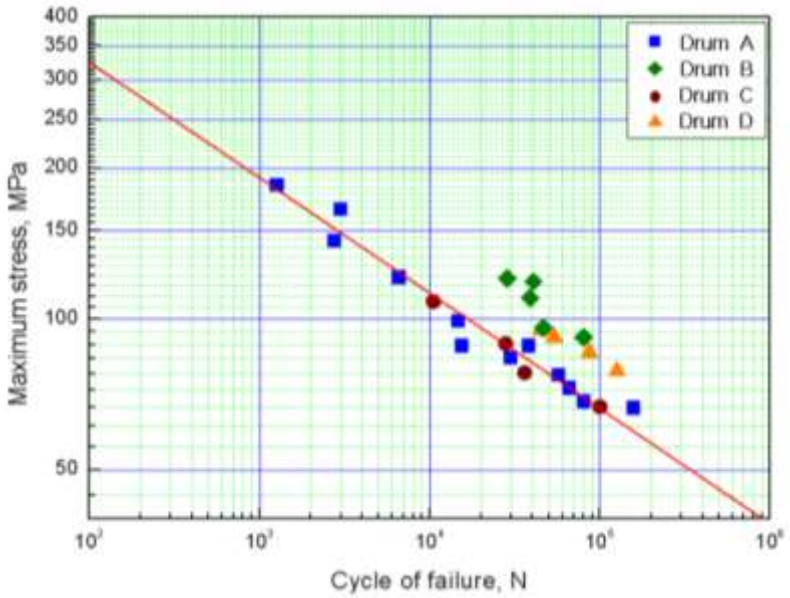

Fig. 3 Results of fatigue test according to shape of caulking


Fig. 4 The origin of crack in caulking part

The shape of caulking and the radius of inflexion were set in 3 cases(1.4mm, 1.6mm, 1.8mm). Also, a caulking tool removed after compression on the 0.5t stainless sheet. The analysis was finished after a sufficient time passing because the spring back phenomenon occurs. The shape of the caulking was shown in Fig. 5 (a) after analysis finished. The stress distribution of the load direction was checked in the folding part, and as the result, in case of R=1.4, the residual stress of the folding part was 256MPa, and in case of R=1.6, 200MPa and in case of R=1.8, 183MPa like Fig. 5 (b). In other words, the residual stress decreases when the inflexion radius increases, and it have an effect on tensile strength and fatigue life.

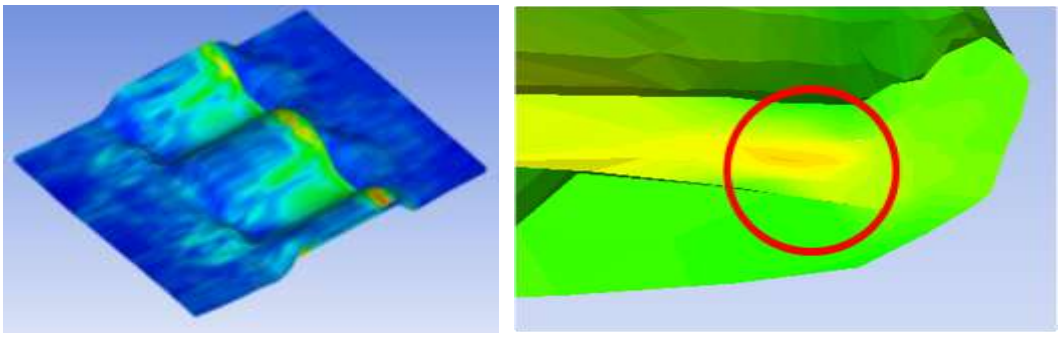

(a) (b)

Fig. 5 (a) Figure of caulking process analysis after finish,
(b) Figure of the origin of crack in caulking part after analysis

5. Conclusion

(1) The tensile strength and fatigue life seriously change depending on the shape of the caulking, and the tensile strength has an opposite tendency as compared to the fatigue life.
(2) If the caulking part exposes to fatigue load, the crack will initiate at the folding part of the caulking. Therefore, the residual stress of the folding part was checked by finite element analysis. As the result, residual stress decreases when the inflexion radius increases until specific value is approched.

6. Acknowlegment

This work was supported by the National Research Foundation of Korea(NRF) grant funded by the Korea government(MEST) (No. 2011-0020024) and the National Research Foundation of Korea(NRF) funded by the Ministry of Education, Science and Technology(No. 2012M2A8A1029423).

7. References

[1] Y. Kim,, 2006, “Finite Element Analysis and Experimental Study on Multi-Stage Seaming Process for Improving the mechanical Bonding Strength,” *National Univ. of Pusan Master’s thesis*
[2] (2) E. S. Kim, M. L. Jung, B. M. Kim, 2008, “Selection of the Optimum Seaming Condition for Spin Drum Using Statistical Method,” *Journal of the Korean Society for Precision Engineering*, Vol. 25, No. 1, pp. 99~107
[3] (3) N. Nong, O. Keju, Z. Yu, O. Zhiyuan, T. Changcheng, L. Feipeng, 2003, “Research on press joining technology for automotive metallic sheets,” *Journal of Materials Processing Technology*, Vol. 137, pp. 159~163
[4] (4) E.S. Kim, B. M. Kim, 2007, “An experimental study on improvement of joining strength of the spin drum seaming division in washing machine,” *Journal of Materials processing Technology*, Vol. 187~188, pp. 155~158
[5] (5) Y. B. Lee, Y. K. Park, C. S. Chung, H. K. Kim, 2000, “An Experimental Study on the Strength Evaluation of Mechanical Press Joint,” *Trans. of the KSME (A)*, Vol. 24, No. 2, pp. 438~447

E227

An Electromagnetic Vibration Exciter in Multiple Modules of an Electrostatic Precipitator

Ji-Hyun Choi
Electric Motor and Actuator Laboratory, Department of Mechanical Engineering, Yeungnam University, Gyeongsan, Gyeongbuk, 712-749, Korea
jihyun.m.choi@gmail.com

Ki-Bum Lee
Electric Motor and Actuator Laboratory, Department of Mechanical Engineering, Yeungnam University, Gyeongsan, Gyeongbuk, 712-749, Korea
bumbum@ynu.ac.kr

Su-Jeong Lee
Electric Motor and Actuator Laboratory, Department of Mechanical Engineering, Yeungnam University, Gyeongsan, Gyeongbuk, 712-749, Korea
leesujeong@ynu.ac.kr

Jin-ho Kim
Electric Motor and Actuator Laboratory, Department of Mechanical Engineering, Yeungnam University, Gyeongsan, Gyeongbuk, 712-749, Korea
jinho@ynu.ac.kr

Abstract
It was the key point that matching mechanical natural frequency of the electrostatic precipitator (ESP) and input frequency of current which is approved in electromagnetic vibration exciter to improve dust rapping efficiency. The single unit of prototype ESP which includes sets of dust collecting plates and one electromagnetic vibration exciter was vibration modeled and experimentally analyzed in previous research. By frequency response experiments, resonance frequency of dust collecting plates is found. And it was confirmed that these two natural frequencies matched up for effective resonance. Going one step forward, it is necessary that make multiple modules of the ESP system for practical utilization in industrial settings such as underground tunnels and sites. Thus, we looked for the best arrange way for more than two ESP systems, and their electromagnetic vibration exciters. Each ESP module can be arranged in both series and parallel and specification of the exciter can be increased than before without adding more exciters. However, as the number of modules increased or specification of the electromagnetic vibration exciter changed, frequency response analysis is also required again for verifying resonance frequency of the new multiple module system. We also proposed synchronization methods for more than two electromagnetic vibration exciters.

<A previous single module electrostatic precipitator using electromagnetic vibration exciter>

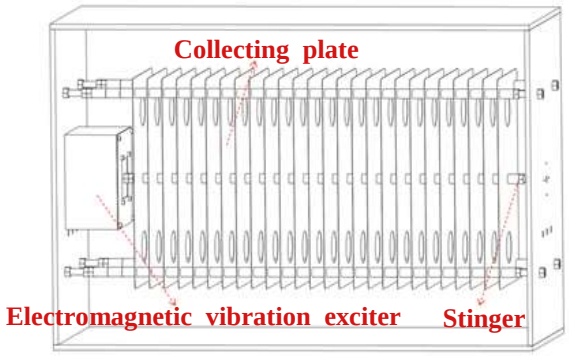

Fig. 1(a). Schematic diagram of the ESP system

Fig. 1(b). The Prototype of single ESP system

<Applied electromagnetic vibration exciter and its operating diagram>

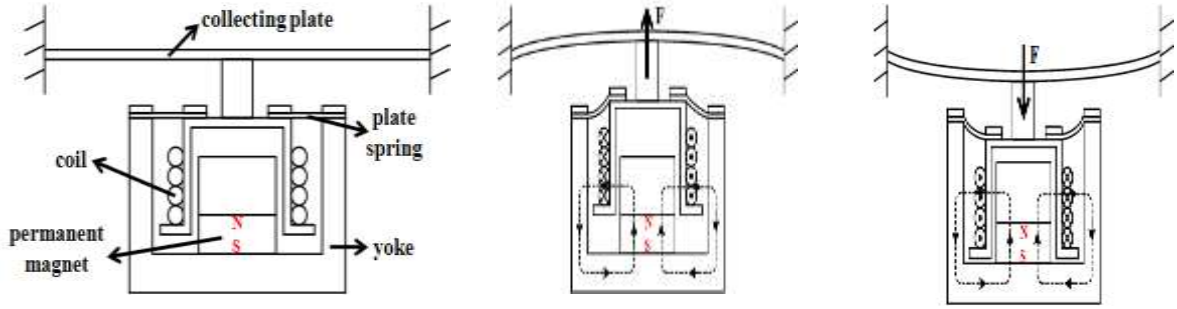

Fig. 2(a). Initial position **(b).** at upper position **(c).** at lower position

<Possible array method for electromagnetic vibration exciters and multiple ESP systems>

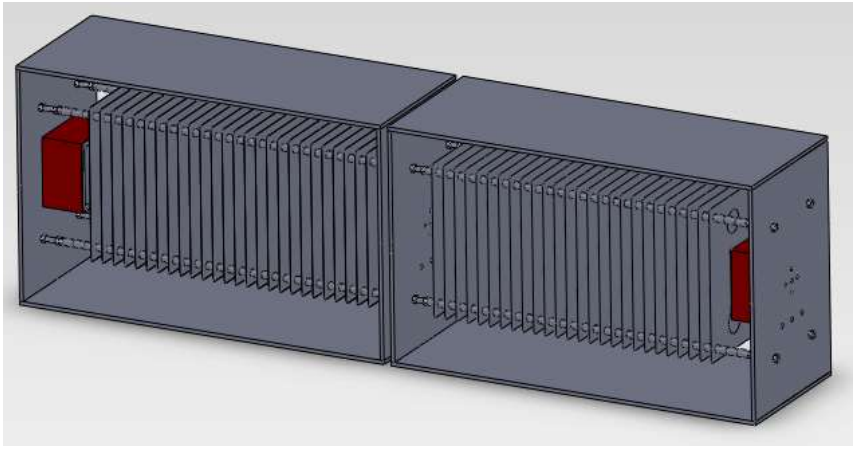

Fig. 3(a). Series connection and two exciters are placed on both sides

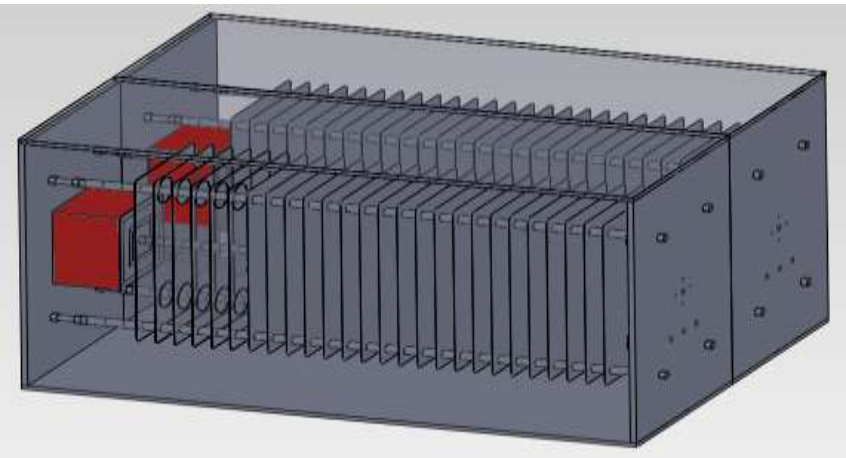

Fig. 3(b). Parallel connection and two exciters are placed on same side

Fig. 3(c). Parallel connection and one exciter with a connecting plate

E229

Optimization of Leaf Spring with High Fatigue Life Applied To Horizontal Linear Vibrating Actuator

Ki-Bum Lee
Electric Motor and Actuator Laboratory, Department of Mechanical Engineering, Yeungnam University, Gyeongsan, Gyeongbuk, 712-749, Korea
bumbum@ynu.ac.kr,

Jae-Hee Kim
Electric Motor and Actuator Laboratory, Department of Mechanical Engineering, Yeungnam University, Gyeongsan, Gyeongbuk, 712-749, Korea
jaehee@ynu.ac.kr,

Ji-Hyun Choi
Electric Motor and Actuator Laboratory, Department of Mechanical Engineering, Yeungnam University, Gyeongsan, Gyeongbuk, 712-749, Korea
jihyun.m.choi@gmail.com,

Su-Jeong Le
Electric Motor and Actuator Laboratory, Department of Mechanical Engineering, Yeungnam University, Gyeongsan, Gyeongbuk, 712-749, Korea
leesujeong@ynu.ac.kr,

Jin-ho Kim
Electric Motor and Actuator Laboratory, Department of Mechanical Engineering, Yeungnam University, Gyeongsan, Gyeongbuk, 712-749, Korea
jinho@ynu.ac.kr

The corresponding author: Jin-Ho Kim

This paper aims to optimize the leaf spring with high fatigue life which guides the moving part of the horizontal linear vibrating actuator. One of the most significant parts of horizontal vibrating linear actuator is the guide spring which supports moving part of actuator and enables actuator to vibrate elastically.

Nowadays, with development of science technology and information industry, the function of smart phone has been various and the size of smart phone has become larger for many objectives. Thus, making thin smart phone is one of hottest issue in the present smart-phone industry. The vertical linear vibrating actuator has been used as the vibration device for haptic and alarm function on smart phone.

Fig. 1 Schematic diagram of typical horizontal linear vibrating actuator

However, the vertical linear vibrating actuator has a major cause on the limitation to make smart phone slim because of its own characteristic of vertical direction vibration. Moreover, the thickness of the vibration actuator is one of most thickness parts in the smart phone components. For this reason, the horizontal linear vibrating actuator which does not need vibration space in vertical direction has been developed for smart phone slimness in recent years. However, one of difficulties in developing horizontal linear vibrating actuator is the design of guide spring. Because when guide spring is reciprocating motion, this spring gets fatigue-fractured by receiving cyclic compression and tension loads. Thus, one of the most significant parts of horizontal vibrating linear actuator is the guide spring which supports moving part of actuator and enables actuator to vibrate elastically.

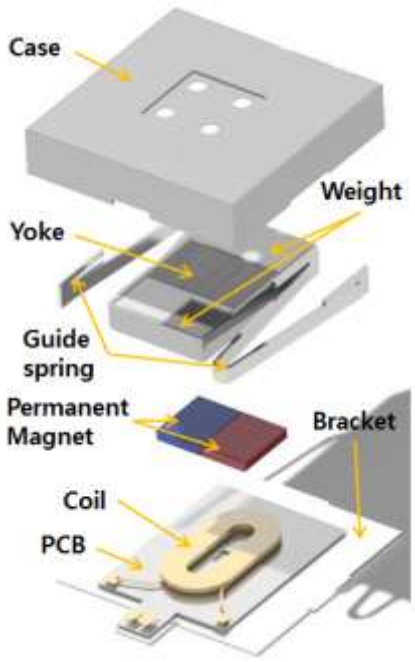

Fig. 2 View of horizontal linear vibrating actuator

A horizontally vibrating linear motor shown in Figure 2 was suggested by Kim et al. And this actuator has 3 mm of thickness and about one million of fatigue life at about 1.9 G.

This paper aims to optimize the leaf spring with high fatigue life, and can be adapted less than 2.5 mm of thickness. Various types of leaf springs were designed to find optimization leaf spring and analyzed to get the required stiffness with high fatigue life through the stress analysis using commercial structural analysis program, ANSYS, and commercial optimization software, PIAnO. (PIAnO basically integrates and automates the analysis process with CAEs and then provides the MDO solution through application of advanced design techniques as DOE, Optimization, RA and etc.) The experiments were performed with prototypes to measure vibration acceleration and life time of leaf spring.

E234

Fabricate Shoetrees Using Four-Axis NC Machines

Alan C. Lin
Department of Mechanical Engineering
National Taiwan University of Science and Technology
43, Keelung Road, Section 4, Taipei 106, TAIWAN
alin@mil.ntust.edu.tw

Tzu-Kuan Lin
Department of Mechanical Engineering
National Taiwan University of Science and Technology
43, Keelung Road, Section 4, Taipei 106, TAIWAN

The corresponding author: Alan C. Lin

Abstract
The fabrication of shoetrees is traditionally viewed as a manual and time-consuming craft. They require experienced workers and are difficult to modify even not much precision is needed. This paper proposes a method to automate the machining of shoetrees using a four-axis CNC milling machine. The scopes of this research include: (1) planning tool orientations, (2) avoidance of interference, (3) generating CL data, and (4) generating NC data.
Keyword: Four-axis NC machining, shoetree, Cutting tool orientation, collision avoidance

1. Introduction

People with abnormal foot shapes may not be able to find comfortable shoes on the market and have to consider customized shoes instead. In this case, a shoetree that mimics their foot shape should be manufactured before the customized shoes are made. This research focuses on the method to rapidly generate four-axis NC (numerical control) data for the customized shoetree using scanned data points as shown in Figure 1.

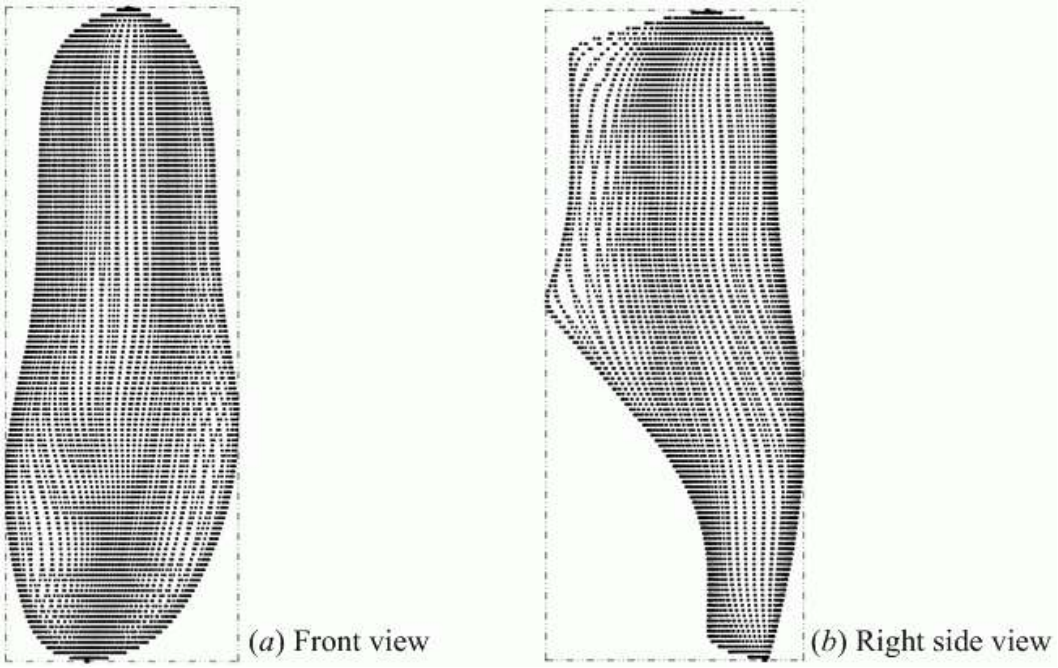

Figure 1. Raw points of shoetree.

CL (cutter location) data must be produced before generating NC data. To generate CL data, three common methods are used: (1) create a surface of workpiece from raw points and offset the surface by the radius of ball-end mill [1, 2], (2) generate cutter contact (CC) data on the surface of workpiece, and obtain CL data from the CC data [3], and (3) obtain CL data directly from point data [4]. These methods were only applicable to three-axis milling. This paper uses shoetree as a case study to explore the method for generating four-axis NC data and machining shoetree. It includes the following steps:

(1) Planning tool orientations: A section-center method is proposed to let the cutting tool not collide with the workpiece, and make the variations of tool orientation smooth.
(2) Avoiding interference: The distances between the tool axis and interference checking points (CKPs) are the crucial condition for interference avoidance. Calculating the distances for every data points to retract tool along the direction of tool orientations make the interference disappear.
(3) Generating CL points and their tool orientations: Retracting tool along tool orientations can generate CL points, which is similar to the method of generating CL data using an offset surface.
(4) Generating NC data: The CL points and their tool orientations are transformed to the coordinates and rotation angles for four-axis machining. Meanwhile, constant value of relative feedrate is adopted to improve the quality of the machined surface.

The details of each of the steps will be addressed in the following sections.

2. Planning of tool orientations

Tool orientation should be carefully taken into account while generating tool paths for four-axis machining. Tool orientation is a unit vector on tool axis with the direction from the tool tip to the

tool holder. This research proposes a ‘section-center method’ to eliminate the shortcomings of the above two methods. In the proposed method, the tool orientation is aligned with the direction from the section center to the section contour as shown in Figure 2. The method to determine the section center is as follows:

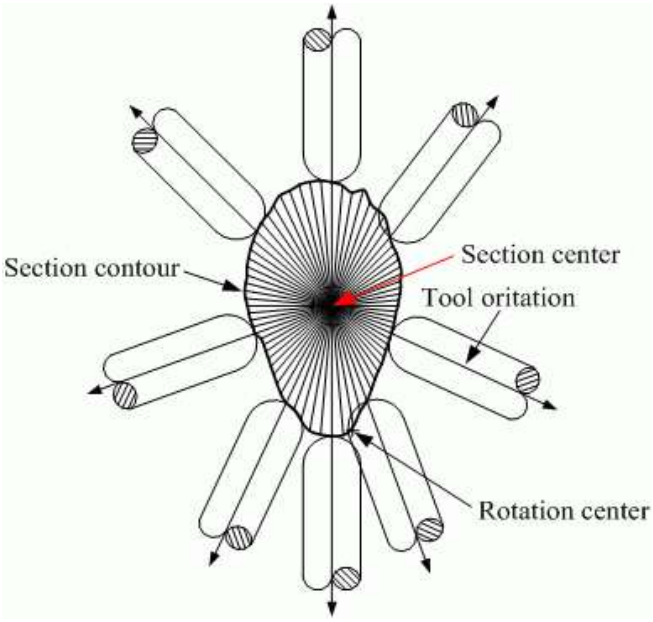

Figure 2. Determination of tool orientations using the proposed section-center method.

(1) If the entire section contour is convex, the geometric center is adopted as the section center.

(2) If any concave region exists, then use the following steps:

(*a*) Find the points on a specific concave region.

(*b*) Determine the areas to be discarded, which are on one side of tangent lines of points on the concave region, as shown in Figure 3(*a*) and (*b*).

(*c*) Repeat the above two steps for all concave regions in order to find the final area feasible for locating the section center, as shown in Figure 3(*c*).

(*d*) Adopt the geometric center of the useful area as the section center, as shown in Figure 3(*d*).

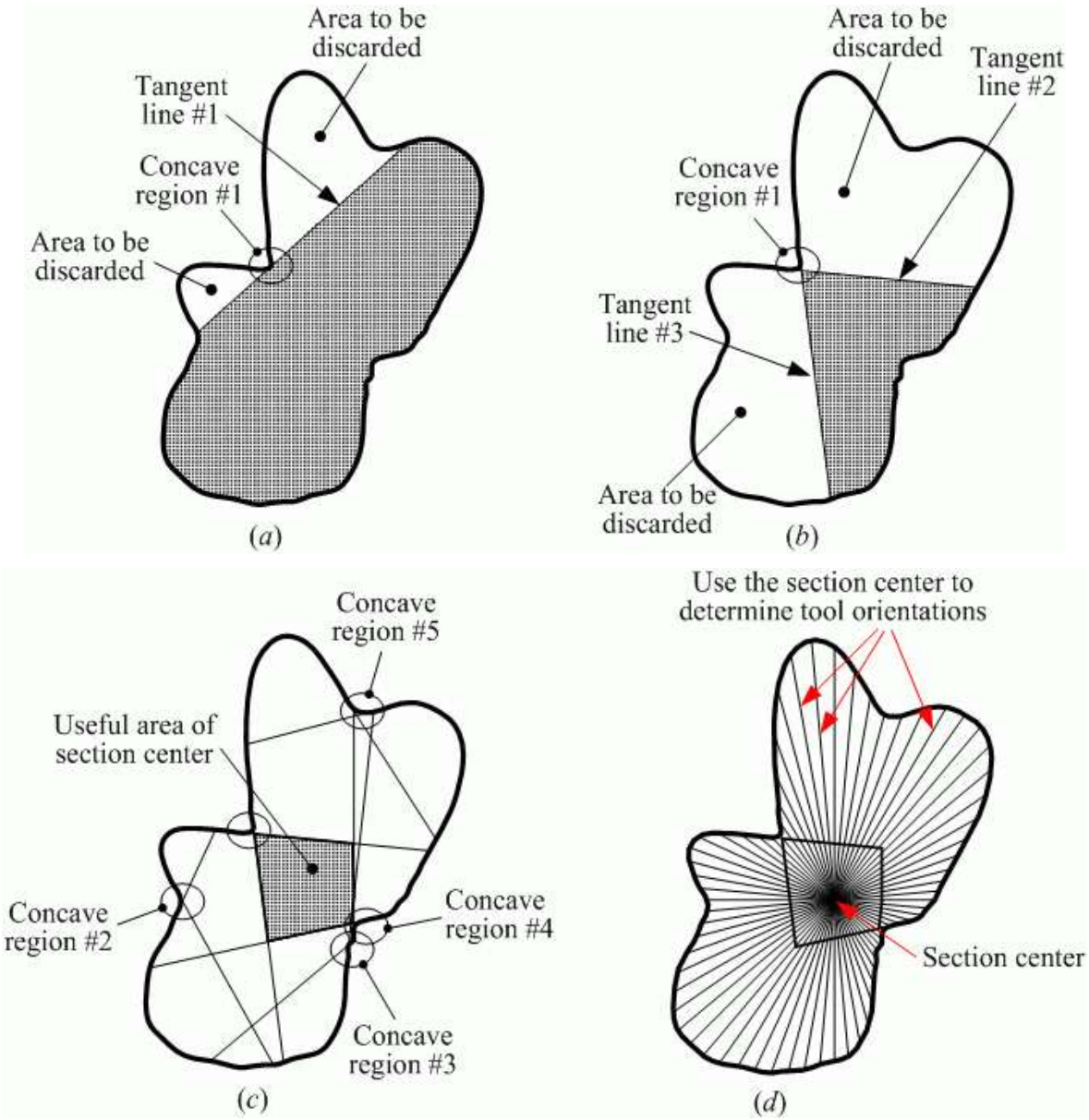

Figure 3. Determination of section center for concave regions.

3. Avoidance of interference

The method to avoid interference is to raise the cutting tool along the direction of tool orientation until the interferences are all excluded. The points of destination are herein called 'raised points' after they had gone through the raising process.

The derivation of the equation used to calculate the raising distance is illustrated in Figure 4. The equation is:

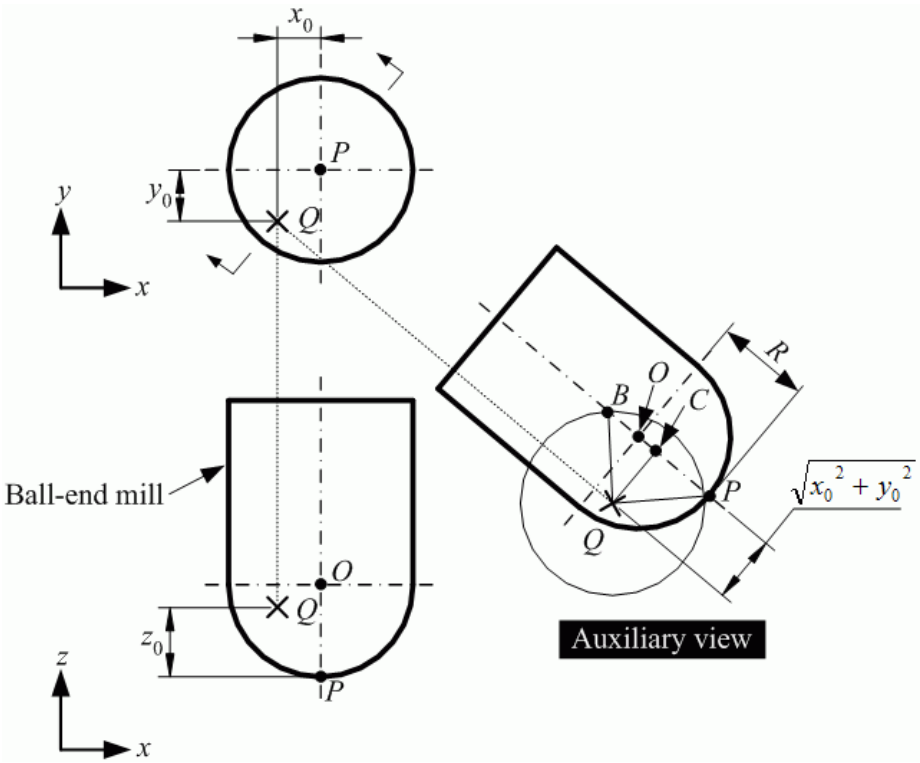

Figure 4. Calculation of raising distance to avoid interference.

$$\overline{OB} = \overline{PB} - R = \overline{PC} + \overline{BC} - R = Q_z - P_z + \sqrt{R^2 - x_0^{\ 2} - y_0^{\ 2}} - R \qquad (1)$$

A data point may meet many CKPs. A raising distance must be derived for every single CKP. Among these raising distances of CKPs for a data point, the maximum value is the truly required raising distance for avoiding interference along the tool orientation. After adding the maximum raising distance to every data point, the raised points can be obtained as shown in Figure 5.

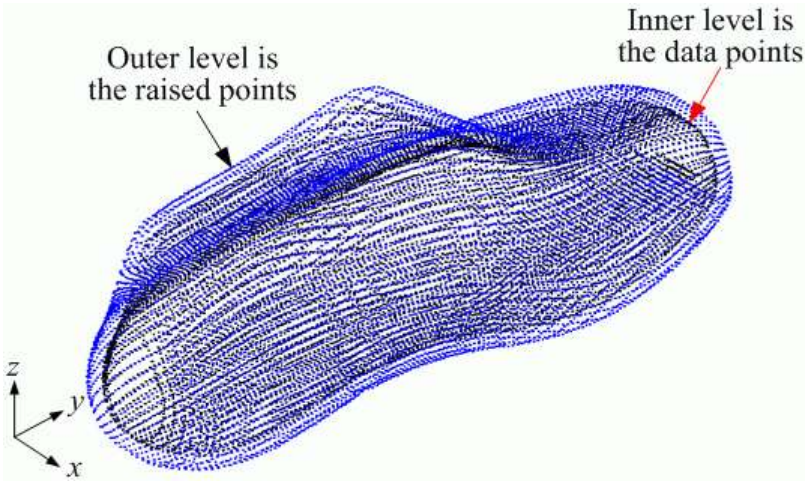

Figure 5. Data points and raised points.

4. Generation of CL points and their tool orientations

Although raised points are the points without interference, if CL points are obtained directly from the raised points, the surface will be too rough after machining. Therefore, interpolating longitudinal and transverse curves base on the raised points along these curves are necessary before generating CL points. The interpolation method is the same with the method of interpolating CKPs discussed in Section 3.

In this research, the radius of the ball-end mill R = 5 mm. In the interpolation, the longitudinal and transverse distances between two nearby raised points are both equaled to 0.5 mm. The tool orientations are planned using the aforementioned section-center method. Every CL point is accompanied with a tool orientation. Figure 6(a) depicts some CL points. Figure 6(b) shows the CL points of tool center, but tool orientations are not plotted.

x	*y*	*z*	*i*	*j*	*k*
-2.923	5.059	52.5172	0	0	1
-3.41735	5.059	52.4362	-0.01225	0	0.999925
-3.90614	5.059	52.3166	-0.02444	0	0.999701
-4.38676	5.059	52.1606	-0.03651	0	0.999333
-4.85659	5.059	51.9701	-0.04844	0	0.998826
-5.31302	5.059	51.7474	-0.06017	0	0.998188
-5.75342	5.059	51.4945	-0.07166	0	0.997429
-6.17518	5.059	51.2135	-0.08286	0	0.996561
-6.57581	5.059	50.9064	-0.09371	0	0.995599
-6.95474	5.059	50.5754	-0.10422	0	0.994555
-7.31279	5.059	50.2228	-0.11439	0	0.993436
-7.65085	5.059	49.8505	-0.12427	0	0.992249
-7.9698	5.059	49.4609	-0.13387	0	0.990999
-8.2705	5.059	49.056	-0.14321	0	0.989693
-8.55384	5.059	48.6381	-0.15231	0	0.988333
-8.82069	5.059	48.2092	-0.16119	0	0.986923

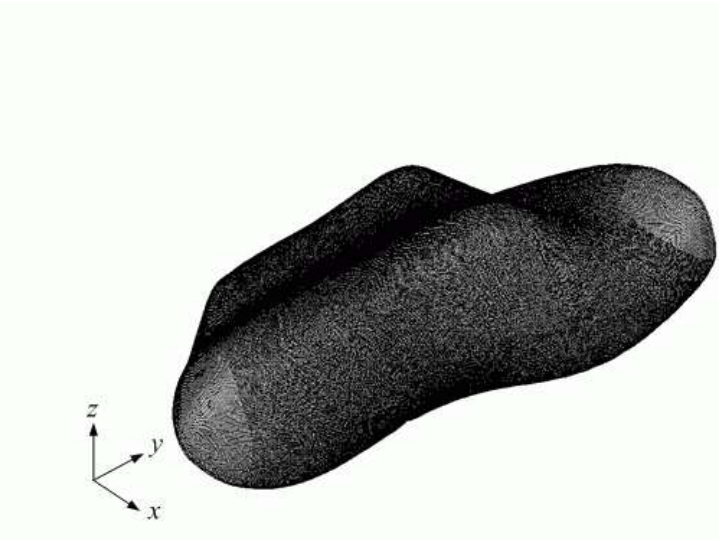

(*a*) (*b*)

Figure 6. (*a*) Part of CL data, (b) Tool path of ball end mill.

5. Generation of four-axis NC data

During the process of generating CL points, the workpiece is assumed to be fixed, and every tool orientation is aligned with the direction from section center to CL point based on the workpiece coordinate system, but NC data is based on the machining coordinate system which can be set by G54 code. Therefore, every CL point and its tool orientation should be rotated to align with the direction of the spindle that is (0, 0, 1), as shown in Figure 7. Assume the coordinate of CL point is $P(x, y, z)$, the tool orientation is $\vec{N}(N_x, 0, N_z)$, the rotation center is point $C(0, y, 0)$, and the angle between the tool orientation vector and the *z*-axis is *B*. The point $P'(X, Y, Z)$ is obtained after rotating point $P(x, y, z)$ about the *y*-axis. Rotation angle *B* and point P' are derived as discussed below.

(1) Rotation angle of NC data

Figure 32 shows that rotation angle B can easily be calculated by $B = \tan^{-1}(N_x / N_z)$. A positive rotation angle B is defined such that the workpiece rotates clockwise about the y-axis. Angle B is defined to be between 0° and 180° when $N_i \geq 0$, and between 180° and 360° when $N_i < 0$.

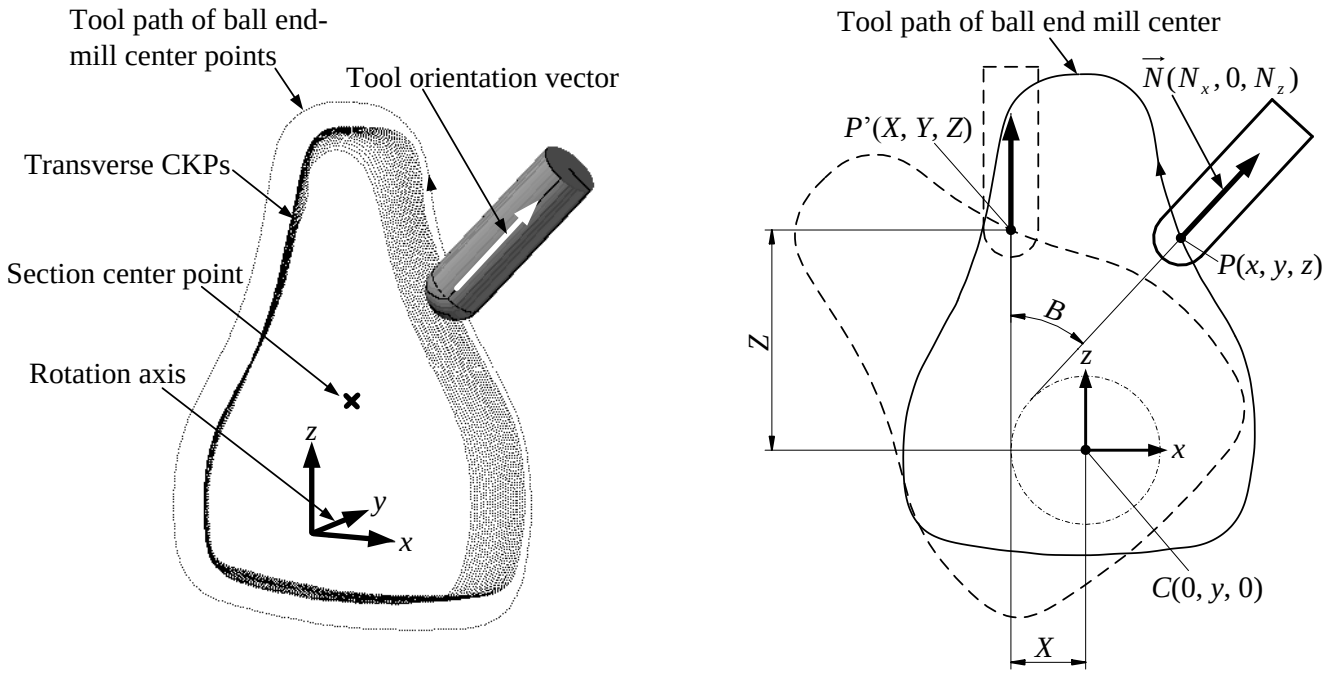

Figure 7. The coordinates of four-axis NC data points transformed from the toolpath points.

(2) Point coordinates of NC data

The coordinate transformation matrix for the rotation of the workpiece about the y-axis by angle θ is given by:

$$Rot(y,\theta) = \begin{bmatrix} \cos\theta & 0 & \sin\theta \\ 0 & 1 & 0 \\ -\sin\theta & 0 & \cos\theta \end{bmatrix} \quad (6)$$

Rotation angle B is defined as positive if the workpiece rotates clockwise about the y-axis, so $\theta = -B$. Substituting $\sin B = N_x, \cos B = N_z$, and $\theta = -B$ into Equation (6) yields the following rotation matrix:

$$Rot(y,-B) = \begin{bmatrix} \cos(-B) & 0 & \sin(-B) \\ 0 & 1 & 0 \\ -\sin(-B) & 0 & \cos(-B) \end{bmatrix} = \begin{bmatrix} \cos B & 0 & -\sin B \\ 0 & 1 & 0 \\ \sin B & 0 & \cos B \end{bmatrix} = \begin{bmatrix} N_z & 0 & -N_x \\ 0 & 1 & 0 \\ N_x & 0 & N_z \end{bmatrix} \quad (7)$$

The relationship between NC point P' and CL point P can thus be written as follows:

$$P'(X,Y,Z) = Rot(y,-B)\cdot P = \begin{bmatrix} N_z & 0 & -N_x \\ 0 & 1 & 0 \\ N_x & 0 & N_z \end{bmatrix} \begin{bmatrix} x \\ y \\ z \end{bmatrix} = \begin{bmatrix} x\,N_z - z\,N_x \\ y \\ x\,N_x + z\,N_z \end{bmatrix} \qquad (8)$$

6. System implementation

Programming language Visual C++ and geometry kernel ACIS are adopted to develop a software package for generating NC data of massive points using the algorithms described above. In the circumstance of the software package, raw points of the shoetree surface can be read and modified to produce data points and interpolate CKPs. The raising distances are automatically calculated to exclude gouging and to generate CL points. The coordinates of NC data points are found base on CL data and the feedrates are adjusted to keep the relative velocity constant during post-processing, Figure 8(*a*) shows a part of NC data. The parameters of the machining NC data for machining the shoetree are: the radius of ball-end mill is 5 *mm*, the space between two nearby CKPs is 0.5 *mm* along longitudinal and transverse directions, and the relative feedrate was 1000 *mm/min*. The finished product is shown in Figure 8(*b*).

```
%
O1234
/ G91 G28 Z0
/ G28 X0 Y0
G54
G90 G00 X0 Y0
Z100.
S3000 M3
G90 G00 X-2.923 Y5.059 B0
Z67.517
G01 Z47.517 F1000
X-2.774 Z47.474 B0.702 F984
X-2.626 Z47.396 B1.400 F986
X-2.479 Z47.286 B2.093 F989
X-2.333 Z47.144 B2.777 F992
X-2.190 Z46.973 B3.450 F995
X-2.048 Z46.774 B4.110 F998
X-1.910 Z46.549 B4.753 F100
X-1.776 Z46.299 B5.377 F100
X-1.646 Z46.025 B5.982 F101
X-1.520 Z45.730 B6.569 F101
X-1.397 Z45.415 B7.139 F101
X-1.277 Z45.083 B7.693 F102
```

(*a*) (*b*)

Figure 8. (*a*) Part of NC data, (*b*) finished shoetree.

7. Conclusions

This research contributes a method for machining massive data points using a four-axis CNC machine. Processes from reading the raw points to the generation of NC data are all automatically. The methods proposed in this paper successfully validate the output of NC data and the manufacturing using four-axis machines. The methods can be applied not only to shoetrees, but also to any objects with complex surfaces.

8. Acknowledgements

This project was supported in part by the National Science Council, Taiwan, under project number NSC 100-2221-E-011-024-MY2.

9. References

1. K. I. Kim and K. Kim, "A new machine strategy for sculptured surfaces using offset surface", *International Journal of Production Research*, Vol. 33, No. 6, 1995, pp. 1683-1697.
2. K. Tang, C.C. Cheng and Y. Dayan., "Offsetting surface boundaries and 3-axis gouge-free surface machining", *Computer Aided Design*, Vol. 27, No. 12, 1995, pp. 915-927.
3. H. Li and H.Y. Feng, "Efficient five-axis machining of free-form surfaces with constant scallop height tool paths", *International Journal of Production Research*, Vol. 42, No. 12, 2004, pp. 2403-2417.
4. A.C. Lin and H.T. Liu, "Automatic Generation of NC Cutter Path from Massive Data Points," *Computer Aided Design*, Vol. 30, No. 1, 1998, pp. 77-90.

E236

Estimation of Mechanical Properties of Thermal Barrier Coating measured by Nano-Indentation

In-Hwan Shin
Mechanical Engineering, SungKyunKwan University,
300 Cheon-cheon dong, Jang-an gu, Suwon, Korea
sihwan@skku.edu

Chang-Sung Seok
Mechanical Engineering, SungKyunKwan University,
300 Cheon-cheon dong, Jang-an gu, Suwon, Korea
seok@skku.edu

Jae-Mean Koo
Mechanical Engineering, SungKyunKwan University,
300 Cheon-cheon dong, Jang-an gu, Suwon, Korea
kjm9000@hanmail.net

Sung-Ho Yang
G/T Technology Team, KPS Gas Turbine Technology Service Center,
647 Kyoung-seo dong, Seo gu, In-cheon, Korea
shyang@kps.co.kr

The corresponding author: Chang-Sung Seok

Abstract
Plasma-sprayed Thermal Barrier Coating (TBC) is applied to protect the blades of a gas turbine system from high-temperature gas and lower the surface temperature of the blades. The failure of TBC is directly connected with the failure of blades because the spallation of a ceramic layer will lead to the acceleration of excessive local corrosion and oxidation at the location of failure. Therefore, the estimation of mechanical properties of TBC is very important in the evaluation of the reliability of a gas-turbine blade. In this study, isothermal oxidation tests and thermal fatigue tests were performed at 1,100℃. Then, nano-indention tests were performed for TBC specimens that were thermally aged. From the results of the nano-indentation test to compare two different conditions, there were no significant differences between the mechanical properties of the TC and BC. But those of the TGO remarkably decreased when the aging time increased from 100 h to 200 h and 2cycle to 20cycle by thermal fatigue.
Keyword: Thermal Barrier Coating (TBC), Thermally Grown Oxide (TGO), Isothermal Oxidation, Thermal Cyclic, Nano-Indentation

1. Introduction

A technique of thermal barrier coating (TBC) is applied to protect the components of aircraft engines and gas turbines from high temperatures and to lower the surface temperature of the components. The temperature drop resulting from the TBC is known to be 100℃~150℃ [1-3].

TBC usually consist of a MCrAlY(where M=Ni, Co or both) bond coat, a ceramic (7~8 wt% ZrO_2-Y_2O_3) top coat, and a thermally grown oxide (TGO). The TGO is formed at the interface between the top coat and the bond coat via oxidation of the bond coat during the operation of the gas turbine. Temperature dropped mostly in the top coat, but the top coat deposited directly onto the blade increases the probability of failure at the interface because of the difference in thermal expansion coefficient between the top coat and the substrate. So, an intermediate bond coat layer is applied between the top coat and the substrate to increase the bond strength of the top coat and to relieve the thermal stress [4].

TBC applied between aircraft engine applications and gas turbine blades are exposed to cyclic oxidation conditions, and cyclic oxidation has the most influence on coating failure, especially aircraft engine applications [7, 8]. Therefore, most work relating to the reliability of TBC has been carried out by cyclic oxidation tests where the life of the TBC is usually evaluated by the number of cycles until the spallation (fully-delamination) of the top coat occurs.

For the evaluation of the reliability of TBC, experiments using real coated blades are ideal, but very hard due to the complex shape and cost of a blade. Thus, cyclic oxidation test using cylinder-shaped [9-11] or coin-shaped [4, 10] TBC samples are generally adapted instead.

The aim of this study is to evaluate the variation of the mechanical properties of TBC applied for a gas turbine blade according to the degradation between isothermally aged and thermal fatigue conditions. For this purpose, isothermal oxidation tests and thermal fatigue tests were performed at 1,100℃ and then, nano-indention tests were performed for TBC specimens that were thermally aged.

2. Experimental Details

2.1 Materials and Coating Technology

All of tests were carried out on coin-shaped specimens with the dimensions Φ25.4mm (3mm thickness) and coated on the upper face of specimens. Thermal barrier coating specimens consist of a Ni based super-alloy substrate, a MCrAlY bond coat and a ceramic (7~8 wt% ZrO_2-Y_2O_3) top coat. Table 2.1 shows the composition and thickness at each layer of TBC specimen.

Table 2.1 Composition of thermal barrier coating specimen

	Material	Coating Type	Thickness
Substrate	GTD-111DS	-	3 mm
Bond Coat	MCrAlY	LVPS	240 ㎛
Top Coat	7~8%Y_2O_3-ZrO_2	APS	598 ㎛

2.2 Isothermal Oxidation Test and Thermal Cyclic Test

Isothermal tests, which were to evaluate the relationship between the bond strength and the isothermally aging time of TBC, were performed at 1100℃. For each test were intentionally stopped at 100, 200, 400 hours. Thermal cyclic tests were performed by a furnace and an automated moving system with a timer. 1 cycle of the test consisted of 45-min holding in the furnace and 15-min cooling with compressed air. Thermal cyclic tests, which were to evaluate the spallation life of the plasma-sprayed TBC by cyclic oxidation, were performed at 1100℃. Thermal cyclic tests were performed until the spallation of TBC. Thermal cyclic tests, which were to evaluate the relationship between the bond strength and the number of cycles of oxidation of TBC, were performed at 1100℃. Tests were intentionally stopped at 1, 2, 5, 10 and 20 cycles.

2.1 Nano-Indentation Test

Nano-indentation tests were performed for the TBC specimens, which were thermally aged between the isothermal oxidation test and thermal cyclic test. It is known to the bond strength gradually decreased with the increase between aging time and the number of thermal cycles. The spallation lives of TBCs were assumed to be the time which the bond strength became zero and the spallation lives were determined by the linear curve fittings for the results of nano-indentation tests at each test conditions.

3. Test Results

The elastic modulus of the TGO is considerably higher when compared to those of the two phases in the BC (Bond Coat) and TC (Top Coat). Such large differences in the elastic modulus of the TGO could lead to severe thermal stress near the TGO, which may be the reason why the failure of TBC. The sintering was so active as to lead to an increase of the elastic modulus between an aging time of 100 h and thermal fatigue of 2 cycles as compared to the as-sprayed properties, and then remained constant afterwards. There was no significant difference in the nano hardness of TC, TGO and BC under isothermal oxidation. But the nano hardness of BC is higher in thermal fatigue. It seems to be related to the inter-diffusion at the boundary of TC and BC is active under thermal fatigue.

4. Conclusions

(1) From results between isothermal oxidation tests and thermal fatigue tests using coin-shaped TBC specimen, TBC is fully spalled due to the degradation of BC, the component of Al depletion and the layer of TGO growth.

(2) From the results of the nano-indentation test to compare two different conditions, there were no significant differences between the mechanical properties of the TC and BC. But those of the TGO remarkably decreased when the aging time increased from 100 h to 200 h and 2cycle to 20cycle by thermal fatigue.

(3) The nano-indentation technique is a very effective way to evaluate the degradation of TGO. It is possible to catch the initiation point of delamination by observing the change in the mechanical properties of TGO both aging time and thermal fatigue increase by using the nano-indentation technique.

5. References

[1] K. Vaidyanathan, E. H. Jordan, M. Gell, Surface geometry and strain energy effects in the failure of (Ni/Pt)Al EB-PVD thermal barrier coating, Acta Materialia, Vol. 52, pp. 1107-15, 2004.

[2] J. A. Thompson, T. W. Clyne, The effects of heat treatment on the stiffness of zirconia top coats in plasma sprayed TBCs, Acta Materialia, Vol. 49, pp. 1565-75, 2001.

[3] K. W. Schlichting, N. P. Padture, E. H. Jordan, M. Gell, Failure modes in plasma-sprayed thermal barrier coatings, Materials Science & Engineering A, Vol. 342, pp. 120-30, 2003.

[4] A. Nusair Khan, J. Lu, Behavior of air plaspa sprayed thermal barrier coatings, subjected to intense thermal cycling, Surface and Coatings Technology, Vol. 166, pp. 37-43, 2003.

[5] G. G. Levi, E. Sommer, S. G. Terry, A. Catanoiu, Alumina grown during deposition of thermal barrier coatings on NiCrAlY, Journal of American Ceramic Society, Vol. 86, No. 4, pp. 676-685, 2003.

[6] W. J. Quadakkers, V. Shemet, D. Sebold, R. Anton, E. Wessel, L.Singheiser, Oxidation characteristics of a platinized MCrAlY bond coat for TBC systems during cyclic oxidation at 1,000℃, Surface & Coatings Technology, Vol. 199, pp. 77-82, 2005.

[7] Mats Eskner, Mechanical behavior of gas turbine coatings, Doctoral Thesis, 2004.

[8] N. P. Padture, M. Gell, E. H. Jordan, Thermal barrier coatings for gas-turbine engine applications, Science, Vol. 296, pp. 280-284, 2002.

[9] R. A. Miller and C. E. Lowell, Failure mechanisms of thermal barrier coatings exposed to elevated temperatures, Thin Solid Films 95, pp. 265-273, 1982.

[10] R. V. Hillery, B. H. Pilsner, R. L. McKight, T. S. Cook, and M. S. Hartie, Thermal barrier

coating life prediction model development - final report, NASA-CR-180807, 1988.
[11] J. Shi, A. M. Karsson, B. Baufeld, M. Bartsch, Evolution of surface morphology of thermo-mechanically cycled NiCoCrAlY bond coats, Materilas Science and Engineering A, Vol. 434, pp. 39-52, 2006.

E241

A Two-stage Priority based Genetic Algorithm for Closed-loop Supply Chain Network

Y.T.Chen
Department of Industrial and Systems Engineering
Hong Kong Polytechnic University, Hong Kong
yongtong.chen@connect.polyu.hk

F.T.S Chan*
Department of Industrial and Systems Engineering
Hong Kong Polytechnic University, Hong Kong
f.chan@inet.polyu.edu.hk

S.H.Chung
Department of Industrial and Systems Engineering
Hong Kong Polytechnic University, Hong Kong
mfnick@inet.polyu.edu.hk

The corresponding author: F.T.S Chan

Abstract
Closed-loop supply chain network has gained increasing attention throughout this decade. In this paper, a six-level close-loop supply chain network has been studied. Due to the complexity of this model, a two-stage priority based Genetic Algorithm (GA) is developed. This algorithm contains a newly developed two-stage and priority based encoding method, which makes GA more powerful in solving this kind of problems. Three numerical experiments have been done to test the proposed algorithm. The results show that, this proposed GA can get a reliable and higher quality results with shorter computational time comparing with LINGO and spanning-tree based GA.
Keyword: Closed-loop supply chain, Genetic algorithm, Reverse distribution, Linear programming

1. Introduction

Environmental issues have gained increasing attentions in these decades, many research related to it have been done in the area of supply chain, which include both academic one and industrial applications. Considering both environmental and economic issues simultaneously, Closed-Loop Supply Chain (CLSC) emerged to coordinate the flow of materials between forward and reverse logistics. CLSC focuses on taking back products from customers and recovering added value by reusing the entire product, and/or some of its modules, components, and parts [1].

In this academic area, many researchers established various optimal CLSC networks. Barros *et al.* [2] proposed a two-level location model for the sand problem and considered its optimization using heuristic procedures. Sheu *et al.* [3] proposed a linear multi-objective programming model to solve an integrated CLSC problem. Paksoy *et al.* [4] formulated a linear program model to balance the equilibrium between various costs. Ozkir and Basligil [5] proposed a mixed integer

linear program model to describe a CLCS network, in which three ways of recovery process were considered. Besides using linear programming to formulate this kind of problem, Yang *et al.* [6] optimized the equilibrium state of the CLSC network using the theory of variation inequalities. Shi *et al.* [7] developed a mathematical model to maximize the total profit of the CLSC network by analyzing the pricing and production decisions simultaneously.

Since the problems mentioned above are NP-hard problems, heuristic algorithm such as Genetic Algorithm (GA) becomes an efficient method and gains more popularity. Wang and Hsu [8] established a generalized closed-loop model as an integer linear programming model which integrated forward and reverse logistics, a revised spanning-tree based GA was proposed. Kannan *et al.* [9] developed a multi echelon, multi period, multi product CLSC network model for product returns, GA is also applied as an efficient methodology.

In this study, a two-stage GA using priority based calculation to solve the CLSC network problem is proposed. In the numerical experiments, the proposed GA is used to solve several different scales of problems and the results indicate that, the proposed GA can solve the integrated closed-loop problem with higher quality and more efficiently.

2. Problem Description

Many mathematical models have been designed to describe the CLSC problem. In this study, Wang and Hsu's model [8] in "A closed-loop logistic model with a spanning-tree based genetic algorithm" (which will be called original paper in the following content) is used as an illustrative example to show how the priority based two-stage GA works. From the numerical results, the efficiency and accuracy of the proposed GA can be proved.

Indices

I	the number of suppliers with i=1,2,...,I
J	the number of manufacturers with j=1,2,...,J
K	the number of distribution centers with k=1,2,...,K
L	the number of customers with l=1,2,...,L
M	the number of dismantlers with m=1,2,...,M

Parameters

a_i	capacity of supplier i
b_j	capacity of manufacturer j
Sc_k	total capacity of forward and reverse logistics in the Distribution Center (DC) k
pd_k	the percentage of total capacity for reverse logistics in DC k
pc_l	recovery percentage of customer l
pl_m	the landfilling rate of dismantler m
d_l	demand of the customer l
e_m	capacity of dismantler m
s_{ij}	unit cost of production in manufacturer j using materials from supplier i

t_{jk} unit cost of transportation from each manufacturer j to each DC k
u_{kl} unit cost of transportation from DC k to customer l
v_{km} unit cost of transportation from DC k to dismantler m
w_{mj} unit cost of transportation from dismantler m to manufacturer j
Ru_{lk} unit cost of recovery in DC k from customer l
f_j fixed cost for operating manufacturer j
g_k fixed cost for operating DC k
h_m fixed cost for operating dismantler m
φ fixed cost for landfilling per unit

Variables

x_{ij} Quantity produced at manufacturer j using raw materials from supplier i
y_{jk} Amount shipped from manufacturer j to DC k
z_{kl} Amount shipped from DC k to customer l
o_{km} Amount shipped from DC k to dismantler m
Rd_{mj} Amount shipped from dismantler m to manufacturer j
Rz_{lk} Quantity recovered at DC k from customer l

$$\alpha_j = \begin{cases} 1 & \text{if production takes place at manufacturer j} \\ 0 & \text{otherwise} \end{cases}$$

$$\beta_k = \begin{cases} 1 & \text{if DC k is opened} \\ 0 & \text{otherwise} \end{cases}$$

$$\delta_m = \begin{cases} 1 & \text{if dismantler m is opened} \\ 0 & \text{otherwise} \end{cases}$$

Object function:

$$\min \quad TC = \sum_i \sum_j s_{ij} x_{ij} + \sum_j \sum_k t_{jk} y_{jk} + \sum_k \sum_l u_{kl} z_{kl} + \sum_k \sum_m v_{km} o_{km} + \sum_m \sum_j w_{mj} Rd_{mj}$$
$$+ \sum_l \sum_k Ru_{lk} Rz_{lk} + \sum_j f_j \alpha_j + \sum_k g_k \beta_k + \sum_m h_m \delta_m + \varphi \sum_m \left\lfloor pl_m \sum_k o_{km} \right\rfloor \qquad (1)$$

Subject to

$$\sum_j x_{ij} \le a_i, \qquad \forall \text{i} \qquad (2)$$

$$\sum_k y_{jk} \le b_j \alpha_j, \qquad \forall j \qquad (3)$$

$$\sum_l z_{kl} + \sum_m o_{km} \le Sc_k \beta_k, \qquad \forall k \qquad (4)$$

$$\sum_m o_{km} \le \lfloor pd_k Sc_k \beta_k \rfloor, \qquad \forall k \quad \lfloor \ \rfloor \text{: floor for Guass'symbol} \qquad (5)$$

$$\sum_j Rd_{mj} + \left\lfloor pl_m \sum_k o_{km} \right\rfloor \le \text{e}_m \delta_m, \qquad \forall m \qquad (6)$$

$$\sum_k Rz_{lk} \ge \left\lceil pc_l \sum_k z_{kl} \right\rceil, \qquad \forall l \quad \lceil \ \rceil \text{: ceiling for Gauss'symbol} \qquad (7)$$

$$\sum_i x_{ij} + \sum_m Rd_{mj} = \sum_k y_{jk}, \qquad \forall j \tag{8}$$

$$\sum_j y_{jk} = \sum_l z_{kl}, \qquad \forall k \tag{9}$$

$$\sum_l Rz_{lk} = \sum_m o_{km}, \qquad \forall k \tag{10}$$

$$\sum_k o_{km} = \sum_j Rd_{mj} + \left\lfloor pl_m \sum_k o_{km} \right\rfloor, \qquad \forall m \tag{11}$$

$$\sum_k z_{kl} \geq d_l, \qquad \forall l \tag{12}$$

$$\alpha_j, \beta_k, \delta_m \in \{0,1\}, \qquad \forall j,k,m \tag{13}$$

$$x_{ij}, y_{jk}, z_{kl}, o_{km}, Rd_{mj}, Rz_{lk} \in N \cup \{0\} \qquad \forall i,j,k,l,m \tag{14}$$

The objective is to minimize the total cost which consists of transportation and operation costs as represented by objective function (1). Constraints (2) and (3) formulate the capacity limitation of suppliers and manufacturers. Constraint (4) represents that the total capacity of DC must be able to cover the gross flows of forward and backward. Constraints (5) and (6) show the capacity limitation in reverse logistics for distribution centers and dismantlers. Constraint (7) explains the relationship between customer recovery and recovery rate. Constraints (8), (9), (10) and (11) guarantee the in-flow equal to out-flow. Constraint (12) restrains that the customer demand must be satisfied. Constraints (13) and (14) represent the binary and integer variables respectively.

3. Two-stage priority based genetic algorithm

In this study, a two-stage priority based GA is developed to solve the problem mentioned above. Since the objective of the CLSC model is to find an appropriate delivery route and delivery flow to minimize the total cost of transportation and facility operation, the proposed GA implements a two-stage encoding and priority based flow allocation to solve this problem.

3.1 The first stage of encoding

The first stage of encoding is to determine the appropriate route. Since this CLSC model has six levels, the chromosome has six sections to represent each level respectively. In each section, the number of genes equals to the product of the number of suppliers and the number of demanders. Totally in a chromosome, the number of genes is $I \times J + J \times K + K \times L + L \times K + K \times M + M \times J$. For simplicity, the first and second section in the chromosome will be taken as an example. Other four sections have the similar principle.

Assuming I=3, J=5, K=2 which means that three suppliers provide materials to five manufacturers, and this five manufacturers will provide finished products to two DCs. Each gene contains a binary number, 1 means the delivery route is used and 0 means not. The chromosome at this stage is shown in the upper part of Fig. 1, and the corresponding delivery route is shown in Fig. 2. Obviously, the first section of the chromosome has 3*5=15 genes: the first five genes represent the situation of supplier one providing materials to manufacturers two and four but not providing materials to manufacturers one, three and five. The second five genes represent supplier two, and the third five genes represent supplier three. The second section of the chromosome has 5*2=10 genes: The first two genes represent the situation of manufacturer one providing finished products to neither of the two DCs, the second two genes represent manufacturer two, and so on.

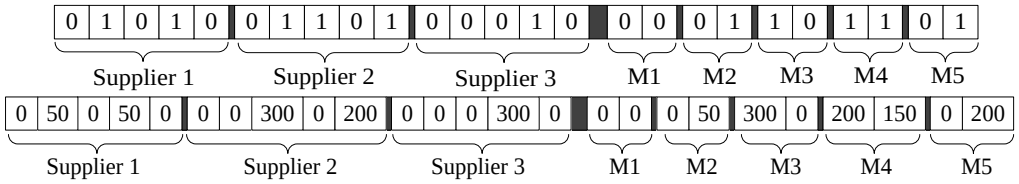

Fig. 1 The first and second section in the chromosome

3.2 The second stage of encoding

After the first stage, a chromosome representing the delivery route has been established, according to this route, the second stage is to decide the delivery flow of materials or products which called generate flow. The lower part of Fig. 1 shows the chromosome after the second stage of encoding.

In this model, the demand of entities in each level must be satisfied, so the process of generate flow actually is the process of allocate the demand flow to different suppliers. In this problem, each delivery route has its own unit shipping cost. The route whose shipping cost is low has the priority to be firstly used for delivery. Since the demand must be satisfied, the flow allocation has to be started at the last stage of the supply chain. That mean, the flow allocation will start at the level of distribution centers delivery to customers.

The process of flow allocation contains four steps:
Step 1 is to find out the lowest unit shipping cost from manufacturers to distribution center one. Step 2 is to compare the supply and the demand, and allocate the transport flow with the small one. Step 3 is to update the corresponding capacity and demand to check whether manufacturer can provide any products. Step 4 is to return to Step 1.

This process can be seen in Fig. 2, and the numbers in parentheses mean the unit shipping cost of that delivery route. The demand of distribution centers and the capacity of suppliers and manufacturers are represented by the numbers in the circles.

4. Numerical examples

To test the proposed two-stage priority based GA, three examples are computed. The dataset are the same with the original paper [8], which is shown in Table 1.

Table 1 Scale of numerical examples

	Suppliers	manufacturers	DCs	Customers	Dismantlers
Basic Scale	3	5	3	4	2
Second Scale	6	10	6	8	4
Third Scale	12	20	12	16	8

4.1 Results and validation of the basic scale problem

After computing with the proposed GA, the results turn out to be the same as the original paper, which is to say, the total cost of the basic scale problem is the same, while the flow delivered among each stage is slightly different. Since this model is a NP hard problem, it is good news to find out another optimal solution. This result can be verified by drawing out this CLSC, which is shown in Fig. 3.

4.2 Results and comparison of all numerical examples

These three scale problems also have been optimized with Lingo 11.0. Table 2 shows the results and the comparison with the results provided by the original paper [8].

Table 2 results and comparison

30 Times each problems		Numerical examples		
		1	2	3
Lingo 8.0 in original paper	Optimal(US$)	29848	58306	114805
	Time(s)	6	13	>1200
Revised ST-GA (population size=100) in original paper	Min-cost(US$)	29848	58368	115866
	[absolute deviation]	[0]	[62]	[1061]
	[standard deviation]	[0]	[0.11%]	[0.92%]
	Ave-cost(US$)	29966.8	58999.6	117524.9
	Ave-time(s)	2.04	6.35	22.49
	[percentage of time]	[34%]	[48.85%]	[<3.74%]
Lingo 11.0	Optimal(US$)	29848	58306	114805
	Time(s)	1	12	>1000
Two stage priority based GA (population size=40)	Min-cost(US$)	29848	58325	115252
	[absolute deviation]	[0]	[19]	[447]
	[standard deviation]	[0]	[0.03%]	[0.39%]
	Ave-cost(US$)	29931.5	58867.8	116865.3
	Ave-time(s)	0.3	2.1	9.6
	[percentage of time]	[30%]	[17.5%]	[<1.92%]

The first half of Table 2 presents the results in the original paper using a PC with Intel® Pentium® M processor 1.86GHz, 1.0G RAM. The remaining part of Table 2 shows the results worked out by the developed GA, using a PC with Intel(R) Core(TM) i7-2600 CPU @ 3.4GHz, 8.0G RAM. From Table 2, it is easy to observe that, whether compared with Lingo or compared with the revised ST-GA in the original paper, the developed GA gave higher quality results with shorter computing time.

5. Conclusions

This paper studied a six-level CLSC model which can be formulated into an integer linear programming model. For the small scale of this model, it can be solved by LINGO. However, the complexity of this model grows with the scale of it, for the larger one, LINGO cannot solve it within an acceptable period of time. Wang and Hsu [8] proposed a spanning-tree based GA to solve it. In this paper, a two-stage priority based GA has been developed to improve the solution of the same model. Three numerical examples which have the same dataset as Wang and Hsu's experiment have been implemented [8], and the results show that, this newly developed algorithm can achieve reliable and higher quality solution with shorter computing time.

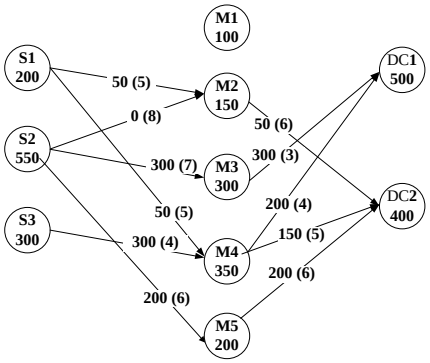

Fig. 2 Result of the illustrative case

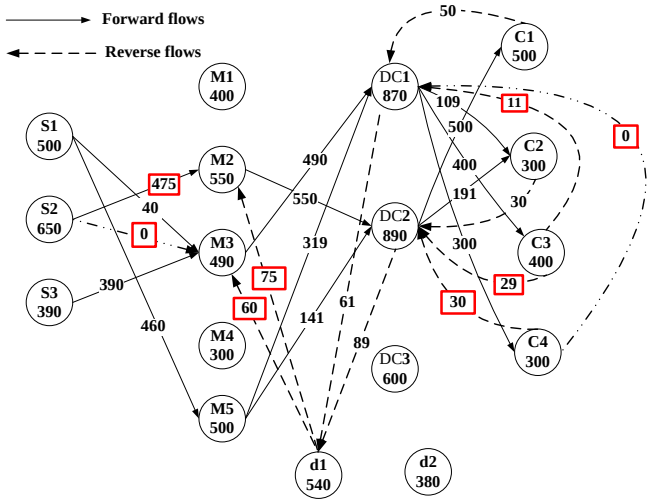

Fig. 3 Result of the basic scale problem

Acknowledgment

The authors would like to thank The Hong Kong Polytechnic University Research Committee for the financial and technical support.

6. References

[1] Guide, V. and L.N. Van Wassenhove, The Evolution of Closed-Loop Supply Chain Research. *Operations Research, 2009. 57(1): p. 10-18.*

[2] Barros, A.I., R. Dekker and V. Scholten, A two-level network for recycling sand: A case study. *European Journal of Operational Research, 1998. 110(2): p. 199-214.*

[3] Sheu, J.B., Y.H. Chou and C.C. Hu, An integrated logistics operational model for green-supply chain management. *Transportation Research Part E-Logistics and Transportation Review, 2005. 41(4): p. 287-313.*

[4] Paksoy, T., T. Bektas and E. Ozceylan, Operational and environmental performance measures in a multi-product closed-loop supply chain. *Transportation Research Part E-Logistics and Transportation Review,* 2011. 47(4): p. 532-546.

[5] Ozkir, V. and H. Basligil, Modelling product-recovery processes in closed-loop supply-chain network design. *International Journal of Production Research, 2012. 50(8): p. 2218-2233*.

[6] Yang, G.F., Z.P. Wang and X.Q. Li, The optimization of the closed-loop supply chain network. *Transportation Research Part E-Logistics and Transportation Review,* 2009. 45(1): p. 16-28.

[7] Shi, J.M., G.Q. Zhang and J.C. Sha, Optimal production and pricing policy for a closed loop system. *Resources Conservation and Recycling, 2011. 55(6SI): p. 639-647.*

[8] Wang, H.F. and H.W. Hsu, A closed-loop logistic model with a spanning-tree based genetic algorithm. *Computers & Operations Research, 2010. 37(2): p. 376-389.*

[9] Kannan, G., P. Sasikumar and K. Devika, A genetic algorithm approach for solving a closed loop supply chain model: A case of battery recycling. *Applied Mathematical Modeling, 2010. 34(3): p. 655-670.*

Engineering III

Pullman Bangkok King Power, 2F Meeting Room GAMMA

2013/1/27 Sunday 10:30-12:00

Session Chair: Ramli Nazir

E226
Constantly Usable Self-Rechargeable Generator embedded in Cellular Phone
Se Myung Park | *Yeungnam University*
Su Jeong Lee | *Yeungnam University*
Jin Ho Kim | *Yeungnam University*
Ji Hyun Choi | *Yeungnam University*
Ki Bum Lee | *Yeungnam University*

E177
Strength Characteristics of Sustainable Concrete with Cement Partially Replaced by Malaysian Clay
Noor Faisal bin | *Abas Universiti Sains Malaysia*
Zakariah Abd | *Ghani Institut Pendidikan Guru*

E168
Ground Improvement Work On Soft Soil At Universiti Tun Hussein Onn, Johor, Malaysia.
Ramli Nazir | *Universiti Teknologi Malaysia*
Ismail A. Rahman | *Public Works Department Malaysia, Kuala Lumpur*

E236
Estimation of Mechanical Properties of Thermal Barrier Coating measured by Nano-Indentation
In Hwan Shin | *Sung Kyun Kwan University*
Chang Sung Seok | *Sung Kyun Kwan University*
Jae Mean Koo | *Sung Kyun Kwan University*
SungHo Yang | *KPS Gas Turbine Technology Service Center*

E248
Secure and Reliable Satellite-based Tracking System for Emergency Management
Jyri Rajamäki | *Laurea University of Applied Sciences*
Pasi Kämppi | *Laurea University of Applied Sciences*

E226

Constantly Usable Self-Rechargeable Generator embedded in Cellular Phone

Se Myung Park
Department of Mechanical Engineering, Yeungnam University,
Gyeongsan, Gyongbuk 712-749, Korea
parksemyung@ynu.ac.kr

Su Jeong Lee
Department of Mechanical Engineering, Yeungnam University,
Gyeongsan, Gyongbuk 712-749, Korea
leesujeong@ynu.ac.kr

Jin Ho Kim
Department of Mechanical Engineering, Yeungnam University,
Gyeongsan, Gyongbuk 712-749, Korea
jinho@ynu.ac.kr

Ji Hyun Choi
Department of Mechanical Engineering, Yeungnam University,
Gyeongsan, Gyongbuk 712-749, Korea
Jihyun.m.choi@gmail.com

Ki Bum Lee
Department of Mechanical Engineering, Yeungnam University,
Gyeongsan, Gyongbuk 712-749, Korea
Bumbum@ynu.ac.kr

The corresponding author: Jin Ho Kim

Abstract

The development of information industry and technologies is accelerated in today's society. Similarly, cellular phone of modern people's necessity is developed gradually from simple telecommunication terminal equipment to multimedia equipment. The development of technologies makes to increase battery capacity. Although battery capacity is increased, the available time of rechargeable battery is getting shorter by increasing usage of the cellular phone. Therefore, we propose a tubular type permanent magnet linear self-generator embedded in cellular phone to correct the flaw. The characteristics of the proposed generator are investigated by analysis using electromagnetic analysis software, 'MAXWELL'. The linear self-generator enables you to charge phone by shaking and working motion in our daily life. In case of walking motion, amplitude of magnet is too small to use generator. So we need to increase amplitude of

magnet by using resonance in walking motion. We are expecting constantly usable possibility by charging through working motion in many environments.
Keyword: Tubular Linear generator, Electromagnetic force, Load analysis,
Resonance, Base excitation

1. Introduction

The development of information industry and technologies is accelerated in today's society. Similarly, cellular phone of modern people's necessity is developed gradually from simple telecommunication terminal equipment to multimedia equipment that is made available various functions such as web surfing and even excitement and fun. The performance of cellular phone should be improved, and the battery capacity should be increased. The development of technologies makes to improve the performance of cellular phone and to increase battery capacity. Although battery capacity is increased, the available time of rechargeable battery is getting shorter by increasing usage of the cellular phone. Accordingly, cellular phone users may have experienced inconvenience that users cannot use original function of cellular phone such as communication with others due to battery discharge.

In order to solve such an inconvenience, small and medium-sized self-generators for battery charging in emergency have been developed among academies [1][2][3]. As most of these generators are energy conversion devices utilizing human biomechanical energy generated from human activity, researches on the characteristics of human energy are needed and have been conducted [4].

Now, one of the most representative device in early devices is now commercializing, which converts kinetic energy derived from human biomechanical energy into electric energy by using external linear generator, and can recharge the battery of cellular phone. However, this external type generator always should be detached from cellular phone and carried for the purpose of recharging battery, because it is impossible to build inside of cellular phone due to its relatively large size. Thus, this device has disadvantages when considering user's convenience and constant recharging the battery.

In this research, in order to overcome the drawbacks of above-mentioned external type generator, we develop an internal type linear generator for self-recharging the battery of cellular phone. The proposed internal type linear generator need not to carry separately and can recharge the battery constantly as converting kinetic energy from walking motion of user into electric energy, because it is small enough to install inside of cellular phone. Also, In case of emergency such as full-discharge of the battery, the proposed device will generate enough charge to enable them to complete a quick phone call after the user shakes the device up a bit.

In general, linear electrical generator can be divided into two types such as TPMLG(Tubular type Permanent Magnet Linear Generator) and FPMLG(Flat type Permanent Magnet Linear Generator). TPMLG type has simple structure and structural stability, it has the merit of

producing less vertical force which tends to prevent the slider of the linear generator from vibrating vertically [5].

Accordingly, we introduce a TPMLG which is built inside of cellular phone to overcome the drawbacks of FPMLG. Also, in order to satisfy the DC voltage 4.2[V] which is minimum requirement for recharging battery in the case of shaking motion and even walking motion, we can get enough amplitude to use generator in walking motion by using mechanical resonance. Lastly, the load-analysis is applied to verify the electrical performance of newly designed linear generator through commercial electromagnetic analysis software, MAXWELL.

2. Linear Electric Generator

2.1 The Structure of Linear Electric Generator (LEG)

Fig. 1 shows the cross-sectional diagram of newly proposed linear electric generator.

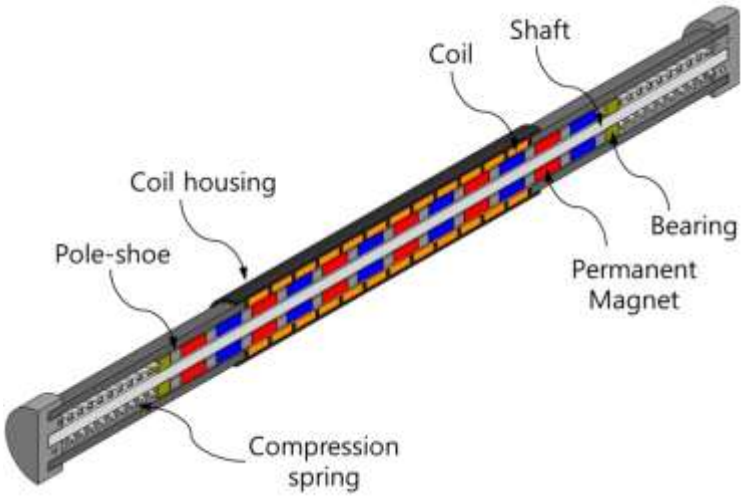

Fig. 1 Cross-sectional diagram of the proposed linear generator

The LEG is composed of two main parts of slider and stator. The slider includes 13 cores and a combination of axially magnetized permanent magnet between cores. The permanent magnets are arranged with halbach array method that increase flux linkage. The steel bar, get through magnet center, ties up magnets and cores. The steel bar is called pole shoes and serves as conductors of the magnetic flux. The stator consists of coil, coil housing. Also, coil winding is formed by several 2-pole 3-phase formations. The rest of device is two springs and linear ball-bush on the ends of the slider and casing for the overall parts.

Fig. 2 shows how to work the linear generator.

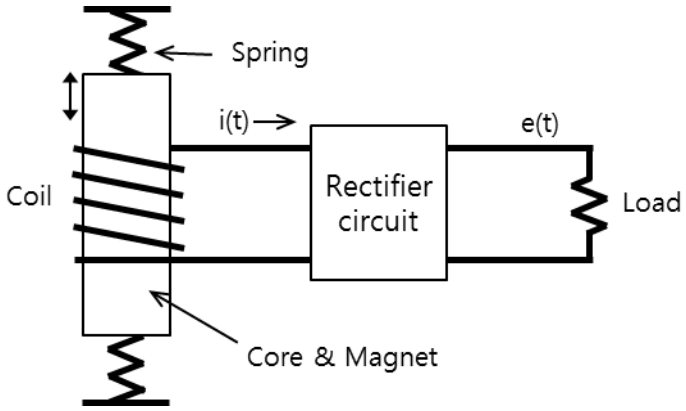

Fig. 2 Conceptual diagram of the linear generator

Up & down motion of the slider changes magnetic flux density in coil. And the change of magnetic flux density generates induced current by Faraday's law. The amount of Electro Motive Force (EMF) is calculated by Faraday's law and can be expressed by the following equation (1).

$$\mathbf{e}_{EMF} = \mathbf{\imath} N \frac{d\varphi}{dz}\frac{dz}{dt} \tag{1}$$

where N is the number of turns per coil, φ is the magnetic flux passing in each turn in real time t, dz/dt is speed of the slider, and z is the distance along z-direction. So, the EMF is proportional to the speed of the slider, the number of coil turns and the amount of flux, which interlinks to the solenoid.[4]

2.2 Vibration Characteristic Analysis of the Linear Electric Generator

In order to verify the vibration characteristics of the linear generator, we supposed it as a base excitation.

Fig.3 shows mathematical modeling of linear generator.

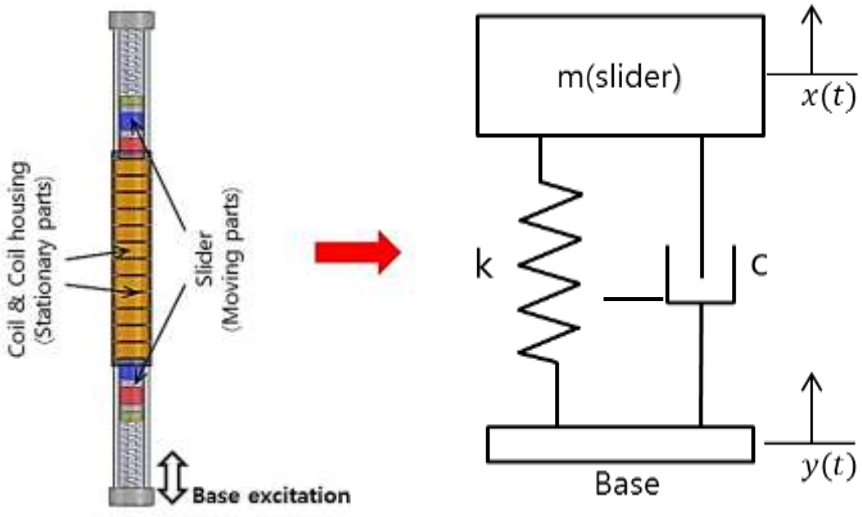

(a) (b)

Fig. 3 Mathematical modeling of linear generator

In Fig. 3(b), we assumed that stationary parts are base structure and moving parts are slider. The displacement of the base and slider is denoted $\mathbf{y(t)}$ and $\mathbf{x(t)}$.
The application of Newton's second law of motion to the system gives the equation of motion as below (2).

(2)

The walking and shaking motion are reciprocating action. Then, $\mathbf{y(t)}$ is supposed as $\mathbf{y}\sin\omega_b t$.
So, amplitude of $\mathbf{x(t)}$ is calculated as below equation (3).
The frequency of walking motion is in the range of 1.8 Hz to 2.2 Hz. Also, the shaking frequency is in the range of 3.0 Hz to 3.3 Hz.

$$, \quad r = \frac{\omega_n}{\omega_b}$$

ω_n : Natural frequency
ω_b : Base excitation frequency (3)

In case of walking motion, amplitude of magnet is too small to use generator. But in case of shaking motion, amplitude is enough. So we need to increase amplitude of magnet in walking motion.

If exciting frequency is resonance frequency; resonance, exciting force is accumulated and exciting object has too large amplitude. By using mechanical resonance, we can get enough amplitude to use generator in walking motion.
Fig.4 shows displacement ratio of X/Y.

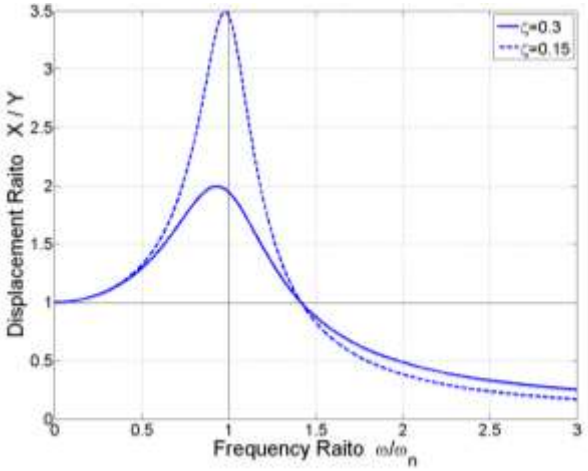

Fig. 4 Displacement Ratio (Input Y & Output X)

Increasing damping ratio is 0.15 to 0.3, amplitude is gradually lower in fig.4. So, damping value is modified low to get high amplitude.

3. The Simulation Result of LEG

We simulated our proposed generator using MAXWELL. The load of generator is 1mA constant current source. And excitation frequency is 2.2Hz.

Fig. 7 shows the induced generated voltage versus time at input frequency 2.2Hz. Fig. 7(a) is 3-phase result and Fig. 7(b) is 6-phase result.

In figure, the settling voltage is approximated 4.5V. This value is larger than 4.3V, lithium ion Battery charging voltage. So, proposed generator makes possible to charge Li-ion battery in 1mA current. However, both cases have about 1.1V ripple voltage at 4.4Hz frequency. This ripple voltage is 2 times of excitation frequency because rectifier circuit makes double frequency of excitation frequency. Reducing ripple voltage, external filter must be used. But, the ripple voltage has too low frequency. So, if we use passive filter, the filter size becomes too large. To resolve this problem, we apply 'Low Drop Out voltage regulator (LDO)'.

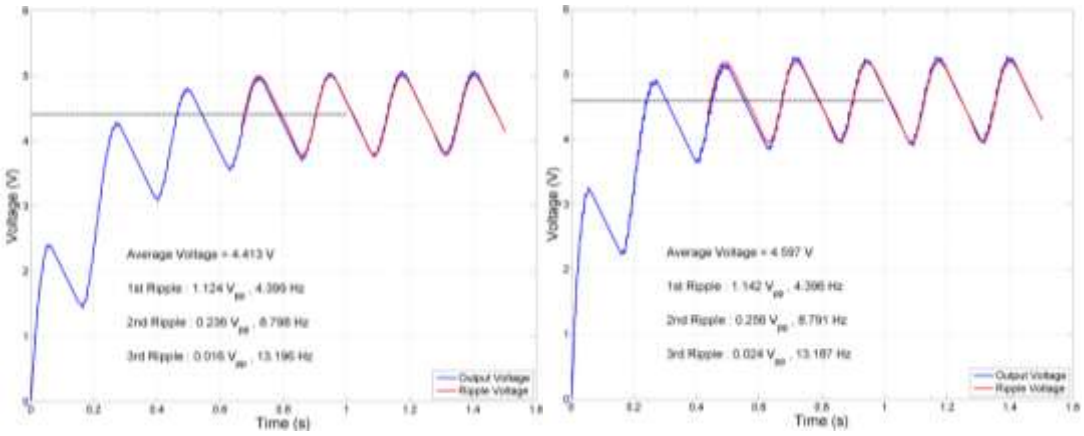

(a) (b)

Fig. 7 Induced EMF (Input frequency 2.2Hz)

In figure, the settling voltage is approximated 4.5V. This value is larger than 4.3V, lithium ion Battery charging voltage. So, proposed generator makes possible to charge Li-ion battery in 1mA current. However, both cases have about 1.1V ripple voltage at 4.4Hz frequency. This ripple voltage is 2 times of excitation frequency because rectifier circuit makes double frequency of excitation frequency. Reducing ripple voltage, external filter must be used. But, the ripple voltage has too low frequency. So, if we use passive filter, the filter size becomes too large. To resolve this problem, we apply 'Low Drop Out voltage regulator (LDO)'.

4. Conclusions

In this paper, we proposed internal type small linear electric generator. The linear electric generator was mathematically modeled the base excitation. We increased amplitude of magnet in working motion by using resonance for constantly usable linear generator. Also, the output voltage of sine waves is changed DC voltage by applying rectifier circuit that consists of diodes and capacitor. In simulation result, generated voltage in 1mA current is about 4.5V, larger than 4.3V Li-ion battery charging voltage. The result also show that the possibility for recharging the battery at walking motion.

5. Acknowledgment

This work (Grants No. 00045555) was supported by Business for Cooperative R&D between Industry, Academy, and Research Institute funded Korea Small and Medium Business Administration in 2011.

6. References

[1] Sang-Yong Jung; Ho-Yong Choi; Hyun-Kyo Jung; Yang-Seung Choi; Kyu-Man Choi, 2001 " Performance evaluation of permanent magnet linear generator for charging the battery of mobile apparatus", *Electric Machines and Drives Conference, IEMDC*, pp. 516-521

[2] L.I. ANATYCHUK, V.YA. MYKHAILOVSKY, L.T. STRUTYNSKA, 2011 "Self-Contained Thermoelectric Generator for Cell Phones", *Journal of ELECTRONIC MATERIALS*, Vol. 40, No.5, p.p 1119-1123

[3] Ruellan, M.; Turrim S.;Ahmed, H.B.; Multon, B. 2005, "Electromagnetic resonant generator", Industry Applications Conference, IAS, Vol.3, p.p. 1540-1547

[4] T. Matsushita, M. Sanada, S. Morimoto, and Y. Takeda, 2005 "Study of the Configuration and the Magnetic Pole Pitch of the Linear Generator for Wave Power Generation", *IEEJ Trans*, Vol. 5, No. 069, pp. 83-84

[5] Gwon O-Chang, Kim Ji-Hyun, Jang Ki-Bong, Kim Gyu-Tak, 2009 "The Design of Tubular type Permanent Magnet Linear Synchronous Generator for wave power generation", *KIEE conference*, pp. 79-81

E177

Strength Characteristics of Sustainable Concrete with Cement Partially Replaced by Malaysian Clay

Noor Faisal bin Abas,
Universiti Sains Malaysia, Pulau Pinang, Malaysia,
nfaisal@usm.my

Zakariah Abd. Ghani
Institut Pendidikan Guru, Kampus Sultan Abdul Halim, Malaysia
zag_5737@yahoo.com

Abstract
The use of pozzolanic materials as admixtures in partial replacement of Portland cement in mortars and concrete increased significantly in the last 20 years. Some pozzolanic materials, such as silica fume, fly ash, and rice husk ash, are by-products of industrial and agro industrial processes, which further contribute to reduce both environmental and economical problems that would be associated with their disposal. The study has been taken to investigate the engineering properties of concrete with partial cement replacement of Malaysian raw clay. Five different concrete design mix by replacing the cement content with raw clay of labu sayong in the ratio 5%, 10%, 15% and 20%. The concrete grade 50 was designed in this study as a control mix. The study shows that, replacing cement in the range of 5% to 20% with raw clay result in increasing the long term development of compressive and flexural strength. The design mix of 5% replacement of cement with raw clay has the highest compressive strength at the all age of specimen compared with the other mix.

Keywords: Pozzolanic material, Environmental problems, Cement replacement, Compressive strength, Flexural strength.

1. Introduction

The world is now more concerned about the pollution occurred. Many agencies are increasingly concerned over the environmental quality in the world. This awareness is also felt in the construction industry. For example, an architect board has introduced the index of green building (GBI) as a way to reduce the greenhouse effect in the design and use of building materials for the building. This awareness also has led many researchers to carry out research to produce new building materials that's more environmentally friendly. One of building materials to receive serious attention in the research study is concrete.

The main ingredient in the production of concrete is cement. Production of cement by the cement factory plant has contributed many environmental pollutants. T. W. Bremner on his thesis of environmental aspects of concrete was stated that there is a numbers of environmental problems come from cement industries such as carbon dioxide (CO2) emissions, nitrous oxide emissions, noise pollution, water pollution and particulate air emissions. The carbon dioxide and nitrous

oxide are among the greenhouse gases. The emission of these two gases to the atmosphere will cause the greenhouse effect to our earth.

Rationally, there are 2 simple solutions for the all environmental problem above. Firstly is by reducing the production of cement and secondly is by replacing the cement content in concrete with viable alternatives where is possible. However, it seems impossible for the cement manufacturers to reduce their total production of cement because the cement demand is increasing every year. This method may not be agreed upon by most of the cement as it will impact the amount of their income. Therefore, the method of replacement of cement with other substances that have characteristics similar or almost similar to the characteristics of cement is seen as the most effective solution for manufacturers of cement.

Many studies have been conducted by the researchers in the past 2 or 3 decade to utilize effectively wastes material and find a suitable alternative for partial cement replacement in concrete without decreasing the strength and durability of the conventional concrete. The use of waste material as partial replacement of cement in concrete also can preserve the environment and get to solve problems of waste disposal from industry.

The use of pozzolanic materials as admixtures in partial replacement of Portland cement in mortars and concrete increased significantly in the last 20 years. The name of pozzolan was taken in conjunction with the name of the village, Pozzuoli, near Napoli in Italy (Sersale, 1958 cited in Kitsopoulos, 1996, p. 576). Some pozzolanic materials, such as silica fume, fly ash, and rice husk ash, are by-products of industrial and agro industrial processes, which further contribute to reduce both environmental and economical problems that would be associated with their disposal (G. C. Cordeiro, 2008).

Metakaolin is one of the examples of pozzolanic material. It is obtained from calcining the kaolin (clay) within the certain temperature. Thermal activation of clay minerals between 600–900 °C by dehydroxylation leads to the breaking down or partial break down of the structure forming a transition phase with high reactivity (Ambroise et al., 1986 and Sayanam et al., 1989 cited in R. Siddique, 2009, p. 393). Metakaolin is poorly crystallized transition phase obtained by calcining kaolin in the temperature range 700 – 800 °C (M. Murat, 1983 and J. Ambroise, 1989 cited in Ambroise et al., 1994, p. 161)

The mechanical properties of concrete with partial cement replacement with metakaolin were improved compared to the normal concrete using 100% ordinary Portland cement. The previous research has reported, the compressive strength of concrete will increased by replacing 5% to 15% weight of cement with metakaolin. C. –S. Poon et al. 2001 was reported that the cement pastes containing 5% to 20% metakaolin had higher compressive strength than the control at all ages of test.

The use of metakaolin from different origin also will affect the performance of the concrete. The clay from the different resources had a different chemical content. It is one of the reasons why the concrete with partial cement replacement of cement with metakaolin from different origin had different compressive strength. F. Curcio et al., 1998 in the research on metakaolin as pozzolanic microfiller for high performance mortars was using the four different origin of

metakaolin. He found that the use of metakaolin from the different origin at the similar percentage replacement will contribute the different compressive strength. Based on the above reason, this paper will discuss the mechanical properties of concrete with partial cement replacement with raw clay of labu sayong. The aims of this paper are to study the compressive strength and flexural strength of concrete containing partial cement replacement of raw clay of labu sayong.

2. Methodology

2.1 Material used

ASTM Type I ordinary Portland cement was used in all concrete mixtures. Mineral admixture that was used in this research is raw clay, in the form of yellowish powder, collected from the area of Sayong, Perak. The chemical composition of ordinary Portland cement and raw clay is given in Table 1

Table 1: Chemical composition of cement and mineral admixture

Chemical composition %	formula	Portland cement type 1	Raw clay
Silicon dioxide	SiO2	20.90	53.40
Aluminum oxide	Al2O3	4.76	27.78
Iron oxide	Fe2O3	3.41	2.16
Calcium oxide	CaO	65.41	0.11
Magnesium oxide	MgO	1.25	0.12
Sulphur trioxide	SO3	2.71	0.13
SiO2 + Al2O3 + Fe2O3		**-**	**83.34**

The coarse aggregate used in this study is the locally available aggregate with nominal size greater than 5.00mm and less than 20.00mm. The fine aggregate which is used in the concrete mix for this research is from river sand. The range size of the river sand particles used in concrete mix design is around 5 mm below. Sieve analysis test is done according to the British standard specification BS 882: 1982 and that is with the sieve size of between 5 mm to 0.15 mm.

2.2 Sample preparation

The concrete specimens were prepared in this study. The concrete grade 50 (the compressive strength at 28 days is >50 N/mm²) is used as the control specimen. Than the concrete with raw clay of labu sayong as a partial cement replacement in different ratio namely C2 (5%), C3 (10%), C4 (15%), and C5 (20%) were prepared. The mix proportions of the concrete are shown in Table 2 below.

Table 2: mix proportion of concrete

Sample name	Concrete grade (N/mm²)	w/c ratio	w/b ratio	Mix proportion kg/m³					
				Portland cement	Aggregate		Admixture	Water (w/c + w/b)	Super plasticizer
					Course	Fine	Raw		

							clay		
C1	50	0.44	-	477.00	959.28	753.72	-	210	4.77
C2	50	0.44	0.61	453.15	959.28	753.72	23.85	224.55	4.53
C3	50	0.44	0.61	429.30	959.28	753.72	47.70	239.10	4.29
C4	50	0.44	0.61	405.45	959.28	753.72	71.55	253.65	4.05
C5	50	0.44	0.61	381.60	959.28	753.72	95.40	268.19	3.82

2.3 Experimental program

a. *Compressive Strength*

Concrete cube with dimension 100 x 100 x 100mm was used to determine the compressive strength. The concrete were casting using Portland cement with partial cement replacement of raw clay at 5%, 10%, 15%, and 20%.the specimens were vibrated using vibrator table to assist the compaction. The concrete samples were demoulded after 24 hours (1 day) casting and cured in water until the testing age. The compressive strength of all concrete specimens was determined at ages of 3, 7, 14, 28 and 60 days. Three cubes were used for each test.

b. *Flexural Strength*

Concrete prism with dimension 100 x 100 x 500mm was used to determine the flexural strength. The concrete were casting using Portland cement with partial cement replacement of raw clay at 5%, 10%, 15%, and 20%.the specimens were vibrated using vibrator table to assist compaction. The concrete samples were demoulded after 24 hours (1 day) casting and cured in water until the testing age. The compressive strength of all concrete specimens was determined at ages of 3, 7, 14, 28 and 60 days. Three cubes were used for each test.

3. result and discussion

The result of compressive strength test of concrete with partial cement replacement of raw clay was shown in Figure 1. The value of compressive strength is the average value of three cubes for each age. Figures 1 show that the compressive strength of concrete with 5% replacement of cement with raw clay (C2) has highest result. The compressive strength increased 74.34%, increased 41.20%, increased 47.03%, increased 50.67% and increased 52.29% respectively at 3 days, 7 days, 14 days, 28 days and 60 days of specimen ages.

The development strength of C3 (concrete with 10% replacement of raw clay) is slightly below the control mix for the early age of curing, but it is become higher than the control mix after 28 days of curing. At the age of 60 days, the compressive strength of C3 is 23.36% higher than the control mix. While the C4 and C5 compressive strength are below the compressive strength of control mix at every age of specimen. However, the different of strength are decreasing when the age of specimen increase. The C4 mix (concrete with 15% replacement of raw clay) has slightly the same strength with the control mix.

Based on the figure 1 below, it looks like the concrete with replacement 5% to 20% of cement with raw clay will become same or maybe higher than the control mix strength when the age of specimen increased. The graph of C3 to C5 is still increased while the C1 was start decreased or remain constant after the age of 60 days.

Figure 1: Compressive strength of concrete grade 50 (N/mm^2)

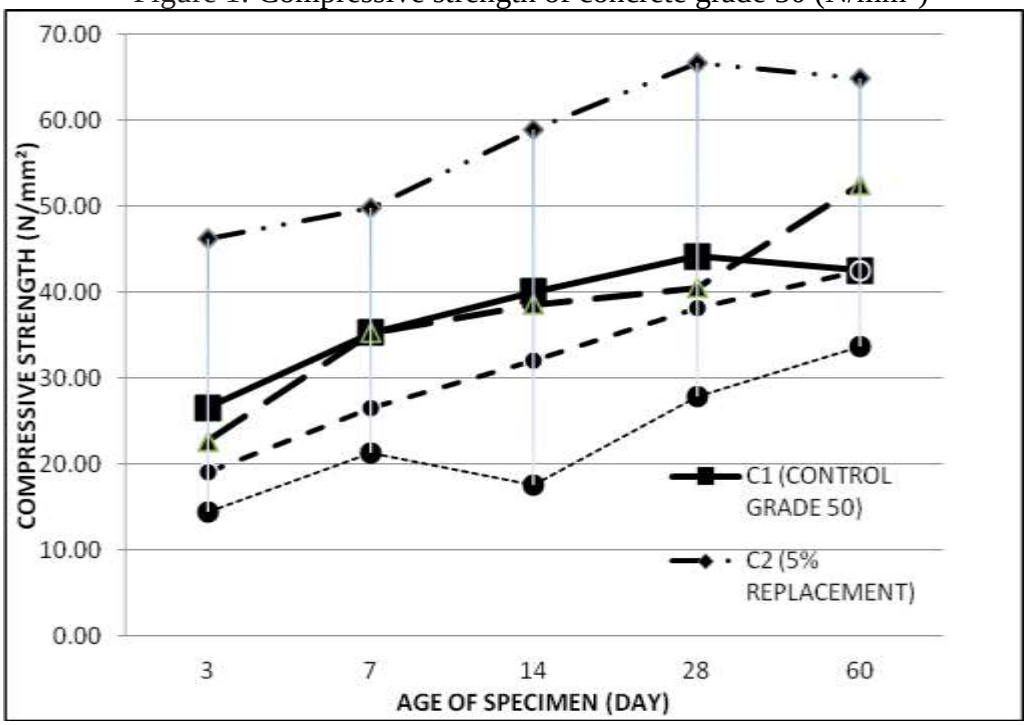

The result of flexural strength test of concrete with partial cement replacement of raw clay was shown in Figure 2. The value of flexural strength is the average value of two prisms for each age of specimen. From the result below, the average flexural strength varies from 2.20 to 5.47 N/mm^2. Figure 2 show that the distributions of flexural strength of concrete with replacement 5% to 20% of cement with raw clay are inconsistent at the early age of specimen compared the control mix. However, the flexural strength was more consistent at the age of 28days and above. C2 show the highest development of flexural strength compared to the other mixes. At the age of 60 days, C2 has exceeding 21.56% of control mix strength.

The C3, C4, and C5 mixes however still have the lower flexural strength than the control mix. Even the flexural strength still lower than control, but the strength is indirectly perpendicular with the age of specimen increase. That means when the age of specimen increase, the different of strength between the C3, C4, and C5 with the control mix decrease. Besides, the C2, C3, C4, and C5 shows that their strength will still increase after the 60 days curing period while the control mix does not show that it will be increased in strength after 60 days.

Figure 2: flexural strength of concrete grade 50 (N/mm^2)

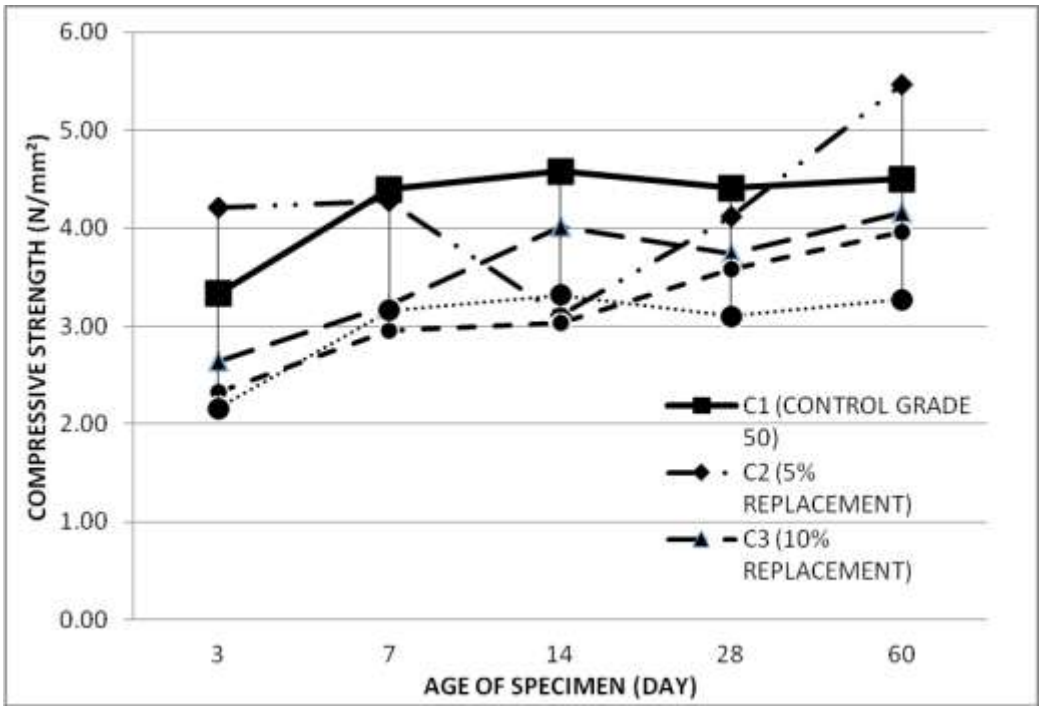

4. Conclusion

Based on the results indicate that, an increase of compressive strength and flexural strength of concrete is definitely noticed with the addition of mineral admixtures (raw clay of labu sayong). The result also show that, by replacing 5% t0 15% of cement with raw clay will increasing the long term strength development of compressive and flexural strength. Thus, it will improve the engineering properties of the concrete. The concrete with 5% replacement of cement with raw clay has the highest compressive strength at all the age of specimen.

5. REFERENCES

[1] Bremner, T. W. (2001). Environmental Aspects of Concrete: Problem And Solutions . *1st All – Russian Conference on Concrete and Reinforced Concrete*. 9 – 14 September 2001.

[2] Heulandite and mordenite – rich tuffs from Greece: a potential source for pozzolanic materials.

[3] Cordeiro, G. C. Filho, R. D. T. Tavares, L. M. Fairbairn, E. M. R. , (2009) Ultrafine Grinding of Sugar Cane Bagasse Ash for Application as Pozzolanic Admixture In Concrete. *Cement and Concrete Research.* (39), pp. 110–115.

[4] Ambroise, J. Maximilien, S. Pera, J., 1994. Properties of metakaolin blended cement. Advanced Cement Based Materials (1), pp. 161 – 168.

[5] Siddique, R. Klaus, J., 2008. Influence of metakaolin on the properties of mortar and concrete: A review. Applied Clay Science, (43), pp. 392 – 400.

[6] Rate of pozzolanic reaction of metakaolin in high-performance cement pastes.

[7] Curcio, F. DeAngelis, B.A. Pagliolico, S., 1998. Metakaolin as a pozzolanic microfiller for high-performance mortars. *Cement and Concrete Research*. 28, (6), pp. 803–809.

E168

Ground Improvement Work On Soft Soil At Universiti Tun Hussein Onn, Johor, Malaysia.

Ir. Ramli Nazir, Phd, Assoc. Professor.
Faculty of Civil Engineering, Universiti Teknologi Malaysia,
81300 Skudai, Johor, Malaysia
ramlinazir@utm.my

Ir. Ismail A. Rahman, M. Eng. Senior Engineer.
Department of Civil, Structure and Bridge Specialist Work, Public Works Department Malaysia,
Kuala Lumpur.
ismail@jkr.gov.my

The corresponding author: Ir. Ramli Nazir, Phd, Assoc. Professor.

Abstract
The paper presents the history of ground improvement work adopted in the campus development for Universiti Tun Hussein Onn, Batu Pahat, Johor. Due to the limitation of construction cost, ground improvement work is to be limited for roads and parking lot only. 11 numbers of boreholes and 13 numbers of CPT tests were performed to established soil parameters needed for the design works. Excessive long term settlement was the major concern for the area due to the existing of soft soil within the area. In order to minimize the long term settlement, ground treatment would be required. Various ground treatment methods had been assessed and it was decided to use surcharge and Prefabricated Vertical Drain (PVD) method for the soft soil treatment due to its financial value and simplicity in its works. Real time prediction using Asaoka's Observatory Procedure shows a reliable agreement for prediction of settlement in ground improvement works for soft soil.
Keyword: Ground Improvement, Prefabricated Vertical Drain, Simplicity, Financial

1. Introduction

Universiti Teknologi Tun Hussein Onn is located in Parit Raja, about 25km to the east of Batu Pahat Town. The area is considerably flat with existing ground level ranges generally between 1.2m to 2.4m above Sea Level. The construction begins in 2007 within an area of 145 Ha. It comprises of construction for the Library and Chancellery, Faculty of Civil Engineering and Environment, Faculty of Electrical and Electronic Engineering, Faculty of Technology Information and Multimedia, Faculty of Mechanical Engineering and Manufacturing, Faculty of Technical Education and Lecture Hall. The existing area which is to be developed has a Reduce Level varies from +1.4m to +1.8m in the open area. A propose final platform level will be RL 2.5m since flood contributed by Sungai Semberong and Sungai Simpang Kanan was estimated to be at highest level of +2.3m. However as a centre of attraction, the Library building will be placed on a higher level than others at a R.L of +3.5m. The layout plan for the development area is as shown in Figure 1.0.

Figure 1.0 Location of site

2. Subsurface Conditions

Prior to the ground improvement work a site investigation scheme was performed throughout the propose development area. The scheme suggested comprises of 11 boreholes and 13 CPT point with Dissipation test from selected boreholes and CPT point respectively and laboratory test on extracted samples. The laboratory testing includes strength and settlement parameters and also physical testing. The subsoil information from the development area is divided into 3 zones. Base from the overall soil profile cross section i.e:

i) Zone A (Profile BH1,BH2 and BH11)
ii) Zone B (Profile BH8, BH4, BH7)
iii) Zone C (Profile BH5, BH6, BH10)

Generally, the soil layer can be described as below:-

Table 1.0 Generalised Soil Profile

Soil Layer	Description	Ground Level (m RL)	Remark
Layer 1	Very Soft Clay	From **EGL to -20m RL	Existing Highly Compressible soft Alluvial.
Layer 2	Stiff to Very Stiff Clay	From -20m CD to -24m RL	Less compressible. Assume insignificant settlement
Layer 3	Stiff to Very Stiff Silt Clay	From -24m CD to -28m RL	Insignificant settlement
Layer 4	Hard to Very Hard Silt Clay	Below -28m RL	Good bearing Stratum

** EGL at about +1.4m to +1.8m RL.

Water level that has been monitored through boreholes ranged from 0m to 0.5m below the ground surface. The water levels are slightly erratic initially but stabilized during most of the

monitoring period. To minimize the future settlement of the platform for infrastructure such as roads, parking and open area after the completion of the development, subsoil treatment is necessary due to the existence of soft layer within the development area. Figure 2.0 shows a typical cross section of boreholes acquired during the site investigation work.

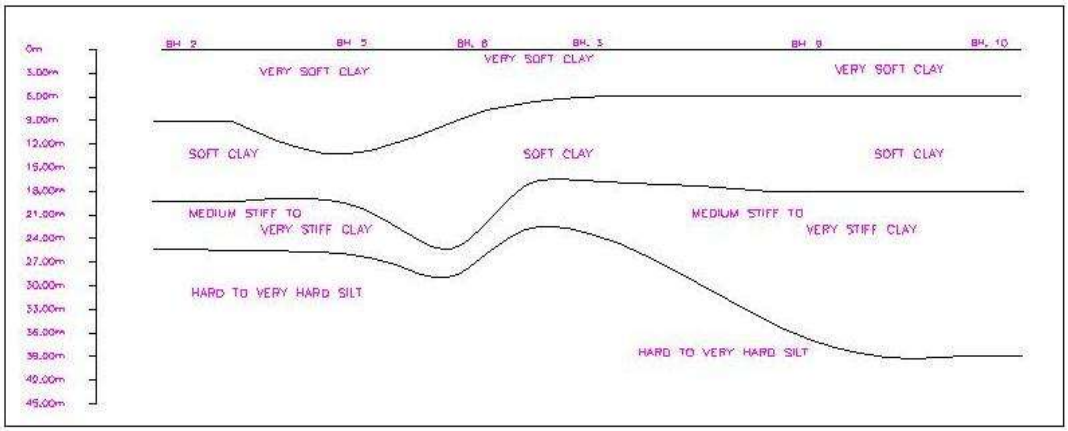

Figure 2.0 : Typical cross section of the area.

3. **Subsoil Treatment Method**

Excessive post construction settlement of the area is the main concern. Various ground treatment methods has been considered. After consideration of time, cost, effectiveness and practicality of various subsoil treatment methods, Surcharge + Vertical Drain was chosen. This method had been used for most of the project in Malaysia that encounter with the soft alluvial deposit. For this project, earth fill surcharge was adopted due to its cost effective compared with other methods. However to accelerate the process of settlement Vertical Drain will be associated with surcharge in order to shortened the drainage path for the process of excess pore pressure dissipation. Sand drains and prefabricated band shape drains are common types of vertical drains.

For this exercise, prefabricated vertical drain (PVD) was adopted. The PVD was installed at 1.5m spacing. With the help of the vertical drains, water within the soft layer not only flows vertically but also flows horizontally to the vertical drains. Thus, the drainage path is significantly shortened. With shorten drainage path and higher horizontal permeability as mention by Hansbo(1979), the consolidation process can be accelerated tremendously. The proposed surcharged and PVD system targeted to treat the subsoil to more than 90% consolidation settlement attributed to permanent loading from platform level of +2.5m. In order to increase the shear strength of the soil base, geogrid system is introduced. The use of geogrid will allow base strengthening on a soft formation and permit embankment construction to take place in a controlled and safe manner. Depending on the design requirement, it can be placed as a single or multiple layer reinforcement at the embankment base to intersect potential failure surfaces extending to the surrounding area. Figure 3 to Figure 4 shows the selected area to undergo ground improvement programme.

Figure 3: Installation of PVD prior to surcharge

Figure 4: Complete Surcharge at Resting Period.

4. Monitoring Programme

Due to the inherent uncertainty of subsoil, it is very difficult to estimate precisely the magnitude of settlement and the rate of settlement of the reclaimed platform especially when only limited numbers of boreholes were made and distributed over large area. Monitoring of the subsoil performance during construction is essential. Geotechnical instruments inclusive of inclinometers, piezometers and settlement markers were installed during the process of reclamation to monitor the subsoil performance. In the monitoring work, readings are taken once a week from the beginning of filling activity until full surcharge load. The instrumentations that have been installed are as follows:

i.	Settlement Plates	-	25	Nos
ii.	VW Piezometer	-	15	Nos
ii.	Magnetic Probe Extensometer	-	2	Nos
iv.	Inclinometer	-	2	Nos
v.	Permanent Datum	-	2	Nos

Results are plotted using measured instrumentation readings such as settlement versus time, pore pressure development versus time and lateral movement versus time. These plots will show the trend or behaviour of the soil related to the soil improvement work. A typical type of instrumentation protective casing is as shown in Figure 5.

Figure 5 : A Typical Instrumentation protective casing installed on the Embankment.

5. Results and Discussions

The results will be discussed into three main criteria:-

1. Embankment Stability
2. Monitoring Evaluation
3. Performance Analysis

5.1 Embankment Stability

Stability analysis need to be performed to ensure that embankment slope will not collapse during the full load application. The specification allows a minimum Factor Of Safety of 1.5 for the embankment. Figure 6(a) shows a deformation occurs at full load. The settlement occurs is 262mm which is within the estimated value of elastic settlement calculated before. The FOS obtained is 1.7 which is more than specified in the work specification. The value is as shown in Figure 11(b). Separator at grade TS30 is used since stability of the embankment is not a critical issue. Zone A was selected for stability analysis since the area is more critical than Zone B and Zone C.

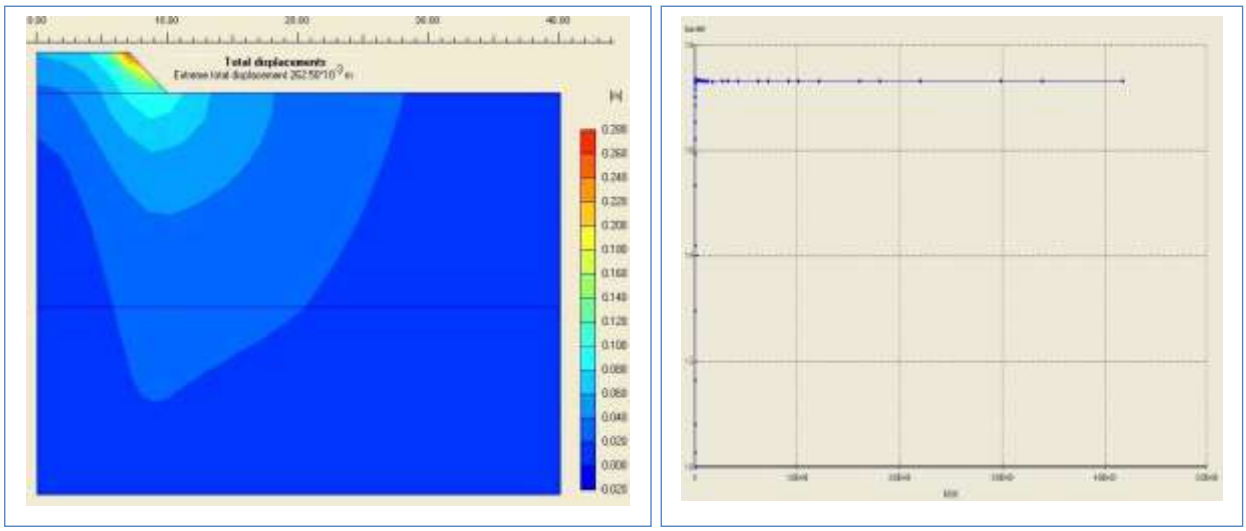

(a) (b)

Figure 6: Slope Deformation and Factor of Safety through Simulation

5.2 Monitoring Evaluation

Due to an assumption on several soil parameters such as coefficient of horizontal consolidation, horizontal permeability and well effect, evaluation base on theoretical or prescriptive value will be used as guidance in obtaining the magnitude of related ground improvement. To ensure the real time performance of the ground improvement, instrumentations were installed and monitored. Monitoring was done once a week. It should be noted that from the specification provided, the residual settlement should be limited to a maximum of 100mm within 5 years post construction period. Figure 7(a) and Figure 7(b) shows a typical result obtained from monitoring Magnetic Extensometer and Pressuremeter respectively. Inclinometer that is used to detect movement of the embankment toe is plotted as shown in Figure 8. While a typical plots of settlement plate is as shown in Figure 9. Based on the measured field data, back analysis to verify the design assumptions and to predict the total primary consolidation settlement can be carried out. Although back analysis always involves a number of simplifying assumptions which may compromise the reliability of the compute values, Asaoka (1978) had applied his back analysis method successfully based on field settlement observation using simple graphical procedures. In this procedure the settlement analysis was employed using the latter method.

5.3 Performance Analyses

The final stage of evaluating the instrumentation reading is to provide performance analyses base on its settlement and embankment stability. Throughout the resting period, the data was acquired and it will be terminated whenever readings obtained from settlement plate are constant for a minimum of three consecutive readings or by observing the piezometer readings and extensometer readings.

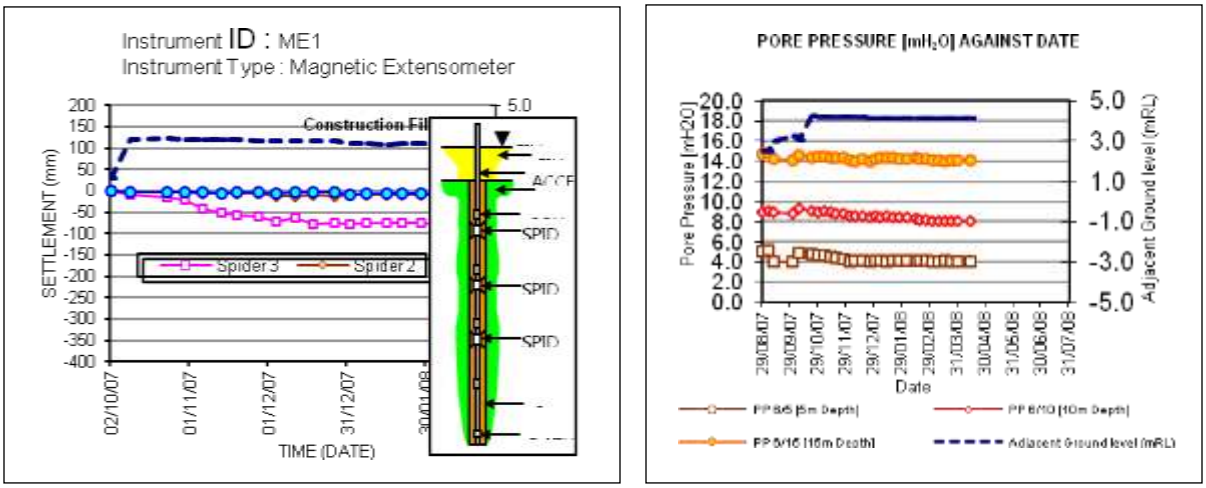

(a) (b)

Figure 7: Typical reading for Magnetic extensometer (a) and Menard Pressuremeter installed in pre bore hole.

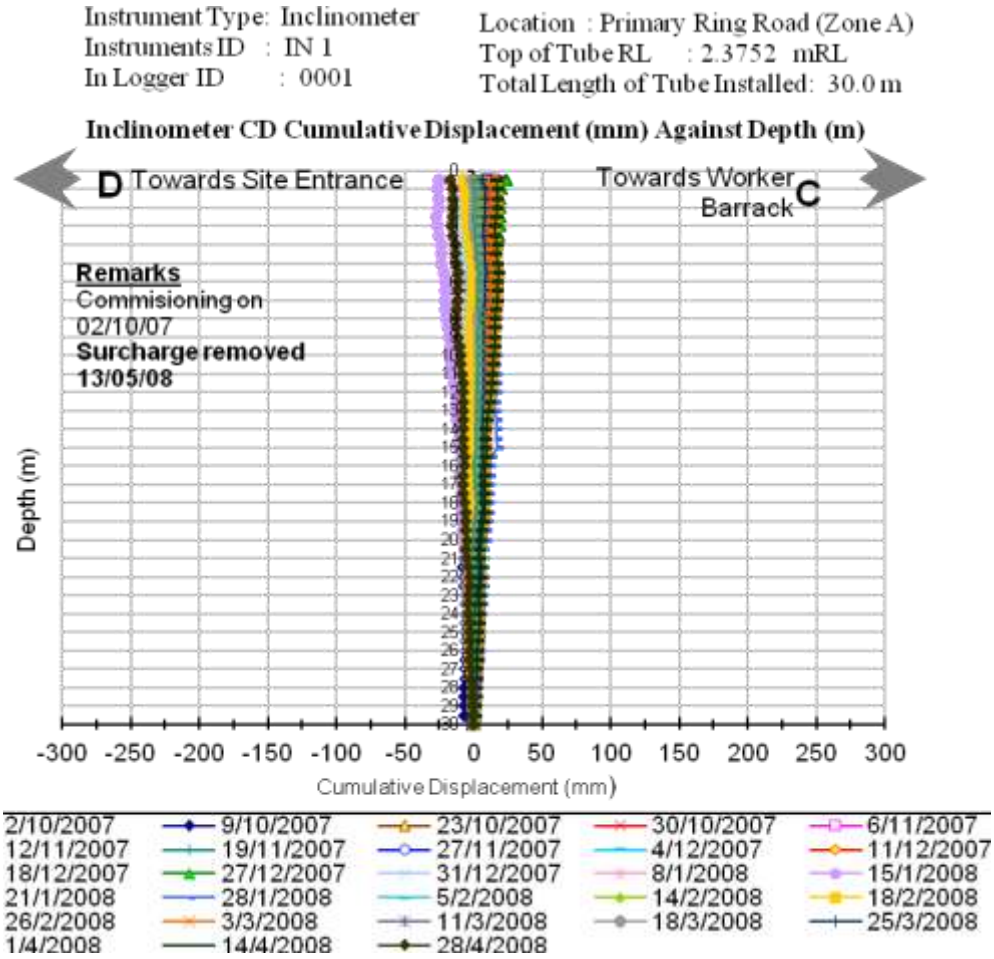

Figure 8: Typical Results for Inclinometer located at the toe of an Embankment

Embankment stability in terms of settlement and slope instability will be observed through the settlement plate via Temporary Bench Marking point and Inclinometer respectively. This will provides a real time performance observation during improvement period. At the initial stage, a total settlement predicted to occurs are 800mm, 486mm and 572mm for Zone A, Zone B and Zone C respectively. These values are inclusive of elastic settlement that occurs immediately after the filling is place on the improved site. Base from observational procedure by Asaoka(1978) the average value of settlement obtained from the analysis are as shown in Table 2.

Table 2: Prediction of Settlement using Asaoka's Observation Procedure and Terzaghi One Dimension Consolidation.

Zone	Asaoka's Average (mm)	Terzaghi's Predicted Settlement(mm)
A	490	675
B	460	360
C	420	450

At average all zones shows a settlement between 420mm and 490mm. In most cases, the settlement from back analysis shows that Asaoka's plots is lower than predicted except for Zone B. The different in reading is expected, since the use of an analytical solution such as Terzaghi one dimensional consolidation is not always effective factors concerning settlement magnitudes in which sometimes it is quite uncertain in engineering practices. Figure 9 and 10 shows selected typical results for Asaoka's plot representing the zones. SP6 representing Zone A, while SP8 is representing Zone B. Finally SP9 and SP10, is representing Zone C.

6. Conclusions

The whole area of the development sits on soft clay which is highly compressible. Due to construction time constrain, a ground improvement need to be done to expedite the settlement process of the area. A task of less than six month was given to improve the site before other infrastructure works will be commencing. Surcharge method incorporated with PVD was used as a ground improvement programs. The method was selected due to its simplicity and economical in comparison with other available method within the region. The work was done by stages starting from Zone A until Zone C. Settlement at each zone reached its final value within a period of 5months from the day of the ground improvement work started. The surcharge height used was 2.5m for both Zone A and B and 2.75m for Zone C. The final settlement occurs were 490mm, 400mm and 254mm for Zone A, Zone B and Zone C respectively. Geotechnical instrument were installed to monitor the performance of subsoil. Back analysis based on settlement monitoring results predicted using Asaoka's Observatory method shows a reliable agreement with Terzaghi's one dimensional consolidation. It was thought to be useful to understand the history of the development site before any settlement prediction is done to eliminate overestimating of surcharge materials which might incurs to extra cost in construction.

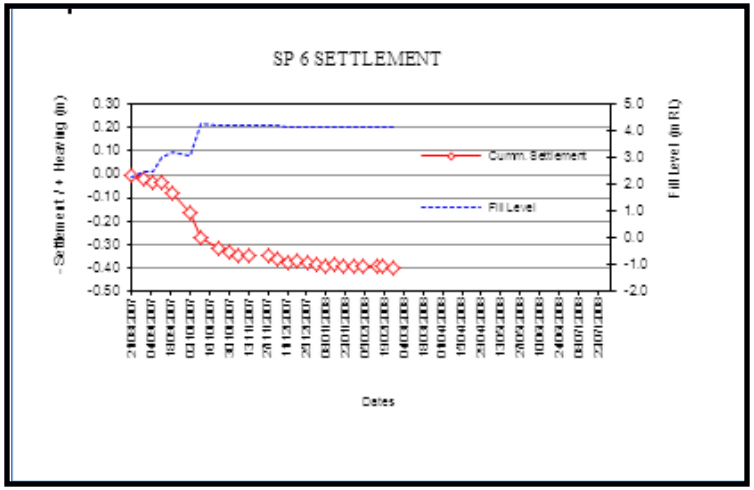

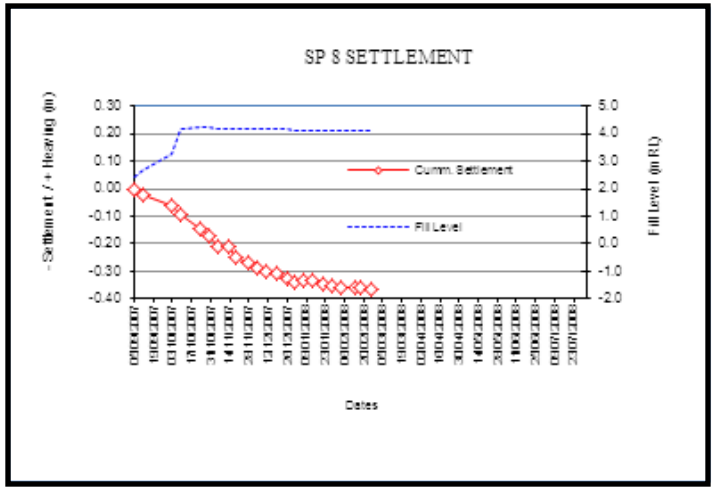

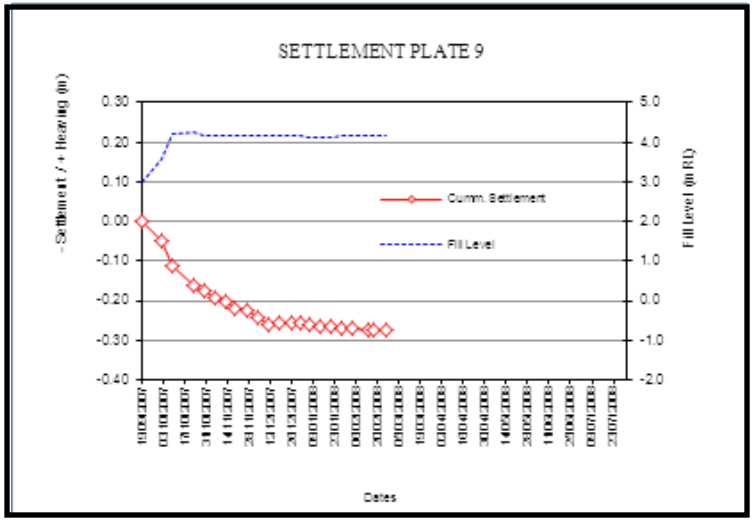

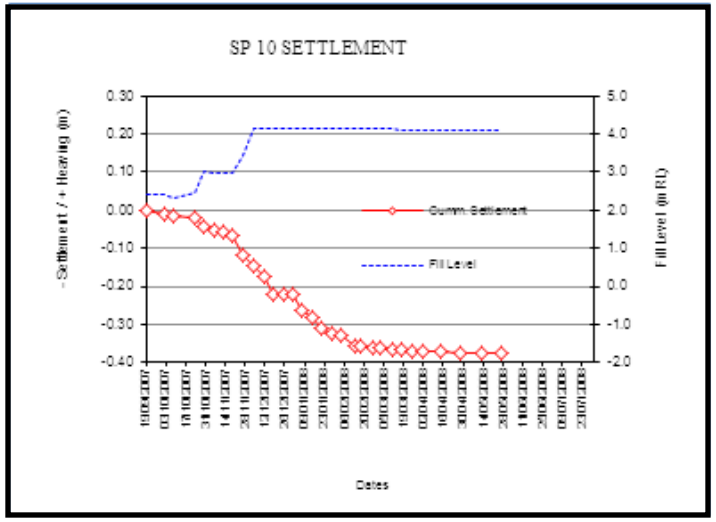

Figure 9 : Typical reading monitor from Settlement Plate

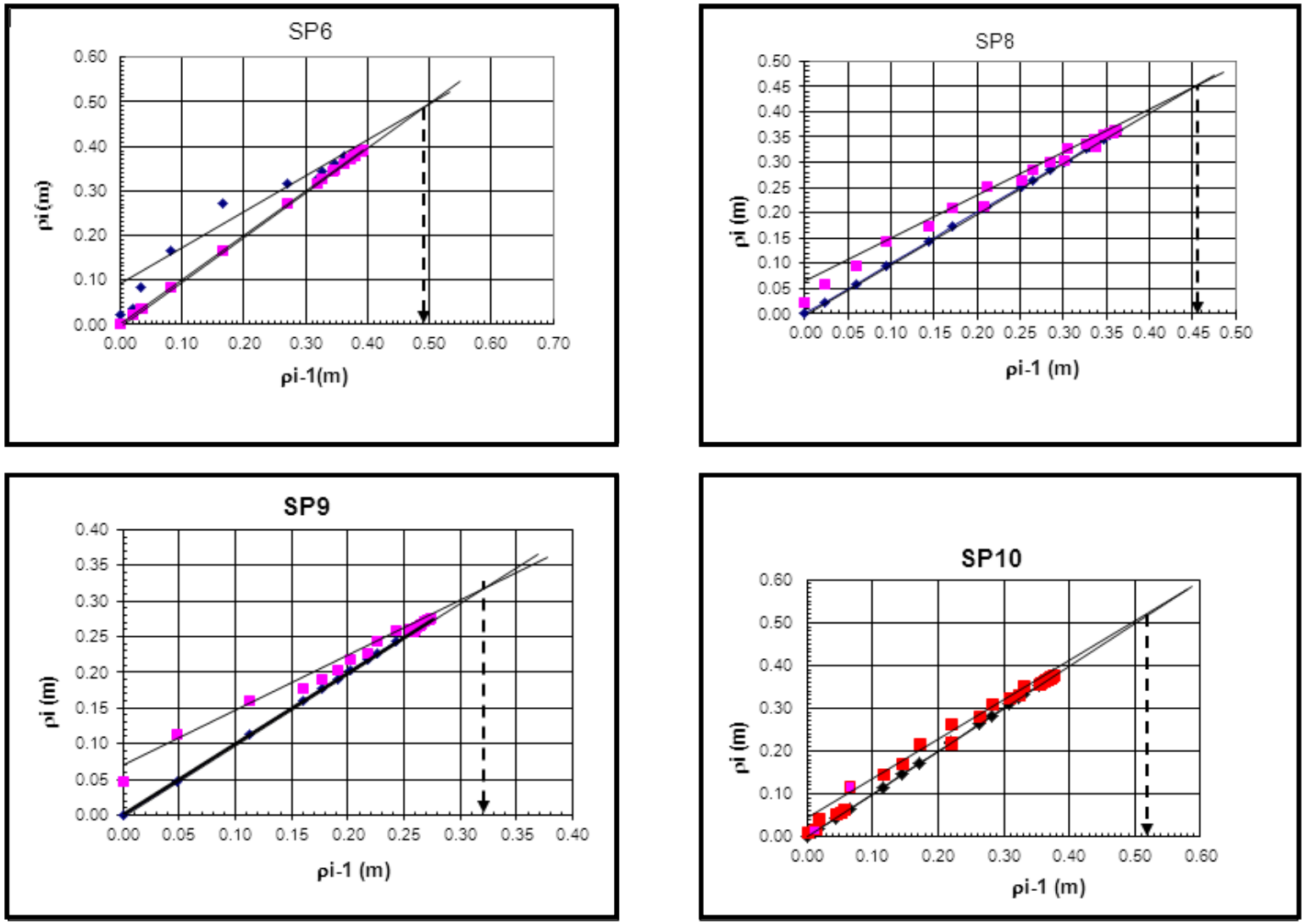

Figure 10 : Typical value of Asaoka's plot for settlement prediction

7. Acknowledgement

The authors' wishes to thank to all personnel involve during the construction and monitoring of the ground improvement on site. Appreciation is to be given to UTHM, JKR and Ecovest Sdn. Bhd. for allowing publishing the data available.

8. References

[1] Asaoka, A. 1978. Observational Procedure of Settlement Prediction. Soils and Foundations, Vol. 18, No. 4, Dec. 1978. Japanese Society of Soil Mechanics and Foundation Engineering. pp. 87- 101

[2] Hansbo, S. 1979. Consolidation of clay by band-shaped prefabricated drains. Ground Engineering, July, Vol. 12, No.5.

[3] Hansbo, S. 1981. Consolidation of fine-grained soils by prefabricated drains. Proceedings, 10th International Conference on Soil Mechanics and Foundation Engineering, Vol. 3, Stockholm.

[4] Terzaghi, K. 1948. Teorethical Soil Mechanics. John Wiley and Sons, New York.

E236

Estimation of Mechanical Properties of Thermal Barrier Coating measured by Nano-Indentation

In-Hwan Shin
Mechanical Engineering, SungKyunKwan University,
300 Cheon-cheon dong, Jang-an gu, Suwon, Korea
sihwan@skku.edu

Chang-Sung Seok
Mechanical Engineering, SungKyunKwan University,
300 Cheon-cheon dong, Jang-an gu, Suwon, Korea
seok@skku.edu

Jae-Mean Koo
Mechanical Engineering, SungKyunKwan University,
300 Cheon-cheon dong, Jang-an gu, Suwon, Korea
kjm9000@hanmail.net

Sung-Ho Yang
G/T Technology Team, KPS Gas Turbine Technology Service Center,
647 Kyoung-seo dong, Seo gu, In-cheon, Korea
shyang@kps.co.kr

The corresponding author: Chang-Sung Seok

Abstract

Plasma-sprayed Thermal Barrier Coating (TBC) is applied to protect the blades of a gas turbine system from high-temperature gas and lower the surface temperature of the blades. The failure of TBC is directly connected with the failure of blades because the spallation of a ceramic layer will lead to the acceleration of excessive local corrosion and oxidation at the location of failure. Therefore, the estimation of mechanical properties of TBC is very important in the evaluation of the reliability of a gas-turbine blade. In this study, isothermal oxidation tests and thermal fatigue tests were performed at 1,100℃. Then, nano-indention tests were performed for TBC specimens that were thermally aged. From the results of the nano-indentation test to compare two different conditions, there were no significant differences between the mechanical properties of the TC and BC. But those of the TGO remarkably decreased when the aging time increased from 100 h to 200 h and 2cycle to 20cycle by thermal fatigue.

Keyword: Thermal Barrier Coating (TBC), Thermally Grown Oxide (TGO), Isothermal Oxidation, Thermal Cyclic, Nano-Indentation

1. Introduction

A technique of thermal barrier coating (TBC) is applied to protect the components of aircraft engines and gas turbines from high temperatures and to lower the surface temperature of the components. The temperature drop resulting from the TBC is known to be 100℃~150℃ [1-3].

TBC usually consist of a MCrAlY(where M=Ni, Co or both) bond coat, a ceramic (7~8 wt% ZrO_2-Y_2O_3) top coat, and a thermally grown oxide (TGO). The TGO is formed at the interface between the top coat and the bond coat via oxidation of the bond coat during the operation of the gas turbine. Temperature dropped mostly in the top coat, but the top coat deposited directly onto the blade increases the probability of failure at the interface because of the difference in thermal expansion coefficient between the top coat and the substrate. So, an intermediate bond coat layer is applied between the top coat and the substrate to increase the bond strength of the top coat and to relieve the thermal stress [4].

TBC applied between aircraft engine applications and gas turbine blades are exposed to cyclic oxidation conditions, and cyclic oxidation has the most influence on coating failure, especially aircraft engine applications [7, 8]. Therefore, most work relating to the reliability of TBC has been carried out by cyclic oxidation tests where the life of the TBC is usually evaluated by the number of cycles until the spallation (fully-delamination) of the top coat occurs.

For the evaluation of the reliability of TBC, experiments using real coated blades are ideal, but very hard due to the complex shape and cost of a blade. Thus, cyclic oxidation test using cylinder-shaped [9-11] or coin-shaped [4, 10] TBC samples are generally adapted instead.

The aim of this study is to evaluate the variation of the mechanical properties of TBC applied for a gas turbine blade according to the degradation between isothermally aged and thermal fatigue conditions. For this purpose, isothermal oxidation tests and thermal fatigue tests were performed at 1,100℃ and then, nano-indention tests were performed for TBC specimens that were thermally aged.

2. Experimental Details

2.1 Materials and Coating Technology

All of tests were carried out on coin-shaped specimens with the dimensions Φ25.4mm (3mm thickness) and coated on the upper face of specimens. Thermal barrier coating specimens consist of a Ni based super-alloy substrate, a MCrAlY bond coat and a ceramic (7~8 wt% ZrO_2-Y_2O_3) top coat. Table 2.1 shows the composition and thickness at each layer of TBC specimen.

Table 2.1 Composition of thermal barrier coating specimen

	Material	Coating Type	Thickness
Substrate	GTD-111DS	-	3 mm
Bond Coat	MCrAlY	LVPS	240 ㎛
Top Coat	7~8%Y_2O_3-ZrO_2	APS	598 ㎛

2.2 Isothermal Oxidation Test and Thermal Cyclic Test

Isothermal tests, which were to evaluate the relationship between the bond strength and the isothermally aging time of TBC, were performed at 1100℃. For each test were intentionally stopped at 100, 200, 400 hours. Thermal cyclic tests were performed by a furnace and an automated moving system with a timer. 1 cycle of the test consisted of 45-min holding in the furnace and 15-min cooling with compressed air. Thermal cyclic tests, which were to evaluate the spallation life of the plasma-sprayed TBC by cyclic oxidation, were performed at 1100℃. Thermal cyclic tests were performed until the spallation of TBC. Thermal cyclic tests, which were to evaluate the relationship between the bond strength and the number of cycles of oxidation of TBC, were performed at 1100℃. Tests were intentionally stopped at 1, 2, 5, 10 and 20 cycles.

2.1 Nano-Indentation Test

Nano-indentation tests were performed for the TBC specimens, which were thermally aged between the isothermal oxidation test and thermal cyclic test. It is known to the bond strength gradually decreased with the increase between aging time and the number of thermal cycles. The spallation lives of TBCs were assumed to be the time which the bond strength became zero and the spallation lives were determined by the linear curve fittings for the results of nano-indentation tests at each test conditions.

3. Test Results

The elastic modulus of the TGO is considerably higher when compared to those of the two phases in the BC (Bond Coat) and TC (Top Coat). Such large differences in the elastic modulus of the TGO could lead to severe thermal stress near the TGO, which may be the reason why the failure of TBC. The sintering was so active as to lead to an increase of the elastic modulus between an aging time of 100 h and thermal fatigue of 2 cycles as compared to the as-sprayed properties, and then remained constant afterwards. There was no significant difference in the nano hardness of TC, TGO and BC under isothermal oxidation. But the nano hardness of BC is higher in thermal fatigue. It seems to be related to the inter-diffusion at the boundary of TC and BC is active under thermal fatigue.

4. Conclusions

(1) From results between isothermal oxidation tests and thermal fatigue tests using coin-shaped TBC specimen, TBC is fully spalled due to the degradation of BC, the component of Al depletion and the layer of TGO growth.

(2) From the results of the nano-indentation test to compare two different conditions, there were no significant differences between the mechanical properties of the TC and BC. But those of the TGO remarkably decreased when the aging time increased from 100 h to 200 h and 2cycle to 20cycle by thermal fatigue.

(3) The nano-indentation technique is a very effective way to evaluate the degradation of TGO. It is possible to catch the initiation point of delamination by observing the change in the mechanical properties of TGO both aging time and thermal fatigue increase by using the nano-indentation technique.

5. References

[1] K. Vaidyanathan, E. H. Jordan, M. Gell, Surface geometry and strain energy effects in the failure of (Ni/Pt)Al EB-PVD thermal barrier coating, Acta Materialia, Vol. 52, pp. 1107-15, 2004.

[2] J. A. Thompson, T. W. Clyne, The effects of heat treatment on the stiffness of zirconia top coats in plasma sprayed TBCs, Acta Materialia, Vol. 49, pp. 1565-75, 2001.

[3] K. W. Schlichting, N. P. Padture, E. H. Jordan, M. Gell, Failure modes in plasma-sprayed thermal barrier coatings, Materials Science & Engineering A, Vol. 342, pp. 120-30, 2003.

[4] A. Nusair Khan, J. Lu, Behavior of air plaspa sprayed thermal barrier coatings, subjected to intense thermal cycling, Surface and Coatings Technology, Vol. 166, pp. 37-43, 2003.

[5] G. G. Levi, E. Sommer, S. G. Terry, A. Catanoiu, Alumina grown during deposition of thermal barrier coatings on NiCrAlY, Journal of American Ceramic Society, Vol. 86, No. 4, pp. 676-685, 2003.

[6] W. J. Quadakkers, V. Shemet, D. Sebold, R. Anton, E. Wessel, L.Singheiser, Oxidation characteristics of a platinized MCrAlY bond coat for TBC systems during cyclic oxidation at 1,000°C, Surface & Coatings Technology, Vol. 199, pp. 77-82, 2005.

[7] Mats Eskner, Mechanical behavior of gas turbine coatings, Doctoral Thesis, 2004.

[8] N. P. Padture, M. Gell, E. H. Jordan, Thermal barrier coatings for gas-turbine engine applications, Science, Vol. 296, pp. 280-284, 2002.
[9] R. A. Miller and C. E. Lowell, Failure mechanisms of thermal barrier coatings exposed to elevated temperatures, Thin Solid Films 95, pp. 265-273, 1982.
[10] R. V. Hillery, B. H. Pilsner, R. L. McKight, T. S. Cook, and M. S. Hartie, Thermal barrier coating life prediction model development - final report, NASA-CR-180807, 1988.
[11] J. Shi, A. M. Karsson, B. Baufeld, M. Bartsch, Evolution of surface morphology of thermo-mechanically cycled NiCoCrAlY bond coats, Materilas Science and Engineering A, Vol. 434, pp. 39-52, 2006.

E248

Secure and Reliable Satellite-based Tracking System for Emergency Management

Jyri Rajamäki
Laurea University of Applied Sciences, Espoo, Finland
jyri.rajamaki@laurea.fi

Pasi Kämppi
Laurea University of Applied Sciences, Espoo, Finland
pasi.kamppi@laurea.fi

The corresponding author: Jyri Rajamäki

Abstract
A Geographic information system (GIS) offers great deal of assistance in emergency management. Satellite-based tracking has long been considered a technology that compliments GIS operations. However, current satellite-based tracking systems have serious technical flaws and vulnerabilities. This paper presents a detailed modular system-level description for the satellite-based tracking system including control, space, tracking, communication, data processing, end-user and external applications segments. The paper further discusses and suggests how the technical vulnerabilities of satellite based tracking systems could be avoided taken in e.g. a hybrid tracking segment and multichannel communication paths.
Keyword: emergency management; geographic information system; security; multichannel communications; tracking;

1. Introduction

Emergency management needs geographic information for emergency response and planning operations. Geographic information system (GIS) can combine many layers of different information. GIS enables emergency managers to quickly access relevant data about an affected area during emergencies. GIS' objectives are to have a general view of the theatre of operations with its geographic characteristics, troop's location, roads and railways and fighting location [1]. Satellite-based tracking and navigation has gained broad popularity during past years. The primary focus of satellite-based tracking systems within the GIS arena has traditionally been based around global positioning system (GPS) that collects, stores and transfers data from a field system to an office-based GIS [2].

Integration of information systems is a current trend in all businesses and organizations [3]. The trend is towards larger mobility and the Internet plays a major role in providing critical business and operational data, applications and services for mobile users. In this respect, service-level requirements play an important role in the process. However, service-level requirements are difficult to quantify during the project planning phase. The following intangible values could be used as guide lines for drawing up the operational constraints and goals required: 1) usability, 2) performance, 3) scalability, 4) reliability, 5) availability, 6) extensibility, 7) maintainability, 8) manageability and 9) trustworthiness and security. Only after deployment these attributes can be quantified. To meet pertinence requirements, the production (communication) system needs changing and tuning; if not possible, service-level requirements should be readjusted to conform the operational environment. The reason for the existence of any Internet based system is to support business and organizational needs. A shift of focus may be needed in any new project and Internet architecting activities should be given more effort, attention and seriousness. [4]

A satellite-based tracking system combines navigation and telecommunication technologies. The system is relatively complicated and consists of many technical segments, including the control, space, tracking, communication, data processing, application interface for external applications and end-user segment [5]. The basic principle is that a tracked device is positioned by Global Navigation Satellite Systems (GNSS) and positioning data is delivered for post-processing via mobile networks, the Internet or a secure network. The end-user segment might be e.g. an office-based GIS for emergency management. The manner in which GNSS used with GIS is wide and varied allowing users to determine the way GIS and GNSS are used together to best meet their needs.

GNSS-based tracking devices are able to calculate and deliver position information for post processing. Today many mobile phones (smart phones) include GPS receivers and phones are easy to turn into tracking devices by client software. For professional services like emergency management, TETRA clients and tracking-only clients without communications functionality are available. New positioning devices expected to support all four major systems (GPS, GLONASS, Compass and Galileo) so that several techniques can be used simultaneously to guarantee better positioning accuracy and availability. GNSS-based tracking is used in many applications, e.g. in logistics, fleet management, road tolls, traffic signal management. Also, emergency management is using them e.g. for following troop's location.

Very often only the benefits of the satellite-based tracking solutions are advertised while the risks and weak points are forgotten. However, current GNSS-based tracking systems have serious vulnerabilities [5]. The systems are complex and open to several kinds of data delivery problems, data losses and cyber-attacks. The systems are GPS and GSM dependent for positioning and communications. They include no cross-over possibilities; positioning is not based on parallel satellite systems, known WLAN networks, mobile phone cell location, RF/DF etc. Also, intelligence is lacking from the systems; they can be commanded but they do not have the capability of self-reacting and alerting. Furthermore, available commercial products are vulnerable to jamming without jamming detection possibilities and their power consumption is not always optimized. [5]

This paper studies current threats of satellite-based tracking systems in the field of emergency management. It also presents a detailed modular system-level description for the satellite-based tracking system. This paper proposes how the vulnerabilities of satellite-based tracking systems could be avoided utilizing multi-GNSS (Galileo, GPS, CLONASS, Compass) capable equipment, taken a hybrid tracking segment and multichannel communication paths into account. Paper also discusses self-protection, counter measure protection, jamming detection as well as power consumption optimizing.

2. Threats of Current Satellite-based Tracking Systems

Identifying threats of satellite-based tracking in order to avoid the problem of limited existing data or limited knowledge of the risk analysis team, it is necessary to investigate the requirements of the applications and operations/business. An application can have technical requirements that have not been levied on prior uses of the system. If the system cannot offer service with certain requirements, then it is a threat for the application. The requirements of the operations/business can create technical requirements, and the technical limitations of the system causes threats to those requirements being met. Using this approach, we were able to generate a model for identifying threats with regard to satellite-based tracking, shown in Figure 1.

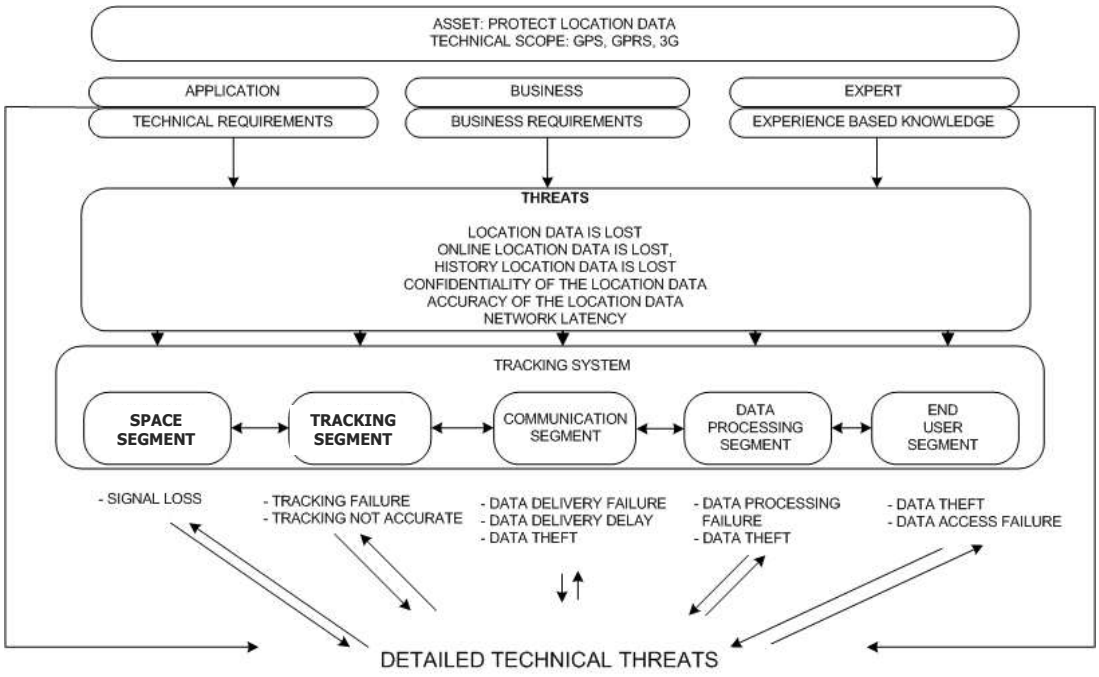

Figure 1. Model for identifying technical threats of satellite-based tracking

We started identifying threats by listing well known technical threats. The asset we chose to investigate was location data. First, we defined the segments of the system and then we group the threat according to the segments in which they occur. We discovered that a single technical threat can be the cause for some higher-level threat. For example, the cause of a tracking failure can be a technical problem in tracking device. The technical problem is the lower-level threat and the tracking failure is the higher-level threat. Also, we noticed that higher-level threats can help to find lower level threats. Data privacy threats are caused by certain technical reasons. The data privacy is higher level threat and the technical reason is the lower level threat. Next, we investigated if higher-level threat could occur in the other segments of the system. For example, privacy threats can be caused by many technical reasons in many segments. This cycle generated relations between all threats and segments.

When we had sorted all well-known threats we added operational/business requirements. Table 1 shows the threats resulting from this methodology grouped by system segments and categories.

Table 1 Technical vulnerabilities in satellite-based tracking systems

System segment	**Threats**
Control segment	Error in monitoring data, Error in adjustment commands
Space segment	Natural disasters (e.g. solar storms, ash cloud from volcano eruption), Collisions in the orbit, Unintended interface, Intentional interface, Atmospheric conditions, Multipath propagation, Selective availability, Total signal loss

Tracking segment	HW fault, SW fault, Power feed break-down, Clock drift, Signal attenuation, Information security diminution
Communication segment	Capacity, Radio coverage, Roaming, Latency, Information security diminution
Data processing segment	HW fault, SW fault, Power feed break-down, Capacity, Information security diminution, Database corruption
End-user segment	HW fault, SW fault, Power feed break-down, Capacity, Information security diminution

3. Improved Tracking System for Emergency Management

Previous chapter investigates the main threats of today's satellite-based tracking systems. These systems have no cross-over possibilities for positioning and communications as the tools are GPS and GSM dependent. In emergency situations, some of these threats (e.g. power feed breakdown) are more probable to realize. For this reason, we propose an improved tracking system for emergency management, shown in Figure 2.

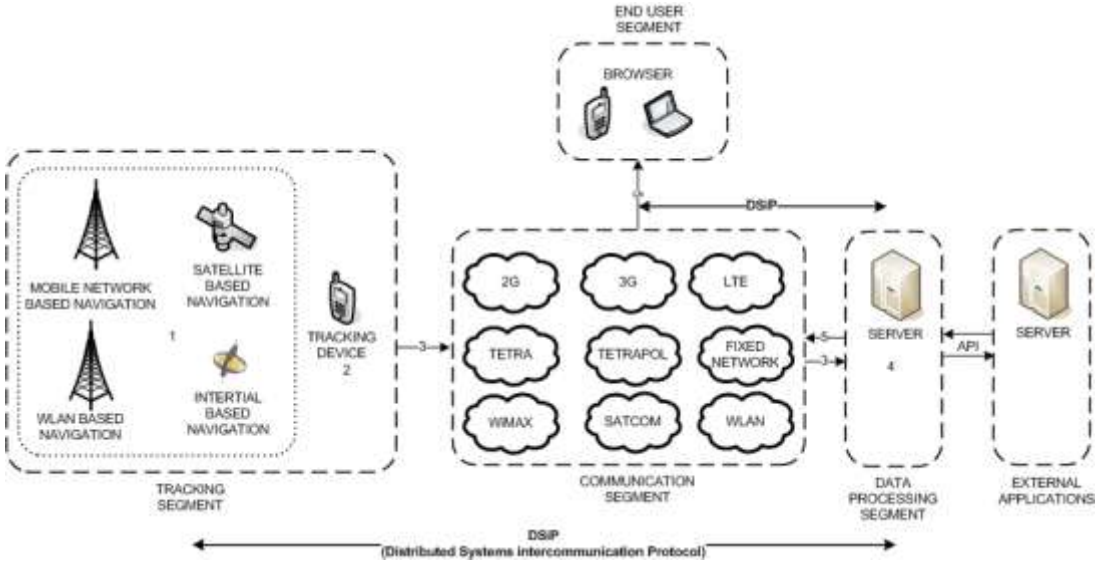

Figure 2. Modular system-level description of improved tracking system for emergency management

The improved tracking system for emergency management includes three main segments: (1) Integrated tracking segment where the location could be calculated based on several satellite systems, known WLAN-networks, mobile phone cell location, etc.; (2) multichannel communication segment which could utilize the best available communication path or several parallel paths; and (3) GIS integrated data processing, API and end-user segments.

New tracking devices should support all four major GNSS systems (GPS, GLONASS, Compass and Galileo) so that several techniques can be used simultaneously to guarantee better positioning accuracy and availability. For robustness reasons, relying on only one technology (GNSS) is not enough. For example, electromagnetic

interference might interrupt all GNSS operations in a certain area. Utilizing known WLAN-networks, mobile phone and TETRA/TETRAPOL cell location, etc. information could give notable additional value for calculation of the location. In emergency situations, the power consumption of the tracking device could be a critical factor. Combining device's power consumption optimization with utilizing energy harvesting from ambient vibrations, wind, heat or light and new high energy rechargeable battery technologies, a multiply running time could be achieved. Outfitting the tracking device with jamming detection ability requires access to GNSS chips Automatic Gain Control (AGC) software and comparing the chances in gain and signal to noise ratio. Furthermore, the devices could have artificial intelligence for self-reacting and/or alerting when certain abnormalities occur.

A multichannel data communication concept provides a uniform way to communicate over virtually any type of communications media in such a way that multiple, sometimes parallel communication paths appear as a single robust, uninterruptable, secure and reliable communication link between communicating peers. For example, a solution named DSiP (Distributed Systems intercommunication Protocol) makes it possible to distribute all telecommunication among several operators and methods, resulting in a true multichannel communication system. The DSiP telemetry system increases reliability, security and integrity in telecommunication and allows regular communication methods to be used in mission critical telemetry systems. This is achieved by (1) splitting risks between operators and communication channels, (2) better routing and priority capabilities that takes security and intrusion risks into account and (3) adding modularity. [6]

There are many ways that GIS and tracking technologies can and already do work well together. From complete commercially available data collection and data maintenance systems, to help with the management of spatial features and attribute data, through to very flexible software development kits, to assist in the creation of unique and sophisticated field applications [2]. In the future, office-based command and control rooms will more and more be replaced by mobile and field command systems.

4. Discussions and Conclusions

Geographic information systems can combine many layers of different information, creating products that are more sophisticated than flat maps. GIS can map and access data — from flood zones and local infrastructure to population density and road closures — before, during, and after an emergency. By linking maps to databases GIS

enables users to visualize, manipulate, analyze, and display spatial data. The primary focus of satellite-based tracking systems within the GIS arena has traditionally been to collect, store and transfer data from a field system to an office-based GIS. All the time, satellite-based systems are becoming more popular and positioning information becomes more important in managing field operations. However, there is no interoperability standard to exchange location information and simple GIS information.

A satellite-based tracking system integrates satellite-based positioning, mobile and fixed communication networks as well as data processing and administration. Most satellite-based tracking systems are based on GPS operated by the United States Air Force who, however, cannot guarantee to maintain global uninterrupted service. If GPS signals were switched off in some part of the Globe tomorrow, emergency management efficiency would suffer heavily jeopardizing the public safety. E.g. in Europe, Public Protection and Disaster Relief (PPDR) operators can only be self-dependent if their tracking is based on Galileo, the only European global navigation satellite – supported by other GNSS systems. Galileo will allow positions to be determined accurately even in high-rise cities, where buildings obscure signals from today's satellites. Galileo will also offer several signal enhancements making the signal more easy to track and acquire and more resistant against interferences and reflections. European GNSS will deliver much more precise and much more reliable services than the American and Russian systems. By placing satellites in orbits at a greater inclination to the equatorial plane, Galileo will also achieve better coverage at high latitudes, making it particularly suitable for operation over northern Europe, an area not well covered by GPS. However, presuming on only one technology (GNSS) is not enough and utilizing known WLAN-networks, mobile phone and TETRA/TETRAPOL cell location, etc. information could give notable additional value for location data availability.

The power consumption of the tracking device could be a critical factor, especially during emergencies. Combining device’s power consumption optimization with utilizing energy harvesting from ambient vibrations, wind, heat or light and new high energy rechargeable battery technologies, a multiplied running time could be achieved.

There is a lack of interoperability between different technical systems in use by emergency services. When managing troops during emergencies, communications is critical. Mobile devices make use of different communication networks. In general,

they are legacy systems without a homogeneous and/or secured configuration and their default encryption is weak and very easy to hack. Often, even one single point attack can compromise the complete network connection and bring the network down. At present, the roaming features of TETRA/TETRAPOL networks are inadequate to apply them in cross-border PPRD operations. Therefore, the need for secure multichannel communication is global and exploding. DSiP is a solution allowing regular communication methods to be used in mission critical communication systems. It also enables a combination of all kinds of telecommunication resources: IP traffic and non-IP traffic over TETRA, radio links, satellite communications, serial connections etc. can all co-exist forming a single uniform and maintainable system.

This article presents a modular system-level description of improved tracking system for emergency management. Within GNSS systems a tracking device calculates its location itself and sends this information for post-processing. In most other system, the tracking device – 'tag' – sends no location data. Instead, the system calculates the location of the tag. With current knowledge the integration of these different technologies is easy to realize.

5. Reference

[1] Sauvagnargues-Lesage, S and Ayral, P-A. (2007) "Using GIS for emergency management: a case study during the 2002 and 2003 flooding in south-east France", International Journal of Emergency Management, Vol. 4, No. 4, pp. 682 – 703.

[2] Harrington, A. (1999) "GPS/GIS Integration: GPS Can Play a Major Role in GIS Data Maintenance?" GeoWorld, Daneilson, Todd (ed.), Vol.12 No.10, Arlington Heights: Adams Business Media.

[3] Litan, D. and Mocanu, A-M. (2011) "Information systems integration, a new trend in business", in Proc. 9th WSEAS International Conference on Applied Electromagnetics, Wireless and Optical Communications (ELECTROSCIENCE '11),

[4] Tumin, S. and Encheva, S. (2011) "A brief look at Web architecting", in Proc. 9th WSEAS International Conference on Applied Electromagnetics, Wireless and Optical Communications (ELECTROSCIENCE '11), Meloneras, Gran Canaria, Canary Islands Spain, March, pp. 245-249.

[5] Rajamäki, J., "Cross-border Satellite-based Tracking: Needs, Approach, Benefits and Competition", In proceedings of 2nd International Conference on Ubiquitous Positioning, Indoor Navigation and Location-Based Service, UPINLBS2012, Helsinki, October 3-4, 2012.

[6] Holmstrom, J., Rajamäki, J. and Hult, T. (2011) "The future solutions and technologies of public safety communications - DSiP traffic engineering solution for secure multichannel communication", International Journal of Communications, Issue 3, Vol. 5, pp.115-122.

Information

Pullman Bangkok King Power, 2F Meeting Room BETA I

2013/1/27 Sunday 13:00-14:30

Session Chair: Jyri Rajamäki

E158

Digital Image Authentication and Recovery Based on Secret Sharing

Shu Fen Tu｜*Chinese Culture University*

Ching Sheng Hsu｜*Ming Chuan University*

E247

Service Standardization to Utility Model: Process, Technology and Contracts

Jyri Rajamäki｜*Laurea University of Applied Sciences*

Markus Vuorinen｜*HP Enterprise Services*

E253

Multi-Agency Cooperation in Cross-border Operations: Information Exchange between Law Enforcement Authorities

Jyri Rajamäki｜*Laurea University of Applied Sciences*

Petter Ruohomäki｜*Laurea University of Applied Sciences*

E158

Digital image authentication and recovery based on secret sharing

Shu-Fen Tu
Department of Information Management, Chinese Culture University
No.55, Huagang Rd., Shihlin District, Taipei City 11114, Taiwan
dsf3@ulive.pccu.edu.tw

Ching-Sheng Hsu
Department of Information Management, Ming Chuan University
No.5, Deming Rd., Gueishan Township, Taoyuan County 333, Taiwan
cshsu@mcu.edu.tw

The corresponding author: Ching-Sheng Hsu

Abstract
This paper proposed a fragile watermarking scheme to verify the integrity of digital images. The image feature values are converted into a series of authentication message and then concealed in the image. Except for authenticating images, this study attempted to employ a threshold secret sharing scheme to split recovery message into four shares, and gathering any three shares can reconstruct the original recovery message. By doing so, we can cut down the length of recovery message carried by a pixel. The experimental results showed that the proposed method outperforms other method in the image restoration quality.
Keyword: fragile watermarking, image tamper detection, image recovery

1. Introduction

Data integrity is always an important issue for digitalized data since they are prone to suffer from malicious attacks. If receivers fail to detect tampering, disputes may arise. Take news photos for example. Tampered news photos may distort the fact or cause damage to a person's reputation. Therefore, authenticating image integrity effectively becomes an important research issue. There are two main techniques to authenticate image integrity: one is digital signature, and the other is digital watermarking. Digital signature can be seen as image features and is appended to the transmitted image. When authenticating, we can follow the same steps to extract the image feature and compare it to the digital signature. If they are not the same, we can know that the image may be tampered. However, digital signature cannot provide any information regarding to the tampering location. Compared to digital signature, a fragile watermarking scheme is more helpful for us to find out where the tampering area is. A fragile watermark, containing important features of an image, is embedded into a

cover image, and by comparing the fragile watermark and image features, integrity can be authenticated. Many researchers have proposed least significant bitplane (LSB) substitution methods to embed an authentication message into the least significant bits of image pixels [1-8].

In addition to the ability to judge which regions are tampered with, an ideal tampering detection method should also provide the ability to recover the affected areas. Recently, some tampering detection schemes with the capability of image recovery have been proposed [2, 6-9]. The basic idea of these methods is to embed the recovery message of a block (e.g., the average pixel values of a block or the index of a code-book for vector quantization) into other blocks. Thus, when detecting a tampered block, one can recover this block by the recovery messages gathered from other untampered blocks. In 2008, Lee and Lin proposed a tamper detection and recovery scheme [7]. Their distinguish feature is that two copies of recovery and authentication messages are embedded in the image. Because dual watermark is stored, their scheme increases the opportunities to successfully retrieve the recovery message. But the consequence is that the bits of recovery message carried by a pixel increases as well. Besides, duplicating authentication message is not so necessary hence may waste some spaces. The other problem is that only the last three bits of a pixel is used to judge the tampering status. If someone makes modifications only to the first five bits of a pixel, such tampering cannot be detected by Lee and Lin's scheme.

In this paper, we shall propose a hierarchical tampering detection and recovery scheme to reach better detection error rate and better image quality of recovered images. The proposed method utilizes the concept of secret sharing to cut down the bits of recovery message carried by a pixel. The shares of recovery message will be spread over the image to raise their survivability. In addition, the proposed scheme employs Hsu and Tu's two-stage image authentication scheme [10], and add a third stage to decrease the false negative rate. Generally speaking, decreasing false negative rate can increase the quality of the recovered image. Finally, we will conduct a series of experiments to evaluate the performance of the proposed method.

2. The proposed scheme

2.1 Generation and embedding of recovery and authentication message

If the original image H is an $m \times n$ undistorted gray image, m denotes the image height, and n denotes the image width. The recovery information is generated and embedded by the following algorithm:

Step 1: The image H is split into nonoverlapping 2×2 blocks; and then all blocks are

scrambled randomly. Let $t = ((m \times n)/4) - (((m \times n)/4)$ **mod** 3) and B denote the set of scrambled blocks, where $B = \{b_i \mid i = 0..(t-1)\}$.

Step 2: Set $i = 0$.

Step 3: For each triple of adjacent blocks b_i, b_{i+1}, b_{i+2} of B, we compute their average pixel values avg_i, avg_{i+1}, and avg_{i+2}, respectively. Let

$$c_j = \begin{cases} avg_{i+j} >> 2 & \text{if } (avg_{i+j} >> 2) < 61 \\ 60 & \text{otherwise,} \end{cases} \quad \text{where } j = 0..2.$$

Step 4: Calculate four shares s_1, s_2, s_3, and s_4 by Eq.(1):

$$f(x) = c_0 + c_1 x + c_2 x \textbf{ mod } 61, \tag{1}$$

where $s_k = f(k)$ and $k = 1..4$.

Step 5: Let $(b_{k5}\ b_{k4}\ b_{k3}\ b_{k2}\ b_{k1}\ b_{k0})_2$ denote the bit-string of share k. Distribute each bit of the four shares to the next triple blocks $b_{(i+3) \bmod t}$, $b_{(i+4) \bmod t}$, and $b_{(i+5) \bmod t}$ as shown in Figure 1. Note that P_0 to P_{11} denote the 12 pixels of these three blocks, and B_0 to B_7 denote each bit of a pixel.

Step 6: Set $i = i + 1$. Repeat step 3 to step 5 until $i > (t - 4)$.

Step 7: Rearrange all blocks according to the original order.

Step 8: For each block, generate 4-bit authentication message by means of Hsu and Tu's scheme. Then, embed it to the last bit of each pixel.

	B_7	B_6	B_5	B_4	B_3	B_2	B_1	B_0
P_0						b_{11}	b_{12}	
P_1						b_{13}	s_{14}	
P_2						b_{15}	b_{16}	
P_3						b_{21}	b_{22}	
P_4						b_{23}	b_{24}	
P_5						b_{25}	b_{26}	
P_6						b_{31}	b_{32}	
P_7						b_{33}	b_{34}	
P_8						b_{35}	b_{36}	
P_9						b_{41}	b_{42}	
P_{10}						b_{43}	b_{44}	
P_{11}						b_{45}	b_{46}	

Figure 1 The embedding rule of recovery message

2.2 Tampering detection and recovery

To authenticate an image, we first perform Hsu and Tu's two-stage tampering detection and get a binary matrix M_0 of size $(m \times n)/4$ as the detection result. Each element of M_0 indicates the tampering status of a block. If the element is true (*i.e.* '1'), the corresponding block is detected as tampered (or called positive); otherwise, the corresponding block is detected as untampered (or called negative). Then, a further

detection, called a "sliding-window" stage, is performed to adjust the matrix so that the false negative rate can be decreased more. When a block is detected as negative, the recovery scheme does not think this block needs to be fixed. But if it is a false negative, this block actually needs to be repair. Therefore, decreasing false negative rate as much as possible can make most tampered block be recovered and hence increase the quality of the recovered image. For each block detected as tampered, its recovery message is retrieved and used to fix them. However, some recovery message cannot be retrieved successfully due to attacks. When such situation happens, those tampered blocks will be recovered by their neighborhood blocks. Below we explain the proposed scheme in detail.

Stage 1 and 2 tampering detection:

Step 1: Let T denote the image to be authenticated. Perform Hsu and Tu's scheme on T and thus get a binary matrix $M_0 = [d_{ij}]_{(m/2) \times (n/2)}$, where $d_{ij} \in \{0, 1\}$ and 1 denotes positive and 0 denotes negative.

Stage 3 tampering detection:

Step 2: Initialize another binary matrix M_1 of size $(m \times n)/4$.

Step 3: Position a window W of size $k \times k$ to up-left corner of M_0. Note that k is predefined by the user.

Step 4: Let A denote the area of M_0 falling within W. Count the number of '1' within A. If the number is greater than a predefined threshold θ, set each element of M_1 corresponding to the same position of A to 1. Otherwise, set each element of M_1 to the same value of A.

Step 5: If the window W reaches the end column of M_0, go to step 6. Else, move W one column and go to step 4.

Step 6: Move W one row and back to the first column of M_0.

Step 7: If W reaches the right-bottom corner of M_0, go to step 8; otherwise go to step 4.

Stage 1 recovery:

Step 8: Split T into nonoverlapping 2×2 blocks; and then all blocks are scrambled randomly using the pseudo-random number generator seeded with the same key as the above section. Let $t = ((m \times n)/4) - (((m \times n)/4)$ **mod** $3)$ and B denote the set of scrambled blocks, where $B = \{b_i \mid i = 0..(t - 1)\}$. Scramble all element of M_1 with the same seed as well.

Step 9: For each block b_i whose detection result is true, set $g = (i/3) + 1$.

Step 10: If the detection status of $b_{g\times3}$, $b_{g\times3+1}$, and $b_{g\times3+2}$ are not true, retrieve any three shares from these three blocks.

Step 11: With the three shares, use Lagrange interpolation [11] to reconstruct the

polynomial as Eq. (1) and get the three coefficients c_0, c_1, and c_2.

Step 12: Recover the block b_i with the value $c_{i \bmod 3} << 2$.

Step 13: Repeat step 9 to 12 until all blocks are processed. Rearrange the order of all blocks and all elements of M_1.

Stage 2 recovery:

Step 14: For those blocks whose detection result are true and are not fixed at stage 1 recovery, use their neighbors' average pixels to recover them.

3. Experimental Results and Discussions

3.1 Measurements

In order to verify the performance of our method, the following measurements are used:

(1) PSNR (Peak Signal to Noise Ratio) measures the similarity between two images I_1 and I_2. Usually speaking, two images look similar if the PSNR is greater than 30.

$$PSNR(I_1, I_2) = 10 \times \log \frac{255^2}{MSE} \text{ (dB)}, \tag{2}$$

where

$$MSE = \frac{1}{m \times n} \sum_{i=1}^{m} \sum_{j=1}^{n} (p_{i,j} - p'_{i,j})^2 \tag{3}$$

.

In Eq. (3), $p_{i,j}$ and $p'_{i,j}$ are pixels located at (i, j) of images I_1 and I_2, respectively. The PSNR measurement plays two roles in the proposed scheme. One role is to measure the imperceptibility of the proposed scheme. The so-called imperceptibility means that the difference between the original and watermarked image cannot be perceived by human eyes. The other role is to measure the similarity between the watermarked and recovered image to show the quality of the recovered image.

(2) FNR (False Negative Rate) and FPR (False Positive Rate) measure tampering detection accuracy [10].

$$\text{FNR} = \text{FN}/(\text{FN} + \text{TP}). \tag{4}$$

$$\text{FPR} = \text{FP}/(\text{FP} + \text{TN}). \tag{5}$$

In Eq.(4) and Eq.(5), FN is the number of False Negative pixels, TP is the number of True Positive pixels, FP is the number of False Positive pixels, and TN is the number of True Negative Pixels.

(3) Tampering ratio ρ is defined as follows [10].

$$\rho = (\text{FN} + \text{TP})/(m \times n). \tag{6}$$

3.2 Results and Discussions

Figure 2(a) and 2(b) are the test image and watermarked image, respectively. The

proposed scheme uses the PSNR to measure the similarity between the original and watermarked image. The PSNR value indicates that the imperceptibility of the proposed scheme is good. Figure 2(d) is the detection result of figure 2(c) after three-stage authentication, and figure 2(e) is the recovered image. Table 1 lists the FNR and FPR from stage 1 to stage 3 when figure 2(c) is detected. Table 1 shows that our third stage indeed decreases FNR of Hus and Tu's authentication scheme.

Below we provide three experiments to compare the recovery quality between ours and Lee and Lin's scheme. In figure 3, we copy the upper right corner of the watermarked image and past to the bottom right corner. Since the rectangle area is only copied and pasted and not changed, Lee and Lin's scheme cannot detect such tampering. As a result, the tampering area cannot be recovered successfully. On the contrary, our scheme can detect such tempering and hence fix the tampering successfully. Figure 4 and figure 5 display image synthesis attacks with different tampering ratios. The PSNR values of the recovered images show that our scheme recovers the image better than Lee and Lin's scheme does.

In Lee and Lin's scheme, ten bits of the recovery message are embedded into a 2×2 block; hence, 2.5 bits are carried by a pixel averagely. In our scheme, four 6-bit shares of the recovery messages are embedded into three 2×2 blocks; hence, 2 bits are carried by a pixel averagely. Obviously, our scheme can shorten the bits of the recovery message carried by a pixel.

(a) Original image (b) Watermarked Image (PSNR = 37.9755) (c) Attacked image (d) Detection result (e) Recovered image

Figure 2 The original and watermarked images of the proposed scheme

Table 1 FNR and FPR of the three authentication stages

	Stage 1	Stage 2	Stage 3
FNR	0.0414	0.0174	0.0073
FPR	0.0024	0.0024	0.0031

Methods	Attacked image (ρ = 5.75%)	Detection result	Recovered image
Lee and Lin		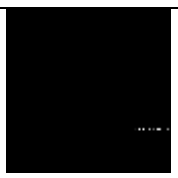	
	(a)	(b)	(c) PSNR = 23.6321

Ours			
	(d)	(e)	(f) PSNR = 33.9023

Figure 3 Comparison experiment 1

Methods	Attacked image (ρ = 8.63%)	Detection result	Recovered image
Lee and Lin			
	(a)	(b)	(c) PSNR = 32.5821
Ours		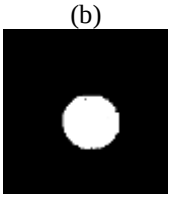	
	(d)	(e)	(f) PSNR = 34.8037

Figure 4 Comparison experiment 2

Methods	Attacked image (ρ = 17.75%)	Detection result	Recovered image
Lee and Lin			
	(a)	(b)	(c) PSNR = 25.5617
Ours			
	(d)	(e)	(f) PSNR = 29.8359

Figure 5 Comparison experiment 3

4. Conclusions

This paper proposed a tampering detection and recovery scheme for digital images. The recovery message is split into four shares and spread over the image. By doing so, we can cut down the bits of the recovery message carried by a pixel and increase the survivability of the recovery message. Averagely, two bits are carried by a pixel and are shorter than Lee and Lin's 2.5 bits. The authentication message is hashed from the information of user id, user password, block number, pixel average, …, etc. and is

embedded into the last bit of pixels. When an image is suspect to be tampered, the authentication message is used to judge the tampering status and locate the tampering area. The tampering detection goes through Hsu and Tu's two-stage authentication followed by the proposed sliding-window stage. The purpose of the third stage is to decrease the false negative rate so that the quality of the recovered image can be increased. Observing from the values list in Table 1, the proposed third stage indeed decreases the false negative rate. Compared to Lee and Lin's scheme, the proposed scheme can recover the image better. Besides, our scheme can detect the copy-and-paste attack successfully.

5. Acknowledgement

This work was supported in part by a grant from the National Science Council of the Republic of China under the projects NSC 100-2221-E-130-014- and NSC 100-2221-E-034-011-.

6. References

[1] C.K. Chan and L.M. Cheng, Hiding data in images by simple LSB substitution, *Pattern Recognition*, 37(3), 2004, pp.469-474.

[2] P.L. Lin, C.K. Hsieh, and P.W. Huang, A hierarchical digital watermarking method for image tamper detection and recovery, *Pattern Recognition*, 38, 2005, pp.2519-2529.

[3] C.C. Chang, Y.S. Hu, and T.C. Lu, A watermarking-based image ownership and tampering authentication scheme, *Pattern Recognition Letters*, 27, 2006, pp.439-446.

[4] F.H. Yeh and G.C. Lee, Content-based watermarking in image authentication allowing remedying of tampered images, *Optical Engineering, 45*(7), 2006, pp.1-10.

[5] S.H. Liu, H.X. Yao, W. Gao, and Y.L. Liu, An image fragile watermark scheme based on chaotic image pattern and pixel-pairs, *Applied Mathematics and Computation*, 185, 2007, pp.869-882.

[6] C.C. Chang, Y.H. Fan, and W.L. Tai, Four-scanning attack on hierarchical digital watermarking method for image tamper detection and recovery, *Pattern Recognition*, 41, 2008, pp.654-661.

[7] T.Y. Lee and S.D. Lin, Dual watermark for image tamper detection and recovery, *Pattern Recognition Letters*, 41, 2008, pp.3497-3506.

[8] C.W. Yang and J.J. Shen, Recover the tampered image based on VQ indexing, *Signal Processing, 90*, 2010, pp.331-343.

[9] X. Zhang, S. Wang, Fragile watermarking scheme using hierarchical mechanism, *Signal Process*, 89, 2009, pp.675-679.

[10] C.S. Hsu and S.F. Tu, Probability-based Tampering Detection Scheme for Digital Images, *Optics Communications*, 283(9), 2010, pp.1737-1743.

[11] E.T. Whittaker and G. Robinson, Lagrange's Formula of Interpolation, in: *The Calculus of Observations: A Treatise on Numerical Mathematics*, 4th ed. New York: Dover, 1967, pp. 28-30.

E247

Service Standardization to Utility Model: Process, Technology and Contracts

Jyri Rajamäki
Laurea University of Applied Sciences, Espoo, Finland
jyri.rajamaki@laurea.fi

Markus Vuorinen
HP Enterprise Services, Helsinki, Finland

The corresponding author: Jyri Rajamäki

Abstract
IT Services are currently delivered in very heterogeneous and customized delivery methods to client organizations. Clients have tailored processes, contracts and technology managed by both internal and external suppliers. The IT service terms, process and technology have been often fully tailored based on client organizations wishes. The next IT Megatrend - utility computing – is very controversy. In utility computing IT services are highly standardized. Same services are provided for multiple clients simultaneously to any device over the network with same terms and conditions. Suppliers have invested to automation to be able to provide the service to as many clients as possible with little or no manual work. With utility computing client organizations could achieve considerable savings, quality improvements and strategic initiatives as they would pay only based on the actual usage. The transformation journey from highly tailored service model to highly standardized services requires some careful preparations in order to succeed. This paper studies and presents that processes, technologies and contracts should be standardized in order organizations to be mature enough to take the benefits of utility computing. The benefits of standardization are described in detail as well some potential issues if standardization is not done.
Keyword: Utility services; IT outsourcing; service management

1. Introduction

IT services are under evolution phase. The traditional IT services which used to be built of hardware and software components are coming as commodity services. Organizations notices that model where everyone used to build up their own services may not be most effective solution. Using shared large scale utility services is more flexible both from service quality perspective and financially. Multiple standard utility services are out there already. CRM's, managed OS, e-mail, instant messaging and file

sharing to name only few of the services. Deployment can be done often in minutes and charging is based on actual usage, time, transactions or other measurable unit with price tag. Deployment of utility services has been typically automated making it very effective to duplicate the service to multiple clients. From business perspective this approach is warmly welcome – time for deployment projects is cut drastically and heavy investments are not required. Additionally even service pilots can be done in very short time and with minimal investments.

In the paper a case is made for standardizing the processes, technology and contracts surrounding IT services. Both advantages of standardizing and disadvantages of not standardizing are discussed. A new method is presented for organization how they could prepare to take the benefits of utility computing and also briefly pointed the dangers of jumping in to cloud computing without being mature enough to manage dangers of it. The paper is a descriptive paper resulting in practical recommendations in the field.

2. Rationale

The utility services are defined "collection of technologies and business practices that enables computing to be delivered seamlessly and reliably across multiple computers" and "capacity is available as needed and billed according to usage" [1]. In this type of model organizations are able to use resources when they need it and as much as they need it.

Traditional IT services have been insourced or outsourced and the platform is fixed for organization only. This means that organization using the IT service has dedicated environment for them. Organizations has been possibility to have their own technologies which are partly legacy, their own support methods and processes and also custom contracts both internally and externally.

In utility services the platform is shared and there are multiple customers using the service and the platform underneath. As the service is shared the customers in multi-tenancy environment have very little or no possibilities to have special tailoring for their service. In shared service, all customers' need to follow the service lifecycle and service conditions much more strictly than they are probably use to do earlier [2].

Non-standard custom built technologies supported by informal processes and gentleman agreements are common in organizations. As a contrast - global utility computing service suppliers having thousands of customers from different cultures, have very standard technologies, processes and contracts for their service catalog. Next chapters describes why and how organizations should standardize their technologies,

processes and contracts in order to gain the benefits of utility computing.

3. Review of Literature

3.1 IT Architecture and Technology

Ross [1] has studied several large different types of outsourcing arrangements and based on the research he had made some conclusions how organizations can achieve better outsourcing agreements.

Ross also expects that in future organizations will continue outsourcing as part of utility computing. Smaller organization will more likely make a partnership with one-supplier where larger organizations are more likely to use selective sourcing with a network of suppliers [1].

Organization are likely moving more and more their services to cloud as utility services, because using resources only when needed is strategically feasible. In order firms to use cloud resources strategically, their architecture should be very standardized. A heterogeneous environment cannot get the benefits of utility computing and therefore a strong global standardization is required.

For some organizations, looking for a partner for helping them to incrementally standardize the environment might be strategically more feasible than a big-bang approach. This would allow organizations to have roadmap for utility services though they would not have the ability to transform themselves.

In order organizations to survive in the future, going into more standardized architecture is needed. IT services should be transferred towards a commodity type of services. In order IT organizations to succeed they should have a strong strategy for IT technology standardization. This allows organizations to have cost effective outsourcing models and to move towards utility computing incrementally.

3.2 Computing Exchange and Contracting

Buyya &al [2] have studied how cloud computing as utility is going to chance the computing model. They have presented a model in which computing capacity is provided by same models than electricity exchange. In today's electricity exchange, the market prices are changing based on the demand and supply. Similar model could work in IT domain where holders of major datacenter capacity could sell their capacity for market price and those requiring it could buy it for the best price. Within this model there are brokers who buy and sell capacity (computing, storage e.g.) and enterprises who buy this capacity where they can get it for cheapest and run their services on top of it [2]. Transition from physical servers lying in office corner to buying computing capacity for a daily spot price is a long way. Different technologies for moving the IT

services from server to another, sliced into different virtual machines (VM's) are developed. The idea of computing exchange sounds an effective way for managing the demand and supply of computing capacity globally. However, the technology and standards that support the movement of IT services between different supplier's datacenters on fly do not exist yet.

Addition to the technical boundaries, also he trm of agreements should be considered to make computing exchange possible. Contracts for computing capacity should be standardized. Possible risks would include that supplier is selling capacity more than he actually holds and that might cause unavailability of service, performance issues or unavailability to transfer the service between the suppliers. Different type of Quality of Service (QoS) agreements must be in place together with penalties and aligned with Service Level agreements and key performance indicators.

Several ways to measure performance exist, e.g. computing can be measured by instructions per second or floating-point operations per second; storage by size (Mb) or by performance (input/output operations per second, IOPS); network performance by speed or by latency. Therefore, a standard computing unit that could be applied for any service is complicated to have. The hosted application should be guaranteed with certain transaction time or turnaround time. Transaction speeds and turnaround times would describe if the application is performing as expected. In order to make computing exchange possible, all different type contract terms for computing exchange should be standardized and preferably categorized.

3.3 Demand Management and Processes

Salle [3] presents the history of IT management from the 70's until the beginning of 21st century. He describes how the IT domain started to work in more structured way and how same IT service management practices have spread around the world. Also, core IT processes are looking similar in most organizations. Salle describes also how the roles of companies' IT managers are changing from technical IT experts to organizations' strategic business partners who manage the services based on the business requirements.

In the early years of IT computing, no common processes or practices existed for problem management. IT was seen only as technology and not as a service towards business organization. The IBM Information Systems Management Architecture (ISMA) was first service management practice that was created to respond to this problem. ISMA was later extended and refined with for example with Information Technology Infrastructure Library (ITIL), HP IT Service Management (ITSM) and Microsoft Operations Framework (MOF) which are taking broader look into service

management and defining core functions and processes in more detailed and practical way.

The trainings for different IT Service Management practices have been growing continuously over the years. Organizations are increasingly aware that in order IT to be managed efficiently, some standard service management frameworks need to be followed. When organizations consider changing a part of the business support into utility services, they should validate their capability to operate with a supplier which is following ITSM principles. For client organization, the challenge is not to manage the technology any longer but to master the demand from business and work with supplier accordingly. One of the strategic changes for client organizations is to understand that IT is no longer only a expense to be controlled but rather and investment that can be managed.

4. Three Pillars of IT Services

We pose three pillars of IT services that should be standardized on the journey to utility services: (1) technology, (2) contracts and (3) processes; presented in Table 1. Next we briefly present the benefits for both supplier and customer organizations that will arise when these pillars are widely standardized.

Table 1 - Service Standardization

	Standardized	**Non-Standardized**
Technology and Architecture	*Operations can be automated. Commodity, cost effective to run, transferrable from supplier to another. No special knowledge required.*	*Tailored and heterogeneous. No automation, a lot of manual work and client specific special knowledge.*
Contracts	*Predefined Service Levels and penalties, formal papers and agreements.*	*Based on gentleman agreements, no official warranties or penalties.*
Process	*Ability to operate with practically any supplier. Capabilities to manage changes and problems between the companies not only between people.*	*Based on people relationships, no roles. Does not scale to support large business models.*

The first standardization aspect is technology and architecture. Let's look e.g. a client which is looking for the most efficient hosting solutions for their web application developed with PHP. PHP is a popular web application development language. There can be found hundreds of hosting services which provides managed hosted server where clients can install their own PHP applications. Clients are not required to have their own teams around the clock to maintain the availability of servers; this is done by the supplier. These types of utility services are often cost effective as the same platform can be shared among tens of clients with no customization or manual work. However, if

this web application has a requirement to be able to run some custom scripts on the host operating system level time to time with root access, the service offering is diminishing. Usually, none of the suppliers have such option to access to data files on OS level and run scripts in their portfolio. This would make the management complex, if users would have customized access and cause security concerns, if they would have access to each other's data. In such case, the client would be required to have non-standard and usually dedicated service for them which is considerably more expensive. Applications which are not built to run on standard technology based on best-practices can be very expensive in a long run.

The next standardized aspects are contracts. They would describe the service performance, availability, support hours etc. These are usually referred as different Service Level Agreements (SLAs). If the contract between the supplier and the client does not have any warranties about e.g. performance or service hours, the client (or the supplier) could be in trouble later. Clients should validate if their suppliers are capable to deliver services based on their contractual requirements such as 24*7 hour support or four hour response time for contact center. If contracts are standardized and they describe the service detailed enough, it is possible to compare the service between different suppliers helping both clients and suppliers.

The last aspect is process standardization. Within all main ITSM frameworks, some processes are very similar. Change Management, Problem Management and Incident Management are some of the most common ITSM processes. All of these processes have certain roles from both suppliers' and clients' perspectives. Communication and collaboration is very complex if no common understanding exists what is incident or what are the responsibilities of change manager. A typical issue would be that clients who are unfamiliar with ITSM practices are requesting for support from certain people or asking for contact persons where they should be looking for corresponding role to help them in their matters. However, people tend to be on holiday and change positions. This means that all requests cannot be managed by single person anyway. Organizations which are used to work with gentleman agreements need to revise their requirements on their journey. Standardized processes are beneficial for both the client and the supplier.

5. Discussion

Over the past decades, the history of IT services has been usually based on the collaboration of two companies; client and supplier or even customer and engineer. Such a service model has been based on personal relationships instead of role based responsibilities. However, when the service model is changing so that a supplier has

multiple customers for the same service or a client has multiple suppliers for different services, then technology, processes and contracts should be standardized.

On the journey to utility computing, IT services should be standardized. Neither clients nor suppliers can utilize the benefits of utility computing unless the services are very standardized. The benefits of standardized technology, processes and contracts are obvious. Clients are able to change their supplier more flexible if the service is transferrable from a supplier to another. The technology must be commodity compliant so clients are able to move their services from provided to another. The suppliers are having more providers of commodity service. The price of standard utility services is decreasing and in order clients to be able to take the advantage of the trend, they need to be compliant with standard service platforms, contracts and processes.

Due to the nature of utility services, the standardization should be driven by a group of suppliers rather than e.g. legal requirements. The standards should be voluntary defined by consortia of organizations. This type of De facto standards, typically created by individual firms, groups of companies or in industrial associations, could be flexible and easily adopted by the community of service suppliers and clients. Ownership of standard development should be owned by similar way as the ITSM processes, where consortia of organizations are maintaining the industry practices. [4, 5]

6. Conclusion

The state of current IT services is very heterogeneous; the services are usually tailored for each customer's requirements. Clients have had their own customized technologies, processes and contracts for each supplier. As the IT services are changing to utility services, the tailoring of services is vanishing. Same services are provided for multiple customers with same technology, terms and conditions and processes. Cloud computing provides the benefits of massive scales. Services are provided over the network almost fully automated and charged based on actual usage. For most clients, it is strategically more feasible to use resources when they are needed.

In order clients and suppliers to get the best benefits out of their IT services, they should focus on De Facto standardization of IT services:

- Organizations should focus how to standardize their technology and architecture to be technically compliant with utility services. All tailored nonstrategic solutions should be planned for retirement or migration.
- Organizations need to assure that they are mature with global ITSM methodologies. ITIL framework is a good industry standard to be followed. To effectively work with IT suppliers, ITIL processes should be followed.
- Organizations should validate their maturity with contracts. Gentleman

agreements must be changed to standard contracts. Terms of SLA's and QoS must be agreed with supplier in order to assure service quality and make services transferable.

This paper deals ITSM from strategy perspective looking at its overall picture. However, the methodologies in multi-supplier management in ITIL core processes have not been studied yet. The multi-supplier operating framework for some of the ITIL main processes, such as change management, incident management and problem management, would be important to be studied for providing organizations more practical approaches in operational duties.

Each organization has its own requirements for IT services. When external suppliers are providing IT services, standard services might be inflexible for the multi-tenant service base. Suppliers' standard services might not respond to all client requirements. The ways how organizations could manage the gaps between the supplier's standard services and clients requirements is vital to understand and study. Our approach is not looking the dependencies between the different IT services for a multi-supplier service base but only from a single IT service perspective. In the future, synergies and/or conflicts between different IT services should be studied within a multi-supplier service base. Additionally, the difference between traditional outsourcing and cloud sourcing governance methodologies should be investigated.

7. References

[1] Ross J. W., Westerman G., 2004. Preparing for utility computing: The role of IT architecture and relationship management. IBM SYSTEMS JOURNAL, VOL 43, NO 1, 2004

[2] Buyya R., Yeo C., Venugopal S., Vision, Hype, and Reality for Delivering IT Services as Computing Utilities, 2008, IEEE

[3] Salle M., IT Service Management and IT Governance: Review, Comparative Analysis and their Impact on Utility Computing, HP Laboratories, HPL-2004-98, June 2, 2004

[4] Kivimäki, Anri, Wireless telecommunication standardization processes, 2007, University of Oulu, Department of Information Processing Science, University.

[5] OSCON (Open Source Convention) 09: Simon Wardley, "Cloud Computing - Why IT Matters". July 20-24, 2009. San Jose, California.

E253

Multi-Agency Cooperation in Cross-border Operations: Information Exchange between Law Enforcement Authorities

Jyri Rajamäki and Petteri Ruohomki
Laurea University of Applied Sciences, Espoo, Finland
jyri.rajamaki@laurea.fi

Abstract
The nature of crime has internationalized. Therefore the transmitting of tracking and other status information between Law Enforcement Authorities should become an everyday business. The goal of this paper is to present a possible solution for international cooperation between authorities. The proposed solution is based on Public Key Infrastructure operation model built for the financial sector companies.
Keyword: Law enforcement; Public key infrastructure, Public protection and disaster relief

1. Introduction

Organized crime is a real threat around the globe. Law Enforcement Authorities (LEAs) are constantly seeking new technological recording, retrieving and monitoring solutions that would facilitate their combat against criminal organizations. Organized crime is an international business whereas operational LEAs are mostly national organizations. This creates a pressure for improved cooperation between LEAs. However, LEA organizations increasingly face interoperability issues at all levels (technical, operational and human) as they interact with other national, regional or international organizations. Not only assets and standards must be shared to empower joint responses to threats and crisis in an increasingly interconnected network, but also LEA organizations have to benefit from interoperability functionality in their day-to-day work.

1.1 MACICO Project

LEAs are not the only Public Protection and Disaster Relief (PPDR) organizations that need more cross-border cooperation. Multi-Agency Cooperation in Cross-border Operations (MACICO) Celtic project [1] will develop a concept for interworking of security organizations in their daily activity. It deals with cooperation of PPDR organizations that do not use the same radio network, but in some missions could take benefit of a share of their respective infrastructure. Use cases such as cross-border surveillance and pursuit of criminals across a border require LEA organizations from both countries to communicate together and to continue to communicate with their

control room. Also, exchanging of sensor data is highly needed between LEAs of multiple countries.

MACICO's main goal is addressing in a short-term perspective the needs for improved systems, tools and equipment for radio communication in cross-border operations (cross-border surveillance, cross border pursuit,…) as well as during operations taking place on the territory of other member states (high scale civil crisis operations or complex emergencies needing support of PPDR services from other countries). On the other hand, MACICO encompasses the interoperability issues European countries will be faced to in a long term perspective, tackling the necessary transition between currently deployed legacy network and future broad band networks.

Celtic is a European research and development programme, designed to strengthen Europe's competitiveness in telecommunications through short and medium term collaborative R&D projects. Celtic is currently the only European R&D programme fully dedicated to end - to – end telecommunication solutions. MACICO Celtic project has partners from France, Spain and Finland. It started December 2011 and lasts 2.5 years.

MACICO project is centered on the PPDR sector (police, fire, paramedic, custom, …). Nevertheless, other sectors divided by end-user application as Professional Mobile Radio (PMR) and Private Access Mobile Radio (PAMR) could profit by the outcomes of MACICO. Such sectors are e.g. critical infrastructure protections and military. In areas, such as Asia and Oceania, where the developed European PMR solutions perfectly match, the interoperability would be a decisive advantage to gain the market.

1.1 Target of the Paper

The ICT services supporting LEAs' surveillance operations have usually been developed by national agencies, although some commercial devices are nowadays more widely in use. Many of the solution providers offer integrated systems, where sensors and mapping software are combined. Traditionally these systems are designed to be standalone services with no built-in way to communicate with other mapping systems. If some interface and protocol exists, the possibility to send properties and status information, so-called metadata, is still missing. Differences between devices, protocols and background systems have caused problems for international cooperation, simply due to lack of commonly agreed operational procedures and technical interfaces. [2]

This paper presents a system how LEAs can exchange and share critical information. The paper answers how to provide efficiency and consistent Public Key Infrastructure functionality. The main question is how LEAs can identify the counterparty player securely. A LEA organization must be able to trust outputs and inputs.

2. Proposed System

Operational procedures should be as follows: Decisions should be taken at the lowest appropriate level with coordination at the highest necessary level. The doctrine and training describe the way in which people, processes and technology combine to enhance decision making through the use of a common operating picture that provides mission critical information available to appropriate staff.

When building up LEAs' multinational sensor data exchange system, increased costs are minor when compared to benefits of international cooperation of authorities. Shared data should be considered critical information, and therefore appropriate data protection is required. More and more information and communications have become network-based, and accordingly the number of cyber-security incidents has increased. Although some nations have already established critical information infrastructure protection (CIIP) laws [3], international legislation is still missing.

When an information infrastructure is installed and all functions are tested, the system should be tested against external and also internal cyber-attacks to find possible vulnerabilities. Protection against external attacks and alternative routing with different IP addresses should be tested to provide necessary reliability for the system. Ref. [4] is one useful aid for planning security tests.

Suitable ways for exchanging and sharing information between LEAs with no delays should be found; certain protocols and operational procedures are needed. The possibility to adopt already existing methods, for example from military organizations, should be considered. Currently the National Marine Electronics Association (NMEA) protocol [5] is used in some international situations, but for real-time surveillance it is not sufficient. For example, the NMEA protocol does not provide the possibility to send metadata.

2.1 Network Topology

The lack of a transmission protocol is not the only issue in developing a multinational LEA network; also the network topology has to be agreed. Figure 1 shows a possible

network topology, in which all data transfer is encrypted and protected with a virtual private network (VPN). If the data should be encrypted inside VPN, the easiest way is to use a common Public Key Infrastructure (PKI) solution. All the public keys should be stored in one server connectible via VPN.

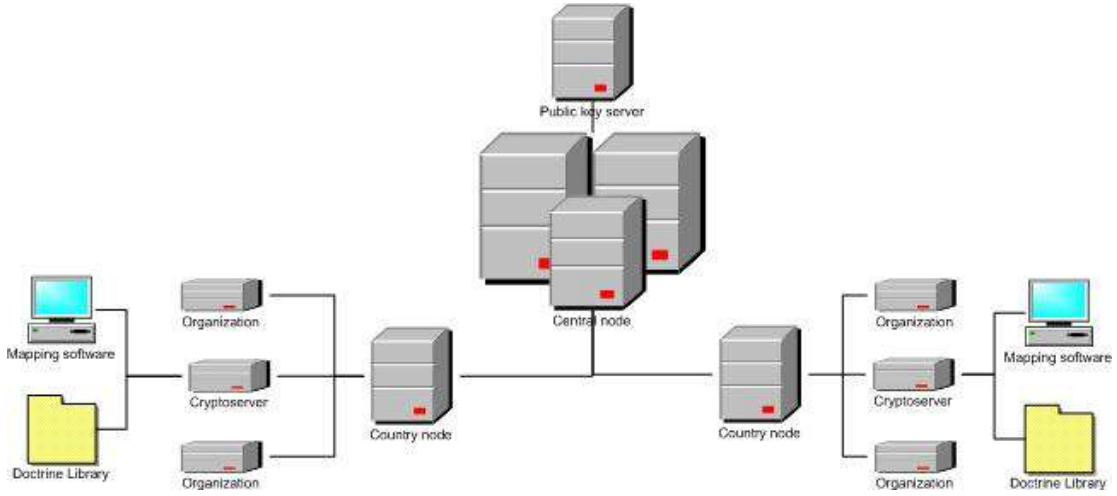

Figure 1. Network Topology

When a connection to another LEA organizations' data source is needed, the transmitting server acquires needed public keys from the dedicated server, then encrypts and sends messages to the receiver. When the receiving server gets a new encrypted message, it automatically decrypts the data.

Also, reliable ways to exchange additional information during cross-border operations is needed. This so-called metadata contains necessary information about the target and therefore should also be transmitted to the foreign LEAs. Metadata can include details about the target vehicle, possible risks of the target (e.g. armed) and preferred actions against the target. Like always, all data should be encrypted. All metadata should be sent along with the spatial information.

2.1 PKI Operations Model

Public Key Infrastructure operations model idea is based on ISF (Information Security Forum) best practices and modified for a financial company. The model idea is that it serves as a basic package to new PKI projects. The model is divided to 16 different processes as shown in Figure 2. All these processes have their own role and owners. Process owners have divided to four different roles. Sometimes process significance might be trivial, other times the process might prove vital for the project. Good example is the Policy and standard process. First time an organization must build this document, it might be a large undertaking for the organization. However, in next

project this process is only applied for updating valid policies.

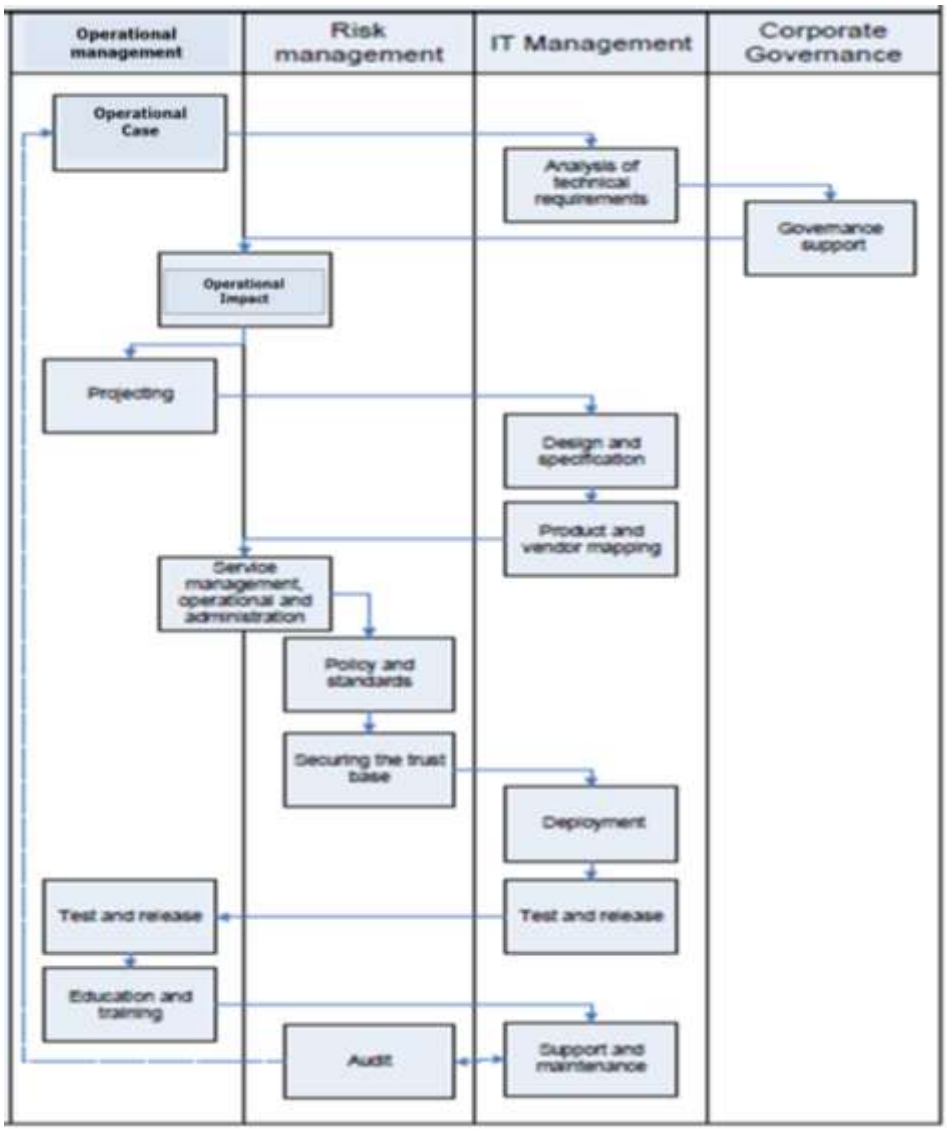

Figure 2. PKI Operations Model

Everything starts from LEAs operational needs. It is important that the operational part is leading this conversation. IT management and Risk management is supporting this report. This is an important phase because it is here that most of the metrics are defined. In the end these metrics define how successful the project was. Model is PKI project best practices. This is the reason why all processes are described separate processes. All phases give advice on what must be done and what should be done. In the end it's always a company or project decision what to do in the different kind of PKI projects. This is not a model for how to run a PKI project. It does not concern with how to come up with a project budget, or how to keep project meetings. When a certain project adapts this model it assumes that all basic project process practices are defined beforehand. Normally organizations have their own project model what they

follow or they can follow PMBOK guide [6].

Operational case phase is a regular operational process case. This process should come from LEA's own operational environment. There are no specific PKI demands in the operational case phase. From a security point of view these phases should have their own detailed guide on how to estimate what are the costs to security environment. How to estimate what is really needed so future projects do not build extra secure or fully automated environments without any benefit.

In the analysis of technical requirements the organization should follow know standards like ISO 27000 or PCI. Good example is best practices in [7]. It is important to go through all in the analysis stage as LEA can easily notice if some area, like the physical environment, is missing. Normally projects think only for valid environments. There might be similarities and projects can save cost and time. Also, if environment is outsources it helps environment deployment.

Governance support like senior management support is vital for the security projects. These are persons who can make decisions so projects avoid delays because of lack of decisions. Model gives basic knowledge for governance support but this is normally depended on the manager. E.g., an inside project manager has better connections to senior management. Sometimes this is a good thing and at other times this is a problem.

Operational impact phase needs more detail information how to evaluate real impact. This phase needs a check list for the actors. There is always something what must be taken in the consideration. That is the reason why best practice check list is needed.
Projecting phase is a standard stage in the projects. This phase should give more detail information where project manager can find guidelines and best practices on how to set up a project.

Design and specification phase is what to write so an environment can be done. This is more technical than others. It is important that technical personnel of the project are participating. At this phase all operational needs must be known by the project design group. These specifications should be reviewed with the operational personnel.

Product and vendor mapping phase are decisions what service provider or program company are using. This phase needs more information from e.g. ITIL; the project can find of processes for finding right product and vendor. There should be e.g. specified

RFO (Request for Order) and RFP (Request for Proposal) processes.

Service management, operational and administration phase is fully implemented from ITIL. Maybe some special detail for PKI or security can be found. Basically these processes are almost same in all IT sector. Model should follow ITIL process steps with PKI information.

The policy and standards phase is more detailed to PKI and security issues. PKI and security have their own security policies and practice statement models what to follow. During this phase it is always important to remember that organizations have their own security policies what they must follow.

Securing the trust base phase tells company what was the PKI policy state because this phase is based on that. In this phase all the PKI policy stages must be checked so that all is done as in the defined policy. PKI policy is an inclusive guide, ranging from technical to legal issues. So this phase needs time to pass.

Deployment phase is about the technical issues. In this phase all plans are built to use. It is very important to follow specifications so all is done in the right order and in the right way. Normally in this phase it is noticed whether something is not planned. These new specification add-ons must be described and approved by the management. Also it is import calculate new costs.

Test and release phase is where project needs more hands on personnel because there are lots of different tasks. Normal situation an organization has its own test and release processes. If not, organization should follow some known standard or best practice like ITIL. ITIL has already solved basic problems with this phase. This implementation model should follow more ITIL process. These basic ITIL processes need all kind of authorities.

Education and training phase is easiest to drop out from the plans. Yet it is still an important part. This phase is for the new users and for the rest of the company to know what this project focuses on. Company should have its own security education and training program. This should be only one part of that. Project has massive work to do if company does not have any program of its own. This must be taken care of in the project time table.

Support and maintenance phase is important for continuity. LEA should have already

working support and maintenance processes. This is only for PKI implementation to that. Also this is lighter if services are outsourced because of some services are provided by the vendor. LEA should follow ITIL processes if company does not have already these processes on place. During this phase LEA must consider whether the PKI services are open always or can the hours be limited to business hours.

The audit phase is compulsory for some sectors. This means that LEA should have an audit process on place like specification audits and environment audits. Normally these are added to LEA's own project processes. During the audit phase LEA should use COBIT models. Company separate full COBIT implementation from project work.

3. Discussions

The paper result is the artifact of Public Key Infrastructure operations model. This model offers the first steps on what must be done in PKI project. It provides a partial answer on how to develop faster, more efficient, and safer PKI services. The paper results are derived from a real PKI project in the financial sector, but these kinds of projects are comparable with one another.

The model phases in Figure 2 are not at the same operational level. Some phases are light business/operational decisions and so are detailed technical assignments. Model needs some kind of estimation about the timet-able. Every phase should have its own duration estimate. Also, the model needs an estimate on what phases can be done at the same time and what phases are depended on each other. It also needs actors. Every phase should have information concerning who is responsible for that phase and who must participate in that phase. Project manager carries the overall responsibility but every phase needs its own responsible person such as the audit risk manager or for technical environment setups the technical architect.

4. References

[1] CELTIC-Plus, MACICO Project Information, http://www.celticplus.eu/Projects/Celtic-projects/Call8/MACICO/macico-default.asp

[2] Viitanen, J., Happonen, M., Patama, P. & Rajamaki, J., "Near Border Procedures for Tracking Information", WSEAS TRANSACTIONS on SYSTEMS. Issue 3, Volume 9, March 2010.

[3] Park, S. & Yi, W., "The Evaluation Criteria for Designation of Critical Information Infrastructure", in Proceedings of the 8th WSEAS International Conference on EActivities, Information Security and Privacy (ISP), Puerto de la Cruz, Spain, December 2009, pp. 77-83.

[4] Patriciu, V.-V.& Furtuna, A. C., "Guide for Designing Cyber Security Exercises", in Proceedings of the 8th WSEAS International Conference on E-Activities, Information Security and Privacy (ISP), Puerto de la Cruz, Spain, December 2009, pp. 172-177.

[5] National Marine Electronic Association, http://www.nmea.org

[6] *A Guide to the Project Management Body of Knowledge (PMBOK Guide)*, Project Management Institute, 4th Edition 2008.

[7] Barker, E., Barker, W., Burr ,W. & Polk ,W. & Smid, M., *Key Management Inserts for Security Plan Templates*. 2002.

Program – Poster Sessions

Engineering A

Pullman Bangkok King Power, 2F

2013/1/26 Saturday 10:00-12:00

E185

A Study on Optimization of DVC Type Thermal Barrier Coatings Applied to Gas Turbine Blade

Dongkeun Lee｜*Sungkyunkwan University*
Dongkeun Lee｜*Sungkyunkwan University*
Inhwan Shin｜*Sungkyunkwan University*
Yongseok Kim｜*Sungkyunkwan University*
Jae Mean Koo｜*Sungkyunkwan University*
Chang Sung Seok｜*Sungkyunkwan University*

E199

The Performance Evaluation of Port Crane using Next-generation Port Simulator

Young Min Kim｜*Dong A University*
Jong Il Bae｜*Pukyong National University*
Kwon Soon Lee｜*Dong-A University*

E214

Apply Low Energy ELA to Anneal and Improve Au Nanoparticle Embedded Nonvolatile Memory

Kuan Yuan Shen｜*National Taiwan University*
Chieh Hsiung Kuan｜*National Taiwan University*

E218

Kinetics of the Biogas Production from Chlorella Vulgaris at Different Ultrasonic Dose of Pretreatment

Phrompol Chantrasakdakul｜*Konkuk University*

E185

A Study on Optimization of DVC Type Thermal Barrier Coatings Applied to Gas Turbine Blade

Dongkeun Lee
Graduate school of mechanical engineering, Sungkyunkwan University,
2066, Seobu-ro, Jangan-gu, Suwon, South Korea
positive47@hanmail.net

Inhwan Shin
Graduate school of mechanical engineering, Sungkyunkwan University,
2066, Seobu-ro, Jangan-gu, Suwon, South Korea
sihwan@skku.edu

Yongseok Kim
Graduate school of mechanical engineering, Sungkyunkwan University,
2066, Seobu-ro, Jangan-gu, Suwon, South Korea
dmsnake@naver.com

Jae-Mean Koo
Department of mechanical engineering, Sungkyunkwan University,
2066, Seobu-ro, Jangan-gu, Suwon, South Korea
Kjm9000@hanmail.net

Chang-Sung Seok
Department of mechanical engineering, Sungkyunkwan University,
2066, Seobu-ro, Jangan-gu, Suwon, South Korea
seok@skku.edu

The corresponding author: Chang-Sung Seok

Abstract

Nowadays, various types of TBCs (thermal barrier coatings) applied to gas turbine blade have been developed and researched. However, DVC (dense vertically cracked) coating has not been lively researched, although DVC coating has been widely applied to commercial gas turbine blades.

In the case of DVC coating, vertical cracks which influence fatigue life and stress distribution in the coating are artificially inserted to improve the performance of coating. Especially, density and depth of the inserted cracks are main variables changing coating's characteristic. To research this, thermal fatigue test was performed by using a coin-type specimen. Also, the finite element analysis of the transient heat transfer and thermal stress was performed.

From the thermal fatigue test result, it have been seen that a fatigue life of specimen with high crack density is longer than that with low crack density. And from the FEA result, it have been seen that the narrower the crack interval is, the smaller the maximum stress is, but there is no change of the stress below a particular density.
Keyword: DVC(dense vertically cracked), TBC(thermal barrier coating), thermal stress, thermal fatigue, crack

1. Introduction

Thermal barrier coating (TBC) is applied to protect the core components of a gas turbine from high temperature flame and to reduce the surface temperature of the components. The coating layer is composed of a metallic bond coat (MCrAlY) and a ceramic top coat.

Major failure mechanisms of the TBC is thermal stress, which is caused by the mismatch in the thermal expansion coefficients between the two coats.[1] Various researches to increase the reliability of thermal barrier coating have been conducted because the failure of thermal barrier coating can seriously damage not only the blade itself but also the whole turbine system.

Among the various coating methods applied to gas turbine blades, DVC is a well-known coating method that increases the coating life efficiently. In the case of DVC coating, vertical cracks which influence fatigue life and stress distribution in the coating are artificially inserted to improve the performance of coating. [2] Especially, density and depth of the inserted cracks are main variables changing coating's characteristic. To research this, thermal fatigue test was performed. Also, the finite element analysis of the transient heat transfer and thermal stress was performed.

2. Thermal Fatigue Test of DVC TBC

2.1 Thermal Fatigue Test

The thermal fatigue test was conducted for 4 cases of different crack densities for each specimen, and the relationship between crack density and thermal fatigue life was verified. The specimens used in this study were coin-shaped specimens,which are widely used in thermal fatigue tests. The metalic bond coat thickness was about 0.25mm and ceramic topcoat thickness about 0.5mm.

Fig. 1 shows the equipment used for the thermal fatigue test. This equipment was composed of a vertical electric furnace, an auto moving system and a forced air-cooling system.

The heating period was 15minutes and the cooling period was 5 minutes . The temperature in the furnace was maintained from 1100℃, which is a widely applied as the temperature range for thermal fatigue tests[3]. The time to perfect delamination of the coating layer from the substrate was considered as the coating life.

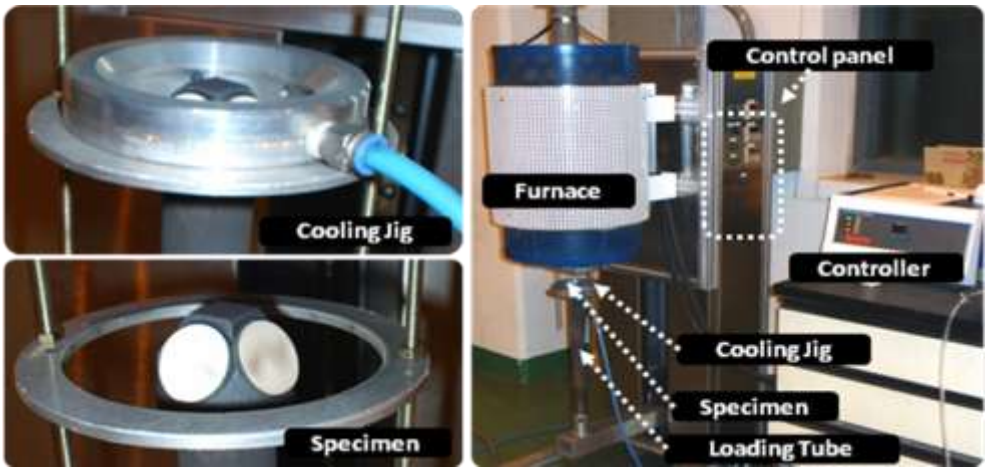

Fig. 1 Experimental Equipment

2.2 Test Result

From the result of the thermal fatigue test of the DVC specimen, we could know that delamination occured at the top coat-bond coat interface.

Fig. 2 shows the relationship between crack density and fatigue life of 4 cases. The x-axis indicates the density of the inserted cracks, and the Y-axis indicates the number of cycles to coating failure.

Based on the test result, the thermal fatigue life of a specimen increased when the inserted vertical crack density increased.

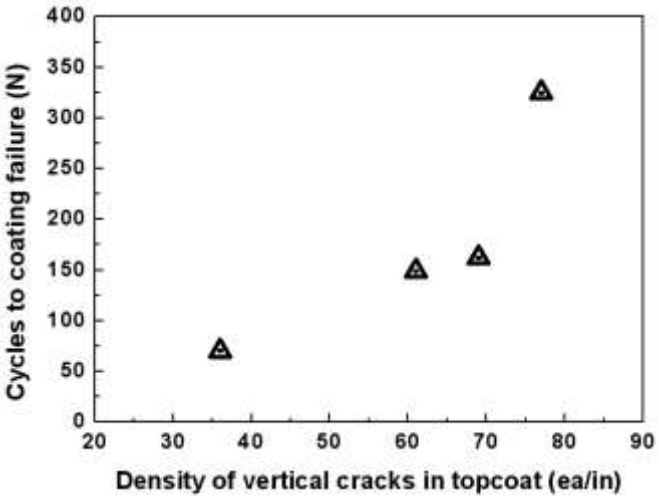

Fig. 2 Fatigue life-crack density diagram(N-ea/in)

3. Optimization of DVC TBC by FEA

3.1 Thermal stress analysis by crack density

A 2-dimensional analysis model of a part of a blade was used in the finite element analysis. In the case of the DVC coating, approximately 1 crack exists within 0.1~1.3mm (crack density, 20~200ea/inch)[2]. In this study, therefore, heat transfer analysis and thermal stress analysis of 9 cases of crack density in the range of 0.1~1mm were conducted.

Fig. 3 shows the 2D modeling and FEA mesh that were applied to simulate the crack geometry of DVC. ABAQUS commercial finite element analysis program was used and CPS4R type was used in the thermal stress analysis. The number of nodes and elements of FE model was approximately 10,000. The temperature applied to the top of the top coat layer was 1260℃, and the temperature applied to the bottom of the substrate was 285℃. In addition, the unit cell condition was applied to x-axis, which has infinite periodic condition.[4]

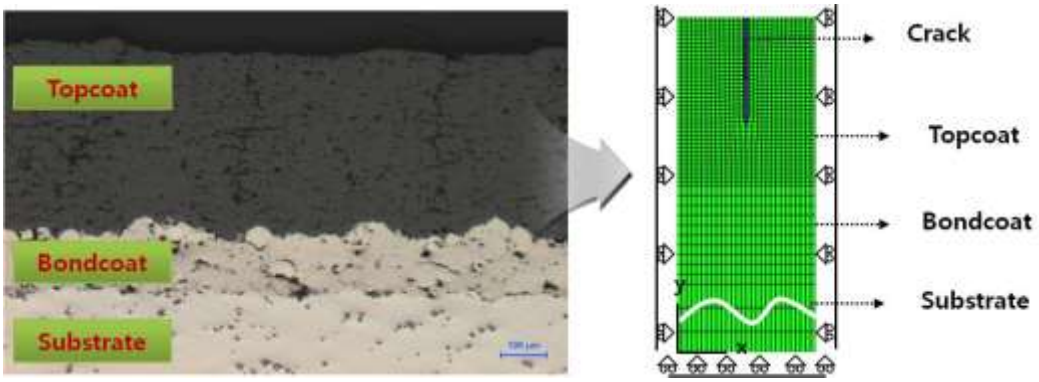

Fig. 3 FEA Condition of DVC-TBC

3.2 Result of FEA

The change of maximum stress in the interface between the top coat and the bond coat in the vertical direction was analyzed. Generally, delamination occurs at top coat and bond coat interface .

In Fig. 4, result of the finite element analysis shows the maximum tensile stress in the vertical direction at the interface. The x-axis indicates the distance of adjacent cracks, and the y-axis indicates the maximum stress.

The figure shows that the maximum vertical stress at the interface decreases when the crack interval decreases. The maximum vertical stress converges between the crack intervals of 0.2mm; this stress is equivalent to a crack density of 70ea/inch.
Based on the FEA result, it is expected that the thermal fatigue life of the coating will increase with the decrease of the maximum vertical stress at the interface, which is a well-known factor of coating fracture. In other words, the thermal fatigue life of a coating increases when the interval of cracks decreases. This is similar to the result of thermal fatigue test.

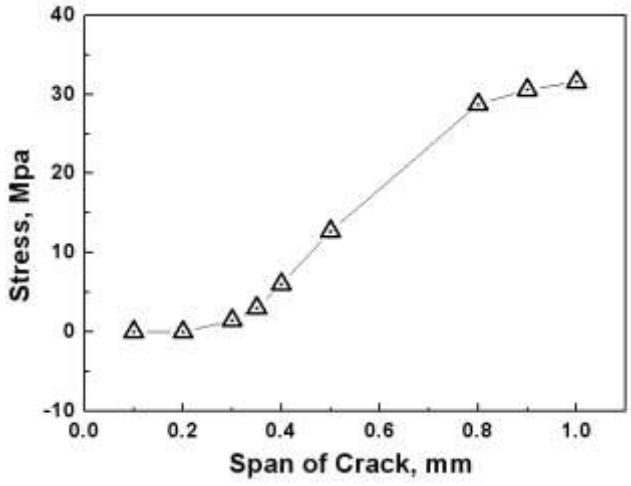

Fig. 4 Max tensile stress of interface of top-bond coat

4. Conclusion

1. The result of thermal fatigue test showed that when the crack density in DVC coating increases, the thermal fatigue life of the coating increases.
2. The result of FEA showed that the maximum vertical tensile stress at the interface, which is known as the most important factor of coating fracture, decreases when the

crack interval decreases(crack density increases), and converges around the crack interval of 0.2mm (crack density 70ea/inch; Optimized density).

5. Acknowledgments

This work was supported by the R&D program of the Korea Institute of Energy Technology Evaluation and Planning (KETEP) grant funded by the Korea government Ministry of Knowledge Economy (No. 20111020400020).

6. References

[1] Manish Madhwal, Eric H. Jordan, Maurice Gell, "Failure mechanisms of dense vertically-cracked thermal barrier coatings", Materials Science and Engineering A, Vol 384, pp. 151-161, 2004.

[2] D.K Lee, I.H Shin, J.M Koo, C.S Seok, T. W Lee, B.S Kim, "Estimation of the effect of crack on DVC-TBC applied gas turbine blade", Korean Society for Precision Engineering autumn conference collection of dissertations, pp. 815-816, 2010.

[3] D.J Kim, "The Estimation of Delamination Life of the Plasma-Sprayed Thermal Barrier Coating for Gas Turbine Blade", A doctoral dissertation of Sungkyunkwan Univ, 2009.

[4] A. A. Spector, M. Ameen, and A. S. Popel, "Simulation of Moter-Driven Cochlear Outer Hair Cell Electromotility," Biophysical Journal, Vol. 81, 11-24, 2001.

E199

The Performance Evaluation of Port Crane using Next-generation Port Simulator

Young Min Kim
Dong-A University, Hadan-dong, Saha-gu, Busan, Korea
kdudals119@naver.com

Jong Il Bae
Pukyong National University, Daeyeon-dong, Nam-gu, Busan, Korea
jibae@pknu.ac.kr

Kwon Soon Lee
Dong-A University, Hadan-dong, Saha-gu, Busan, Korea
kslee@dau.ac.kr

The corresponding author: kdudals119@naver.com

Abstract

In this study, the innovative operation system performance was evaluated for port competitiveness improvement at port distribution industry field. We conducted the 3D modeling of existing crane and suggested crane. The loading and unloading simulation was fulfilled for each crane in accordance with developed port simulator scenario. We compared loading and unloading performance of each crane based on the simulation result.

Keyword: Port simulator, Two trolley elevator crane, Crane evaluation, 3D modeling

1. Introduction

A port distribution industry field is a competitive field for the initiative between countries and demands continuous development of operation system. To anchor bigger vessel, and to provide services as fast loading and unloading with lower costs are considered as most important in harbor competitiveness. The advanced country major ports are in development for introducing entirely new innovative operation system. It is considered necessary to assess such innovative system and to develop technology of port innovative simulator for design optimization.[1,2]

In this study, we conducted 3D modeling of crane structure based on blueprint of currently used cranes both domestic and foreign harbor. The simulation was conducted following the physical data as modeling data, unloading algorithm, crane velocity and acceleration, and then provided real time process status to user while simulating container loading operation. Through this, we try to review performance

and productivity of each crane by comparing performances of existing crane and suggesting crane

2. 3D modeling and operation condition design

2.1 3D modeling and simulator design

In this study, we conducted 3D modeling by analyzing data and properties based on drawings of existing crane (Single Trolley Crane), Chinese 2PMC crane (Buffered Crane), and suggested new-generation port crane TTEC (Two Trolley Elevator Crane). Through this, we strived to evaluate performance and productivity of each crane.
All simulation display models are produced in 3D to observe in various angle, and <Figure 1> is 3D model of existing crane, Chinese ZPMC, and suggesting crane with contain two Trolleys and Elevator.

(a) Single Trolley Crane (b) Buffered Crane (c) Two Trolley Elevator Crane

<Figure 1> 3D Modeling of Crane Used In Simulator

The simulator was produce based on Microsoft.NET Framework v1.1, and Visual C# was used for development language. Especially, Library for expressing 3 dimensional graphic, we used CsGL(C# OpenGL Library) of OpenGL.[3,4,5]
All simulation display models are produced in 3D to observe in various angle, and <Figure 1> is 3D model of existing crane, Chinese ZPMC, and suggesting crane with contain two Trolleys and Elevator.

2.2 Operation condition design

For operation condition of crane simulation, we selected operation of loading all containers of one section in 8030TEU class container vessel. We assumed that the container trailer(LMTT, Linear Motor-based Transfer Technology) is always at ready, and it starts when spreader loads the container. Moreover, as shown in <Figure 2>, we can set the velocity of Hoist and Trolley in the Speed Setting. For Hoist, velocity V and Acceleration A is modifiable, and for Trolley, setting for VLoaded and ALoaded(Marked as (L) in the simulator) for loaded condition, and VEmpty and AEmpty(Marked as (E) in the simulator) is available. Also, in Container Quantity section, setting for the number of simulated container is available, and when selecting "On Deck," it can conduct simulation for 8030TEU class vessel based upper line of container hatch cover, and when selecting "On Deck + In Hold," it can be set to conduct simulation for upper or lower line of container hatch cover. All conditions that can affect simulation as crane motor performance or container vessel size are set identically.

For simulation scenario composition, one of each crane anchor for loading, and calculated required time for unloading containers in one section under setting conditions of "On Deck" and "On Deck + In Hold".

3. 3D simulator execution and performance comparison

3.1 3D simulator setting

First, execute simulator program and select Simulation Configuration menu and display for supplement of each crane selection appears.

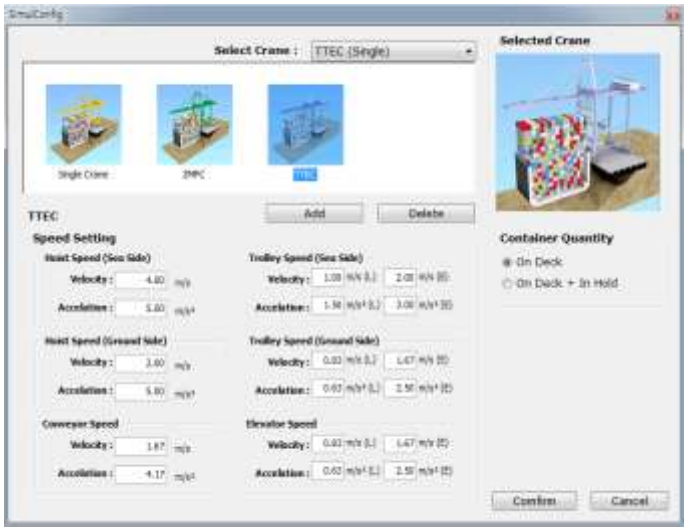

<Figure 2> Velocity, Acceleration Condition Setting for Each Crane

Select crane in "Select Crane" section and press "Add" button to set performance of each crane as shown in <Figure 2>. Set performance of each crane and select

Container Quantity in “On Deck” and press “Confirm” button to see simulation ready display as shown in <Figure 3>.

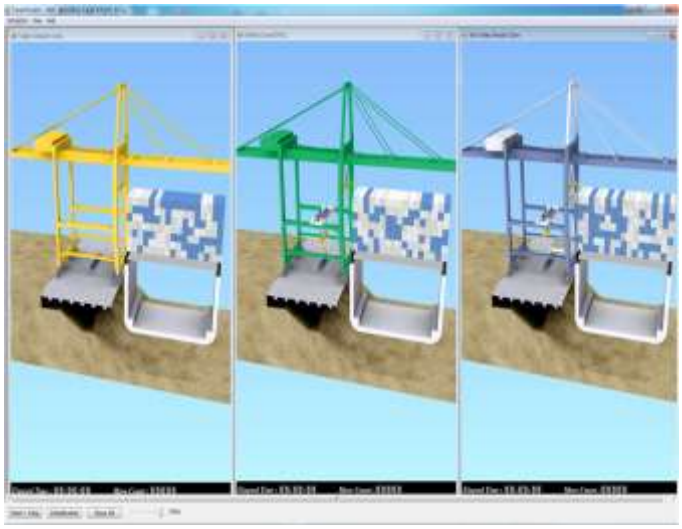

<Figure 3> Simulation Display

Developed 3D simulator provide following functions in order to observe closely of simulation in progress.

- Zoom In/Zoom Out : +/- (Or mouse wheel)
- Viewpoint Movement : Drag while holding mouse right button
- Crane Rotation : Drag while holding mouse left button
- Automatic Rotation On/Off : 8

Moreover, the simulator can control simulation using button located at the bottom as shown in <Figure 3>. It can start or pause simulation using “Start/Stop” button, and can stop all simulation in progress shown in the simulator and return to initial condition using “Initialization” button. It can stop all open simulation and shut windows by pressing “Close All” button, and can modify simulation speed by 1x, 5x, 10x, 50x, 100x, and 500x by using track bar located next to the “Close All: for it takes very long if conducted simulation in real speed.

3.2 Simulation execution and performance comparison

Conclude simulation setting and execute simulation by pressing “Start/Stop” button, and result of the simulation appears as shown in <Figure 4(a)>.

Likewise, if simulation is conducted as “On Deck + In Hold” setting in Container Quantity section, the result appears as shown in <Figure 4(b)>.

(a) On Deck (b) On Deck + In Hold

<Figure 4> Simulation Result

Above result shows average load time (Sec) per container, and number of loaded containers per time(EA/h). <Table 1> indicates arranged result.

<Table 1> Simulation Execution Result

Container Quantity	Crane Type	Total Load Time (Sec)	Load Time per Container (Sec)	Number of Containers Loaded per Time (EA/h)
On Deck (119EA)	Single Trolley Crane	6692	56.2	64.0
	Buffered Crane	6208	52.2	69.0
	Two Trolley Elevator Crane	5147	43.3	83.2
On Deck + In Hold (252EA)	Single Trolley Crane	16639	66.0	54.5
	Buffered Crane	15430	61.2	58.8
	Two Trolley Elevator Crane	12685	50.3	71.1

4. Conclusion

In this study, we developed new-generation port simulator, and conducted simulation comparing existing crane and suggested crane. The result is as below.

First, comparing conditions of “On Deck” and “On Deck + In Hold” A load time per container increased by 15% generally and number of containers loaded per time decreased by 14% generally for “On Deck + In Hold” has longer crane movement distance than “On Deck.” This indicates decreases of crane efficiency as crane movement distance increases.

Second, in “On Deck” condition, existing Single Crane handle 64.0 containers per hour, and Chinese Buffered Crane handled 69.0 containers per hour. Suggested TTEC handled 83.2 containers per hour showing performance improvement compared to prior cranes by 30.0%, and 20.6%, respectively.

Third, in “On Deck + In Hold” condition, existing Single Crane handle 54.5 containers per hour, and Chinese Buffered Crane handled 58.8 containers per hour. Suggested TTEC handled 71.1 containers per hour showing performance improvement compared to prior cranes by 30.5%, and 20.9%, respectively.

Through this, developed simulator in this study can be applied from plan stage to design and application of new port terminal crane construction and development, and is expected to obtain further economic reduction effect, and is believed to be used for new performance assessment measures different from port container load system development by applying to port system performance assessment that will be installed henceforth.

5. References

[1] Oh se Woong, Yeo Ki Tae and Lee Seoul Young,”Study on Dynamic Model Between Port and Regional Economy.”, Korean Port Society Autumn Symposium Collection of Dissertations, pp. 15-23, 2000.

[2] Kim Dong Young, Choi Han Soo, Kim Dae Joon and Lee Jae Ki, “Port Load Equipment 3 Dimensional Simulator Development.”, Korean Information Science Institute Presentation Collection, Vol. 26, No. 2, pp. 742-744, 1999.

[3] Richard S. Wright Jr. and Michael Sweet, OpenGL Super Bible, Waite Group Press, 1996.

[4] Woo Sang Woo, OpenGL Programming, Cyber Publishing Company, 1997.

[5] Ron Fosner, OpenGL Programming for Windows 95 and Windows NT, Addison-Wesley, 1998.

E214

Apply Low Energy ELA to Anneal and Improve Au Nanoparticle Embedded Nonvolatile Memory

Kuan-Yuan Shen
EEII, R129, National Taiwan University, Taipei, 10617, Taiwan(R.O.C)
flmanfree@gmail.com

Chieh-Hsiung Kuan
EEII, R129, National Taiwan University, Taipei, 10617, Taiwan(R.O.C)
kuan@cc.ee.ntu.edu.tw

The corresponding author: Kuan-Yuan Shen

Abstract

One of the major advantages of excimer laser annealing (ELA) is that it provides localized heating without thermally damaging other parts of a device. This feature greatly fits the requirement of fabricating nanocrystal embedded oxide, which is the floating gate in novel nonvolatile nanocrystal memory. During conventional thermal annealing process, the atoms of nanocrystals usually diffuse into surrounding oxide and become oxide traps that degrade the charge retention performance. This work proposes applying low-energy ELA to anneal the gold nanocrystal (AuNC) embedded silicon dioxide thin film. The low-energy ELA is first test on silicon dioxide thin film and analyzed with FTIR spectrum. The AuNC embedded oxide also fabricated as MOS capacitor with electrical characterization. The result of high frequency capacitance-voltage (C-V) measurement shows the reduction of oxide traps after ELA. The retention performance is tested and analyzed to study the relaxation behaviors of charges stored in AuNCs and traps. The calculated result implies that the low-energy ELA eliminates the oxide traps, increase the ratio of charges stored in AuNCs, and therefore improves the charge retention performance. When increasing the energy of ELA, it contrarily creates traps and degrades the retention performance.

Keyword: excimer laser annealing, nanocrystal memory, nonvolatile memory, FTIR spectrum, charge retention

1. Introduction

Excimer laser process has been widely used in electronics and display device industries. The high energy UV photons with well-controlled energy, pulse time, exposing area provide instantaneous heating or melting are used in many manufacturing processes, such as pulsed laser deposition, dopant activation, laser

lift-off, and laser annealing. In the application of annealing, that ELA provides preferentially localized heating while keeping the substrate or other parts of a device relatively cool would be highly advantageous especially when they are sensitive to thermal damage. This feature fits the requirement of annealing the nanosrystal embedded oxide thin film, which is used as floating gate in novel nonvolatile nanocrystal memory devices.

In the fabrication of nanocrystal embedded oxide, it usually needs to be thermally annealed to reduce oxide traps and defects, which will become leakage paths and degrade charge retention performance. However, conventional thermal annealing process causes another series problem of atom diffusion [1,2]. Atoms with thermal energy will easily diffuse into surrounding oxide and become trap centers resulted in leakage. Furthermore, as to the metal nanocrystal that is able to provides higher charge storage, the diffused metal atom can even turn into contamination. To solve this problem, based on the feature of localized heating of ELA, we propose the low-energy ELA process on AuNC embedded SiO_2 thin film to improve the charge retention performance.

2. Experiment

To investigate the effect of low-energy ELA, a 1.5μm SiO_2 thin film is deposited by Plasma-enhanced chemical vapor deposition (PECVD) system on p-type silicon substrate, and then annealed with KrF excimer laser with different erengies (pulse width 15ns and 1Hz for 30shots). The annealed thin film is characterized with FTIR spectrum. To test the localized heating of ELA, the AuNC embedded SiO_2 thin film is fabricated and ELA annealed. The chemical synthesized AuNCs (~20nm in diameter) are deposited on 3nm thermal oxide on p-type silicon substrate. This AuNC layer is then deposited with 40nm SiO_2 thin film by PECVD system and ELA processed by KrF excimer laser with different energies from 70mJ/cm^2 to 200mJ/ cm^2. To characterize the retention performance, top and bottom Al metal contact is deposited to from a MOS capacitor, which is to be tested with HP4284 LCR meter. Fig.1 shows the TEM picture and the diagram of device structure. That the AuNC after ELA process is maintained spherical as original without distortion or aggregation implies that there is no diffusion of Au atoms as reported in ref. [2]

3. Results and Discussion

3.1 FTIR spectrum of ELA on SiO2 thin film

As shown in Fig.2, after low-energy ELA, the absorbance of Si-O-Si (stretching

mode~1090cm^{-1}) and Si-O (rock mode ~450cm^{-1}) are increased, and Si-H (~660cm^{-1}) Si-OH (~935cm^{-1}) are decreased [3]. It implies that the low-energy ELA eliminates the –H and –OH related bonds and enhances the formation of Si-O-Si bonds, which might be resulted from Si-OH + Si-OH →Si-O-Si + H2O [4]. Contrarily, the result of high-energy ELA shows weak bonds of Si-O-Si.

3.2 Electrical characterization of AuNC embedded MOS

Fig.3 shows the high-frequency (1MHz) Capacitance-Voltage (C-V) hysteresis curves with sweep voltages from ± 1V to ± 15V. Fig.4 shows the neutral flat-band voltages (V_{FB}), which is calculated from C-V hysteresis at very small sweep voltage. The shift of V_{FB} toward positive implies that low-energy ELA anneals out traps and reduces the fixed oxide charges. However, when increasing the energy of ELA higher than 150mJ/cm^2, there are more fixed oxide charges created and makes the neutral V_{FB} shift toward much negative value.

To test the retention performance, the Capacitance-Time (C-T) curve is measured at fixed voltage biased of V_{FB}. The corresponding stored charge percentage is calculated from C-T curve and C-V curve. Fig.5 shows the results of stored charge percentage after 1hour of retention test. The retention performance is improved with decreasing energy of ELA and is best with ~80mJ/cm^2 ELA. Since the charges stored in not only the AuNCs but the traps in oxide, the curve of stored charge percentage various with time is then fitted with following charge relaxation equation (1) to obtain different charge loss behaviors in AuNCs and traps respectively.

$$\text{Stored Charge \%} = C_{AuNCs} \cdot \exp(-\frac{t}{\tau_1}) + C_{traps} \cdot \exp(-\frac{t}{\tau_2}) \quad (1)$$

Fig.6 shows one example of curve fitting with equation(1). Comparing the different charge relaxation behaviors in AuNCs and traps, the drastically decreased curve (blue one) implies that charges stored in traps escape rapidly. Contrarily, the gently decreased curve (red one) implies that charges stored in AuNCs are well confined and therefore shows good retention performance.

Fig.7(a) and 7(b) show two groups of the fitting parameters: the larger τ_1 (>8000s) and related coefficient C_{AuNCs} representing the relaxation time and ratio of charges stored in AuNCs; the smaller τ_2 (<300s) and related coefficient C_{Traps} representing that of charges stored in traps. The increased relaxation times, τ_1 and τ_2, at lower energy imply that low-energy ELA eliminates shallow traps that lead to leakage and therefor enhance the charge retention. Contrarily, the decreased of relaxation times at higher

energy imply that high-energy ELA might create more traps and degrade charge retention. On the other hand, the increased coefficient C_{AuNCs} and decreased C_{Traps} at lower energy imply that the low-energy ELA reduce traps and therefore the ratio of charge stored in AuNCs increases while that in traps decreases.

Furthermore, the effect of ELA to stored charge can be investigated from the memory window contributed from charge stored in traps and AuNCs (Fig.8), which is calculated from C-V hysteresis curves (Fig.3) and fitting parameters (Fig.7(a) and (b)). The memory window contributed from traps decreases with low-energy ELA while that increases with high-energy ELA. It shows that low-energy ELA eliminates traps but high-energy ELA create traps. The memory window contributed from AuNCs stays as constant at low-energy ELA, decreases with higher-energy ELA, and drastically decreases with much higher-energy ELA. It implies that the low-energy ELA effectively eliminates traps without damaging AuNCs. However, if the energy increases highly, the Au atoms might start to diffuse and therefore the charge stored in AuNCs reduced.

4. Conclusion

Based on the feature of localized heating, the low-energy ELA fits the requirement of annealing the AuNC embedded silicon dioxide, where there is usually diffusion of Au atoms with conventional thermal annealing. The positive shift of neutral V_{FB} shows the reduction of oxide traps with low-energy ELA. The stored charge retention test also shows the best retention with low-energy ELA. To further study on the charge relaxation behaviors in AuNCs and traps, the fitting parameters imply that with low-energy ELA the oxide traps are reduced and therefore enhance the relaxation time constants and the ratio of charge stored in AuNCs is increased. When the ELA energy increases much higher, it will contrarily create oxide traps and degrade the charge retention.

5. References

[1] M. Yang, Effect of annealing on charge transfer in Ge nanocrystal based nonvolatile memory structure, *Journal of Applied Physics*, 106, 2009, 103701.

[2] Jungmok Seo, Trade-Off Relationship of Size and Density of Platinum Nanocrystal in Nonvolatile Memory Characteristics, *Japanese Journal of Applied Physics*, 49, 2010, 104003.

[3] J.A. Luna-López, FTIR, AFM and PL properties of thin SiOx films deposited by HFCVD, *Materials Science and Engineering B*, 174, 2010, pp.88.

[4] Yasuo Hiroshige, Formation of High-Quality SiO2 and SiO2/Si Interface By Thermal-Plasma-Jet-Induced Millisecond Annealing and Postmetallization Annealing, *Japanese Journal of Applied Physics*, 49, 2010, 08JJ01.

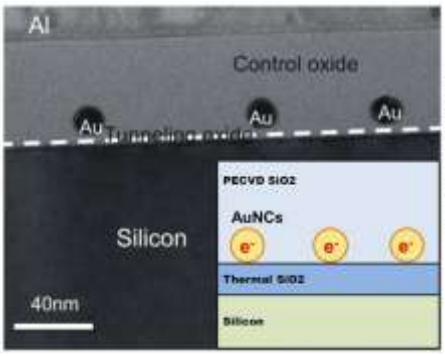

Fig. 1. The cross-sectional TEM picture and diagram of device structure.

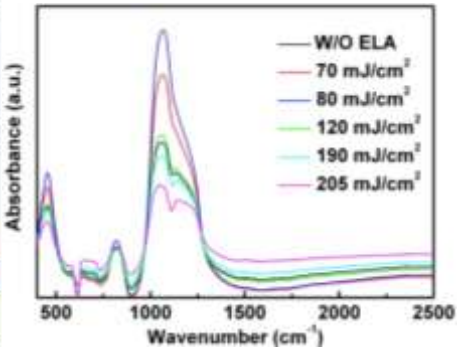

Fig. 2. FTIR spectrum of SiO_2 thin film with different ELA energies.

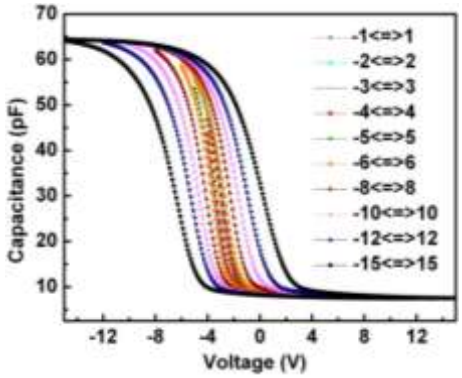

Fig. 3. High frequency C-V hysteresis curves.

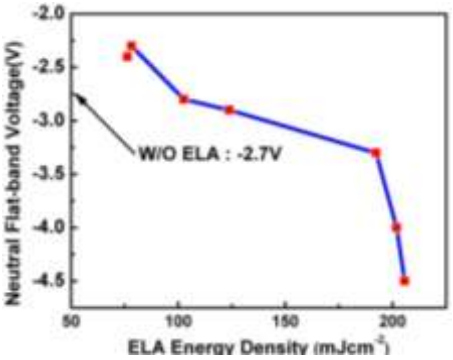

Fig. 4. Neutral V_{FB} of devices with different ELA energies.

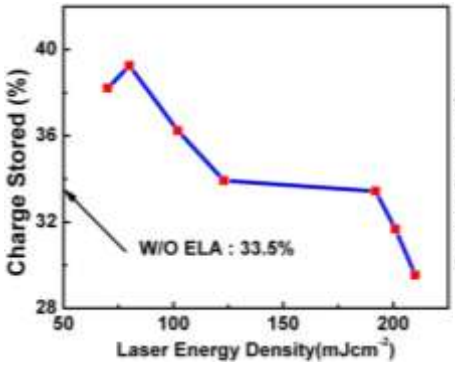

Fig. 5. Percentage of stored charges after 1hour retention test with different ELA energies.

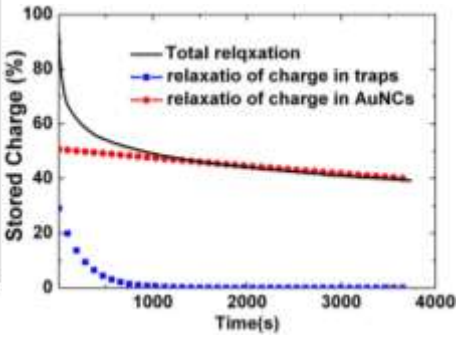

Fig. 6. One example of time-varing percentage of stored charges curve fitting with equation(1).

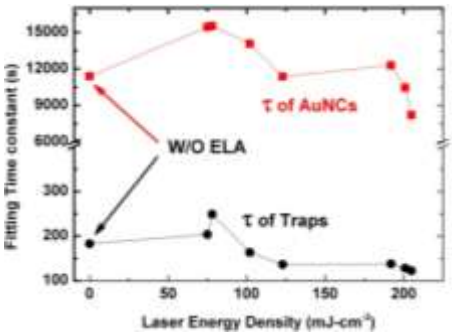

Fig. 7(a). fitting parameter of relaxation time constant.

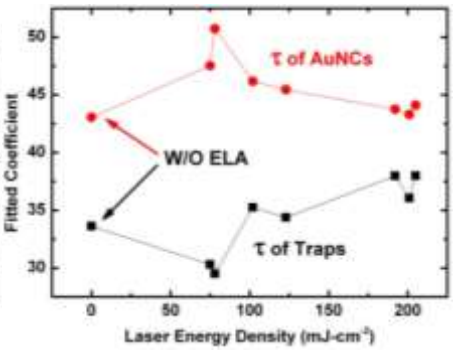

Fig. 7(b). fitting parameter of coefficient of relaxation.

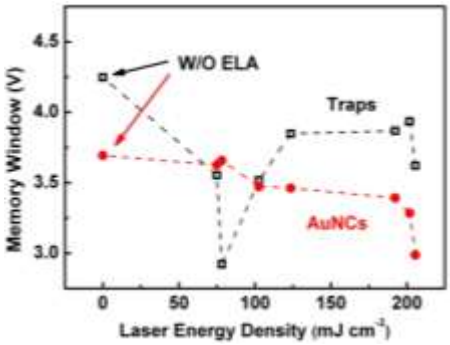

Fig. 8. The memory window contributed from charges stored in traps and AuNCs respectively.

E218

Kinetics of the biogas production from *Chlorella vulgaris* at different ultrasonic dose of pretreatment

Phrompol Chantrasakdakul
Department of Civil and Environmental System Engineering, Konkuk Uiversity, Seoul, South Korea
phrompol@konkuk.ac.kr,

Kwan Yong Lee
Department of Civil and Environmental System Engineering, Konkuk Uiversity, Seoul, South Korea
kwanyonglee@gmail.com,

Ki Young Park
Department of Civil and Environmental System Engineering, Konkuk Uiversity, Seoul, South Korea
kypark@konkuk.ac.kr

Abstract

The biogas is one of the alternative bioenergy source due to their high growth rate of microalgae. Anaerobic digestion is a promising technology for bioenergy recovery from waste microalgal biomass. However, the hard cell wall of microalgae is a major drawback of microalgae anaerobic digestion. The pretreatment of microalgae cell by ultrasonic wave was used to render the intracellular organic matter accessible to anaerobic bacteria in anaerobic process in order to improve the biogas production. The BMP test was conducted to evaluate the accumulation of biogas production. Modeling equation will be used to predict the biogas production at different ultrasonic dose of 10 J/mL, 50 J/mL, 200 J/mL, 500 J/mL, 1,000 J/mL and 5,000 J/mL respectively.

Keyword: kinetic, modeling, ultrasonic, biogas, microalgae, Chlorella

1. Introduction

The use of microalgae for nutrient removal and biofuel production has been widely discussed as an alternative green energy due to high growth rate. Moreover, microalgae also has ability to fix carbon dioxide gas and to remove nutrients (N, P). Microalgae can be cultured in non-arable lands so that microalgae grown for biogas production will not compete with crops for human nutrition [3]. Although algal biomass contains high amount of lipids and proteins which is suitable for anaerobic bacteria in anaerobic process, the resistance of cell wall is one of the limiting factors for cell digestibility [1]. The pretreatment of algal biomass is necessary to render the intracellular organic matter to anaerobic microorganism, and therefore to improve biogas and methane production.

There are various pretreatment were studied to improve biogas production in anaerobic digestion. Pretreatment of microalgae were used to rupture cell wall resulting in release of organic substances to outside of the cell. These organic substances can be easily hydrolyzed by extracellular enzyme of

anaerobic microorganism leading to improve biogas production in anaerobic process. The order of pretreatment efficacy for improve biogas production was ultrasonication, thermal pretreatment by autoclave, thermal pretreatment with hot water and freezing, respectively [4]. Ultrasonication has been investigated as microalgae pretreatment process. In first stage of sonication, the structure of algal cell would be disintegrated [6]. In the subsequent stage, some portion of the insoluble particulate organic matter could be transformed into soluble state [5].

In this study, the effect of ultrasounds on disintegration and methane production of microalgae *Chlorella vulgaris* was investigated. The biomethane potential (BMP) test was conducted to evaluate the anaerobic biodegradability in batch assay for each different ultrasonic dose. The cumulative biogas production of pretreated *Chlorella vulgaris* cell was compared to the modified Gompertz equation for studying the possibility of predicting the biogas production.

2. Materials and methods

2.1 Preparation of microalgae

The Chlorella sample used in this study (*Chlorella vulgaris*) was supplied by Daesang Co. Ltd., (Korea) with concentration of 10% total solids (TS). The TS concentration of *Chlorella vulgaris* was diluted to 1% TS with distilled water. Total suspended solids (TSS) and total volatile suspended solids (TVS) before and after ultrasonic disintegration was determined according to Standard Methods (APHA, 2005).

2.2 Cell disruption

Cell disruption of *Chlorella vulgaris* was performed by ultrasonic homogenizer model STH-750S. The maximum unit has a maximum power output of 750W and operated at a constant frequency of 20 kHz and constant power input of 150 W. This unit is equipped with dia.20x123mm horn. The different ultrasonic dose which applied to 100 mL of *Chlorella vulgaris* were 10 J/mL, 50 J/mL, 200 J/mL, 500 J/mL, 1000 J/mL, 5000 J/mL respectively.

The equation of ultrasonic dose is shown in Eq.1

Ultrasonic dose:

$$\text{Ultrasonic dose} = \frac{P \times t}{V} \qquad \text{(Eq.1)}$$

Where,

P = ultrasonic power in Watt

t = ultrasonic duration in seconds (s)

V = Volume of sonicated microalgae in milliliter (mL)

The soluble COD release was used as a direct measurement of *Chlorella vulgaris* cell disintegration. When *Chlorella vulgaris* cell was sonicated, the intracellular *Chlorella vulgaris* cell was released into the aqueous phase. An increased soluble COD after ultrasonic disintegration was an indication of *Chlorella vulgaris* cell disintegration efficiency. Soluble COD released of *Chlorella vulgaris* was

determined for each operation condition as per HACH method 8000. The samples were centrifuged at 4,000 rpm for 5 minutes and supernatant was filtered through 0.45 μm pore size membrane filter then used for soluble COD analysis.

2.3 Biochemical Methane Potential (BMP)

BMP test was carried out to determine the anaerobic biodegradability by comparing methane and biogas production for different sonication conditions applied. The 160 mL of serum bottles were used for BMP test. Anaerobic digester sludge in wastewater treatment plant was used as an inoculum for BMP test. *Chlorella vulgaris* cell was sonicated at constant power input of 150W and constant frequency of 20 kHz with different ultrasonic dose of 10 J/mL, 50 J/mL, 200 J/mL, 500 J/mL, 1,000 J/mL and 5,000 J/mL respectively.

The ratio of inoculum and substrate used was 1:1 by mass of volatile solids. The amount of necessary nutrients for anaerobic microorganism was added into each BMP serum bottle [7]. The difference to 100 mL (sample volume) was filled up with distilled water.

In BMP test, serum bottles capped with butyl rubber stoppers. All the serum bottles were sealed and headspace was also purged with oxygen free nitrogen gas. Serum bottles were kept in 35^{o}C incubator until they stop producing biogas. Daily biogas was measured by inserting needle attached to a syringe (10 mL). The blank was undertaken without adding substrate to determine the actual biogas production for only substrate.

2.4 Kinetic Model

Most kinetic model derived from an experimental data which called empirical equation. The empirical model or statistical analysis can be used to explain the biochemical mechanism or bacterial growth rate. The kinetic model can provide better guidance in process design and control. In this study, the modified Gompertz equation and first-order equation were conducted to predict the biogas accumulation from Chlorella vulgaris by SigmaPlot software and compare both models to the experimental data.

The modified Gompertz equation was shown below.

$$M_p = P\exp\left[-\exp\left\{\frac{R_m e}{P}(\lambda - t)+1\right\}\right] \quad \text{(Eq. 2)}$$

Where

M_p = cumulative biogas production (mL/gVS)

P = biogas yield potential (l/gVS)

R_m = maximum biogas production rate (mL/gVS.d)

λ = Duration of lag phase (days)

t = time at which cumulative biogas production M_p is calculated (days)

V = Volume of sonicated microalgae in milliliter (mL)

The first order equation was shown below.

$$Mp = P(1-\exp(-k_h t)) \qquad \text{(Eq.3)}$$

Where

M_p = cumulative biogas production (mL/gVS)

P = biogas yield potential (l/gVS)

k_h = the apparent hydrolysis rate coefficient

t = time at which cumulative biogas production M_p is calculated (days)

3. Results and Discussion

3.1 Effect of ultrasonic pretreatment on disintegration

Figure 1 shows the effect of ultrasonic pretreatment of microalgae. There were 7 different ultrasonic dose: 0 J/mL (unsonication), 10 J/mL, 50 J/mL, 200 J/mL, 500 J/mL, 1,000 J/mL and 5,000 J/mL. The microalgae which used for ulrasonication was *Chlorella vulgaris* of 1% TS. The total suspended solids (TSS) and volatile suspended solids (VSS) of each sample with different ultrasonic dose were the same trend. For the sample at ultrasonic dose of 0 J/mL (nonsonication), the total suspended solids concentration of 13,200 mg/L and for the final ultrasonication (5,000 J/mL), the total suspended solids concentration of 12,950 mg/L. This results show that the concentration of total suspended solids and volatile suspended solids were decreased significantly by ultrasonication. This result has been proved that the insoluble particulate organic matter could be transformed into soluble state by ultrasonic disintegration.

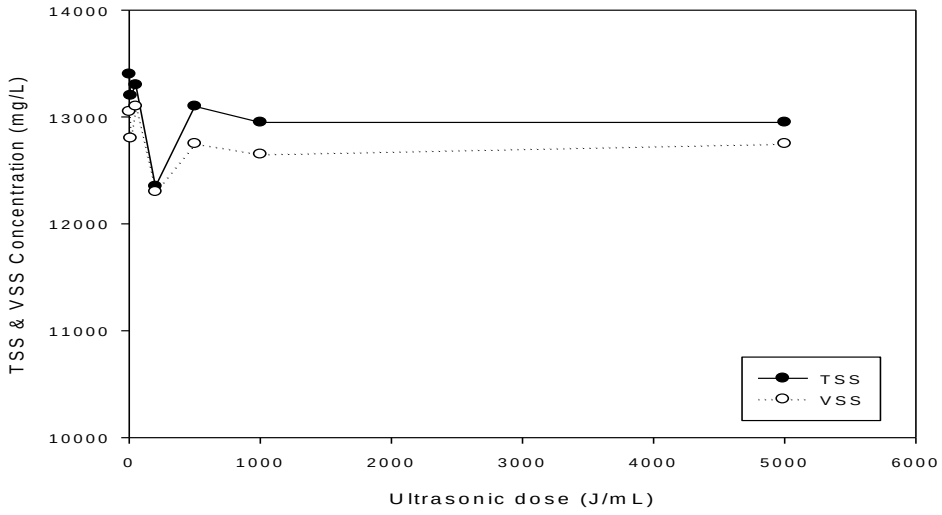

Fig. 1. Total suspended solids and volatile suspended solids in each ultrasonic dose

Figure 2 shows the relationship between ultrasonic dose and soluble COD concentration. For the sample at ultrasonic dose of 0 J/mL (unsonication), the soluble COD concentration of 6,250 mg/L and for the final ultrasonication (5,000 J/mL), the soluble COD concentration of 6,400 mg/L. This results show that the trend of soluble COD concentration were increased by ultrasonication and proved that the intracellular organic matter was released due to broken of microalgae cell wall by ultrasonication.

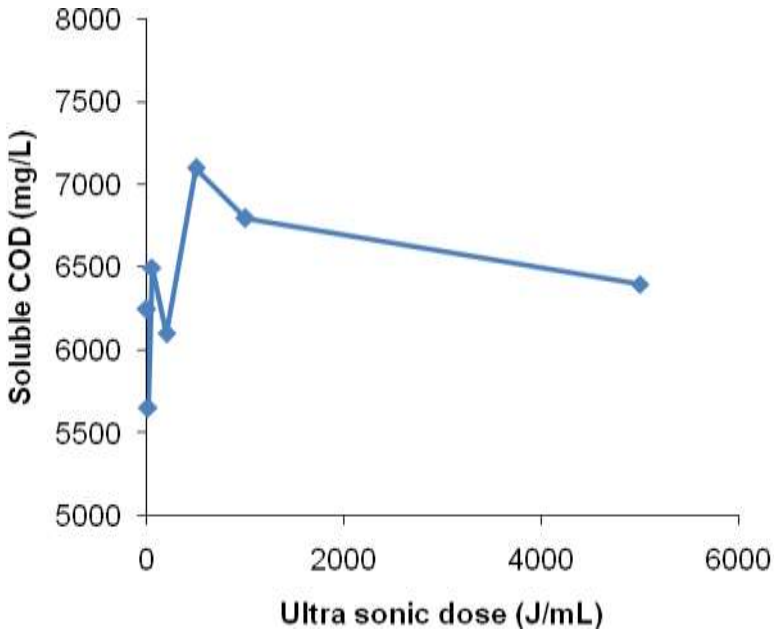

Fig. 2. Soluble COD concentration in each ultrasonic dose

3.2 Effect of ultrasonic pretreatment on BMP test

In figure 3 and 4 shows the accumulation of biogas production and fit curve model in 1% TS of *Chlorella vulgaris*. The biogas production rate was increased exponentially and after 13 days it was retarded due to substrate limitation or VFA accumulation. In the 36 days, the accumulated biogas production reached the maximum and became steady value. In figure 3 shows the highest accumulated biogas production came from the highest ultrasonic dose of 5,000 J/mL and the lowest accumulated biogas production came from the nonsonicated sample (0 J/mL). The biogas production potential of *Chlorella vulgaris* in ultrasonic dose of 5,000 J/mL, 1,000 J/mL, 500 J/mL, 200 J/mL, 50 J/mL, 10 J/mL and 0 J/mL (nonsonicated) were 529.90 mL/gVS, 457.02 mL/gVS, 452.45 mL/gVS, 461.89 mL/gVS, 427.00 mL/gVS, 419.43 mL/gVS and 389.85 mL/gVS, respectively. The results of all ultrasonic dose show that biogas production depends on how much ultrasonic dose applied to the samples. It can be concluded that to render microalgae cell wall by ultrasonication can increase soluble organic matter and improve the biogas production due to organic matter accessible to anaerobic microorganism.

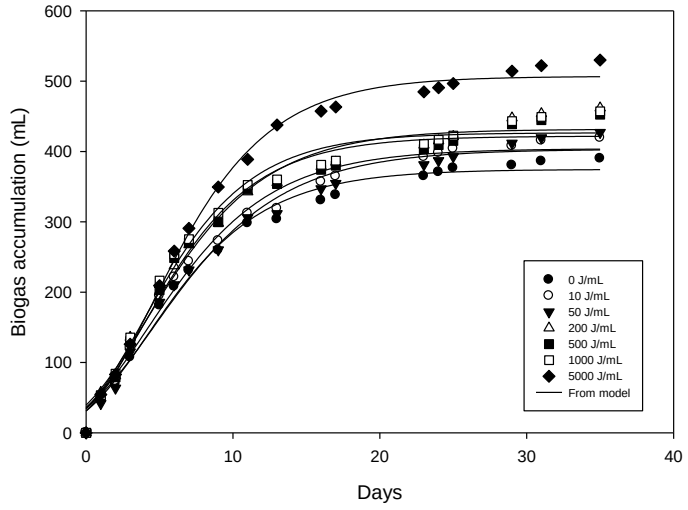

Fig. 3 Biogas accumulation and Fit curve model by Gompertz equation

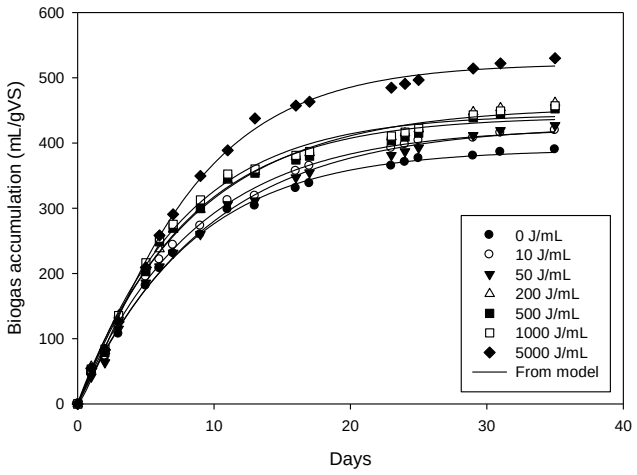

Fig. 4 Biogas accumulation and fit curve model by first-order equation

3.3 Kinetics Model of biogas production

For an assumption that biogas production is a function of bacterial growth, Modified Gompertz equation and first-order equation were used to predict the cumulative biogas production compare to the experimental data at different ultrasonic dose. The values of biogas yield potential (P), the maximum biogas production rate (R_m), the duration of lag phase (λ) and the apparent hydrolysis rate coefficient (k_h) obtained from the equation by fit curve data with SigmaPlot software are listed

in Table 1. The line curve of model equation plot from modified Gompertz equation and first-order equation at different ultrasonic dose are shown in Fig.3 and Fig.4

Table 1. Summary of kinetics data

Ultrasonic dose (J/ml)	Biogas Yield From exp.data (mL/gVS)	Modified Gompertz parameters P (mL/gVS)	Rm (mL/gVS.d)	λ (days)	R^2	First-order parameter P (mL/gVS)	k_h	R^2
0	389.85	374.50	30.42	-0.39	0.9886	390.30	0.135	0.9978
10	419.43	404.00	31.18	-0.57	0.9874	423.30	0.1195	0.9980
50	427.00	403.10	29.41	-0.52	0.9842	427.50	0.1078	0.9966
200	461.89	431.70	34.18	-0.59	0.9834	455.80	0.1094	0.9956
500	452.45	421.80	36.17	-0.33	0.9840	440.60	0.1375	0.9944
1000	457.02	426.60	37.71	-0.33	0.9847	444.40	0.1426	0.9952
5000	529.90	506.80	41.89	0.12	0.9946	522.10	0.1936	0.9976

From the Table 1, The R square values of model from Gompertz equation at ultrasonic dose of 0 J/mL (nonsonicated), 10 J/mL, 50 J/mL, 200 J/mL, 500 J/mL, 1,000 J/mL and 5,000 J/mL are 0.9886, 0.9874, 0.9842, 0.9834, 0.9840, 0.9847, 0.9946, respectively and the R square values of model from first-order equation are 0.9978, 0.9980, 0.9966, 0.9956, 0.9944, 0.9952 and 0.9976 respectively. Those results showed that the first-order equation is more suitable than modified Gompertz equation for predicting the accumulated biogas production. For another reason in Gompertz equation, the shape of the model curve at t = 0, the $\lambda<0$ which has no physical meaning. Despite of this case, the mainly point was focused on the evaluation of P and R_m to consider the biogas production. However, the Gompertz equation showed that the maximum biogas production rate (R_m) was affected by the ultrasonic dose. The greatest increase in the maximum biogas production rate was achieved under ultrasonic dose of 5,000 J/mL.

4. Conclusion

Due to high biomass of microalgae, anaerobic digestion of microalgae is the promising renewable energy to solve the lack of energy sources nowadays. Pretreatment of microalgae by ultrasonication followed by the anaerobic process can be improved the biogas production. Pretreatment at different ultrasonic dose can affect to different biogas production rates. With high ultrasonic dose (since 5,000 J/mL), the prediction of biogas accumulation by modified Gompertz equation will be correctly due to high organic substrate release to outside of the microalgae cell.

5. Acknowledgement

This subject is supported by Korea Ministry of Environment as "Eco-Innovation Project"(Project No.: E211-40005-0035-0). This work is financially supported by Korea Ministry of Environment (MOE) as “Waste to energy recycling human resource development Project”.

6. References

[1] B. Sialve, N. Bernet, O. bernard, Anaerobic digestion of microalgae as a necessary step to make microalgal biodiesel sustainable, Biotechnology advances 27 (2007), pp.409-416.

[2] Jagadish H. Patil, Malourdu Antony Raj., P.L. Muralidhara, S.M. Desai, G.K. Mahadeva Raju, Kinetics of Anaerobic Digestion of Water Hyacinth Using Poultry Litter as Inoculum, International Journal of Environmental Science and Development, Vol.3, No.2 (2012), pp. 94-98.

[3] Marta Alzate Andrade, Sara Isabel Elvira-Perez, Raul Munoz Torre., Optimization of biogas production from algal biomass (2010). Acquired on internet June 1, 2012. iqtma.uva.es/girta/pdf/P-Algae_Digestion.pdf

[4] Q. Wang, J.C. Chen, K. Kakimoto, H. Ogawa, Y. Kato, Pretreatment of waste activated sludge results in enhancement of its anaerobic digesting efficiency, Journal of the Society of Water Environment (Japan) 18 (1995), pp. 875-882.

[5] Tatsuo S., Kudo K., Nasu Y, Anaerobic waste activated sludge digestion-a bio conversion mechanism and kinetic model, Biotechnol. Bioeng. 41 (1993), pp. 1082-1091.

[6] Tiehm A., Nickel K., Neis U., The use of ultrasound to accelerate the anaerobic digestion of sewage sludge, Water Sci. Technol. 36 (11) (1997), pp. 121-128.

[7] Young J.C., Tabak H.H., Multi-Level protocol for assessing the fate and effect of toxic organic chemicals in anaerobic reactions, Water Environ. Research 65 (1993), pp. 34-45.

Biomedical Engineering

Pullman Bangkok King Power, 2F

2013/1/26 Saturday 14:00-16:00

BENS77
Lethargic Repair Process in DNA Condensates with A basic Clustered Damage
Prolay Das｜*Indian Institute of Technology Patna*

BENS127
Control of Bioprosthetic Hand Based on Multimodal Biosignals Recognition and Feedback Signals from the Prosthesis Sensors
Marek Kurzynski｜*Wroclaw University of Technology*
Andrzej Wolczowski｜*Wroclaw University of Technology*

BENS160
Induced lpa (Low Phytic Acid) Mutant in Pigeonpea (Cajanus cajan (L.) Millsp.) Sanjay Pralhad Giri ｜*Arts, Commerce and Science College Satral*

BENS175
Lipoteichoic Acid (LTA) Isolated from Lactobacillus Plantarum has Inhibited Effects of Lipopolysaccharide (LPS)-Induced Proinflammation Cytokine and MAPK Siganaling
Gaeun You｜*Kyunghee University*
Dae Gyun Chung｜*Kyunghee University*
Han Geun Kim｜*Saintlouis Universuty*

BENS176
The Improvement of Intestinal Immunity by Lb. Plantarum LTA
Bong Jun Jung｜*Kyunghee University*
Han Geun Kim｜*Saint Louis University*
Dae Kyun Chung｜*Kyunghee University*

BENS177
Different effect of Lactobacillus Plantarum and Staphylococcus Aureus LTA on Immune

System

Hye Rim Kim ｜*Kyunghee University*
Dae Kyun Chung｜*Kyunghee University*
Han Geun Kim｜*Saint Louis University*

BENS178

Encapsulation of Bovine Serum Albumin within Banana Starch-Alginate Hydrogel Beads for Controlled Protein Drug Release

Warin Pimpa | *Naresuan University*

BENS180

Characterization of the Hemagglutinin of Influenza by Cold-Adaptation as a Novel Approach to Increase the Safety of the Vaccine Candidates

Yoon Jae Lee | *Yonsei University*
Yo Han Jang | *Yonsei University*
Yun Ha Lee | *Yonsei University*
Kwang Hee Lee | *Yonsei University*
Baik Lin Seong | *Yonsei University*

BENS186

Fabrication of Highly Aligned Collagen Micro-Scaffolds and its Evaluation by SHG Microscopy and Mechanical Tensile Test

Keisuke Yoshiki | *University of Hyogo*
Nobutaka Goami | *University of Hyogo*
Takahiro Namazu | *University of Hyogo*
Shozo Inoue | *University of Hyogo*

BENS206

Multiple Growth Factors-Immobilized Bioactive Porous Beads as an Injectable Bulking Agent

Jin Ho Lee | *Hannam University*
Sang June Kim | *Hannam University*
Se Heang Oh | *Hannam University*

BENS213

Redox Environment Modifies the Antimutagenic Functionality of Bifidobacterium Bifidum

Rémy Cachon｜*Université de Bourgogne*
Bruno Ebel｜*Université de Bourgogne*
Coralie Dumont｜*Université de Bourgogne*
Isbelle Séverin｜*Université de Bourgogne*
Patrick Gervais｜*Université de Bourgogne*
Marie-Christine Chagnon｜*Université de Bourgogne*

BENS135

Chemically-Induced Bacterial Ghosts

Nagarajan Vinod｜*Pai Chai University*
Sung Oh｜*Pai Chai University*
Seongdae Kim｜*Pai Chai University*
Chang Won Choi｜*Pai Chai University*
Sei Chang Kim｜*Pai Chai University*

BENS238

The Molecular Mechanism of CDV-Induced Apoptosis

Hung Yi Wu｜*National Pingtung University of Science and Technology*
Chia Ying Lin｜*Sheng Jie Veterinary Hospital*
Perng Chih Shen｜*National Pingtung University of Science and Technology*
Ching Dong Chang｜*National Pingtung University of Science and Technology*
Shinn Shyong Tsai｜*National Pingtung University of Science and Technology*

BENS239

Enhancement of Osteogenic and Chondrogenic Differentiation of Human Embryonic Stem Cells by Mesodermal Lineage Induction with BMP-4 and FGF2 Treatment

Byung Soo Kim｜*Seoul National University*

BENS139

Comparison of the Biomechanical Effects on Lumbar Spine between Pedicle-Based Composite and Rigid Rod Devices

Kyoung Tak Kang｜*Yonsei university*
Heoung Jae Chun｜*Yonsei university*
Hyoung Taek Hong｜*Yonsei university*
Ji Hoon Nam｜*Yonsei university*

BENS77

Lethargic Repair Process in DNA Condensates with Abasic Clustered Damage

Vandana Singh[a], Prolay Das[b,*]
[a]**Department of Chemistry, Indian Institute of Technology Patna**, Patna- 800013, Bihar, India
Email: vandanasingh@iitp.ac.in

[b]**Department of Chemistry, Indian Institute of Technology Patna,** Patna- 800013, Bihar, India
Email: prolay@iitp.ac.in

EXTENDED ABSTRACT

Abasic Clustered DNA damages results from stripping off the purine or pyrimdine bases in a DNA double helix structure within one or two helical turns of the DNA. These clustered damages, among other types, are potential signature of ionizing radiation induced DNA damages and have been proven to be repair resistant and potentially mutagenic. Repair of abasic clusters involves a series of enzymes including ApeI, common to Base Excision Repair pathway (BER) of DNA. Action of ApeI on abasic sites can result in double strand breaks if damaged lesions are present in opposite strands.

Oligomer DNA duplexes (47 bp) were designed to have deoxyuridine in the middle of the sequences (25th and 22nd base from 5' end of the two single strands DNA respectively). The deoxyuridine residues were converted into abasic sites by treatment with UDG enzyme. Thus one clustered damage site was created by two abasic sites close to one another in opposite strands in precise positions. This oligomer duplex having compatible cohesive ends was ligated to pUC19 plasmid, linearized with HindIII restriction endonuclease. The plasmid-oligomer conjugates were transformed into condensates by treating them with spermidine following standard methods as described elsewhere. Formation of condensates was observed and characterized by Dynamic Light Scattering (DLS) study. The efficiency of double strand breaks; initiated by Ape I enzyme was determined by timed incubation under physiological conditions followed by denaturing PAGE for both the oligomer and the oligomer-plasmid conjugate. Quantitative gel analysis revealed the efficiency of double strand breaks in the oligomer, the linear ligated plasmid-oligomer conjugate and the plasmid-oligomer conjugate condensate models.

We found significant differences in ApeI induced repair rate or generation of double strand breaks between the linear and the condensate model. Rate of double strand break generation is significantly reduced in the DNA condensates as compared to the oligomer DNA duplex or the linear ligated oligomer-plasmid conjugate. This suggests that the ApeI enzyme have difficulty to access the abasic sites located deep into the condensates leading to repair refractivity of the damages. In addition, we found that presence of a polyamine like spermidine has no significant effect in the incision activity of ApeI enzyme in linear DNA duplexes.

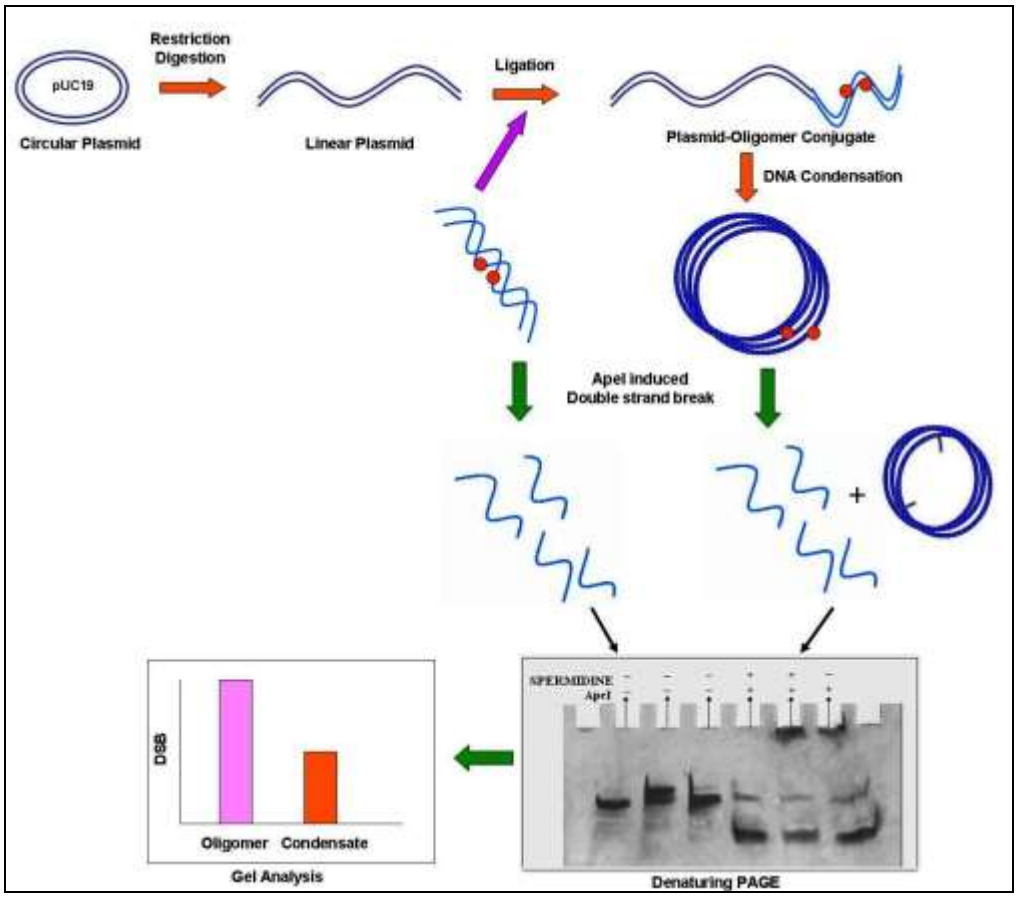

References:

1. Georgakilas A. G., Bennett P. V., David M. Wilson III D. M. and Sutherland B. M. Processing of bistranded abasic DNA clusters in γ-irradiated human hematopoietic cells. *Nucl. Acids Res.*2004, 32: 5609-5620.

2. Paap B, Wilson III D M and Sutherland B M Human abasic endonuclease action on multilesion abasic clusters: implications for radiation-induced biological damage. *Nucleic Acids Res.* 2008, 36: 2717-2727.

3. Das P. and Schuster G. B. Effect of Condensate formation on long-distance radical cation migration in DNA. *Proc. Natl. Acad. Sci. USA* 2005, 102: 14227-14231.

BENS127

Control of Bioprosthetic Hand Based on Multimodal Biosignals Recognition and Feedback Signals from the Prosthesis Sensors

Marek Kurzynski[a,]*, Andrzej Wolczowski[b]
[a]**Wroclaw University of Technology**, Department of Systems and Computer Networks, Wroclaw, Poland
E-mail address: marek.kurzynski@pwr.wroc.pl

[b]**Wroclaw University of Technology**, Department of Systems and Computer Networks, Wroclaw, Poland
E-mail address: andrzej.wolczowski@pwr.wroc.pl

ABSTRACT
The paper presents an advanced method of recognition of patient's intention to move of multijoint hand prosthesis during the grasping of objects. The proposed method is based on two-level multiclassifier system (MCS) with homogeneous base classifiers dedicated to EEG, EMG and MMG biosignals and with combining mechanism using a dynamic ensemble selection scheme and probabilistic competence function. Additionally, the feedback signal derived from the prosthesis sensors is applied to the correction of learning algorithm and classification result. The performance of proposed MCS was experimentally compared against three benchmark MCSs using real data concerning the recognition of six types of grasping movements. The systems developed achieved the highest classification accuracies demonstrating the potential of multiple classifier systems with multimodal biosignals for the control of bioprosthetic hand.

Keywords: Bioprosthetic hand, biosignals, multiclassifier system, competence function

1. INTRODUCTION

Existing active prostheses of hand (the bioprostheses) are generally controlled on myoelectric way – they react to electrical signals that accompany the muscle activity (called electromyography signals – EMG signals). The control is feasible since after the amputation of the hand, there remain a significant number of the muscles in the arm stump that normally controlled the finger action. The tensing of these
muscles still depends on the patient will and may express her/his intentions as to the workings of her/his prosthesis [11, 22].

At the decision level this control can be reduced to the recognition of the patient intent based on EMG signals. Nevertheless, reliable recognition of intended movement control based on EMG signal analysis is a hard problem [2, 3, 6, 8, 11, 14, 17]. The difficulty increases along with the cardinality of prosthesis movement repertoire (e.g. with prosthesis dexterity). Considering this fact, there is still a need for research in developing EMG signal recognition methods that could increase the reliability of recognition of handicapped person movement decisions.

According to the author's recent experience ([8, 9, 14, 15, 16, 17, 18]), increasing the efficiency of the recognition stage may be achieved through the following activities:

- by introducing the concept of simultaneous analysis of different types of biosignals, which are the carrier of information about the performed hand movement;
- by taking into account in classification algorithm the feedback signal derived from the prosthesis sensors for the correction of learning algorithm;

- through the use of multiclassifier system with the ensemble of base classifiers dedicated to particular registered biosignals;
- through development of the paradigm of dynamic ensemble classifier selection system using measures of competence as results of appropriate optimization problems.

Taking into account above observations and suggestions, the paper aims to solve the problem of recognition of the patient's intention to move the multiarticulated prosthetic hand during grasping and manipulating objects in a skillful manner, by measuring and analyzing multimodal signals coming from patient's body and from prosthesis sensors. The adopted solution takes into consideration the advantages given by the fusion of the EEG, EMG and MMG signals. The concept combines the recognition of EEG, EMG and MMG signals performed by multiclassifier system working in the two-level structure, with tuning the classifier competence measure in dynamic manner by data coming from prosthesis sensors. The approach proposed in this paper leads to the prosthesis decision control system presented in Fig. 1.

The paper arrangement is as follows. Chapter 2 provides an insight into steps of the whole decision control procedure and presents the key recognition algorithm based on the multiclassifier system with the dynamic ensemble classifier selection strategy. Chapter 3 presents experimental results confirming adopted solution and chapter 4 concludes the paper.

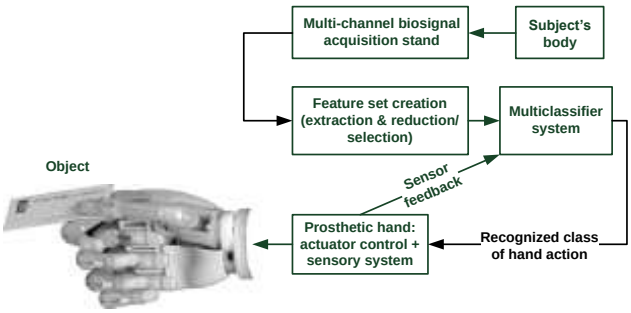

Fig. 1. Block-diagram of the prosthesis decision control based on the recognition of biosignals and feedback signals from the prosthesis sensors

2. MULTICLASSIFIER SYSTEM

2.1 Preliminaries

In the multiclassifier system (MCS) we assume that a set of trained classifiers $\Psi = \{\psi_1, \psi_2, \dots, \psi_L\}$ called base classifiers is given. A classifier ψ_l ($l = 1,2, \dots, L$) is a

function $\psi_l : X \to \Omega$ from a feature space to a set of class labels $\Omega = \{1,2, \dots, M\}$. Classification is made according to the maximum rule:

(1)

where $[d_{l1}(x), d_{l2}(x), \dots, d_{lM}(x)]$ is a vector of class supports produced by ψ_l. Without loss of generality we assume, that $d_{lj}(x) \geq 0$ and $\sum_j d_{lj}(x) = 1$.

The ensemble Ψ is used for classification through a combination function which, for example, can select a single classifier or a subset of classifiers from the ensemble, it can be independent or

dependent on the feature vector *x* (in the latter case the function is said to be dynamic), and it can be non-trainable or trainable [7]. The proposed multiclassifier system uses dynamic ensemble selection (DES) strategy with trainable selection/fusion algorithm. The basis for dynamic selection of classifiers from the pool is a competence measure $[\![c(\psi)]\!]_l|x)$ of each base classifier (l=1,2,…,L), which evaluates the competence of classifier ψ_l i.e. its capability to correct activity (correct classification) at a point $x \in X$.

In this paper trainable competence function is proposed what leads to the assumption that a validation set containing pairs of feature vectors and their corresponding class labels is available, viz:

$$V = \{(x_1, j_1), (x_2, j_2), \dots, (x_N, j_N)\}; x_k \in X, j_k \in \text{I} \quad . \tag{2}$$

2.2 Measure of Classifier Competence

The construction of the competence measure is based on the original concept of a hypothetical classifier called a Randomized Reference Classifier (RRC) [19, 20]. The RRC is a stochastic classifier defined by a probability distribution which is chosen in such a way, that RRC acts, on average, as an modeled base classifier $\psi_l \in \Psi$. It means, that RRC can be considered equivalent to the modeled base classifier ψ_l, and therefore it is justified to use the probability of correct classification of RRC as the competence of the classifier ψ_l at the validation point $x_k \in V$, i.e. $C(\psi_l|x_k) = Pc^{(RRC)}(x_k)$. The Matlab code for calculating $Pc^{(RRC)}(x_k)$ was developed [20] and it is freely available for download [21].

Using the normalized Gaussian potential function method [7, 20] for extending competence values to the entire feature space *X*, we get competence function for base classifier ψ_l ($l = 1,2,\dots,L$):

, (3)

where $dist(x,y)$ is the Euclidean distance between the objects *x* and *y*.

2.3 Dynamic Ensemble Selection System

Since recognition of the patient's intent is made on the basis of analysis of three different biosignals (EEG, EMG and MMG), the multiple classifier system – according to the proposed concept of the recognition method – consists of three submulticlassifiers, each of them dedicated to particular types of data. It leads to the two level structure of MC system presented in Fig. 2, in which the DES method is realized at the first level, whereas combining procedure at the second level is consistent with the continuous-valued dynamic fusion scheme.

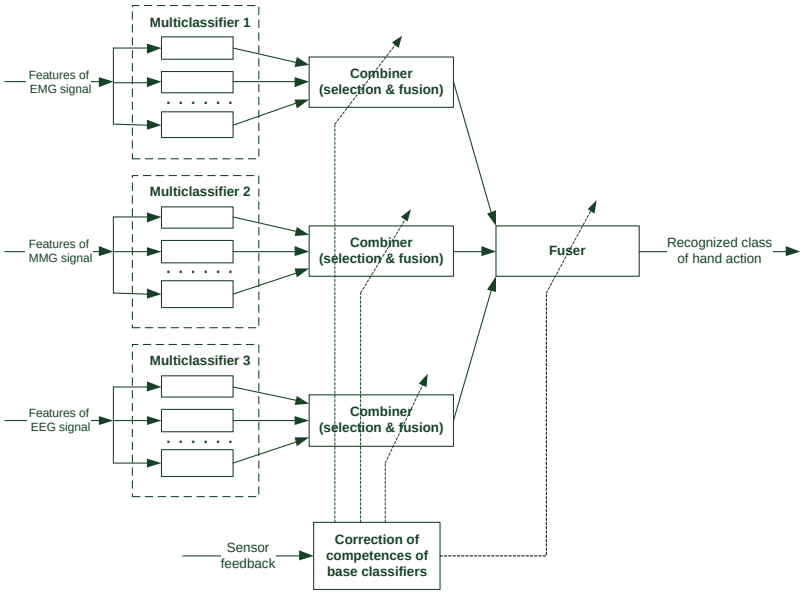

Fig. 2. Block-diagram of the proposed multiclassifier system

1) DES Systems at the First Level: Let $\Psi_i \ (i = 1,2,3)$ denote sets (ensembles) of base classifiers dedicated to the EEG, EMG and MMG signals, respectively. The DES system for the ensemble Ψ_i is constructed using developed measure of competence and classifies the feature vector $x^{(i)} \ (i = 1,2,3)$ in the following manner.

First, the competence function $c(\psi_k^{(i)}|x^{(i)}) \ (k = 1,2, \dots, L_i)$ are constructed for each classifier $\Psi_i'(x^{(i)})$.

in the ensemble. Then, a subset of base classifiers with the competences greater than the probability of random classification is selected. The selected classifiers are combined on the continuous-valued level [9], viz.

. (4)

2) Fusion Procedure at the Second Level: At the second level of MC, supports (4) are combined by the weighted sum:

$$d_j(x) = \sum_{i=1,2,\mathbf{3}} c^{(i)}(x^{(i)})\mathbf{d}_j^{(i)}(x^{(i)}), \tag{5}$$

where weight coefficients $c^{(i)}(x^{(i)})$ denote mean competence of base classifiers from $\Psi_i'(x^{(i)}) \ (i = 1,2,\mathbf{3})$.

Finally, the MC system classifies $x = (x^{(1)}, x^{(2)}, x^{(3)})$ using the maximum rule (1).

2.4 Tuning of Competence Measure

The feedback signal from the bioprosthesis sensors can be the source of information about a correct class of hand movement. This signal contains the data defining relation between the finger postures during the grasp, univocally connected with the classification result and the grasping object

which in turn explicitly determines the correct type of hand action (class of hand movement) [18]. In other words, the feedback signal coming in the course of recognition of testing hand movement, can help us answer the question if the classification result is correct or – if not – what is the set of classes into which the correct classification belongs. This proposition is the basis of an additional sequential learning procedure through the tuning of competence measures of base classifiers. The suggested algorithm for a base classifier ψ_l is the following.

Input data:
x – the testing point;
ψ_l – the base classifier;
i – the result of classification of $\bar{x}$ by ψ_l ;
$I_{\bar{x}}$ – the subset of classes determined by feedback information from bioprosthesis sensors.
If then do
Begin

1. Calculate competence of ψ_l at the point $\bar{x}$:

$$[\![C(\psi)]\!]_l(\bar{x}) = \frac{1}{([\![|I]\!]_{\bar{x}}|) \sum_{k \in I_{\bar{x}}} P^{(RRC)}(k|\bar{x})} \quad (6)$$

where $P^{(RRC)}(k|\bar{x})$ denotes the probability of classification of object $\bar{x}$ to the k-th class by RRC;

2. Calculate new competence measure $[\![c(\psi)]\!]_l(x)$ according to (3)with $V = V \cup \{\bar{x}\}$.

End

3. EXPERIMENTS

3.1 Experimental Setup

In order to study the performance of the proposed method of EEG, EMG and MMG signals recognition, some computer experiments were made. The experiments were conducted in MATLAB using PRTools 4.1 [5] and Signal Processing Toolbox. In the recognition process of the grasping movements 6 types of grips (tripoid grip, pinch grip, power grip, hook grip, column grip and mouse grip [1]) were considered.

The experiments were carried out on healthy persons. Biosignals were registered using 2 EEG sensors, 3 EMG electrodes and 3 MMG microphones [12]. EMG and MMG sensors were located on a forearm above the appropriate muscles and signals were registered in specially designed 16-channel biosignals measuring circuit (Bagnoli Desktop EMG System made by DELSYS Inc.) with sampling frequency 1 kHz. EEG electrodes were located over the hand sensorimotor cortex (in the frontal lobe) and signals were registered using EEG MobiLab System made by g.Tec Medical Engineering Inc. The results of classification were the basis of control of actuation system of artificial hand constructed in the Biocybernetics Laboratory of Wroclaw University of Technology presented in Fig. 3. During experiments its sensors located at tips and joints of digits produced feedback signals.

The dataset set used to test of proposed classification method consisted of 500 measurements, i.e. pairs “EEG, EMG and MMG signals segment/movement class”. Each measurement lasted 6 s and was preceded with a 10 s break. The values from Short Time Fourier Transform (STFT) product corresponding to the k = 3, 4, 5 most representative time slices were considered as feature vector [9]. Consequently, we got 3 datasets each containing 400 objects describing by different number of features.

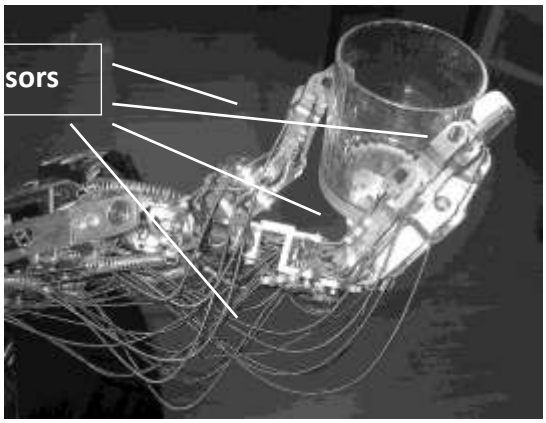

Fig. 3. The laboratory artificial hand with sensors

The training and testing sets were extracted from each dataset using two-fold cross-validation. A half of objects from the training dataset was used as a validation dataset and the other half was used for the training of base classifiers. Four experiments were performed which differ in the biosignals used for classification (EEG signals, EMG signals, MMG signals, all EEG, EMG and MMG signals). Each ensemble Ψ_i (i=1,2,3) was constructed using 20 feed-forward backpropagation neural network classifiers with one hidden layer (containing 10 neurons) and the number of learning epochs set to 80. Each classifier was trained using randomly selected 70% of objects from the training dataset.

The performances of the systems constructed (MC-, MC+ – without using and with using the signals from the bioprosthesis sensors) were compared against the following three multiple classifier systems: (SB) – The single best classifier in the ensemble [*7*]; (MV) – Majority voting (MV) of all classifiers in the ensemble [7]; (LA) – DCS-local accuracy (LA) system: this system classifies x using selected classifier with the highest local competence (the competence is estimated using *k* nearest neighbours of *x* taken from the validation set [13].

3.2 Results and Discussion

Classification accuracies (i.e. the percentage of correctly classified objects) for methods tested are listed in Table 1 (*k* denotes the number of time slices per signal channel). The accuracies are average values obtained over 10 runs (5 replications of two-fold cross validation). Statistical differences between the performances of the DCS-MC and DES-CS systems and the four MCS's were evaluated using Dietterich's 5x2cv test [4]. The level of $p < 0.05$ was considered statistically significant. In Table 1, statistically significant differences are given under the classification accuracies as indices of the method evaluated, e.g. for the dataset with $k = 3$ and EMG signals the MC- system produced statistically different classification accuracies from the SB and MV methods.

These results imply the following conclusions:

1) The both MC- and MC+ systems produced statistically significant higher scores in 55 out of 72 cases (12 datasets x 3 classifiers x 2 systems developed);
2) There are no statistically significant differences between scores of MC- and MC+ systems.
3) The multiclassifier systems using EEG, EMG and MMG signals achieved the highest classification accuracy for all datasets.

Table 1. Classification accuracies of MSCs compared in the experiment (description in the text). The best score for each dataset is highlighted

	Classifier / Mean accuracy [%]						Classifier / Mean accuracy [%]				
k	SB (1)	MV (2)	LA (3)	MC - (5)	MC+ (6)	k	SB (1)	MV (2)	LA (3)	MC - (5)	MC+ (6)
	EEG signals						MMG signals				
3	43.7	45.8	46.2	47.6 1, 2	**48.1** 1, 2, 3	3	63.6	61.7	**66.2**	65.1 1, 2	65.6 1, 2
4	47.7	48.3	**49.3**	48.9 1	48.6	4	66.8	69.2	68.3	**71.9** 1, 2, 3	71.4 1, 2, 3
5	49.3	49.2	50.3	**50.8** 1, 2	50.4 1, 2	5	70.7	71.5	73.3	74.5 1, 2	**74.9** 1, 2, 3
	EMG signals						EEG, EMG and MMG signals				
3	76.4	73.5	78.2	78.6 1, 2	**79.3** 1, 2, 3	3	85.8	87.2	88.1	90.3 1, 2, 3	**90.6** 1, 2, 3
4	79.4	80.5	83.6	84.6 1, 2	**85.1** 1, 2, 3	4	87.7	88.9	90.1	**92.6** 1, 2, 3	92.3 1, 2, 3
5	82.6	**86.3**	84.2	85.7 1, 3	84.9 1	5	90.5	92.7	93.2	94.1 1, 2	**94.8** 1, 2, 3

4. CONCLUSION

Experimental results indicate that proposed methods of grasping movement recognition based on the dynamic ensemble selection with probabilistic model of competence function, produced accurate and reliable decisions, especially in the cases with features coming from the EEG, EMG and MMG biosignals. Unfortunately, experimental tests did not confirm that proposed algorithm for tuning of competence measure is an effective tool for recognition of patient's intent in the bio-prosthesis control systems. This results from the fact, that presented concept of using feedback signals from bioprosthesis sensors has preliminary character and the proposed procedure of additional adaptive learning requires both theoretical analyses and experimental investigations. The problem of deliberate human impact on the mechanical device using natural biological signals generated in the body can be considered generally as a matter of "human – machine interface". The results presented in this paper significantly affect the development of this field and the overall discipline of signal recognition, thereby contributing to the comprehensive development of civilization. But more importantly, these results will also find practical application in the design of dexterous prosthetic hand - in the synthesis of control algorithms for these devices, as well as development of computer systems for learning motor coordination, dedicated to individuals preparing for a prosthesis or waiting for a hand transplantation [10].

Acknowledgement. This work was financed from the National Science Center resources in 2012-2014 years as a research project No ST6/06168.

5. REFERENCES

[1] Bebionic v2. *Product brochure*, Chapter: Grip patterns, RSLSteeper, Issue 2 July 2011

[2] Boostanl B., and Moradi M.: Evaluation of the forearm EMG signal features for the control of a prosthetic hand, *Physiolog. Measurement* 24, 309-319 (2003)

[3] De Luca C: *Electromyography. Encyclopedia of Medical Devices and Instrumentation*, (John G. Webster, Ed.) John Wiley Publisher, 98-109 (2006)

[4] Dietterich T.: Approximate statistical tests for comparing supervised classification learning algorithms, *Neural Computation* 10, 1895-1923 (1998)

[5] Duin R, Juszczak P, et al.: *PRTools4. A Matlab Toolbox for Pattern Recognition*, Delft University of Technology (2007)

[6] Englehart K.: Signal representation for classification of the transient myoelectric signal, *Ph.D. Thesis*, University of New Brunswick, Fredericton, New Brunswick (1998)

[7] Kuncheva I.: *Combining Pattern Classifiers: Methods and Algorithms*, Wiley-Interscience (2004)

[8] Kurzynski M.,Wolczowski A.: Dynamic selection of classifier ensemble applied to the recognition of EMG signal for the control of bioprosthetic hand, *Proc. 11 th Int. Conf. on Control, Automation and Systems*, Seoul, 175-182 (2011)

[9] Kurzynski M., Wolczowski A., Tito A., Control of Bioprosthetic Hand Based on EMG and MMG Signals Recognition Using Multiclassifier System with Feedback from the Prosthesis Sensors, *Proc. 2nd International Conference on Systems and Control*, pp. 127-135 ,Marrakesch 19-21.06.2012.

[10] Kurzynski M., Wolczowski A., Classification of EMG Signals in a System for Training of Bioprosthetic Hand Control in One Side Handless Human, *Proc. International Conference on Electrical Engineering and Computer Science EECS12*, pp. 566-576, Szanghai 18 – 22.08.2012

[11] Nishikawa D.: Studies on Electromyogram to Motion Classifier, *Ph.D. Thesis*, Graduate School of Engineering, Hokkaido University, Sapporo (2001)

[12] Orizio C.: Muscle sound: basis for the introduction of a mechanomyographic signal in muscle studies, *Critical Reviews in Biomedical Engineering* 21, 201-243 (1993)

[13] Smits P.: Multiple classifier systems for supervised remote sensing image classification based on dynamic classifier selection. *IEEE Trans. on Geoscience and Remote Sensing* 40, 717-725 (2002)

[14] Wolczowski A., Kurzynski M.: Human – machine interface in bioprosthesis control using EMG signal classification, *Expert Systems* 27, 53-70 (2010)

[15] Wolczowski A., Kurzynski M.: Control of artificial hand via recognition of EMG Signals, *Lecture Notes on Computer Science* 3337, Springer Verlag, 356-367 (2004)

[16] Wolczowski A.: Smart hand: The concept of sensor based control, *Proc. of 7th IEEE Int. Symposium MMAR*, 783-790, Miedzyzdroje (2001)

[17] Wolczowski A., Krysztoforski K.: Artificial hand control via EMG signal classification - experimental investigation of alghoritms. *Progress in robotics* [ed.] K. Tchon. Warszawa WKL, 97 - 122 (2008)

[18] Wolczowski A., Suchodolski T.: Bioprosthesis control: human machine interaction problem, [in] *Challenges for assistive technology*, [Ed.] Eizmendi G., Azkoitia J.M. Craddock G., Amsterdam, IOS Press, 558-560 (2007)

[19] Woloszynski T., Kurzynski M.: A measure of competence based on randomized reference classifier for dynamic ensemble selection. *Proc. 20th Int. Conf. on Pattern Recognition*, 4194 – 4197, IEEE Computer Press, Istanbul (2010)

[20] Woloszynski T., Kurzynski M.: A probabilistic model of classifier competence for dynamic ensemble selection. *Pattern Recognition* 44, 2656-2668 (2011)

[21] Woloszynski T, *Classifier competence based on probabilistic modeling (ccprmod.m) at Matlab central file exchange* URL http://www.mathworks. com/matlabcentral/fileexchange/ 28391-classifier-competence-based-on-probabilistic-modeling (2010)

[22] Zecca M., Micera S., Carrozza M., and Dario P.: Control of Multifunctional Prosthetic Hands by Processing the Electromyographic Signal, *Critical Reviews in Biomedical Engineering* 30, 459-485 (2002)

BENS160

Induced lpa (Low Phytic Acid) Mutant in Pigeonpea (Cajanus cajan (L.) Millsp.)

S.P. Giri[a,*], B.J. Apparao[b]

[a]**Arts, Commerce and Science College,** Satral, Tal-Rahuri, Dist-Ahmednagar (MS), PIN 413 711.
Email: sanjaygiri2005@rediffmail.com

[b]**Jijamata College of Science and Arts,** Dnyaneshwarnagar, Bhende Tal-Newasa, Dist-Ahmednagar, (MS), PIN 414 605.

ABSTRACT

Phytic acid is considered to be an antinutritional substance in human diets because it binds mineral cations and reduces their bioavailability. Isolation of low phytic acid content (P) in seeds is a desired goal of genetic improvement in several crops. The present investigation reports induction of low phytic acid (=Low phosporous) mutant in Pigeonpea as a result of treatment with 200Gy and 300Gy gamma rays. These mutants are named as Vegetable type mutant (VTM) and Energy saving mutant (ESM). These mutants were characterized by significant decrease in phosphorus content as compare to its control counterpart. Result indicate that the genotypes of pigeonpea with low phytic acid content could be identified and used in breeding program to improve their nutritional value and utilization.

Keywords: Pigeonpea, Gamma rays, Phosphorous, Phytic acid.

1. INTRODUCTION

Phytic acid (myo-inositol 1,2,3,4,5,6-hexakisphosphate) is an abundant component of plant seed grains and is deposited in protein bodies as a mixed salt of mineral cations, such as K^+, Mg^{2+}, Ca^{2+}, Zn^{2+}, and Fe^{3+}(Shi *et al*., 2003). Low-phytic acid mutants have used in genetic breeding, but it is not known what genes are responsible for the low-phytic acid phenotype. Although phytic acid as an antioxidant is suggested to have potential functions of reducing lipid peroxidation and some protective effects, phytic acid is considered to be an anti nutritional substance in animal feed and reduces human diets because it binds mineral cations and reduces their bioavailability (Zhou and Erdman, 1995). Additionally, Phytic acid is a strong chelating agent that can bind metal ions, reducing availability of Fe, Zn, and Mg, therefore reducing phytic acid content would increase nutritional value (Gehan, A.E.El-Emery and Ayman Y. Amin, 2010). Isolation of reduced phytic acid content in seeds is a desired goal of genetic improvement in several crops including maize, rice, barley, wheat, soybean and pigeonpea. Pigeonpea (*Cajanus cajan* L.) is important grain legume of Indian subcontinent and good source of protein, minerals and vitamins for million of people in the world. Phytic acid content (mg/g) is 12.7 in pigeonpea, on an average, phytic acid constituted 78.2 percent of the total phosphorous content (Chitra *et al*., 1995). In the present investigation an effort was made to induce low phytic acid (=Low Phosporous) mutant in pigeonpea by employing Gamma rays.

2. MATERIAL AND METHODS

Dry dormant seeds of Pigeonpea ICPL-87 (Moisture content 10-11%) were irradiated with 100, 200, 300 and 400Gy gamma rays from the source of CO^{60} from institute of Science, Aurangabad. 250 treated seeds from each treatment including control were sown on the same day in well-prepared seed beds in the field. The seeds were sown in randomized block design (RBD) in rows of 5M long and 60 cm between rows, at a spacing of 25 cm between plants, in the

experimental fields of Padmashri Vikhe Patil College, Pravaranagar during the Kharif 2007. Seeds from M_1 progeny were harvested separately and carefully from each treatments as well as control and sown to raise M_2 progeny in Kharif 2008. In M_2 progeny plants were carefully screened for the occurrence of any novel, morphological mutants. The seeds of twelve isolated morphological mutants (Table) were also analyzed in laboratory for Phosphorous (P) content by Vanadomolybdate yellow colour method as described by Bhargava and Raghupathi (2005).

3. RESULTS AND DISCUSSION

In M_2 generation twelve morphological mutant isolated viz. High yielding mutant, Bushy mutant, Vegetable type mutant, Dwarf mutant, Spreading mutant, White Seed mutant, Coffee colour mutant, Bold seeded mutant, Early mutant, Tall mutant, Late mutant and Energy saving mutant. Out of this Vegetable type mutant (VTM) and Energy Saving mutant (ESM) shows reduced phosphorous content and named as lpa mutants. These mutants were isolated from M_2 progeny of 200Gy, and 300Gy gamma rays administered pigeonpea cultivar respectively. The lpa mutant of Pigeonpea exhibits a 40% reduction in seed phytic acid with an equivalent increase in inorganic phosphorus. It is indirectly responsible to decrease in phytic acid content. Differences observed among morphological mutant and corresponding control plants is shown in the table. Similar results of low phytic acid mutants are also reported by, Raboy *et al*., (2000, 2001) in maize, Li *et al*., (2001) in Barley, Shi *et al*., (2003), Nguyen Thi Lang *et al*., (2007) in rice, and Raboy (2008), Tambe, (2009) in Soybean. Result indicate that the genotypes of pigeonpea with low phytic acid content could be identified and used in breeding program to improve their nutritional value and utilization.

Table: Phosphorous content of Viable mutants in M_2 in Pigeonpea

Sr. No	Mutant	Phosphorus %	Shift mean
1.	Control	0.24	0.00
2.	High yielding mutant	0.30	+0.06
3.	Bushy mutant	0.25	+0.01
4.	**Vegetable type mutant**	0.15*	-0.09
5.	Dwarf mutant	0.21	-0.05
6.	Spreading mutant	0.27	+0.03
7.	White Seed mutant	0.20	-0.04
8.	Coffee colour mutant	0.28	+0.04
9.	Bold seeded mutant	0.37	+0.13
10.	Early mutant	0.31	+0.07
11.	Tall mutant	0.36	+0.12
12.	Late mutant	0.24	00
13.	**Energy saving mutant**	0.16*	-0.08
CV % : 3.68		CD 1% : 0.021	
SE ± 0.0054		CD 5% : 0.015	
*Significant decresase in Phosporous content			

4. ACKNOWLEDGEMENTS

Authors are grateful to Principal R.S. Shinde, Arts, Commerce and Science College, Satral, Tal-Rahuri, Dist-Ahmednagar (MS), for his keen interest and constant encouragement. Thanks are due to Dr. S. R. Walunj, Principal and Dr. P. G. Reddy, Head Department of Botany of Padmashri Vikhe Patil College of Arts, Science and Commerce, Pravaranagar, Mahatma Phule Agriculture University Rahuri (MS) and Krishi Vigyan Kendra Babhaleshwar for providing facilities to carry out research work.

5. REFERENCES

Bhargava B.S. and Raghupathi H.B. (2005); Methods of Analysis of soils, Plants, Waters, Fertilizers and Organic Manures; Second ed[n] edited by Tondon HLS., Fertilizer Development and Consultation organization, New Delhi Pp-87-88.

Chitra, U., Vimala V., Singh U. and Geervani P. (1995). Variability in phytic acid content and protein digestibility of grain legumes. *Plant Foods for Human Nutrition*. **47**: 163-172.

Gehan, A. E. El-Emery and Ayman Y. Amin, (2010). Assessment Level of Some Antinutritional and Nutritional Factors in some Egyptian Cultivate Soybeans and Barley. Agriculture and Biological Sciences, **6**(4): 481-486.

Li, Y.C., Ledoux D.R, and Veum T.L.(2001). Bioavailability of Phousporous in Low Phytic Acid in Barley. *J. App. Poultry Res.* **10**:86-91.

Nguyen Thi Lang, Tran Anh Nguyet, Nguyen van Phang and Bui Chi, Buu. (2007); Breeding for low phytic acid mutants in rice (*Oryza sativa* L.); *Omonrice*, **15**: 29-35.

Raboy V. (2008); Induced mutation-facilated genetic studies of seed phosphorus, *International symposium on induced mutations in plants*, 12 -15 Aug., FAO/IAEA, Vienna, Pp. 68.

Raboy V., P. Gerbasi, KA Young, JA Dooch, and A Cook (2001); Genetics and breeding seed with low phytic acid; *J. Plant Physiol*, **158**: 489-497.

Raboy Vicror, Paola F. Gerbasi, Kevin A. Young, Sierra D. Stonebertg, Suewiya G.Pikett, Andrew T. Bauman, Pushpalatha P.N Murthy, William F. Sheridan and David S. Ertl. (2000). Origin and seed Phenotype of Maize low phytic acid 1-1 and low phytic acid 2-1[1]. *Plant Physiology*.**124**: 355-368.

Shi, Jinrui, Hongyu Wang, Yunsheng Wu, Jan Hazebroek, Robert B. Meeley and DavidS. Ertl. (2003). The Maize Low- Phytic Acid Mutant lpa-2 is Caused by Mutation in an Inositol Phosphate Kinase Gene. *Plant Physiology*.**131**: 507-515.

Tambe A.B. (2009); Induction of Genetic Variability in Soybean [*Glycine max* (L.) Merrill.] For yield Contributing Traits.; Ph.D. Thesis, University of Pune.

Zhou J.R and Erdman J. W. (1995).Phytic acid in health and disease. Crit Rev. *Food Sci Nutr* **35**:495-508.

BENS175

Lipoteichoic acid(LTA) isolated from *Lactobacillus plantarum* has inhibited effects of lipopolysaccharide(LPS)-induced proinflammation cytokine and MAPK siganaling

Ga Eun You Dae[a,]*, Gyun Chung[b]
[a]**Soechen-dong**, Kiheung-gu, Yongin-si, Gyeonggi-do 449-701, South Korea
E-mail address: twlovege@naver.com

[b]**Soechen-dong**, Kiheung-gu, Yongin-si, Gyeonggi-do 449-701, South Korea
E-mail address: dkchung@khu.ac.kr

ABSTRACT
Shigella flexneri is well known as pathogen that can cause bacillary dysentery, rectocolitis, septic shock and inflammation etc. One of the most important reason causing diseases is bacteria cell wall component. Lipopolysaccharide(LPS) is Gram negative bacteria cell wall component, this causes inflammation by inducing proinflammation cytokine in macrophage/monocyte. LPS induces proinflammation cytokine, including IL-8, IL-6 and TNF-alpha, which is induced by NF-κb and MAPK activity. LPS from *Shigella flexneri* induces phosphorylation of ERK, JNK and p38 kinase, and degrades IKBα and IKBβ. Therefore NF-κb is translocated into nucleus by this mechanism, NF-κb and phosphorylated ERK, JNK and p38 kinase induce transcription of proinflammation cytokine.
Lactobacillus sp. is known to exhibit anti-inflammation activity. Investigation of whole cell of Lactobacillus sp. had led to suppress of inflammation activity is well known. We found that one of the most important roles of inflammation is bacteria component LTA, it has effective inhibitory effects on inflammation mediators. Lipoteichoic acid(LTA) is cell wall component of gram positive bacteria, Lactobacillus sp. LTA is well known as anti-inflammation molecule. Our result show that *Lactobacillus plantarum* LTA(pLTA) inhibites protein level of proinflammation cytokine(IL-8, TNF-alpha) that is induced by LPS in human monocyte(THP-1). This pLTA effect is caused by pLTA pretreatment, pLTA pretreatment suppress MAPK signaling – increased proinflammation cytokine. We examined protein level of MAPK signaling by western blot, We found that pLTA decrease MAPK signaling protein level, including ERK, JNK and p38 kinase, in THP-1. In conclusion, these datas suggest that pLTA may have therapeutic effects for LPS-induced inflammation.

Keywords: Inflammation, Lipoteichoic acid, THP-1, *Lactobacillus plantarum*

BENS176

The improvement of intestinal immunity by *Lb. plantarum* LTA

Bong Jun Jung[a,*], Dae Kyun Chung[b]
[a]**KyungHee University Collge of Life Science 1 Soechen-ri**, Kiheung-eup, Yongin-si, Gyunggi-do 449-701, South Korea
E-mail address: along0@khu.ac.kr

[b]**KyungHee University Collge of Life Science 1 Soechen-r**i, Kiheung-eup, Yongin-si, Gyunggi-do 449-701, South Korea
E-mail address: dkchung@khu.ac.kr

ABSTRACT
Until now, lactobacilli have been known as the probiotic bacteria, which are good for ameliorating the intestinal health. However, the studies using live lactobacilli have taken the majority of the literature on the immune response of the large intestine. In this study, we analyzed the effect of the *lactobacillus plantarum* Lipoteichoic acid (pLTA) on the intestinal immune system. The objective of the study is to analyze the effect of the pLTA on the induction of immune enhancement in the HT29, the colon epithelial cells. In our studies, pLTA suppressed the infection of the pathogenic bacteria, *Staphylococcus aureus*, which is known for the cause of the irritable bowel syndrome. Also, it suppressed the expression of the pathogenic bacteria-induced pro-inflammatory cytokines. Moreover pLTA is thought to enhance the intestinal immune responses by suppressing the excessive signaling. This pLTA-mediated inhibition accompanied the inhibition of nuclear factor (NF)-kappa B and MAPKs.
Such results of our study indicate that the significance of pLTA on the amelioration of intestinal immune system, and suggest that lactobacillus may provide the major components to enhancing intestinal immune response

BENS177

Different effect of *Lactobacillus plantarum* and *Staphylococcus aureus* LTA on immune system

Kim, Hye rim[a], Chung, Dae kyun[b,*]
[a]**College of Life science, 1 Soechen-dong**, Kiheung-gu, Yongin-si, Gyeonggi-do 449-701, South Korea
Lookatme48@khu.ac.kr

Chung, Dae kyun
[b]**College of Life science, 1 Soechen-dong**, Kiheung-gu, Yongin-si, Gyeonggi-do 449-701, South Korea
dkchung@khu.ac.kr

ABSTRACT

Bacteria is classified gram positive and gram negative bacteria, according to the major components of the cell wall. These components are lipoteichoicacid (LTA), composed to the gram positive bacteria cell wall and lipopolysccharide (LPS), composed to the gram negative gram negative bacteria cell wall.

Both *Staphylococcus aureus* and *Lactobacillus plantarum* are Gram positive bacteria. However they show different effects on the human immunity. *Staphylococcus aureus* is recognized as a pathogen, causing serious diseases such as sepsis. By contrast, *Lactobacillus plantarum* is non-pathogenic and is known as probiotics. Bacteria that beneficial to the host organism called probiotics, most of probiotics are Lactic acid bacteria. Lactic acid bacteria has many effects such as intestinal regulation, immune system regulation, skin moisturizing, anti-Aging and skin whitening. These different immunological effects of *S.aureus* and *Lb.plantarum* are expected due to the LTA.

In this experiment, THP-1 cells were treated with LTA isolated from *S.aureus* (aLTA) and *Lb.plantarum* (pLTA), confirmed that effects on the human innate immune response. THP-1 cells were stimulated with various concentrations of aLTA and pLTA, TNF-α production were measured by ELISA. When treated with aLTA, TNF-α production was increased in a dose-dependent manner. However, pLTA had no significant influence on TNF-α production compared with aLTA treated cells. Interestingly, THP-1 cells pretreated with pLTA followed re-treatment with aLTA significantly inhibited aLTA-induced TNF-α production. The difference of the MAP kinase signal transduction in THP-1 cells measured by western blot. Phosphorylation of ERK, JNK and p38 was increased by aLTA, but pLTA scarcely induced the phosphorylation of the MAP kinase. Moreover, pLTA significantly inhibited aLTA-induced phosphorylation of MAP kinase.

These results suggest that pLTA did not cause an immune activation, but inhibit excessive inflammatory response. Thus, pLTA may be an effective prevention and therapeutic substances against gram-positive septic shock.

Keywords: *Lactobacillus plantarum*, Lipoteichoic acid, Gram positive sepsis, Immune response

BENS178

Encapsulation of bovine serum albumin within banana starch-alginate hydrogel beads for controlled protein drug release

Warin Pimpa[a,*], Chakkrit Pimpa[b], Tipawan Thongsook[c], Pensiri Nabheerong[d]
[a]**Department of Agro-Industry, Faculty of Agriculture, Natural Resource and Environment**,
Naresuan University, Phitsanulok 65000, Thailand
e-mail: warin@nu.ac.th

[b]**Northern Region Operation Division**, Electricity Generating Authority of Thailand,
Phitsanulok 65000, Thailand
e-mail: chakkrit.p@egat.co.th

[c]**Department of Agro-Industry, Faculty of Agriculture, Natural Resource and Environment**,
Naresuan University, Phitsanulok 65000, Thailand
e-mail: tipawant@nu.ac.th

[d]**Department of Biology, Faculty of Science**, Naresuan University, Phitsanulok 65000, Thailand
e-mail: pensirin@nu.ac.th

ABSTRACT
A hydrogel system comprised of two natural, hydrophilic polymers: sodium alginate and banana starch was studied as a carrier of bovine serum albumin (BSA) which was used as a model protein. The purpose of the present study was to investigate the release of BSA from banana starch-alginate hydrogel beads. The effect of different banana starch concentration in prepared blending solution on the BSA release profile in phosphate buffer pH 7.4, simulated intestinal fluid, was investigated. Incorporation of banana starch in the alginate gels resulted in improved BSA release by increasing the protein-release rate. The banana starch-alginate hydrogel beads prepared using gelation technique exhibited high BSA loading efficiency for all formulations. Scanning electron microscope revealed a smooth surface with characteristic large wrinkles and spherical in shape of the hydrogel beads. Thus, banana starch is a potentially useful natural material for making controlled release protein-loaded hydrogel beads.

1. INTRODUCTION

Nowadays protein drugs are becoming a very importance class of therapeutic agents. However, there are several problems associated with administration of the protein drugs. Such drug agents present short in half lives degrade by enzymes and poorly pass through biological barriers due to the diffusivity and low partition coefficient [1]. For these reasons the use of swelling polymeric matrices for the encapsulation and controlled release of drugs has received significant attention. This is because the encapsulation process could be performed in a simple, mild and safe condition.

Alginate hydrogels are considered biocompatible materials [2] with mucoadhesive properties [3] and have been widely used in controlled delivery of protein or drug molecules [4-7]. Wong et al. [8] reported that the starch-packed alginate beads have better visual quality, good flowability, higher mechanical strength and lower porosity. The hydrogel carrier could be improved by packing with high concentration of starch granules [8]. Starch is a biodegradable polymer with excellent biocompatibility and non-toxicity [9]. It is often compounded with other polymers in the fields of drug controlled release [10]. Although green banana (Khuai Hom Tong) has a large

amount of starch around 30% (based on dry basis) [11], the banana starch is not popularly used. With regard to the excellent digestion resistance property of banana starch [12], we wish these banana starch-alginate hydrogel beads can lead to a successful application for localized drug delivery in *vivo* and in *vitro* environment.

Therefore, the present study was to investigate the release of brovine serum albumin, a model protein from alginate-banana starch hydrogel beads. Particularly, this study focuses on the effect of different banana starch formulations and drug loading on the release behavior in phosphate buffer pH 7.4, simulated intestinal fluid. SEM microscopy was also examined for detail information regarding their external morphological features.

2. MATERIALS AND METHODS

2.1 Materials

A simple extraction of banana starch was modified from the method employed by Pimpa et al. [13]. All other chemicals used were analytical grade reagents.

2.2 Preparation of banana starch-alginate hydrogel beads

The formation of the hydrogel beads was based on the gelation technique with varying banana starch concentration ranging from 0-4% (w/v) and 2% (w/v) sodium alginate. The resulting dispersion was added dropwise into 1.5% (w/v) CaCl2 solution with constant stirring. Hydrogel beads were allowed for 30 min curring time, washed with distilled water, dried in oven at a temperature below 40oC and stored in desiccators for further use. To make drug loaded hydrogel beads, 100 mg BSA was dissolved under stirring in 100 ml of each one of formulated banana starch-alginate solutions to make them completely homogeneous and applied the same method as describe above.

2.3 Entrapment efficiency

Accurate weighed drug loaded hydrogel beads were crushed in a glass mortar-pestle and added to phosphate buffer pH 7.4. The drug encapsulation efficiency was determined and calculated as described by Sachan et al. [14].

2.4 Drug release experiments

The in vitro release studies were performed in phosphate buffer pH 7.4 (10 mM KH2PO4-NaOH buffer solution) at 37oC. 30 mg drug loaded banana starch-alginate hydrogel beads were suspended in glass vessels containing 50 ml of medium. The samples were taken at the time intervals for a total period of 5 h and they were replaced with the same amount. BSA contents were measured spectrometrically at 280 nm. All the experiments were done in triplicates.

2.5 Scanning electron microscopy analysis (SEM)

SEM was carried out at an accelerating voltage of 15 kV using scanning electron microscope (Leo 1455 Vp). The hydrogel beads were mounted on stub, and gold coated by Sputter coating Sc-7620.

3. RESULTS AND DISCUSSION

It was observed that in the fully swollen state, the hydrogel beads of all systems are semitransparent with almost perfect spherical shape (Fig. 1). The particle size increased significantly by increasing banana starch concentration. The viscosity of the polymer solution significantly affected the size distributions which have diameter ranging from 0.940 mm. to 2.689

mm. The scanning electron microscopy revealed that the presence of banana starch has impact on the external morphology of the hydrogel beads. The hydrogel beads presented a rough surface with characteristic large wrinkles. This might be due to the surface pressure and unequal water loss through the surface [15].

Using the gelation method, the banana starch-alginate hydrogel beads were found to encapsulate more than 98% of BSA and the encapsulation efficiency was not affected by the banana starch concentration. The influence of the different composition of banana starch in the drug loaded banana starch-alginate hydrogel beads on the drug release capacities in phosphate buffer pH 7.4 are shown in Fig. 2. The overall release studies showed that the incorporation of banana starch, even at small amount, in the alginate solution altered the release of BSA. In terms of the structure of the polymeric network this is associated with the interactions between alginate, banana starch and the protein. The polymeric network is dominated by physical entanglements between the BSA and alginate or starch chains rather than electrostatic interaction [16]. At high concentration of the banana starch, 70% BSA was released from the banana starch –alginate hydrogel beads in about 3 h while nearly 100% was released in 5 h. Phosphate containing media lead to degradation of alginates while porous structures provide more surface area and hence exhibit release capacity.

Banana starch-alginate hydrogel beads with different drug loaded amount (50 and 100 mg/100 ml prepare hydrogel solution) were studied in the same release solution cited in in vitro drug release study. The more drug loaded, the higher the drug cumulative release was (Fig. 3). In addition, the stability indicating assay shows that there was no significant change in the drug content of drug-load hydrogel beads, store at room temperature after 28 days of study.

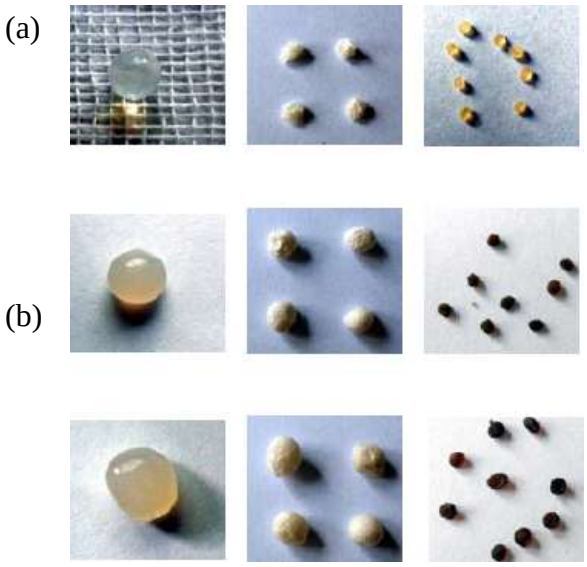

Fig. 1: Representative digital photograph of the three banana starch: alginate formulation (a) 0:2, (b) 2:2 and (c) 4:2 (%w/v) in three different states (from left to right): swollen, freezed dried and oven dried BSA loaded-banana starch-alginate hydrogel beads.

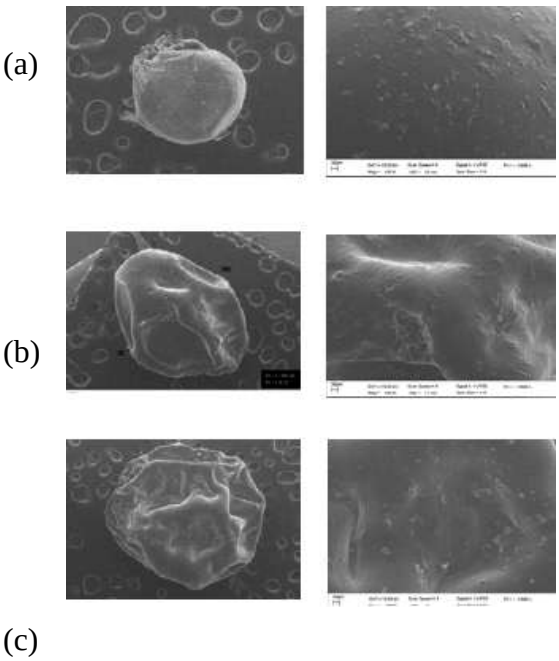

Fig. 2: Scanning electron microscopy image of the three banana starch: alginate formulation (a) 0:2, (b) 2:2 and (c) 4:2 (%w/v)

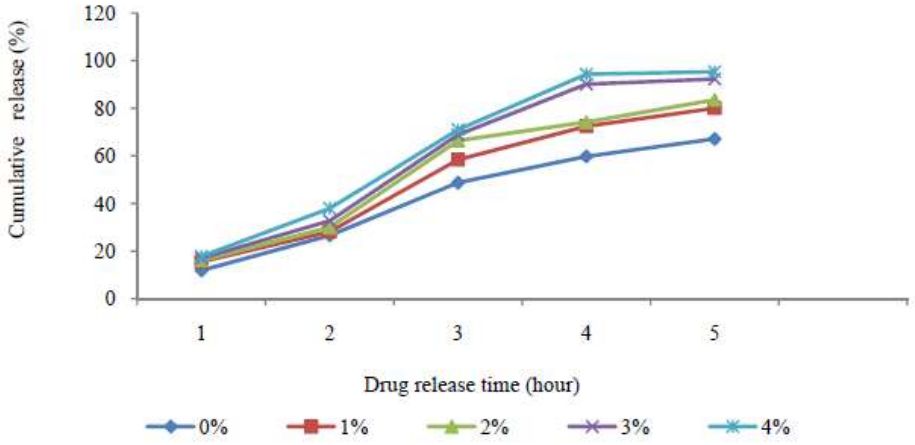

Fig. 3: *In vitro* release studies of BSA from banana-alginate hydrogel in phosphate buffer pH 7.4 at different starch concentration

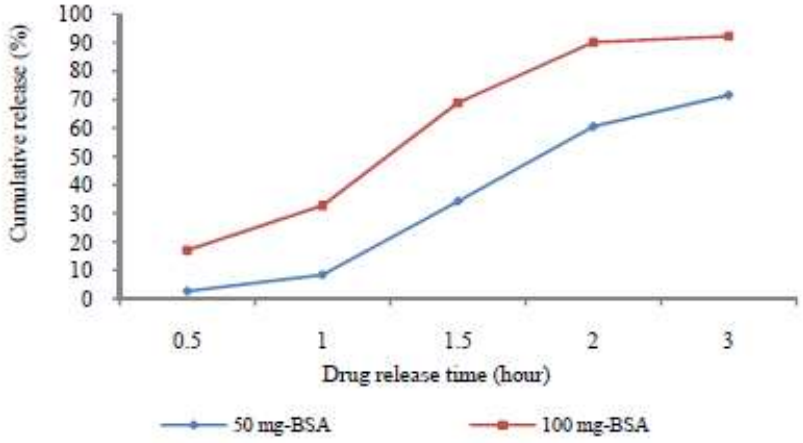

Fig. 4: Influence of the composition of the drug loaded in banana starch-alginate hydrogel beads on the controlled drug release process in buffer pH 7.4

4. CONCLUSION

In concluding the present study, the gelation method was used to prepare calcium alginate hydrogel beads with or without incorporation of banana starch. The banana starch-alginate hydrogel beads exhibited high BSA loading efficiency for all formulations. The presence of

banana starch increased the *In vitro* release ability in phosphate buffer pH 7.4. The data suggest that it is potential to use banana starch-alginate hydrogel beads as drug carriers to regulate the release of protein drug.

5. ACKNOWLEDGEMENT

This work was funded through the research grants 2012 by Naresuan University.

6. REFFERENCES

[1] Lee V H L. Enzymatic barriers to peptide and protein absorption. *CRC Crit. Rev. Therap. Drug Carr. Sys*., 1988, 5:69-97.

[2] Klock G, Pfeffermann A, Ryser C, Grohn P, Kuttler B, Hahn H. Biocompatibility of mannuronic acid-rich alginates. *Biomaterials*, 1997, 18:707-713.

[3] Gombotz W P, Wee S F. Protein release from alginate matrices. *Adv. Drug Deliv. Rev.*, 1998, 31:267-285.

[4] Bodmeir R, Paeratakul O. Spherical agglomerates of water-insoluble drugs. *J. Pharm. Sci.*, 1989, 78:964-967.

[5] Fernandez-Hervas M J, Holgado M A, Fini A, Feki J T. In vitro evaluation of alginate beads of a diclofenac salt. *Int. J. Pharm.* 1998, 163:23-34.

[6] Rasmussen M R, Snabe T, Pedersen L H. Numerical modeling of insuli and amyloglucosidase release from swelling Ca-alginate beads. *J. Controlled Releases.*, 2003, 91:395-405.

[7] Nochos A, Douroumis D, Bouropoulos N. In vitro release of brovine serum albumin from alginate/HPMC hydrogel beads. *Carbohyd. Polym.*, 2008, 74:451-457.

[8] Wong S L, Ravindra P, Lee J S, Chan E S. Effect of starch-packing on alginate hydrogel carrier quality: Particle characterization. In Proc. *XVth International Workshop on Bioencapsulation*, Vienna, Au., Sept 6-8 2007, pp. 1-4.

[9] Herman J, Remon J P, De Velder J. Modified starches as hydrophilic matrices for controlled oral delivery. 1. Production and characterization of thermally modified starches. *Int. J. Pharm.*, 1989, 56:51-63.

[10] Wang Q, Hu X, Du Y, Kennedy J F. Alginate/starch blend fibers and their properties for drug controlled release. *Carbohydr. Polym.*, 201, 82: 842-847.

[11] Bello-Perez L A, Agama-Acevedo E, Sanchez-Hernandez L, Paredes-Lopez O. Issolation and partial characterization of banana starches. *J. Agric. Food Chem.*, 1999, 47:854-857.

[12] Pimpa W, Pimpa C, Jansangsree P. Development of biodegradable films based on durian seed starch. *Adv. Mat. Sci.*, 2012, 506:311-314.

[13] Sachan N K, Ghosh S K, Bhattacharya A. Pharmaceutical utility of Assam Bora Rice for controlled drug delivery. *World Appl. J.*, 2011, 14(11):1687-1695.

[14] Sachan N K, Ghosh S K, Bhattacharya A. Evaluation of glutinous starch based matrix microbeads using scanning electron microscopy. *J. Chem. Pharm. Res.*, 2010, 2(3): 433-452.

BENS180

Characterization of the hemagglutinin of influenza by cold-adaptation as a novel approach to increase the safety of the vaccine candidates

Yoon-Jae Lee[a,*], Yo-Han Jang[b], Yun-Ha Lee[b], Kwang-Hee Lee[b], Baik Lin Seong[a,b]

[a]Department of biomaterials science & engineering, College of Life Science and Biotechnology, Yonsei University, Seoul, Korea

[b]Department of Biotechnology, College of Life Science and Biotechnology, Yonsei University, Seoul, Korea

1. BACKGROUND

Cold-adapted live attenuated influenza vaccines (CAIVs) have served as reliable vaccine platform. The attenuated phenotypes of the CAIV are attributed to genetic mutations accrued during cold-adaptation process. Mutations of the two surface antigens, HA and NA, are disregarded, because they would be replaced with those of circulating strains. In the cases where the HA and NA from wild type virus are still significantly virulent, the reassortant vaccine might also become virulent accordingly, raising the safety concern of the vaccine.

2. PURPOSE & METHODS

To analyze the attenuating mutations accumulated in the HA of live vaccine donor strain, we sequenced the nucleotides of the HA and NA of the cold-adapted X-31 strain (X-31 ca), and compared them with the parental strain, X-31 (X-31 wt). There were found four amino acid changes in the HA but not in the NA of the X-31 ca, compared to the X-31 wt. To characterize the degree of attenuation of these mutations of the HA ca, we generated two recombinant viruses, each carrying either the HA ca or HA wt, in the genetic background of A/Puerto Rico/8/34 virus. These two viruses were compared in cold-adapted, temperature-sensitive, and attenuated phenotypes, both in vitro cell culture and in vivo animal model.

3. RESULT

The HA ca provided the virus with the appreciable level of cold-adapted and temperature sensitive phenotypes, as compared to the HA wt-containing virus. Remarkably, the virulence of the HA ca-containing virus in mice was approximately a tenth that of the HA wt-containing virus, and its viral replications in the tissues were also significantly reduced, showing the attenuated phenotype. Alignment of the amino acid sequences among diverse influenza strains revealed that the replacement of the amino acids were also feasible to other influenza virus strains.

4. CONCLUSION

Our results are the first report demonstrating that the HA also has the specific mutations that participate in the overall attenuation of influenza live vaccine donor strain. The attenuating effect of these mutations was considerable increasing the mouse lethal dose 50 by ten times when incorporated into virulent virus. If these mutations are introduced into other HA of the virulent

viruses, such as the highly pathogenic H5N1 avian influenza virus, the safety level of the vaccine could be increased. To be more practical, the contribution of individual mutation and possible

BENS186

Fabrication of Highly Aligned Collagen Micro-Scaffolds and its Evaluation by SHG Microscopy and Mechanical Tensile Test

Keisuke Yoshiki*, Nobutaka Goami, Takahiro Namazu, and Shozo Inoue
Department of Mechanical and Systems Engineering Graduate School of Engineering
University of Hyogo 2167 Shosha, Himeji, Hyogo 671-2201, JAPAN
E-mail address: yoshiki@eng.u-hyogo.ac.jp

We propose a micro fabrication system of higher oriented micro electrochemical aligned collagen (ELAC) for cell culturing under micro-fluid system.

Cell culture using Micro-Total Analysis Systems (μ-TAS) is useful to estimate cell response to environmental chemicals; for instance, to estimate the efficiency and toxicity of a drug [1]. Especially, the response to few chemicals, such as endocrine disrupters, is investigated using μ-TAS systems. However, in addition to responding to chemicals, cells also respond to physical conditions, such as temperature, pH, ion strength and stress. In biological tissues, cells have the ability to accommodate mechanical stress. When mechanical stress is applied to biological tissues, the cells degrade and the collagen fibers restructure to relieve the stress in the extracellular matrix around the cells [2]. In this report, we focus on mechanical stress and the scaffolds because mechanical stress is more difficult to apply than other environmental factors.

In conventional μ-TAS, the scaffold for cell culture is a surface of glass or polymer coating, which makes it difficult for a mechanical force equivalent to that in actual tissues to be applied. Furthermore, in contrast to actual tissues, which consist of highly oriented collagen fibres, the orientation of the polymer is homogeneous. Therefore, we propose a highly aligned micro-scaffold for cell culture in a μ-TAS with a micro-mechanical tensile tester. ELAC fibers are used for culturing cells [3] and we observed that the size of the crystal could be controlled under certain preparation conditions. Using second-harmonic generation (SHG) microscopy, the prepared ELAC fibers were compared to tendon tissue to determine if the ELAC fibers have the same optical properties as those of tendon tissue. We found that SHG microscopy was useful for estimation of the scaffold.

Figure 1 shows a image and an equivalent mechanical model of the micro-tensile tester device. The device consists of two probes that apply tensile stress to a collagen fiber. One side of each probe was connected to a weight supported on a frame by four springs whose stiffness was compensated by the resonance frequency of a spring-mass system. The resonator was actuated by an interdigitated electrode, which in turn was actuated by a sinusoidal signal with an amplitude of 7 V and offset of 5 V. The resonance frequency was 1210 Hz, which indicates the 1st resonance frequency and in-plane vibration mode. The spring stiffness was estimated to be 116 N/m, which is in good agreement with the result from a conventional tensile tester using a load cell (114 N/m). The deviation from the design specification of 200 N/m was due to an error in the manufacturing process. The other side of the probe was connected to the frame through springs. We held and moved both probes by a linear transfer stage driven by a micrometre.

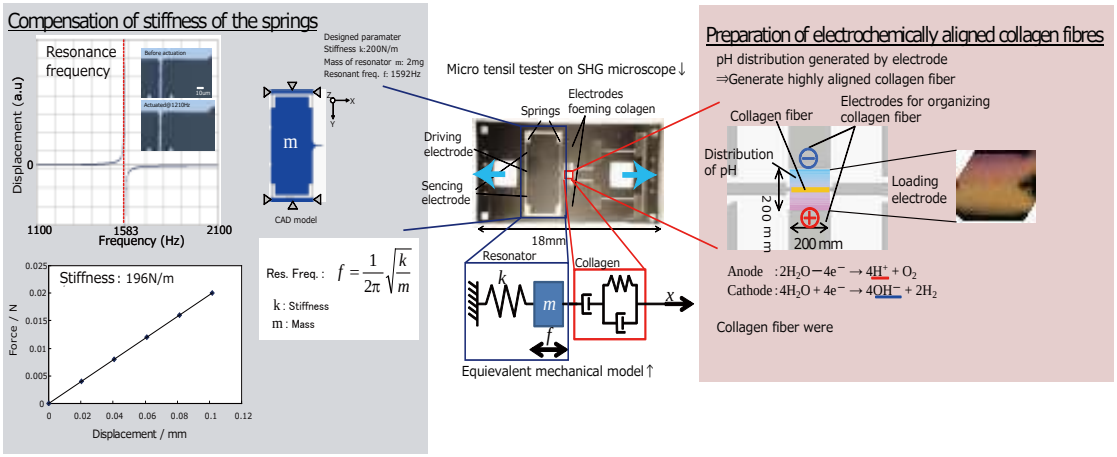

Figure 1: Micro-tensile tester device on the SHG microscope

We report the result of measurement of the mechanical tensile load on collagen scaffolds using SHG microscopy. The optical arrangement of the SHG microscope is shown in Fig. 2. We measured the dependence of SHG intensity on stress and strain applied to a collagen fiber. Using the dependence, we converted the distribution of SHG intensity to stress and strain distribution. Therefore, it will be possible to obtain images of the stress and strain distribution of biomaterials. Figure 3 illustrates the change in the SHG signal from collagen when stress and strain are applied. Both intensity of transmission SHG and reflection SHG increased, and the ratio of these intensities deceased with strain. This indicates that the orientation of molecules becomes homogeneous and the size of the crystal is decreased due to the mechanical stress. The results make it possible to calculate the quantitative value of stress.

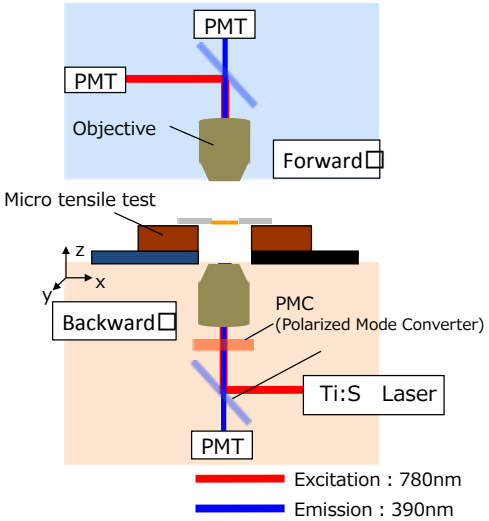

Figure 2: SHG microscope

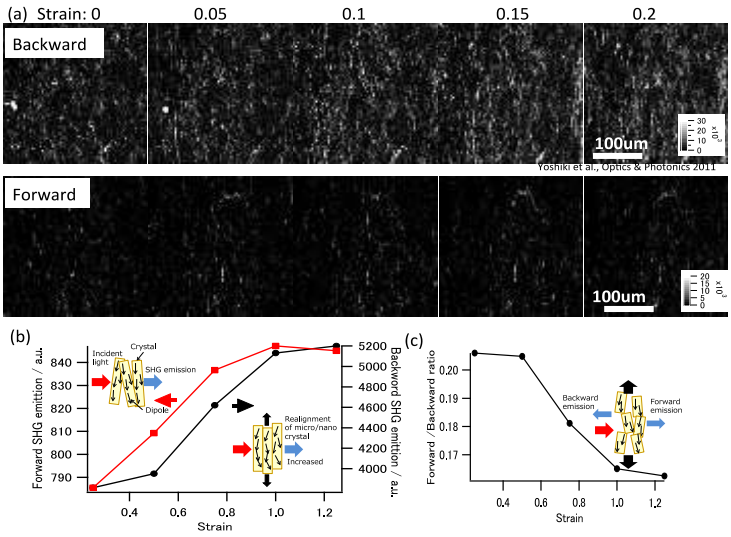

Figure3: Dependence of SHG intensity on strain

REFERENCES

[1] B. G. Chung, L. A. Flanagan, S. W. Rhee , P. H. Schwartz , A. P. Lee , E. S. Monuki and N. L. Jeon, Lab Chip, 2005, 5: 401–406.

[2] M. Kjaer, Physiol. Rev. 2004, 84: 649–698.

[3] X. Cheng, U. A. Gurkan, C. J. Dehen, M. P. Tate, H. W. Hillhouse, G. J. Simpson and O. Akkus, Biomaterials 2008, 29: 3278–3288.

BENS206

Multiple Growth Factors-Immobilized Bioactive Porous Beads as an Injectable Bulking Agent

Sang June Kim, Se Heang Oh, and Jin Ho Lee*

Dept. of Advanced Materials, Hannam University, Daejeon 305-811, South Korea

E-mail address: jhlee@hnu.kr

ABSTRACT

The injection of bulking agents has usually been used as the first line therapy for the treatment of urinary incontinence. However, the injection volume decrements with time caused by particle migration and resorption in the body have been considered as a critical problem. In this study, polycaprolactone (PCL)/Pluronic F127 porous beads were fabricated by an isolated particle melting/melt-molding particulate-leaching method as an injectable bulking agent. Three growth factors [GFs; basic fibroblast growth factor (bFGF), vascular endothelial growth factor (VEGF) and nerve growth factor (NGF)] were respectively immobilized onto the porous beads for the effective treatment of urinary incontinence. The GFs were easily immobilized onto the surfaces of the PCL/F127 porous beads via heparin binding. The GFs immobilized onto the pore surfaces were continuously released for up to 35 days. The GFs-immobilized porous beads had a positive effect for the differentiation of muscle-derived stem cells into target cells (smooth muscle cells/nerve cells). And it was also observed that the porous beads had effective cure behaviors for urinary incontinence as follows: the narrowed urethral lumen and the regeneration of smooth muscle/nerve around the urethra and thus functional recovery of urethral sphincter.

Keywords: Injectable bulking agentt, Growth factors, Porous beads

1. INTRODUCTION

Urinary incontinence, which is defined as the involuntary loss of urine, causes serious medical and social problems, having a deep influence on a patient's psychological state [1]. Stress urinary incontinence, one type of the urinary incontinence, may be caused by urethral hypermobility and/or intrinsic sphincter deficiency [2]. The main idea for the treatment of stress urinary incontinence has been referred to increment of urethral resistance to intra-abdominal pressure by coaptation or narrowing of the urethral lumen. Injectable bulking agents, such as polytetrafluoroethylene particle, silicone particle, carbon particle, glutaraldehyde cross-linked collagen, and autologous fat, have been used in the treatment of stress urinary incontinence. However, injection volume decrement with time caused by particle migration and resorption in the body has been main problems for them. In this study, we prepared multiple growth factors-immobilized porous polycaprolactone (PCL)/Pluronic F127 beads as an injectable and bioactive bulking agent which can provide bulking effect and stimulate the defect tissues around urethra for the effective treatment of urinary incontinence.

2. EXPERIMENTAL

The PCL/Pluronic F127 porous beads were fabricated by an isolated particle-melting method

(for nonporous beads) and the following melt-molding particulate-leaching method (for porous beads) developed by our laboratory [3]. The Pluronic F127 chains exposed onto the PCL bead pore surfaces were used to bind heparin and the following growth factor [basic fibroblast growth factor (bFGF), vascular endothelial growth factor (VEGF) or nerve growth factor (NGF)] which may improve the sphincter muscle function around the urethra. The morphology, growth factor release behaviors, and the animal study (using an urinary incontinence rat model) to investigate the effectiveness of the growth factors-immobilized porous beads as a bioactive bulking agent were conducted.

3. RESULTS

It was observed that the random-shape PCL crushed particles were changed into spherical nonporous beads with similar sizes through the isolated particle-melting method. The porous beads fabricated by the melt-molding particulate-leaching method showed highly uniform pore structures. From the growth factor release experiment, it was observed that the growth factors immobilized onto porous PCL/F127 porous beads were continuously released up to 35 days, regardless of growth factor types. We confirmed from the *in vivo* animal study that the multiple growth factors-immobilized porous beads have a significantly faster smooth muscle and nerve regeneration and higher cure rate for the urinary incontinence than the single growth factor-immobilized porous bead groups as well as the porous bead group without the growth factor immobilization. From the results, it was expected that the multiple growth factors (bFGF, VEGF, and NGF)-immobilized PCL porous beads may be a good candidate as an injectable bioactive bulking agent.

4. ACKNOWLEDGEMENTS

This work was supported by a grant of the Korean Health Technology R&D Project, Ministry of Health & Welfare, Republic of Korea (A120357) and a Pioneer Research Program for Converging Technology funded by the Ministry of Education, Science and Technology (2012-0001052).

5. REFERENCES

[1] Abrams P, et al., *Scand J Urol Nephrol Suppl.*, 1988, 114:5-19.

[2] Blaivas J, et al., *J Urol.*, 1997, 157:818-820.

[3] Lim SM, et al., *J Biomed Mater Res.*, 2009, 90B: 521-530.

BENS213

Redox environment modifies the antimutagenic functionality of *Bifidobacterium bifidum*

R. Cachon[a,*], B. Ebel[a], C. Dumont[b], I. Severin[b], P. Gervais[a], MC. Chagnon[b]

[a]UMR A 02.102 Procédés Alimentaires et Microbiologiques, AgroSup Dijon / Université de Bourgogne, équipe PMB, 1 esplanade Erasme, 21000 Dijon

E-mail address: remy.cachon@u-bourgogne.fr

[b]Laboratoire Nutox – Inserm U866, AgroSupdijon, 1 esplanade Erasme 21000 Dijon

ABSTRACT

Bifidobacteria are probiotic bacteria isolated from the human gastrointestinal tract. They are the most prevalent microbes in the large intestine but are also implanted throughout the distal jejunum and ileum in the small intestine. The oxidoreduction potential E_h plays an essential role in microbial cell physiology. Obligate aerobes are metabolically active in an environment with a positive E_h, whereas obligate anaerobes require a negative E_h. The aim of this work was to study the effect of the E_h on the functionality of *Bifidobacterium bifidum*. In order to modify E_h, gases were employed; two gases were used: pure nitrogen (N_2) or nitrogen (96%) / hydrogen (4%) (N_2-H_2). By modulating E_h with gas, human gastrointestinal conditions could be reproduced: an oxic condition (Control; considered to mimic those encountered in zones adjacent to the mucosal surface), a reducing condition (N_2-H_2; considered to mimic those encountered in the intestinal lumen) and an intermediary oxidant anoxic condition (N_2). We studied the impact of the change in E_h on antimutagenic functionality of *Bifidobacterium bifidum*. The antimutagenic effect of *Bifidobacterium bifidum* was determined on a pro-oxidant molecule and mutagen, 4NQO. The supernatant of the co-incubation bacteria / 4NQO has been in contact with a human colorectal cell line (Caco-2), and the genotoxic potential assessed with the comet assay. This study shows that *Bifidobacterium bifidum* grown on the control medium is able to significantly reduce the mutagenic effect of 4NQO. This feature is significantly increased with oxidizing and reducing anaerobic environments. A change in membrane surface properties could explain this phenomenon.

BENS135

Chemically-Induced Bacterial Ghosts

Nagarajan Vinod[a], Sung Oh[b], Seongdae Kim[c], Chang Won Choi[d], Sei Chang Kim[e,*]
[a]**Department of Biology & Medicinal Scienece**, Pai Chai University, Daejeon 302-735, Korea
E-mail address: biovinz@yahoo.com

[b]**Department of Biology & Medicinal Scienece**, Pai Chai University, Daejeon 302-735, Korea
E-mail address: 5star@pcu.ac.kr

[c]**Department of Biology & Medicinal Scienece**, Pai Chai University, Daejeon 302-735, Korea
E-mail address: khboy111@pcu.ac.kr

[c]**Department of Biology & Medicinal Scienece**, Pai Chai University, Daejeon 302-735, Korea
E-mail address: choicw@pcu.ac.kr

[d]**Department of Biology & Medicinal Scienece**, Pai Chai University, Daejeon 302-735, Korea
E-mail address: kimsc@pcu.ac.kr

ABSTRACT
The Bacterial Ghost (BG) platform technology is an innovative system for vaccine, drug or active substance delivery and for technical applications in different biotechnological applications. BG is an empty cell envelopes derived from Gram-negative bacterium. BG is devoid of all cytoplasmic content but has a preserved cellular morphology and native surface antigenic structures including bioadhesive properties. In this study, we are introducing a new method for BG preparation using chemical agents. The method is based on minimum inhibitory concentration (MIC) of NaOH, $(NH_4)_2SO_4$, $CaCl_2$ and EDTA, respectively. The MIC values of each chemical for the treatment of *Escherichia coli* DH5α were 3.125 mg/mL of NaOH, 187.5 mg/mL of $(NH_4)_2SO_4$, 125 mg/mL of $CaCl_2$, and 25 mg/mL of EDTA. These values of each chemical were used to produce BG cells. Light microscope and scanning electron microscope have been used to characterize the BG. Spectrophotometric analysis and SDS-PAGE was used to evaluate the amount of protein in BG preparation. Spectrophotometric analysis and agarose gel electrophoresis also have been used to determine the existence of any residue of DNA after BG preparation. The chemicals used in this method that are safe to use and their costs are relatively cheap.

Keywords: Bacterial ghost, Chemical agents, Minimum inhibitory concentration (MIC)

1. INTRODUCTION

Bacterial Ghost (BG: empty bacterial cell envelope) raised from Gram-negative bacteria are under investigation as vaccine candidates and carriers of foreign antigens [1-3]. The most common method used for BG production by protein E-mediated lysis is based on the tightly controlled expression of the cloned lysis gene E of bacteriophage PhiX174. The gene E encodes a hydrophobic polypeptide of 91 amino acids that forms a transmembrane tunnel in the bacterial cell wall through which the cytoplasmic contents are expelled [4-9]. The resulting BGs share functional and antigenic determinants of the envelope with their living counterparts, as the the protein E does not cause physical or chemical denaturation to bacterial surface structures [6, 10].

There are various applications of BG. The live attenuated and inactivated bacterial cells prove to be an effective delivery system for recombinant antigens and nucleic acids [11]. BG candidate

vaccines are highly immunogenic and in many instances induce protective immunity against lethal challenge in animal models. BG cells are able to stimulate the innate and adaptive immune system without any addition of exogenous adjuvants. Furthermore, BGs are not considered as genetically manipulated organisms (GMO), as they are nonliving and devoid of genetic information. Therefore, BG can be used as a delivery system for protein, nucleic acids, drugs and soluble compounds for various medical and technical applications [12, 13]. The combination of enterohemorrhagic Escherichia coli (EHEC) and protein E is used to produce oral EHEC vaccine [14]. BG cells from Mannheimia Haemolytica were used for site-specific delivery of doxorubicin (DOX) to human colorectal adenocarcinoma cells (Caco2) [15]. In addition, BG cells have been used recently as DNA delivery system by immobilizing the plasmid DNA [16]. The inner space of BG's empty envelope, can carry antigen, DNA or mediators of the immune response [17], representing a new highly efficient gene delivery platform as an alternative to current viral and bacterial methods in vaccine development [18].

Minimum inhibitory concentration (MIC) of an antimicrobial will inhibit the visible growth of a microorganism after overnight incubation, and minimum growth concentration (MGC) as the lowest concentration of antimicrobial that will prevent the growth of an organism [19, 22]. MIC is typically used by diagnostic laboratories mainly to confirm resistance. In this paper we present data indicating the MIC values of chemicals (NaOH, (NH4)2SO4, CaCl2 and EDTA), which would inhibit the growth of E. Coli DH5α. These chemicals have been proven to affect bacterial cell walls. We also present a newly designed method for BG preparation without the need for E lysis gene.

2. MATERIALS AND METHODS

2.1 Bacterial strain

Bacterial strain E. Coli DH5α was maintained in our laboratory. E. Coli was grown in Luria-Bertani (LB) broth at 37^{o}C in shaking incubator at 200 rpm.

2.2 Determination of minimum inhibitory concentration

The MIC values of NaOH, (NH4)2SO4, CaCl2 and EDTA was determined by using the two-fold broth dilution method [20, 21]. Starting from a chemical agent solution, serial dilutions were prepared in LB inoculated with the test bacterial populations ≥ 106 CFU/mL. Then tubes were incubated at 37^{o}C for 18 hr. Minimum inhibition of E. Coli DH5α growth was determined by measuring the absorbance at 600 nm.

2.3. Bacterial Ghost production

The biomass of the E. Coli DH5α culture was collected by centrifuging the bacterial broth at 8000 rpm for 5 min. E. Coli DH5α cells were collected, washed and adjusted to concentration ≥ 106 CFU/mL. Stock solutions (5x) of NaOH, (NH4)2SO4, CaCl2 and EDTA have been prepared from MIC which was determined as above. One mL of 5x NaOH, (NH4)2SO4, CaCl2 and EDTA, respectively, has been added to 2 mL of the bacterial suspension to make up the volume to 5 mL and to give a final concentration equal to 1x for each NaOH, (NH4)2SO4, CaCl2 and EDTA. Then, all the tubes were incubated at 37^{o}C for 1 hr. After incubation, BG cells were harvested by centrifugation at 8000 rpm for 5 min. After harvesting, BG cells were washed by saline (0.5%) to remove any debris, fatty materials as well as DNA and protein.

2.4. Determination of Protein concentration

Protein analysis of BG cells was done using the spectrophotometer at 280 nm. The protein concentration was derived from Bovine Serum Albumin standard curve.

2.5. Determination of *E. Coli* ghosts viability

The various preparation of BG cells has been investigated for the presence of any viable cells by

subjecting them to grow in LB medium. Where 25 µL from each sample has been transferred to the surface of LB plate and has been allowed to grow for 48 hr at 37ºC.

2.6. SDS-PAGE and agarose gel electrophoresis

BG samples were electrophoresed in 12% SDS-PAGE. The samples were denatured in Laemmili buffer and then loaded in SDS-PAGE under constant 40 mA. The gel was stained in Coomassie brilliant blue solution for 4 hr at room temperature and immerged in destaining solution (45% methanol; 10% acetic acid; 45% distilled water, v/v/v) until the protein bands clearly visible. The presence of genomic DNA in BG cells was analyzed using 1% agarose gel containing 0.5 g/mL of ethidium bromide.

3. RESULTS AND DISCUSSION

The MIC of each chemical was determined by serial dilution method. The MIC of NaOH, (NH4)2SO4, CaCl2 and EDTA was 3.13 mg/mL and 5.37 %, 187.50 mg/mL and 17.00 %, 125 mg/mL and 0.09 %, 25 mg/mL and 8.14% , respectively (Table 1). All chemicals tested showed the effective inhibition of bacterial growth.

Table 1. Minimum inhibitory concentration of NaOH, $(NH_4)_2SO_4$, $CaCl_2$ and EDTA.

Sample No.	Chemical agents	MIC (mg/ml)	MIC %
1	NaOH	3.13	5.368
2	$(NH_4)_2SO_4$	125.00	17.067
3	$CaCl_2$	125.00	22.803
4	EDTA	9.38	0.087

The MIC will give us the minimum amount of the chemicals, which is responsible for killing the bacteria while MGC will give the minimum concentration while allow the bacterial cells to survive. The method depends on growing the bacterial cells in condition allowing a correct cell wall formation then subjecting the cell wall to chemicals which could affect it. While vegetative cells are more sensitive to those chemicals used, a fully grown and three days old culture cells are expected to have more resistant cell wall, meaning that it will have less effect on the quality of cell wall. Light microscope was used for quality of the cells, which based on the bacterial structure as either being correct or deformed. BG cell viability is determined by spreading it on LB agar plate. After 18 hr incubation, LB plates showed no viable cells in BG sample. In our case NaOH, $(NH_4)_2SO_4$, $CaCl_2$ and EDTA showed good effect (Fig. 1).

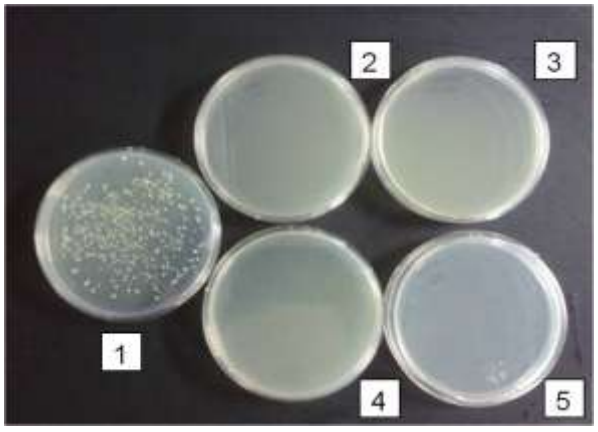

Figure 1. Determination of *Escherichia Coli* ghosts viability. Non-treated (1), NaOH-treated (2), $(NH_4)_2SO_4$-treated (3), $CaCl_2$-treated (4), and EDTA-treated (5) *E. Coli* DH5α.

Table 2. Determination of bacterial ghosts protein concentration

Sample No.	Chemical agents	Protein Concentration (µg/ml)
1	Control (*E. Coli* DH5α)	15600.00
2	NaOH	90.00
3	$(NH_4)_2SO_4$	450.00
4	$CaCl_2$	75.00
5	EDTA	225.00

Spectrophotometer was used to estimate protein concentration in BG cells. Table 2 shows the protein content in the control as compared with the prepared BG cells. As it is clearly seen the protein content in non-treated control is higher because of the presence of both cytoplasmic proteins and cell wall proteins. Whereas the protein content in BG cells are much less than those of non-treated control, because it may have only cell wall proteins to maintain BG. Remaining protein and DNA content of BG cells were evaluated by SDS-PAGE and agarose gel electrophoresis. Fig. 2A showed the total protein in the non-treated control and four chemicals-treated BG cells. However, the protein concentration in non-treated control is much higher than that in BG cells. This is evident because the amount of protein in non-treated control is much higher than that of each chemical-treated BG. SDS-PAGE was able to confirm that we were able to produce BG which is devoid of cytoplasmic protein. Agarose gel electrophoresis showing perfectly that the DNA was completely degraded in BGs as compared to non-treated *E. Coli* DH5α which clearly shows the band for DNA (Fig. 2B). [Samples were given for SEM images and currently we are working for the images.]

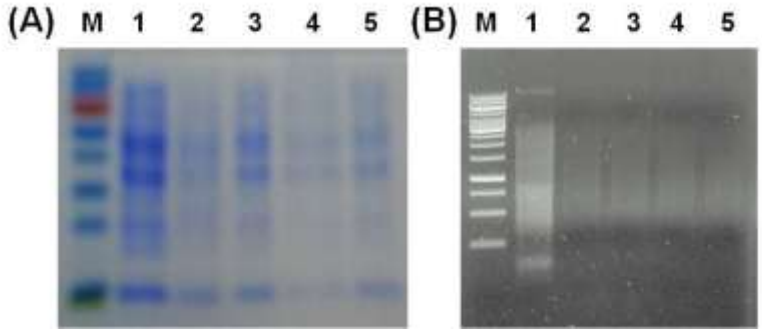

Figure 2. (A) SDS-PAGE Analysis of bacterial ghosts. M: Protein Marker, non-treated *E. Coli* DH5α (lane 1), NaOH-treated (lane 2), $(NH_4)_2SO_4$-treated (lane 3), $CaCl_2$-treated (lane 4), and EDTA-treated (lane 5). (B) Agarose gel electrophoresis of bacterial ghosts. M: 1kb Marker Ladder, non-treated *E. Coli* DH5α (lane 1), NaOH-treated (lane 2), $(NH_4)_2SO_4$-treated (lane 3), $CaCl_2$-treated (lane 4), and EDTA-treated (lane 5).

While preparation of BG cells, complete cell lysis should be avoided. High release of each of DNA and protein indicates that the cells have lost their cytoplasmic content and turned into BG cells. This protocol can be used with any kind of bacterial strain which is affected by using the chemical used in this method.

4. ACKNOWLEDGEMENTS

This research was financially supported by the Leading Industry Development for Economic Region of the Chungcheong Leading Industry Office (CCLIO), Korea Institute for Advancement of Technology (KIAT) and Ministry of Knowledge Economy (MKE).

5. REFERENCES

[1] Szostak M, Wanner G, Lubitz W. Recombinant bacterial ghosts as vaccines. Res. Microbiol,

1990, 41: 1005-1007.
[2] Szostak M, Hensel A, Eko F O, Klein R, Auer T, Mader H, Haslberger A, Bunka S, Wanner G, Lu-bitz W. Bacterial ghosts: non living candidate vaccines. J. Biotechnol, 1996, 44: 161-170.
[3] Hensel A, Van Leengoed L A G, Szostak M, Windt H, Weissenboeck H, Stockhofe-Zurwieden N, Katinger A, Stadler M, Ganter M, Bunka S, Papst R, Lubitz W. Induction of protective immunity by aerosol or oral application of candidate vaccines in a dose-controlled pig aerosol infection model. J. Biotechnol, 1996, 44: 171-181.
[4] Henrich B, Lubitz W, Plapp R. Lysis of *Escherichia coli* by induction of cloned PX174 genes. Mol. Gen. Genet, 1982, 185: 493-497.
[5] Blaesi U, Henrich B, Lubitz W. Lysis of Escherichia coli by cloned gene E depends on its expression. J. Gen. Microbiol, 1985, 131: 1107-1114.
[6] Witte A, Lubitz W. Biochemical characterizationof PhiX174 protein E-mediated lysis of *Escherichia coli*. Eur. J. Biochem, 1989, 180: 393-398.
[7] Witte A, Blaesi U, Halfmann G, Szostak M, Wanner G, Lubitz W. PhiX174 protein E-mediated lysis of *Escherichia coli*. Biochimie, 1990, 72: 191-200.
[8] Witte A, Wanner G, Blaesi U, Halfmann G, Szostak M, Lubitz W. Endogenous transmembrane tunnel formation mediated by PX174 lysis protein E. J. Bacteriol, 1990, 172: 4109-4114.
[9] Schoen P, Schrot G, Wanner G, Lubitz W, Witte A. Two-stage model for integration of the lysis protein E of bacteriophage PhiX174 into cell envelope of *Escherichia coli*. FEMS Microbiol. Rev, 1995, 17: 207-212.
[10] Witte A, Wanner G, Lubitz W. Dynamics of PhiX174 protein E-mediated lysis of *Escherichia coli*. Arch. Microbiol, 1992, 157: 381-388.
[11] Kany H Y. Immune responses dependent on antigen location in recombinant attenuated *Salmonella typhimurium* vaccine following oral immunization. FEMS Immunol. Med. Microbiol, 2003, 85: 99-104.
[12] Susanne Paukner, Thomas Stiedl, Pavol Kudela, Jozef Bizik, Firas Al Laham, Werner Lubitz. Bacterial ghosts as a novel advanced targeting system for the drug and DNA delivery. Expert Opin. Drug Deliv, 2006, 3: 11-22.
[13] Tabrizi C A, Walcher P, Mayr U B, Stiedl T, Binder M, McGrath J, Lubitz W. Bacterial ghosts--biological particles as delivery systems for antigens, nucleic acids and drugs. Curr. Opin. Biotechnol, 2004, 15: 530-537.
[14]Ulrike Beate Mayr, Christoph Haller, Wolfgang Haidinger,, Alena Atrasheuskaya, Eugenij Bukin, Werner Lubitz, Georgy Ignatyev. Bacterial Ghosts as an Oral Vaccine: a Single Dose of *Escherichia coli* O157:H7 Bacterial Ghosts Protects Mice against Lethal Challenge. Infect. Immun, 2005, 73: 4810–4817.
[15] Paukner S, Kohl G, Lubitz W. Bacterial ghosts as novel advanced drug delivery systems: antiproliferative activity of loaded doxorubicin in human Caco-2 cells. J. Control. Release, 2004, 94: 63-74.
[16] Mayrhofer P, Tabrizi C A, Walcher P, Haidinger W, Jechlinger W, Lubitz W. Immobilization of plasmid DNA in bacterial ghosts. J. Control. Release, 2005, 102: 725-735.
[17] Jechlinger W, Azimpour Tabrizi C, Lubitz W, Mayrhofer P. Minicircle DNA immobilized in bacterial ghosts: in vivo production of safe non-viral DNA delivery vehicles. J Mol Microbiol Biotechnol, 2004, 8: 222-231.
[18] Weiner D B. Introduction to Dna vaccines issue. Vaccine, 2006, 24: 4459-4460.
[19] Jennifer M Andrews. Determination of minimum inhibitory concentrations. J. Antimicrob. Chemother, 2001, 48: 5-16.
[20] Thereza C V Penna**,** Priscila G Mazzola, Alzira M Silva Martins. The efficacy of chemical agents in cleaning and disinfection programs. Infec. Dis, 2001, 1: 1-8.
[21] Tavares L C, Vessoni Penna T C, Amaral A T. Synthesis and biological activity of nifuroxazide and analogs. Boll. Chim. Farm, 1997, 136: 244-249.
[22] Manimozhi D M, Sankaranayanan S, Sampathkumar S. Evaluating the antibacterial activity of

flavonoids extracted from *Ficus Benghalensis*. Int. J. Pharm. Bio. Res, 2012, 3: 7-18.

BENS238

The molecular mechanism of CDV-induced apoptosis

Hung-Yi Wu[a,*], Chia-Ying Lin[c], Perng-Chih Shen[b], Ching-Dong Chang[a], Shinn-Shyong Tsai[a], Tsung-Chou Chang[a], Ming-Hui Liao[a]

[a]Department of Veterinary Medicine National Pingtung University of Science and Technology, 912, Taiwan, ROC

E-mail address: hungyibob@yahoo.com.tw

[b]Department of Animal Science, National Pingtung University of Science and Technology, 912, Taiwan, ROC

[c]**Sheng Jie Veterinary Hospita**l

ABSTRACT

Canine distemper virus（CDV）causes generalized infection in dogs with prominent respiratory, gastrointestinal and nervous signs. Not only dogs, CDV can infect other carnivores, ferret, mink, marine mammals and so on. CDV has highly contagiously pathology and it is classified into the Morbillivirus genus of the family Paramyxoviridae. The previous studies showed that CDV induced apoptosis in the caspase-dependent pathway through the activated caspase-3/-8/-9. But it did not explain the entire relationship between the apoptotic proteins related the CDV-induced cell damages. Thus, our studies revealed that the caspase-dependent pathway was not the only one apoptotic pathway in CDV-infected cells, the caspase-independent apoptotic pathway in CDV-induced cell death also played an important role. We showed the CDV-induced apoptosis in the TUNEL and Annexin V assay and evaluated the effect of AIF, Endo G and caspases with the immunofluorescence studies. We analyzed the intracellular distribution of CDV in cells treated with CDV and caspase inhibitor by immunofluorescence assay. We also realized the intracellular effects of AIF and Endo G in CDV-infected cells by western blot analysis. Thus, we clarified CDV-induced apoptosis also via caspase-independent pathway.

Keywords: canine distemper virus, apoptosis, AIF, Endo G

BENS239

Enhancement of osteogenic and chondrogenic differentiation of human embryonic stem cells by mesodermal lineage induction with BMP-4 and FGF2 treatment

Byung-Soo Kim

School of Chemical and Biological Engineering, Seoul National University, Seoul, Republic of Korea

ABSTRACT

Recently, it was reported that bone morphogenetic protein 4 (BMP4) alone or BMP4 combined with fibroblast growth factor 2 (FGF2) treatment enhanced mesodermal differentiation of human embryonic stem cells (hESCs) that were cultured feeder-free on Matrigel. In this study, we show that mesodermal lineage-induced embryoid bodies (EBs) generate greater numbers of osteogenic and chondrogenic lineage cells. To induce the mesodermal lineage, hESCs were treated with BMP4 and FGF2 during the EB state. Quantitative real-time reverse transcription-polymerase chain reaction analysis showed that the treatment decreased endodermal and ectodermal lineage gene expression and increased mesodermal lineage gene expression. Importantly, the mesodermal lineage-induced EBs underwent enhanced osteogenic and chondrogenic differentiation after differentiation induction. This method could be useful to enhance the osteogenic or chondrogenic differentiation of hESCs.

BENS139

Comparison of the Biomechanical Effects on Lumbar Spine between Pedicle-Based Composite and Rigid Rod Devices

Kyoung-Tak Kang, Heoung-Jae Chun, Hyung-Taek Hong
School of mechanical engineering, Yonsei University, Seoul, Korea

Abstract

In this study, comparison of the biomechanical characteristics of woven composite rod with rigid-rod lumbar fusion is introduced. Adjacent segment degeneration has been reported as the one of late serious complication after spinal fusion surgery. The immediate rigidity produced by instrumentation causes more stress leading to accelerated degeneration at adjacent levels. Posterior dynamic stabilization has been used to overcome the adjacent segment degeneration. Non-fusion technologies were adopted to reduce negative effects from arthrodesis. The popularity of non-fusion implants is based more on the lack of satisfaction with conventional spinal fusion rather than their proved superiority. Screw breakage can easily occur in posterior dynamic stabilization system, surgical technique without cage. However composite posterior dynamic stabilization has a good fatigue-failure characteristic. Finite element analysis was conducted to compare effects on the load-sharing properties of posterior dynamic stabilization device. Disc stress and range of motion of the woven composite rod model were similar to those of the intact spine, and the stress on the adjacent level was decreased in comparison with a fused spine. These results suggest that the use of the posterior dynamic stabilization devices can restore functionality similar to that of the intact spine and confirm that stiffness should be an important parameter in the design of dynamic stabilization devices.

Keywords: Finite element analysis, Pedicle screw, Woven Composite Rod

1. INTRODUCTION

Adjacent segment degeneration (ASD) has been reported as the one of late serious complication after spinal fusion surgery [1-3]. Presumably, the immediate rigidity produced by instrumentation causes more stress leading to accelerated degeneration at adjacent levels [2]. Many previous studies have been corroborated a trend toward earlier development of ASD with instrumentation as well. In contrast, posterior dynamic stabilization (PDS) has been used to overcome the adjacent segment degeneration, one of the serious complications after lumbar fusion. Non-fusion technologies have been developed with the goal of reducing the incidence of arthrodesis-related morbidity. Implant types include total disc replacements, prosthetic nuclear implants and posterior dynamic stabilization devices. Although implants offer some theoretical advantages over fusion, new potential problems such as mechanical failure, device migration, same level degeneration and implant subsidence are associated with new technologies. Furthermore, the efficacy of non-fusion implants in the prevention of adjacent level degeneration was not yet proved. The popularity of non-fusion implants is based more on the lack of satisfaction with conventional spinal fusion rather than their proved superiority. In addition, implants failure (17% of 24 patients) after a 2-years follow-up was found in one study [4]. The stress concentration was suspected to be the main cause of screw breakage [5]. Screw breakage can easily occur in PDS system, surgical technique without cage. However composite material has a good fatigue-failure characteristic. Thus it is appropriate for PDS material. Therefore, in this study, comparison of the biomechanical property of woven composite rod (WCR) with rigid-rod lumbar fusion was evaluated.

2. MATERIALS AND METHODS

2.1 Intact Model

A three-dimensional (3D) nonlinear FE model of the lumbar spine that consisted of four lumbar vertebrae, three intervertebral discs, and associated spinal ligaments was developed. Geometrical details of the human lumbar spine (L2-L5) were obtained from high-resolution computed tomography (CT) images of a 46-year-old male subject who had no spinal deformities. Digital CT data were imported to a software program (Mimics; Materialise Inc., Leuven, Belgium) that was used to generate the 3-dimensional geometrical surface of the lumbar spine. Exported IGES files from the Mimics software were input into Unigraphics NX 3.0 (Siemens PLM Software, Torrance, CA) to form solid models for each vertebral segment. The solid model was then imported into Hypermesh 8.0 (Altair Engineering, Inc., Troy, MI) to generate FE meshes. The FE method was analyzed with commercially available software (ABAQUS 6.6-1; Hibbitt, Karlsson and Sorenson, Inc., Providence, RI).

Three-dimensional homogenous and transversely isotropic solid elements were used to model the cortical and cancellous cores, the posterior bony parts of the vertebrae. The anterior longitudinal ligament, posterior longitudinal ligament, intertransverse ligament, ligament flavum, capsular ligament, interspinous ligament, and supraspinous ligament were modeled using tension-only truss elements

2.2 Material properties

Material properties were selected based on various literature sources (Table.1.)[6]. The cortical and cancellous regions of the vertebrae were modeled independently. Differentiation between cortical and trabecular bone in the posterior region was difficult to delineate; therefore, the posterior elements were all assigned a single set of material properties.

Table.1. Material properties in the present FE models.

Component	*Young's modulus (MPa)*	*Cross-section (mm^2)*	*Poisson's ratio*
Cortical bone	E_x = 11300 E_y = 11300 E_z = 22000 G_x = 3800 G_y = 5400 G_z = 5400		υ_{xy} = 0.484 υ_{xz} = 0.203 υ_{yz} = 0.203
Cancellous bone	E_x = 140 E_y = 140 E_z = 200 G_x = 48.3 G_y = 48.3 G_z = 48.3		υ_{xy} = 0.45 υ_{xz} = 0.315 υ_{yz} = 0.315
Posterior elements	3500		0.25
Disc Nucleus pulposus Annulus (ground substance) Annulus fiber	 1.0 4.2 358 – 550		 0.4999 0.45 0.30
Cartilaginous endplate	24.0		0.40
Ligaments			
Anterior longitudinal	7.8(<12%) 20(>12%)	63.7	
Posterior longitudinal	10(<11%) 20(>11%)	20.0	
Ligamentum flavum	15(<6.2%) 19.5(>6.2%)	40.0	

Capsular	7.5(<25%) 32.9(>25%)	30.0	
Interspinous	10(<14%) 11.6(>14%)	40.0	
Supraspinous	8.0 (<20%) 15(>20%)	30.0	
Intertransverse	10(<18%) 58.7(>18%)	1.8	
Fusion mass	3500		0.25
Pedicle screws, rod (Ti6Al4V)	110000		0.3

The annulus fibrosus was modeled as a composite of a solid matrix with embedded fibers (via the REBAR parameter) in concentric rings surrounding a nucleus pulposus, which was considered to be an incompressible inviscid fluid. Element members with hybrid formulation (C3D8H) combined with low elastic modulus and large Poisson ratio definitions were applied to simulate the nucleus pulposus. Eight-node brick elements were employed to model the matrix of the ground substance. Each of four concentric rings of ground substance contained two evenly spaced layers of annulus fibers oriented at ±30° to horizontal. The reinforcement structure annulus fibers were represented by truss elements with modified tension-only elasticity. In the radial direction, four double cross-linked fiber layers were defined, and those fibers were bounded by the annulus ground substance and both endplates. In addition, these fibers had proportionally decreased elastic strength from the outermost (550 MPa) to the innermost (358 MPa) layer [7].

The articulating facet joint surfaces were modeled using surface-to-surface contact elements in combination with the penalty algorithm with normal contact stiffness of 200 N/mm and a friction coefficient of zero. The thickness of the cartilage layer of the facet joint was assumed to be 0.2 mm. The initial gap between the cartilage layers was assumed to be 0.5 mm. The cartilage was assumed to be isotropic, linear elastic with a Young's modulus of 35 MPa and a Poisson's ratio of 0.4 [8]. Spinal ligaments were represented with nonlinear material properties. Naturally changing ligament stiffness (initially low stiffness at low strains, followed by increasing stiffness at higher strains) was simulated through a "hypoelastic" material designation (Table 1). Three-dimensional truss elements were used to simulate ligaments, which were active only in tension.

2.3 Implanted Model

The implanted models were constructed after modifying the intact model to simulate post-operative changes with these kinds of pedicle screw systems: one kind of WCR devices and a conventional rigid fixation system (Table.2). Since our models were designed to simulate the biomechanical behavior after healing, the bone–implant interface behavior was accomplished via the 'tie' contact condition, which enables the screw threads and vertebrae to be bonded together permanently by full constraint (Fig.1) .

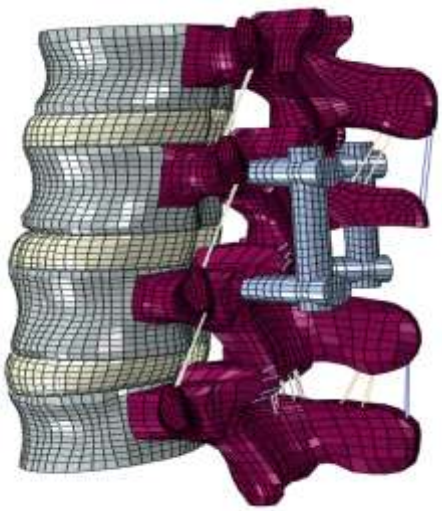

Fig.1. Implanted model current study.

Table.2. Material properties and design specification of longitudinal rod.

Implant Type	Diameter	Design	Elastic Modulus (Gpa)
Woven composite (Carbon/Epoxy)	5mm	Cylindrical	64
Ti -alloy	5mm	Cylindrical	114

To validate the model, the same loading conditions used in Yamamoto et al's study were applied [9]. Therefore, 10 Nm flexion, 10 Nm extension 10Nm torsion, and 10 Nm lateral bending moment under the 150 N preload were imposed on the L2 vertebral body, respectively. To reach 10 Nm moments, the five load steps were applied to models.

2.4 Loading and Boundary Conditions.

The loading and boundary condition was the hybrid testing protocol, which was implemented during the flexibility testing of the FE models as described by Goel et al [10] for the study of adjacent level biomechanics. The follower load technique was used to simulate the vector sum of trunk muscle co-activation by using a single internal force vector that acts tangent to the curvature of the spine passing through each segmental center of rotation. This "follower" path acts tangent to the curvature of the spine, thus mimicking the physiologic compressive loads on the lumbar spine seen in vivo. The 400 N compressive follower loads was simulated at each motion segment in the model by a pair of 2-node thermo-isotropic truss elements.

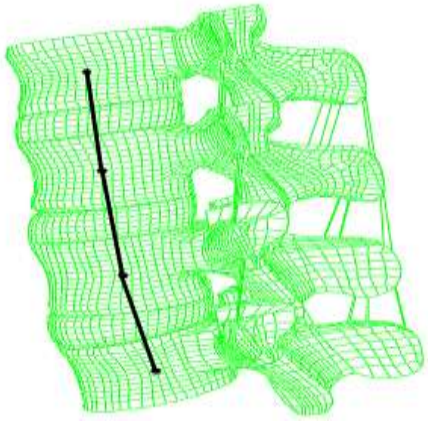

Fig.2. Lateral view of the finite element model showing follower load trusses at each level.

3 RESULTS

The intact *L3-L5* model was validated in our laboratory, as reported in our prior publications [2-3]. The increase of stress in the disc corresponding level was compared among the rigid fixation, the WCR and intact model. The rigid fixation had greater increase of stress in the disc at the *L3-L4* segment in flexion, extension, torsion and lateral bending than the fusion WCR model. The WCR demonstrated less increase of stress in the disc at the *L3-L4* segment than the rigid fixation, but greater increase was inspected in the intact model (Fig.3).

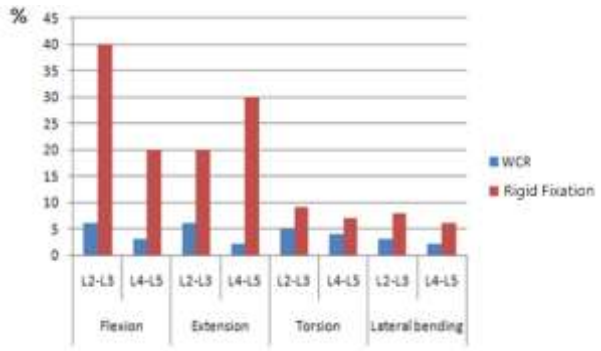

Fig.3. The comparison of the percent change of stress of the intervertebral disc at each corresponding segment in the two models.

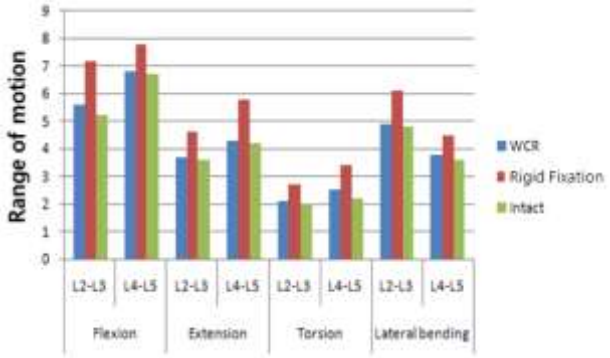

Fig.4. The comparison of the range of motion at each corresponding segment in three models (the intact vs. the WCR vs. the rigid fixation).

Under flexion moment, the largest difference of motion at the L2–3 segment (proximal adjacent segment) was observed between the rigid fixation model and the intact model (7.2^0 vs. 5.2^0), and the relatively distal adjacent segment (L4–L5 segment) was less influenced by fusion. In the WCR model, there was less increased motion (5.4^0) at the proximal adjacent segment (L2–3), compared to the rigid fixation model (7.2^0). The distal adjacent segment was less affected depending on the instrumentation in flexion moment than the proximal adjacent segment (Fig. 4) L3–4 fusion also produced increased motion at both adjacent segments under extension moment. Changes of adjacent segment motion in the rigid fixation model became more pronounced than in the WCR model. Proximal adjacent segment in the rigid fixation model had 4.6^0 of ROM while the corresponding segment in the WCR model had 3.8^0 of ROM. Furthermore, compared to flexion moment, difference of ROM in distal adjacent segments (L4–5) (1.5^0) between rigid fixation and WCR model had similar to the proximal adjacent segment (L2–3) (1.2^0). Similar patterns of changes of motion to flexion and extension moment were also shown under torsion (axial rotation) and lateral bending moment. L3–4 fusion (rigid fixation and WCR model) caused increased motion at both adjacent segments, and the changes became more prominent in the rigid fixation model than in the WCR model (Fig.4)

4. CONCLUSIONS

In conclusion, the ROM and disc stress of the WCR model were similar to those of the intact spine, and the stress on the adjacent level was decreased in comparison with a fused spine. These results suggest that the use of PDS devices can restore functionality similar to that of the intact spine and suggest that stiffness should be an important parameter in the design of dynamic stabilization devices. Although an FE model of the lumbar spine was used to verify the usefulness of the PDS device and to investigate its design parameters, this verified FE model with tuned parameter values can also be used for designing other types of spinal implants.

5. REFERENCES

[1] P. Park, H. Garton and V. Gala "Adjacent segment disease after lumbar or lumbosacral fusion: review of the literature". *Spine*, Vol. 29, pp 1938-4, 2004.

[2] K. Kang, H. Chun and J. Son "The Change of Biomechanical Milieu after Removal of Instrumentation in Lumbar Arthrodesis Stiffness of Fusion Mass: Finite Element Analysis". *The KSME annual fall conference*, Jeju, Vol. 1 pp. 664-667, 2008.

[3] H. Kim, H. Chun and K. Kang "A validated finite element analysis of nerve root stress in degenerative lumbar scoliosis", *Med Biol Eng Comput*, Vol. 47, pp. 599–605, 2009.

[4] K. Schnake, S. Schaeren and B. Jeanneret "Dynamic stabilization in addition to decompression for lumbar spinal stenosis with degenerative spondylolisthesis", *Spine,* Vol. 31, pp. 442–449, 2006

[5] J. Cotler and A. Star *"Complications of spine fusions"* 1st Edition, Springer-Verlag, 1990.

[6] V. Goel, Y. Kim and T. Lim, "An analytical investigation of the mechanics of spinal instrumentation". *Spine* Vol. 13, pp. 1003-1011, 1988.

[7] A. Polikeit, S. Ferguson and L. Nolte, "Factors influencing stresses in the lumbar spine after the insertion of intervertebral cages: finite element analysis". *European Spine Journal*, Vol.12, pp. 413-420, 2003.

[8] H. Schmidt, F. Galbusera and A. Rohlmann, "Effect of multilevel lumbar disc arthroplasty on spine kinematics and facet joint loads in flexion and extension: a finite element analysis". *European Spine Journal* , Accepted, 2010.

[9] I. Yamamoto, M. Panjabi and T. Crisco "Three-dimensional movements of the whole lumbar spine and lumbosacral joint" *Spine* Vol. 14, pp. 1256–1260, 1989.

[10]V. Goel, J. Grauer and T. Patel "Effects of charité artificial disc on the implanted and adjacent spinal segments mechanics using a hybrid testing protocol". *Spine* Vol. 30, pp. 2755-2764, 2005.

Civil Engineering

Pullman Bangkok King Power, 2F

2013/1/26 Saturday 14:00-16:00

BENS182

Estimation of Route Travel Time Using Collected Bus data

Young-Woo Lee｜*Daegu University*

BENS182

Estimation of Route Travel Time Using Collected Bus data

Young-Woo Lee
Civil Engineering, Deagu University, Jillyang, Gyeongsan, Gyeongbuk 712-714 S. Korea
E-mail address: yw209@daegu.ac.kr

ABSTRACT

Recently the demands for traffic information tend to increase, and travel time might one of the most important traffic informtion. To effectively estimate exact travel time, highly reliable traffic data collection is required. Bus Information System (hereafter called BIS) data would be useful for the estimation of the route travel time because BIS is collecting data for the bus travel time on the main road of the city on real-time basis. Traditionally use of BIS data has been limited to the realm of bus operating but it has not been used for a variety of traffic categories. Therefore, this study estimates a route travel time on road networks in urban areas on the basis of real-time data of BIS and then eventually constructs regression models. These models use an explanatory variable that corresponds to bus travel time excluding service time at the bus stop. The results show that the coefficient of determination for the constructed regression model is more than 0.950. As a result of T-test performance with assistance from collected data and estimated model values, it is likely that the model is statistically significant with a confidence level of 95%. It is generally found that the estimation for the exact travel time on real-time basis is plausible if the BIS data is used.

Keywords: Route travel time, BIS, Regression model

Engineering B

Pullman Bangkok King Power, 2F

2013/1/27 Sunday 10:00-12:00

E263

Optimum Cutting Condition Decision System for Ultra Precision Machining

Hyun Chul Kim｜*Inje University*

E277

Thermal Performance Tests and Modeling of Tubular Evaporative Condensers of Water Chillers

Liang Han Chien｜*National Taipei University of Technology*

E289

Numerical Simulation of Temperature Profiles of a Two-Layer Sample during Irradiation

Darya Alontseva｜*East Kazakhstan State Technical University*

E259

Non-Dendritic A356 Al alloys Synthesized via Cooling Slope Technique

Yao-tin Chen｜*National Cheng Kung University*

Chi-Yuan Albert Tsao｜*National Cheng Kung University*

Chun-Hsien Chiang｜*National Cheng Kung University*

E263

Optimum cutting condition decision system for ultra precision machining

Thanh-Hung Duong
Department of Mechanical Engineering, Inje University, Gimhae, Korea
duongthanhhung86@gmail.com

Hyun-Chul Kim
High Safety Vehicle Core Technology Research Center, Department of Mechanical & Automotive Engineering, Inje University, Gimhae, Korea
mechkhc@inje.ac.kr

The corresponding author: Hyun-Chul Kim

Abstract

In ultra-precision machining for micro pattern, the deformation occurs with high frequency. High aspect ratio, high cutting speed, high feed rate, etc… all lead to deformation. This paper presents a theoretical prediction model for optimization of feed rate in manufacturing the micro rectangular pattern. The model contains cutting force prediction and deformation forecasting. To forecast deformation phenomenon, the rectangular pattern was considered as a cantilever beam with a distributed load, and then the maximum principle stress which acts on micro rectangular pattern can be determined. Furthermore, for verifying this solution, several experiments have been carried out to have rectangular pattern by single point diamond turning. The maximum different between the prediction cutting force and experimental cutting force was approximately 0.01N and the maximum error is 10%. The optimum feed rate prediction model was applied for 2 difference cutting speed 150rpm and 300rpm.

Keyword: Ultra-precision machining, Micro channel, Machining process, Deformation, Diamond machining

1. Introduction

Liquid crystal displays (LCDs) are one of the major products of flat panel displays, and have a wide range of applications. The current product trend of an LCD is lightweight, low-power consumption, high brightness, and low cost. A typical edge-type BLU [1] includes a light source, a wedge-shaped light guide plate (LGP) and light-scattering dots or pattern [2-4], a diffusion film for scattering light, and some prism sheets for condensing light. The surfaces of these optical elements are not flat; they have micro patterns. The use of high aspect ratio grooves would reduce the number of sheet and enhance light efficiency, but for a given cutting parameters, there is the limit to the achievable aspect ratio due to deformation phenomenon. Due to its fragile nature, the way for increasing aspect ratio causes the instability of machining processing such as deformation or fracture of pattern and cutting tool [5,6].

Until now, the most common method which is used to manufacture the optical elements with micro pattern is ultra precision diamond turning. For this kind of machining process, the cutting conditions play an important role in the efficient use of a machine tool. Because of the high cost of numerically controlled machines, compared with their conventional counterparts, there is an economic need to operation these machines as efficiently as possible in order to obtain the required payback. The cutting conditions determine not only the cost of turning on these machines but also the maximum achievable aspect ratio of micro pattern. So the optimum values of cutting condition have to be determined before a part is put into production.

This study presents a developed Matlab program, an optimization system for avoiding the deformation of rectangular patterns in machining and for minimization of machining time. The cutting force, the permissible bending stress and deflections of the rectangular pattern are main constraints in the developed program. A theoretical solution for predicting cutting force and forecasting the deformation phenomenon of micro rectangular patterns with high aspect ratio have been built; subsequently, optimum cutting conditions, which are cutting speed and feed rate, can be predicted in ultra precision diamond turning.

2. Optimum cutting condition

2.1 Cutting force analysis

In ultra precision turning, cutting force is one of the main factors which lead to deform. Normally, cutting force vector of turning process is composed of three components: cutting force, thrust force and radial force.

In orthogonal cutting, for an uncut chip with height h and width b, the cutting force can be estimated as the following equation:

$$\vec{F}_{ortho} = \begin{bmatrix} F_c \\ F_t \end{bmatrix} = \begin{bmatrix} \dfrac{\cos(\beta - \gamma_o)}{\cos(\phi_o + \beta - \gamma_o)} \\ \dfrac{\sin(\beta - \gamma_o)}{\cos(\phi_o + \beta - \gamma_o)} \end{bmatrix} \frac{\tau_s bh}{\sin(\phi_o)} \qquad (1)$$

The friction coefficient □ and shear stress □s are unknown, and only determined by using experiment data. They are considered as experimental constants and are determined for the purpose of minimizing the error between the measurement cutting force and the prediction cutting force. In our experiment, the minimum depth of cut is 2 um, the noise radius of diamond cutting tool is relatively smaller than 1 um, hence, there is no side effect and the rake angle □o is considered as zero. The shear angle □□ □ is determined by using Ernst-Merchant's prediction model:

$$\phi_o = 45 - 0.5(\beta - \gamma_o) \qquad (2)$$

However, this model neglected the radial force, and considers that it equals zero. Therefore, an idea has been come out, dividing solution. The cross-section of uncut chip will be divided into several parts; each part will be applied the Merchant's theory to determined the local cutting force and local thrust force; and the total cutting force will be determined by combining these local forces.

There are many ways to divide the rectangular uncut chip. Because the cutting is done by 3 tool edges, the dividing way as shown in Fig 1, three pieces linearly dividing, is chosen for using in calculation of this paper. The study on the effective and different of the dividing methods will be discussed in future.

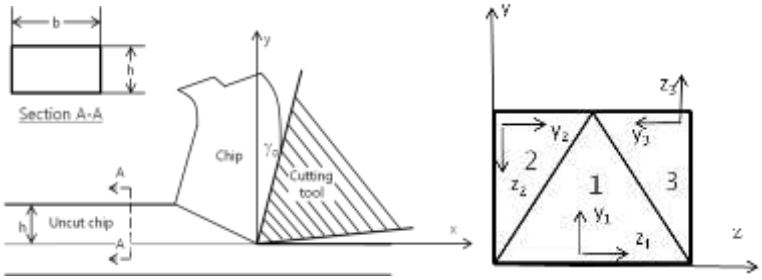

Fig. 1: Cross section of divided uncut chip

Piece number 1 is calculated in coordinate axes $x_1y_1z_1$, piece number 2 is calculated in $x_2y_2z_2$ and similarly, $x_3y_3z_3$ is applied to calculated cutting force on piece number 3.
By following these rules, the total cutting force F_{total} can be expressed as :

$$\vec{F}_{total} = \vec{F}_1 + \vec{F}_2 + \vec{F}_3 = \begin{bmatrix} F_{1c} \\ -F_{1t} \\ 0 \end{bmatrix} + \begin{bmatrix} F_{2c} \\ 0 \\ -F_{2t} \end{bmatrix} + \begin{bmatrix} F_{3c} \\ 0 \\ F_{3t} \end{bmatrix} = \begin{bmatrix} F_{1c} + F_{2c} + F_{3c} \\ -F_{1t} \\ -F_{2t} + F_{3t} \end{bmatrix} \quad (3)$$

In addition, the dividing method is symmetric; hence the part number 2 and part number 3 have the same area, so

$$\vec{F}_{total} = \begin{bmatrix} F_{ct} \\ F_{tt} \\ F_{rt} \end{bmatrix} = \begin{bmatrix} F_{1c} + 2F_{2c} \\ -F_{1t} \\ 0 \end{bmatrix} = \begin{bmatrix} \dfrac{\cos(\beta - \gamma_o)}{\cos(\phi_o + \beta - \gamma_o)} \\ \dfrac{\sin(\beta - \gamma_o)}{2\cos(\phi_o + \beta - \gamma_o)} \\ 0 \end{bmatrix} \dfrac{\tau_s bh}{\sin(\phi_o)} \quad (4)$$

In the end, we obtain the same cutting force as the conventional orthogonal cutting estimation, the thrust force reduces half of it and the radial force still equals zero. However, with the dividing solution, the force which acts on the side face of groove can be estimated and its amplitude equals the thrust force F_{2t} or F_{3t}.

2.2 Deformation analysis

In ultra precision machining, there are several reasons for the deformation occurrence. In this work, the radial cutting force, F_r, one of three cutting force components is considered as a main cause. It creates a normal stress on side face of micro pattern. We call this stress side stress. Depending on the large of this stress, micro pattern can be deformed elastically or plastically. For the sake of simplicity, in this paper, we will neglect the impacts of chip flows, and only concentrate on the impact of the radial force component on the side of the micro pattern.

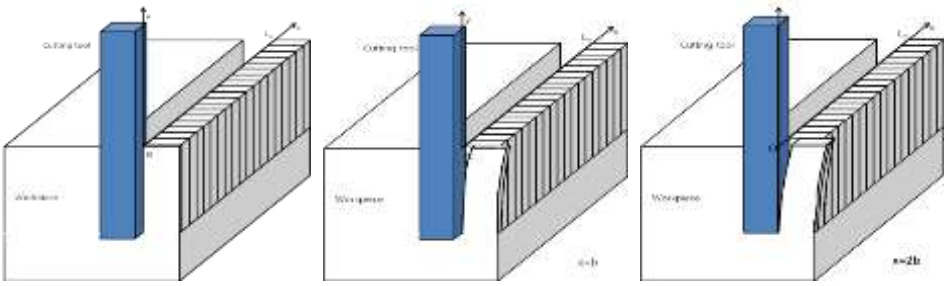

(a) (b) (c)

Fig. 2: The modeling of the deformation of a micro pattern

For modeling, we considered that the micro channel consists of many rectangular thin plates, as shown in Fig.2. All plates have the same dimensions: height L, width h and thickness b. During the machining process of cutting step i, the cutting tool edge moves along the X-axis, from 0 to L_w. In case where the deformation occurs, it grows along the micro channel, as shown in Fig. 2. At position of cutting edge x=b, the first thin plate is deformed with maximum deflection $\square_i$. When cutting edge moves to position 2b, the second thin plate is also deformed. And the same thing happens to the other plates. For the sake of simplicity, we assumed that there is no interaction between these plates, they are deformed separately. The study on the deformation with interaction between these plates will be discussed in future. Moreover, because all thin plates have the same dimension and the cutting force is constant in one cutting step, the maximum deflection of deformation plate will be the same value. Hence, the maximum deflection of a thin plate equals the maximum deflection of the micro pattern.

When compared to the width and the thickness of a thin plate, normally, its height is significantly larger. Plus, the radial force is perpendicular to the thin plate. In case where deformation occurs, the bottom of a thin plate is laterally and rotationally fixed, and the top of a thin plate is free to move along the Z-axis. All this characteristics are similar to the features of a cantilever beam. By rotating 90^o, we can consider the thin plate as a cantilever beam, as shown in Fig.3. In addition, the radial forces F_r can be considered as the distributed load $\square\square$

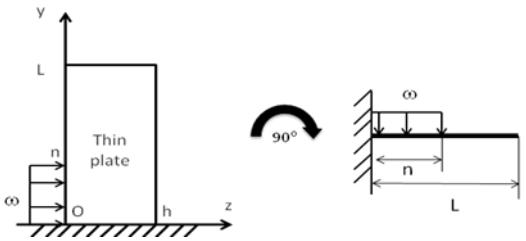

Fig. 3: The uniform distributed load on the cantilever beam

As we considered in cutting force analysis, in all cutting force component, there is local thrust force of piece number 3 which acts on the side wall, thus, to calculate the stress which acts on the micro pattern, the thrust force, F_{3t}, component of piece number 3 is used. This force is converted to a uniform distributed load □, by the following expression:

$$\omega = \frac{F_{3t}}{n} \qquad (5)$$

With distributed load □, the maximum stress σ_{max} on the micro pattern can be calculated as the following equation:

$$\sigma_{max} = \frac{3\omega\left(\frac{n}{h}\right)^2}{b} \qquad (6)$$

In the other hand, the yield strength σ_y of workpiece material is very important in predicting process. It not only is used to determine the type of deformation but also is used in deformation calculation. Normally, for popular materials such as copper, steel, aluminum, its yield strength can be found in many books or researches without any difficulty. However, because of size effect, the yield strength may not be the same as the value in these books. Due to the development rapidly of material industry, many new materials have been created, and, of course, its yield strength cannot be found in any books. In this study, for acquiring yield strength with accuracy, the micro-indentation hardness test was carried out.

2.3 Optimization and Matlab program

The flow diagram for determining the maximum feed rate is shown in Fig 4. The maximum side stress is considered as a main factor to decide. The current feed rate will be increased until the maximum side stress go beyond the yield strength of workpiece.

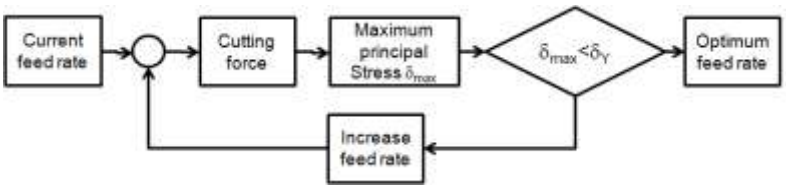

Fig. 4: Flow diagram for optimum feedrate

3. Experiment and discussion

To validate the theoretical analysis in this paper, the cutting forces and the deformation of micro pattern has been measured. Machining conditions are shown in the table 1. The experiment for this study was conducted by machine tool Nanotech HDL 1800. The roll mold is made of steel with copper coated.

Table 1.Machining condition

Parameter	Description
Machine tool	Nanotech HDL 1800
Cutting tool	W50□m, H205□□m, A0° Diamond tool
Workpiece	Copper coated steel, lathe □150 mm
Cutting speed	150,300 rpm

In our experiments, the cutting speeds are 150 and 300 rpm and feed rates were different from 0.15mm/min to 1.65mm/min. The cutting forces are measured by a dynamometer of Kistler and data are transfer to computer through a DAQ card and LabView. For each combination of feed rate's values and cutting speed's values, five micro rectangular pattern were machined. In the end of each cutting step, the SEM images of rectangular patterns are taken. From above analysis, a Matlab program has been built to support the prediction of cutting force and proposing cutting conditions.
The experiments are separated into 2 groups: one for building the model and the other for verifying the prediction. The micro pattern's shapes of each experimental group are shown in the fig. 5.

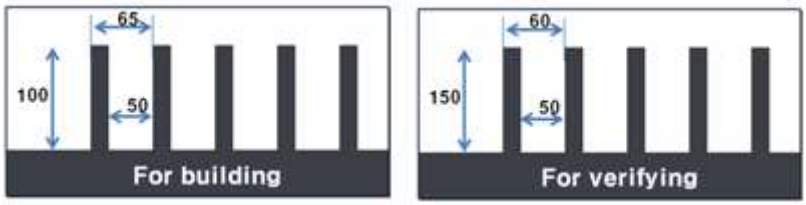

Fig. 5: The rectangular pattern's shapes for building (left) and verifying (right)

The cutting force predicted by the developed model was compared to the experimental data from the second experimental groups. The maximum different between experiment and prediction is 0.01N. The percentage errors between measurement and prediction are also relatively small, from 2% to 10%. Furthermore, except to the feed rate 0.15mm/min and 0.4mm/min, the rest of errors of cutting force prediction are smaller than 3%. With these result, it was proved that the cutting force prediction model for rectangular pattern worked well.

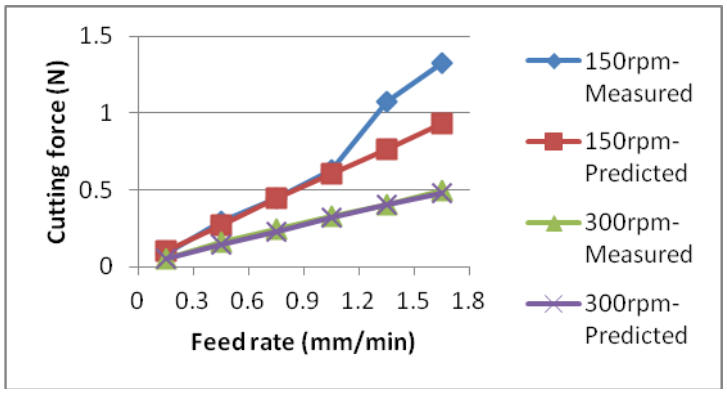

Fig 6: Cutting force model developed from experimental data of micro pattern.

By applying the current cutting conditions, it predicted the maximum feed rate is 0.7mm/min for 150 rpm and 1.35mm/min for 300rpm. For 150rpm case, the deformation has started with the feed rate between 0.6 and 0.8 mm/min, and for 300rpm case, it's started with the feed rate between 1.4 and 1.6 mm/min. It means the prediction was correct for 150 rpm case but not for 300rpm case. In spite of the forecasting was wrong for the case 300rpm, the prediction value is still smaller than the real value, that means it's an acceptable value for manufacturing.

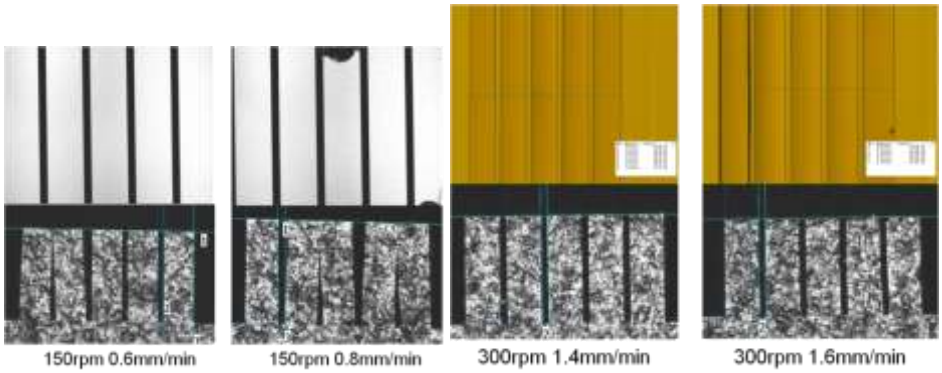

Fig. 7: Verification for deformation prediction

4. Conclusion

This study presented a cutting force prediction method and a machining condition proposal in term of deformation. This proposal reduces machining time effectively.

The maximum difference between cutting force prediction and cutting force measurement is 0.01N, plus, almost the percentage errors are around 2-3%. It means that the method agrees with the real data.

The cutting force prediction and deformation analysis are used to proposal the optimum feed rate for given cutting parameters. It predicted correctly for 150 rpm case but not accuracy for 300rpm case. However, both proposal cutting conditions are machining-applicable and more efficiency than the current cutting conditions.

In this paper, only rectangular shape is applied, but this solution shows its potential to be used with the others shape such as triangle, trapezoid etc.

5. Acknowledgement

This research was supported by Basic Science Research Program through the National Research Foundation of Korea (**NRF**) funded by the Ministry of Education, Science and Technology (2012R1A1B4001609), and also financially supported by the Ministry of Knowledge Economy(MKE), Korea Institute for Advancement of Technology(KIAT) and Southeast Area Leading Industry Office through the Leading Industry Development for Economic Region.

6. References

[1] Alting, L., Kimura, F., Hansen, H.N., Bissacco, G., 2003, "Micro engineering," CIRP Annals - Manufacturing Technology, Vol. 52, pp. 635-657, 2003.

[2] Malek, C.K, Saile, V., "Applications of LIGA technology to precision manufacturing of high-aspect-ratio micro-components and -systems: a review," Microelectronics Journal, Vol. 35, pp. 131–143, 2004.

[3] Park, H.K, Onikura, H., Ohnishi, O., Sharifuddin, A., "Development of micro-diamond tools through electroless composite plating and investigation into micro-machining characteristics," Precision Engineering, Vol. 34, pp. 376–386, 2010.

[4] Gabler, J., Pleger, S., "Precision and micro CVD diamond-coated grinding tools," International Journal of Machine Tools & Manufacture, Vol.50, pp. 420–424, 2010.

[5] Je, T.J., Lee, K.W., Park, S.C., Kim, J.G., Choi, D.S., Park, K.T., Whang, K.H., "Influence of tool deflection on micro channel pattern of 6:4 brass with rectangular tool," Transactions of nonferrous metals society of China, Vol. 19, pp. 164-170, 2009.

[6] Takeuchi, Y., Suzukawa, H., Kawai, T., Sakaida, Y., "Creation of ultra-precision microstructures with high aspect ratios," CIRP Annals - Manufacturing Technology, Vol. 55, pp. 107-110, 2006.

E277

Thermal Performance Tests and Modeling of Tubular Evaporative Condensers of Water Chillers

Liang-Han Chien
National Taipei University, Department of Energy and Refrigerating Air-conditioning Engineering
No. 1, Sec. 3, Chung-Hsiao E. Rd., Taipei 10608, TAIWAN,
Email: lhchien@ntut.edu.tw

Chien-Yeh HSU
National Taiwan University, Department of Mechanical Engineering
No. 1, Sec. 4, Roosevelt Rd., Taipei 10617, TAIWAN,
Email:crane12_24@hotmail.com

The corresponding author: Liang-Han Chien

Abstract

In this manuscript, an analytical thermal performance model of the evaporative condenser is presented. A computer program of chiller performance was established based on this model. The program was verified by experimental data of a 33 kW chiller equipped with an evaporative condenser and two compressors. The system COP_s (= cooling capacity/total power consumption), accounting for the power consumed by the fan and the pump in the condenser, of the evaporative cooled chiller are 4.12 and 4.27 at full load and half load, respectively. The evaporative condenser yields 47.7% greater COP_s as compared with the COP_s of an air-cooled chiller (2.79) in the Chinese National standard. The discrepancy between the test data and simulation results are less than ± 8%. The predictions of the present model show that the air flow rate has more significant influence on COP than water flow rate. The COP increased from 3.8 to 5.1 as the air flow rate increased from 0.39 to 1.28 kg/s.

Keyword: Engineering, Air-conditioning, Water chiller, Evaporation, Condenser

1. Introduction

The evaporative condenser is a highly efficient method of heat rejection involving latent heat of vaporizing water. Water is sprayed on the heat exchanger surface directly and heat is rejected by evaporation of the water in contact with the heat exchanger. As compared with an air-cooled chiller, the power consumption of the compressor of an evaporative cooled chiller is reduced at a reduced condensing temperature. The required air flow rate and fan power of evaporative condenser are smaller than an air-cooled unit for the same condensing capacity because heat transfer to air is in both sensible and latent forms. The COP of evaporative of an evaporative cooled unit is significantly greater than an air-cooled one because of the reduced power consumption of the compressor and the fan. Evaporative condensers are widely used in large units of air conditioner. In the present project, a 10 RT water chiller, having evaporative condenser and two parallel connected scroll type compressors, has been developed, and a computer program of chiller performance was

completed.

2. Experiment and Prediction Model

2.1 Evaporative cooled chiller facility

The evaporative cooled chiller is shown in Fig. 1. The main components of the prototype are: two scroll type compressors, a brazed plate type evaporator, and an evaporative condenser. Micro-fin tubes with outside diameter of 9.52mm are used in the condenser. The tube arrangement of the condenser is shown in Fig. 1. The cooling air temperature, relative humidity, and velocity were measured at the inlet and exit. The flow rate, inlet and outlet temperature of chilled water were measured to calculate the cooling capacity. The temperature distribution on the tube surface of circulating cooling water was measured by thermocouples as shown in Fig. 1. The refrigerant temperature distribution was measure by the thermocouples on tube wall temperature with a layer of 5 mm thick, 20 mm width insulation surrounding the tube. Power consumptions of the compressor and the entire system were measured separately with two power meters. Tests were conducted at 35^{o}C dry ball and 24^{o}C temperatures with 0.98 kg/s air flow and 120 LPM water flow rate. The cooling capacity at full load and half load are 33.07 kW and 18.23 kW, respectively. The system COP_s (= cooling capacity/total power consumption, accounting for the power consumed by the fan and the pump in the condenser) are 4.12 and 4.27 at full load and half load, respectively.

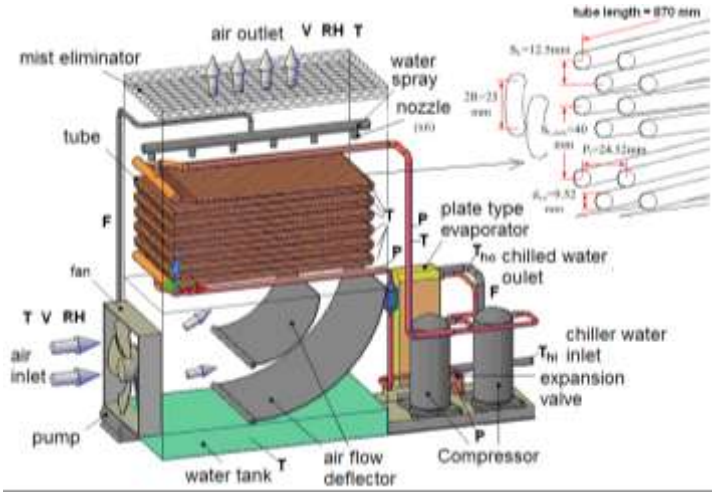

Fig.1 the evaporative cooled water chiller.

2.2 Prediction of chiller with evaporative condenser

(1)Evaporative condenser model

A computer program was developed to predict the performance of the evaporative cooled chiller in Fig. 1. In the evaporative condenser, refrigerant is cooled and condensed in the tube. Water

evaporated on the tube surface into the air passing the tube bundle (Fig. 2). The assumptions in the present model are: 1. steady state, 2. no heat loss to the environment, 3. negligible water loss by splashing, 4. negligible thermal radiation, 5. constant heat-mass transfer coefficient, 6. uniformly wet tube outer surface, 7. negligible temperature variation across the water film.

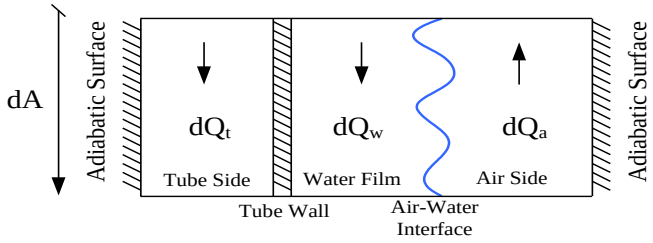

Fig.2 Heat transfer model of a tubular evaporative condenser

The heat transfer process of a segment of the condenser tube is shown in Fig. 2(b). The energy balance of a segment of the condenser tube is given by Eq. (1).

$$dQ_t + dQ_w + dQ_a = 0 \quad (1)$$

The heat transferred into the refrigerant is: $dQ_t = \dot{m}_r di_r$, where i_r is the enthalpy of refrigerant. The energy change of the cooling air is: $dQ_a = -\dot{m}_a di_a$. The energy change of the water film (dQ_w) on the tube wall includes latent heat and sensible heat, and is given by Eq. (2), where $C_{p,w}$ is the heat capacity of water, and $i_{f,w}$ is water liquid enthalpy.

$$dQ_w = d\dot{m}_w i_{f,w} = \dot{m}_w di_{f,w} + i_{f,w} d\dot{m}_w \approx \dot{m}_w C_{p,w} dT_w + i_{f,w} d\dot{m}_w \quad (2)$$

Heat transfer analysis of the refrigerant flows through the tube wall to the water film on the tube surface gives Eq. (3), where U_o is the overall heat transfer coefficient. T_r and T_w are the refrigerant and water temperatures, respectively.

$$\dot{m}_r di_r = -U_o (T_r - T_w) dA \quad (3)$$

Consider the mass balance of evaporated water vapor into the air stream, the energy change of air stream is given by Eq. (4), where K_m is the mass transfer coefficient, Le_f is the Lewis factor, $C_{p,a}$ is the specific heat constant of air, $i_{g,w}$ is water vapor enthalpy. The w_a and $w_{a,int}$ are the specific humidity of the air stream and at the air-water interface, respectively.

$$-\dot{m}_a di_a = Le_f C_{p,a} K_m (T_{a,\text{int}} - T_a) dA + K_m (w_{a,\text{int}} - w_a) i_{g,w} dA - K_m (w_{a,\text{int}} - w_a) i_{f,w} dA \quad (4)$$

As the water evaporated and mixed into the air stream, the mass change of water film and air stream is given by Eq. (5).

$$\dot{m}_a dw_a = d\dot{m}_w = -K_m (w_{a,\text{int}} - w_a) dA \quad (5)$$

Substituting Eq. (5) into Eq. (4) and replacing $i_{f,w}$ by $C_{p,w}T_w$, one obtains Eq. (6).

$$\frac{dT_w}{dA} = -\frac{K_m}{\dot{m}_w C_{p,w}}\left\{\left(i_{a,\text{int}} - i_a\right) + \left(Le_f - 1\right)\left[\left(i_{a,\text{int}} - i_a\right) - \left(w_{a,\text{int}} - w_a\right) i_{g,w}\right]\right\} + U_o\left(T_r - T_w\right) \quad (6)$$

The overall heat transfer coefficient of the refrigerant flows through the tube wall to the water film on the tube surface can be calculated by Eq. (7), where h_i and h_{film} are the heat transfer coefficients of tube side and water film, respectively. The R_{int} is the conduction resistance of water film, and it is neglected by assuming constant water film temperature across the water film.

$$UA = \left[\frac{1}{h_i A_i} + \frac{\ln\left(d_{t,out}/d_{t,in}\right)}{2\pi k_t L} + \frac{1}{h_{film} A_o} + R_{\text{int}}\right]^{-1} \quad (7)$$

For condensation section, Shah correlation is used for predicting condensation heat transfer coefficient of smooth tube. Calvallini [1] and Han and Lee [2] are used for condensation in micor-fin tubes. The prediction with the Calvalini [1] correlation for condensation yields reasonable well agreement with the experimental result. For either 44.3 kg/m^{2}s (half load) or 83.5 kg/m^{2}s (full load), the micro-fin tube yielded about 130% condensation heat transfer enhancement over the smooth tube.

The refrigerant enters the condenser as superheat vapor, and leaves as subcooled liquid. It is modeled as three sections: 1- superheated vapor section, 2-condensing section, and 3-subcooled liquid section. Correlations of single phase convections are used for the first and third sections. For smooth tubes, the Dittus Boelter correlation is used to calculate single (liquid or vapor) phase internal convection. For tubes having internal micro-fins, the water-side heat transfer coefficient (h_i) is calculated using the Carnovo's correlation. For condensation section, Shah [3] correlation is used for predicting condensation heat transfer coefficient of smooth tube. Calvallini [1] and Han and Lee [2] are used for condensation in micor-fin tubes.

Previous work on evaporative cooling of plain tubes includes experimental test and thermal analysis. Empirical correlations of heat-mass transfer of evaporative water-air flow and heat transfer of water film on tube surface were provided [4-7]. Heyns and Kroger [7] derived correlations of falling water film convection coefficient and the air-water mass transfer coefficient, for 0.7 <G_a < 2.6 kg/m^{2}s, and 1.8 < G_w < 4.7 kg/m^{2}s. Comparing the predictions by these methods, the Heyns and Kroger [7] correlation showed the most reasonable agreement with the present tests.

(2) Evaporator correlation

For the heat transfer and pressure drop calculation of evaporator, the correlations developed by Lin [8] are used in the present model.

(3) Correlations of compressors and fans

In the present model, the refrigerant flow rate and compressor power consumption were correlated

as function of given evaporator and condenser pressures. These correlations agree with the tabulated compressor performance data provided by the vendor (uncertainty < ±2%). The tube bundle pressure drop has been tested with various air flow rate, and compared with the fan curves from vendor.

3. Results

3.1 Comparisons of prediction and experiment

In this study, the discrepancy between the test data and simulation results are shown in Fig. 3. The given conditions in the predictions are: air flow rate = 0.98 kg/s, water flow rate 120 LPM, isentropic efficiency of the compressor = 70%, 5.56°C superheat at the evaporator exit, 1.5°C subcooling at the condenser exit.

As shown in Fig. 3, the cooling capacity of the chiller is predicted with ± 5% and ± 8% maximum discrepancy at full load and half load, respectively. The cooling capacity decreases with increasing wet ball temperature (Fig. 3). The system COP_s at half load, ranging from 3.97 to 4.27, is about 30% greater than that at full load (COP_s = 3.57~4.12). This is because that the sizes of condenser and evaporator do not change while the heat transfer rate reduced by an half. The increase of A/Q ratio results in an increase of heat exchanger effectiveness, and this in turn results in an increase of chiller COP_s as the operation shift from full load to half load.

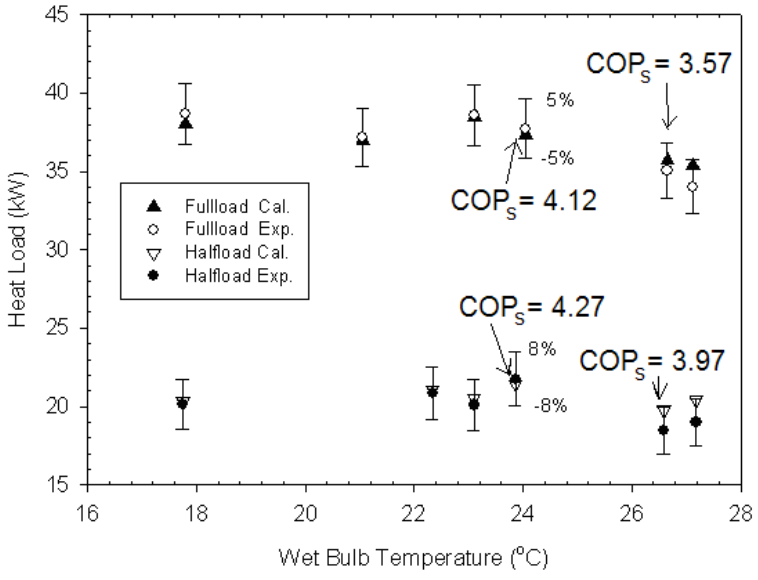

Fig.3 Comparison of prediction and experiment on heat transfer rate of the chiller

Empirical correlations of heat and mass transfer coefficient are determined by comparing the tests results with the calculation of several correlations. Fig. 5 shows the predicted and measured temperature distribution of refrigerant, tube wall and water film from the inlet to the outlet of the

condenser. The calculated refrigerant temperature is similar to the temperature measured by the thermocouples attached on tube wall with a layer of insulation surrounding the tube. The measured water temperature is about 0.6^{o}C higher than the predicted value, because the temperature variation across the water film has been ignored.

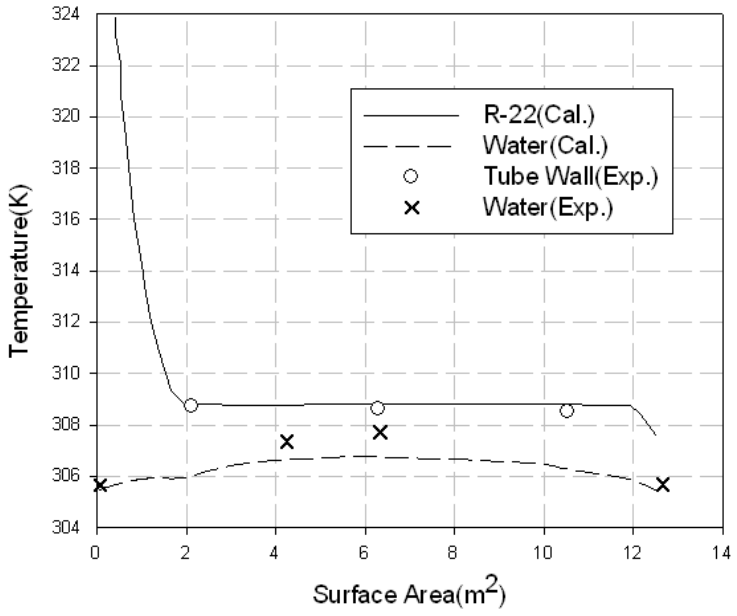

Fig. 4 Predicted and measured temperatures of the condenser

3.2 Parametric study on chiller performance

Parametric study on the effects of the circulating flow rate of cooling water and air flow rate have been conducted with the computer code based on the present thermal performance model of the chiller. Fig. 5 shows the COP (excluding the power consumed by the fan and the pump of the condenser) and sensible heat transfer coefficient (h_{sens}) variation with cooling water flow rate. The air flow rate has more significant influence on COP than water flow rate. The water flow rate has negligible influence on the COP in the range of 0.7~2.3 kg/s (G_w = 1.6~4.6 kg/m^{2}s). This is because the pumping power decreases with decreasing flow rate. This offsets the influence of the decreased heat transfer coefficient at a reduced water flow. The COP increased from 3.8 to 5.1 as the air flow rate increased from 0.39 to 1.28 kg/s.

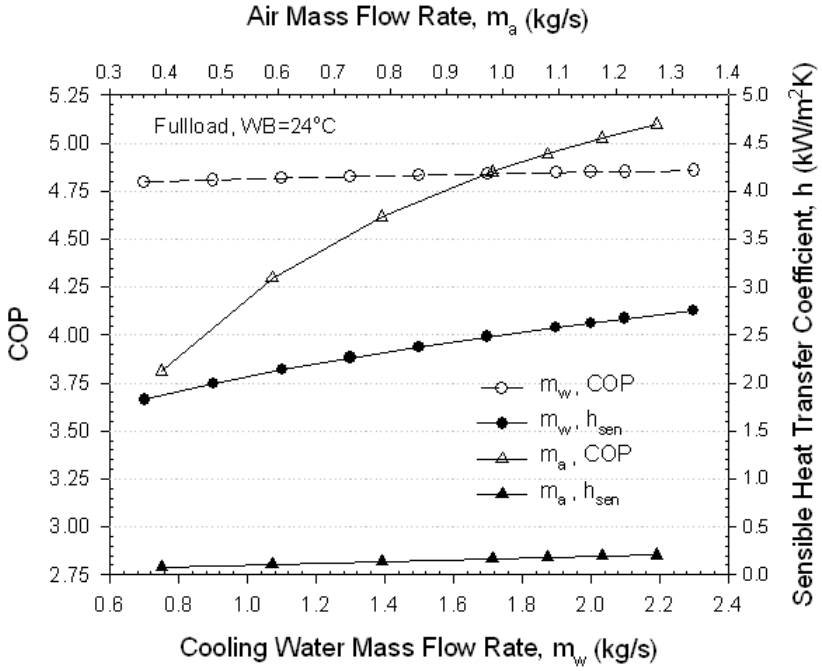

Fig.5 Effects of flow rates of air and water

Several designs predicted by the present model. For a fixed cross-sectional area of condenser using the same type of blower, the air flow rate decreases with the increase of the number of tube rows because the system impedance increases. The refrigerant flow rate also decreases as the total cross-sectional area increases with increasing number of tubes per pass. Therefore, the improvement of overall COP due to the increment of heat transfer area is not as significant as expected. When the outside air wet bulb temperature is 24 ℃ and the heat transfer area increases from 8.9 to 14.8m^2(original), the COP increases from 4.7 to 4.87. By reducing the number of tubes, a cost reduced design results in a reduction of COP by less than 1%.

4. Conclusion

A thermal performance model of evaporative cooled chiller has been developed. It predicts the system COP_s (= cooling capacity/total power consumption including fan and pump) with less than ± 8% uncertainty. At 24^{o}C wet ball temperature and 35^{o}C dry ball temperature, the system COP_s of the evaporative cooled chiller are 4.12 and 4.27 at full load and half load, respectively. It yields 47.7% greater COP_s as compared with the COP_s of an air-cooled chiller (2.79) in Chinese National standard. The present model shows that the air flow rate has more significant influence on COP than water flow rate. The COP increased from 3.8 to 5.1 as the air flow rate increased from 0.39 to 1.28 kg/s.

5. Acknowledgments

We are thankful for the supported of I-Min Engineering Co., and National Science Council of

Taiwan (Project no.: NSC-99-2622-E-027-027-CC3, NSC-100-2622-E- 027-016-CC3).

6. References

[1] Cavallini A., Censi G., Del-Col D., Doretti L., Longo G.A., Rossetto L., Zilio C., “Condensation inside and outside smooth and enhanced tubes — a review of recent research”, Int. J. of refrigeration, 26 (2003).

[2] Han D., Lee K.J., “Experimental study on condensation heat transfer enhancement and pressure drop penalty factors in four microfin tubes”, Int. J. Heat Mass Transfer, 48 (2005).

[3] Shah M. M., “A general correlation for heat transfer during film condensation inside pipes”, Int. J. Heat Mass Transfer, 22 (1989).

[4] Mizushina T., Ito R., Miyasita H., “Experimental study of an evaporative cooler”, International Chemical Engineering, 7 (1967).

[5] Niitsu Y., Naito K., Anzai T., “Studies on characteristics and design procedure of evaporative coolers”, Journal of SHASE, 43 (1969).

[6] Hasan A., Sirén K., “Theoretical and computational analysis of closed wet cooling towers and its applications in cooling of buildings”, Energy and Buildings, 34 (2002).

[7] Heyns J.A., Kröger D.G., “Experimental investigation into the thermal-flow performance characteristics of an evaporative cooler”, Applied Thermal Engineering, 30, (2010).

[8] Lin L.W., “Performance test and analysis of water-R22 plate type heat exchanger”, Master Thesis of National Center University (2004).

E289

Numerical Simulation of Temperature Profiles of a Two-Layer Sample During Heating By The Electron Beam

Darya Alontseva
East – Kazakhstan State Technical University, 69, Protazanov St., 070004 Ust-Kamenogorsk, Kazakhstan
dalontseva@mail.ru

Alexander Krasavin
East – Kazakhstan State Technical University, 69, Protazanov St., 070004 Ust-Kamenogorsk, Kazakhstan
alexanderkrasavin@mail.ru

Tatyana Kolesnikova
East – Kazakhstan State Technical University, 69, Protazanov St., 070004 Ust-Kamenogorsk, Kazakhstan
takol@list.ru

Alyona Russakova
Eurasian National University, 5,Munaitpasov St., 010008 Astana, Kazakhstan
arussakova@gmail.com

The corresponding author: Darya Alontseva

Abstract
The paper presents the calculation of the distribution of the temperature profile in two-layer metallic materials under direct current low-energy electron beam irradiation and proposes explicit parameters of the electron beam for modification of thick (150-300 microns) plasma detonation Ni-based coatings by irradiation. Ni-based coatings deposited onto steel substrates were interpreted as a Ni-Fe two-layer sample irradiated on the coating side. The numerical simulation methods were used for solving the heat equation. The model takes into account the electron beam travelling, dependence of heat conductivity and specific thermal capacity coefficients on the temperature and heat loss for emission from the surface. The design modes were used to carry out the modification by e-beam.
Keyword: electron beam irradiation, plasma detonation coatings, heat equation, temperature profile, numerical simulation

1. Introduction

The efficiency of advanced technology of getting protective coating by means of pulsing plasma jet deposition of Ni-based powders onto steel items often falls due to the porosity of the received coatings and their poor adhesion to the substrate [1,2]. To eliminate these disadvantages the coatings are modified by the plasma jet or electron beam [1]. The processes of diffusion and formation of new phases in materials under the influence of electron irradiation happen very quickly, the temperature being one of the main factors influencing these processes. However the temperature measurement under irradiation conditions is difficult and unreliable. Development of a mathematical model of temperature distribution in a material depending on irradiation parameters makes it possible to assume the kind of structures and phases that form in the material during irradiation (on the basis of the received values of temperature and the known phase diagrams). Based on this model, one can choose the parameters of irradiation so as to develop sufficiently high temperatures on the boundary of the coating to the substrate to accelerate the diffusion processes in order to improve adhesion of the coating to the substrate. The sources devoted to the development of such a model [3, 4] testify the relevance of this problem, but they do not provide a comprehensive solution.

The aim of this work is to propose a model of temperature distribution in two-layer metal absorbents during irradiation by a direct current electron beam depending on the energy and beam current density; on the basis of a simulation experiment on the calculation of temperature profiles to recommend specific irradiation modes; to carry out the exposure to radiation according to these modes.

2. Results and Discuss

2.1 Experiment and modeling

The protective coatings with a thickness of 150 to 300 microns were formed on a substrate of quality carbon steel St3 (20x30x10 mm3 samples) using "Impulse-6" plasma-detonation facility. They were deposited with the PG-10N-01 and PG-AN-33 (Russian standards) Ni-based powder alloys.

The irradiation of samples on the side of the surfaces according to the calculated modes was carried out in vacuum by an electron beam on "U-212" generator with an accelerating voltage of 30 kV. The scan is sawlike; the beam travel speed in the horizontal direction is 360 mm/min; the diameter of the electron beam on the sample is 10 mm; the current amperage is 20-30mA.

The need for a detailed explanation of the coating structure scheme stems from the fact that in order to develop a mathematical model of temperature distribution in the coating during irradiation we have to justify the choice of material and thickness of the irradiated layers. Resting on reliable experimental data [5-7] we proposed a layered scheme of the coating structure [8]. A thin layer (less than 5 microns) with mostly Cr oxides and carbides forms on the coating surface. Then comes the main layer of the Ni-based coating, 100-300 microns thick, then a layer of Fe (substrate), 10 000

microns thick. Because of the small thickness of the Cr layer on the surface, this layer was neglected when calculating the temperature profile during electron irradiation, and Ni-Fe double-layer coatings irradiated from the Ni side were considered.

In order to formulate the problem of describing the heating of the coated sample by a moving electron beam as a boundary problem of heat conductivity theory, it is necessary to specify the density of heat sources in a composite solid body. Since the thickness of the coating layer in which the electron beam is almost completely absorbed is very small compared to the thickness of the coating, and we are interested primarily in the temperature field at the boundary surface between the coating and the substrate, we simulate a moving beam of electrons by a moving flat normal-circular source of a given power, i.e. we assume that the specific heat flux at a distance r from the point of intersection of the symmetry axis of the beam with the sample surface is given by expression (1) (without considering losses):

$$q(r) = q_{max} \exp(-kr^2) \qquad (1)$$

where $q_{max}=kN/\pi$ (N- beam power, $N=U_kI$, where U_k- cathode voltage, and I – the beam amperage), and the heat flux concentration ratio k is correlated with the heating spot radius R_b (the beam radius) by the formula $k=1.125/R_b^2$. The analytical solution of the problem of heating a plate of finite thickness with a moving normal-circular source presented in the literature [9] makes it possible to roughly estimate the maximum heat value of the points on the unheated sample surface. The corresponding calculations for the given ranges of beam energies and the geometrical dimensions of the sample show that the maximum heating (the difference between the maximum temperature reached by a point and the initial temperature of the sample) for the points on the ends and the "back" side of the plate does not exceed 3° C. Thus, the nature of the heat exchange with the environment on the unheated plane of the substrate and the ends of the sample has little effect on the temperature distribution in the contact area of the substrate and coating; and we simulate a sample by an infinite plate of thickness h lying on the surface of the semi-infinite space filled with a material with desired thermal characteristics.

Introducing the Cartesian coordinates by the method indicated in Fig. 1 (X and Y axes lie in the plane of the surface coating, Z axis points into the sample), we believe that at the time t0=x0/v a normally circular source begins to operate at the surface, its center moves uniformly with velocity v along the axis X, and switches off at time t1=-t0 (and at time t=0 corresponds to the passage of the beam center point with the coordinates O(000).

Since the heating occurs in vacuum, we believe that the only mechanism of heat loss from the heated surface of the coating is the heat emission described by the Stefan-Boltzmann equation

$$P = \sigma\varepsilon T^4 \qquad (2)$$

where p - beam surface power density [W/m^2] σ - the Stefan-Boltzmann constant, ε – the emissivity

factor for the coating material.

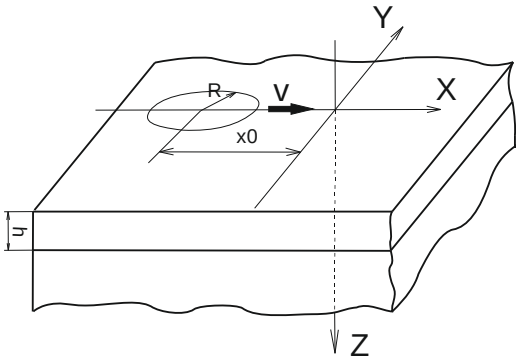

Fig. 1. Schematic representation of a two-layer sample with a moving spot during heating by the electron beam, indicating the choice of the coordinate system.

Thus, we have the following problem of heat conductivity theory: find function $T_1(x,y,z,t)$ (temperature of the coating) and $T_2(x,y,z,t)$ (substrate temperature), as defined in areas S_1 and S_2 respectively (area S_1 is defined by the inequalities $0 \le z \le h$, $t_0 \le t \le t_1$, while are S_2 is defined by the inequalities $h \le z \le \infty$ and $t_0 \le t \le t_1$, at that for both areas $x\epsilon(-\infty,\infty)$ and $y\epsilon(-\infty,\infty)$), that comply in these areas with the differential equations (3) and (4):

$$\frac{\partial T_2}{\partial t} = \frac{1}{c_2\rho_2}\left(\frac{\partial}{\partial x}\left(\lambda_1 \frac{\partial T_1}{\partial x}\right) + \frac{\partial}{\partial y}\left(\lambda_1 \frac{\partial T_2}{\partial y}\right) + \frac{\partial}{\partial z}\left(\lambda_1 \frac{\partial T_2}{\partial z}\right)\right) \quad (3)$$

$$\frac{\partial T_2}{\partial t} = \frac{1}{c_2\rho_2}\left(\frac{\partial}{\partial x}\left(\lambda_2 \frac{\partial T_1}{\partial x}\right) + \frac{\partial}{\partial y}\left(\lambda_2 \frac{\partial T_2}{\partial y}\right) + \frac{\partial}{\partial z}\left(\lambda_2 \frac{\partial T_2}{\partial z}\right)\right) \quad (4)$$

where $\lambda_1=\lambda_1(T)$ the thermal conductivity of the coating material, considered as a function of temperature and $\lambda_2=\lambda_2(T)$ the thermal conductivity of the substrate material, also considered as a function of temperature. In the calculations for computing the values of the functions $\lambda_1(T)$ and $\lambda_2(T)$ we used polynomal interpolation on tabulated values of thermal conductivity of nickel and iron, $c_1=c_1(T)$ and $c_2=c_2(T)$ – specific heat capacity of the coating and the substrate, respectively, also considered as a function of temperature; ρ_1 and ρ_2 the density of the coating and the substrate materials (the constants), when the initial and boundary conditions described below are met: the initial conditions: $T_1(x,y,z,t_0)=T_0$ and $T_2(x,y,z,t_0)=T_0$, where T_0 - the initial temperature of the sample set equal to $T_0=20$ ℃; the boundary conditions (5), (6) , (7) и (8): at the boundary $z=0$ (the coating surface) –condition (5)

$$k_1((T_1)_p)x\left(\frac{\partial T_2}{\partial z}\right)_p = q_{max}\exp(-kr^2) - \sigma\varepsilon((T_1)_p)^4 \quad (5)$$

where $P(x,y,0)$ – the point on the surface of the coating, and $(T_1)_p=T_1(x,y,0)$ and $\left(\frac{\partial T_1}{\partial z}\right)_p$ respectively, the values of the temperature and the normal derivative of temperature at the point P, k_1 – thermal conductivity of the coating material (depending on the temperature), $r = \sqrt{(X_u(t)-x)^2} + y^2$ – the distance from point P to the center of the normally circular source $(X_u(t)=X_0+vt)$; at the boundary between the coating and the substrate (plane z = h) must be met the two conditions (6) and (7):

$$k_1((T_1)_{z=h}) \times (\frac{\partial T_1}{\partial z})_{z=h} = k_2((T_2)_{z=h}) \times (\frac{\partial T_2}{\partial z})_{z=h} \quad (6)$$

where $k_2 = k_2(T_2)$ the thermal conductivity of the substrate material, considered as a function of temperature

$$T_1(x, y, h) = T_2(x, y, h) \quad (7)$$

that is, for all *x, y* and any *t*, belonging to the interval (t,t_0) at *z* tending to infinity, the temperature tends to the initial temperature of the sample T_0, condition (8)

$$\lim_{z \to \infty} T_2(x, y, z, t) = T_0 \quad (8)$$

2.2 Experiment results

The problem was being solved by the finite-difference method. We used the data [10] for the values of the thermal conductivity, emissivity, specific heat and density of Ni and Fe. Fig. 2 shows the dependence of the temperature at the point with the coordinates *(0,0,h)* (the point that lies at the boundary surface between the coating and the substrate) on the time at the following design parameters: coating thickness h=300 μm, the beam power *N=300W* (cathode voltage U_k=30 kV , beam amperage *I*=20 mA), beam radius R_b=5 mm, beam velocity *v*=0.004 m/s, calculation time interval t_1-t_0=14s (t_0=7.0s), correspondingly x_0=-28 mm. Fig. 2b displays the corresponding temperature dependence on the *z* coordinate for the point with the coordinates *x*=0, *y*=0 at the time *t*=0 at the above calculated parameters (the source switches on at the time t_0=7.0 s, time *t*=0 corresponds to the center of the source passing the point with the coordinates (0,0,0)).

The samples of Ni-based coatings were additionally irradiated according to the modes recommended in the result of numerical simulation calculation: electron beam current density – 20 mA/cm^2, accelerating voltage – 30 kV, in the continuous exposure regime.

For practical calculations at low electron energies we needed to turn to the experimentally obtained patterns. The empirical evidence [11] suggests that the 1-2 mm thick Ni layer at the energies of the electron beam of 30 keV is being completely absorbed. Since the depth of the total absorption of electrons is extremely small in comparison with the thickness of coatings, a model of surface distributed sources of heat can be taken for the construction of the temperature profile in the sample. In our proposed model not only a high temperature in the boundary zone is achieved, but also long enough, the order of several seconds, holding of the area in the high temperature diapason of 400° C is provided, which allows for diffusion processes. The model enabled to choose low current density values, which allows one to save energy for further processing, without penetration into the coating or substrate.

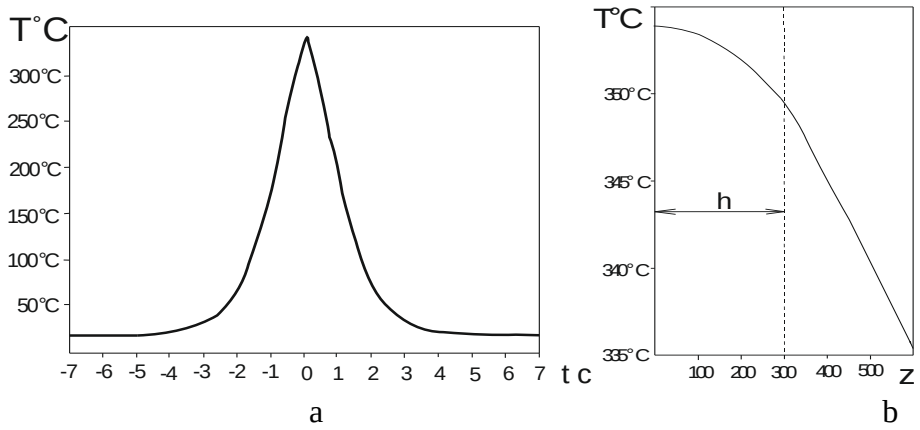

Fig. 2. Dependence of the temperature of a sample point on the boundary of the substrate and the coating on the time at the surface heating by a moving beam of electrons (a) and the corresponding temperature dependence on the coordinate *z* (b)

Based on the model of temperature distribution in two-layer absorbents with the surface distribution heat sources, the temperature profiles were calculated according to the irradiation parameters and conditions. The choice of materials and thicknesses of absorbent layers is based on the experimentally developed scheme of the structure of thick plasma-detonation powder coatings. Basing on the calculations we proposed the modes of exposure leading to the formation of high temperatures in the coating - substrate contact zone to accelerate diffusion processes.

2.3 Acknowledgments

This work was funded by the Ministry of Education and Science of Kazakhstan for the two projects: “Study of nanostructure formation in the Ni and Co-based plasma detonation coatings and the search for scientifically justified modes of coating modification by irradiation” and “Development of scientific basis of innovation technology of protective coatings modification by e-beam and plasma-jet irradiation”.

3. References

[1] K.K. Kadyrzhanov, F.F. Komarov, A.D. Pogrebnyak, V.S. Russakov, T.E. Turkebaev, Ion-beam and Ion-plasma Modification of Materials. MGU: Moscow, 2005, 425c.

[2] E. Celik, I. Ozdemir, E. Avci, Y. Tsunekawa, “Corrosion behavior of plasma sprayed coatings”, Surface and Coatings Technology, vol. 193, 2005, pp. 297-302.

[3] G.Z.Ganeev, S.B. Kislitsin, “The calculation of temperature fields, thermal stresses, thermal erosion during pulsed irradiation by an electron flow”, in: Abstract Book of 7th International Conference Nuclear and Radiaion Physics, Almaty, Kazakhsnan, 2009, p. 34.

[4] N.I. Pischasov, A.V. Nikolaev, “Modification of the structure and properties of hard alloys of WC-Co system by high-current beams of charged particles”, Communications of Omsk University 2, 1996, pp.39-43.

[5] D.L. Alontseva, S.N. Bratushka, A.A. Borysenko, N.V. Prokhorencova, V.T. Shablya, :Formation of Micro-and Nanostructured Phases in Coatings Based on Ni-Cr and Co-Cr, Their Structure and Properties”, Metallofizika I Noveishie Teknologii, vol. 33, 2011, pp. 721-745.

[6] D. Alontseva, “The study of using plasma technologies for the deposition of Ni-Cr based coatings on steel substrate andmodification of their properties by duplex treatment”, Przegląd Elektrotechniczny, vol. 86, N7, 2010, pp. 42-44.

[7] A.D. Pogrebnjak, Sh.M. Ruzimov, D.L. Alontseva, “Structure and properties of coating

s on Ni base deposited using a plasma jet before and after electron a beam irradiatio n", Vacuum, vol. 81, 2007, pp. 1243-1251.

[8] D.L. Alontseva, "Creating the Firm, Wear-Proof and Corrosion-Resistant Coatings on B ase Of Ni-Cr and Co–Cr Powder Alloys by Plasma Detonation Method", in: Abstract Book of the Fourth International Conference "Deformation & Fracture of Materials an d Nanomaterials", Moscow, 2011, pp. 446-447.

[9] N.N. Rykalin, Calculations of thermal processes in welding. Moscow: Mashgiz, 1951, p. 297.

[10] C.I. Smithells, Metals Reference Book, Moscow: Metallurgiya, 1980 p. 447.

[11] I.A. Abroyan, A.N. Andronov, A.I. Titov, Physical basis of electronic and ionic techno logy, Higher, 1984 p. 320.

E259

Non-Dendritic A356 Al alloys Synthesized via Cooling Slope Technique

Y. T. Chen
Dept. of Materials Science and Engineering, and Center for Micro/Nano Science and Technology, National Cheng Kung University, Tainan, TAIWAN
N5694145@mail.ncku.edu.tw

Chi Y. A. Tsao
Dept. of Materials Science and Engineering, and Center for Micro/Nano Science and Technology, National Cheng Kung University,Tainan, TAIWAN
tsao_cya@alum.mit.edu

C.-H. Chiang
Metal Industries Research & Development Center, 1001 Kaonan Highway, Kaohsiung, Taiwan
samchiang@mail.mirdc.org.tw

The corresponding author: tsao_cya@alum.mit.edu,

Abstract
The cooling slope technique has been developed in recent years, which controls the nucleation and growth of the primary grains during solidification to achieve fine and non-dendritic microstructures. In this study, A356 Al alloys were processed through a modified cooling slope technique to obtain fine, non-dendritic microstructures, in which the cooling rate of the cast crucible was controlled. Three process parameters, namely pouring temperature, inclined slope angle, and the cooling rate of the cast crucible, were varied during the processing. The cooling slope was water-cooled with a constant water flow rate. The solid fraction and the size distributions of the primary grains along the vertical and horizontal positions of the cast ingots were measured individually. The macro-segregation was examined in terms of the distribution of the solid fraction. The yields of the ingots were calculated for studying the efficiency of the cooling slope technique. The effects of the three process parameters on the microstructures, macro-segregation, and yields were studied by the Taguchi method.
Keywords: Semi-Solid Processing, Modified Cooling Slope, A356 Al Alloys, Non-Dendritic Structure

1. **Introduction**

Semi-solid metal forming process has been developed since 1971 [1]. The key feature of this process is that the metals are processed in the semi-solid state. The semi-solid melt has high viscosity as well as thixotropic and pseudoplastic flow behavior, which allow them as a solid at rest and having fluid properties when sheared [2].

The essential of the semi-solid metal forming process is to have non-dendritic-structured materials to begin with. Many processing routes have been developed to obtain the fine and non-dendritic microstructure, such as mechanical stirring, electromagnetic stirring, and so on [3]. In order to reduce costs and the time of production further, the New Rheocasting process (NRC) has been developed by UBE Industries Ltd in 1996 [4]. This process is different from the previous two, because it produces fine and non-dendritic microstructure without using any external force. In the

NRC process, a slightly superheated melt pour into the inclined steel crucible and directly touch the wall of the steel crucible, where the melt temperature drops down to the semi-solid range and nucleation occurs. Subsequently, by controlling the melt cooling rate, constitutional supercooling is reduced to inhibit dendritic grain formation and non-dendritic structures are obtained [5]. The Cooling Slope [6] is another technique developed to make semi-solid slurry with non-dendritic grains. In the process, melt is charged and flows over a water-cooled slope, which provides high thermal supercooling, so a greater numbers of small nuclei are obtained in the melt. Because the large number of the nuclei limit the space between them, grain size is fine.

In the present work, the concepts of the NRC process and Cooling Slope are combined to become a modified Cooling Slope technique, including a water-cooled steel slope and a steel crucible that is preheated to a desired temperature and temperature-controlled. Therefore, it has the advantage of the cooling slope, which is a greater numbers of small nuclei are obtained in the melt., and the advantage of the controlled cooling rate, which is reducing the constitutional supercooling, promoting the non-dendritic structures.

In the present work, the effects of pouring temperature, inclined slope angle and the cooling rate of the steel crucible on the microstructures and yields were analyzed and studied with the experiments designed by the Taguchi method.

2. Experimental methods

The material used was the commercial A356 aluminum alloy with the chemical composition as shown in Table 1. The A356 was heated in an electric resistance furnace and became fully molten when temperature reached 615˚C. Subsequently, the melt was heated to 625˚C, 635˚C, and 645˚C with superheats of 10~30˚C, and then poured onto a water-cooled inclined slope (200mm in length and 50mm in width). The surface of the water-cooled inclined slope was coated with a thin layer of boron nitride, and the inclined angles used were 20˚, 25˚, and 30˚, separately. Two K-type thermocouples were placed at the top entrance and the bottom exit of the inclined slope to measure the temperatures of the melt on the slope. Subsequently, the melt was cast into a steel crucible (70mm in diameter, and 150mm in height) preheated to 400˚C. A temperature controlling devices was used to control the cooling rate of the melt in the steel crucible. A K-type thermocouple was placed inside the cast crucible at a distance of 10 mm from the bottom and 5mm from the wall to monitor the cooling rates of the cast billets. The temperature controlling device included a heating source from an induction coil, and a cooling source from air or nitrogen cooling.

Table 1 Chemical Composition of A356.

A356	Si	Mg	Fe	Zn	Cu	Ti	Mn	Al
Wt%	6.8	0.4	0.2	0.1	0.2	0.2	0.1	Rem.

In order to investigate the effects of the parameters on the yields of the cat billets, the experiments were divided into two parts. In the first set of the experiments, equal weight (600g) of the material were used to obtain the effects of the pouring temperature and inclined slope angle on the yield. In the second set, the resulting volumes of the cast billets were controlled to be the same to eliminate the influence of the ingot size on the microstructures. The sizes of the billets were 70mm in diameter and 40mm in height. Samples of the billets were taken at six positions as shown in Fig. 1, which were etched with Keller's reagent for 10 sec. The grain size, shape factor and solid fraction were analyzed using the Optimas Image Analysis software.

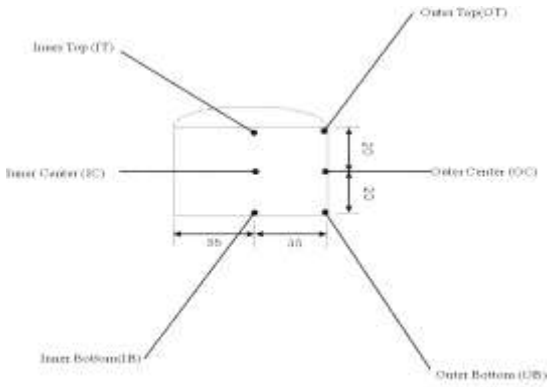

Fig. 1 Sample positions on the billet

The process parameters of the experiments include pouring temperatures of 625˚C, 635˚C and 645˚C, inclined slope angle of 20˚, 25˚ and 30˚, and melt cooling rate inside the steel crucible of 0.1˚C/s, 0.5˚C/s and 1˚C/s. The Taguchi method was applied to design and analyze the experiments to study the effects of the three parameters on the microstructures and yields. Table 2 shows the nine experiments designed by the Taguchi method with three process parameters and three levels for each process parameter.

Table 2 Nine experiments designed by Taguchi method

	I	II	III	IV	V	VI	VII	VIII	IX
Pouring Temperature(°C)	625	625	625	635	635	635	645	645	645
Inclined slope angle	20°	25°	30°	20°	25°	30°	20°	25°	30°
Melt cooling rate(°C/s)	0.1	0.5	1	0.5	1	0.1	1	0.1	0.5

3. Results and Discussion

Process Parameters vs. Yields of the Cast Billets. Table 3 shows the results of the first part of the experiments, which are the yields of the billets made in the experiments, defined by the billet weight/charged weight. Table 4 and Fig. 2 show the results analyzed by the Taguchi L9 method, which shows that the higher the pouring temperature and the larger the inclined slop angle, the better the yield. Higher pouring temperature resulted in higher melt temperature, which restricted melt from solidifying on the cooling slope, giving a larger yield for the cast billet. Larger inclined slope angle made melt flow on the cooling slope at a faster speed, which reduced the time available for solidification, also giving a larger yield for the cast billet.

Table 3 Yield in first part of the experiments.

	I	II	III	IV	V	VI	VII	VIII	IX
Weight	176.3g	218.7g	322.8g	223.4g	305.1g	392.9g	269.4g	415.0g	510.0g
Yield	29%	37%	54%	37%	51%	66%	45%	69%	85%

Table 4 Pouring temperature vs. yield and inclined slope angle vs. yield.

Pouring Temperature	625°C	635°C	645°C	Inclined slope angle	20°	25°	30°
Yield	40%	51%	66%	Yield	37%	52%	68%

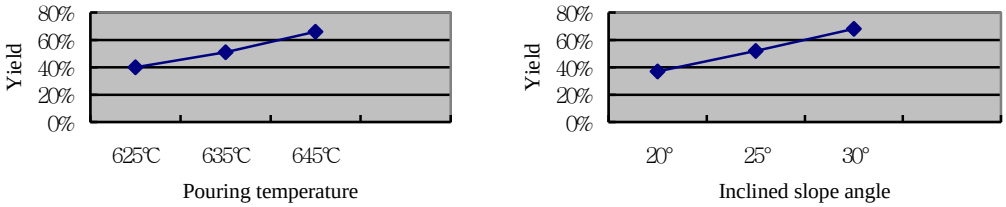

(a) (b)

Fig. 2 (a) Pouring temperature vs. yield. (b) Inclined slope angle vs. yield.

Process Parameters vs. Microstructures. Table.5 shows the melt temperatures on the top entrance and bottom exit of the inclined slope and their difference, ΔT, supercooling, in the second part of the experiment. The effects of the inclined slope angle on theΔT are shown in Table 6. TheΔT decreases as the inclined slope angle increases due to shorter time available for the melt to cool down on the slope.

Table 5 Tt , Tb and ΔT on the inclined slope.

	I	II	III	IV	V	VI	VII	VIII	IX
Tt	603°C	604°C	604°C	607°C	610°C	608°C	612°C	611°C	610°C
Tb	588°C	590°C	592°C	593°C	597°C	598°C	595°C	594°C	594°C
ΔT= Tt - Tb	15°C	14°C	12°C	14°C	13°C	10°C	17°C	17°C	16°C

Table 6 Inclined slope angle vs. supercooling (ΔT)

Inclined angle	ΔT (°C)
20˚	15.3
25˚	14.7
30˚	12.7

Fig. 3 shows the original as-cast structures, which consists of as-cast structures consists of coarse dendritic structure of the primary α-Al phase with inter-dendritic eutectic phase. Fig. 4 shows the microstructures of the as-cast billets from experiments I, IV and VII. In the billets made via modified cooling slope method, the primary α-Al phase became of rosette-like or globular morphology.

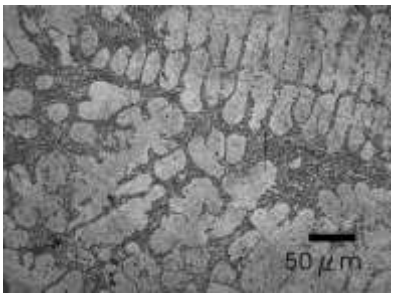

Fig. 3 Micrograph of as-cast A356 alloy

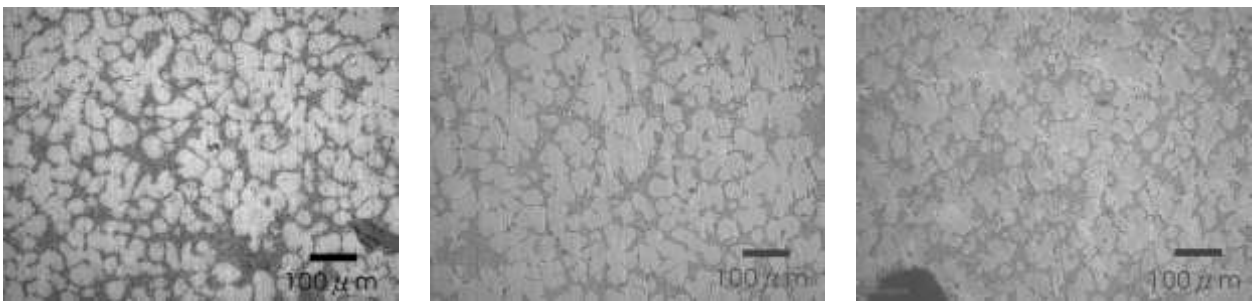

(a) (b) (c)

Fig. 4 Micrographs of A356 alloys obtained from experiment (a) I (b) IV, and (c) VII.

The effects of the three parameters on the average grain sizes were analyzed as shown in Table 7. As shown in Table 7, the increase of the pouring temperature results in somehow larger grain size. However, the effect of the pouring temperature on the grain size is not very significant, as shown in Table 7. At lower pouring temperature, rapid nucleation occurs on the cooling slope and the great numbers of nuclei limit the space between them, resulting in finer solidified grains [7]. In contrast, nucleation doesn't occur abundantly at higher pouring temperature, which renders less numbers of nuclei, providing more space for grain growing to larger sizes.

The relationships between the inclined slope angle and the grain size are shown in Table7. There is nearly no effect of the inclined slope angle on the grain size. There are two contributions of the inclined slope angle that compete with each other. High inclined slope angle causes the melt to flow faster and, thus, decreases the time of its staying on the slope, so the thermal supercooling of the melt at exit of the slope decreases with increasing inclined angle. On the other hand, for the same melt pouring rate, high inclined slope angle gives faster flow rate, but thinner melt flow, which is, thus, cooled at faster cooling rate, giving larger thermal supercooling. Therefore, the degree of the supercooling, which controls the nucleation rate and thus, the grain size, is a balance between these two contributions. The fact that there is no effect of the inclined slope angle on the grain size is a clear evidence of this balance.

The effects of the melt cooling rate on the grain size are shown in Table 7. Higher melt cooling rate provides less time for grain to grow and coalesce, so the grains are finer than those for lower cooling rate. For those grains near the walls of steel crucibles that have higher cooling rates, the effects are more significant.

Table 7 Pouring temperature vs. grain size (μm), Inclined slope angle vs. grain size (μm) and Melt cooling rate vs. grain size (μm).

Pouring Temperature	Grain size (All)	Grain size (OB)	Inclined slope angle	Grain size (All)	Grain size (OB)	Melt cooling rate	Grain size (All)	Grain size (OB)
625°C	69.0	67.3	20°	70.1	68.0	0.1°C/s	71.8	71.3
635°C	70.3	68.7	25°	70.1	68.3	0.5°C/s	70.1	68.3
645°C	71.4	70.0	30°	70.6	69.7	1°C/s	69.9	65.3

The distributions of the solid fractions at the six positions for each billet are shown in Table 8. It is shown that the distribution of the solid fraction inside each billet is within 5%, which means that the macro-segregation is not significant for the billets made by modified Cooling Slope technique.

Table 8 Solid fraction distribution. (%)

	I	II	III	IV	V	VI	VII	VIII	IX
IT	70	72	72	74	70	72	67	71	71
IC	73	70	69	71	70	69	70	70	71
IB	71	73	69	71	73	70	70	69	70
OT	68	70	67	71	69	70	68	69	71
OC	70	70	71	72	71	70	73	73	73
OB	69	70	66	69	71	70	72	68	72

4. Conclusions

In the A365 billets made via modified cooling slope method, the primaryα-Al phase became of rosette-like or globular morphology, in contrast to the dendritic morphology for the conventional

cast A356 alloy. The higher the pouring temperature and the larger the inclined slop angle, the better the yield of the billet made with the cooling slope technique. The increase of the pouring temperature results in somehow larger grain size. However, the effect of the pouring temperature on the grain size is not very significant. There is nearly no effect of the inclined slope angle on the grain size due to the two contributions being balanced. Higher melt cooling rate provides less time for grain to grow and coalesce, so the grains are finer than those for lower cooling rate. The macro-segregation is not significant for the billets made by modified Cooling Slope technique.

5. References

[1] D.B. Spencer, R. Mehrabian, M.C. Flemings: Metall. Trans. 3 (1972), p. 1925–1932.

[2] S. Nafisi, O. Lashkari, R. Ghomashchi, F. Ajersch, A. Charette: Volume 54, Issue 13 (2006), p. 3503–3511.

[3] E. Cardoso, H. V Atkinson and H. Jones: *Microstructural evolution of A356 during NRC processing* (8th Int. SSP. Conf. Limassol, Cyprus, 21-23 September 2004, published by TMS).

[4] A. Mitsuru, S. Hiroto, H. Yasunori, S, Tatsuo, S. Satoru, Y. Atsushi: *Method and Apparatus for Shaping Semisolid Metal*s (UBE Patent EP0745694 A1, 1996).

[5] D.J. Browne, M.J. Hussey, A.J. Carr and D. Brabazon: *Direct Thermal Method: new Process for Development of Globular Alloy Microstructure* (Int. Journal of Cast Metals Research, 16, No.3, 2003, p. 1-9).

[6] Toshio Haga, P. Kapranos: *Simple rheocasting processes* (Journal of Materials Processing Technology 130–131 (2002), p. 594–598).

[7] P. J. Uggowitzer, H. Kaufmann: *Evolution of Globular Microstructure in New Rheocasting and Super Rheocasting Semi-Solid Slurries*. (steel research int. 75 (2004) No.8/9, p.525-530).

Chemical Engineering

Pullman Bangkok King Power, 2F

2013/1/27 Sunday 14:00-16:00

BENS120
Study of Tribology Characteristics of Rice Straw Biolubricant
Jeng Haur Horng｜*National Formosa University*
Shou Yin Yang｜*National Formosa University*
Kai Wei Chen｜*National Formosa University*

BENS193
Two-Stage Static Cultivation of g. Lucidum for the Production of Pharmaceutical Bioactive Compounds: Triterpenoids and Ganoderic Acids
Zhang Jinming｜*Ngee Ann Polytechnic*
Indirakumar Balasubramanian｜*Ngee Ann Polytechnic*
Anli Geng｜*Ngee Ann Polytechnic*

BENS194
Simultaneous Higher Production of Ganoderic Acid and Polysaccharides Using Fungal Elicitors by Submerged Cultivation of Ganoderma Lucidum
Indirakumar Balasubramanian｜*Ngee Ann Polytechnic*
Jinming Zhang｜*Ngee Ann Polytechnic*
Anli Geng｜*Ngee Ann Polytechnic*

BENS120

Study of Tribology Characteristics of Rice Straw Biolubricant

Jeng-Haur Horng[a], Yang Shou-Yin[a], Chen Kai-Wei[c]
[a]**Department of Power Mechanical Engineer**ing, National Formosa University, Taiwan
E-mail address: jhhorng@gmail.com

[b]**Department of Power Mechanical Engineering, National Formosa University,** Taiwan
E-mail address: Ianyan@nfu.edu.tw

Chen Kai-Wei
[c]**Department of Power Mechanical Engineer**ing, National Formosa University, Taiwan
E-mail address: yoyoqqq66@gmail.com

ABSTRACT
An environmental-safe biolubricant was emphasized due to the environment protection and the rapid depletion of world fossil fuel reserves. If rice straw can the used as bio-additive of lubricant, it will be an important source of renewable and sustainable energy. The aim of this study was to assess the tribological characteristics of rice straw biolubricant in ring-disk testing machine for the different speeds and loads. The rice straw oil is obtained by using fast pyrolysis method. The effects of friction coefficient, workpiece temperature and contact resistance of interface were investigated to evaluate biolubricant performance. In this paper, the three-body contact model also is used to analysis rice straw biolubricant effect.
In the work, comparison of lubrication characteristics between rice straw biolubricant and general mineral oil, the mixed 8% rice straw to the mineral oil as an additive which decreases the values of friction coefficient and temperature of interfaces from thick film lubrication to mixed lubrication even at higher load. The biolubricant has better antiwear property than that of mineral oil from mixed lubrication to boundary lubrication. However, the mixed biolubricant made from rice straw have to modify the VI property in order to increase viscosity stability.

Keywords: Biolubricants, Pyrolysis, Rice Straw, Contact Resistance, Three-Body Microcontact

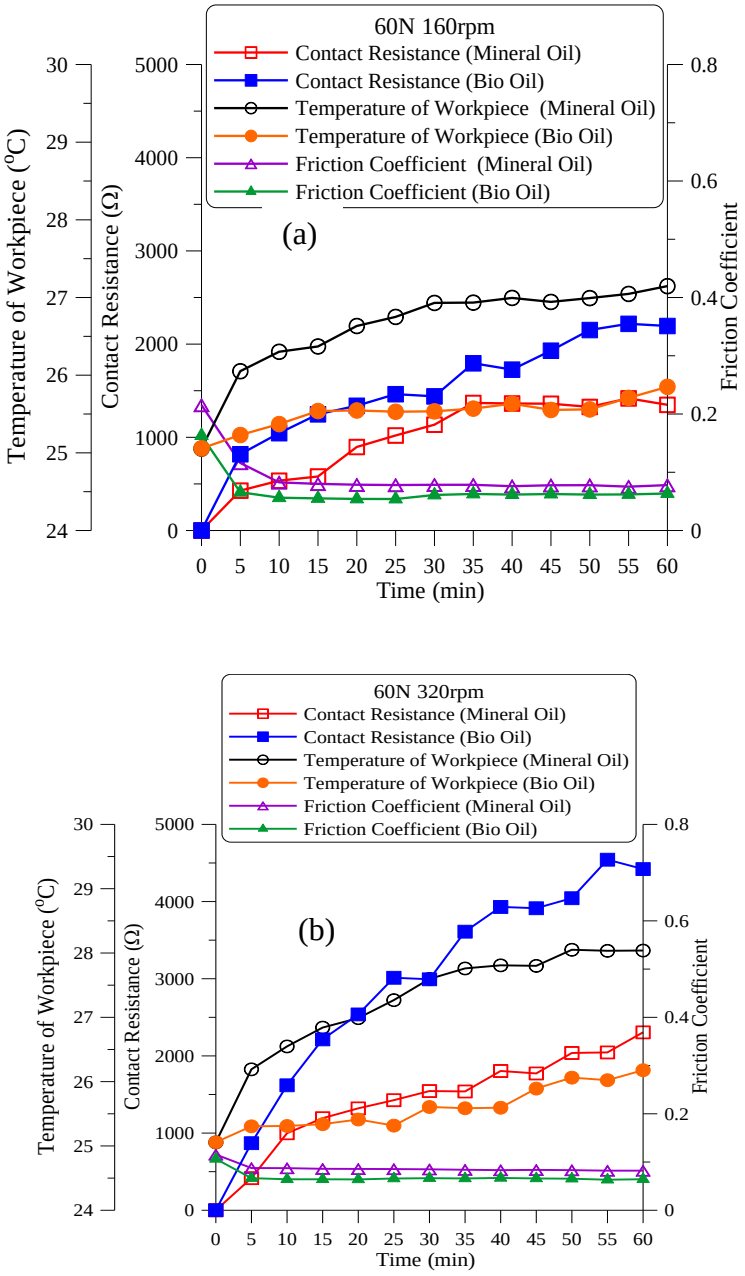

Fig. 1 Comparison between mineral oil and biolubricant for contact resistance, workpiece temperature and friction coefficient varying with test time at the load of 60 N and the speed is (a) 160 rpm. (b) 320 rpm.

BENS193

Two-stage static cultivation of *G. lucidum* for the production of pharmaceutical bioactive compounds: triterpenoids and ganoderic acids

Jinming Zhang[a], Indirakumar Balasubramanian[b], Anli Geng[c,*]
[a]School of Life Sciences and Chemical Technology, Ngee Ann Polytechnic, Singapore
E-mail address: zji2@np.edu.sg

[b]School of Life Sciences and Chemical Technology, Ngee Ann Polytechnic, Singapore
E-mail address: bin2@np.edu.sg

[c]School of Life Sciences and Chemical Technology, Ngee Ann Polytechnic, Singapore
E-mail address: gan2@np.edu.sg

ABSTRACT

G.lucidum is a basidiomycete white-rot fungus which has been used for medicinal purpose for centuries in Asia. Much work has been done and revealed that this medicinal mushroom is presently untapped source of a wide range of new compounds with biological activities. It has been proved that a number of substances from this medical mushroom have the important properties of antitumor, immune modulating, cardiovascular, antihypercholesterolemia, antiviral, antiparasitic, hepatoprotective and antidiabetic activities, to name a few. The main bioactive compounds from the ethanolic extracts are triterpennoids, while the ganoderic acids are the major constitutes. Our present work focuses on the improvement of the production of total triterpennoids and ganoderic acids from the cultivation of *G.lucidum*. In order to hyper produce triterpenoids and ganoderic acids; a two-stage static cultivation was applied with a first stage cultivation in shake-flasks and the second stage in the tissue culture bottles. Liquid volume loading, the liquid surface area and the shift time between the two stages were investigated. A maximum total triterpenoids production of 2900 mg/L was obtained and ganoderic acids production was 1400 mg/L. To further improve the production of the bioactive metabolites, a wide range of elicitors and inducers such as metal ions, oligosaccharides, proteins, unsaturated fatty acid and some Chinese medicines were investigated on their improvement of bioactive compounds production by *G. lucidum*.

Keywords: *Ganoderma lucidum*, static cultivation, bioactive compounds, triterpenoids, ganoderic acids

BENS194

Simultaneous higher production of Ganoderic acid and Polysaccharides using fungal elicitors by submerged cultivation of *Ganoderma lucidum*

Balasubramaniam Indrakumar[a], Jinming Zhang[b], Anli Geng[c,*]
[a]**School of Life Sciences and Chemical Technology, Ngee Ann Polytechnic**, Singapore
E-mail address: bin2@np.edu.sg

[b]**School of Life Sciences and Chemical Technology, Ngee Ann Polytechnic**, Singapore
E-mail address: zji2@np.edu.sg

[c]**School of Life Sciences and Chemical Technology, Ngee Ann Polytechnic**, Singapore
E-mail address: gan2@np.edu.sg

ABSTRACT
Ganoderic acid and polysaccharides from *Ganoderma lucidum* are medicinally valuable and a popular remedy for many chronic diseases. Therefore, it is essential and commercially important to have a simultaneous higher production of polysaccharides and ganoderic acid. In this study we investigated the optimal conditions of *Ganoderma lucidum* submerged cultivation for simultaneous and effective production of polysaccharides and ganoderic acids. To achieve this, various strategies such as fed-batch optimization and addition of various fungal elicitors were studied. Fed-batch cultivation followed by ultrafiltration concentration of the broth produced comparable amount of extracellular polysaccharides and high-yield of ganoderic acid. The addition of fungal elicitors increased both the production of polysaccharides (2.56 g/L) and ganoderic acids (562.5 mg/L) by multiple folds compared to the control without elicitors. Whole elicitors from *Arthroderma otae* up surged the production of both cell biomass and polysaccharides.

Keywords: *Ganoderma lucidum*, Polysaccharides, Ganoderic acid, submerged culture, elicitor

Natural Sciences

Pullman Bangkok King Power, 2F

2013/1/27 Sunday 14:00-16:00

BENS103
Theoretical Studies of Population Dynamics of Species in Two Predators-One Prey System
Sai Krishna｜*JNTUH College of Engineering*
Madhusudana Rao P｜*JNTUH College of Engineering*

BENS107
The Fine Structure and Phylogeny of Minutocellus Sp. (Penatae, Cymatosiraceae) from China Sea
Zhenghong Sui｜*Ocean University of China*
Chunyan Wang｜*Ocean University of China*
Kyoung Ho Kang｜Chonnam National University
Wei Zhou｜*Ocean University of China*

BENS111
Total Phenolic Contents, Total Flavonoid Contents and in Vivo Anti-Angiogenic Properties of Blueberry Pomace Extracts
Janyawat Vuthijumnonk｜*Massey University*

BENS118
New Production of Haloketides by the Marine-Derived Fungus Aspergillus sp.
Byeng Wha Son｜*Pukyong National University*
Alain Simplice Leutou｜*Pukyong National University*
Keumja Yun｜*Pukyong National University*

BENS140
Pathogenicity of Tomato Leaf Curl Virus (TYLCV) Infectious Clones Agroinoculated into Nicotiana Benthamiana and Tomato Plants
Chang Won Choi｜*Pai Chai University*
Sung Oh｜*Pai Chai University*
Seongdae Kim｜*Pai Chai University*
Nagarajan Vinod｜*Pai Chai University*
Young Shik Kim｜Sangmyung University

BENS151
Pistacia Chinensis Inhibits NO Production via PI-3K/Akt Pathway in LPS-Activated RAW264.7 Cells
Man Hee Rhee｜*Kyungpook National University*
Hyun Dong Ji｜*Kyungpook National University*

BENS170
In Vitro Bioaccessibility Assessment of Lycopene in Raw Tomato and Tomato Sauce With and Without the Addition of Olive Oil
Ahmad Rashid Allafi｜*Kuwait University*

BENS148
Differential Drug Response of E. Coli Biofilm against Gentamycin, Ciprofloxacin and Ofloxacin on Externally Implantable Devices
Preetam Verma｜*MNNIT Allahabad*
Vishnu Agarwal｜*MNNIT Allahabad*

BENS246
Salt Stress-Related Function of Pdsa Gene in Aspergillus Nidulans
Dong Soo Park｜*Chungnam National University*

BENS103

Theoretical studies of two Predator and single prey model

Banda Sai Krishna[a,*], P.Madhusudana Rao[b]
[a]**JNTUH College of Engineering**, JNTUH, Hyderabad – 500 085, Andhra Pradesh, India
E-mail address: bandasaikrishna@gmail.com

[b]**JNTUH College of Engineering**, JNTUH, Hyderabad – 500 085, Andhra Pradesh, India
E-mail address: pmrphy@yahoo.co.in

ABSTRACT
The present work deals with prediction of a mathematical model for a system containing two predators and single prey .and later this model is extended to various cases. The system taken contains two predators and one prey. Differential equations are proposed for the population change of each species based on Logistic Growth model. The model considers parameters like growth rate, death rate, predation rate of each predator on prey and predator to predator negative impact rate]. The thrust of this work is to explain the possible pattern of change of population of each species over longer period of time. Two types of systems are considered here. One is that both the predators depend on same prey and they are long term rivals. Other is both predators depend on same prey while one of the predators also diets on other predator, thus making itself top in food chain in present system .Considering some random fixed values for model parameters differential equations are solved numerically and population of each species over period of time were plotted using MATLAB. For a given model parameters, it was observed that the initial and maximum populations of each species determine the pattern of change of populations over the time.

1. INTRODUCTION

Theoretical interpretation of Predator Prey population dynamics could be helpful to Ecologists and Biologists. Ever since Lotka-Volterra model many other models have been proposed and developed for understanding predator-prey dynamics. The present work considers Logistic growth model as basis and proposes model equations. The system considered consists of two predators and single prey. Here two types of system are considered. One is that both the predators are not just competitors for the prey but they are long term rivals. The other is where one of the predators diets on other predator along with prey making it top on food chain in this system. The general equation of Logistic growth model is given below (1)

$$\frac{dN}{dt} = rN\left(1-\frac{N}{K_N}\right) \quad \text{.....(1)}$$

Where N represents species population at the time
r represents net growth rate of the species
K_N is the carrying capacity or maximum population possible for the species.

It is observed that when r is positive, the population of the species increases logistically to maximum value of K_N and then it becomes constant.

The system taken consists of three species, two predators A, B and single prey N. Equations based on Logistic Growth model are proposed. In these equations growth rate of N is explained based on natural birthrate, predation rates of A and B. Growth rate of A and B are based on positive impact of N on them, their natural death rates and death rates caused a predator on other. Each species competes with itself.

SYSTEM TYPE 1. A and B predate on N and they are long term rivals
Model equations are given (2) ,(3), (4) below

$$\frac{dN}{dt}=\left(r-p_AA-p_BB\right)N\left(1-\frac{N}{K_N}\right) \qquad \ldots\ldots\ldots\ldots\ldots\ldots\ldots\ldots\ldots\ldots\ldots\ldots\ldots\ldots(2)$$

$$\frac{dA}{dt}=\left(g_AN-d_A-i_BB\right)A\left(1-\frac{A}{K_A}\right) \qquad \ldots\ldots\ldots\ldots\ldots\ldots\ldots\ldots\ldots\ldots\ldots\ldots\ldots\ldots(3)$$

$$\frac{dB}{dt}=\left(g_BN-d_B-i_AA\right)B\left(1-\frac{B}{K_B}\right) \qquad \ldots\ldots\ldots\ldots\ldots\ldots\ldots\ldots\ldots\ldots\ldots\ldots\ldots\ldots(4)$$

Here r is natural birthrate of N while g_A, g_B are positive impact N causes on A, B populations respectively

p_A, p_B are predation rates of A, B on N respectively.

K_A, K_B, K_N are carrying capacities or maximum population possible by A, B, N respectively.

d_A, d_B are natural death rates of A, B.

i_A is death rate of B caused by A while i_B is death rate of A caused by B.

In each equation two brackets were observed. First bracket shows the net growth rate of each species depending on different parameters and other species populations. It is assigned based on Lotka-Volterra Predator-prey model[1]. Second bracket shows the competition of species with itself. Giving random values to all model parameters mentioned in equations population dynamics of A, B, N were observed. It is clear that for given fixed values of model constants like birthrates, natural death rates and others which were mentioned in the equations, the dynamics of populations of three species depends upon initial values A_0, B_0, N_0. Keeping the model constants fixed and then based on different initial values of A, B, N and respective carrying capacities, five different cases were observed. The constants mentioned in the model were mostly fixed except few changes which were observable in the table.

Table 1

Parameters	Case 1.1	Case 1.2	Case 1.3	Case 1.4	Case 1.5

r	2	2	2	2	2
p_A	0.03	0.03	0.03	0.03	0.001
p_B	0.025	0.025	0.025	0.025	0.002
g_A	0.008	0.008	0.008	0.008	0.008
g_B	0.009	0.009	0.006	0.009	0.009
d_A	0.4	0.4	0.4	0.4	0.5
d_B	0.3	0.3	0.3	0.3	0.4
i_A	0.0095	0.0095	0.0095	0.0095	0.015
i_B	0.009	0.009	0.009	0.009	0.009
K_A	70	70	30	44	70
K_B	40	40	43	40	50
K_N	150	150	98	98	150
A_0	9	25	32	38	30
B_0	8	6	29	24	12
N_0	12	65	65	70	130

These five cases represent five different possibilities of dynamics of populations of the three species taken. These cases were explained along with graphs representing the change of populations of A, B, N over period of time. The population curve of N is represented by solid line while the population curves of A, B are represented by dotted and dashed line respectively. Same trend is followed for all the graphs presented in the present work.

Case 1.1

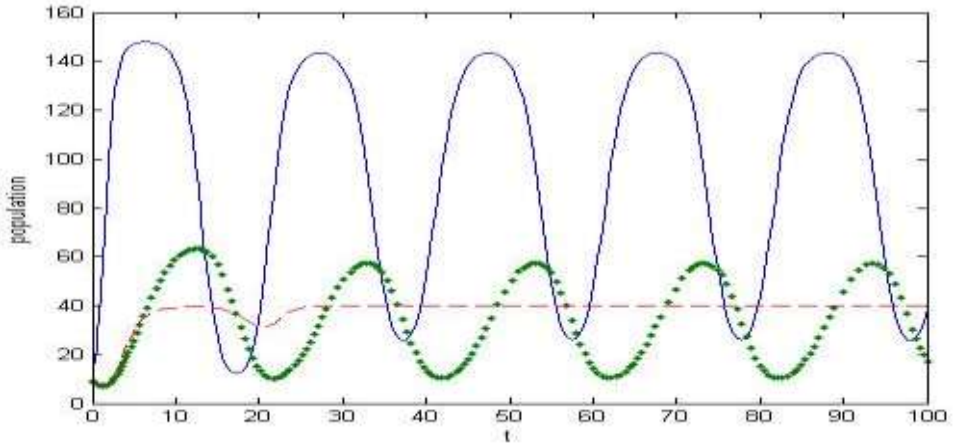

Figure 1.1

We observe that the three species populations oscillate in initial periods of time like in single predator-single prey model. Later population of B reaches maximum while A and N oscillate continuously. Thus in this case once B reaches maximum population the system changes to single predator-single prey type where

the predator A and prey N populations oscillate continuously. These oscillations are periodic and both have same amplitude. The population of B is effected by other two species initially, but later it remains constant.

Case 1.2

F

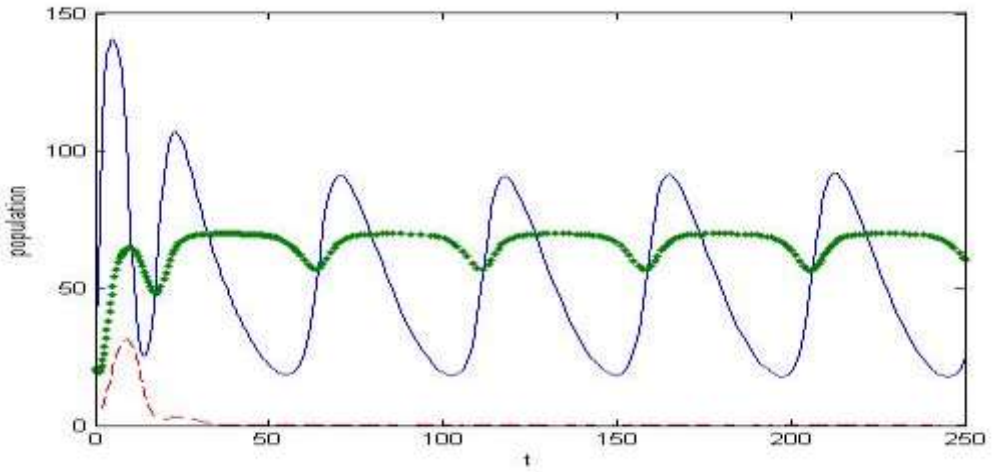

Figure 2.2

Here too all three species populations oscillate initially. However B is observed to be get extinct after some time. A and N oscillate continuously as system has become single predator-single prey type. This is the case which explains the extinct of the species. It is observable from the table that the only change made from case 1 is initial values of A, B, N

Case 1.3

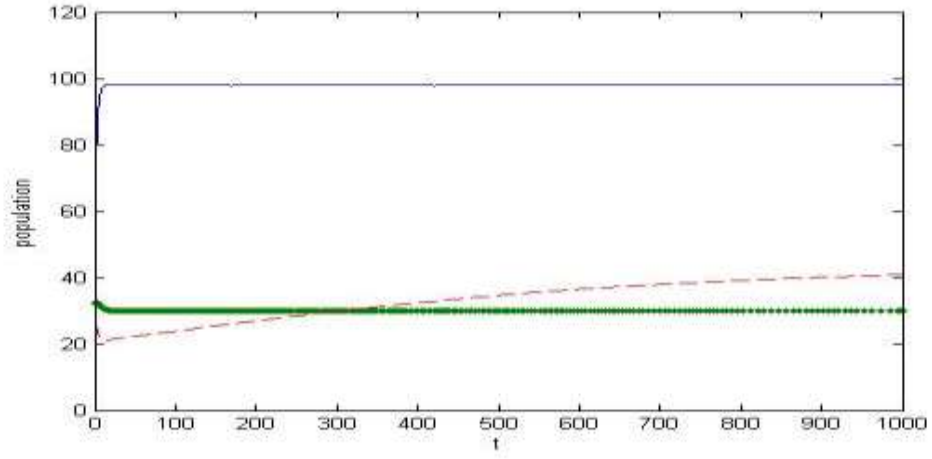

Figure 1.3

In this case we observe the population of the three species goes to their respective maximum. When A and N reach their maximum population during initial periods B takes longer time to reach its maximum population. Oscillations of population of species are not observed in this case. This kind of situation is generally possible when the initial values of the species are close to maximum population of them respectively.

Case1.4

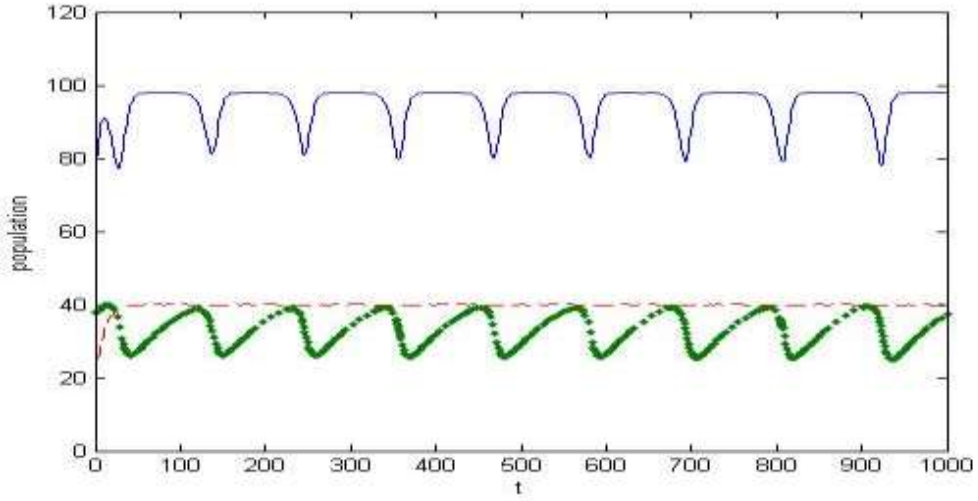

Figure 1.4

This is also similar to case 1. The only difference from that is B reaches maximum value while A and N population oscillate with amplitude equal to maximum population of the respective species.

Case 1.5

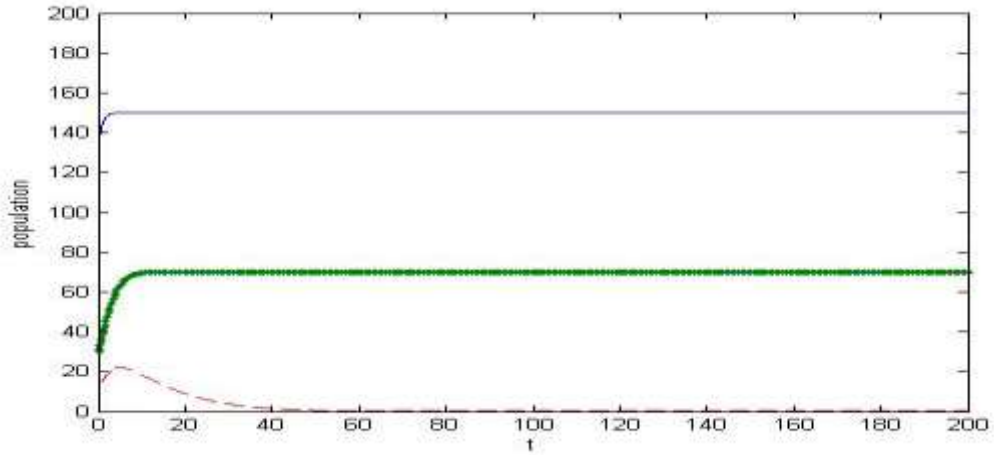

Figure 1.5

Here B gets extinct while other two species reaches their respective maximum population.

SYSTEM TYPE 2. A Predates On N While B Predates On N and A.

Model equations

Model equations describing the population dynamics of the three species are given as:

$$\frac{dN}{dt} = \left(r - p_A A - p_B B\right) N \left(1 - \frac{N}{K_N}\right) \quad \text{.....(5)}$$

$$\frac{dA}{dt} = \left(g_A N - p_b B - d_A\right) A\left(1 - \frac{A}{K_A}\right) \quad \text{.....(6)}$$

$$\frac{dB}{dt} = \left(g_B N + g_b A - d_B\right) B\left(1 - \frac{B}{K_B}\right) \quad \text{.....(7)}$$

The constants defined are same as mentioned in eq(4) ,(5),(6) . The new constants defined here are g_b which represent growth rate of B due to A. p_b represent the predation rate of B on A.

Here too different fixed values for model constants are taken equations are solved numerically using MATLAB. Then graphs are obtained describing the dynamics of population of them. Four different cases were observed here.

Table 2

Parameters	**Case 2.1**	**Case 2.2**	**Case 2.3**	**Case 2.4**
r	2	2	2	3
p_A	0.03	0.03	0.03	0.03
p_b	0.032	0.032	0.01	0.01
p_B	0.025	0.025	0.025	0.025
g_A	0.008	0.008	0.008	0.009
g_b	0.003	0.003	0.003	0.003
g_B	0.004	0.004	0.004	0.004
d_A	0.3	0.3	0.29	0.3
d_B	0.6	0.6	0.44	0.5
K_A	80	50	60	60
K_B	100	100	100	45
K_N	150	200	150	100
A_0	35	25	15	40
B_0	22	30	10	25
N_0	65	65	50	65

Here the four different cases represent four different possibilities of dynamics of populations of three species with respect to each other. Here too solid line in graphs represent population of N while that of A and B are represented by dotted and dashed lines respectively.

Case 2.1

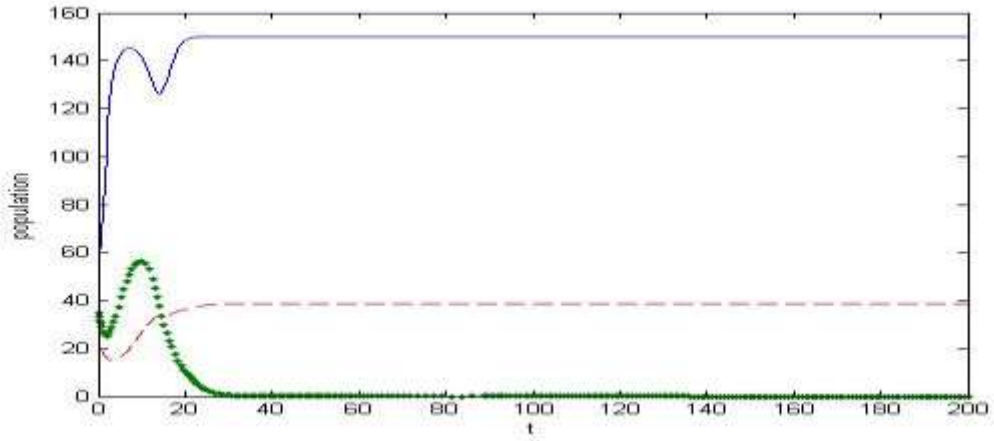

Figure 2.1

As from graph it can be observed that A gets extinct out while other two species remain constant. While N remains constant at its maximum population, population of B remains constant at lower value compared to its maximum population.

Case 2.2

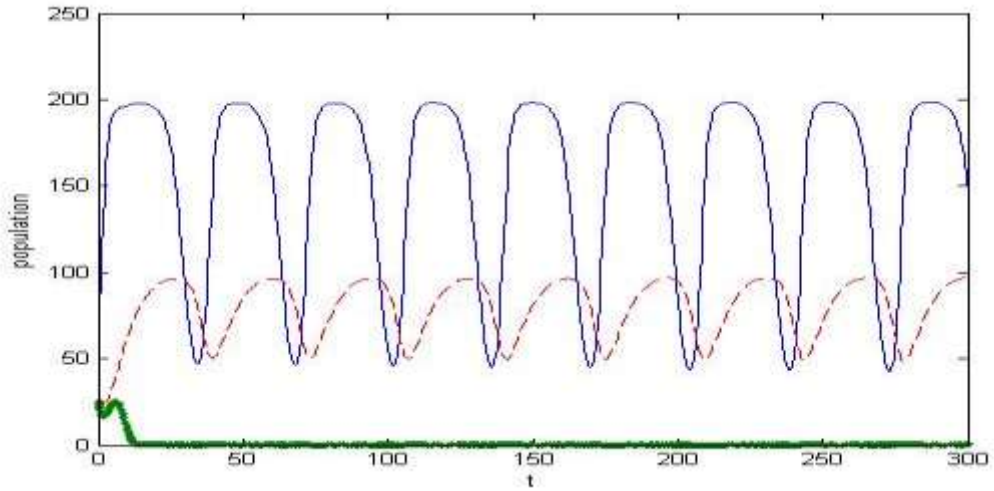

Figure 2.2

Here too it is observed that A gets extinct out while N and B populations curve oscillates periodically. While in case 1 N and B remain constant over time here their populations change periodically.

Case 2.3

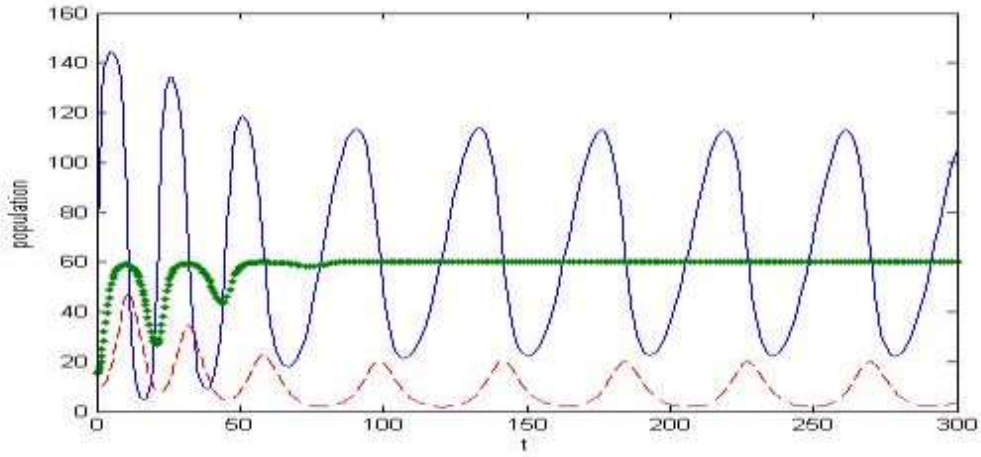

Figure 2.3

Here population curves of three species oscillate initially. Later N and B populations change periodically while population of A becomes constant at its maximum population.

Case 2.4

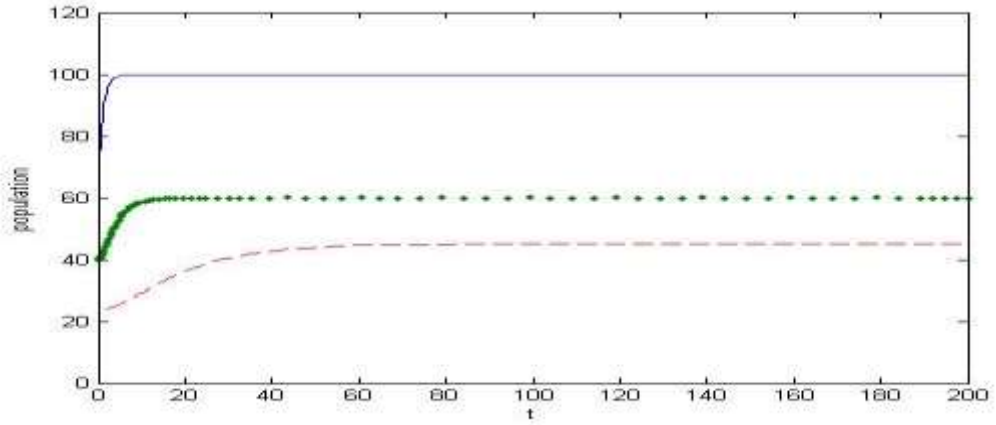

Figure 2.4

Here all the three species populations were observed to reach maximum and then become constant.

2. DISCUSSION AND CONCLUSION

Thus using the model equations and solving them numerically by using some random fixed values for model constants and varying the initial population values we were able to get different types of dynamics of populations of three species. There can be some more types of dynamics possible but the intention of this paper to focus on the dynamics where the three species coexist or where one of the species specifically a predator gets extinct out. Considering system type 1 it was observed that in Case(1.1),Case(1.2), Case(1.4) B gets extinct out or its population remains constant after reaching its maximum while other two species population oscillate periodically . Thus in these cases after certain period of time when population of B gets extinct or remains constant, system of three species changes to system of two species like a

single predator –single prey system. Dynamics of populations of the two species follow similar to Lotka-Volterra single predator single prey model. In Case(1.3) the three species population grow to their respective maximum in logistic manner and remain constant thereafter. In Case(1.5) however B gets extinct out while other two species grow logistically to their respective maximum.

Considering system type 2 it was observed that in Case (2.2) and Case(2.3) population of N and B oscillate periodically while population of A gets extinct out or remains constant after reaching maximum. Thus here too 3 species system is converted to two species system after certain period. In Case (2.4) it was observed that population of the species grow in logistic manner and all three species attain their respective maximum population.

Initial population values of the species and their respective maximum populations determine the pattern of dynamics of population of them for given fixed model constants. Some of the constants were however slightly changed to obtain a better plot of curves. Using this model for both system types coexistence of the three species was successfully explained. Other cases were also explainable like extinction of a species.

3. ACKNOWLEDGEMENTS

I B.Sai Krishna hereby thankful to University Grants Commission for giving support by funding. I am also thankful to Professor, Principal and other Academic persons.

4. REFERENCES

[1] George Seifert ,A Lotka –Volterra Predator Prey system involving two predators,Methods and Applications of Analysis, 2(2) 1995,pp,248-255.
[2] Global Properties of three –dimensional Predator-Prey Lotka-Volterra systems, A.Korobeincov, G.C.Wake, Journal of Applied mathematics and Decision Sciences ,3(2) 1999 , pp,155-162.
[3] A Lotka –Volterra three species food chain , Erica Chauvet, Joseph E. Paullet, Joseph E. Previte, Zack Walls, Mathematical Magazine , vol 75 , NO.4,October 2002, Page 243-255.
[4] Dynamics of species in a model with two predators and one prey, Ta Viet Ton, Nguyen Trong Hieu ,Non Linear Analysis, 74(2011) , 4868-4881.
[5] On stoichiometric two predators on one prey discrete model, Xinyuan Liao,Shengfan Zhou, Zigen Ouyang, Applied Mathematics Letters, 20(2007), 272-278.

BENS107

The Fine Structure and Phylogeny of Minutocellus Sp. (Penatae, Cymatosiraceae) from China Sea

WANG Chunyan[a,c], KANG KyoungHo[b], Zhou Wei[a], SUI Zhenghong[a,*]
[a]**Key Laboratory of Marine Genetics and Breeding Ministry of Education**, Ocean University of China, Qingdao 266003, China
E-mail address: suizhengh@ouc.edu.cn

[b]**Department of Aquaculture**, Chonnam National University, Yeosu 550-749, Korea

[c]**Putian Marine and Fishery Environmental Monitoring Station**, Putian Marine and Fishery Bureau, Putian 351100, Fujian Province, China

ABSTRACT

In the present paper, a new nanoplanktonic diatom was isolated and classified by using scanning electron microscopy (SEM), transmission electron microscopy (TEM) and molecular biological techniques. The cells were elliptical or near elliptical from valve view under TEM observations with the length of 2.2~7.0μm and width of 2.1~4.4μm. A protuberant structure alike a short funnel could be seen. The cells were cylindrical from side view under SEM, and from the girdle view the oriented drapes was displayed regularly. There was no pili structure on the cell valve. A tubular process was elongated from one side of the valve. Two to three clustered tubules was on the fringe of the cell valve. The valve were rich in stria, normally 50 within 10 μm, which was covered by pseudoseptum with 2~6 perforation on it. The new isolate was ascribed to *Minutocellus* Halse, Von Stosch et Syvertsen (Penatae, Cymatosiraceae) according to their characterized structure revealed by light microscope and electron microscope observations and molecular biological analysis data. It was morphological similar to but still different from *M. polymorphus*. Due to absent of more information both from morphology and molecular biology, further taxonomic attribution of the new isolate was inappropriate. It was suggested that the new isolated nano-diatom was either a variety of *M. polymorphus* or a new species of *Minutocellus* Hasle, Von Stosch et Syvertsen. This is the first report of the fine structure of the species of this genus.

Keywords: 18SrDNA, *Minutocellus* sp., SEM, taxonomy, TEM.

1. INTRODUCTION

Nanoplankton has been defined as a class of planktonic organism with the size between 2 and 20 μm, including photosynthetic and non-photosynthetic organisms [1], and is predominated by eukaryotic protists [2]. Studies of size classes within the plankton by a variety of analytical and observational techniques have led to a realization of the importance of nanoplankton in the microbial food web. The smaller nanoplankton (less than 10 pm; principally microflagellates) are frequently found to dominate phytoplankton assemblages both numerically and by biomass [3,4,5,6,7,8]. Similarly, this size fraction of the phytoplankton often accounts for most of the primary productivity [8,9,10,11,12,13]. In addition, nanoplankton is also important

live feed source for aquaculture.

However, despite of much knowledge on its significant contributions on primary productivity and marine ecosystem, fine structure describing on nanoplankton species are limited due to sampling methods used before which will normally discard most of the plankton within this size fraction.

Minutocellus Hasle, Von Stosch et Syvertsen belongs to Pennatae, Cymatosiraceae [14]. Till now, totally three species were recorded in the family as M. polymorphus, M. pseudopolymorphus and M. scriptus. M. polymorphus was illustrated as Bellerochea polymorphus by Hargraver and Guillard [15]. There were distribution reports of Minutocellus species around Japanese coastal sea [16], North Atlantic, Long Island of USA, Sargasso Sea and along the coastal region of Peru [17] . M. polymorphus and M. pseudopolymorphus were reported as red tide species [18]. Due to the highly sensitivity to heavy metal, M. polymorphus was suggested as sensitive indicators of environmental change and used in the assessment of risk and development of environmental regulations for metals [19]. However, there is no systematic and fine structural description for Minutocellus, and little information is available at present.

In the present paper, a new nanoplanktonic diatom was isolated and classified using SEM, TEM and molecular technique as a variety of M. polymorphus or a new species of Minutocellus (Minutocellus sp.). Fine structure of the species of this genus was first reported here.

2. MATERIALS AND METHODS

2.1 *Sample collection and isolation of algae*

Seawater sample was collected from North Yellow Sea, China (121.59925E and 38.0607000N) on October 22 th 2007, with the water temperature and salinity of 21℃ and 32 PSU, respectively. A volume of 200ml water sample was filtered by a mesh with the pore size about 25 μm to remove large particles and organisms. The filtrate were newly filtered onto a 3μm nucleopore filter and cultivated in F/2 enriched sea water medium at 21℃, with salinity of 33 PSU, and at constant photon irradiance of 37μmol photons m-2 s-1 with a day: night cycle of 12:12h. Algae were purified and clonally isolated by limiting dilution method usually exploited during preparation of monoclonal antibody. Cell dimensions were determined by measuring the length and width of 20 cells using an ocular micrometer under a light microscope. Cell numbers were determined by hemacytometer count.

2.2 *Electron microscopy*

Samples were prepared for examination using a Millipore vacuum filtration apparatus containing a 25mm diameter, 3 μm pore size polytetrafluoroethylene (PTFE) membrane (General Electric Osmonics, Minnetonka, MN). The material was first washed with 250 ml distilled water, re-suspended in 5ml distilled water and treated with sulphuric acid (H_2SO_4) in a boiling water bath for 20-30min. Then saturated potassium permanganate ($KMnO_4$) was added and maintained for 24h. Hydrogen Peroxide (H_2O_2) was added until the sample turned transparent. The sample was subsequently rinsed several times with distilled water. For transmission electron microscopy (TEM), a drop of liquid containing the rinsed frustules was placed on a

Formvar-coated copper grid (mesh size 100/200nm) and left to dry, the grids were examined under a JEOL-1010 microscope. For scanning electron microscopy (SEM), samples collected by centrifugation without acid-treatment were also prepared. Each drop was placed on a round glass cover slip, left to dry, and then adhered to a stub, under a JEOL-1010 microscope for observations.

2.3 *DNA extraction*

Approximately 20 ml of exponential phase were concentrated by gentle centrifugation, pelleted cells were frozen in liquid nitrogen. DNA was extracted using DNA extraction kit (Tiangen, China) following the instruction of the manufacturer's.

2.4 *PCR and Sequencing*

18SrDNA fragments were amplified via PCR using primers 5'-CCGTAGTAATTCTAGAGCTAATAC and 5'-AAACCTTGTTACGACTTCACC. ITS region were amplified via PCR using primers 5'-CGGTGAGGACTCGGGACTGT and 5'-CAGATTGAGTAA GACTACCCGCT .The amplification condition were as follow: pre-denaturing at 94℃ for 5 min, then denaturing at 94℃ for 1 min; annealing at 60℃ for 1 min; and extension at 72℃ for 2min.This cycle was repeated 30 times and followed by a final extension step at 72℃ for 5min. At last 5μl PCR product were used in agarose gel electrophoresis to check the success of the amplification. The products with expected length were recovered and cloned using pMD18T vector (TaKaRa, Japan) following the instruction of the manufacturer's. Clone with rightness inserted fragment was sent for commercial sequencing service at Huada Gene (Shanghai, China).

2.5 *Phylogenic analyses*

Blast searches (http://www.ncbi.nlm.nih.gov/BLAST) were performed on all obtained DNA sequences to verify its taxa attribution. The sequence was assembled and edited using Clustal version 1.83. 18SrDNA sequences from 14 species within bacillariophyta were selected to construct the phylogenic tree (Table 1).

Table 1 18SrDNA sequences information analyzed in this study

Species	Length /bp	Genbank accession number
Cf. Minutocellus sp.	1762	AY485520
Minutocellus polymorphus	1690	AY485478
Papiliocellulus elegans	1802	X85388
Stephanodiscus neoastraea	1764	DQ514906
Cyclostephanos sp.	1757	DQ514913
Thalassiosira guillardii	1756	DQ514869
Porosira pseudodelicatula	1712	AY485469
Odontella aurita	1761	EU818944
Odontella sinensis	1802	Y10570

Psammoneis pseudojaponica	1710	AB433339
Bellerochea malleus	1719	DQ514845
Plagiogramma atomus	1783	AB433338
Biddulphiopsis titiana	1752	AF525669
Attheya longicornis	1791	AY485450

Phylogenic and molecular evolutionary analyses were performed with two different tree-building methods: neighbor-joining (NJ) and minimum evolution (ME). Both of the two reconstructions were obtained using the program MEGA3.1. For both methods (NJ and ME), bootstrap analysis with 1000 replicates was used assess robustness of tree nodes, and the model of both the methods is Kimura 2-parameter.

3. RESULTS

3.1 *Light microscope (LM) observations*

The side view of cells under LM was rectangle or foursquare. They were mostly pelagic individually with the length of 2.2~7μm and width of 2.1~4.4μm. No cell chain structure was observed.

3.2 *Transmission electron microscope (TEM) observations*

The cells were elliptical or near elliptical from valve view under TEM observations (Figs. 1~6). The valve were rich in stria, which were round pseudo-pores with the diameter of 0.05~0.15μm. There were about 50 pseudo-pores within 10μm on the surface of cell valve, more than those reported [17]. Normally 2~6 perforation were observed on the pseudo septum (five perforation was displayed in Fig. 5). In both end of apical axis of the cell valve, protuberant structure alike a short funnel could be seen, named clustered tubules [17, 20] (Figs. 1 ~5). Sometimes, 3 clustered tubules were shown on the cell valve (Figs. 2 and 3). The center of the cell was characterized by electronic density substances (Fig. 6).

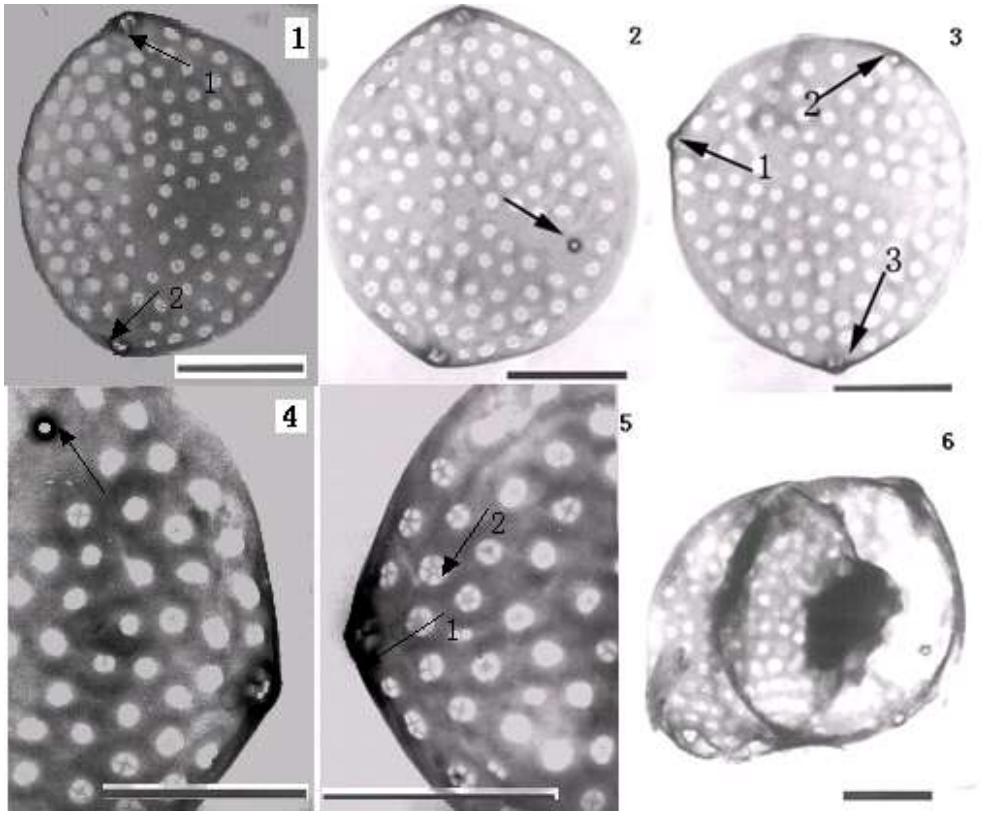

Figs 1-6 Transmission electron microscope (TEM) observation of *Minutocellus sp.*. Figs 1~3 showed valve view, arrows indicated clustered tubules; Fig. 4 and 5 showed details of clustered tubules, arrow in Fig. 4 and arrow 1 in Fig. 5 showed enlarged structure of clustered tubules, arrow 2 in Fig. 5 showed five perforation on the pseudoseptum; Fig. 6 showed TEM of the whole cell. Figs. 1-6, Bar =1μm

3.3 ***Scan electron microscope (SEM) observations***

The cells were cylindrical from side view under SEM. Valve view was still near elliptical. Two to three clustered tubules was on the fringe of the cell valve, with the in-radial about 0.07μm and out-radial of 0.13μm (Fig. 7). A tubular process [17,20] was shown on one of the valve (Fig. 8). Thickened valve on one side or in the center part was usually obtained (Figs. 9 and 10), which may be produced by cell fission. Regularly oriented drapes were displayed from girdle view (Figs. 7~13).

The sulphuric acid treatment was done to get rid of silicon substances to show the texture on the cell surface. According to different time length of sulphuric acid treatment, the elimination level of the surface silicon wall was different. If treated shorter, pseudo-pores with stria structure could be seen (Figs. 13 and 15). If treated longer, the pseudo septum will be destroyed and perforated (Fig. 14). The clustered tubules was also clearly disclosed under FESEM as constructed by 2 to 4 apertures with a thicken fringe (Figs. 16 and 17).

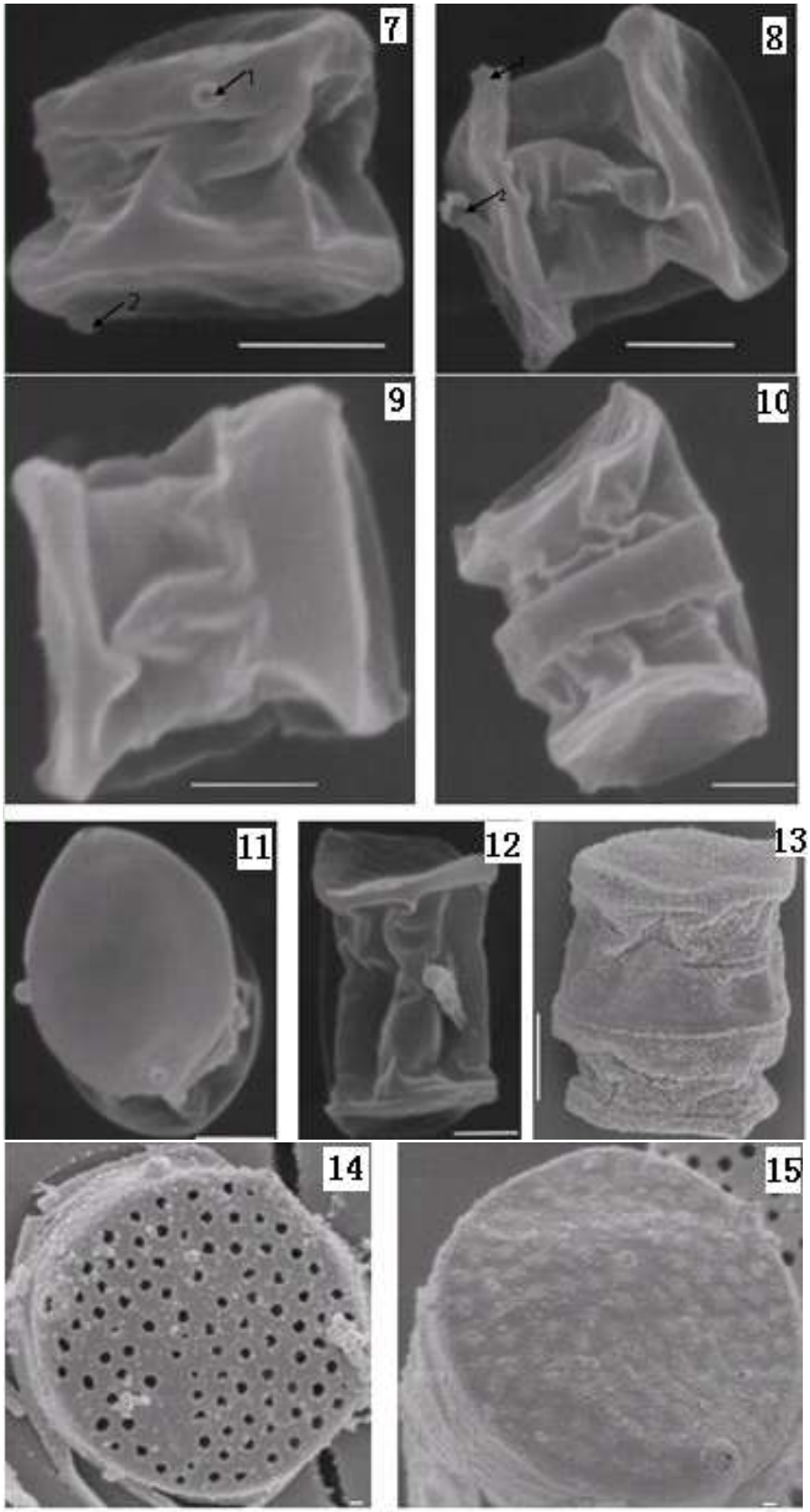
7
8
9
10
11
12
13
14
15

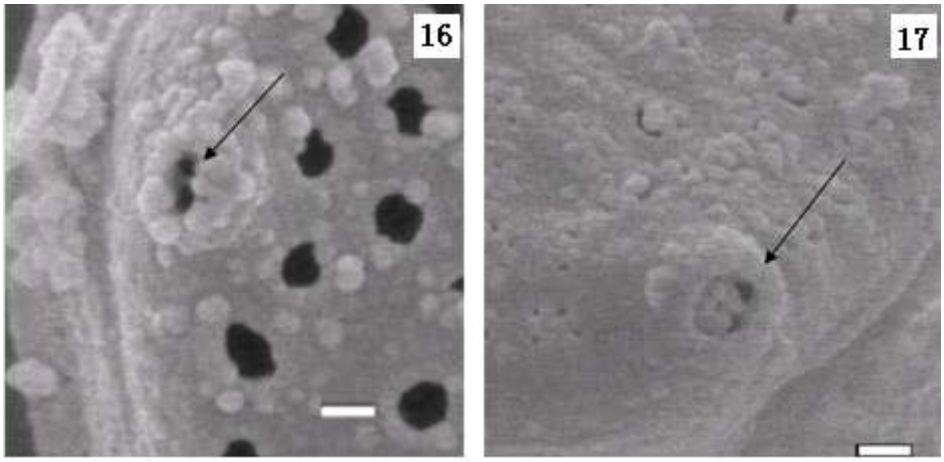

Figs. 7-17 Scan electron microscope (SEM) observations of *Minutocellus sp.* Figs. 7~12 showed various views of *Minutocellus sp* under SEM, arrows in 7 and arrow 1 in 8 indicated clustered tubules and arrow 2 in 8 indicated tubular process; Figs. 13~17 showed cell surface structure after sulphuric acid treatment under Field Emission Scanning Electron Microscope（FESEM）, Fig. 14 and 15 showed valve view after sulphuric acid treatment with different time length, Fig. 16 and 17 showed the details of clustered tubules (Arrows indicated). Bar: Figs. 7~13=1μm; Figs. 14~17=100nm.

3.4 *Phylogenic analyses*

We have jointed the 18SrDNA sequences and the ITS rDNA sequence , and the sequence accession number in GenBank is GQ245763.The genetic distance based on 18S rDNA sequences between the newly isolate and 14 diatom species was 0~0.071 (Tab. 2). There was no genetic distance between the new isolate and M. polymorphus. The genetic distance between the new isolate and Papiliocellulus elegans is 0.020, while those between this isolate and other diatom species were relative larger, from 0.060 to 0.071. The relationship reflected by two phylogram trees was basically accord, with the new isolate closely related to Minutocellus species (Figs. 18 and 19). It was concluded that the new isolate belonged to Minutocellus Halse, Von Stosch et Syvertsen.

Table 2 Genetic distance between 14 representative species of diatoms and *Minutocellus sp.* based on 18SrDNA sequence

Species	1	2	3	4	5	6	7	8	9	10	11	12	13	14
Cf. Minutocellus sp.														
Minutocellus polymorphus	0.000													
Minutocellus sp.	0.000	0.000												
Papiliocellulus elegans	0.020	0.020	0.020											
Stephanodiscus neoastraea	0.069	0.069	0.069	0.069										
Cyclostephanos sp.	0.071	0.071	0.071	0.071	0.001									
Thalassiosira guillardii	0.065	0.065	0.065	0.063	0.027	0.028								
Porosira pseudodelicatula	0.065	0.065	0.065	0.058	0.056	0.058	0.046							
Odontella aurita	0.073	0.073	0.073	0.067	0.089	0.090	0.086	0.075						
Odontella sinensis	0.068	0.068	0.068	0.067	0.071	0.073	0.072	0.069	0.069					
Psammoneis pseudojaponica	0.071	0.071	0.071	0.074	0.093	0.093	0.077	0.077	0.097	0.082				
Bellerochea malleus	0.071	0.071	0.071	0.072	0.094	0.094	0.079	0.075	0.094	0.080	0.010			
Plagiogramma atomus	0.076	0.076	0.076	0.078	0.091	0.091	0.079	0.078	0.096	0.081	0.028	0.025		
Biddulphiopsis titiana	0.060	0.060	0.060	0.051	0.074	0.076	0.061	0.060	0.080	0.059	0.064	0.062	0.066	
Attheya longicornis	0.069	0.069	0.069	0.067	0.078	0.080	0.072	0.066	0.088	0.075	0.074	0.073	0.071	0.065

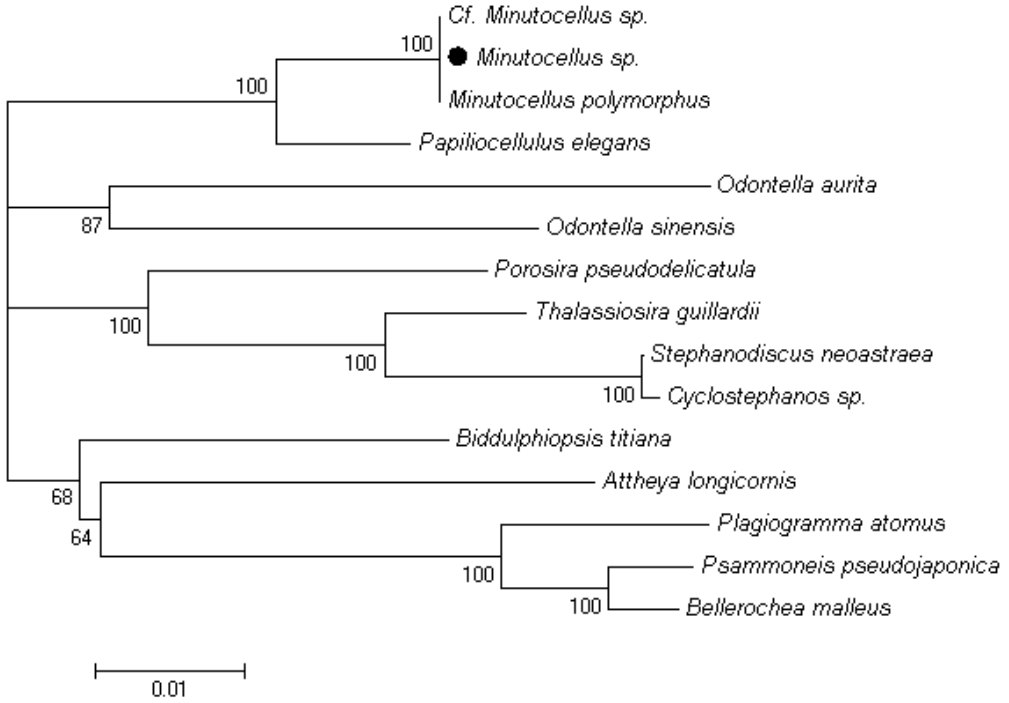

Figure 18 Phylogram NJ tree based on 18Sr DNA sequences of 14 species within bacillariophyta and *Minutocellus sp.* It was produced using the program MEGA3.1. Bootstrap analysis with 1000 replicates was used assess robustness of tree nodes. Model: Kimura 2-parameter. ●shows *Minutocellus sp.*

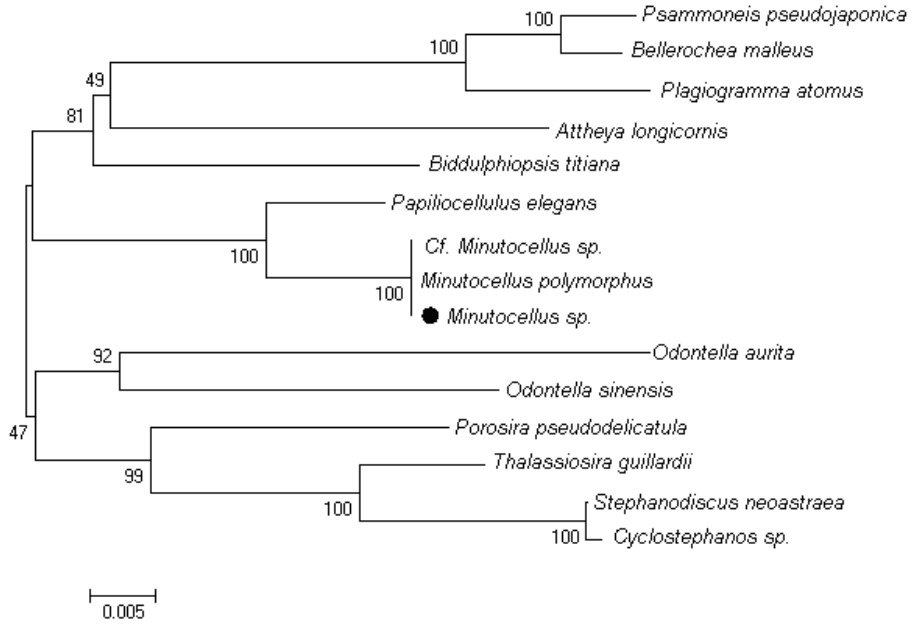

Figure 19 Phylogram ME tree based on 18Sr DNA sequences of 14 species within bacillariophyta and *Minutocellus sp.* It was produced using the program MEGA3.1. Bootstrap analysis with 1000 replicates was used assess robustness of tree nodes. Model: Kimura 2-parameter. ●shows *Minutocellus sp.*

4. DISCUSSIONS

Living species belonging to the Cymatosiraceae were observed in detail by Hasle et al [14], who reported that tubular process and the present of a pseudo septum were main characteristics of *Minutocellus* Halse, Von Stosch et Syvertsen. The study provided details description of the new isolate as revealed by SEM and TEM techniques. Based on the morphological similar between the new isolate and *Minutocellus* species, especially from the similar cell surface textures, the new isolate was ascribed to *Minutocellus* Halse, Von Stosch et Syvertsen [14,17, 21, 22]. However, compared with the structural data of *Minutocellus* species obtained till now, the new isolate was different from anyone. *M. scriptus* is bigger than *Minutocellus* sp. and *M. polymorphus* with the cell size more than 10 μm (Fig. 22). *M. polymorphus* displays flat tri-dimensional structure (Fig. 21), is contrary to *Minutocellus* sp. with cylindrical one (Figs. 7~13). The valve view of the new isolate is elliptical or near elliptical, while those of *M. polymorphus* is sometime navicular (Fig. 21). In addition, there are cater-corner elongated pili in *M. polymorphus* and *M. scriptus* (Figs. 21 and 22), no such structure were detected in the new isolate either under light microscope or under EM.

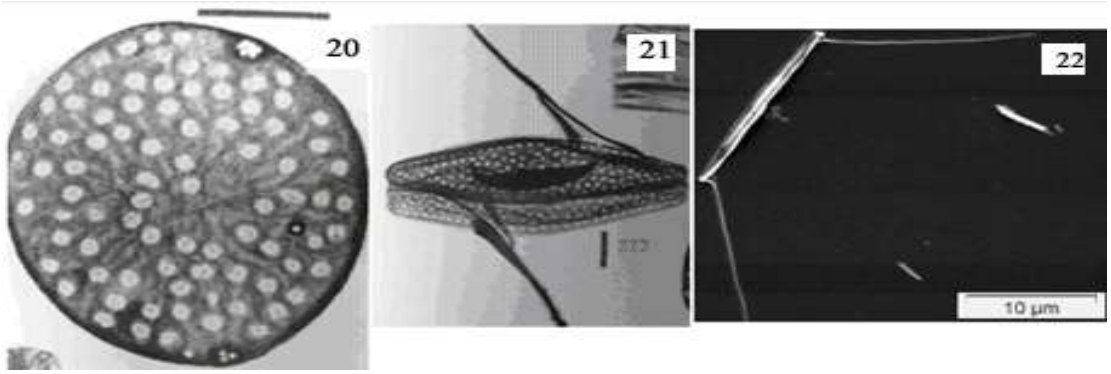

Figs 20-22 EM observations of reported *Minutocellu* species
Figs 20 and 21 showed valve view of *Minutocellus polymorphus* under TEM [17]; Fig. 22 showed SEM of *Minutocellus scriptu* (from http://www.ifremer.fr/crela/recherche/equipes_de_recherche/ateliers_transversaux/plateau_microscopie/pages_species_photos/centric_diatoms/Minutocellus_scriptus.htm)
Figs 20, 21 Bar= 1 μm; Fig. 22 Bar=10 μm.

The new isolate has the similar surface stria structure to *M. polymorphus*, however more than *M. polymorphu* in number (Fig. 2 and Fig. 20). It is not clear as if the number of stria will be also one of the taxonomic evidence, or if the number of stria will change according to certain environment factor or cell life stages. On the other hand, the fine structural description of *Minutocellus* Hasle, Von Stosch et Syvertsen species was scarce at present.

Molecular biological data of 18SrDNA sequence analysis also confirmed that the new isolate belonged to *Minutocellus* Halse, Von Stosch et Syvertsen [14]. However, due to shortage of ITS sequence information of *Minutocellus* species deposited in Genbank database, further attribution of the isolate to species level is impossible at present.

5. ACKNOWLEDGMENT

The work was supported by the grant from National Marine Survey Project of China (908-01-ST02) and 'The Twelfth Five-Year-Plan' in National Science and Technology For the Rural Development in China (2012AA100811-3).

6. REFERENCES

[1] Sieburth J M, Smetacek V, Lenz J. Pelagic ecosystem structure: heterotrophic compartments of the plankton and their relationship to plankton size fractions. *Limnology and Oceanography*, 1978, 23: 1256-1263.
[2] Davisl P G, Caron D A, Johnson P W, Sieburth J M C N. Phototrophic and apochlorotic components of picoplankton and nanoplankton in the North Atlantic: geographic, vertical, seasonal and diel distributions. *Marine Ecology Progress Series*, 1985, 21: 15-26.
[3] Ballantine D. Comparison of the different methods of estimating nanoplankton. *Journal of Marine Biological Association of United Kingdom*, 1953, 32: 129-147.
[4] Beers J R, Reid F M H, Stewart G L. Microplankton of the North Pacific Central Gyre: population structure and abundance, June 1973. Int. Revue ges. *Hydrobiology*, 1975, 60: 607-638.
[5] Beers J R, Reid F M H, Stewart GL. Microplankton population structure in southern California nearshore waters in late spring. *Marine Biology*, 1980, 60: 209-226.
[6] Beers J R, Reid F M H, Stewart GL. Seasonal abundance of the microplankton population in the North Paclfic Central Gyre. *Deep Sea Reserch*, 1982, 29: 227-245.
[7] Booth B C, Lewin J, Norris RE. Nanoplankton species predominant in the subarctic Pacific in May and June 1978. *Deep Sea Reserch*, 1982, 29: 185-200.
[8] Hannah F J, Boney AD. Nanophytoplankton in the Firth of Clyde, Scotland: seasonal abundance, carbon fixation and species composition. *Journal of Experimental Marine Biology and Ecology*, 1983, 67: 105-147.
[9] Malone T C. The relative importance of net plankton and nanoplankton as primary producers in neritic and oceanic tropical waters. *Limnology and Oceanography*, 1971,16: 633-639.
[10] Mccarthy J J, Taylor W R, Loftus M E. Significance of nanoplankton in the Chesapeake Bay estuary and problems associated with the measurement of nanoplankton productivity. *Marine Biology*,1974, 24: 7-16.
[11] Platt T, Subba Rao D V, Irwin B. Photosynthesis of picoplankton in the oligotrophic ocean. *Nature*, 1983, 301: 702-704.
[12] Li W K W, Subba Rao DV, Harrison W G, Smith J C, Cullen J J, Irwin B, Platt T. Autotrophic picoplankton in the tropical ocean. *Science*, 1983, 219: 292-295.
[13] Seoane S, Laza A, Orive E. Monitoring phytoplankton assemblages in estuarine waters: the application of pigment analysis and microscopy to size-fractionated samples. *Estuarine, Coastal and Shelf Science*, 2006, 67: 343–354.
[14] Hasle G R, Von Stosch H A, Syvertsen E E. Cymatosiraceae, a new diatom family. *Bacillaria*, 1983, 6: 9-156.
[15] Hargraver P E, Guillard R R L. Structural and physiological observations on some small marine diatoms. *Phycologia*, 1974, 13(2): 163-172.

[16] Takano H. A new diatom from sand-flats in Mikawa Bay. Japan. *Bulletin of Tokai Regional Fisheries Research Laboratory No. 115*, 1985, pp29-37.
[17] Cheng Zhaodi, Gao Yahui, Liu Shicheng. *Nano-diatom along coastal of Fujian Province*, Ocean Press, Beijing, 1993.
[18] Richardson K. Harmful or Exceptional Phytoplankton Blooms in the Marine Ecosystem. *Advances in Marine Biology*, 1997, 31: 301-385.
[19] Levy J L, Stauber J L, Jolley D F. Sensitivity of marine microalgae to copper: The effect of biotic factors on copper adsorption and toxicity. *Science of The Total Environment*, 2007, 387(1-3): 141-154.
[21] Hasle G R, Syvertsen E E. Marine Diatoms. In: *Identifying marine diatoms and dinoflagellates* (Tomas, C.R. eds), Academic Press, 1996, pp. 5-385.
[20]Tomas C R, Hasle G R. Identifying marine diatoms and dinoflagellates. USA: Academic Press. 1997.
[22] Takano H. Diatoms. In: *Red tide organisms in Japan-An illustrated taxonomic guide*. (Fukuyo, F., et al., eds), Uchida Rokakuho, Tokyo, 1990, pp. 162-331.

BENS111

Total Phenolic Contents, Total Flavonoid Contents and in Vivo Anti-Angiogenic Properties of Blueberry Pomace Extracts

J. Vuthijumnonk

A. L. Molan, J. A. Heyes Institute of Food, Nutrition and Human Health, Massey University

ABSTRACT

By-products of blueberry juice processing (blueberry pomace) contain high amount of phenolic compounds which possess several health benefits such as protection against cancers, obesity, neurodegenerative diseases and heart diseases. Total phenolic content (TPC) of blueberry pomace extracts (BPE) of three rabbiteye blueberry genotypes (Maru, Rahi and Tifblue) were determined using Folin-Ciocalteu method. TPC value of Tifblue BPE was the highest among three tested genotypes at 4 mg gallic acid equivalent (GAE)/g frozen weight followed by Maru and Rahi at 3.97 and 3.40 mg GAE/ g frozen weight, respectively. Total flavonoid content (TFC) of the BPEs has been determined using aluminium chloride colorimetric assay. BPE of Tifblue genotype also showed the highest TFC value (1.10 mg catechin equivalent (CE)/ g frozen weight) followed by Maru (1.05 mg CE/ g frozen weight) and Rahi (0.88 mg CE/ g frozen weight).

Angiogenesis plays a key role for cancer growth and metastasis, therefore inhibition of blood vessel formation may result in lower rate of cancer metastasis. In the present study, BPEs were studied for their anti-angiogenic properties using chicken chorioallantoic membrane (CAM) assay. The number of blood vessels in a 0.25 cm^2 field of view was counted using Image J software then the percentage inhibition was calculated in comparison to control membranes treated with water only. The BPEs of three genotypes elicited anti-angiogenic properties when compared with control samples at a concentration of 1 g frozen weight/ml. BPE of Tifblue genotypes exhibited 66% inhibition of newly-formed blood vessels followed by Maru (61%) and Rahi (50%) in comparison with control CAMs treated with MilliQ water.

Interestingly, total phenolic content and total flavonoids content of three BPEs were strongly and positively correlated. While correlation does not equal cause, it seems likely that phenolic compounds especially flavonoids contribute to anti-angiogenic properties of blueberry fruits.

BSNS118

New Production of Haloketides by the Marine-Derived Fungus Aspergillus sp.

Alain S. Leutou, Keumja Yun, Byeng-Wha Son
Department of Chemistry, Pukyong National University, Nam-gu, Busan608-737, Korea
E-mail address: sonbw@pknu.ac.kr

ABSTRACT

Marine-derived microorganisms continue to attract attention as a rich source of structurally novel bioactive metabolites that are potential lead compounds for the development of new drugs.[1] When the marine-derived microorganisms were cultured under saline condition, they rarely produced interesting biological halogenated metabolites (e.g., salinosporamide A3 of a highly potent inhibitor of the 20S proteasome and its halogenated derivatives). [2] Encouraged by the detection of halogenated marine analogs, we manipulated the fermentation of *Aspergillus* sp. by the addition of halide salts in an effort to gain access to a wider cross-section of halogenated secondary metabolites. This presentation describes the production, isolation, and identification of brominated methyl dihydroxyphenylacetates as well as dihydroxyphenylacetic acid. We will also show the radical-scavenging activity of these compounds.

[1] Jensen, P. R., Fenical, W., "*Marine microorganisms and drug discovery: current status and future potential*", In "*Drugs from the Sea*", (ed Fusetani, N.) pp. 6–29 (Karger, Basel, 2000).

[2] Lam, K. S., Tsueng, G., McArthur, K. A., Mitchell, S. S., Potts, B. C. M., Xu, J., *J. Antibiot*., 2007, 60, 13-19.

BENS140

Pathogenicity of *Tomato leaf curl virus* (TYLCV) infectious clones agroinoculated into *Nicotiana benthamiana* and tomato plants

Sung Oh[a], Seongdae Kim[b], Nagarajan Vinod[c], Chang Won Choi[d,*], Young Shik Kim[e], Mun Haeng Lee[f]

[a]**Department of Biology & Medicinal Scienece, Pai Chai University**, Daejeon 302-735, Korea
5star@pcu.ac.kr

[b]**Department of Biology & Medicinal Scienece, Pai Chai University**, Daejeon 302-735, Korea
khboy111@pcu.ac.kr

[c]**Department of Biology & Medicinal Scienece, Pai Chai University**, Daejeon 302-735, Korea
biovinz@yahoo.com

[d]**Department of Biology & Medicinal Scienece, Pai Chai University**, Daejeon 302-735, Korea
choicw@pcu.ac.kr

[e]**Department of Plant Science & Technology, Sangmyung University**, Cheonan, Chungnam 330-720, Korea
advenia@empas.com

[f]**Tomato Experimental Station, Buyeo**, Chungnam, 323-814, Korea
dogue24@korea.kr

ABSTRACT

Tomato yellow leaf curl virus (TYLCV)-Bus (accession number GQ141873), -Bos (accession number GU325634) and -Hwas (accession number GU126513), respectively, were isolated from tomato (*Solanum lycopersicum*) plants in Korea. TYLCV-Bus and -Bos belong to TYLCV group II (old Japan cluster), while TYLCV-Hwas belongs to group I (new Japan cluster) that was only reported in Japan, China and the New World. Their unit-lengths of DNA-A genome were amplified by polymerase chain reaction (PCR) and used to construct dimer genomes of each isolate using restriction enzyme digestion and ligation. The resulting constructs were cloned into binary vector pRI101-AN, respectively. To prove the infectivity of clones, each construct was transformed into *Agrobacterium tumefaciens* cells and agroinoculated into young leaves of *Nicotiana benthamiana* and tomato plants. In *N. benthamiana*, the plants inoculated with infectious clones, respectively, caused pronounced disease symptoms such as plant stunting, downward leaf curling and crinkling. To discriminate resistant, tolerant and susceptible tomato cultivars, each infectious clone was agroinoculated into some tomato cultivars carrying *Ty1*, *Ty2*, and/or *Ty3* resistant genes. Response of tomato plants were various from no symptom to severe plant

stunting and leaf yellowing, curling and crinkling. The virus concentration in each plant was determined by ELISA using TYLCV C4 protein-specific antibody in each sample. Symptom severity of tomato plants corresponded with the concentration of virus and the presence or absence of *Ty* gene in each tomato cultivar.

Keywords: *Tomato yellow leaf curl virus* (TYLCV), infectious clone, agroinoculation, symptom severity, tomato Ty gene

1. INTRODUCTION

Tomato yellow leaf curl virus (TYLCV) belongs to the Old World *Begomovirus* that consists of a single circular DNA molecule of 2.7 kb. TYLCV is transmitted by the whitefly *Bemisia tabaci* in a circulative manner, which causes severe losses in tomato (*Solanum lycopersicum*) yield worldwide. Recently, tomato (*Solanum lycopersicum*)-infecting begomoviruses are epidemic nationwide in Korea. TYLCV has been present in Korea since 2007 and cause annual epidemics of disease in tomato crops [1, 2]. In a previous study, we grouped five Korean TYLCV isolates into three clusters such as old Japan cluster, new Japan cluster and China cluster based on the phylogenetic analyses. These TYLCV isolates caused typical symptoms in tomato plants, such as small leaves with yellow margins, curling upward at the erected axillary shoots, and/or stunted appearance of plants with a bushy appearance when plants were infected at an early growth stage [1].

Use of resistant and/or tolerant tomato cultivars provides the most promising approach to control TYLCV disease. Resistance is considered one host factor preventing virus infection, while tolerance is another host factor allowing virus to spread systemically but developing milder symptom than highly susceptible cultivars. There has been significant progress in the development of markers for numerous TYLCV resistance genes. The first gene, *Ty1*, which originated from *S. chilense* (Dunal), was mapped near a molecular marker on tomato chromosome 6 [3]. A second TYLCV resistance gene, *Ty2*, which originated from *S. habrochaites*, was mapped on tomato chromosome 11 [4]. A third TYLCV resistance gene, *Ty3*, was identified on the chromosome 6 of *S. chilense* lines [5]. Unlike *Ty1* and *Ty2*, which are effective against only monopartite TYLCV, *Ty3* is effective against TYLCV and a bipartite begomovirus. In addition, *Ty1* and *Ty2* genes express complete or nearly complete dominance, while *Ty3* is more additive [5]. Recently, *Ty4* was mapped on chromosome 3 of tomato and this gene with *Ty3* showed the highest level of resistance in recombinant inbred lines [6].

To estimate the resistance, tolerance and susceptibility levels of a tomato cultivar against TYLCV infection, several parameters were developed based on the ratio of infected plants, virus titer and symptom severity. However, the lack of good methods to evaluate plant resistance/tolerance is a limiting factor in tomato breeding strategy. Although diagnostic tools are available for its detection in plants, suitable tools for estimating viral loads in plants are needed to compare tomato cultivars.

To investigate the infectivity of Korean TYLCV isolates, infectious clones of TYLCV-Bus (accession number GQ141873), -Bos (accession number GU325634) and -Hwas (accession number GU126513) were constructed respectively, and

agroinoculated into *Nicotiana benthamiana*. Regardless of clones, they showed a systemic infection with symptoms and viral replication in plants. Therefore, *Agrobacterium* containing pRI-TYLCV-Bus was selected to inoculate into 8 commercial tomato cultivars in Korea. To estimate the degree of resistance and tolerance of plants to virus infection, symptom severity of plants and virus titer and were used as parameters. To quantify the virus titer, enzyme linked immuno-sorbent assay (ELISA) was performed with tomato plants agro-inoculated with pRI-TYLCV-Bus clone.

2. RESULTS AND DISCUSSION

2.1. Vector construction

A full-length genome of TYLCV-Bus, -Bos and -Hwas cloned into a pGEM-T Easy vector in our previous study, which were used as a primary template in this study. Firstly, the full-length genome (1mer) was amplified using a set of genome-specific primers.

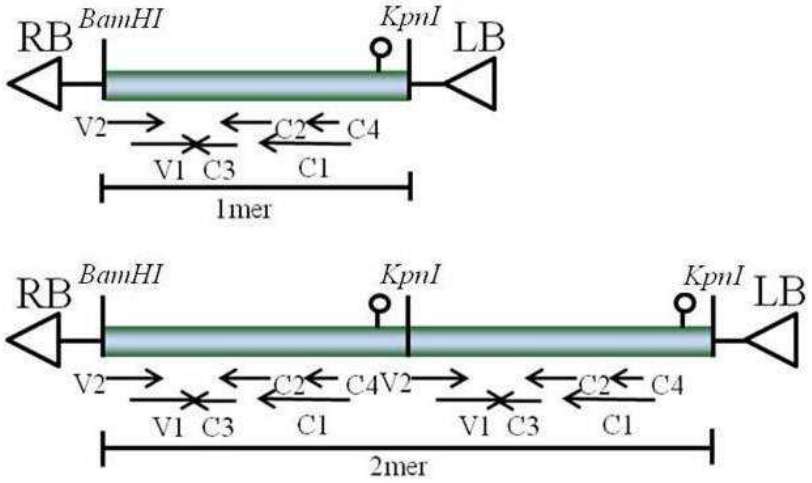

Fig. 1. Construction of infectious clone of TYLCV. The open circles indicate the stem-loop-forming region. The arrows represent predicted open reading frames in both orientations (**v** for viral sense and **c** for complementary sense). The restriction enzyme sites used for cloning. Constructs are monomer (1mer, top) and dimer (2mer, bottom) of TYLCV genome.

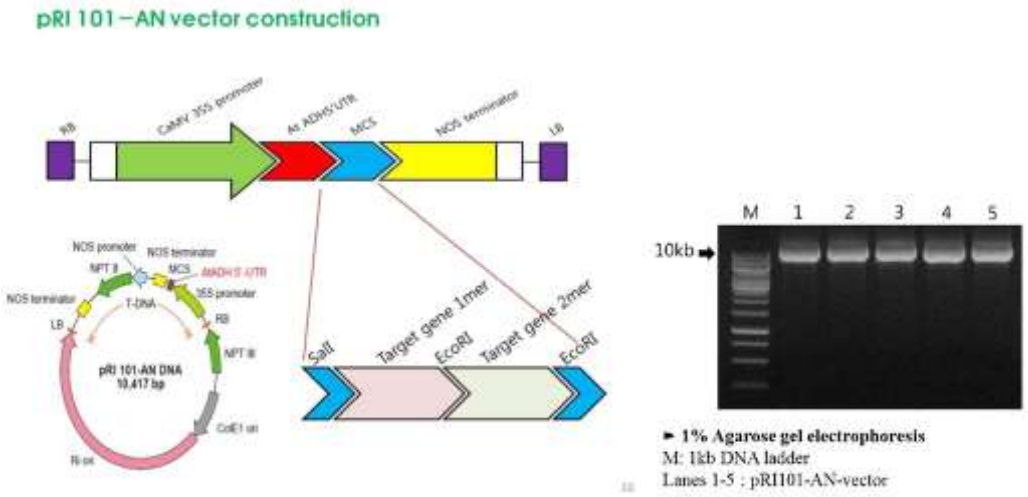

Fig. 2. Ligation of the insert (dimer of TYLCV genome) into pRI101-AN (right).

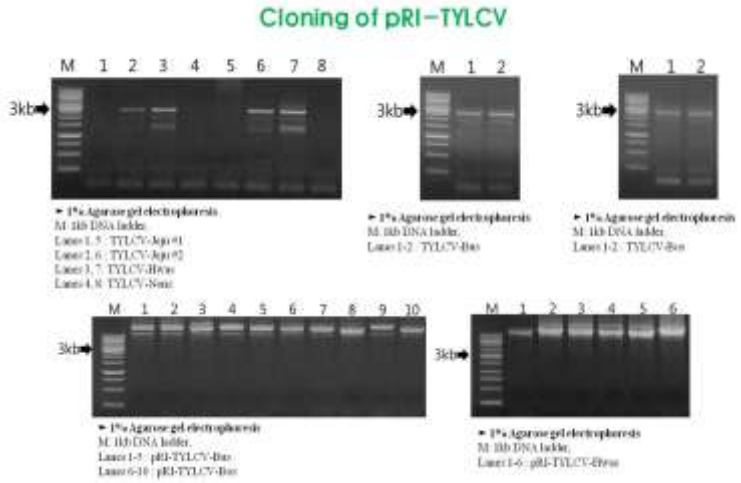

Fig. 3. Top: PCR amplification of TYLCV genomes (monomer). Bottom: The amplified products were double-digested with *Sal*I and *Eco*RI, respectively and cloned into pRI101-AN vector (Takara, Japan) which was digested with same restriction enzymes. The resulting vector was named pRI-TYLCV-Bus 1mer, pRI-TYLCV-Bos 1mer and pRI-TYLCV-Hwas 1mer.

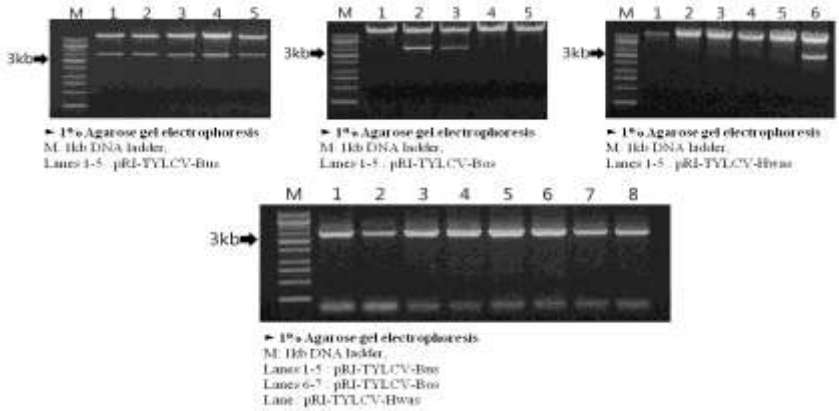

Fig. 4. The presence and orientation of the insert in pRI-TYLCV-Bus 1mer, pRI-TYLCV-Bos 1mer and pRI-TYLCV-Hwas 1mer, respectively, were confirmed by the restriction enzyme digestion with *Sal*I and *Eco*RI (top) and PCR amplification

using the genome-specific primer pairs (bottom).

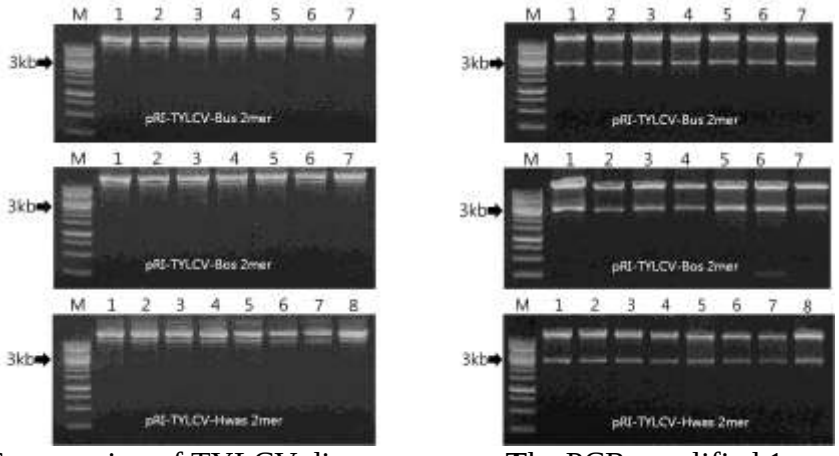

Fig. 5. Construction of TYLCV dimer genome. **T**he PCR-amplified 1mer product digested with *EcoR*I that was ligated with *EcoR*I-digested pRI-TYLCV-Bus 1mer, pRI-TYLCV-Bos 1mer and pRI-TYLCV-Hwas 1mer, respectively, to make two copies of TYLCV genome in a vector. The resulting vectors were named as pRI-TYLCV-Bus-2mer, pRI-TYLCV-Bos 2mer and pRI-TYLCV-Hwas 2mer.

2.2. Infectivity of TYLCV clones using agroinofiltration into *N. benthamiana*

To confirm that pRI-TYLCV-Bus, pRI-TYLCV-Bos and pRI-TYLCV-Hwas can be infectious, *Agrobacterium* containing three clones, respectively, were infiltrated into lower leaves of *N. benthamiana* using a needleless syringe. Test plants were monitored for symptom development at weekly intervals and symptoms were recorded. Plants were assayed for the presence of TYLCV DNA using V1 gene-specific primers in PCR at 35 days post-infiltration (dpi).

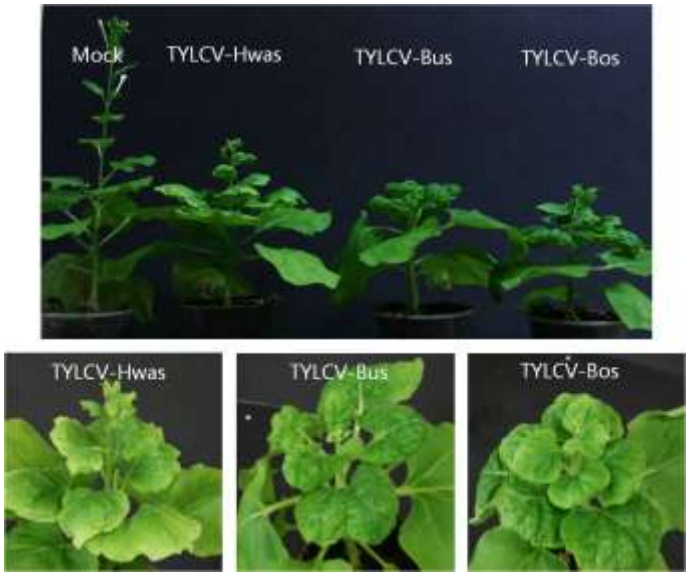

Fig. 6. Symptom development in *Nicotiana benthamiana* inoculated with Agrobacterium harboring pRI-TYLCV-Bus-2mer, pRI-TYLCV-Bos 2mer and pRI-TYLCV-Hwas 2mer, respectively, in 5 weeks after infiltration.

2.3. Tomato accessions, agroinoculation, and symptom rating

Seeds of 8 commercial tomato cultivars were obtained (Table 1). These included plants with different sized and shaped fruits and exhibited different levels of viral resistance, ranging from fully susceptible to resistant. The TYLCV resistant, tolerant or susceptible tomato genotypes were screened for resistance to TYLCV infectious clone under glasshouse conditions. Tomato seeds were sown in nursery pots and transplanted (spacing of 2 x 3 feet) into plastic containers filled with soil and compost, which were kept in an insect-proof glasshouse. Ten-day-old tomato seedlings were inoculated with cloned viral DNA by the agroinfiltration method using needless syringe. The inoculated plants of each cultivar were compared with their respective control of mock inoculated plants (exposed to infiltration buffer) of the same cultivar in terms of monitoring symptom development and virus accumulation in the inoculated plants. Plants were visually examined for development of disease symptoms up to 10 weeks post-inoculation. Symptom development was evaluated according to the symptom severity scale as follows: 0 = no visible symptoms, inoculated plants show same growth and development as noninoculated plants; 1 = very slight yellowing of leaflet margins on apical leaf; 2 = some yellowing and minor curling of leaflet ends; 3 = a wide range of leaf yellowing, curling and crinkling, with some reduction in size, yet plants continue to develop; and 4 = very severe plant stunting and yellowing, pronounced leaf cupping and curling, crinkling and plant growth stops. Plants with no symptoms were also collected. Leaf samples were collected from tomato plants exhibiting at least one of the foliar symptoms of TYLCD, namely, yellowing, leaf curling or reduced leaf size.

Table 1. Reaction of commercial tomato cultivars inoculated with TYLCV-Bus clone at 10 weeks pdi.

Cultivar (Type)	Origin / Source	Infection[1]	Severity[2]				Ty gene[3]		
			1	2	3	4	*Ty1*	*Ty2*	*Ty3*
TY Miracle (cherry)	Sky Seed, Korea	16/16	0	4	4	8	nd	nd	nd
Dotaerang (globe)	Takii, Japan	16/16	9	7	0	0	*ty1ty1*	*ty2ty2*	*ty3ty3*
Hoyong (globe)	Sakata Korea, Japan	11/11	3	0	2	6	*ty1ty1*	*ty2ty2*	*ty3ty3*
Keri TY (globe)	Sunseed, Korea	4/16	4	0	0	0	*Ty1ty1*	*ty2ty2*	*ty3ty3*
Pinkie107 (globe)	Konong Seed, Korea	12/12	3	9	0	0	*ty1ty1*	*ty2ty2*	*ty3ty3*
Pinkie127 (globe)	Konong Seed, Korea	9/12	0	0	0	9	*ty1ty1*	*ty2ty2*	*ty3ty3*
Ruby King (cherry)	Bunong Seed, Korea	0/16	0	0	0	0	*ty1ty1*	*Ty2ty2*	*ty3ty3*
Gold sugar	Bunong Seed, Korea	15/16	2	4	3	6	nd	nd	nd

(plum)

[1]symptomatic plants / inoculated plants
[2]Rating was scored in symptomatic plants
[3]Ty genes were determined by Tomato Experimental Station in Korea (nd: not determined).

2.4. ELISA

Total proteins were extracted from the most upper 3 leaves which were selected from 3 tomato plants, using PBS buffer (20 mM phosphate, 150 mM NaCl, pH 7.4) containing 1.5% SDS , and adjusted to 1 μg/μl with coating buffer (35 mM $NaHCO_3$, 15 mM Na_2CO_3, pH 9.6). Each dilution was added in triplicates to the coating wells (100 μl per well) in the ELISA plate, and incubated at 4˚C overnight. Total proteins (1 μg/μl) extracted from healthy plants were used as a negative control. The wells were washed five times with PBS containing 0.05% (w/v) Tween 20 (PBST) and blocked with 200 μl of 1% (w/v) BSA in PBS for 2 h at 37˚C. After saturation, 100 μl of polyclonal IgG (1:1000 dilution in PBS, v/v) purified from rat antiserum against *Escherichia coli* expressed recombinant C4 protein, was used as a primary antibody. After 2 h incubation, the multiwell plates were washed five times with PBST and incubated at 37°C for 2 h in the presence of 100 μl per well of goat anti-rat IgG alkaline phosphatase conjugate (Sigma) at 1:20,000 dilution in PBS containing 1% BSA. The wells were washed five times with PBST, after which 100 μl of substrate solution (alkaline phosphatase yellow liquid substrate system for ELISA, Sigma) was added and incubated for 30 min at room temperature in the dark. The optical density at 405 nm (OD_{405}) was measured using a Model iMark Microplate Reader (Bio-Rad, USA). The sample was considered to be positive when its absorbance value was three times greater than that of the negative control. The quantity of antigens in the sample, respectively, was determined by comparing its absorbance with that of standard curve that was made by suitable dilution of purified recombinant TYLCV-C4 protein.

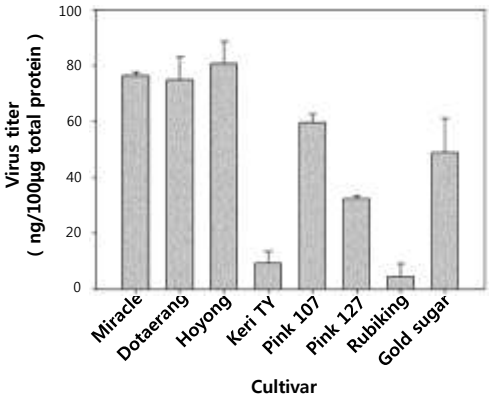

Fig. 7. TYLCV concentration in commercial tomato cultivars inoculated with TYLCV infectious clone was probed with antibody to recombinant TYLCV C4 protein in ELISA.

There were substantial differences in viral C4 protein accumulation among the different cultivars tested. In essence, the correlation between resistance level and viral

protein accumulation held true for the resistant cultivars as well. Cultivars of Kery TY and Rubyking carrying *Ty1ty1* and *Ty2ty2*, respectively, showed the lowest level of viral C4 protein. Therefore, these two lines exhibited the highest level of resistance.

2.5 Acknowledgments

This study was supported by Basic Science Research Program through the National Research Foundation of Korea (NRF) funded by the Ministry of Education, Science and Technology (2010-0009984).

3. REFERENCES

[1] Kim S H, Oh S, Oh T-K, Park J S, Kim S C, Kim S H, Kim Y S, Hong J K, Sim S-Y, Park K S, Lee H G, Kim K J, Choi C W. Genetic diversity of tomato-infecting *Tomato yellow leaf curl virus* (TYLCV) isolates in Korea. *Virus Genes*, 2011, 42, 117–127.

[2] Wang Y, Ji J, Oh T-K, Oh S, Kim S H, Lee H J, Shim M Y, Kim S H, Kim I-S, Kim Y S, Choi C W. Occurrence of *Honeysuckle yellow vein virus* (HYVV) containing a monopartite DNA-A genome in Korea. *Eur. J. Plant Pathol*., 2011, 129, 361–370.

[3] Zamir D, Ekstein-Michelson I, Zakay Y, Navot N, Zeidan M, Sarfatti M, Eshed Y, Harel E, Pleban T, Van-Oss H, Kedar N, Rabinowitch H D, Czosnek H. Mapping and introgression of a *Tomato yellow leaf curl virus* tolerance gene, TY-1. *Theor. Appl. Genet*. 1994, 88, 141-146.

[4] Ji Y, Scott J W, Hanson P, Graham E, Maxwell D P. Sources of resistance, inheritance, and location of genetic loci conferring resistance to members of the tomato-infecting begomoviruses. In *Tomato yellow leaf curl virus disease: Management, molecular biology, breeding for resistance*, (Czosnek H ed.), Dordrecht, Netherlands: Kluwer, 2007, pp 343–362.

[5] Ji Y, Schuster D J, Scott J W. Ty-3, a begomovirus resistance locus near the *Tomato yellow leaf curl virus* resistance locus *Ty-1* on chromosome 6 of tomato. *Mol. Breed*., 2007, 20, 271–284.

[6] Ji Y, Scott J W, Schuster D J. Molecular mapping of *Ty-4*, a new Tomato yellow leaf curl virus resistance locus on chromosome 3 of tomato. *J. Amer. Hort. Sci*., 2009, 134, 281-288.

BENS151

Pistacia Chinensis Inhibits NO Production via PI-3K/Akt Pathway in LPS-Activated RAW264.7 Cells

Man Hee Rhee, Hyun Dong Ji

Laboratory of Veterinary Physiology and Cell Signaling College of Veterinary Medicine and Stem Cell Research Therapeutic Institute, Kyungpook National University, Daegu 702-701, Republic of Korea

ABSTRACT

Pistacia chinensis has been used for various purposes in China including as an understock for grafting Pistacia vera. However, little attention was given to its health promoting effects. Therefore, in this study, we investigated the effect of Pistacia chinensis methanolic extract (PCME) containing resorcinol class of phenolic lipids on pro-inflammatory mediators and heme oxygenase-1(HO-1) in lipopolysaccharide stimulated RAW264.7 cells.

Nitric oxide (NO), MTT assay (cytotoxicity test), Real time PCR (gene expression) and western blot (protein expression) were employed in PCME treated or untreated RAW264.7 cells.

While PCME (2.5–10 μg/ml) inhibited mRNA expressions of inducible nitric oxide synthase (iNOS), cyclooxygenase 2 (COX-2), tumor necrosis factor (TNF)-α, interleukin (IL)-1β, and IL-6, it up-regulated HO-1 expression. Likewise, PCME inhibited iNOS protein expression, but not COX-2, and reduced nitric oxide (NO) release. Moreover, Phosphorylated c-Jun N-terminal Kinase (JNK) was attenuated dose-dependently in PCME pre-treated RAW264.7 cells. In addition, PCME up-regulated HO-1 protein expression was diminished by pre-treatment of PI-3K inhibitor. Furthermore, nuclear factor erythroid 2 related factor 2 (Nrf 2) repressor was attenuated time-dependently during PCME treatment.

Our study showed (for the first time) that PCME inhibited NO production and up-regulated HO-1 induction via PI-3K/Akt pathway, suggesting the role of Pistacia chinensis as potential sources of anti-inflammatory and antioxidant natural compounds.

REFERENCES

Tomaino, A., M. Martorana, T. Arcoraci, D. Monteleone, C. Giovinazzo and A. Saija. Antioxidant activity and phenolic profile of pistachio (Pistacia vera L., variety Bronte) seeds and skins. Biochimie 92: 1115–1122, 2010

Giudice, A., C. Arra and M.C. Turco. Review of molecular mechanisms involved in the activation of the Nrf2–ARE signaling pathway by chemopreventive agents. Methods Mol. Biol. 647: 37–74, 2010.

BENS170

In Vitro Bioaccessibility Assessment of Lycopene in Raw Tomato and Tomato Sauce With and Without the Addition of Olive Oil

Ahmad R. Allafi
Department of Family Sciences, College for Women, Kuwait University, P.O.Box: 5969, Safat 13060, Kuwait.
E-mail address: ahmadallafi@yahoo.com

EXTENDED ABSTRACT

Carotenoids exhibit diverse metabolic effects and diets rich in carotenoids are associated with reduced risk of chronic diseases. An antioxidant carotenoid, lycopene, found in the reddish fruits and vegetables including tomatoes, watermelon, pink grape fruit, guava and papaya, is implicated for anti-carcinogenic properties and curative efficacies in cardiovascular diseases, neurological disorders, hypertension, osteoporosis, male infertility and many other complications.

An important component of the Kuwaiti diet is the consumption of a traditional tomato sauce which is prepared by cooking fresh tomatoes, olive oil, garlic, salt and spices on medium heat. No studies, so far, have investigated lycopene bioaccessibility of tomato sauce and, therefore, the present study investigates lycopene bioaccessibility in raw tomato and Kuwaiti tomato sauce (Daqous) with and without olive oil addition using an *in vitro* digestion model. *In vitro* digestion models simulate digestion process and helps in understanding the bioaccessibility of nutrients.

Intact, digestate and micellar fractions of both raw and tomato sauce were thawed and vortexed. For extraction, 2 ml of each sample were mixed with 0.7 ml of internal standard (1 µg β-apo-8'-carotenal in 100 ml methanol) in order to assess extraction loss and then each sample was extracted twice with 1 ml of hexane/ethanol/acetone (50:25:25) followed by centrifugation and separation of upper layer. Combinations of the two extracts from each sample were dried at room temperature in the presence of nitrogen stream and were frozen at −80^{o}C before HPLC analysis.

So far, the lowest lycopene contents among the micelles were observed in fresh tomato samples (2.5µg/g). Lycopene contents of tomato sauce were 10.2µg/g while the samples of sauce added with olive oil had 16.5µg/g lycopene.

Keyword: Lycopene, Tomato, Tomato Sauce, HPLC, Antioxidants

References

1. Bose KSC, Agarwal BK: Effect of lycopene from cooked tomatoes on serum antioxidant enzymes, lipid peroxidation rate and lipid profile in coronary heart disease. Singapore Med J 2007;48(5):415–420.
2. Gartner C, Stahl W, Sies H: Lycopene is more bioavailable from tomato paste than from fresh tomatoes. Am J Clin Nutr 1997;66:116–122.
3. Donaldson M S: Nutrition and cancer: A review of the evidence for an anti-cancer Diet. Nutr J 2004;3:19. doi:10.1186/1475-2891-3-19
4. Kong K, Khoo H, Prasad K N, Ismail A, Tan C, Rajab N F: Revealing the power of the natural red pigment lycopene. Molecules 2010;15:959–987.
5. Kim AY, Jeon S, Jeong Y, Park YB, Jung UJ, Choi M. Preventive Effects of Lycopene-Enriched Tomato Wine againstOxidative Stress in High Fat

Diet-Fed Rats. J Food Sci Nutr 2011;16: 95–103.
6. Hedges LJ, Lister CE: Nutritional attributes of tomatoes. Crop & Food Research 2005; Confidential Report No 1391, New Zealand Institute for Crop & Food Research Limited.
7. Chauhan K, Sharma S, Agarwal N, Chauhan B. Lycopene of tomato fame: Its role in health and disease. Int J Pharmaceut Sci Rev Res 2011;10(1):99-115.
8. Singh P, Goyal G K. Dietary lycopene: Its properties and anti-carcinogenic effects. Comp Rev Food Sci Food Safety 2008;7:255–270.
9. Fielding JM, Rowley KG, Cooper P, O'Dea K: Increases in plasma lycopene concentration after consumption of tomatoes cooked with olive oil. Asia Pac J Clin Nutr 2005;14(2):131–136.
10. Fish WW, Davis AR: The effects of frozen storage conditions on lycopene stability in watermelon tissue. J Agric Food Chem 2003;51:3582–3585.

BENS148

Differential Drug Response of E. Coli Biofilm against Gentamycin, Ciprofloxacin and Ofloxacin on Externally Implantable Devices

Preetam Verma, Vishnu Agarwal*
Faculty of Biotechnology, Department of Biotechnology, Motilal Nehru National Institute of Technology, Allahabad, 211004
E-mail address: Vishnu_agarwal02@rediffmail.com

ABSTRACT

Several types of infection caused by *Escherichia coli* (e.g.Urethral catheter, Biliary tract prosthesis, Biliary tract infection,Lithangiuria, Urinary tract infection andmanyother diseases) are associated with biofilm formation which leads to an inability to eradicate the infection due to its intrinsic nature to resist high levels of antibiotics. Biofilm related infection are major cause of conditions leading to morbidity and mortility. New drug formulation and therapies are ineffective to combat biofilm related infection specially to those which are related to device surfaces. The present study deals with biofilm related infection on four different market available externally implantable devices (EID) taking *E.coli* as model organism. Biofilm was formed by standard method on four different EIDs. Rubber catheter (RC), foleys catheter (FC), endotracheal tube (ETT), eternal feeding catheter (EFC) for 24 hrs 48 hrs and 72 hrs. It was found that maximum biofilm was developed on rubber catheter after 48 hrs. The efficacy of gentamycin, ofloxacin and ciprofloxacin against *E. coli* biofilm was checked on different device surfaces. It was found that minimum biofilm inhibitory concentration (MBIC) value for different drugs differs in case of all four selected indwelling devices. The rubber catheter showed highest value for MBIC (61 µg/ml for ciprofloxacin). The atomic force microscopy (AFM) study demonstrated morphological differences among device surfaces. The study concludes that different quantity of biofilm and its response to antibiotics vary with indwelling devices and MBIC values are not correlated with biofilm formation or its minimum inhibitory concentration (MIC) value.

Keywords: Biofilms, externally implantable devices, minimum inhibitory concentration, minimum biofilm inhibitory concentration

BENS246

Salt stress-related Function of *pdsA* Gene in *Aspergillus nidulans*

Dong Soo Park, Pil Jae Maeng*
Department of Microbiology, School of Bioscience & Biotechnology, Chungnam National University

ABSTRACT

Aspergillus nidulans is a homothallic ascomycete which has been used as a model system for molecular genetic studies due to its versatile life cycle, its amenability to genetic manipulation, and the open availability of its genome sequence. It is also a reference for basic studies in fungal morphogenesis and gene regulation. Asexual differentiation is a common mode of reproduction for avariety of filamentous fungi. During asexual development, conidiophores, multicellular structures containing several types of differentiated cells, such as foot cells, stalk cells, vesicles, metulae and philalides are formed from the vegetative mycelia that acquired developmental competence. Several hundred genes are involved in the process of asexual development yielding developmental structures, however, only a limited number of these genes have been functionally identified and characterized to date.

In the previous studies, we have analyzed the microarrays of *A.nidulans* genome in time-course manner from vegetative stage to asexual development by statistical analysis, and selected 51 putative transcription factors. The array revealed stage-dependent expression of distinct sets of genes which were hierarchically clustered into groups with respect to their expression profiles over the time course of vegetative growth and asexual differentiation.

pdsA, one of the 51 genes encoding putative transcription factors. In this study, I present the identification and characterization of *pdsA* and demonstrate that correlation of *pdsA* gene with salt tolerance. Deletion of *pdsA* resulted in delay of asexual reproduction and partial fluffy phenotype, elevated of salt resistance.

Possible roles of the vacuole and channel in osmoadaptation. vesicles are Ions and nutrients Trafficking towards the apical tip plays a key role in the Asexual development and hyphal growth. and vacuoles roles of efflux of extra ions and nutrients, proteins degradation. From these observation, I observated that *pdsA* knock-out mutant was enlarged the vacuole in salt stress conditions. I propose that *pdsA* is probably a regulator for salt tolerance.